A. C. Hoffmann
L. E. Stein

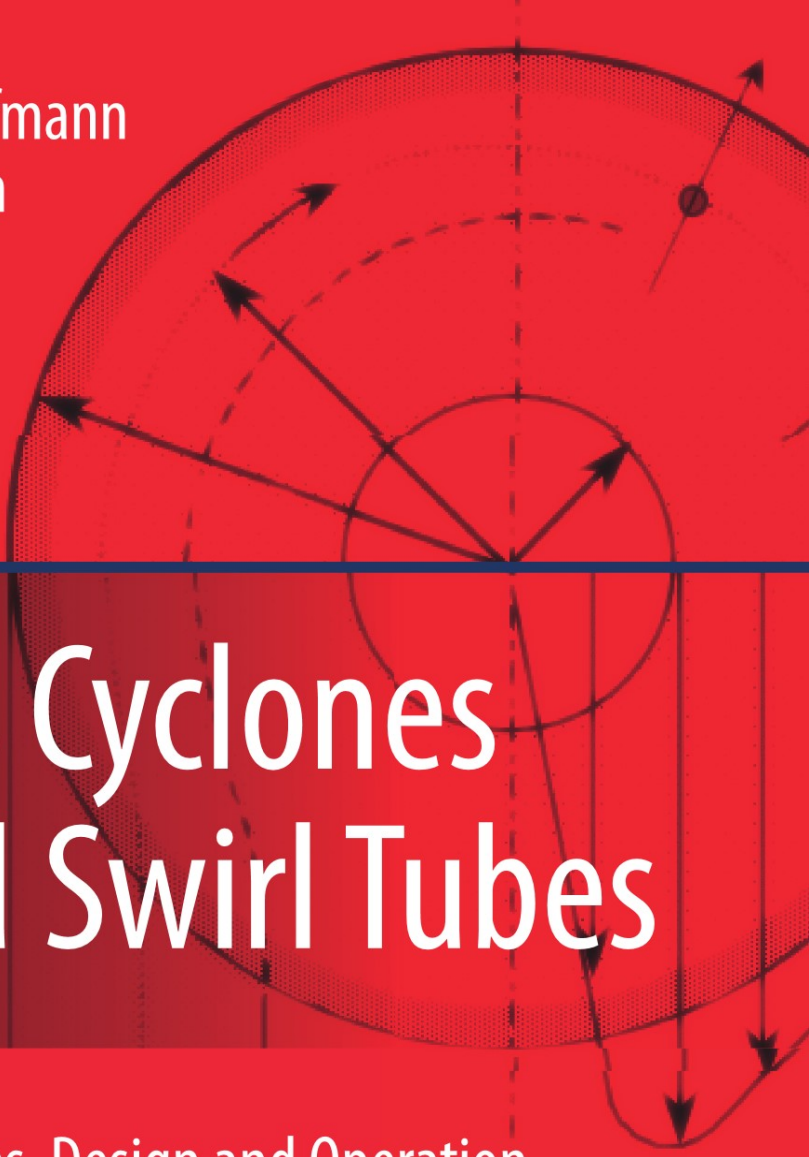

Gas Cyclones and Swirl Tubes

Principles, Design and Operation

Second Edition

Springer

Alex C. Hoffmann · Louis E. Stein

Gas Cyclones and Swirl Tubes

Alex C. Hoffmann · Louis E. Stein

Gas Cyclones and Swirl Tubes

Principles, Design and Operation

Second Edition

With 218 Figures and 14 Tables

Springer

Prof. Dr. Alex C. Hoffmann
University of Bergen
Dept. of Physics and Technology
Allegt 55
5007 Bergen
Norway
alex.hoffmann@ift.uib.no

Dr. Louis E. Stein
Process Engineering Consultant
Mechanical Separations
5818 Autumn Forest Dr.
Houston TX 77092
USA
lestein@swbell.net

Library of Congress Control Number: 2007934931

ISBN 978-3-540-74694-2 2nd Edition Springer Berlin Heidelberg New York
ISBN 978-3-540-43326-2 1st Edition Springer Berlin Heidelberg New York

Typesetting: Data supplied by the authors
Production: LE-TEX Jelonek, Schmidt & Vöckler GbR, Leipzig
Cover Design: eStudioCalamar S.L., F. Steinen-Broo, Girona, Spain

SPIN 12113378 60/3180/YL 5 4 3 2 1 0 Printed on acid-free paper

To our long-suffering families

Preface

This book has been conceived to provide guidance on the theory and design of cyclone systems. For those new to the topic, a cyclone is, in its most basic form, a stationary mechanical device that utilizes centrifugal force to separate solid or liquid particles from a carrier gas. Gas enters near the top via a tangential or vaned inlet, which gives rise to an axially descending spiral of gas and a centrifugal force field that causes the incoming particles to concentrate along, and spiral down, the inner walls of the separator. The thus-segregated particulate phase is allowed to exit out an underflow pipe while the gas phase constricts, and—in most separators—reverses its axial direction of flow and exits out a separate overflow pipe.

Cyclones are applied in both heavy and light industrial applications and may be designed as either classifiers or separators. Their applications are as plentiful as they are varied. Examples include their use in the separation or classification of powder coatings, plastic fines, sawdust, wood chips, sand, sintered/powdered metal, plastic and metal pellets, rock and mineral crushings, carbon fines, grain products, pulverized coal, chalk, coal and coal ash, catalyst and petroleum coke fines, mist entrained off of compressors and various processing units, and liquid components from scrubbing and drilling operations. They have even been applied to separate foam into its component gas and liquid phases in recent years.

This book strives to provide a long overdue overview of the state of the art in this specialized, albeit, important area of separation technology. Theory and design methods are presented covering the important classical topics, including particle cut-size, grade-efficiency, overall efficiency and pressure drop. In addition, many special topics are covered on basis of the authors experiences and interests. These include discussions and sections on a very wide variety of topics that, in one way or the other, relate to cyclone technology:

- particle characterization, motion, size distribution, sampling
- swirl flow and flow patterns
- important cyclone separation and pressure drop models

- static and dynamic pressure
- computational fluid dynamics
- vapour-liquid (demisting) and foam-breaking cyclones
- swirl-tube type cyclones
- wall roughness and solids loading effects
- model predictions and comparison with experiments
- dimensional analysis and scaling rules
- sampling and performance measurement
- in-leakage (up-flow) effects and hopper crossflow
- dipleg backup
- hopper venting
- forces acting on a flapper valve
- erosion and erosion protection methods
- particle settling in conveying lines
- high vacuum operation
- estimating feed drop sizes distribution
- non-uniform inlet flow distribution
- inlet, overflow and underflow geometries and configurations including inlet vane design
- cyclone length and the natural vortex length
- parallel and series arrangements and multiclones

A number of cyclone models of varying degree of complexity are given. The modeling approach instigated by Walter Barth, and further developed by Edgar Muschelknautz and co-workers to account for solids loading and wall roughness effects is given special treatment due to its overall practical usefulness.

Many drawings and photographs are included to help illustrate key concepts or interesting aspects. A number of worked example problems are included to help firm-up ideas presented in the textual discussions.

Even with today's modern tools, the complexity of cyclone behaviour is such that experimental studies are necessary if one is to truly understand the phenomena governing their behaviour. Thus, laboratory-scale studies are discussed on basis of the writers understanding and experiences in this central area.

For the researcher in gas cleaning and cyclone technology, the basic concepts underlying the working of centrifugal separators are set out, with references to literature where the topics are treated in more detail. Understanding the peculiarities of swirling flows and the basic description of fluid dynamics in rotation-symmetric coordinate systems is very much the key to appreciating the topic at hand. Other essential topics are elements of particle characterization and fluid-particle interaction. Although it is not possible to give the derivations of all the model equations in full, the basic reasoning behind each is discussed, and references are given to the original articles with full accounts of the derivations. Dimensional analysis is another key topic for understanding

cyclone technology and the basis for cyclone modeling and scaling. Computational fluid dynamics (CFD) simulations of the fluid and particle flows in cyclones has become a hot topic, and it has clear advantages for understanding the details of the flow in cyclones, but also limitations in terms of modelling cyclone separation performance accurately.

Obviously, the design of cyclone systems requires some expertise in many diverse areas of the physical sciences and engineering disciplines. For the benefit of the reader who works in either a manufacturing plant, a contractor or engineering-design firm, an engineering division of a company, or as an independent consultant, the book tries to go beyond the research or mathematical aspects of cyclone behaviour and to provide examples of how one designs, sizes and evaluates commercial-scale equipment. Those who have the responsibility to design, operate, evaluate, troubleshoot or modify cyclone systems must not only understand the theory and principles underlying their performance, but must also learn how to apply this understanding in a practical, cost- and time-effective manner. Because so many variables or factors govern the performance of cyclones, one must understand them well enough to know which variables are important and which are not, in any given situation. One must be able to see the whole picture and not be content, for example, with having developed a mathematical or computer model of cyclone behaviour.

The cyclone separator is one of the most efficient and most robust dust and mist collectors available for the cost. Its robustness is largely the result of its lack of moving parts and ability to withstand harsh operating environments. Cyclones can be fabricated from a wide variety of materials of construction including carbon steel, stainless steel and exotic alloys, or they may be made from castings. Some are molded in plastic or heat-formed from plastic sheets. Where conditions require they may be equipped with refractory, rubber, fluorocarbon, or specially hardened metal liners or electro- polished surfaces. Furthermore, cyclones are particularly well suited for high pressure applications and severe solids and liquid loadings, where filter media is sensitive to abrasion, sparks, oil, humidity, temperature, et cetera, and in applications wherein the separator must operate unattended for extended periods of time—up to several years in some refinery processing units. Nevertheless, things can and will go wrong. When they do, it tends to happen at the discipline or equipment interfaces. We are referring here to the fact that design, fabrication and installation work is often performed by isolated groups or by individuals and, unless all aspects or components of the system are examined from the standpoint of their impact on all other aspects or components, the system may fail to perform up to expectations. This applies to both the process and the mechanical aspects of their design. A simply spray nozzle, for example, can shut down a huge commercial operation if it fails to atomize the water, and a jet of water impacts an 800°C cyclone nearby. Because such things will happen, good communication and an appreciation of how the various components of the entire system interact will prevent most such problems.

Experience teaches that the more one understands and learns about cyclones, and the more performance and equipment experience one obtains, the more successful and confident one becomes in applying his or her knowledge in a laboratory or operating plant environment. And, with this understanding, some of the mystery surrounding these deceptively simple looking devices will vanish.

We recognize that the International System of Units (SI) has become the fundamental basis of scientific measurement worldwide and is used for everyday commerce in virtually every country except the United States. As painful as it may be for those of us who have learned and practiced the British or US Customary system of units, we feel that it is time to put aside the units of the industrial revolution and adopt the SI system of measurement in all aspects of modern engineering and science. For this reason, SI units have been adopted as the primary system of units throughout this book. However, it is recognized that US customary or British units are still widely used in the United States and some use of them is provided herein for the benefit of those who still relate closely to them. Dimensional constants specific to the British system, such as g_c, have been left out of the formulae.

In this book, we have tried to capture not only the state of the art pertaining to cyclone technology but to also capture and convey as much of our 55 cumulative years of experience as possible and, in some few cases, permissible. Still, there are areas where further research and analysis is required to fill the gaps in the checkerboard of our understanding. We hope this book will be a stepping-stone and an aid to all those who work with cyclones and who find them as useful and fascinating as we do.

Bergen and Houston,
April 2007

Alex C. Hoffmann
Louis E. Stein

Foreword to the First Edition

The cyclone is one of the most elegant pieces of engineering equipment—a triumph, one might say, of the particle technologist's art. Here is a device with no moving parts and virtually no maintenance which enables particles of micrometres in size to be separated from a gas moving at 15 m/s or so, and without excessive pressure-drop. It gets better: the harder you drive it (up to a point), the better the efficiency; the heavier the particle loading, the less the pressure drop. There can be few examples of engineering equipment that are so forgiving. It is for this reason that cyclones have become ubiquitous in processes. In catalytic cracking they are the main reason why the catalyst stays in the process. In power generation and innumerable manufacturing plants, they are the first line of defence of the environment. In air intakes to turbines on trains and helicopters[1] they are essential components. Even in the home they now enable vacuum cleaning without frequent bag cleaning.

Where did the principle come from and why do we design them as we do? The first design is probably lost in the mists of time. There are reports that the first Renault car factory, in late 19th century France, was equipped with an extraction system incorporating cyclones, but the idea must go back much further than that - probably to the flour milling industry. Their subsequent development is an interesting story of design evolution, with largely empirical optimisation studies being carried out simultaneously and apparently independently in the USA (Lapple, Leith and others), the UK (chiefly Stairmand), Japan (Iinoya and others) and the Eastern bloc countries. Seldom could it have been more clearly demonstrated that good engineering will converge on the same range of designs, wherever it is performed. Despite many attempts to improve on those basic general-purpose designs, they still represent the bulk of the industrial units installed today.

A full understanding of how the cyclone works and how individual particles behave within it has been slow in following these pioneering industrial devel-

[1] As discovered on President Carter's ill-fated rescue mission of the Iranian hostages in 1980.

opments. Little could be done until the invention of the measuring equipment necessary to measure fluid velocities within the cyclone (particularly laser Doppler anemometry - LDA), the assembly of theoretical models (largely in Germany, by Barth, Muschelknautz, Löffler and others), and ultimately the development of computational fluid dynamics (CFD) codes (pioneered by Swithenbank) which could accurately model swirling flows. Armed with these devices and techniques, it became clear that cyclones are in fact far from simple, and there is still much to know. At the same time, new uses have been found and new designs developed. Despite (or because of) its simplicity, the cyclone is not about to disappear.

It seems odd that there has not been before now an attempt to put together what is known empirically and theoretically about this most essential of separation devices. This book is both necessary and fascinating - a useful guide, complete with worked examples, for those attempting to design and use cyclones, and the first authoritative assembly of what is known both experimentally and theoretically for the benefit of those skilled in the art.

Jonathan Seville
University of Birmingham

Gas Cyclones and Swirl Tubes—Principles, Design and Operation is a valuable and necessary work in the field of gas cyclones. It will become a classic in this field because of the comprehensive manner in which it covers the study and usage of cyclones. In addition, this work provides unbiased presentations of the many theories used to describe and calculate the performance of cyclones, empirical methods of cyclone design, and the practical aspects of using cyclones.

Cyclones have the ability to provide for fine particle collection while arguably also providing for the most robust methods of construction and simplicity of design. If one is faced with a particle/gas separation application a cyclone should be the first technology examined. Low capital cost, low operating cost, and reliability are the reasons for this placement within the hierarchy of technologies that may be selected. Cyclones have been successfully used in industrial applications from the most common to the most severe, including highly erosive applications—a topic that this book discusses in some detail. Cyclones are routinely used in applications where the operating temperatures exceed 1000°C and in applications where the pressures may exceed 100 bar. Cyclones may be safely designed to handle highly explosive powders or py-

rophoric materials. They can be used to recover pharmaceuticals without the loss of expensive product due to contamination.

This then raises the question, why not use a cyclone for all particle-gas separation applications. The two cases where a cyclone may not be the correct choice are:

The engineering and data collection required to design a cyclone to meet the requirements of the application are too high, and

The cost of the cyclones required to meet the particulate collection requirements exceeds that of other technologies.

Although it is relatively simple to fabricate a cyclone for severe duty, it is not so simple to select the geometry and subsequently accurately predict the performance of a cyclone. As shown herein, predicting the particle collection performance of a cyclone also requires accurate particle size and loading data at the inlet of the proposed cyclone. While this may be worthwhile and feasible for a severe duty industrial application, it may not be for the operator of a small wood shop whose neighbors are complaining about the dust.

Cyclones may be designed to effectively remove virtually any size particulate from a gas stream. Several worked examples of this are presented herein. The barriers to cyclone usage for small particle collection are largely those of economics. Small cyclones are routinely used for particulate as small as .5 micron with 90% removal efficiency. Unfortunately, these small cyclones are not an attractive economical choice for many industrial applications. Conversely though, cyclones are now able to satisfy environmental and process requirements on particulate that is much finer than is commonly believed. With the advances in cyclone design that have begun in the late 20^{th} century cyclones are commonly used for emission control and product recovery on particulates with average particle sizes below 10 microns.

Gas Cyclones and Swirl Tubes–Principles, Design and Operation provides a valuable tool in the advancement of the design and usage of cyclones. The authors, a scientist and an industrialist, bring varied backgrounds and strengths to this work. The result is the most comprehensive work in the field of cyclones to date. Although it would be impossible to provide a complete treatise of all of the subjects covered, this work covers a wide array of the most critical, to a depth that allows the reader to understand the concepts and applications that are appropriate for designing or using a cyclone.

William L. Heumann
President and CEO, Fisher-Klosterman Inc.

Foreword to the Second Edition

Rarely does the technical community have the opportunity to learn from the accumulated efforts of a first-rate academic author of impeccable qualifications teamed with an also-academically qualified and broadly experienced practitioner, and where both individuals are natural teachers. Such an opportunity is available in this book. Comprehensive methods are presented, coupled with real-life examples gathered from the published literature and from the authors' own experiences in cyclone research and application. Those charged with responsibility for cyclone design or trouble-shooting will eagerly study and absorb this book's teachings—from theoretical basis to worked example problems.

For particles from a few microns upward, cyclones provide an attractive process alternative for particle separation from a fluid. Knockout pots are fine in applications where particle size is large, but for smaller sized particles, effective separation requires agglomerating or filtering the particles, or increasing the effective gravity force acting on them. Cyclones are often the preferred choice, as the authors show. While the physical principles of cyclone performance are intuitively clear, internal flow fields are quite involved. Rotational fields are coupled with secondary flow vortices and their interactions with particles, most often of varying size, density, or both. After separation, the solids must flow to a quiescent region away from the central vortex to avoid being re-entrained into the swirling fluid. There are virtually no standards of geometric proportion. Prediction of overall cyclone performance as a separation device has proven to be quite a challenge, and even overall pressure loss is not completely understood.

Professor Hoffmann and Dr. Stein have expanded by some hundred-plus pages the first edition of this book. Chapter 1 has an interesting section on the history of cyclones. An explanation of centrifugal force is given in Chapter 2. A beautifully clear explanation of the vortex equations is given in Chapter 3. Improved material on cyclone pressure drop in Chapter 4 is enhanced by better illustrations. Chapters 5 and 6 are virtually the same as in the earlier edition, but a new curve-fit is included useful for computerized cyclone

design, with emphasis on Muschelknautz' method. The computational fluid dynamics presentation in Chapter 7 is a welcome new segment, since flow profiles in a cyclone even without the complications of particles are inherently three-dimensional fields. Breakthrough work remains in coupling effective turbulence models to the small length scales associated with fine particles. Chapter 8 has a very useful applied section on scaling cyclone pressure loss and separation performance with Stokes, Euler, and Reynolds Numbers.

New material on the end-of-vortex phenomenon in reverse flow cyclones and swirl tubes is given in Chapter 9. Chapters 10 and 11 emphasize the importance of base-line performance of a new cyclone, tracer measurements, and post-separation problems including hopper design. Prudent advice is given regarding suggested focus on underflow mechanics when operational problems arise. Substantial changes were made in Chapter 12, with new material and illustrations added on erosion of the vortex finder's outer wall in view of recent CFD results, and use of wetted walls, sprays, and electrostatic fields in cyclones.

New sections and illustrations were added to Chapter 13 arising from the authors' recent research on re-entrainment of particles, and on wall film flow. Chapter 14 has an improved discussion of foams. Extensive additions to Chapter 15 include new material on vortex finder geometry and length, the design of inlet vanes, and rectifying vanes for pressure recovery. New material is included on design of the cyclone roof, and use of a pressure recovery diffuser chamber, along with experimental data illustrating its effectiveness. An appendix is added on construction of a vane cutout pattern. An expanded discussion is given in Chapter 16 on application of multiple cyclones nested together.

The changes included in this second edition show that cyclone technology is indeed still evolving. Those involved in cyclone design, operation and selection will welcome the effort put into the new material, and the authors' effectiveness in presenting the subject with enthusiasm and clarity, always with an eye on rigor.

Moye Wicks III
Consulting engineer, fluid flow phenomena

Acknowledgments

We wish to separately thank and acknowledge those who have inspired and helped us write this book:

I, Alex C. Hoffmann, wish to thank Professor John G. Yates of University College London, for introducing me to powder technology, and for many years of productive and very enjoyable collaboration, and Professor Ray W.K. Allen of Sheffield University and Professor Roland Clift of the University of Surrey for introducing me to cyclones and gas cleaning.

I, Louis E. Stein, wish to affectionately thank my former, and now deceased, Professors Frank L. Worley, Jr. and Frank M. Tiller who helped to establish the Chemical Engineering Department of the University of Houston, and engineering consultant, Dr. Moye Wicks, III, for teaching me through their own example the value of hard work, dedication to a cause and personal integrity. Perhaps unsuspecting on their part, they have been my most honored role models and inspiration these past 30 to 40 years.

Together we wish to also thank our friend and professional associate, Ir. Huub W. A. Dries of Shell Global Solutions International of the Royal Dutch/Shell Group for years of collaboration in the cyclone field, and for his expert review and suggestions on the draft copy of the first ediction of this book. Likewise, we wish to acknowledge and thank Mr. William L. Heumann, president and owner of Fisher-Klosterman, Inc. and Professor Jonathan P. K. Seville of the University of Birmingham, Editor-in-Chief of Powder Technology, for their kind and insightful views expressed in the two Forewords they wrote for this book. Valuable contributions were received from Dr. Hugh Blackburn of CSIRO Building Construction & Engineering, from Professors Steve Obermair and Gernot Staudinger of the Institute of Chemical Apparatus Design, Particle Technology and Combustion of the Technical University of Graz, and from Professor Emeritus Frederick A. Zenz, now of PEMM-Corp, New York.

Finally, we wish to express our appreciation and to dedicate this book to our dear wives and children: Doris, Travis, Courtney and Jennifer on Louis'

side; Gloria, Erik and Andrea on Alex's, who relinquished an untold number of hours with us to make this book possible.

All things were made by him; and without him was not any thing made that was made. (John 1:3)

Alex C. Hoffmann
Louis E. Stein

About the Authors

Alex C. Hoffmann is of Danish nationality. He graduated with a Ph.D. from UCL in 1983 in high pressure fluidization. During his studies he worked one year for UOP oil products in Chicago. He worked for three years as a post-doctoral research fellow at Surrey University, stationed at Separation Processes Services at Harwell, acting as Research Engineer and Industrial Consultant in cyclone technology and gas cleaning. In 1987 he moved to the University of Groningen in the Netherlands as a Lecturer and, later, Senior Lecturer. In 2001 he started as Professor in Multiphase Systems at the Department of Physics and Technology at the University of Bergen, Norway.

Professor Hoffmann has carried out a number of research projects in collaboration with processing industry, mainly the oil and gas industry, specializing in particle and multiphase technology. He is the author of more than 110 scientific articles, two scientific/technical monographs and he has two patents to his name. He used to play the classical guitar, but now mostly makes furniture or works in his garden in Norway in his spare time. He is married to Gloria and has two children.

Louis E. Stein graduated with a Ph.D. in Chemical Engineering from the University of Houston in 1974. After graduating he worked as a post-doctoral research fellow at the University of Utah, as a NASA Engineering Aide, and as a process engineer at the Sinclair Refinery, Pasadena Texas. During the period 1970–74, he held the post of Chemical Engineering Instructor at the University of Houston. After an interval as Research Engineer at Envirotech, Salt Lake City, he joined Shell in 1975 and, after several promotions, and numerous company awards, retired in 1999 as a Senior Staff Process Engineer. He remains active as a Separations and Fluid Flow Consultant to industry and as Fluid Mechanics Lead Instructor for Shell.

Dr Stein has eight patents to his name and has held the Presidency of the South Texas Chapter of the International Filtration Society. His interests include math and science tutoring, guitar playing and building and repairing personal computers. He is married to Doris and has 3 children and 2 grandchildren.

Contents

1

Introduction

The subject of this book is centrifugal gas cleaning devices, namely cyclones used as gas-solids separators (for 'dedusting') and as gas-liquid separators (for 'demisting').

1.1 Some Historical Background

The first cyclone patent was granted to John M. Finch of the United States back in 1885 and assigned to the Knickerbocker Company. Although the "dust collector", as it was then called, contained the essence of today's modern cyclones (see Fig. 1.1.1), the dust was allowed to exit out the side of its cylindrical body, rather than out a conical-shaped bottom. It was also a rather complex device and bore little resemblance to today's modern cyclones.

Still, the idea of using centripetal acceleration for separating particles from a gas stream was quite a radical idea back in the late 1800's. After all, everyone knows that dust will settle only when the gas stream carrying the dust is quiet and relatively free of motion for a long time. Indeed, a 10-micron dust particle of unit density requires about $5\frac{1}{2}$ minutes just to settle 1 meter in still air. The beauty of John Finch's discovery is that he devised a solution to the problem of dust "settling" which was just the opposite of conventional thinking or even common sense at the time of his discovery. Rather than devising a large, quiet settling chamber, he introduced the dust-laden air into a small cylindrical housing in a tangential manner and imparted a significant velocity to the mixture, thereby separating the dust from the air under highly turbulent flow conditions using the principle of centripetal acceleration, rather than gravity. In the area of separations technology the concept embodied in Finch's discovery has proven to be one of the most elegant, yet practical inventions of the 19^{th} century. It's a textbook example of the value of "thinking outside the box".

Improvements in the design of cyclones rapidly followed (at least rapid for the times) and, by the early 1900's, there began to appear cyclonic devices

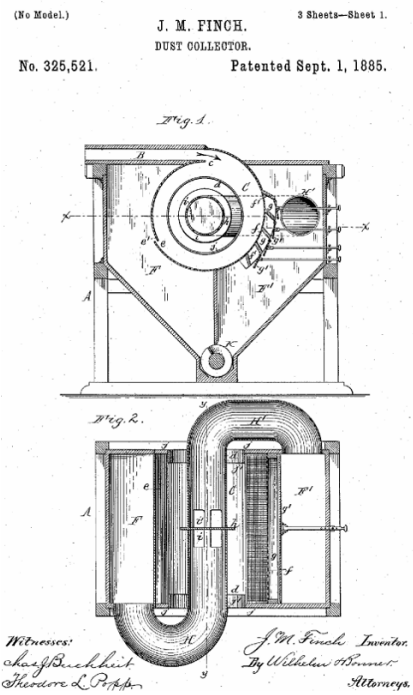

(No Model.) 3 Sheets—Sheet 1.

J. M. FINCH.

DUST COLLECTOR.

No. 325,521. Patented Sept. 1, 1885.

Fig. 1.

Fig. 2.

Witnesses: Inventor. Attorneys.

UNITED STATES PATENT OFFICE.

JOHN M. FINCH, OF JACKSON, MICHIGAN, ASSIGNOR TO THE KNICKERBOCKER COMPANY, OF SAME PLACE.

DUST-COLLECTOR.

SPECIFICATION forming part of Letters Patent No. 325,521, dated September 1, 1885.

Application filed May 13, 1885. (No model.)

To all whom it may concern:

Be it known that I, JOHN M. FINCH, of Jackson, in the county of Jackson and State of Michigan, have invented new and useful Improvements in Dust-Collectors, of which the following is a specification.

This invention relates to an improvement in the class of machines which are employed in mills, factories, &c., for separating dust from air; and the object of the invention is to accomplish the separation in a simple, practical, and inexpensive manner.

Heretofore it has been attempted to separate the dust from the air by compelling the dust-laden air to assume a rotatory motion, either by revolving fan-blades or by its own momentum, thereby imparting to the particles of dust a centrifugal movement which drives them against a perforated case, which separates the current of moving air from a dead air chamber. The separation of dust from air, therefore, takes place only from the fact that the particles of dust, having greater specific gravity than air, tend to follow their lines of direction and so pass through the perforations. In practice I find that much of the dust is of so slight gravity that the moving current of air overcomes the centrifugal force, and that therefore this light dust is carried forward to the outlet by the moving current and escapes from the machine with the air, whereby the object of the machine is to a large extent defeated.

The object of my invention is to overcome this difficulty; and it consists of a machine by which the dust is separated from the air by imparting to the dust-laden air current a rapid rotative motion in a suitable separating-case, thereby causing the dust particles to seek the outer edge or layer of the revolving current and accumulate in the same, then removing or skimming off the outer layer or stratum of air containing the dust through one or more apertures or slots in the case into a dust chamber, in which the air current entering with the dust is permitted to expand and come to a state of comparative rest, whereby the dust is deposited in said chamber while the air is permitted to escape therefrom, as will be hereinafter fully set forth, and pointed out in the claims.

In the accompanying drawings, consisting of three sheets, Figure 1 is a sectional elevation of my improved dust-collector. Fig. 2 is a horizontal section in line *x x*, Fig. 1. Fig. 3 is a side elevation of the machine. Fig. 4 is a vertical section in line *y y*, Fig. 2. Fig. 5 is a sectional elevation showing a modified construction of the machine.

Like letters of reference refer to like parts in the several figures.

A represents the stationary frame of the machine, and B represents the air spout or trunk through which the dust-laden air enters the machine, and which is connected with the middlings-purifier, grain-separator, or other machine from which the dust-laden air is discharged.

C is an approximately cylindrical separating-case, arranged, preferably, horizontally and connected with the air-spout B, to receive the dust-laden air therefrom through the inlet-opening *e*. The spout B is arranged tangentially to the separating-case C, so that the dust-laden air which enters the case C from the spout B with great force and velocity assumes a circular or rotative motion in the casing C, about the axis thereof, whereby the dust particles contained in the air current are all thrown into the outer layer of the air-current against the inner side of the casing. The air-current continues its rotative or gyrating movement in the case C until it escapes at the open ends *d* of the case.

e represents the dust-discharge opening, consisting of a horizontal slot formed in the case C, at a suitable distance from the inlet-opening *e*. The rear edge, *e'*, of the slot *e* stands nearer the center of gyration than the front edge, so that the slot will skim off the thin layer of air and dust which is driven along the wall of the case C and discharge it into the dust-chamber F.

f represents a section of bolting-cloth, or other finely-perforated material, arranged in the case C and forming part of its peripheral wall. The bolting-cloth *f* is supported on ribs *f'*, which divide the space behind the cloth into a number of independent chambers, *g*, each of which is provided with an adjustable discharge-valve *g'*. The very fine dust passes through the meshes of the bolting-cloth into the chambers *g*, and thence into a dust-chamber, F. By regulating the discharge-open-

Fig. 1.1.1. Illustrations of the first cyclone patent

that more closely resemble today's modern units. An example of this is the "dust collector" by the American inventor O. M. Morse who, in 1905, was awarded a patent for purpose of reducing the hazard of dust explosions in flourmills. See Fig. 1.1.2. He wrote—

> My improved machine separates the dust from the air by its own momentum in an extremely simple manner, it employs no moving parts, (and) is very simple in construction...

Due to their simple construction, low manufacturing cost, compactness, lack of moving parts, and relative ease of maintenance, cyclones continued to grow in popularity and improve in both construction and operation. By the 1920s they began to take on the features that characterize today's modern cyclones, as evidenced by two flourmill cyclones shown in Fig. 1.1.3.

Even though the underlying principles governing the behavior of cyclones has not changed since their inception back in the late 1800's, the intervening years of testing and industrial application has resulted in significant design improvements. The geometry and relative proportions of the inlet, roof, vortex finder, barrel, cone, hopper, dust discharge opening, and bewildering array of ancillary features have been the target of numerous investigations. By todays standards, some have been "interesting" to say the least. See, for instance, the

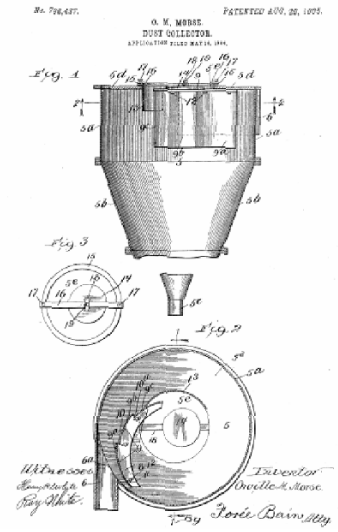

UNITED STATES PATENT OFFICE

ORVILLE M. MORSE, OF JACKSON, MICHIGAN.

DUST-COLLECTOR.

No. 798,437. Specification of Letters Patent. Patented Aug. 29, 1905.

Application filed May 16, 1904. Serial No. 208,068

Fig. 1.1.2. An early cyclone patent featuring a conical dust discharge

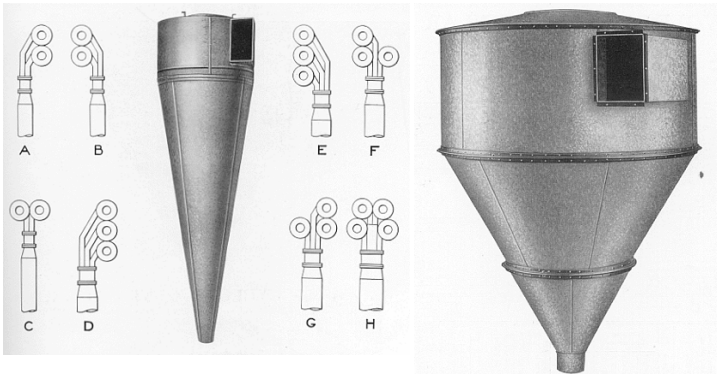

Fig. 1.1.3. Flour mill cyclones manufactured by the Wolf Company (The Wolf Company (1922) Flour Mill Machinery catalog, Chambersburg, Pennsylvania) during the early 1920s. Note the variety of inlet duct designs used to feed multiple cyclones. Courtesy of Theodore R. Hazen and Pond Lily Mill Restorations (http://home.earthlink.net/∼alstallsmith/index.htm)

patented "Rube-Goldberg" like design shown in Fig. 1.1.4 which featured rotating chains, driven by the vortex motion, to keep the lower walls of the cone from clogging up with dust. In addition to such "hardware" considerations, significant attention has been given to the role that velocity, phase densities, viscosity, particle concentration, shape and size distribution has on separation performance. For the most part these investigative efforts have consisted of laboratory and field tests augmented or guided by whatever "theory" and in-

sight was at the investigators disposal at the time. As has been the case with most fundamental inventions, cyclone designs have become very specialized—reflecting the process duties and industries that they serve. Some examples are shown in Fig. 1.1.5.

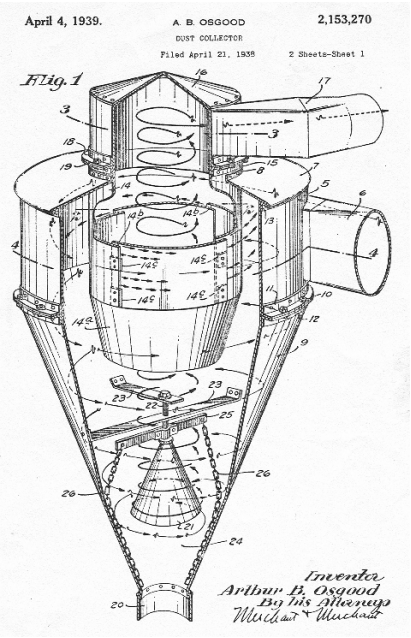

Fig. 1.1.4. 1939 US cyclone patent by A. B. Osgood

Most of the early cyclones were used to collect dust created from mills that processed grains and wood products. In the decades that have followed, however, cyclones have found application in virtually every industry where there is a need to remove particles from a gas stream. Today, cyclone separators are found, for example, in:

- ship unloading installations
- power stations
- spray dryers
- fluidized bed and reactor riser systems (such as catalytic crackers and cokers)
- synthetic detergent production units
- food processing plants
- crushing, separation, grinding and calcining operations in the mineral and chemical industries

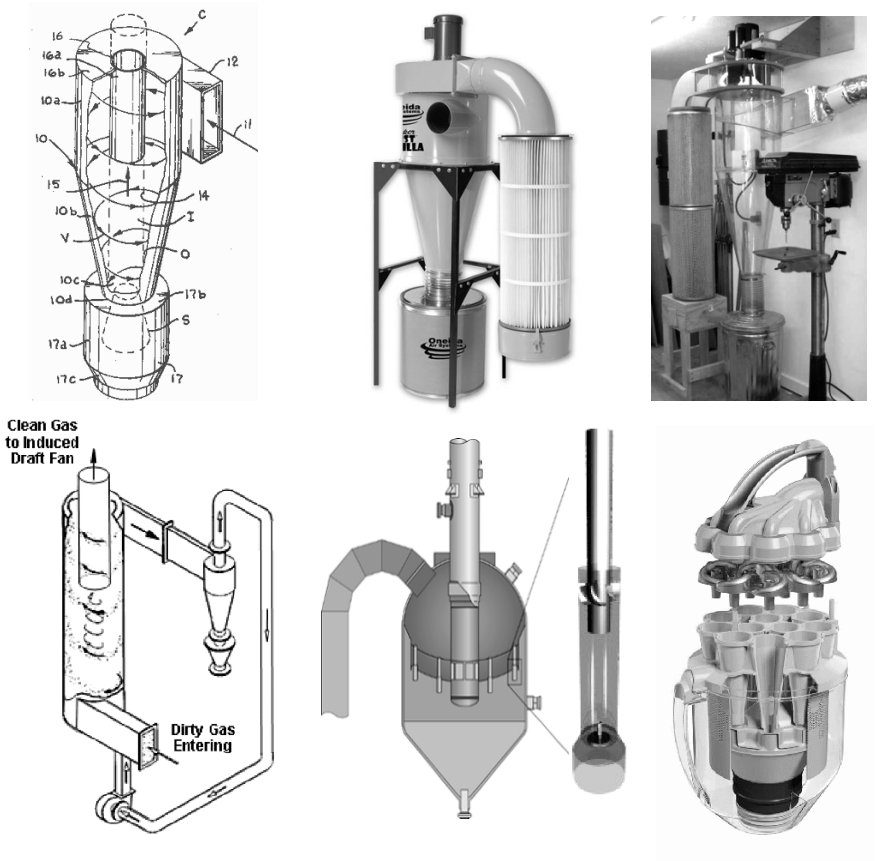

Fig. 1.1.5. Examples of modern cyclones. From top left to bottom right: Polutrol-Europe cyclone (excerpt from US Patent 3,802,570); Oneida wood shop cyclone & cartridge filter; Pentz/Mangano Clear-Vu cyclone; two-stage LSR Core Separator-Butcher (2001); Shell Global Solutions "Third-Stage Separator" multiclone; Dyson vacuum cleaner multiclone

- roasters, sintering plants, rotary kilns, furnaces and converters in the ferrous and nonferrous metallurgical industries
- fossil and wood-waste fired combustion units (normally upstream of a wet scrubber, electrostatic precipitator or fabric filter)
- vacuum cleaning machines
- dust sampling equipment

Cyclones have also been utilized to classify solids on the basis of their aerodynamic characteristic such as their mass, density, size, or shape. Because of their simple construction and high reliability, cyclones are also used very effectively to separate two-phase gas-liquid mixtures, such as the entrained droplets exiting a venturi scrubber or other type of scrubber. Other examples include

the removal of water droplets from steam generators and coolers and oil-mist from the discharge of air compressors. Likewise, they have been widely applied in process machinery to remove entrained oil and hydrocarbon droplets generated from spraying, injection, distillation, or most any process that results in the production of entrained droplets or a two-phase mixture. They have even been used as inlet devices to prevent foaming in gravity separation drums.

The physical laws governing the behavior of today's modern industrial cyclones were firmly established more than a hundred years ago in the works of Sir Isaac Newton and Sir George Gabriel Stokes. Their work provided us with a basis for describing the forces acting on a particle traveling in a fluid medium. P. Rosin, E. Rammler, W. Intelmann and Eugen Feifel, especially, established the basis for scientific calculations. Since then, cyclone development and our understanding of cyclones has continued to expand due to the pioneering and valuable contributions of individuals such as Eugen Feifel, C. J. Stairmand, Ludwig Leineweber, Koichi Iinoya, G. B. Shepherd, C. E. Lapple, A. J. ter Linden, Walter Barth, and Edgar Muschelknautz, to name a few. Eugen Feifel published no less than seven papers between 1938 and 1950 on the theory and principles governing the motion of the fluid and particle phases within cyclones. He appears to have designed the first horizontal cyclone—essentially a cylinder with a horizontally oriented gas outlet on each end and a centrally located, "slot-type" inlet. We rarely see his name mentioned in today's modern literature but his contributions had a major impact on the thinking of investigators for several decades starting in the late 1930's. Walter Barth's theoretical work back in the 1950's has also had a great influence on the work of investigators that followed him, and this influence continues even today.

Still, many unanswered questions remain. In fact, we shall encounter and point out some of these in this book.

The optimization of cyclone performance for any given task is an oft-sought goal but is seldom achieved in practice. Understanding cyclone performance as a function of a cyclone's size, geometry, feed properties, feed flow rates and the system of which it is a part is essential if we wish to successfully design, operate, troubleshoot or predict cyclone performance. We trust that the information presented in this book will help to develop this understanding.

In this first chapter we start by briefly discussing the removal of particles from gases in general, to put the topic in context. We will then focus on centrifugal devices, which are the most widely used gas cleaning devices in industry today. We will explain qualitatively the principle by which centrifugal separators work, and mention the different types that are in use.

1.2 Removal of Particles from Gases

Particulate pollution is a societal concern and has been recognized as a problem for many decades. Airborne particles manifestly cause increase in in-

cidence of disease of the air passages, and constitute a real environmental problem in some urban societies.

It therefore seems appropriate that governments are imposing more stringent limits on particulate emissions from the processing industry. The challenge is to meet these restrictions with robust and efficient technology at minimum cost, retaining, where relevant, as much separated material as possible as useful product and thus minimizing other process waste streams and maximizing profitability.

Aside from meeting ambient air quality targets, various types of separation equipment, including knock-out drums, bag filters, electrofilters/electrostatic precipitators (ESP's), scrubbers and cyclones are also used to capture solid particles for:

- re-use in the process (such as valuable catalytic particles) or
- further processing (grain processing plants) or
- direct sale to the customer (elastomeric particles off a fluid bed dryer).

Another reason for removing particles from process streams is to protect downstream equipment, such as blowers and turbines, from erosion damage caused by particles impacting on, for instance, rotorblades.

If the goal of a given gas cleaning operation is to limit emissions or to collect as much product as is practical, the target is often one of not allowing particles in the emitted gas stream to exceed some maximal allowable concentration . If, on the other hand, the goal is to protect downstream equipment, the target can be in terms of a maximal particle size allowed in the cleaned gas stream.

Particles in gas streams vary so widely in terms of size, density, shape, stickiness, friability, erosiveness, surface charge, and other characteristics that no one method of separation, and not one type of separator, is suitable for processing the entire spectrum of materials. Thus the separation equipment must be capable of processing a very wide variety of material—from pellets to sub-micron powders, from hard minerals, like garnet sand, to soft food products like rolled oats. Some of these materials are very free-flowing, others tend to compact or cake. The products and types of particles shown in Figs. 1.2.1 and 1.2.2 are rather typical of the myriad of substances that can, and have been, successfully conveyed and subsequently classified or separated in modern separation equipment, including cyclones, bag filters and electrofilters.

Figure 1.2.3 shows the approximate size ranges of a number of particle types, and the methods suitable for removing them from a gas stream (Ignatowitz, 1994; Perry, 1997). Below we mention some of the most popular gas cleaning methods with their main advantages and disadvantages.

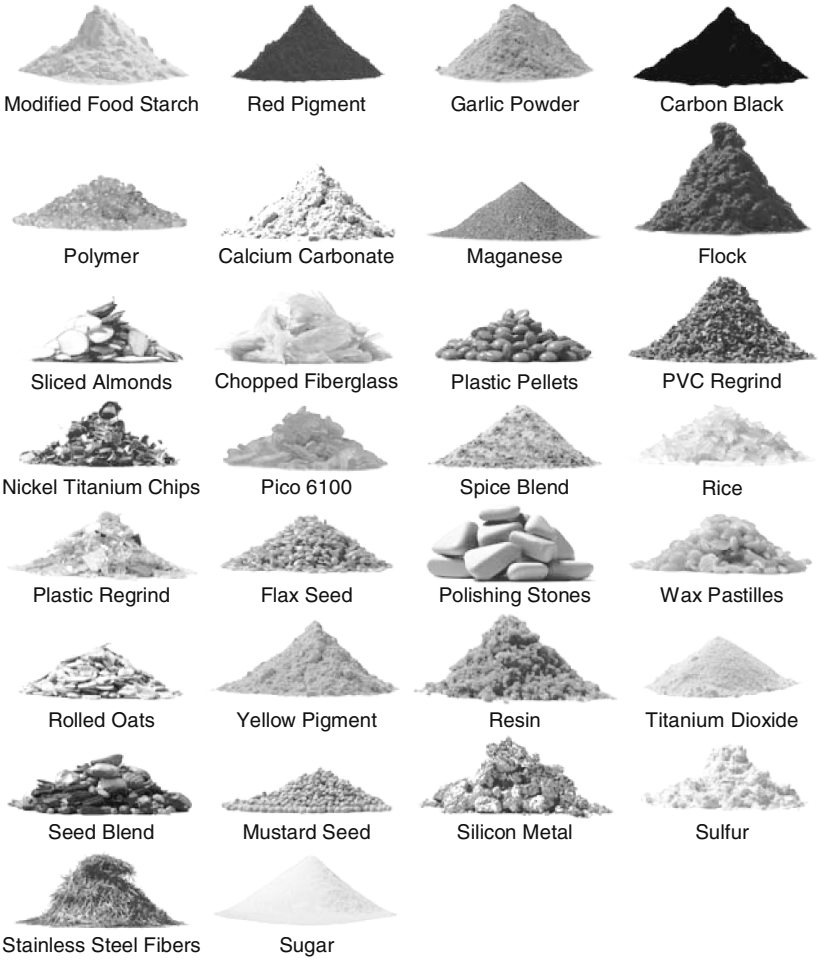

Fig. 1.2.1. Illustration of the diversity of material types that can be conveyed and separated with modern separation equipment. Images courtesy of Flexicon Corporation

1.2.1 Filtration

By far the most common method for removing very fine particles from gas streams is by filtration[1]. The gas stream is led through a filter, which is often a woven or compressed fibrous, cloth-like material.

[1] Here we wish to express our profound thanks to the late Professor Frank M. Tiller of the University of Houston who, for 50 years, performed ground-breaking research in the field of fluid/particle separation, earning wide recognition as the father of modern filtration theory.

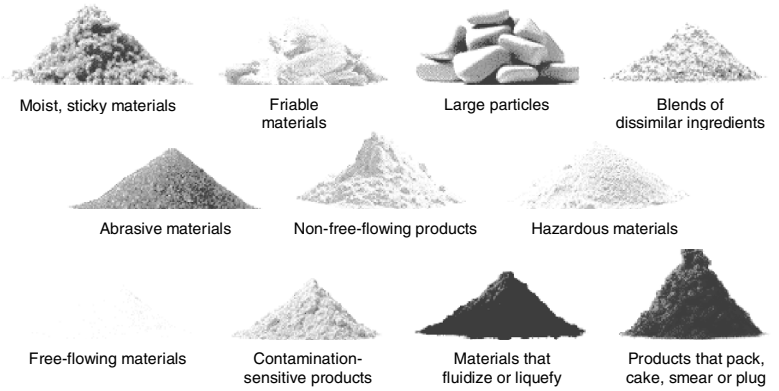

Fig. 1.2.2. Illustration of the diversity of material types that can be conveyed and separated with modern separation equipment. Images courtesy of Flexicon Corporation

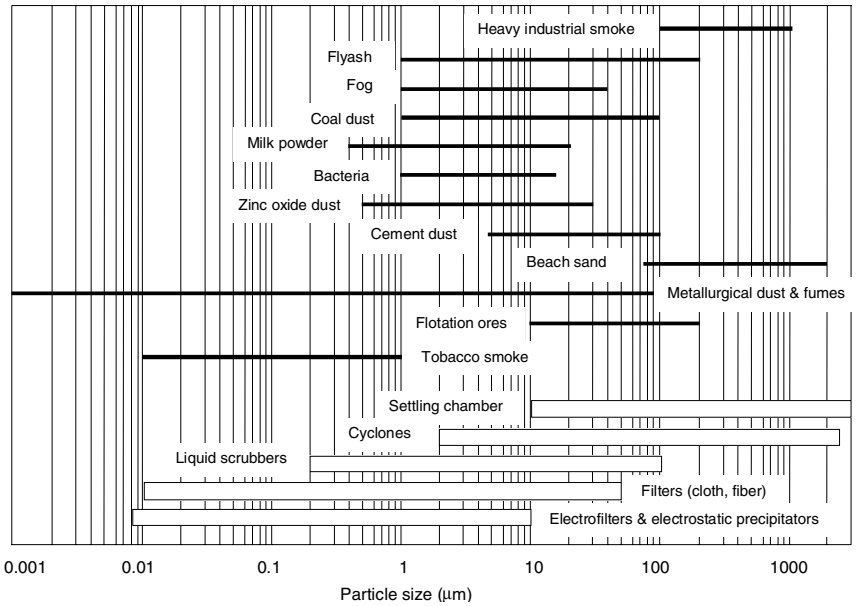

Fig. 1.2.3. Particle size of some materials and suitable methods for removing them from a gas stream; from Ignatowitz (1994) and Perry (1997)

The pore size of the filter material will often be greater than some of the particles that are to be retained. During the first part of the filtration process, particles fill the pores in the filter, and start to build up a layer (a filter 'cake') on the filter. As this layer builds up, the filtration efficiency increases, and so does the pressure drop across the filter. Once the pressure drop exceeds a certain limit, the filter needs to be reconditioned. This is often achieved by a reverse pulse of air, which blows off most the filter cake, allowing it to drop into a hopper, whereafter the filtration process can resume.

The advantage of filtration is its high efficiency. Drawbacks are the oscillating pressure drop, wear of the filter material, handling and disposal of spent filter cartridges or bags, and the fact that filters normally cannot be kept biologically clean so that a food or pharmaceutical product captured in a filter is lost. Cloth filters cannot be used at high temperature (in excess of about 250°C) or in aggressive environments; for such conditions ceramic or sintered metal filters are an option.

A special sort of 'filter' is the electrofilter, sometimes referred to as an electrical or electrostatic precipitator (*i.e.* an 'ESP'). Here, the particles are charged and led through narrow gaps between two oppositely charged plates. The particles are electrostatically attracted to—and deposit on—one of the plates. ESPs have the advantage of being able to collect particles below one micron in size and can operate at elevated temperatures. Some of their disadvantages include failure of electrical components and their large size relative to the amount of solids-bearing gas that they process. They also require a highly uniform distribution of the incoming gas over their collecting plates if they are to operate at peak efficiency. In addition, ESPs may alter the composition of the particles in such a manner as to render them useless for further processing.

1.2.2 Wet Scrubbers

In wet scrubbers droplets are either directly sprayed into the incoming dusty gas or the gas is allowed to shear a source of liquid into droplets, which achieves the same effect. Due to their inertia, the particles impact on the droplets and are incorporated in them. The particle-containing droplets have a larger diameter than the dust particles, which allows them to be separated more easily from the gas stream in inertial type separators such as cyclones, settling chambers or knock-out vessels.

Wet scrubbers can have a high efficiency for small particle sizes, especially the venturi type scrubbers, where the flow is subjected to strong acceleration—a condition that encourages efficient coalescence between particles and droplets. In wet scrubbers, the pressure drop remains constant (except in some relatively rare cases where calcium or other deposits may accumulate in the throat area of the scrubber). Degradation of the separation medium is normally not a problem. However, most scrubbers recycle most of the scrubbing 'water' and the efficiency of the scrubber will suffer if the solids or other

contaminates contained within the recycled scrubbing liquid are not held in check. A more systemic drawback to scrubbers, however, is that the dust, and any water-soluble components within the gas phase, end up in the liquid. This leads to a loss of product in many industries, and the problem of what to do with the slurry stream. Indeed, when considering a scrubber, care must be taken, in some cases, that one does not turn an 'air pollution problem' into a 'water pollution problem'.

1.2.3 Centrifugal/Cyclonic Devices

Centrifugal and cyclonic type separators are the subjects of this book. Compared with the other methods, their advantages are:

- the collected product remains dry and, normally, useful
- low capital investment and maintenance costs in most applications
- very compact in most applications
- can be used under extreme processing conditions, in particular at high temperatures and pressures and with chemically aggressive feeds.
- no moving parts
- very robust
- constant pressure drop
- can be constructed from most any material suitable for the intended service including plate steel, casting metals, alloys, aluminum, plastics, ceramics, etc.
- can be equipped with erosion or corrosion resistant or 'particle repelling' type liners, such as Teflon. Internal surfaces may be electropolished to help combat fouling
- can be fabricated from plate metal or, in the case of smaller units, cast in molds
- can, in some processes, handle sticky or tacky solids with proper liquid irrigation
- can separate either solids or liquid particulates; sometimes both in combination with proper design.

Some disadvantages of cyclones are:

- a low efficiency for particle sizes below their 'cut size' when operated under low solids-loading conditions
- usually higher pressure loss than other separator types, including bag filters, low pressure drop scrubbers, and ESPs
- subject to erosive wear and fouling if solids being processed are abrasive or 'sticky'
- can operate below expectation if not designed and operated properly. Although this problem, as well as the erosion and fouling problem mentioned above, is not unique to cyclones, it is the writers' hope that this book will help in eliminating these type of problems.

1.2.4 Knock-out Vessels and Settling Chambers

For larger particles, adequate separation can be realized if the incoming gas/solids or gas/liquid mixture is allowed to flow slowly through a vessel so that the particles settle out under the influence of gravity. Such vessels share most of the advantages of cyclones, except for low investment costs and compactness since settling chambers, with their 1-G driving force, can be very large. Still, common practice often includes knockout vessels ahead of cyclones. Their performance is less sensitive to flaws in design and operation than that of centrifugal separators. These vessels are normally used to separate out particulate matter (liquids and/or solids) that is greater than about 500 microns in size.

1.3 A Closer Look at Centrifugal Gas Cleaning Devices

We now concentrate on centrifugal devices. In these, the dust-laden gas is initially brought into a swirling motion. The dust particles are slung outward to the wall, and are transported downward to the dust outlet by the downwardly directed gas flow near the wall.

A sketch of a standard reverse-flow, cylinder-on-cone cyclone with a tangential, slot-type inlet is shown in Fig. 1.3.1.

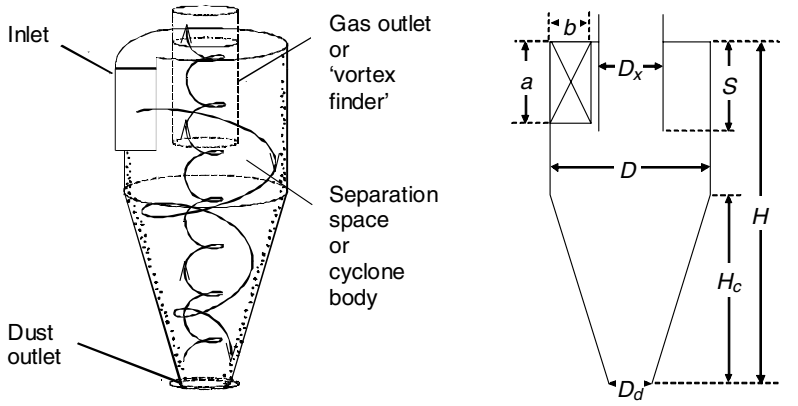

Fig. 1.3.1. Sketches of a reverse-flow, cylinder-on-cone cyclone with a tangential inlet. The geometrical notation is indicated in the right-hand sketch

For the standard, reverse-flow cyclone, (with a so-called 'slot' or 'pipe' type of entry, see below) the swirling motion is brought about by designing the inlet in such a manner that it forces the gas to enter the unit on a tangent to the inner body wall. The inlet is normally of rectangular cross section, as

shown. As the gas swirls, it moves axially downwards in the outer part of the separation space. In the conical part of the cyclone, the gas is slowly forced into the inner region of the cyclone, where the axial movement is upwardly directed. This flow pattern is often referred to as a 'double vortex': an outer vortex with downwardly directed axial flow and an inner one with upwardly directed flow. The gas exits the cyclone through the so-called 'vortex finder', which extends downward from the center of the roof. This outlet pipe goes by many different names, with 'vortex tube' and 'dip-tube' being the most common, aside from 'vortex finder'. The particles in the inlet gas are slung outwards to the wall in the centrifugal field, and are transported to the dust exit by the downwardly directed gas flow near the wall. In the following chapters we shall look in more detail at the flow pattern in the separation space.

The geometry of a cyclone with a 'slot' type inlet is determined by the following eight dimensions:

- body diameter (this is the diameter of the cylindrical section), D
- total height of the cyclone (from roof to dust exit), H
- diameter of the vortex finder, D_x
- length of the vortex finder (from the roof of the separation space), S
- height and width of the inlet, a and b, respectively
- height of the conical section, H_c
- diameter of the dust exit, D_d

All dimensions are understood to be inside, finished dimensions exposed to flow.

1.3.1 Applications of Centrifugal Separators

Centrifugal separators for dedusting and demisting are very widely used throughout industry. Moreover, they come in all sizes and shapes, as shown in Fig. 1.3.2 and elsewhere in this book.

Some of the industries making extensive use of these devices are:

- oil and gas (for instance in fluidized catalytic cracking units, FCCU)
- power generation
- incineration plants
- iron and steel industry/blast furnaces and non-ferrous industries
- ore sintering plants
- wood chip, wood mill and building material plants
- sand plants
- cement plants
- coking plants
- coal fired boilers
- lead, ferrosilicon, calcium carbide, expanded perlite, carbon black plants, etc.
- grain processing facilities such as flour mills (wheat, rice, etc.)

Fig. 1.3.2. A few examples of the variety of cyclone sizes and shapes used in commercial practice. Top photo courtesy of Ducon Technologies Inc., left photo courtesy of Fisher-Klostermann Inc., right photo courtesy of EGS Systems Inc.

- 'chemical' plants (plastics, elastomers, polymers, etc.)
- catalyst manufacturing plants
- food industry
- MTB type plants (similar to FCCU).

Figures 1.3.3 a, b show two commercially available cyclones designed for light industrial use. An example of a much larger scale cyclone installation is presented in Fig. 1.3.4. This is a good example of a complete system—including cyclone, blower, rotary airlock valves and ducting—all supplied by the same manufacturer. Fig. 1.3.5 illustrates a huge spent catalyst regenerator cyclone system typical of today's modern FCCU installations. Such cyclones are used to capture and return the catalyst entrained off the vessel's fluidized bed. Fig. 1.3.6 illustrates where these and other cyclones are typically used in a commercial FCCU refinery process. The left- and right-hand frames in

Fig. 1.3.7 illustrate the first two separation stages of a modern four-stage home vacuum cleaner assembly. Dust-laden air enters on a tangent near the top of the see-through plastic housing. The resulting centripetal energy acting on the incoming dust particles within this first stage separator causes most of the particles to separate to the walls of the housing and to settle within the dust collection bin which comprises the bottom of the housing. The air then flows through a louver or vane type, second-stage separator, which produces a very sharp (180°) flow reversal. The particles inertial prevents most of them from following the air through the bend and, through such action, the vane assembly separates out most particles not captured in the first stage. A circular disk or "separator plate" (item 158 in patent drawing) is employed to help prevent the vortex generated in the upper chamber from re-entraining dust out of the dust collection bin. A porous foam filter and a high-efficiency HEPA filter (not shown) are used to separate micron and most sub-micron sized particles from the air prior to its exit out the cleaning apparatus.

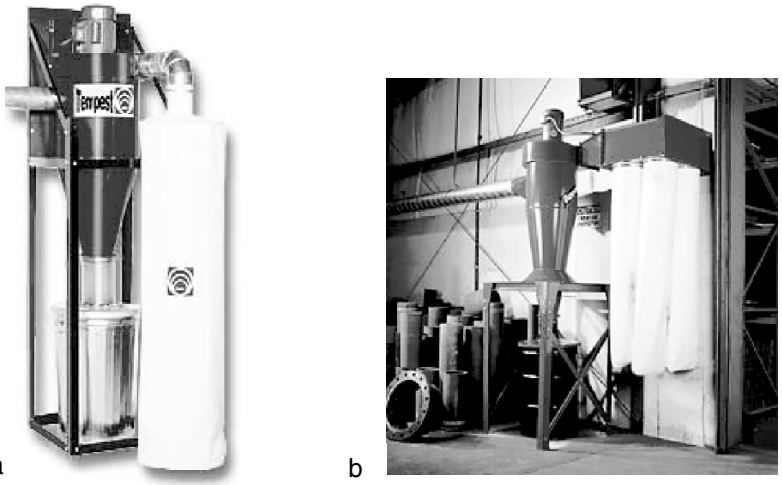

Fig. 1.3.3. Two light commercial slot-type inlet cyclones with an overhead 'pull-through' fan on the clean-gas side and a downstream bag filter assembly. Courtesy of Penn State Industries (**a**) and Torit Products (**b**)

The cylinder-on-cone cyclone with a tangential entry is the industry standard design for centrifugal dedusting or demisting devices. Even so, wide varieties of other configurations are in use and some of these will be discussed in the chapters that follow. We now proceed to look at some of these configurations.

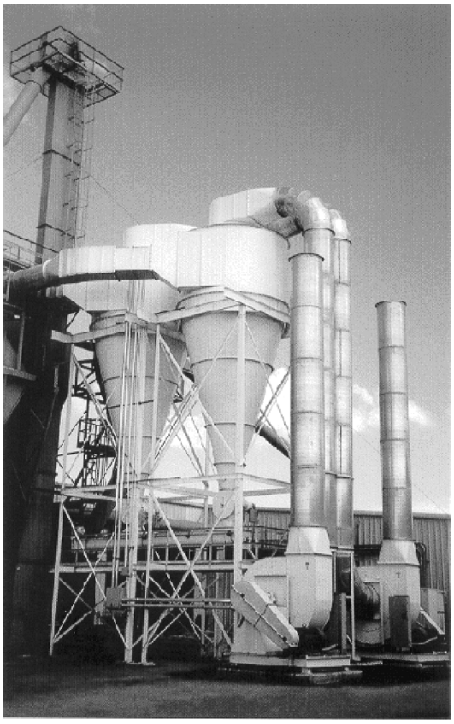

Fig. 1.3.4. A complete pull-through cyclone system for collecting various wood chips, dust and shavings including cyclones, fans and rubber-tipped rotary airlock valves. Note also outside wear plate on inlet bend. Courtesy of Koger Air Corporation

Fig. 1.3.5. A collection of two-stage cyclones suspended from the vessel head of a modern FCCU regenerator prior to installation. Photo courtesy of TapcoEnpro International

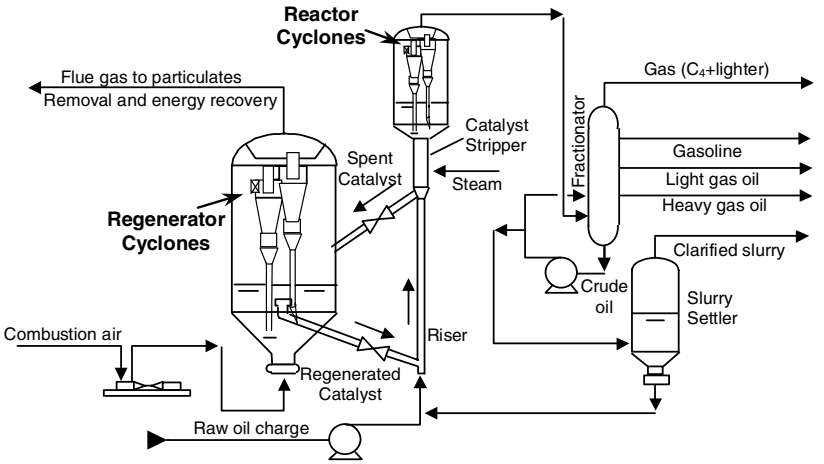

Fig. 1.3.6. A typical Fluid Catalytic Cracking Unit (FCCU) with internal sets of regenerator and reactor cyclones

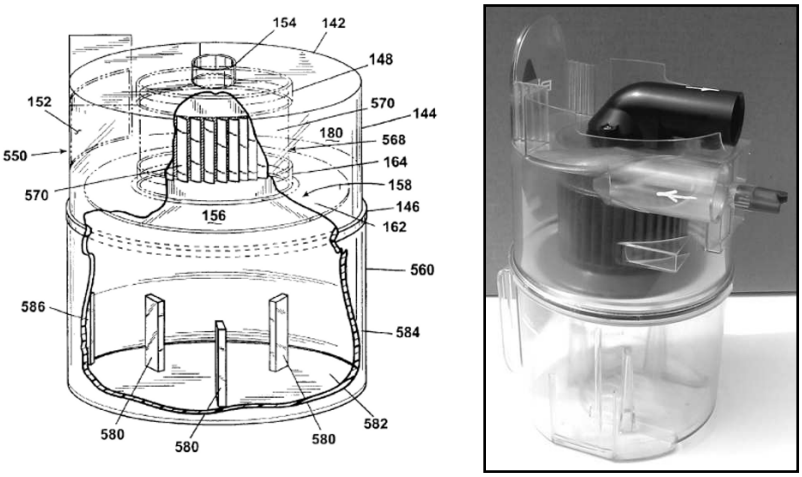

Fig. 1.3.7. An example of a two-stage dust separator comprising a modern home vacuum cleaner. Left frame: Bissell Homecare, Inc. US Patent 6810557 B2. Right frame: commercial example. Photo by L.E. Stein. Image used with permission of Bissell Homecare, Inc.

1.3.2 Classification of Centrifugal Separators

We can classify centrifugal separators according to either:

- their inlet configuration
- the shape of their body

- the flow direction in and out of them

Four main types of inlet configurations are used:

The *first* and simplest is the circular or pipe-type inlet. See Fig. 1.3.8 a. Such inlets are typically found in inexpensive cyclones constructed from sheet-metal wherein some sacrifice in separation performance is acceptable. Many woodshop and grain processing units are designed with this type of inlet. Unlike the slot-type inlet described below, pipe-type inlets eliminate the need to fabricate a round-to-rectangular inlet transition section.

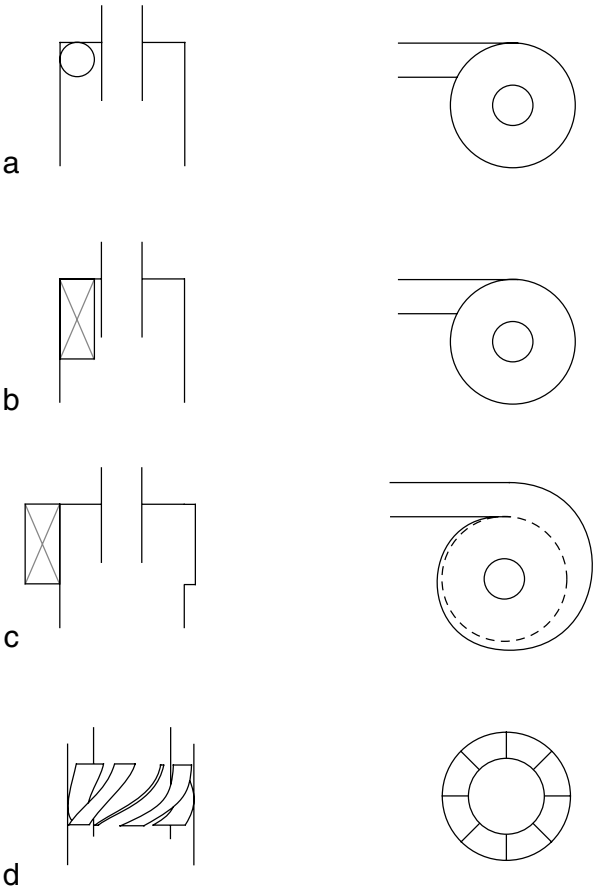

Fig. 1.3.8. Side and top views of the four most used inlet configurations. **a** circular or 'pipe' inlet, **b** 'slot' (also called 'tangential') inlet, **c** 'wrap-around' inlet, and **d** axial inlet with swirl vanes

The *second* inlet type is the 'slotted' inlet, see Fig. 1.3.8 b. Included in this definition is the helical-roof inlet, see for example, Fig. 12.1.3 in Chap. 12. 'Slot'-type inlets are, by far, the most widely used in the chemical and petroleum processing industries. It is sometimes called a 'rectangular' or 'tangential' inlet. However, in this book we reserve the term 'tangential' to denote all cyclones with tangential inflow, in contrast to "axial" cyclones wherein the gas enters along the cylindrical/conical axis of the cyclone (see below). Except in cases where wall stiffening or special reinforcing is required, slot-type inlets are not normally difficult to construct, and they generally give good performance. Since the feed reporting to the cyclone is conveyed in circular pipes, they require the construction of a round-to-rectangular inlet transition duct and this results in some complication in the cyclone's design relative to a simple pipe-type inlet. From a fabrication/strength point of view, it is often preferred that the top of the inlet be located slightly under the roofline, rather than at the same elevation as the roofline (as shown in the figure). This practice, though, can give rise to a ring of dust circulating along the inner roofline. Fortunately, the presence of such a ring does not seem to significantly influence cyclone performance.

The *third* inlet design is the 'wrap-around' inlet, sometimes referred to as a 'scroll' or 'volute' (Fig. 1.3.8 c). In this type of inlet, the gas flow is gradually constricted as the area available for flow decreases. It therefore undergoes some acceleration upstream of the main separation space. Since the scroll's inlet radius is greater than that of any of the other inlet types, this type of inlet produces a greater inlet angular momentum and, as a consequence, a higher spin velocity within the inner core of the vortex. Thus, a scroll inlet is one way of realizing most of the benefits of a larger-bodied cyclone without having to fabricate a larger diameter barrel and cone section. It is preferred in geometries with a wide vortex finder, since the incoming gas and solid mixture will not then impact the wall of the vortex finder. Scroll inlets are also widely used in high solids-loaded cyclones wherein a large fraction of the incoming solids are separated within the scroll section, ahead of the cyclone proper. Figure 1.3.8 c illustrates a 'full', 360° wrap-around scroll. Simpler and more compact 180° and 270° scrolls are also in common usage. For more details, see also Sect. 15.1.2.

The *fourth* type of inlet we wish to describe is that of swirl vanes. As shown in Fig. 1.3.8 d, a swirl-vane assembly allows the gas to enter the cyclone parallel to the axis of the cyclone The swirl-vane assembly is positioned between the vortex finder (or, in case of a 'straight-through' device, see below, a central solid body) and the outer (body) wall of the cyclone. This type of inlet is often inserted in cylindrical-bodied cyclones rather than in cylinder-on-cone or 'conical-bodied' geometries. When it is, we refer to the separator as a *swirl tube*. Swirl tubes are often of small size (by commercial standards) and are most commonly arranged in a parallel array on a common tube-sheet within a pressure-retaining vessel. They are normally fed from, and discharge into, common, but separate overflow and underflow plenums.

One advantage of the axial entry is the high degree of axial symmetry in the flow, which gives some operational advantages. For instance, it eliminates the region prone to fouling on the 'back side' of the vortex finder—that region pointing opposite the inlet opening. Another way of achieving a higher degree of axial symmetry is to distribute the inlet gas over two tangential entries, located 180° apart, rather than only one. Axial inlets also eliminate the need for fabricating a roof or an inlet-transition piece, or for cutting an entry slot in the upper body of the cyclone. The vane elements or "blades" can be bent from metal plate or they can be cast in one piece. Once these are available, the swirl-vane type cyclone is the simplest of all cyclones to assemble.

We have already mentioned the two possible configurations for the shape of the body: cylinder-on-cone and cylindrical. The last classification of centrifugal separators is according to the gas flow direction upon entering and exiting the device. The possible configurations are sketched in Fig. 1.3.9. The gas may leave the cyclone either through the roof, which is called a 'reverse-flow' configuration or through the bottom, in the same direction as the dust, which is called a 'straight-through' (or 'flow-through' or 'uniflow') configuration. Straight-through devices are almost always cylindrical in shape.

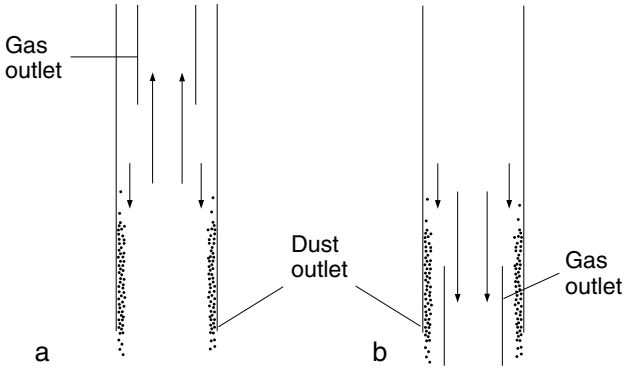

Fig. 1.3.9. Sketch showing the axial gas flow pattern in 'reverse-flow' **(a)** and 'straight-through' **(b)** types of centrifugal dedusters

1.3.3 Two Main Classes—Cyclones and Swirl Tubes

A systematic discussion of all the configurations mentioned above would lead us to spend a disproportionate amount of space on devices that are seldom used in practice. We are therefore concentrating on the two types of devices most used in industry; both are of the reverse-flow type:

- devices with a tangential inlet ('slot' or 'wrap-around') and a cylinder-on-cone body shape, which we will call 'cyclones', and

- devices with an axial inlet with swirl vanes and a cylindrical body shape, which we will call 'swirl tubes'.

We thus make the distinction between vane-type 'axial' inlets and 'tangential' inlets. By tangential inlets, we mean both slot and wrap-around inlets, unless we explicitly distinguish between the two. "Pipe" type inlets are also a type of tangential inlet, which compromises some degree of separation performance for the sake of construction simplicity.

The word 'cyclone' is used as an umbrella designation for all centrifugal separators throughout the scientific and engineering literature, and when using the term in this way swirl tubes can be seen as a special type of 'cyclone'. We have not been able to avoid using the word 'cyclone' in this sense in this book. It should be clear from the context in each case whether the designation 'cyclone' refers to centrifugal separators in general, or to cylinder-on-cone cyclones with tangential inlets in particular. On the other hand when we are saying 'swirl tube', we are referring to the special type of cyclonic separator with cylindrical body and swirl vanes; we could also have called these 'swirl tube cyclones'.

2

Basic Ideas

In order to understand the practical working of cyclones, it is necessary to master a number of topics, which span a range of different disciplines. Fluid mechanics, particularly relating to swirling flows, particle motion in a fluid, and different aspects of particle properties, such as size and size distribution, shape, and density, are all topics relevant to the later chapters.

This chapter contains a series of short discussions of these topics. Due to the nature of the subject matter, it can be difficult to recognize a 'red thread' in this chapter, but the account of each particular topic should be sufficient for appreciating the material in the subsequent chapters. Literature references are given for the reader wishing to study the disciplines more broadly.

2.1 Gas Flow

This section discusses some aspects of fluid mechanics that are particularly relevant to cyclones and swirl tubes.

2.1.1 Swirling Flow

Swirling flow, or vortex flow, occurs in different types of equipment, such as cyclones, hydrocyclones, spray dryers and vortex burners. Swirling flow also plays a central role in the developing fields of fluidics and process intensification. It is also the basis for the operation of foam-breaking or 'defoaming' separators that have received significant industrial attention in recent years.

We derive the equations for the tangential velocity distribution in two types of ideal swirling flows:

1. forced vortex flow, which is swirling flow with the same tangential velocity distribution as a rotating solid body, and
2. free vortex flow, which is the way a frictionless fluid would swirl. The tangential velocity in such a swirl is such that the moment-of-momentum of fluid elements is the same at all radii.

The tangential velocity distribution in real swirling flows is intermediate between these two extremes.

In order to derive these equations, we start by considering the forces acting on a fluid element in a swirling flow, as shown in Fig. 2.1.1. We use a cylindrical coordinate system (r, θ, z) (Weisstein, 1999) fixed in space with the z-axis, the axis of rotation, pointing out of the paper.

As the element rotates, it accelerates toward the center. If it did not accelerate it would continue in a linear path tangent to the orbit toward the axis of rotation. This acceleration is the 'centripetal acceleration'.

If we observe the element from a coordinate system, which is not fixed in space by rotating with the element, the centripetal acceleration will not be observed, but will appear as an *apparent force* directed away from the axis of rotation, the 'centrifugal force' (Fig. 2.1.1 b). This latter force is similar in nature to the gravity force, and acts away from the axis of rotation with a magnitude equal to the mass of the element times the centripetal acceleration.

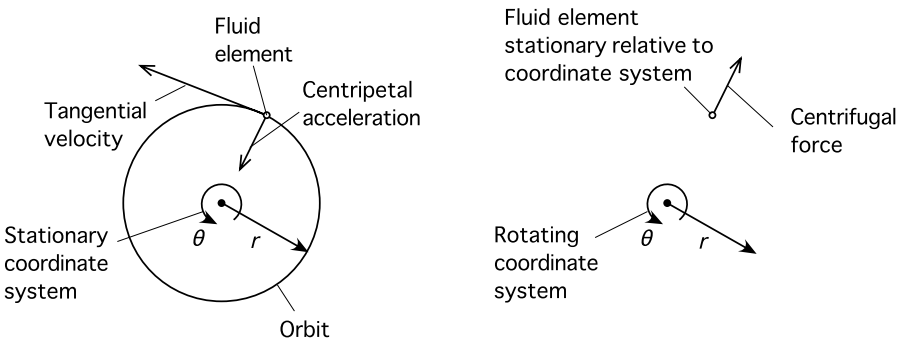

Fig. 2.1.1. A fluid element in a swirling flow, from two different points of view **a** a fixed coordinate system, and **b** a coordinate system rotating with the element

Strictly speaking, Newton's equations of motion apply only in a coordinate system that is not accelerating (in this case, rotating). Nevertheless, for mathematical simplicity, scientists and engineers often use an accelerating coordinate system (a rotating one, for instance), and then devise a non-physical or "pseudo force" (such as the "centrifugal force") in order to apply or preserve the equation of motion. We say "non-physical" because, in a rotating coordinate system, it is not possible to identify a physical object which produces the force needed to satisfy Newton's laws of motion. Also, real forces always occur in pairs yet, if we were to shrink in size and hitch a ride atop a tiny ball connected to a central post by a string and spin around the post, the one and only *force* we would experience would be the inward force (or

tension) exerted by the string. To then explain why the string does not pull us inward toward the post, we create an outwardly directed "pseudo force", called the "centrifugal force", whose magnitude is the mass of the spinning object times the inwardly directed centripetal acceleration, or mv_θ^2/r, where v_θ is the tangential velocity of the ball, and r the length of the string.

For a fluid element (as opposed to a solid or liquid particle, which we will discuss later), the so-called "centrifugal force" is balanced by a force created by a gradient in the static pressure. This pressure gradient acting over the surface of the particle is the "string" tension in our spinning ball example mentioned above. Thus, this latter force acts toward the axis of rotation and keeps the element in its path. This is sketched in Fig. 2.1.2. Depending on our point of view[1], we could also say that this pressure force *gives rise to* the centripetal acceleration or "centrifugal force". As we shall see in Appendix 2.A the pressure in a swirling flow increases with the distance from the axis of rotation.

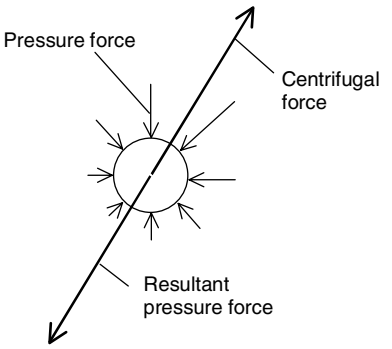

Fig. 2.1.2. Detail of a rotating fluid element in a rotating coordinate system, with the forces acting on it indicated

Now imagine first that the swirling fluid has an *infinite viscosity* (behaves like a solid body). Hence, no shearing motion exists between fluid layers at different radii. In this case fluid elements at all radial positions are forced to have the same angular velocity. The angular velocity, Ω, is measured in radians per unit of time, usually seconds, and therefore has units s^{-1}. It equals v_θ/r, with v_θ the tangential velocity, measured in m/s. Swirl with constant Ω is called 'forced vortex flow' or 'solid-body rotation':

$$v_\theta = \Omega r \tag{2.1.1}$$

This is the first ideal swirl flow.

In the other extreme, if the swirling fluid has *no viscosity*, the motion of a given fluid element is not influenced by the neighboring elements at smaller

[1] In principle, cause and effect cannot be identified in this type of flow

and larger radii. If we, in such a fluid, bring an element to a smaller radius, its tangential velocity will increase, since its moment-of-momentum (mass times tangential velocity times radius of rotation: $mv_\theta r$) will be conserved. We call a vortex where moment-of-momentum is conserved in this way, 'loss free', or 'frictionless'. In such a flow we have $rv_\theta = C$, with C a constant, so that:

$$v_\theta = \frac{C}{r}. \tag{2.1.2}$$

This is the second ideal swirl flow. We should point out that the quantities v_θ, Ω and r are vectors since they have both magnitude and direction. Here, however, we are only interested in their magnitudes and, for this reason, we dispense with the vectorial notation.

These two ideal flow patterns are derived from the fundamental equations of fluid mechanics in Appendix 2.A. This derivation is useful for a fuller understanding of the flow, but it is not essential for appreciating the material in this book as a whole.

A real fluid will have some finite viscosity, which will cause transfer of moment-of-momentum between layers at different radii. An additional transport of moment-of-momentum will be caused by any turbulence present, due to exchange of fluid elements between the layers.

A real swirling flow normally has a core of near solid-body rotation surrounded by a region of near loss-free rotation as sketched in Fig. 2.1.3. This is called a 'Rankine vortex'.

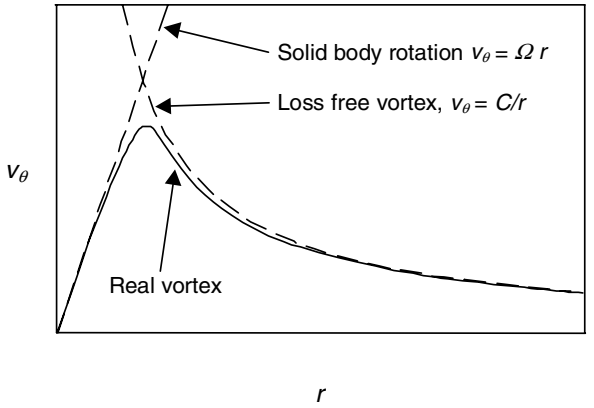

Fig. 2.1.3. Sketch showing the two ideal vortex flows, and the tangential velocity distribution in a real vortex

2.1.2 Static and Dynamic Pressure

The flow and pressure distribution within cyclones and swirl tubes is more easily understood if we make clear the relation between *static* and *dynamic*

pressures: p and $1/2\rho v^2$, respectively, with ρ the density. The well-known Bernoulli equation for steady flow of a frictionless, constant density fluid, which can be derived from the Navier-Stokes equations (Bird et al., 2002), states that:

$$\frac{p}{\rho} + gh + \frac{1}{2}v^2 = \text{constant along a streamline.} \tag{2.1.3}$$

In this equation, we recognize the static and dynamic pressures—the latter is often called the 'velocity head'—as the first and third terms on the left-hand side. They have been divided by the fluid density.

This equation shows that static and dynamic pressures can be interchanged in the flow field. In areas where the velocity is high, the static pressure will be low and *vice versa*. This is the principle used in many flow meters, for instance pitot tubes and venturi meters. It is especially important to appreciate this interdependence between static and dynamic pressure when dealing with swirling flows.

The left-hand side of Eq. (2.1.3) is sometimes called 'Bernoulli's trinomial'. The second term is unimportant relative to the two others when discussing gas cyclones and swirl tubes, since the fluid density is relatively low, and height differences not very large.

In an actual flow situation, the fluid is not frictionless. Frictional dissipation of mechanical energy will therefore cause Bernoulli's trinomial to decrease in the flow direction, *i.e.* the trinomial is no longer constant, but decreases along a streamline.

Frictionless flow is, nevertheless, a reasonably good approximation in the outer part of the swirl in a cyclone, Bernoulli's trinomial does not change very much there.

Friction is taken into account in the 'extended Bernoulli equation', sometimes called the 'frictional form of the Bernoulli equation' or the 'engineering Bernoulli equation' (Bird et al., 2002).

2.2 Particle Motion

We now look at the motion of a solid or liquid particle in a fluid, starting with a general discussion and focusing on the particle motion in swirling gas flows toward the end of the section.

In a gas cyclone or swirl tube, the particles of interest are almost always moving relative to the gas at their *terminal velocity*, and the terminal velocity of a given particle determines whether it will be captured or lost. This terminal velocity is exactly analogous to that of a particle settling in the earth's gravitational field, g, under steady-state conditions except that, for a cyclone, the radially directed centrifugal force, mv_θ^2/r replaces the gravitational one. This will be discussed in detail later.

We are therefore interested in calculating the particle terminal velocity in the swirling flow. We begin with the equation of motion of a particle in a fluid.

Applying Newton's law to a particle moving in a fluid, equating its mass times acceleration to the sum of the forces acting on it, we obtain

$$\begin{pmatrix}\text{mass}\\ \text{times}\\ \text{acceleration}\end{pmatrix} = \begin{pmatrix}\text{body}\\ \text{force}\end{pmatrix} + \begin{pmatrix}\text{fluid}\\ \text{drag}\end{pmatrix} + \begin{pmatrix}\text{unsteady}\\ \text{force}\\ \text{terms}\end{pmatrix}$$

where the body force is normally due to a gravitational field and/or a centrifugal force. Following our earlier discussion, in using the term 'centrifugal force' we are implying that the above force balance is being performed in a reference coordinate systems that is rotating with the particle. The fluid drag is the drag acting on the particle if it moves with a steady velocity relative to the fluid, while the unsteady terms account for the effects of acceleration of the particle relative to the fluid. With appropriate substitution into the above expression the general equation of motion for a particle in a Newtonian fluid becomes Clift et al. (2005):

$$\begin{aligned}\left(\frac{\pi x^3}{6}\right)\rho_p\frac{d\mathbf{U}'}{dt} = \left(\frac{\pi x^3}{6}\right)(\rho_p-\rho)\,\mathbf{a} - C_D\left(\frac{1}{2}\rho\mathbf{U}'\,\|\mathbf{U}'\|\right)\left(\frac{\pi x^2}{4}\right)\\ -\begin{pmatrix}\text{added}\\ \text{mass}\end{pmatrix} - \begin{pmatrix}\text{Basset}\\ \text{term}\end{pmatrix}\end{aligned} \tag{2.2.1}$$

where $\mathbf{U}$' is the particle velocity vector relative to the gas and has cylindrical coordinate components (U_r', U_θ', U_z'); $\mathbf{a}$ is the acceleration vector of an external force field (equal to $\mathbf{g}$ for a gravitational field); ρ_p and ρ are the particle and fluid densities, respectively, and t is time. $\|\cdot\|$ denotes the absolute value (the length) of the vector. Throughout this book we shall represent the particle diameter with the symbol x.

The first term on the right-hand side represents the body force, and the second term the drag $\mathbf{F}_D$ acting on the particle when the flow around it is fully developed, C_D is the drag coefficient.

The two last terms on the right-hand side of (2.2.1) relate to fast, unsteady motion. The added mass term accounts for the fact that when accelerating a particle from rest, the surrounding fluid must also be accelerated. This appears to 'add mass' to the particle. The Basset integral says that the drag will, by rapidly changing motion, depend not only on its instantaneous velocity relative to the fluid, but also on the previous motion since the fluid flow pattern may not have had time to adjust, due to the fluid inertia. These two terms are zero in steady movement.

Clift et al. (2005) showed that ignoring these two unsteady terms (in particular the Basset integral) can lead to errors for a rapidly changing motion in liquid. Fortunately, in the case of gas cyclones we can safely ignore them, even when calculating the rapid, small-scale turbulent motion, since the gas inertia is relatively small. In fact, it turns out that this is true even for the case

of hydrocyclones, where the carrier fluid is a liquid rather than a gas. Also practical plant experience with their design and operation indicates that it is not necessary to include either the added mass or the Basset terms appearing on the right-hand side of (2.2.1).

The second term on the right-hand side in (2.2.1) can be simplified. In gas cyclones we are concerned with small particles (small x) moving in a fluid of low density (small ρ), so that the 'particle Reynolds number':

$$Re_p \equiv \frac{\rho \, \|\mathbf{U}'\| \, x}{\mu} \tag{2.2.2}$$

is relatively low, in spite of the relatively low viscosity μ. For low Re_p, the equations of motion—Eqs. (2.A.1) and (2.A.2) in Appendix 2.A—for the fluid moving around the particle can be solved, and $\mathbf{F}_D$ calculated. If there is no slip between fluid and particle surface (that is: the fluid velocity is equal to the velocity of the surface at the surface), the result is 'Stokes drag law' (Bird et al., 2002):

$$\mathbf{F}_D = -3\pi x \mu \mathbf{U}'. \tag{2.2.3}$$

Comparing this with the expression for the fluid drag term of Eq. (2.2.1) and, by using Eq. (2.2.2), we see that $C_D = 24/Re_p$, which is the particle's drag coefficient under conditions of laminar flow.

These simplifications produce the following equation of motion for the particle:

$$\left(\frac{\pi x^3}{6}\right) \rho_p \frac{d\mathbf{U}'}{dt} = -3\pi x \mu \mathbf{U}' + \left(\frac{\pi x^3}{6}\right) (\rho_p - \rho) \, \mathbf{a}. \tag{2.2.4}$$

If we solve this differential equation in one direction indicated by the index i (replacing the vectors with their components in the i-direction, where i is a Cartesian coordinate), assuming $U_i' = U_{i,0}'$ at $t = 0$, the particle velocity relative to the gas becomes:

$$\begin{aligned} U_i' = \frac{x^2 \, (\rho_p - \rho) \;\; a_i}{18\mu} \left(1 - \exp\left[-\frac{18\mu t}{x^2 \rho_p}\right]\right) + U_{i,0}' \exp\left[-\frac{18\mu t}{x^2 \rho_p}\right] = \\ \left(\frac{\rho_p - \rho}{\rho_p}\right) \tau a_i \left(1 - e^{-t/\tau}\right) + U_{i,0}' e^{-t/\tau} \end{aligned} \tag{2.2.5}$$

where τ is called the 'particle relaxation time':

$$\tau \equiv \frac{x^2 \rho_p}{18\mu}. \tag{2.2.6}$$

For large t the exponential terms go to zero, and the particle reaches its terminal velocity. If $\rho_p \gg \rho$, as it is in gas cyclones, the terminal velocity is (dropping the index i):

$$U_t' = U_{Stk}' = \tau a = \frac{x^2 \rho_p}{18\mu} a \text{ for } \rho_p \gg \rho \tag{2.2.7}$$

where the subscript Stk signifies that this is the 'Stokes' velocity', *i.e.* the terminal velocity of a particle when Stokes' drag law applies. Small particles in gas cyclones reach their terminal velocity quickly. We can see this from Eq. (2.2.5): τ is small for small x (in the cases we are considering it is of the order 10^{-3} s), so the exponential term goes to zero quickly. We may put this into perspective for commercial cyclones for which the particle residence time within the cyclone typically lies within the range of about 50 milliseconds (ms) for small, high velocity cyclones to 1 to 2 seconds for large industrial units such as those in use in large coal conversion units or fluid catalytic cracking (FCC) units. This means that we can ignore the unsteady part of Eq. (2.2.5), even for the rapid, small-scale velocity fluctuations caused by the gas turbulence, and assume the particle will always be at its terminal velocity relative to the gas.

In Fig. 2.2.1 velocity is plotted against time for a 10 μm particle of density 2700 kg/m^3 (a typical density, close to, for instance, those of chalk or sand) dropped in air in the field of gravity. The terminal velocity and τ are indicated. The particle approaches its terminal velocity within a couple of milliseconds.

As mentioned, Stokes' drag law is valid for low particle Reynolds numbers. Another requirement for Stokes' law to apply is that the surrounding fluid can be *considered a continuous medium*. This is not so for very small (sub-micron size) particles in gases, especially for sub-micron particles feeding cyclones operating under high vacuum conditions. In some applications, for example, vacuum assists with the drying of moist or solvent-laden incoming solids. Here we have to take into account the fact that the gas consists of individual molecules. This has two effects:

1. Collisions with gas molecules give rise to a *fluctuating particle motion* ('Brownian motion'). This can be neglected compared to any large-scale turbulent particle dispersion.
2. A *slip* takes place between the gas and the particle as the free space between the gas molecules becomes comparable to the particle size. This is accounted for in the drag law by multiplying the terminal particle velocity calculated from Stokes' law, U'_{Stk}, by the 'Cunningham correction factor', C_c (Allen, 1990):

$$U' = U'_{Stk} C_c = U'_{Stk} \left(1 + \frac{2\lambda}{x}\right) \tag{2.2.8}$$

where λ is the molecular mean free path. This correction factor can be viewed also as a correction to the viscosity term appearing in the denominator of (2.2.7). Thus, the 'effective' viscosity becomes the gas viscosity times the Cunningham correction factor. It has the effect of always decreasing the effective viscosity and, hence, the drag that all particles—not just the the sub-micron particles—experience.

We now turn our attention to the behavior of a particle in a swirling flow. Here, we can apply some of what we have previously discussed about

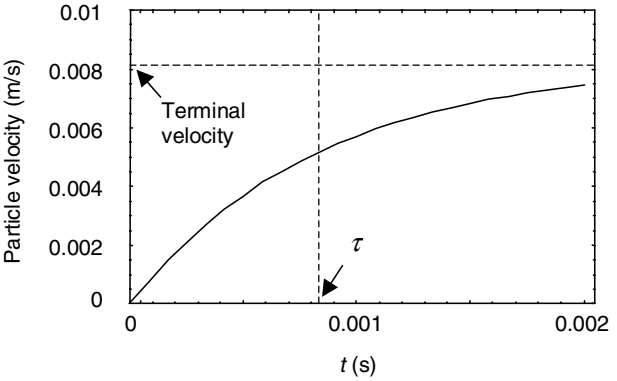

Fig. 2.2.1. The velocity of a particle (x=10 μm, ρ_p=2700 kg/m^3) dropped in air. Calculation is according to Eq. (2.2.5)

a rotating fluid element to a solid or liquid particle. One difference, though, is that the force arising from the pressure gradient in the fluid, which in this context is akin to the buoyancy force acting in a gravitational field, will not keep the particle in its path unless it has the same density as the fluid. In gas cyclones the particle density is much higher than that of the carrier gas, so the 'buoyancy' is low and the particle will move radially outward in the vortex. This, then, becomes and defines the primary mechanism for separation of particles within a cyclone. As we shall see, we can even ignore the buoyancy when calculating the particle's velocity, so that the only significant force opposing the particle's outward radial motion is a drag force.

If the particle moves with the same tangential velocity as the gas, and we choose a coordinate system rotating with the particle, we can consider the centrifugal force as analogous to the force of gravity. This allows us to replace the acceleration a in Eq. (2.2.5) with the magnitude of the centripetal acceleration: v_θ^2/r, and we can say that a centrifugal force equal to $m_p v_\theta^2/r$, where m_p is the mass of the particle, acts on the particle (compare with Eq. (2.A.12) in Appendix 2.A).

When $\rho_p \gg \rho$, the particle will thus be centrifuged outward (see Fig. 2.2.2), resisted by drag, and will move with a terminal velocity relative to the gas of:

$$U_r' = (U_r - v_r) = \frac{x^2 \rho_p}{18\mu}\left(\frac{v_\theta^2}{r}\right) = \tau\left(\frac{v_\theta^2}{r}\right) \text{ for } \rho_p \gg \rho. \tag{2.2.9}$$

This outward movement of the particle is, as mentioned, the principle of separation in all centrifugal separators, both for dedusting and demisting.

In addition to its mean movement, a particle in a cyclone will also have a small scale, fluctuating motion in response to the local turbulence in the gas. This is more severe for smaller particles, which are most affected by the fluctuations in the gas velocity. The turbulent motion gives rise to some dispersion and mixing of the particles.

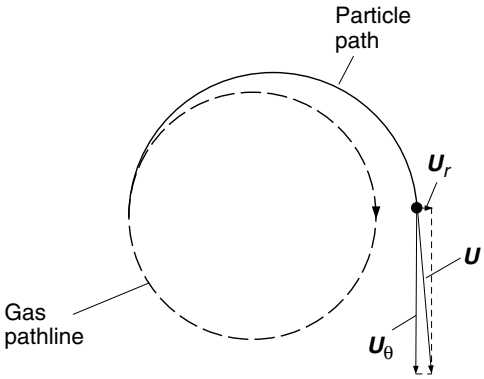

Fig. 2.2.2. Sketch showing gas and particle pathlines in a swirling flow field where the gas has no radial velocity component, that is: $v_r = 0$ in Eq. (2.2.9). The vectors represent the radial, tangential and resultant particle velocity components

2.3 Particle Size

2.3.1 Definitions of Particle Size

The motion of a particle, and its separation in a cyclone, obviously depends on its size, amongst other important factors, such as its density, shape, and tangential velocity. By the term 'size' we normally mean the diameter. The particle diameter can be defined in different ways, and one should be aware which one is used in a given context. Clift et al. (2005) and Allen (1990) review this issue. We mention here the definitions that are most relevant for cyclones.

The 'volume equivalent' diameter is the *diameter of a sphere with the same volume as the actual particle*[2]. The 'surface equivalent' diameter is the *diameter of a sphere with the same surface area as the actual particle*. The 'surface/volume diameter' is the *diameter of a particle with the same surface-to-volume ratio as the actual particle*.

To illustrate this, a cylindrical particle with height $2L$ and diameter L is shown in Fig. 2.3.1, together with its equivalent spheres.

Very central to cyclone technology is the 'dynamically equivalent' particle diameter. This is the *diameter of an equi-dense sphere that has the same terminal velocity as the actual particle*. Calculating this can be difficult in the range of intermediate Reynolds numbers, or when the Cunningham correction is significant. In the region where Stokes drag law applies, we call it the 'Stokesian' diameter.

[2] If all the particles are of the same density, then the volume equivalent diameter is the same as the mass equivalent diameter, since their mass is then proportional to their volume.

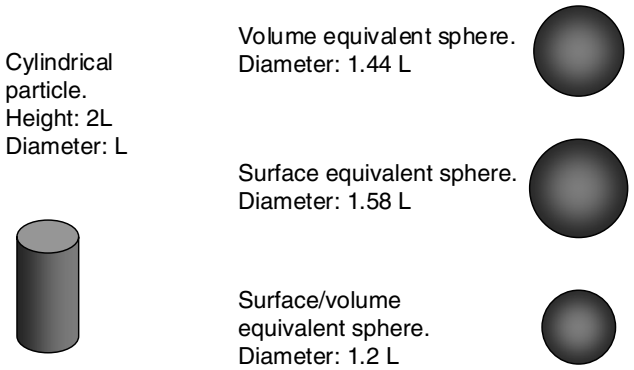

Fig. 2.3.1. Sketch of a cylindrical particle with the different equivalent spheres

A similar measure, which is widely used in aerosol science, is the 'aerodynamic particle size'. This is the *diameter of a sphere of density 1000 kg/m*^{3} *that has the same terminal velocity as the actual particle in air at normal temperature and pressure in a gravity field.*

Figure 2.3.2 from Kaye (1995) shows silhouettes of dynamically equivalent particles. The more nonspherical the actual particle, the larger it needs to be in order for it to settle with the same terminal velocity. The spheres to the right are Stokes diameters, those to the left aerodynamic diameters. Since uranium dioxide is far denser than 1000 kg/m^3, the two diameters differ the most for this type of particle.

2.3.2 Particle Size Distribution

The particle size distribution of a given dust or mist can be reported as a number, length, surface, volume or mass (weight) distribution. Figure 2.3.3 shows number and volume distribution curves for a sample powder. The curves in the figure are *density curves*: the function values $f(x)$ represent *the fraction of particles in a given interval divided by the width of that interval.* The definition of the number density distribution $f_N(x)$ is thus:

$f_N(x)dx$ = the number fraction of particles with a diameter between $x - 1/2\ dx$ and $x + 1/2\ dx$,

and the definition of the volume density distribution $f_V(x)$ is:

$f_V(x)dx$ = the volume fraction of particles with a diameter between $x - 1/2\ dx$ and $x + 1/2\ dx$.

Since the particle volume is proportional to x^3, the larger particles contribute much more to the volume distribution than to the number distribution. This can be seen in the shapes of the curves in Fig. 2.3.3. The larger particles contribute negligibly to the number distribution, which appears to go

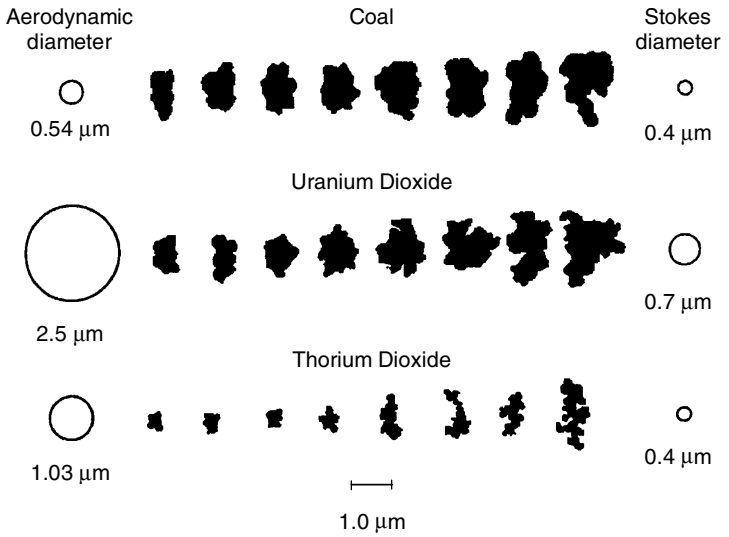

Fig. 2.3.2. Silhouettes of several different particle types along with their equivalent aerodynamic and Stokesian diameters from Kaye (1995)

to zero, while they contribute substantially to the volume distribution. The same holds true for the mass or weight distribution. For this reason it is also difficult to obtain a statistically satisfactory volume distribution from sizing methods based on particle counting if the particle size distribution is wide (many small particles need to be counted for each large one).

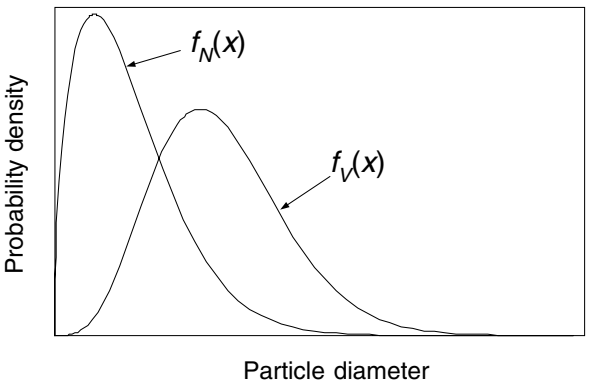

Fig. 2.3.3. Number and volume density distributions for a sample powder

If one of the distributions is known, the others can be calculated; at least this is the case if one assumes the particles to be spherical (Allen, 1990). For instance, we can calculate the volume density distribution from the number density distribution. Since the number fraction of particles in the diameter interval: $x - 1/2\ dx$ and $x + 1/2\ dx$ is $f_N(x)dx$, then:

$$f_V\,(x) \propto \frac{\pi x^3}{6} f_N\,(x)\,dx. \tag{2.3.1}$$

We have to choose the proportionality constant so that the area under our volume density distribution becomes unity:

$$f_V\,(x)\ \mathrm{d}x = \frac{\frac{\pi x^3}{6} f_N\,(x)\ dx}{\int\limits_0^\infty \frac{\pi x^3}{6} f_N\,(x)\ dx}. \tag{2.3.2}$$

In addition to density distributions, a very widely used method of reporting a particle size distribution is through the use of its 'cumulative undersize distribution' $F(x)$, defined as *the fraction of particles with a diameter less than* x. $F(x)$ is related to the density function $f(x)$ by:

$$F\,(x) = \int\limits_0^x f\,(z)\,dz, \qquad f\,(x)\,dx = dF\,(x) \tag{2.3.3}$$

where we have used z as the dummy variable of integration.

In Fig. 2.3.4 the cumulative undersize distributions corresponding to the density functions in Fig. 2.3.3 are shown.

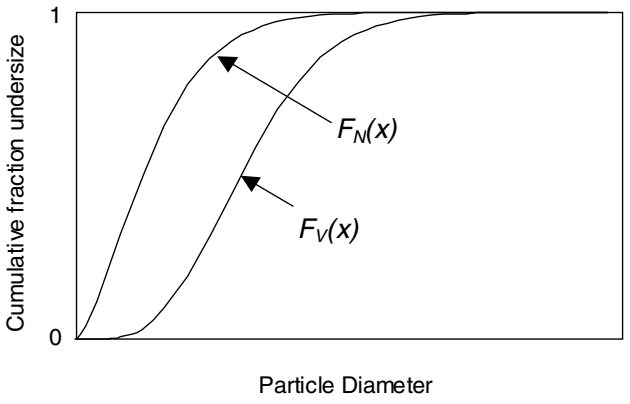

Fig. 2.3.4. Cumulative number and volume distributions for the powder in Fig. 2.3.3

Throughout this book, we shall be using the volume distributions and, in order to simplify the notation, we drop the subscript V from now on. In practice, one frequently encounters the terms 'mass' or 'weight' distributions such

as that obtained from sieve analysis. It is important to recall that, irrespective of the way in which the particle sizes are measured or reported, if the density of the particles comprising the distribution does not change as a function of particle size, then the particles' mass and weight distributions are identical to their volume distribution. This is so because the volume of any one particle or fraction of particles is directly proportional to its mass or weight if its density remains constant.

A number of *model distribution functions* exist, some of which fit the size distributions of many powders quite well. The model functions used most frequently are the 'normal' (or 'Gaussian') distribution, the 'log-normal' distribution and the 'Rosin-Rammler' distribution (Allen, 1990). These are given in Appendix 2.B for reference. The latter two can be fitted particularly well to the volume distributions of a wide range of powders. The Rosin-Rammler distribution was used to produce Figures 2.3.3 and 2.3.4.

It should be added, however, that it is generally not necessary or even necessarily desirable to represent a particle distribution by 'fitting' it to any particular distribution function, *a priori*. Computer programs for designing and evaluating cyclone performance normally utilize the 'raw' particle size distribution data (often in cumulative form) in their internal computations. This technique eliminates any errors pertaining to any differences that may exist between the mathematical 'fit' of the data and the actual data that is being fitted. Often it is observed that some distribution function does 'fit' the majority of the measured distribution data but may, for example, fail to fit the smallest particle size fraction. Under such conditions, if it were important to know about the collection or losses of the 'fines', one would not want to use such a distribution model in practice. Instead, the actual measured distribution data would be utilized for cyclone simulation purposes.

Finally, we consider the mean and spread of a particle size distribution. The mean size can be defined in different ways, depending on which property of the powder is important. A review of this can be found in Allen (1990). In this book, we use the volume distribution, and the 'volume mean' particle size, which is equivalent to the mass mean particle size, is defined as the first moment of the volume distribution around zero:

$$\langle x \rangle = \int_0^\infty x f\,(x)\,dx. \tag{2.3.4}$$

Other characteristic sizes are: the 'median size', x_{med}, defined as the size at which $F(x)$=0.5, and the 'mode', defined as the size where $f(x)$ takes its maximum value.

We note here that the mean and the median sizes are often close in practice, and that, of these two, the median size is much easier to determine by reading directly off the cumulative size distribution. The median is therefore often taken as the 'mean' particle size for a given powder in practice, while in the model distribution functions the mean is that defined in Eq. (2.3.4). We shall

follow common practice by using the median diameter as a measure of the 'mean' particle size in this book, we will refer to it as the '(mass) average' or the 'median' size, but always use the symbol x_{med} when we mean the median.

We may also characterize the particle size distribution through a parameter that characterizes its spread, σ, the square of which is the second moment around the mean :

$$\sigma^2 = \int_0^\infty (x - \langle x \rangle)^2 \, f(x) \, dx. \tag{2.3.5}$$

The above parameters are very useful to characterize powders with only two parameters, for instance for controlled laboratory experiments in which results need to be related to the particle size distribution. However, they rarely enter the considerations in engineering design. Those whose job it is to design and/or troubleshoot cyclone systems in industry are generally faced with designing or evaluating the performance based on what the upstream process delivers, using a measured particle size distribution as a basis for calculations.

2.4 Particle Density

In addition to size, one more particle property plays an important role in determining particle motion in fluids, and therefore also in cyclones: the particle density.

If the particle is a nonporous solid, its density is unequivocal, but if it is porous, we need to distinguish the *density of the solid material* comprising the particle (often called the 'skeletal' density) and the *overall* or *effective* particle density, including both the solid material and the pores. The latter is often called the 'envelope density' or 'the density in a Stokes-settling sense'. In practice, it is the envelope density that determines the behavior of the particle in a fluid, and is therefore the density we wish to determine.

Particle density is often determined by some sort of *pycnometry*. If a liquid is used as the pycnometric fluid, this is mostly done in a so-called 'density bottle', where the masses are determined of:

- the empty bottle, m_1
- the bottle containing the powder sample only, m_2
- the bottle containing the powder sample filled with the liquid, m_3
- the bottle filled with the liquid only, m_4

The mass of the powder sample is given by $(m_2 - m_1)$, while its volume is given by $[(m_4 - m_3) - (m_2 - m_1)]/\rho_l$, where ρ_l is the density of the pycnometric liquid. The density can then be found by dividing the mass of the sample with its volume.

If the pycnometric fluid penetrates into the pores of the particles, the density determined will be the skeletal density. In order to find the envelope

density, some pycnometric fluid has to be found that will penetrate the interstitial space between the particles, but not the pores within the particles. Mercury can be used for this, whereby the mercury is added under vacuum, so that it will penetrate the interstices between the particles properly. If one is interested in the skeletal density, and the pores in the particles are fine, air can be used as the pycnometric fluid in specially designed equipment.

We note that if, during particle sizing, the dynamically equivalent particle size is determined, the problem of determining the appropriate particle density is solved already.

We have now reviewed the most essential topics necessary for an appreciation of the basic working of gas cyclones. We shall make frequent use of these developments in the subsequent chapters, and we shall look at models for cyclone performance based on the above-mentioned basic principles. We hasten to add that a cyclone design based on these principles is only a starting point. Many key issues for practical cyclone design and operation are of a highly complex nature and cannot be described using the basic ideas of single particles in swirling flows alone. Examples are the effect of inlet solids loading on cyclone separation efficiency, the 'natural turning point' of the vortex, the phenomenon of 'hopper crossflow', hopper venting, and the issue of cyclone erosion. We will be discussing these and some related issues later on.

2.A Ideal Vortex Laws from the Navier-Stokes Equations

In this appendix, we will derive the essential equations for swirling flow from the basic equations of fluid mechanics: the Navier-Stokes equations. The Navier-Stokes equations are derived in most textbooks on fluid mechanics, for instance Bird et al. (2002).

The 'equation of continuity' states that material can neither be generated nor destroyed. For an incompressible fluid the equation is:

$$\nabla \cdot \mathbf{v} = 0 \tag{2.A.1}$$

with $\mathbf{v}$ the fluid velocity vector.

The 'momentum conservation' equation states Newton's law for a fluid element: its mass times acceleration equals the sum of the forces acting on it:

$$\rho \frac{D\mathbf{v}}{Dt} = -\nabla p - \nabla \cdot \boldsymbol{\tau} + \rho \mathbf{g} \tag{2.A.2}$$

where ρ is the density, p the pressure and $\mathbf{g}$ the gravitational acceleration. $\boldsymbol{\tau}$ is the deviatoric stress tensor (see below). The terms in (2.A.2) represent from left to right:

- The mass times acceleration per unit volume. This is the density multiplied by the absolute (or 'material') derivative of the velocity. The material

derivative D/Dt gives the acceleration of a fluid element in a Eulerian[3] frame of reference.

- The net force due to normal stresses per unit volume.
- The net force due to shear stresses per unit volume. $\boldsymbol{\tau}$ is the 'deviatoric' stress tensor, meaning that the pressure has been subtracted from the total stress tensor, so that the sum of the three diagonal elements is zero. This essentially leaves us with the shear stresses.
- The gravitational force per unit volume.

Equation (2.A.2) can be expressed in terms of its coordinate components. For cyclones, it is convenient to use a cylindrical coordinate system (r, θ, z), with the z-axis along the cyclone axis. Writing out the θ-component of Eq. (2.A.2) gives (Bird et al., 2002):

$$\begin{aligned} &\rho\left(\frac{\partial v_\theta}{\partial t}+v_r\frac{\partial v_\theta}{\partial r}+\frac{v_\theta}{r}\frac{\partial v_\theta}{\partial \theta}+\frac{v_r v_\theta}{r}+v_z\frac{\partial v_\theta}{\partial z}\right)= \\ &\quad \text{I} \qquad \text{II} \qquad \text{III} \qquad \text{IV} \qquad \text{V} \\ &-\frac{1}{r}\frac{\partial p}{\partial \theta}-\left(\frac{1}{r^2}\frac{\partial}{\partial r}\left(r^2\tau_{r\theta}\right)+\frac{1}{r}\frac{\partial \tau_{\theta\theta}}{\partial \theta}+\frac{\partial \tau_{\theta z}}{\partial z}\right)+\rho g_z \\ &\quad \text{VI} \qquad\qquad \text{VII} \qquad\qquad \text{VIII} \qquad \text{IX} \qquad \text{X} \end{aligned} \tag{2.A.3}$$

In the shear stress components τ, the first index indicates the plane on which the stress acts, and the second its direction.

This complicated looking equation can be simplified to give useful information about swirling flow. In steady, axisymmetrical vortex flow with negligible velocity in the r and the z-directions, the terms listed in Table 2.A.1 can be eliminated[4].

This leaves only term VII, and, since $1/r^2 \neq 0$:

$$\frac{\partial}{\partial r}\left(r^2\tau_{r\theta}\right)=0. \tag{2.A.4}$$

And, because the derivative of the quantity in parenthesis is equal to zero, the quantity itself is a constant, which we call C_1:

[3] In a 'Eulerian' frame of reference time derivatives are stated in a stationary frame. Therefore, in order to write the time derivative of a property φ for a fluid element, we have to include both the *local* derivative (the rate of change of φ at the stationary point) and the *convective* derivative (the rate of change of φ in the direction in which the fluid element is moving). The Eulerian frame is in contrast to a 'Lagrangian' frame where we state time derivatives following a fluid element (or a particle).

[4] We note that this is an idealized flow pattern, if the radial velocity in a cyclone were zero, the cyclone would not function since, then none of the entering fluid could make its way to the inner core, and, hence, out the vortex finder.

Table 2.A.1. Eliminating terms in Eq. (2.A.3)

Term eliminated	Reason
I	steady flow, no change with time
II and IV	no radial velocity
III and VI and VIII	no gradients in the θ-direction (axisymmetric flow)
V and IX	no gradients in the z-direction

$$\tau_{r\theta} = \frac{C_1}{r^2}. \tag{2.A.5}$$

The next step is to relate the shear stress $\tau_{r\theta}$ to the velocity field. The simplest way of doing this is to assume a constant Newtonian viscosity, μ. Then the expression for $\tau_{r\theta}$ becomes (Bird et al., 2002):

$$\tau_{r\theta} = -\mu \left[r \frac{\partial}{\partial r} \left(\frac{v_\theta}{r} \right) + \frac{1}{r} \frac{\partial v_r}{\partial \theta} \right]. \tag{2.A.6}$$

Here the second term on the right-hand side can be eliminated if there are no gradients in the θ direction. Doing this and substituting in the first part of (2.A.4) gives:

$$\frac{\partial}{\partial r} \left[r^3 \left(-\mu \right) \frac{\partial}{\partial r} \left(\frac{v_\theta}{r} \right) \right] = 0 \;\Rightarrow\; \frac{\partial}{\partial r} \left[r^3 \frac{\partial}{\partial r} \left(\frac{v_\theta}{r} \right) \right] = 0 \tag{2.A.7}$$

- since μ is independent of r. The first equation above only implies the second if $\mu \neq 0$. If $\mu = 0$, *any* v_θ profile will satisfy the first part.

The solution to (2.A.7) is:

$$v_\theta = C_1 r + \frac{C_2}{r}. \tag{2.A.8}$$

If we require that v_θ does not become infinite at $r = 0$, C_2 has to be zero, giving the well known equation for a 'forced vortex' or 'solid-body rotation':

$$v_\theta = C_1 r = \Omega r. \tag{2.A.9}$$

This is one ideal vortex motion, where, as mentioned in the main text, the angular velocity Ω is constant.

Another is the 'loss-free' vortex, which is a vortex motion in a fluid with a viscosity of zero. We saw that if $\mu = 0$, any radial v_θ profile would satisfy the first part of (2.A.7) under the assumptions. If we allow a radial velocity, so that fluid elements can move radially in the vortex, this is no longer so. Doing this and setting the viscosity and, therefore, the shear stress $\tau_{r\theta}$ equal to zero, we see that terms II and IV re-emerge, and that term VII of Eq. (2.A.3) is eliminated. This leads to:

$$v_r \left(\frac{\partial v_\theta}{\partial r} + \frac{v_\theta}{r} \right) = 0, \tag{2.A.10}$$

which has the solution:

$$v_\theta = \frac{C}{r} \tag{2.A.11}$$

with C an integration constant. This is the familiar equation for the tangential velocity distribution in a loss-free vortex. In this type of flow the moment-of-momentum of fluid elements is constant in the radial direction.

Note that we could not have derived (2.1.2) by letting C_1 equal zero in (2.A.8) since the viscosity μ was assumed to be nonzero to arrive at (2.A.8) in the first place.

In the same way that (2.A.7) was derived from the θ-component equation of (2.A.2), two other differential equations for the flow field in a vortex motion can be derived from the r- and the z-component equations. They are, respectively:

$$\frac{\partial p}{\partial r} = \rho \frac{v_\theta^2}{r} \tag{2.A.12}$$

and:

$$\frac{\partial p}{\partial z} = \rho g_z. \tag{2.A.13}$$

Equation (2.A.12) is the balance between the centrifugal force (or the mass times the centripetal acceleration) and the pressure force, all on a per unit volume basis. It shows, as we also saw on basis of heuristic arguments in the main text, that the pressure in a vortex flow increases towards the periphery and more so the stronger the tangential velocity. The radial pressure distribution can be obtained by integrating the right-hand side over r.

Equation (2.A.13) simply says that the axial pressure distribution is the hydrostatic pressure, which in gas cyclones is not very interesting, since the fluid density is low.

This completes the derivation of the basic equations for swirling flows from the Navier-Stokes equations. When deriving flow equations, particularly in cylindrical coordinates, this method is safer than using heuristic arguments.

2.B Common Model Functions for Particle Size Distributions

In this appendix, the most frequently used particle size distributions are given for the reader's reference. If you are a researcher interested in these distributions, it is very instructive to program and graph these models using a mathematics package (for instance Mathematica, or a freeware program called MathGV), and have a look at how the shapes of the distributions change with the parameters.

When studying cyclone performance, or any issue in powder technology, it can be advantageous to fit models to the experimentally determined particle size distributions obtained from laboratory measurements. In this way the particle size distribution can be characterized using only two parameters: the

mean size and the spread. Model functions may also make it possible to make up for incomplete information about size distributions, as long as one is aware of the dangers of doing so pointed out in Appendix 3.A.

2.B.1 The Normal Distribution

The density function for the normal distribution is:

$$f(x) = \frac{1}{\sigma\sqrt{2\pi}} \exp\left(-\frac{(x - \langle x\rangle)^2}{2\sigma^2}\right). \tag{2.B.1}$$

To obtain the cumulative undersize function, we must integrate this:

$$F(x) = \int_{-\infty}^{x} \frac{1}{\sigma\sqrt{2\pi}} \exp\left(-\frac{(z - \langle z\rangle)^2}{2\sigma^2}\right) dz. \tag{2.B.2}$$

For this distribution, the mean particle size $\langle x\rangle$, the median, and the mode are all equal, and the spread is σ. In this purely mathematical distribution, x can take on negative values, which is not physically meaningful.

2.B.2 The Log-Normal Distribution

The log-normal distribution is defined as: *the distribution of a variable, the natural log of which is normally distributed*. Thus, for the distribution of the natural log of particle diameters we get:

$$f(\ln x) = \frac{dF'(\ln x)}{d\ln x} = \frac{1}{\sigma\sqrt{2\pi}} \exp\left(-\frac{(\ln x - \langle \ln x\rangle)^2}{2\sigma^2}\right). \tag{2.B.3}$$

To obtain the distribution of the particle diameter itself rather than that of its logarithm, we note that $F'(\ln x)$, the fraction of particles with the logarithm of their diameter less than $\ln x$, is the same as $F(x)$, the fraction of particles with diameter less than x. Thus:

$$F'(\ln x) = \int_{-\infty}^{\ln x} \frac{1}{\sigma\sqrt{2\pi}} \exp\left(-\frac{(\ln z - \langle \ln z\rangle)^2}{2\sigma^2}\right) d\ln z = F(x). \tag{2.B.4}$$

In order to write $F(x)$ in terms of x rather than $\ln x$, we change the variable of integration:

$$F(x) = \int_{0}^{x} \frac{1}{\sigma\sqrt{2\pi}} \exp\left(-\frac{(\ln z - \langle \ln z\rangle)^2}{2\sigma^2}\right) \frac{1}{z} dz, \tag{2.B.5}$$

which shows that the density function of x for the log-normal distribution is:

$$f(x) = \frac{1}{x}\frac{1}{\sigma\sqrt{2\pi}}\exp\left(-\frac{(\ln x - \langle \ln x \rangle)^2}{2\sigma^2}\right). \tag{2.B.6}$$

One should be most careful when converting between cumulative and density distributions for the log-normal distribution.

The log-normal distribution is skewed with a long tail at large particle sizes. It fits the volume distributions of many powders very well. Because it is skewed, the mode, the median and the mean particle sizes are all different.

2.B.3 The Rosin-Rammler Distribution

The Rosin-Rammler distribution is one that applies specifically to dusts generated by crushing. The density function is:

$$f(x) = nkx^{n-1}\exp(-kx^n). \tag{2.B.7}$$

The shape of $f(x)$ depends on the constants n and k. Integrating to find $F(x)$ and adding a constant to make it start at the origin gives:

$$F(x) = 1 - \exp(-kx^n). \tag{2.B.8}$$

For this distribution the mode, median and mean sizes are different. Using Eqs. (2.3.4) and (2.B.7) the mean particle size becomes:

$$\langle x \rangle = k^{-\frac{1}{n}}\Gamma\left(\frac{1}{n} + 1\right) \tag{2.B.9}$$

where Γ is the Gamma function.

Mathematics packages, such as Mathematica, Matlab or Mathcad and MathGV make it easy to fit these model distributions to sets of experimental data. It is often helpful to do so, since this allows the particle size distribution to be described by only two parameters. This also has its limitations, though. We shall come across one in Appendix 3.A.

3

How Cyclones Work

As mentioned in Chap. 1, cyclones work as a result of the centrifugal forces acting on the particles suspended in the swirling gas stream. This causes the particles, which are denser than the gas, to move outward to the cyclone wall, along which they are transported downward to the dust exit. The cleaned gas leaves near the centerline, in a reverse-flow cyclone through the roof. In a 'once-through' or 'flow-through' cyclone, the cleaned gas exits out the bottom[1].

In this chapter we take a first look at the flow of gas and particles in cyclones. We also introduce the two key performance indicators for cyclones: their separation efficiency and their pressure drop.

3.1 Flow in Cyclones

The gas flow pattern in cyclones is fairly well known from experimental evidence collected over decades. For particle trajectories, on the other hand, very little experimental data are available, so for this we shall resort to computational fluid dynamics (CFD) simulations.

3.1.1 Gas Flow Pattern

The velocity field in cyclones has been measured using hot-wire anemometers, pitot tubes and, recently, laser-Doppler anemometry (LDA). See Chap. 10 for more information about these techniques.

[1] In some configurations, cyclones may be oriented at an angle to true vertical and, in the limit, may be oriented horizontally. Such configurations do not violate the rules and equations governing vertical cyclones except in certain 'highly loaded' cyclones, wherein the force of gravity competes with the radially-directed centrifugal force, which the particles experience. In such latter configurations the designer must be especially careful in scaling-up. We shall return to this topic in a later chapter.

Figure 3.1.1 shows a sketch of a standard reverse-flow cylinder-on-cone gas cyclone with a tangential entry. The global flow pattern is indicated. A swirling motion is created in the separation space by the tangential injection of the gas. The gas flows downward in the outer part of the swirl (the 'outer vortex') and upward in the center (the 'inner vortex'). The downward flow in the outer part of the cyclone is critically important as it, and not gravity, is the dominant mechanism for transporting collected solids (those at the wall) out the bottom of the cyclone. In vertically oriented cyclones, gravity will assist but its influence is important only for cyclones operating at high solids-loaded conditions, for which 'mass loading' effects are important. More on this later. At the same time there is a radial flow from the outer vortex to the inner one, this is distributed—though not uniformly with height—over the length of the body under the vortex finder.

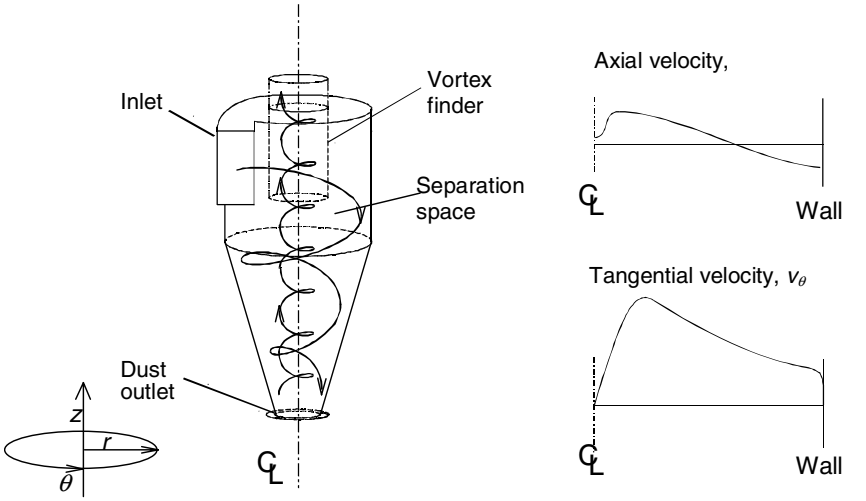

Fig. 3.1.1. Sketch of a tangential-inlet cyclone with the flow pattern indicated. The coordinate directions are shown, normally the z-axis coincides with the axis of the cyclone or swirl tube. To the right, the radial distributions of the axial and tangential gas velocity components are sketched. It is understood that the 'dust outlet' may be the 'liquid' outlet for the case of a demisting cyclone

To the right in Fig. 3.1.1 the radial profiles of the axial and tangential gas velocity components are sketched. The former shows the outer region of downwardly directed axial flow and the inner one of upwardly directed flow. As mentioned, the downward velocity at the wall is the primary mechanism for particle transport out the dust outlet. The axial velocity often shows a dip around the center line. Sometimes this is so severe that the flow there is downwardly directed. The tangential velocity profile resembles a Rankine vortex: a near loss-free swirl surrounding a core of near solid-body rotation.

We do not know enough about the radial velocity to graph it. It is generally much smaller than the tangential velocity and more difficult to measure accurately. It is generally inwardly directed below the lip of the vortex tube, but it is not uniform with height. Rather, the greatest inward flow occurs immediately below the vortex tube opening – this is related to the secondary flows discussed below.

As the discussion in Sect. 2.1.1, and Eq. (2.A.12) show, in order for a rotating fluid element to maintain its equilibrium (static position in the r-direction), the pressure on its surface at higher r must exceed that on its surface a lower r. Thus the static pressure must increase monotonically with increasing radius. This, in fact, is borne out by experiment—a classic example of which is the data of Ter Linden (1953), a sample of which is presented in Fig. 3.1.2. Here the lower curves contained within each set of curves represents the variation in static pressure, p, with radial position; the upper curves, the total pressure, $p+(1/2)\rho v^2$ (static plus dynamic). Comparing with Eq. (2.1.3) and realizing, as before, that the second term in Bernoulli's trinomial is small, we see from the profiles of total pressure in Fig. 3.1.2 that Bernoulli's trinomial is almost constant in the outer, nearly loss-free part of the vortex, while it decreases significantly in the center. This is as we would have expected.

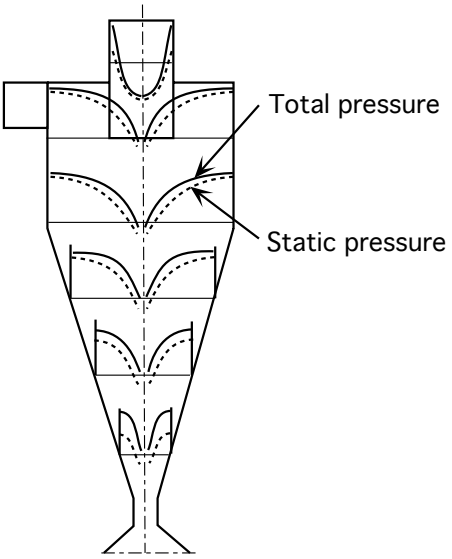

Fig. 3.1.2. Static and dynamic pressure profiles within a cyclone

These data also show that the static pressure within the vortex finder also increases with radial position. This is also what we would expect, since there is still swirl present there. In this "core" region the velocity is approximately that of solid-body rotation, i.e. Eq. (2.1.1). Additionally, the static pressure is

observed to be strongly dependent upon radial position and, like that within the main body of the cyclone, has its maximum value at the wall. Clearly, a simple static pressure measuring tap mounted flush with the inner wall of the vortex finder is not representative of the *average* pressure within this tube. We will have more to say about this in Sect. 4.1.2.

Swirl flow near the walls of concave surfaces is inherently unstable. Pressure gradients caused by the swirling motion create 'secondary flows' in the cyclone body along the walls. We saw in Chap. 2 that the static pressure increases toward the outer part of a swirling flow. This pressure gradient continues to persist through the boundary layers at the roof and at the conical wall. The tangential velocity, on the other hand, is low in these boundary layers. The result is a net inwardly directed force acting on gas pockets in the near-wall region, causing inwardly directed flows along the cyclone roof and the conical wall as indicated in Fig. 3.1.3, so that this net inward force is balanced by frictional drag with the wall and the bulk flow.

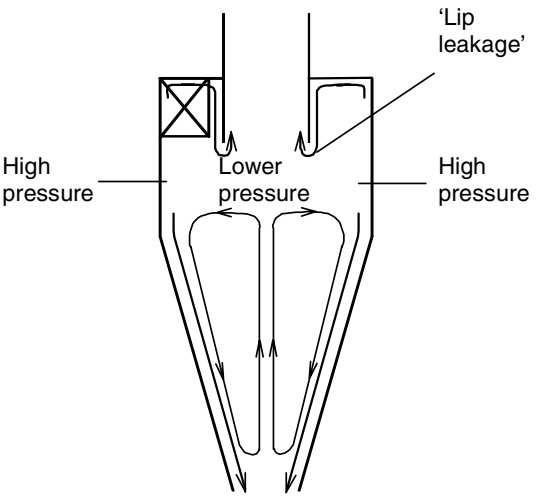

Fig. 3.1.3. The secondary flows caused by the swirl in the cyclone

The strong pressure gradient also has other effects, aside from the secondary flow patterns just mentioned, which are important for the flow near the wall within cyclones and within other such centrifugal devices including swirl tubes and hydrocyclones. In particular, let us apply the above concepts to the region of the boundary layer at the cyclone wall. Here we find that none of the velocity profiles we have discussed thus far apply since none of them predict a sharp decrease in v_θ within this "near wall" region as $r \to R$, where R is the cyclone radius at any given axial position. Nor do they account for the fact that $v_\theta = 0$ at $r = R$. In this wall region, as $v_\theta \to 0$, the 'cen-

trifugal force' that the fluid experiences becomes vanishingly small, and the static pressure experiences a negligible increase with radius. See Eq. (2.A.12), for example, which predicts $dp/dr \to 0$ for $v_\theta \to 0$. Consequently, *wall disturbances can cause the affected portion of the high pressure, solids-laden fluid near the wall to be deflected radially inward. In so doing the fluid will carry some of the previously collected solids with it, thereby degrading separation performance.* In a figurative sense, it is as though the high-pressure fluid near the wall is "just looking for an excuse" to break away from the wall and flow into the low-pressure inner regions of the cyclone. Flow over any concave surface is inherently unstable. This, then, is one reason why cyclone walls should be constructed and maintained as smooth as possible—free of any features which can disturb the flow. This includes such things as: weld seams, warped or distorted walls, solid deposits, damaged refractory or ceramic lining, eroded walls, sight-glasses, thermowells, light-ports, 'manways' or access ports/hatches (that are not flush and contoured to the inside surface of the cyclone), pressure sensors, areas that are hardfaced or 'weld overlaid', flange joints, gaskets that protrude into the flow, and most any area that has been previously repaired that is not in smooth 'like new' condition. This may even include walls that are out-of-round or walls fabricated from plate metal that have been crudely 'braked' and not 'rolled' to render smooth internal surfaces. Such nonideal conditions are virtually impossible to accurately simulate with existing models. Our models can handle uniform wall roughness, once this roughness is known. However, they cannot handle the nonideal wall conditions listed above. Yet, these conditions can strongly impair separation performance. For this reason, plant engineers, maintenance personnel, and designers need to be especially attuned to wall conditions and, should flow disturbances be found, take whatever steps are necessary and practical to render the walls smooth and free from such disturbances.

The secondary flows mentioned above drive others, in turn. For instance, the flow along the roof drives a downward flow along the outer wall of the vortex finder. This contributes to the high radial velocity just under the vortex finder wall, mentioned above, generally referred to as 'lip leakage'.

In addition to these secondary boundary layer flows, there is experimental evidence that a 'swiss roll' type of secondary flow pattern exists in the core of the cyclone body, as indicated in Fig. 3.1.3. Such a flow pattern can cause particles to recirculate in the cyclone body.

In general, many of the features of the flow in cyclones can be understood when considering the effects of the swirling motion on the axial and radial flow pattern. This issue will be discussed in Chap. 4.

3.1.2 Particle Flow

Particles entering the separation space are subject to an inwardly directed drag and an outwardly directed centrifugal force. The 'separation space' starts at the point, where the incoming gas first experiences rotational flow and

the particles carried along in this gas flow first experience a centrifugal force acting radially outwards. This point varies with inlet design and may start, for example, at the leading edge of an inlet scroll or helix upstream of the upper 'barrel' section of the cyclone proper.

Irrespectively, the centrifugal force is proportional to the particle mass and, therefore, the cube of the particle diameter: x^3. The drag force, which is due to the flow of gas from the outer to the inner part of the vortex, is proportional to x, at least when Stokes' law applies which it often does in practice. The largest particles are therefore the easiest to separate.

It is not easy to study the particle flow pattern experimentally. In order to give an impression of the flow of a particle through a cyclone, we can resort to CFD simulations. Figure 3.1.4 shows a series of particle trajectories. The particles are injected at different radial positions along the inlet in a precalculated gas flow field. The swirling motion is not shown.

Although the object is to centrifuge the particles to the wall and capture them, it is interesting to look at particles so fine that some of them are not collected. An extremely fine 1.0 μm particle size was used to generate the particle paths shown in Fig. 3.1.4. Some of the particles can be seen to exit through the vortex finder, while those injected closer to the wall, reach the wall, where they are deemed to be captured and are removed from the simulation.

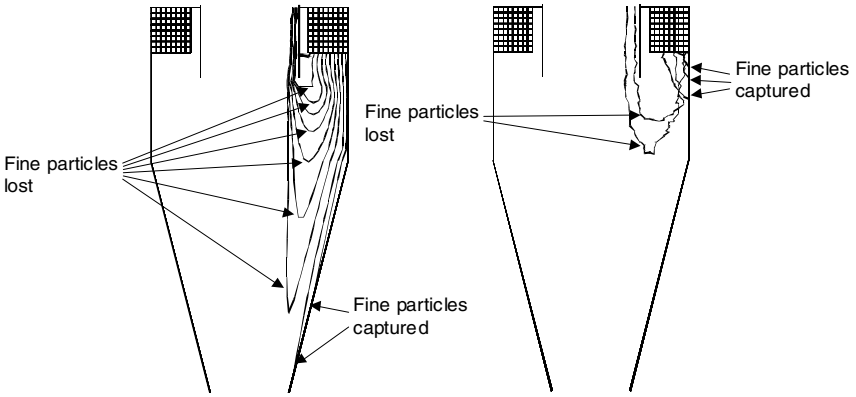

Fig. 3.1.4. Particle tracks in a cyclone by computational fluid dynamics. The swirl components are not shown. On the left 10 tracks are calculated from the mean flow field; on the right 5 particle tracks are shown where the response to the turbulent motion of the gas is taken into account. Conditions: cyclone diameter: 20 cm, gas inlet velocity: 15 m/s, gas at SATP ('standard ambient temperature and pressure', 25°C and 1 atm), particle density: 2730 kg/m^3

3.2 Separation Efficiency

3.2.1 Overall Separation Efficiency

The three particle fractions we are concerned with in cyclone operation are the *feed*, the *captured* (or collected or 'underflow') and the '*overflow*' (or emitted or lost) fractions. Let us represent their masses (or mass flow rates) by the symbols M_f, M_c and M_e, respectively. The mass balance for solids over the cyclone is:

$$M_f = M_c + M_e. \tag{3.2.1}$$

The overall separation efficiency η is simply calculated as the mass fraction of the feed solids captured by the cyclone:

$$\eta = \frac{M_c}{M_f} = 1 - \frac{M_e}{M_f} = \frac{M_c}{M_c + M_e}. \tag{3.2.2}$$

The efficiency is determined by collecting samples and weighing two of the fractions.

The overall efficiency is usually what counts the most in the context of an industrial process. However, it is not a good measure for characterizing the intrinsic separation performance of a particular cyclone, since, for example, it tells us nothing about the separation capability of the cyclone as a function of particle size.

3.2.2 Grade-Efficiency

The separation characteristics of a cyclone are best described by the so-called grade-efficiency curve or GEC, which is the separation efficiency for a given feed particle size or (narrow) range of particle sizes.

If the differential volume or mass density distributions of the charge dust, the captured and overflow (or emitted) fractions are $f_f(x)$, $f_c(x)$ and $f_e(x)$, respectively, the mass balance for particles with diameter between $x - 1/2\ dx$ and $x + 1/2\ dx$ is:

$$\begin{aligned} f_f\,(x)\,dx = \eta f_c\,(x)\,dx + (1-\eta)\,f_e\,(x)\,dx = dF_f\,(x) \\ = \eta dF_c\,(x) + (1-\eta)\,dF_e\,(x)\,. \end{aligned} \tag{3.2.3}$$

To help make this a little less abstract, let us approximate the particle size differential with a finite, yet small value for dx, and also substitute in some numbers obtained from a hypothetical cyclone performance measurement: Thus, let us assume we determine (through measurements) that 10% of the feed solids (by wt. or vol.) lie within a 5-micron (Δx) band centered about some particular particle size, x. In addition, the measurements show that 80% of the particles within this particular 5-micron band are collected and that they comprise 6% of the collected material. Likewise, 30% of the

particles are emitted ("lost") and they comprise 26% of the emitted solids. Our finite approximation to the left three terms of Eq. (3.2.3) then reads:

$$0.10 \times 5 = 0.08 \times 0.06 \times 5 + (1 - 0.80) \times 0.26 \times 5$$

or, cancelling the Δx's (i.e. the 5's):

$$0.10 = 0.048 + 0.052 = 0.10$$

Thus, we see that the cyclone brings about the mathematical equivalent of a partition function, η—it partitions the particles in any given size range, Δx, into the underflow and overflow streams. It does this on the basis of the forces acting on the particles within the separation zone of the cyclone.

Equation (3.2.3) can be integrated term-by-term to give a mass balance for the dust with particle size less than a given size x:

$$F_f(x) = \eta F_c(x) + (1 - \eta) F_e(x) \tag{3.2.4}$$

The grade-efficiency is defined as the fraction of the feed solids with diameter between $x - 1/2\ dx$ and $x + 1/2\ dx$ that is captured in the cyclone:

$$\eta(x) = \frac{M_c f_c(x)\, dx}{M_f f_f(x)\, dx} \tag{3.2.5}$$

Making use of Eq. (3.2.2) and of the mass balances in Eqs. (3.2.3) and (3.2.4) gives:

$$\eta(x) = \eta \frac{f_c(x)}{f_f(x)} = 1 - (1 - \eta) \frac{f_e(x)}{f_f(x)} = 1 - (1 - \eta) \frac{dF_e(x)}{dF_f(x)} \tag{3.2.6}$$

A typical grade-efficiency curve is sketched in Fig. 3.2.1.

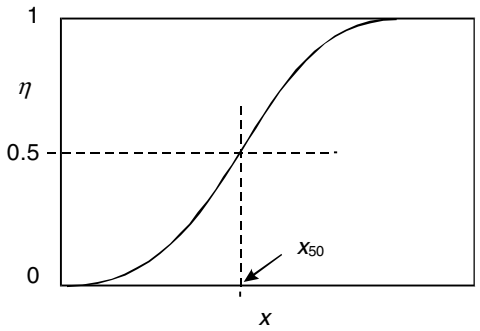

Fig. 3.2.1. Sketch of a typical, s-shaped grade-efficiency curve

If the separation in the cyclone was ideally sharp, the grade-efficiency curve would be a vertical line at the 'critical' or 'cut' size, x_{50}. For a number of reasons—two of which we have considered already—this is not so:

- particles of the same size may be either captured or lost depending on their entry position in the inlet,
- turbulent particle dispersion due to normal fluid turbulence, and enhanced by such things as internal wall roughness and surface irregularities, leads to backmixing,
- particles greater than x_{50}, which were already separated, may be reentrained low in the cyclone or in the dust hopper if the cyclone's lower section is not carefully designed,
- particles smaller than x_{50} may agglomerate with larger ones, and be separated
- particle attrition may take place within the cyclone.

For these reasons we obtain a smooth, s-shaped, grade-efficiency curve in practice. The *cut size*, or 'x-50 cut-point' (often referred to as the 'd-50 cut-point diameter') is taken as the size that is separated with a fractional efficiency of 0.5: x_{50}.

Unlike gross or overall efficiency, a cyclone's x-50 cut-point and grade-efficiency curve are true measures of its intrinsic separation potential. These properties are independent of the size distribution of the feed, at least under low solids loading conditions. We shall return to this issue later.

The x_{50} size is exactly analogous to the openings in an ordinary screen or sieve. In a sieving operation, all feed particles greater than x_{50} will be captured or 'retained', and all less than x_{50} will not be captured. In practice, even a sieve exhibits some nonideal separation with respect to particle size but, generally speaking, a sieve very closely approximates a perfectly sharp separator: it tends to retain all particles greater than its x-50 cut-size or cut-point (sieve opening) while losing those less than its cut-point. In practice, it is often useful to think of a cyclone as a 'sieve', especially when it performs a particle classification duty as opposed to a bulk solids separation task. More on this later.

Furthermore, if the grade-efficiency is reported in terms of an aerodynamic particle size (see Sect. 2.3.1) by calculating this from the actual particle sizes, it is also independent of the density of the feed particles and truly a characteristic of the cyclone. The aerodynamic particle size can be calculated from the actual particle sizes.

The steepness of the grade-efficiency curve around the cut size is an indication of the 'sharpness of the cut' of the cyclone. One measure for this is simply the gradient of the grade-efficiency curve at x_{50}, another is the ratio of the diameters corresponding to two specific fractional efficiencies, for instance 0.25 and 0.75: x_{25}/x_{75}.

The measures of sharpness reported above are two ways of representing the true slope of the grade-efficiency curve near its cut-point, $x_{50.}$ However, in many applications one can mathematically fit the cyclone's measured grade-efficiency data to some functional form $\eta = f(x_i)$ and, with appropriate transformation of the variables, plot the data so that it appears as a straight - or

nearly straight - line. Such a line will also have a 'slope' but this slope will be constant over the entire range of particle sizes and different than the 'true' grade-efficiency curve slope described in the previous paragraph. Nevertheless, both slopes are useful and we will encounter this latter type of slope in Chaps. 5 and 6.

3.2.3 Converting Between Overall Efficiency and Cut-size

We often have occasion to convert between the overall efficiency η and the cut size x_{50}, for instance, when we wish to compare an efficiency determined by testing with the cut-size predicted by a model. There are two ways of doing this: a simple approximation and the precise way.

The simple approximation is to assume the cyclone to have a sharp cut at x_{50}, *i.e.* that all material below x_{50} is lost and all material above is collected. If the cumulative undersize distribution of the feed is $F_f(x)$, then (see Fig. 3.2.2):

$$1 - \eta = F_f\left(x_{50}\right) \tag{3.2.7}$$

The precise way is to use the entire grade-efficiency curve for the cyclone, $\eta(x)$. The fraction of feed lying within the band $x - 1/2\ dx$ and $x + 1/2\ dx$, is captured with a fractional efficiency of $\eta(x) f_f(x) dx$. The total fraction of the feed captured is therefore:

$$\eta = \int_0^\infty \eta\left(x\right) f_f\left(x\right) dx = \int_0^\infty \eta\left(x\right) dF_f\left(x\right). \tag{3.2.8}$$

Experience shows that the approximate method (Eq. 3.2.7) comes out surprisingly accurate, even when the cut of the cyclone is far from sharp. This has very practical implications and is often used when one just needs a rough estimate of overall separation efficiency.

3.3 Pressure Drop

We finally look briefly at cyclone pressure drop. The normal procedure for measuring a pressure drop in the process industry is to measure the static pressure at the wall in the upstream and downstream piping or ducting. This is complicated in cyclones by the swirl in the exiting gas. In the first place, the swirl causes the static pressure at the wall to be higher than the cross-sectional average, and in the second place, there is the issue of what to do with the dynamic pressure stored in the swirling motion. We shall consider the options for solving these problems in Chap. 4. Here it suffices to say that when we talk of the 'pressure drop' over the separator, we mean the drop in *total* pressure: the sum of the static and dynamic pressures.

The pressure drop over a cyclone is normally subdivided in three contributions:

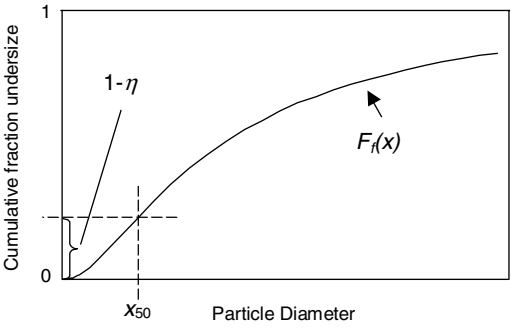

Fig. 3.2.2. Sketch showing the principle of determining the overall efficiency from the cumulative size distribution of the feed and the cut size

1. losses in the entry,
2. losses in the separation space (the main cyclone body), and
3. losses in the vortex finder.

The losses in the entry are often negligible compared to the other contributions, at least in tangential entry cyclones. For swirl tubes with inlet vanes little information is available, but if the vanes are properly contoured aerodynamically, the losses are generally small.

The losses in the cyclone body are higher, but, as we shall see later, their main significance is in limiting the intensity of the swirl in the separation space: more frictional losses at the walls lead to a less intensive vortex. Such *wall losses* do not dominate the overall pressure drop.

The losses in the vortex finder are the largest, in both through-flow and reverse-flow tangential-inlet cyclones. Vortex finder losses may be an order of magnitude larger than the two other contributions. The one notable exception is highly (solids) loaded primary or 'rough-cut' cyclones wherein wall losses associated with frictional drag at the walls can become a significant contribution to the overall pressure loss—at the expense of losses in the vortex core, and the vortex finder.

The pressure drop over a cyclone, Δp, is proportional to—or very close to being proportional to—the square of the volumetric flowrate, as it is in all processing equipment with turbulent flow. To obtain a characteristic measure for pressure drop in a given cyclone, pressure drop is often reported in a dimensionless form known as the 'Euler number':

$$Eu \equiv \frac{\Delta p}{\frac{1}{2}\rho\langle v_z\rangle^2} \tag{3.3.1}$$

where $\langle v_z\rangle$ is the mean axial velocity in the cyclone body, *i.e.* the volumetric flow rate divided by the cross-sectional area of the cylindrical part of the body.

It does not matter which velocity we use to define the Euler number. While the definition in (3.3.1) is popular in research laboratories, most practicing

engineers prefer to use either the inlet velocity or the mean velocity in the vortex finder, since these are the velocities most commonly reported by vendors and designers as part of their overall performance summary:

$$Eu_{in} \equiv \frac{\Delta p}{\frac{1}{2}\rho v_{in}^2}; \qquad Eu_x \equiv \frac{\Delta p}{\frac{1}{2}\rho v_x^2}. \tag{3.3.2}$$

Equation (3.3.2) is especially useful to the plant engineer who wishes to estimate the pressure loss through his or her cyclone system at conditions other than design conditions, or at some flow rate other than one for which the pressure loss is known. We shall see how in Chap. 8, where also the derivation of this and other dimensionless numbers characterizing cyclones and swirl tubes can be found.

With this discussion, we have introduced the basic working characteristics of gas cyclones. In Chaps. 4, 5 and 6 we shall consider the gas flow pattern and the separation in more detail, and also models for predicting them as reported in the research literature. In Chap. 10 we will discuss how cyclone performance can best be determined from laboratory and/or plant measurements.

3.A Worked Example: Calculating a Grade-Efficiency Curve

Let us say that we have measurements of the cumulative undersize distributions for the feed and the lost fractions. The overall fractional efficiency has been measured to be η=0.88. We wish to calculate the grade-efficiency curve.

The cumulative size distributions are:

Feed:

x_i (μm)	1.5	2.5	3.75	5.25	7.0	8.5	9.6	11.4	13.1	14.8	16.8	18.5
$F_f(x_i)$	0	0.01	0.09	0.22	0.37	0.57	0.68	0.78	0.87	0.94	0.98	1.0

Overhead fraction:

x_i (μm)	1.75	2.4	2.9	3.25	3.5	4.0	4.6	5.5	6.5	7.3
$F_e(x_i)$	0.047	0.10	0.30	0.45	0.54	0.70	0.83	0.94	0.99	1.0

Solution

The equation we need to use is Eq. (3.2.6). One option we might consider is to fit model distribution functions, such as the ones we looked at in the

previous chapter, to the data and then using Eq. (3.2.6) directly to determine grade-efficiency performance. However, this will usually not work unless the data are fitted extremely well in the fine end. The small discrepancies between data and fitted function for the smaller size particles of the distributions will otherwise lead to totally wrong grade-efficiency data.

We therefore use the discrete equivalent of Eq. (3.2.6) on the data as they are and calculate, using a spreadsheet for example, the separation efficiency in a series of size intervals, as follows.

The discrete equivalent of Eq. (3.2.6) is:

$$\eta\left(\frac{x_i + x_{i+1}}{2}\right) = 1 - (1-\eta)\,\frac{(F_e\,(x_{i+1}) - F_e\,(x_i))}{(F_f\,(x_{i+1}) - F_f\,(x_i))} \tag{3.A.1}$$

In order to use this equation, we need data for F_e and F_f at the same x_i. We interpolate the function F_f to the points at which we have F_e. Linear interpolation gives:

Feed interpolated:

x_i (μm)	1.75	2.4	2.9	3.25	3.5	4.0	4.6	5.5	6.5	7.3
$F_f(x_i)$	0.0025	0.009	0.036	0.058	0.074	0.112	0.164	0.241	0.327	0.410

Filling in values for the first interval in (3.A.1):

$$\eta\,(2.08) = 1 - (1 - 0.88)\,\frac{(0.10 - 0.047)}{(0.009 - 0.0025)} = 0.022$$

The result of doing this for all the intervals are the points on the grade-efficiency curve shown in Fig. 3.A.1. This completes our solution to the problem.

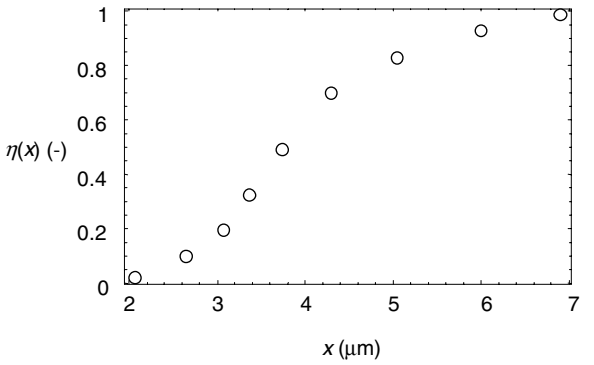

Fig. 3.A.1. Grade-efficiency data calculated from Eq. (3.A.1)

It only takes a small change in the F-data to generate quite different grade-efficiency points, particularly at small x_i. A high quality of size analyses is therefore necessary for generating reliable grade-efficiency curves, especially for the finer particle sizes. Even changing the interpolation from linear to one of higher order changes the first two points. In practice, linear interpolation often works the best, being the least sensitive to small errors in the experimental points.

Generation of accurate grade-efficiency curves is often left to sampling and measurement specialists who are very familiar with the technology under examination and with all the factors that can give rise to erroneous results if they are not adequately accounted for. These include, but are not limited to:

1. Solids maldistribution in the ducts being sampled.
2. Inability to obtain a reasonable match between the velocity entering the sampling probe and that within the duct being measured (*i.e.* inability to achieve 'isokinetic sampling').
3. Flow conditions in which isokinetic sampling is difficult or impossible, such as a skewed velocity profile or strong swirl flow.
4. Insufficient sample mass.
5. Vapor condensation as solids are being withdrawn.
6. Solids agglomeration or dispersion upon measurement of their particle size (after sample is caught).
7. Unsteady gas and/or solids flow conditions during sampling
8. Solids 'reacting' or otherwise being transformed upon sampling into a size distribution other than that which exist in the operating unit.
9. Human error.

Most of these issues will be discussed in Chap. 10.

4

Cyclone Flow Pattern and Pressure Drop

Predicting the separation efficiency of cyclones involves predicting how particles behave in the separation space. In order to do this, we need to know the velocity distribution of the gas. Some researchers have made all-embracing models for both gas flow pattern and separation efficiency; others have concentrated on one or the other. We look at the two issues separately here.

Models for cyclone pressure drop sometimes spring from models for the flow pattern and are based on an estimation of the actual dissipative losses in the cyclone; others are purely empirical.

In this chapter we discuss models for the flow pattern and pressure drop, and in the subsequent two chapters, models for the separation efficiency. We shall not look at all of the models here; an initial discussion will lead to a treatment of a few of the most popular ones. With some regret the authors have to accept that it is not possible to give a full account of the derivations of the model equations. This chapter can only indicate the principles behind the derivations. It is our intent, however, to present enough of the theory and derivations to allow the practicing design and plant engineer to appreciate the 'theory' underlying cyclone performance. It is also our hope that the user of this book will be able to take what is presented herein and apply it towards the design, evaluation and troubleshooting of commercial cyclone installations. The reader wishing to study the details of the derivations is referred to the original papers. At the end of the chapter we will look at how well the model assumptions fit with the real flow in cyclones. Worked examples for calculating cyclone pressure drop can be found in Appendix 4.A.

4.1 Discussion

In this section we will consider some special features of the flow and the pressure drop that are due to the swirling motion in the cyclone. Swirling flow can be awkward to consider intuitively. Nevertheless, we try to look at some of the flow features on an intuitive basis here.

4.1.1 Flow Pattern

The standard way of arriving at flow equations in Transport Phenomena is to balance forces on differential elements. This is tricky in swirling flows in cylindrical coordinate systems. The safest method of deriving flow equations in such systems is to start with the Navier-Stokes equations and simplify them as we did in Appendix 2.A. Nevertheless, to understand the flow pattern in cyclones, and how the models predicting it were derived, it is good also to view the flow pattern intuitively. This can be done by realizing that the tangential momentum balance Equation (Eq. 2.A.4), can also be derived by carrying out a moment-of-momentum balance.

Let's begin by considering the simple swirling flow of an annular fluid element of differential thickness, as sketched in Fig. 4.1.1. Set the change with time in its moment-of-momentum, $\partial/\partial t\,(mv_\theta r)$, equal to the sum of the moments of the forces acting on it, namely the shear forces on the inside and outside of the element.

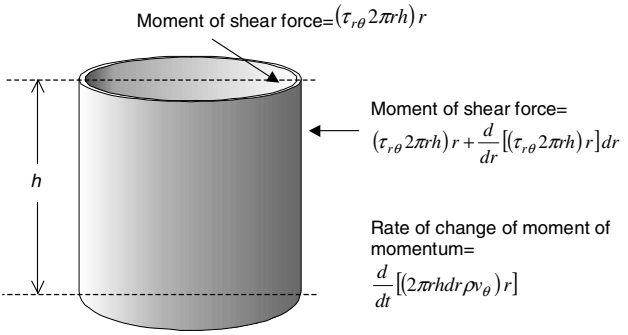

Fig. 4.1.1. Balancing the moments of the forces acting on an annular fluid element of thickness dr

Digressing for a moment, we note that the effect of wall friction on a rotating fluid can be viewed in this way: the moment of the frictional force can be seen as a flow of moment-of-momentum into the fluid, just as shear force can be seen as a flow of momentum in Cartesian coordinates. The moment of the wall friction on a fluid rotating inside a stationary cylindrical wall of radius R_w, height H_w and area $A_w = \pi R_w H_w$ is

$$\text{Moment of frictional force} = \tau_{r\theta} A_w R_w = f\left(\frac{1}{2}\rho v_{\theta w}^2\right)(2\pi R_w H_w)\, R_w \quad (4.1.1)$$

-where f is the friction coefficient. This is used a lot in derivations of models for the pressure drop and separation efficiency in cyclones.

We now return to our intuitive derivation of Eq. (2.A.4), and consider the situation in Fig. 4.1.1 under steady state conditions. In steady state the rate of

accumulation of moment-of-momentum is zero, so if we balance the moments acting on the cylinder we get:

$$(\tau_{r\theta} 2\pi rh)\, r = (\tau_{r\theta} 2\pi rh)\, r + \frac{d}{dr}\left[(\tau_{r\theta} 2\pi rh)\, r\right] dr \;\Rightarrow \frac{d}{dr}\left[(\tau_{r\theta} 2\pi rh)\;\; r\right] dr = 0.$$

However, the entities 2, π, h and since dr is not zero, this simplifies to:

$$\frac{d}{dr}\left(\, \tau_{r\theta} r^2\right) = 0$$

-which is Eq. (2.A.4).

We can thus analyze the tangential flow in a swirling flow field intuitively by carrying out moment-of-momentum balances.

4.1.2 Pressure Drop

The swirling motion can complicate the understanding of cyclone pressure drop:

1. the variation of cyclone pressure drop with some of the geometrical and operational parameters can seem counter-intuitive, and
2. experimentally determined cyclone pressure drops are not straightforward to interpret.

We start with item 1 above. The nature of cyclone pressure drop can be understood only if we make the clear distinction between *static* and *dynamic* pressures: p and $1/2\rho v^2$, respectively, as discussed in Chap. 2.

As gas moves from the outer to the inner part of the vortex in the cyclone body, it is accelerated in accordance with the principle of conservation of moment-of-momentum or, as some would call it, conservation of 'angular' momentum (Chap. 2). In addition, its static pressure decreases (see also Eq. 2.A.12). We can say that the vortex *transforms static pressure into dynamic pressure*. For a given wall velocity, (governed largely by the inlet velocity), the less the frictional loss, the more intense the vortex, the more efficient is this conversion, and the lower is the central static pressure with which the gas enters the vortex finder. The limit, which is never obtained in practice, is a frictionless vortex, where Eqs. (2.1.2) and (2.1.3) are valid. Smooth walled and aerodynamically 'clean' cyclones therefore produce the highest spin in the vortex and the greatest decrease in static pressure within the core, other factors being equal.

Friction at the walls and in the vortex core leads to dissipation of mechanical energy. Just like in normal pipe flow, it is this dissipation which gives rise to the permanent pressure drop over the cyclone. The energy stored as dynamic pressure in the tangential velocity component, $1/2\rho v_\theta^2$ in the gas entering the vortex finder is dissipated in the vortex finder and downstream piping or ducting without much recovery of static pressure (at least in the absence of a rectifying device, see later).

Many are surprised to find that cyclone pressure drop *decreases* with increasing solid load, wall roughness or cyclone body length. After all: all three give rise to increased wall friction in the cyclone body and, from our experience with pipe flow, we expect this to cause increased frictional loss and, therefore, higher pressure drop.

But, with the above ideas about the nature of cyclone pressure drop and some simplistic considerations, we can see intuitively, as shown below, that cyclone pressure drop, indeed, should decrease with increasing wall fraction in the body (we will also present a 'macroscopic' quasi-theoretical model of cyclone performance with predicts such effects later in this book). Consider two extremes for the flow pattern in the cyclone body:

a) an intense swirl with a very low wall loss, and
b) almost complete attenuation of the swirling motion by wall friction in the body.

In case a) a large amount of static pressure is transformed into dynamic pressure. If the inlet velocity is 15 m/s, the tangential velocity in the center could be about 45 m/s. Swirl dynamic pressure of the order of $(1/2\rho 45^2)$ Pa is then dissipated in the vortex finder and downstream piping per unit volume of gas. In case b), on the other hand, with a lot of wall friction robbing the inlet jet of all its dynamic pressure (visualize this by incredibly rough walls reducing the spin to almost zero in the cyclone body), we are dissipating of the order of $(1/2\rho 15^2)$ Pa per unit volume of gas, which is an order of magnitude less. In this second case, the air will then enter the vortex finder without any swirling motion, and at a much higher static pressure. The dissipation in the vortex finder will then be very small. The result is that the dissipation, and therefore the pressure drop, in case a) is higher than in case b).

Thus, the rougher the walls, the less the pressure loss becomes—quite contrary to what our intuition may lead us to think. This being the case, it should not be too difficult to understand that, due to their strong braking action, wall solids in heavily (solids)-loaded cyclones also reduce the overall pressure loss relative to the same cyclone operating with negligible solids loading. Here, drag between the solids and the gas robs the gas of much of its energy. This manifests itself as both a reduction in core spin velocity and a reduction in static pressure loss. Such highly-loaded cyclones exist, for example, at the top of modern FCCU reactor risers and in certain dense-phase pneumatic transport facilities., and in gas/liquid cyclones at high liquid loadings It should also be clear that, other factors being equal, a cyclone built with relatively rough internal refractory liners (for erosion and/or thermal protection), as opposed to one constructed out of smooth metal plate, will also experience less overall pressure loss, despite the increased energy dissipation along the walls. As we shall see later, however, one generally wants to maintain the wall surfaces as smooth as is practical since this leads to the highest core spin velocity and the best separation performance.

Now let us turn to the point mentioned under item 2 above: the interpretation of cyclone pressure drop measurements. Interpreting the measured pressure in the *inlet* of cyclones is not a problem: the static pressure is fairly uniform over the cross section, and can be measured with a pressure tapping in the wall. In fact, in many commercial fluid-bed cyclone installations, the inlet static pressure is, for all practical purposes, simply that existing in the relatively low-velocity, dilute-phase region of the vessel containing the cyclone(s). Interpreting the pressure measured in the *outlet* of cyclones, however, is made difficult by any swirl still present at the point of the pressure tapping:

- dynamic pressure is stored in the swirling motion, and
- the static pressure is not uniform in the swirling flow, but highest at the wall.

The dynamic pressure stored in the swirling motion in the vortex finder can be quite significant. As mentioned, if no pressure recovery or flow rectifying/straightening device is installed in the gas outlet tube, wall friction, along with turbulence and mixing created by downstream bends, expansions, valves, etc., will eventually dissipate it without much recovery of static pressure.

The static pressure at the wall of the vortex finder can be very different from the cross-sectional average. CFD calculations show that pressure drops up to 30 percentage points too low are obtained if the wall pressure is used rather than the cross-sectional average.

One way out of these difficulties lies in the observation that the static pressure at the wall is close to the cross-sectional mean of the static pressure plus the dynamic pressure stored in the swirl (Hoffmann et al., 1992). Or said in another way: the static pressure measured at the wall is close to the static pressure that would be measured after an *ideal rectifier* (or 'pressure recovery diffuser'), which would convert all the swirl dynamic pressure into static pressure. We emphasize that this is not *necessarily* so, it only *happens* to be so because the static pressure in the vortex finder happens to be very nearly a linear function of the radius[1]. Thus, in the absence of pressure recovery devices, the static pressure measured at the wall of the outlet tube minus the static pressure at the inlet gives the true dissipative loss between inlet and the measurement point in the outlet. One should be aware, though, that further dissipation of dynamic swirl pressure will take place in the downstream piping as the spin decays due to friction with the pipe wall, bends, etc.

This completes our short discussion of flow pattern and pressure drop. We now turn to the models. By far most of the modeling work has concentrated on cylinder-on-cone cyclones with tangential inlets. We will therefore talk of 'cyclones' in these sections. Very little direct work on the modeling of the flow pattern and the pressure drop in swirl tubes has been published; our

[1] If the tangential velocity is linear in the radius in the vortex finder (solid-body rotation), the pressure difference between the centerline and a radius r will be proportional to r^2. In reality, the radial profiles of both tangential velocity and pressure in the vortex finder are close to linear.

discussion of the reasoning behind the models should make the reader able to judge to which extent a particular approach can be applied to swirl tubes.

4.2 Models for the Flow Pattern

In the literature there exists a variety of mathematical models intended to predict cyclone velocity distributions. Such distributions are then used in the modeling or prediction of separation performance. For the cyclone separation models, the velocity distribution in:

- the near-wall region, and
- the control-surface *CS* indicated in Fig. 4.2.1

are the most important, as we shall see in the following chapter.

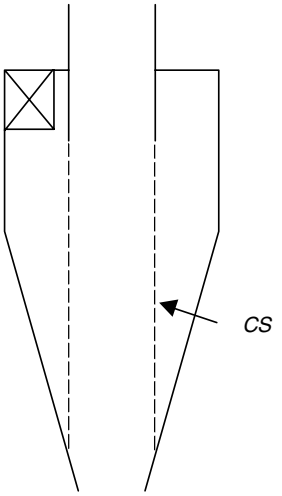

Fig. 4.2.1. The control-surface *CS*

We start with the *radial* velocity, which is computed in a very straightforward manner. Near the wall the radial velocity is neglected, and in the surface *CS* it is assumed uniform, giving:

$$\|v_r\left(R_x\right)\| \equiv v_{rCS} = \frac{Q}{\pi D_x H_{CS}} \tag{4.2.1}$$

where Q is the volumetric flowrate through the cyclone, D_x the diameter of the vortex finder, which is also the diameter of the surface *CS*, and H_{CS} the height of the surface *CS*. $v_r(R_x)$ is the average radial velocity in *CS*. We have called the absolute value of this v_{rCS}.

In reality the radial velocity in CS is not uniform. There occurs a radial, inwardly directed 'lip flow' or 'lip leakage' just below the vortex tube. Thus some portion of the gas tends to 'short circuit' the imaginary cylinder of height H_{CS} and diameter D_x near the top of the cylinder. Such behavior is one cause of the observed nonideal s-shaped grade-efficiency curve discussed in Chap. 3. Another cause is mixing brought about by an axial recirculation of the solids.

The *axial* velocity v_z is also fairly straight-forward: the surface CS is assumed to separate the outer region of downward flow from the inner region of upward flow. The axial velocities in each region is assumed to be uniform over the cross section. This, together with Eq. (4.2.1), allows calculation of the axial velocity from simple geometrical considerations.

Unlike the radial and axial velocities mentioned above, a variety of approaches have been advanced for computing the cyclone's *tangential* velocity v_θ. We give an account of some of the models for this under separate headings below.

4.2.1 n-Type Model

One very simple method of calculating the swirl velocity in the cyclone body, first introduced by Alexander (1949), is to assume that the vortex follows a modified form of the ideal vortex flows introduced in Chap. 2:

$$v_\theta = \frac{C}{r^n} \tag{4.2.2}$$

Thus, if the swirl velocity at one radius is known, that at another can be calculated. In this approach, the swirl velocity at the wall is often taken as being equal to the inlet velocity in cyclones with tangential inlets. This simple model does not distinguish between various inlet design geometries, which may be round pipe, square or rectangular ducting, or a more complex scroll configuration. Thus, the assumption that the wall velocity equals that at the inlet is a rather crude approximation to reality. See also the discussion below.

As discussed in Chap. 2, the index n is 1 for loss-free, and -1 for solid-body rotation. We recall that, in the outer part of the vortex (outside the surface CS in Fig. 4.2.1 above), the swirl is close to loss-free, although some loss is caused by wall friction. As a result of measurements of the tangential velocity profiles within laboratory cyclones, n is found to have a value between 0.7 and 0.8. This is a good approximation for smooth-walled cyclones operating at low solids-to-gas mass ratios (i.e., low 'solids loading'), but not so for cyclones operating at high mass ratios[2].

Alexander gave an empirical expression for n:

[2] What we mean by low and high mass ratios or 'loadings' will be shown later but, generally speaking, a cyclone running at solids concentrations greater than about 0.2 kg solids/kg of gas is considered to be under high mass loading.

$$n = 1 - \left(1 - 0.67D^{0.14}\right) \left(\frac{T}{T_o}\right)^{0.3} \tag{4.2.3}$$

where the body diameter D is measured in meters and the temperature T in degrees Kelvin. T_o can be taken as room temperature: 283 K. This expression indicates that n increases with increasing D and decreasing T. Equation (4.2.3), however, seems to predict values of n that are somewhat low. It also fails to account for the effect of wall friction or solids loading in reducing the swirl intensity.

In general, wall friction has a profound effect on the flow in cyclones and on cyclone performance. We shall discuss this in Chap. 5, when investigating the effect of cyclone body length on cyclone pressure drop and separation efficiency. We shall also discuss the effect of friction in Chap. 9 when looking at the effect of solids loading, which also turns out to be a consequence of the effect of the solids on the wall friction.

4.2.2 Barth

Barth (1956), who pioneered some of the best early practical developments in cyclone modeling, proposed calculating the wall velocity and the tangential velocity at the control cylinder *CS* in steps:

- calculate the wall velocity $v_{\theta w}$ from the inlet velocity v_{in} and
- use this to calculate the tangential velocity, $v_{\theta CS}$ at *CS*.

In some geometries the tangential gas velocity at the wall, and in the entire space between the wall and the vortex finder, can be significantly higher than the inlet velocity due to constriction of the inlet jet. In Fig. 4.2.2, the inlet flow pattern in a cyclone with a 'slot' type of rectangular inlet is compared with one with a 360° 'wrap-around' or 'full scroll' inlet.

In the former, the inlet jet is compressed against the wall, resulting in a decrease in the area available for the incoming flow, and an increase in the velocity. Barth accounts for this by introducing α, which he defined as the ratio of the moment-of-momenta of the gas in the inlet and the gas flowing along the wall:

$$\alpha \equiv \frac{v_{in} R_{in}}{v_{\theta w} R} \tag{4.2.4}$$

where R_{in} is the radial position of the center of the inlet. For a slot inlet $R_{in} = (R - b/2)$ where, as shown in Fig. 4.2.2, b is the width of the inlet chute and R the radius of the inside wall of the cyclone's upper body or 'barrel' section.

Barth suggested taking α as unity for a wrap-around inlet, and gave empirical data for the value of α for slot inlets in graphical form. Muschelknautz (1972, 1980) gave algebraic relations for α, the simplest of which is:

$$\alpha = 1 - 0.4 \left(\frac{b}{R}\right)^{0.5} \tag{4.2.5}$$

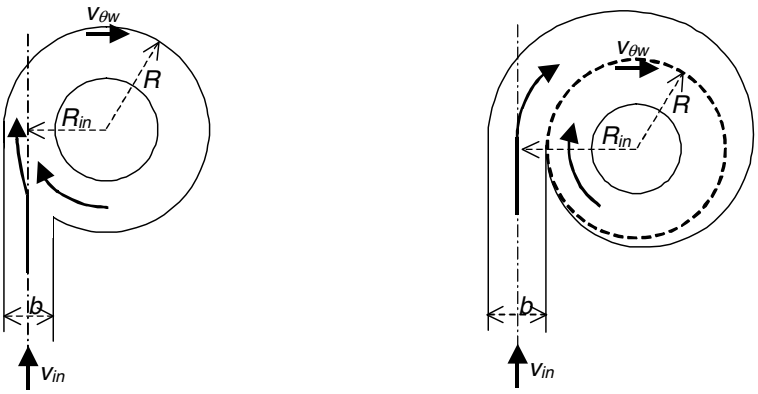

Fig. 4.2.2. Comparison of the inlet flow pattern between a 'slot' and a 360° 'wrap-around' inlet

which fits the graph given by Barth. Equation (4.2.5) is reported to be valid for slot-type inlets with the ratio of inlet to outlet cross-sectional areas in the range 0.9 to 1.8. We see from Eqs. (4.2.4) and (4.2.5) that, for a given R, as b increases, so does $v_{\theta w}$. When designing a cyclone, one should generally avoid making b larger than the annular width between the barrel wall and the vortex tube (i.e. $R - R_x$) in order to prevent large incoming particles from striking and penetrating the outer wall of the vortex tube.

Muschelknautz also gave more sophisticated models for the wall velocity for 360° wrap-around inlets, taking into account the frictional loss of moment-of-momentum. Those expressions do not all give consistent values, and can lead to values considerably larger than 1, which is physically questionable. For the Barth model we will use $\alpha = 1$ for scroll-type inlets and regard the inlet velocity as neither expanding nor contracting upon entering the cyclone.

To get from $v_{\theta w}$ to the tangential velocity at CS,$v_{\theta CS}$, Barth placed an imagined frictional surface in the flow. This surface accounts for the loss of angular momentum due to friction at the cyclone wall. The diameter and height of the friction surface are $(D \times D_x)^{1/2}$ and H_{CS}, respectively. Outside and inside this frictional surface the rotation is assumed to be loss free. This was a most significant advancement in the theory up until that time and, for the first time, a model was developed that could predict, approximately at least, realistic effects of friction upon cyclone performance. Muschelknautz later significantly refined Barth's work (see Chap. 6) but the concept of a frictional cylindrical surface remained a key component to the modeling work that followed.

We shall have to refer to Barth's paper for the details of the derivation, but a differential balance, where the gas loses moment-of-momentum as it flows over the friction surface, leads to the following expression for $v_{\theta CS}$:

$$v_{\theta CS} = \frac{v_{\theta w}\left(\frac{R}{R_x}\right)}{\left(1 + \frac{H_{CS} R \pi f v_{\theta w}}{Q}\right)} \tag{4.2.6}$$

From (4.2.4) and (4.2.6) we can get:

$$\frac{v_{\theta CS}}{v_x} = \frac{R_x R_{in} \pi}{ab\alpha + H_{CS} R_{in} \pi f} \tag{4.2.7}$$

In order to use Eq. (4.2.6) to calculate $v_{\theta CS}$ we need the wall friction factor f.

Before discussing this, however, it is of some practical interest to note that the core spin velocity, $v_{\theta CS,}$ (which has a major impact on separation performance) is not only a function of 'geometry' (R_x, R_{in}, a, b and α), but also a function of internal friction, f. This has very significant practical implications in that, with this approach, the realistic effects of two very important factors influencing commercial cyclone performance—wall roughness and solids loading—can be computed once we have some estimate for the value of f. Furthermore, if we look closely at Eq. (4.2.7), we can also see why simply increasing the height of a cyclone may not always lead to an improvement in performance. This is especially true of cyclones that: must operate under high mass loading conditions and/or with rough refractory or brick-lined walls, or with walls that foul-up with deposits or that significantly roughen over the course of a run.

This phenomenon of wall friction even has a bearing on the performance of otherwise smooth-walled, liquid-irrigated or demisting cyclones wherein the water phase on the walls actually exhibits a surprising large hydraulic roughness. See, for example, Fig. 4.2.3. The extent of the effect of liquid on the friction factor depends, for now at least, on experimental laboratory testing, as little has been reported in the cyclone literature. It would appear, however, that data currently available on the effects of liquid films on the friction factor of common gas flow in ordinary pipes could be applicable to any model development work in this area. This, then is one area that is in need of further research.

Muschelknautz (1972, 1980) gave expressions for f based on experiment. He found that, in a cyclone without dust, f decreases with the Reynolds number, as it does in normal pipe flow, but that the variation is somewhat different. He also found that f increases with increasing dust load due to the relatively slow movement of the separated dust along the cyclone wall. This dust forms a spiral-shaped *dust helix* or "strand" and acts as an additional component augmenting the dust-free wall friction. Such a dust helix can be seen in the laboratory cyclone shown in Fig. 4.2.4. He expressed f in two additive parts: one, which we will call f_{air}, for a dust free cyclone, and the other, f_{dust}, accounting for the effect of the dust.

Determining first f_{air}, he plotted f_{air} against a '*cyclone Reynolds number*'

Fig. 4.2.3. A laboratory air/water cyclone showing wave-producing wall roughness. Photo by L. E. Stein

$$Re_{cyc} \equiv \frac{Re_x}{4\frac{H}{D_x}\left(\frac{D}{D_x}-1\right)} \tag{4.2.8}$$

with Re_x the exit pipe Reynolds number: $(\rho v_x D_x/\mu)$, where v_x is the average axial velocity in the vortex finder. If $Re_{cyc} > 400$, the plots, which are given in Chap. 6, show that f_{air} is about constant, depending only on the relative roughness of the wall, k_s/D[3]. Under these conditions we can read off the values of f_{air} approximately. The values are given in Table 4.2.1.

Table 4.2.1. Value of f_{air} for three values of k_s/D

k_s/D (-)	f_{air} (-)
hydraulically smooth	0.005
$0.5.\times10^{-3}$	0.010
$3.\times10^{-3}$	0.025

[3] For the sake of consistency with the Muschelknautz method, the 'relative roughness' ratio reported in Chap. 6, however, is based on the cyclone radius, R, and is reported therein as k_s/R.

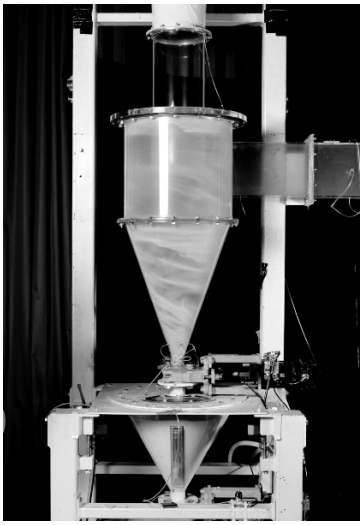

Fig. 4.2.4. A typical dust helix observed in a laboratory cyclone. Courtesy of CSIRO Thermal and Fluids Engineering

Turning to f_{dust}, Muschelknautz gave a simple relation: $f_{dust} = 0.015$ $(c_o)^{1/2}$, where c_o is the mass ratio of dust feeding the cyclone.

We thus get for a cyclone with a smooth wall at a sufficiently high Re_{cyc}:

$$f = f_{air} + f_{dust} = 0.005 \ \left(1 + 3\sqrt{c_o} \right). \tag{4.2.9}$$

In effect, Re_{cyc} is sufficiently high for f_{air} to be constant independent of Re_{cyc} in all cyclones except small ones working under severe vacuum. As in the case of pipe flow, even though we used the term 'smooth' wall above, the wall still exerts a frictional drag on the gas. This drag, however, is accounted for in the f_{air} term just as it is within hydraulically 'smooth' pipes. The added dust, assuming that most of it is collected and in contact with the walls (as has been assumed above), may be regarded as an additional wall roughness, as indicated in the above equation.

This completes our treatment of the models for the flow pattern in the cyclone. We discuss one more model for v_θ, namely that of Meissner and Löffler (1978), in Appendix 4.B. We now examine some of the most used pressure drop models.

4.3 Models for the Pressure Drop

As mentioned, some of the models for cyclone pressure drop are based on a consideration of the dissipative loss in the cyclone while many are purely empirical.

4.3.1 Models Based on Estimating the Dissipative Loss

Stairmand (1949) calculated the velocity distribution in the cyclone from a moment-of-momentum balance, and then estimated the pressure drop as entrance and exit losses combined with the loss of static pressure in the swirl. In line with the discussion of cyclone pressure drop above, Stairmand stated that in practice little of the decrease in static pressure from the outer to the inner part of the vortex can be recovered in the vortex finder, so that this can be counted as lost. His model was worked out in a compact form by Iozia and Leith (1989), who gave the following formulae for calculating cyclone pressure drop:

$$\frac{\Delta p}{\frac{1}{2}\rho v_{in}^2} = Eu_{in} = 1 + 2q^2\left(\frac{2\,(D-b)}{D_x} - 1\right) + 2\left(\frac{4ab}{\pi D_x^2}\right)^2 \tag{4.3.1}$$

with:

$$q = \frac{-\left(\frac{D_x}{2(D-b)}\right)^{0.5} + \left(\frac{D_x}{2(D-b)} + \frac{4A_R G}{ab}\right)^{0.5}}{\left(\frac{2A_R G}{ab}\right)} \tag{4.3.2}$$

whereA_R is the total wall area of the cyclone body, including the inner walls of the lid, the cylindrical and the conical sections and the outer wall of the vortex finder (see also Chap. 6). $G(= f/2)$ is a wall friction factor, which Stairmand set equal to 0.005 for conditions "which normally apply to flow in cyclones".

Barth (1956) estimated the dissipative loss, *i.e.* the loss in the sum of the static and dynamic pressure: $p + 1/2\rho v^2$, as separate contributions from:

- the inlet
- the cyclone body, and
- the vortex finder.

Barth stated that inlet losses could be effectively avoided by design. He estimated the pressure loss in the body as the decrease in dynamic pressure at his imagined friction surface, *i.e.* he considered the decrease in total pressure to arise from the loss of swirl velocity at the friction surface:

$$\frac{\Delta p_{body}}{\frac{1}{2}\rho v_x^2} = \frac{D_x}{D}\left(\frac{1}{\left(\frac{v_x}{v_{\theta CS}} - \frac{(H-S)}{0.5D_x}f\right)^2} - \left(\frac{v_{\theta CS}}{v_x}\right)^2\right) \tag{4.3.3}$$

where f can be calculated with Eq. (4.2.9). We observe that this equation and Eq. (4.3.1), unlike other pressure loss models presented in this section, account for the effect of solids loading upon pressure loss via the total friction factor, f, which includes the effect of solids loading in the incoming gas.

Barth estimated the loss in the vortex finder by a semi-empirical approach, the reasoning behind which is somewhat cryptic. The result is:

$$\frac{\Delta p_x}{\frac{1}{2}\rho v_x^2} = \left(\frac{v_{\theta CS}}{v_x}\right)^2 + K\left(\frac{v_{\theta CS}}{v_x}\right)^{\frac{4}{3}} \tag{4.3.4}$$

where K is found empirically to take on the values 3.41 and 4.4 for vortex finders with rounded and sharp edges, respectively. In normal situations, the model predicts that the loss in the vortex finder is an order of magnitude larger than that in the cyclone body. This equation also accounts for the effect of varying wall friction in the body, but indirectly: as f increases, the swirl velocity decreases (Eq. 4.2.6), and this decreases the vortex finder pressure loss computed from (4.3.4).

Barth stated that the pressure drop could be reduced by 10 to 30% by using a conical vortex finder or outlet diffuser downstream of the cyclone. See also the discussion in Sect. 15.1.5.

4.3.2 Core Model

Our goal in this section is to derive a useful model expression for computing the pressure drop across a cyclone's vortex finder. This model computes the loss in static pressure in the vortex tube as opposed to the permanent or frictional pressure loss. However, as discussed in Sect. 4.1, the energy stored as dynamic pressure in the spinning gas flowing through the vortex finder is usually dissipated therein—and within the downstream piping—without much recovery of static pressure (at least in the absence of a rectifying device). This energy is *completely* dissipated if the gas is allowed to simply exhaust abruptly to the atmosphere. Thus, the pressure decrease resulting from the generation of swirl flow is not recovered very efficiently and it becomes the permanent pressure loss across the vortex finder.

The flow in the vortex finder is assumed to consist of an outer annulus of nonviscous, axisymmetric, potential vortex flow with a uniform axial velocity surrounding a core of solid-body rotation with negligible axial velocity. The derivation here is similar to that presented by Lewellen (1971) and Smith,S Jr. (1962)—both have origins in the original work of Binnie and Hooking (1948).

The model assumes that within a core of radius R_c, the vortex undergoes solid-body rotation with negligible axial flow, see Fig. 4.3.1. As numerous studies have shown (see Slack et al. (2000), for example), the axial velocity within the core region is usually significantly smaller than the tangential velocity. We will be discussing velocity profiles in some detail later in the book. For now, however, we may wish to 'jump ahead' and simply review Slack's data shown in Fig. 7.2. Here we find that, within the vortex core radius of $\pm$ 0.035 m, the rotation closely follows that for solid-body rotation and has a maximum tangential velocity of about 38 m/s. More importantly to the subject at hand, the axial velocity within the core varies from about 10 m/s down to -5 m/s, approximately, and has an average velocity of no more than $+4$ m/s.

We begin our derivation of the 'core flow model' with a flow balance relating the average axial flow velocity, v_a, in the annular region located between radii R_c and R_x, to the average velocity normally computed or measured out the vortex tube, v_x:

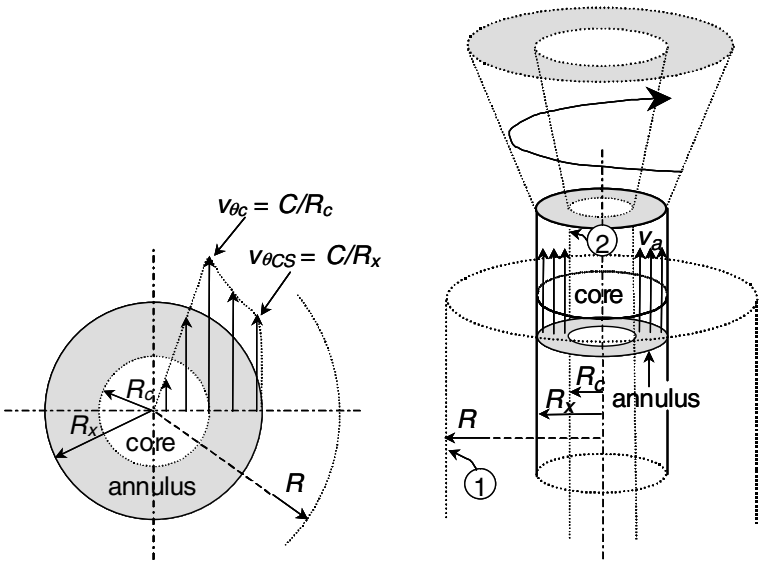

Fig. 4.3.1. Plan (left) and elevation (right) views of the tangential and axial velocity profiles within the vortex tube for the stagnant-core flow model

$$Q = \pi R_x^2 v_x = \pi \left(R_x^2 - R_c^2\right) v_a \tag{4.3.5}$$

where v_a is the average axial velocity through the shaded annular area shown in Fig. 4.3.1 which is enclosed between radii R_x and R_c. From this equation it follows that,

$$v_a = \frac{v_x}{1 - R_{cx}^2} \tag{4.3.6}$$

where,

$$R_{cx} \equiv \frac{R_c}{R_x}. \tag{4.3.7}$$

In addition, for the free-vortex region, the tangential velocity at radius R_x, which we have called $v_{\theta CS}$ elsewhere in this book is, according to Eq. (2.1.2).

$$v_{\theta CS} = \frac{C}{R_x} \tag{4.3.8}$$

and, at radius R_c

$$v_{\theta c} = \frac{C}{R_c} \tag{4.3.9}$$

Thus, upon eliminating the constant C

$$v_{\theta c} = \frac{R_x v_{\theta CS}}{R_c} = \frac{v_{\theta CS}}{R_{cx}} \tag{4.3.10}$$

If we now apply Bernoulli's Equation (Eq. 2.1.3) between point 1 located at the entrance to the cyclone, and point 2, located on the inner surface of the vortex core cylinder, there results

$$p_1 - p_2 = \Delta p_x = \frac{\rho}{2}\left(v_a^2 + v_{\theta c}^2\right) \tag{4.3.11}$$

where p_1 is the *total* pressure entering the cyclone. As this equation shows, our measure of the dynamic pressure in the vortex finder is based on the maximum swirl velocity at the inner edge of the core. It could also have been based on the mean. This would, in most cases, not have made an enormous difference in the predicted pressure drop.

Equation (4.3.11) is the pressure difference between the total pressure entering the cyclone ($p_1 = p + \rho v^2/2$), i.e., static plus dynamic pressure, and the static pressure p_2 at the inner of the vortex core. Yet, one normally regards cyclone pressure drop to be the difference in static pressures only. Therefore, if we wish to compare the results of the core-flow model with measurements (or correlations of measurements) of cyclone delta p for flow out the vortex tube (as we do in Table 4.3.1 later in this chapter) this is permissible providing $\rho v^2/2$ for the gas entering the cyclone is small in comparison with the $\rho(v_a^2 + v_{\theta C}^2)/2$ term that appears on the RHS of Eq. (4.3.11).

Upon substituting (4.3.6) and (4.3.10), this becomes,

$$\Delta p_x = \frac{\rho}{2}\frac{1}{\left(1 - R_{cx}^2\right)^2} v_x^2 + \frac{\rho}{2}\frac{1}{R_{cx}^2} v_{\theta CS}^2. \tag{4.3.12}$$

This equation shows that both axial and tangential velocity components contribute to the static pressure drop across the vortex tube and that these have pressure loss coefficients, or Euler numbers (see also Eq. 3.3.2), that can be defined in terms of the dimensionless core radius R_{cx}.

Before we can apply Eq. (4.3.12) we must be able to compute R_{cx}, which is, in turn, a function of the core radius, R_c. However, R_c is a function of v_x and $v_{\theta CS}$. We will determine the functional relationship between R_{cx} and v_x, $v_{\theta CS}$ by assuming that, for given values of these velocities, the vortex core radius will adjust so that the static pressure loss is a minimum. This, by the way, is equivalent to saying that the core radius will adjust to maximize the flow at a given pressure difference. Thus, we wish to minimize Δp_x with respect to R_{cx}in (4.3.12):

$$\frac{1}{\rho}\frac{\partial \Delta p_x}{\partial R_{cx}} = \frac{1}{R_{cx}^3} v_{\theta CS}^2 - \frac{2R_{cx}}{\left(1 - R_{cx}^2\right)^3} v_x^2 = 0 \tag{4.3.13}$$

which reduces to:

$$v_{\theta CS}^2 = \frac{2R_{cx}^4}{(1 - R_{cx}^2)^3} v_x^2 \tag{4.3.14}$$

This is equivalent to Eq. (6) of Smith's excellent paper (Smith,S Jr., 1962) on swirl flow, although he refers to the paper by Binnie and Hooking (1948) for background on its development. The closest we can get to a physical reasoning is the fact that a creeping flow will adjust so as to maximise the volumetric flow.

We observe from (4.3.14) that, formally, as the dimensionless core radius approaches a limiting value of 1, the tangential-to-axial velocity ratio increases without limit. Thus, a design characterized by intense spin will result in a narrow annulus near the inside wall of the vortex tube through which all the flow will spin and exit the vortex tube. On the contrary, as the dimensionless core radius approaches its limiting value of 0, the tangential-to-axial velocity ratio tends to vanish. Hence, a design characterized by a very weak spin will result in predominately axial flow filling virtually the entire cross-sectional area of the vortex tube.

Our task is to compute R_{cx} from (4.3.14), having found v_x and $v_{\theta CS}$ using methods presented elsewhere in this book. This can be done by trial-and-error. Although this poses no special challenges, it is also not necessary. We have found that the following equation gives an excellent approximation of R_{cx} as a function of the ratio $v_{\theta CS}/v_x$ over the very wide range: $v_{\theta CS}/v_x = 0.01$ to 172, with errors of only about 1%, or less:

$$R_{cx} = \frac{0.0219\,(v_{\theta CS}/v_x)^{-0.686} + 1}{0.700\,(v_{\theta CS}/v_x)^{-0.686} + 1}. \tag{4.3.15}$$

As a point of reference, cyclones usually operate at $v_{\theta CS}/v_x$ ratios of 1 to 2.5 and always less than 5.

Knowing $v_{\theta CS}/v_x$, once R_{cx} is known from Eq. (4.3.14) or (4.3.15), its value may then be substituted into Eq. (4.3.12), along with $v_{\theta CS}/v_x$ and ρ to compute the pressure loss associated with the gas expansion out the vortex tube.

Equation (4.3.12) is still not quite complete since it does not account for any pressure loss associated with the gas *entering* the vortex tube. If, in the limiting case of no rotation, and for a sharp-edged entrance to the vortex tube (thickness of outlet pipe or tube $\ll R_x$, as is the usual case), the gas loses an additional velocity head upon entering the tube, as is the case with gas flow into any protruding entrance. See Blevins (1984) for example. Thus, for the pressure drop model at hand, the total pressure loss associated with gas flow into and out the vortex tube equals that presented by Eq. (4.3.12) with 1 additional velocity head associated with the purely axial contribution:

$$\Delta p_x = \frac{\rho}{2}\left[\left(\frac{1}{(1 - R_{cx}^2)^2} + 1\right) v_x^2 + \frac{1}{R_{cx}^2} v_{\theta CS}^2\right]. \tag{4.3.16}$$

It is both interesting and instructive to compare the 'core flow' pressure drop predictions of Eq. (4.3.16) with those of the Barth model presented above and the Muschelknautz model, which we shall discuss in some detail later (see Chap. 6). For this purpose, we shall divide (4.3.16) by the impact pressure of the axial velocity component. This leads to:

$$Eu_x = \frac{\Delta p_x}{\frac{\rho v_x^2}{2}} = \frac{1}{(1 - R_{cx}^2)^2} + \frac{1}{R_{cx}^2}\left(\frac{v_{\theta CS}}{v_x}\right)^2 + 1 \tag{4.3.17}$$

where R_{cx} may be computed from Eq. (4.3.14) or (4.3.15).

We compare the predictions of the Barth and the Muschelknautz models for pressure loss across the vortex tube with those of Eq. (4.3.17) in Table 4.3.1. In the models of Barth and Muschelknautz, Eu_x is related to the velocity ratio $v_{\theta CS}/v_x$ in a semi-empirical way, based on a curve-fit to experimental data. Muschelknautz and Krambrock (1970) also observed that Eu_x was somewhat dependent upon the vortex tube Reynolds number, Re_x, but that it had little effect for $Re_x > 5 \times 10^4$. Since the vast majority of practical cyclones operate well above this value, we do not attempt to 'fine tune' the model to account for Re_x effects herein. We also want to point out that Muschelknautz and Krambrock's data automatically include the pressure loss associated with gas entering the vortex tube since the 'upstream' static pressure they used to derive their vortex tube loss coefficient (Eu_x) was measured at a point ahead of the vortex tube.

Table 4.3.1. Comparison of various vortex finder pressure drop models

$v_{\theta CS}/v_x$	Barth Eq. (4.3.4)	Muschelknautz Eq. (6.6.2)	Core flow model Eq. (4.3.17)	
	Eu_x	Eu_x	R_{cx}	Eu_x
0.01	0.009	2.01	0.087	2.03
0.05	0.074	2.06	0.181	2.15
0.1	0.191	2.15	0.252	2.30
0.2	0.496	2.39	0.343	2.62
0.5	1.80	3.44	0.487	3.77
1	4.90	6.00	0.601	6.22
2	13.8	13.6	0.706	13.0
5	58.3	52.6	0.818	47.5
10	184	167	0.878	150
50	3218	3055	0.956	2871

We observe that at vanishing spin ($v_{\theta CS}/v_x \to 0$) the Muschelknautz-derived model has a value of 2, but then exponentially increases with increasing dimensionless spin velocity, $v_{\theta CS}/v_x$. The Barth model does not account for an entrance loss, and so the initial value of Eu_x is zero. The Barth and Muschelknautz models agree reasonably well from a $v_{\theta CS}/v_x$ value of about

unity. Most cyclones will operate at $v_{\theta CS}/v_x$ above 1, and well below a value of 5, the latter corresponds to an Eu_x of about 50.

The two columns on the right side of Table 4.3.1 present the predictions of our 'core flow' model. The dimensionless core radius, R_{cx}, was computed on basis of Eq. (4.3.15) for the values of $v_{\theta CS}/v_x$ shown in the leftmost column of the table. Knowing R_{cx} and $v_{\theta CS}/v_x$, Eu_x was then computed from Eq. (4.3.17).

The writers find it rather remarkable that the Eu_x (or 'pressure loss coefficients') predicted by the three methods—two based on experimental measurements, the third on a relatively simple, theoretically-based model— agree so closely over the very wide range of dimensionless spin velocities reported, particularly the Muschelknautz and the core flow model agree closely. Such agreement provides strong support to the assumptions underlying the model and for its use as a method for computing the pressure loss through the gas outlet tube in cyclone separators.

As a final comment, the above development assumed a thin-walled vortex tube. If the tube wall thickness were to be 2% of its diameter, for example, the value of unity, which we added to Eqs. (4.3.16) and (4.3.17), can be expected to take on a value of 0.69. If the thickness were 5% or greater, it would become 0.47. These values are based on experimental data taken on ordinary (axial) flow of gas into protruding (Borda type) inlet pipes. See Blevins (1984), for example.

4.3.3 Purely Empirical Models

A number of empirical models have been proposed for cyclone pressure drop. We shall mention two of the most widely used.

Shepherd and Lapple (1940) suggested:

$$Eu_{in} = \frac{16ab}{D_x^2}, \tag{4.3.18}$$

which is valid for slot-type inlets.

Casal and Martinez-Benet (1983) gave:

$$Eu_{in} = 3.33 + 11.3 \left(\frac{ab}{D_x^2} \right)^2. \tag{4.3.19}$$

Common to these empirical expressions is that they only contain the ratio of the inlet to the outlet areas. Like the common practice of treating the "K" value associated with a particular pipe fitting as a constant, indpendently of the size of the fitting, the preceding simple correlations imply the relatively easy scaling law that the Euler number is independent of the Reynolds number and that it is constant between geometrically similar cyclones. This means that pressure loss measurements performed on a 'model' cyclone, for example, could be expected to give reasonably accurate pressure loss predictions for a

'commercial' cyclone irrespective of whether *Re*-similarity is satisfied. We will be discussing scaling laws for cyclones more thoroughly in Chap. 8. For now we mention that the scaling equation for constant Euler number (based on the inlet velocity, v_{in}) is:

$$(Eu_{in})_{comm.} = \left(\frac{\Delta p}{\rho v_{in}^2}\right)_{comm.} = \left(\frac{\Delta p}{\rho v_{in}^2}\right)_{model} = (Eu_{in})_{model} \qquad (4.3.20)$$

Equation (4.3.20) is known to give good results for smooth walled cyclones operating under fully developed turbulent flow at light to moderate solids loadings. It assumes not only geometric similarity between the 'model' and the 'commercial' unit, but also constant total friction factor. This implies constant relative wall roughness and inlet solids concentration (expressed as mass solids/mass gas or as mass solids/volume of gas). Even so, as we shall see later in Chap. 6, Eq. (6.1.11), the total friction factor is a rather complex function of a large number of dimensional and physical property variables. For this reason, it is not realistic to expect that the total friction factor will remain truly constant between a model cyclone and its commercial counterpart, even if the relative roughness and solids loading are maintained constant. One would not want to use Eq. (4.3.20) to estimate the pressure loss of a heavily solids-loaded, brick-lined commercial cyclone, for example, on the basis of pressure loss measurements performed on a small, smooth-walled model cyclone operating under air-only feed conditions. This would be true irrespective of their dimensional similarity. Fortunately, in most applications involving light to moderate loadings and smooth walled cyclones, the difference in friction factors do not normally impose a serious restriction on the use of Eq. (4.3.20).

4.4 Model Assumptions in Light of CFD and Experiment

In order to obtain analytical models for cyclone performance, investigators have made some rather sweeping assumptions about the flow pattern that actually exists within cyclone separators. We can get some indication of whether these assumptions are reasonable from measurements and numerical simulations.

One important assumption in models predicting cyclone flow pattern and separation performance is that the surface *CS* defines the boundary between axial upflow and downflow. We can test this both experimentally and by CFD. We shall discuss CFD (computational fluid dynamics) for cyclone modeling in Chap. 7.

Figure 4.5 shows results of both experiment and CFD in a swirl tube with a cylindrical body (Peng et al., 2002). In the left-hand figure a series of measurements are shown where the boundary between the up- and downwardly directed flow has been determined using laser-Doppler anemometry (LDA, we

will discuss this technique in Chap. 10). The right-hand side of this figure is a CFD plot wherein this boundary shows up as two dark fuzzy vertical 'lines' symmetrically arranged about the central axis and located about 1/2 the radius out from the centerline[4].

The qualitative picture is the same in the two figures, in fact the measurements and the simulations agree excellently: for the larger vortex finder (D_x is a little larger than 1/2 D, the surface appears to be cylindrical in agreement with the model assumption. For the smaller vortex finder, however, the inner part of the vortex widens under the vortex finder wall, and, in the main part of the body, it becomes practically the same diameter as the larger vortex finder.

Although the general picture therefore is in agreement with the model assumptions, the results in Fig. 4.4.1 indicate that the diameter of the boundary between up- and downward axial flow is determined by D rather than D_x, except right under the vortex finder wall.

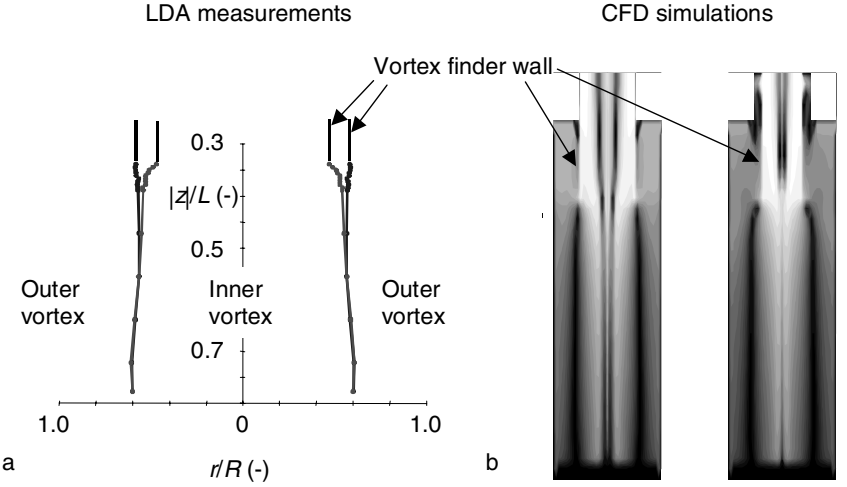

Fig. 4.4.1. LDA measurements and CFD simulations in a swirl tube with different vortex finder diameters. In **a** the boundary between the up- and downwardly directed flow have been pinpointed with LDA. In **b** the loci of zero axial velocity have been made visible in a CFD flow field by plotting contour plots of $\ln(1+v_z^2)$, which shows up the locus as a black region (low contour value)

In much of the cyclone literature the radial position of the boundary between up- and downward flow is held to determine the cut size of the cyclone or swirl tube. However, for a particle caught in the upward flow to be lost, it

[4] The boundary has been made visible in a CFD flow field by plotting contour plots of $\ln(1+v_z^2)$, which shows up the boundary as a black region (low contour value).

still has to enter the vortex finder. Thus, although we see that the radial position of this boundary does not correspond with D_x, D_x remains the parameter determining the cyclone cut size, in accordance with the 'equilibrium-orbit' cyclone separation models, which is one type of model we will discuss in the following chapters. This also means that the separation efficiency to a large extent is determined by the local flow pattern just under the vortex finder wall.

Another assumption made in the models is that the swirl velocity profile (its radial distribution) in the cyclone is constant axially. Figure 4.4.2 shows LDA measurements of the radial profiles of the tangential velocity at a series of axial stations in a cylinder-on-cone cyclone with a conventional slot-type inlet. Figure 4.4.3 shows a similar plot for a swirl tube with a cylindrical body.

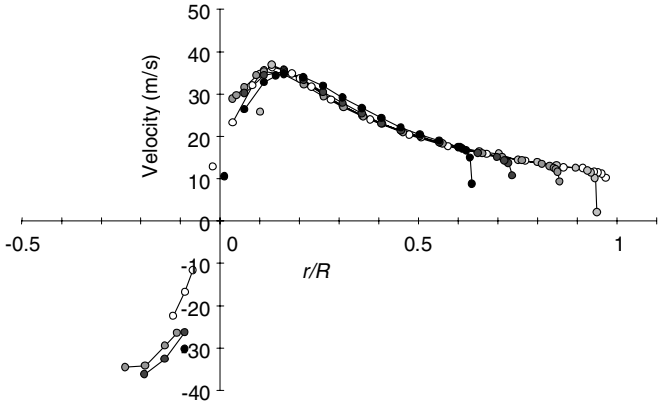

Fig. 4.4.2. The tangential gas velocity as a function of dimensionless radius $r/R.$, measured with LDA at axial stations in a cylinder-on-cone cyclone. The highest station is just in the cylinder, the rest are in the cone. The darker the points the lower the station. The velocities measured beyond the cyclone axis of symmetry (which is at $r/R = 0$) appear with the opposite sign in the output from the LDA

The figures show that the profile of the dimensionless tangential velocity is constant at all axial positions in the cylinder-on-cone cyclone, even until deep in the conical section. In the swirl tube there is a slight tendency for the tangential velocity to decrease as we move down. Overall, the measurements confirm the validity of this model assumption at least for geometries most commonly found in commercial service.

A third assumption made in cyclone performance models is that the radial velocity is uniform over *CS*. The radial velocity is the smallest velocity component, and it is more difficult to measure with LDA than the other components. We can again resort to CFD to get an impression of the flow pattern. Figure 4.4.4 shows profile plots of the radial velocity distribution in both a cylindrical swirl tube and a cylinder-on-cone cyclone with slot inlet.

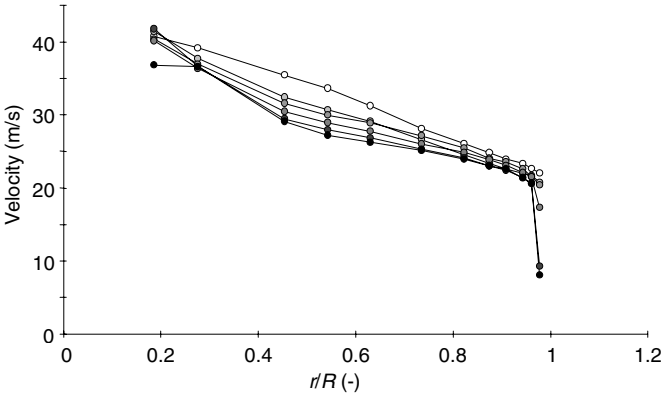

Fig. 4.4.3. The tangential gas velocity measured with LDA at a series of axial stations in a cylindrical swirl tube. The highest station is just under the vortex finder. The darker the points the lower the station

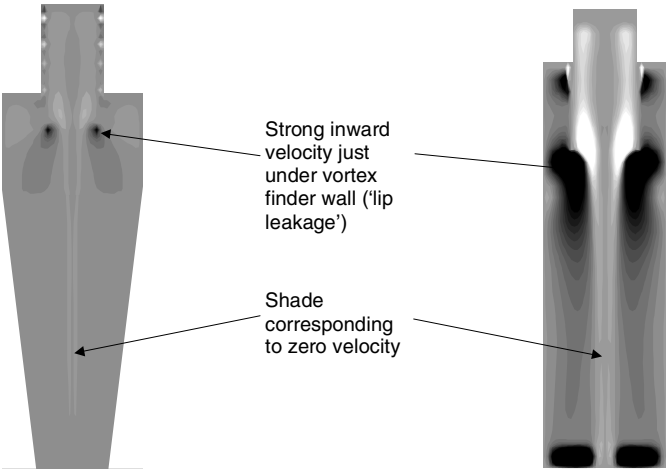

Fig. 4.4.4. Profile plots from CFD simulations of the radial velocity distribution in a cylindrical swirl tube and a cylinder-on-cone cyclone. The main difference between the two is that the radial flow from the outer to the inner vortex is more uniformly distributed axially in the cyclone than in the swirl tube

The figure clearly shows the region of strong inward velocity just under the vortex finder, often referred to as 'lip leakage'. This region is obviously much more localized in the cylinder-on-cone cyclone. Another region of strong inward velocity is visible low in the swirl tube, while the radial velocity is somewhat more uniformly distributed in the cylinder-on-cone design.

The picture is not quite 'fair'. Although the lip leakage appears to be much less of a dominant feature in the cylinder-on-cone cyclone, the maximum

velocity is actually about four times higher than the mean in the cyclone, while it is only two times higher in the swirl tube. Since the gray-shades are evenly distributed from the minimal to the maximal velocities, the flow appears more uniform in the cylinder-on-cone cyclone.

In both cases, the bottom boundary condition was simply a 'no flow-through' condition. The bottom configuration varies in swirl tube designs; some swirl tubes discharge directly to a wider hopper without any bottom plate. Such an arrangement does not encourage gas to suddenly turn inwards at the bottom of the main body cylinder.

4.5 Overview

We finish this chapter with a tabular overview of the models discussed. The models involve different degrees of complexity and vary in terms of the aspects that they account for.

The reader should use his or her own judgment as to which model should be chosen for a particular situation. If the task is to estimate the pressure drop in a smooth-walled cyclone operation at a low solids loading, a simple empirical pressure drop model may well suffice, but if the cyclone in question has rough walls, e.g. due to a refractory lining, or is operating at high loading, the model of Barth or the latest model of Muschelknautz, which we shall discuss in Chap. 6, would be more appropriate. Perhaps also the Stairmand model with a good estimate of the friction factor could be used for situations in which wall roughness plays a role.

Table 4.5.1. Models for the tangential velocity in the cyclone body v_θ

Model	Range of application	Comments
n-type model	All cyclones	The index n is often determined empirically for a given cyclone and operating conditions. Alexander's expression seems to predict somewhat low values of n.
Barth	Cyclones and swirl tubes	Considers the frictional losses in the body. The effects of wall roughness and solids loading are accounted for in the value of the friction factor, f.
Meissner/Löffler	Cylinder-on-cone cyclones with slot inlets at low solids loading	Considers the frictional losses in the body. The friction factors on the cylindrical wall, the conical wall and the roof can in principle be different. The authors themselves did not relate f to the solids loading.

Table 4.5.2. Models for cyclone pressure drop, Δp

Model	Range of application	Comments
Stairmand	Cyclones with tangential inlets.	Considers the frictional losses in the body and vortex finder. Restricted to cyclones with low solids loading if Stairmand's friction factor is used.
Barth	Cyclones and swirl tubes	Considers the frictional losses in the body and vortex finder. Effects of wall roughness and solids loading accounted for in the value of the friction factor, f.
Shepherd-Lapple	Cyclones with tangential inlets. Low solids loading.	Empirical. Only contains inlet and outlet areas.
Casal-Martinez	Cyclones with tangential inlets. Low solids loading.	Empirical. Only contains inlet and outlet areas

4.A Worked Example for Calculating Cyclone Pressure Drop

A large, short-coned, 4 m diameter cyclone is to be installed in a factory. Figure 4.A.1 shows the geometry of the cyclone, which is to operate at varying gas flows; the maximum inlet velocity foreseen is 30 m/s. The gas is ambient air having a density of 1.2 kg/m^3. We are asked to predict the pressure drop over the cyclone at low solids loading.

Solution

We have the model equations in the main text at our disposal. We assume that low loading corresponds to about 2.5 g dust per m^3 of incoming gas.

Let's start with the Stairmand model, Eqs. (4.3.1) and (4.3.2). We need the total wall area of the cyclone separation space. This is (Dirgo and Leith, 1985):

$$A_R = \frac{\pi\left(D^2 - D_x^2\right)}{4} + \pi D\left(H - H_c\right) + \pi D_x S + \frac{\pi\left(D + D_d\right)}{2}\left(H_c^2 + \left(\frac{D - D_d}{2}\right)^2\right)^{0.5}. \quad (4.A.1)$$

Inserting:

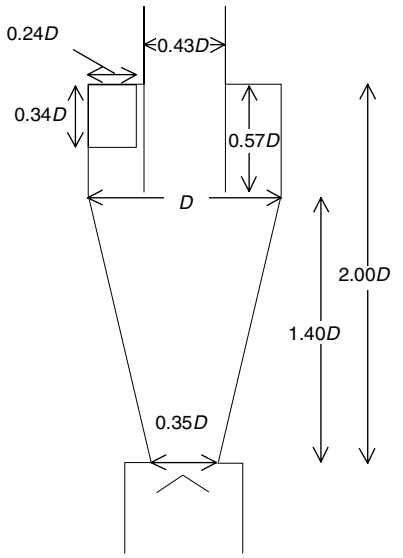

Fig. 4.A.1. Large, short-coned cyclone, $D = 4$ m

$$A_R = \frac{\pi\left(4.0^2 - 1.72^2\right)}{4} + \pi 4.0\,(8.0 - 5.6) + \pi \times 1.72 \times 2.28 + \frac{\pi\,(4.0 + 1.4)}{2}\left(5.6^2 + \left(\frac{4.0 - 1.4}{2}\right)^2\right)^{0.5} = 101.5 \text{ m}^2$$

-which seems reasonable.

We can then fill in Eq. (4.3.2) to get:

$$q = \frac{-\left(\frac{1.72}{2(4.0-0.96)}\right)^{0.5} + \left(\frac{1.72}{2(4.0-0.96)} + \frac{4\times 101.5\times 0.005}{1.36\times 0.96}\right)^{0.5}}{\left(\frac{2\times 101.5\times 0.005}{1.36\times 0.96}\right)} = 1.060$$

and substituting this in (4.3.1) we get:

$$\frac{\Delta p}{\frac{1}{2}\times 1.2\times 30^2} = 1 + 2\times 1.060^2\left(\frac{2\,(4.0 - 0.96)}{1.72} - 1\right) + 2\left(\frac{4\times 1.36\times 0.96}{\pi\times 1.72^2}\right)^2 = 7.33$$

-which gives a pressure drop Δp of 3960 Pa (0.574 psi).

In the same way we can fill in the values in the Barth model equations, (4.3.3) and (4.3.4). This requires some more computations.

First we calculate the wall velocity $v_{\theta w}$ using an α of 0.723 which we compute from Eq. (4.2.5). This gives: $v_{\theta w} = 31.5$ m/s, which is slightly higher than v_{in} due to the constriction of the inlet jet in the slot inlet. We can then calculate $v_{\theta CS}$ from (4.2.6), calculating the friction factor, f, from (4.2.9):

$$f = 0.005(1 + 3(0.0025/1.2)^{0.5}) = 0.00568$$

Note that we divide the solids loading in kg dust/m^3 air with the air density to obtain the loading as a mass fraction. This gives $v_{\theta CS} = 64.1$ m/s.

We then find v_x from v_{in}:

$$v_x = \frac{v_{in}ab}{(\pi D_x^2/4)} = \frac{30 \times 1.36 \times 0.96}{(\pi 1.72^2/4)} = 16.9 \text{ m/s}$$

We now have all the necessary data. Inserting in equations (4.3.3) and (4.3.4) using the value of K for a rounded edged vortex tube, we find that Barth predicts a pressure drop of:

$$\Delta p = \Delta p_{body} + \Delta p_x = 390 + 5910 = \underline{\underline{6300 \text{ Pa}}} \ (0.913 \text{ psi})$$

We can also use the empirical models of Shepherd and Lapple (4.3.18):

$$\Delta p = \left(\frac{1}{2}\rho v_{in}^2\right) Eu_{in} = \left(\frac{1}{2}\rho v_{in}^2\right) \frac{16ab}{D_x^2} = \left(\frac{1}{2}1.2 \times 30^2\right) \frac{16 \times 1.36 \times 0.96}{1.72^2}$$
$$= \underline{\underline{3810 \text{ Pa}}} \ (0.553 \text{ psi})$$

and Casal and Martinez (4.3.19):

$$\Delta p = \left(\frac{1}{2}\rho v_{in}^2\right) Eu_{in} = \left(\frac{1}{2}1.2 \times 30^2\right) \left(3.33 + 11.3 \left(\frac{1.36 \times \ 0.96}{1.72^2}\right)^2\right)$$
$$= \underline{\underline{2990 \text{ Pa}}} \ (0.434 \text{ psi})$$

Obviously the predictions of the models differ considerably. While the models of Stairmand and Shepherd and Lapple agree reasonably well, the Casal/Martinez and Barth models differ by almost a factor of two. In the following chapter we shall put the models for pressure drop to a test: we shall compare their predictions of the effect of cyclone length on pressure drop with experiment.

4.B The Meissner and Löffler Model

In this appendix we discuss one other model for v_θ: the model of Meissner and Löffler (Meissner and Löffler, 1978; Mothes and Löffler, 1988). They performed an intuitively appealing moment-of-momentum balance in the cyclone separation space. Figure 4.B.1 illustrates the principle.

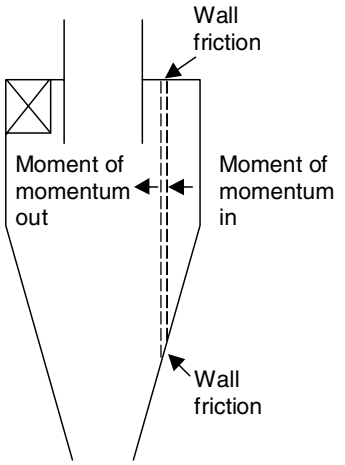

Fig. 4.B.1. A diagram illustrating the moment-of-momentum balance carried out by Meissner and Löffler

They consider a cylindrical element as sketched. Convective flow of moment-of-momentum in and out of the element is balanced with the moment of the wall friction force at the top and bottom walls. An obvious weakness in this approach is that the friction at the cylindrical part of the wall is not easily included. Meissner and Löffler therefore propose a three-step strategy:

- calculate the wall velocity $v^*_{\theta w}$ just after the inlet from the inlet velocity v_{in},
- calculate the velocity reduction due to the friction at the cylindrical wall, giving the tangential wall velocity $v_{\theta w}$,
- calculate the tangential velocity at *CS*, $v_{\theta CS}$

Also here, we shall have to refer to the original paper of Meissner and Löffler for the detailed derivations involved in the two latter steps. The formulae themselves for this model are set out clearer in the paper of Mothes and Löffler (1988).

Like Barth, Meissner and Löffler also consider that the velocity is increased (from v_{in} to $v^*_{\theta w}$) by contraction of the inlet jet just after a slot inlet. They find:

$$\beta \equiv \frac{v_{in}}{v^*_{\theta w}} = -0.204\frac{b}{R} + 0.889 \tag{4.B.1}$$

which is an empirical expression; compare with (4.2.4) and (4.2.5) in the main text.

Meissner and Löffler then perform a moment-of-momentum balance on the gas considering the friction at the cylindrical wall using a wall friction factor, f_{cyl}:

$$v_{\theta w} = \frac{\langle v_z \rangle}{f_{cyl} H^*_{cyl}} \left[\sqrt{\frac{1}{4} + f_{cyl} H^*_{cyl} \frac{v^*_{\theta w}}{\langle v_z \rangle}} - \frac{1}{2} \right] \tag{4.B.2}$$

with:

$$H^*_{cyl} = \frac{a}{R} \left[\frac{-\arccos\left(1 - \frac{b}{R}\right)}{2\pi} \right] + \frac{H_{cyl}}{R} \tag{4.B.3}$$

where $\langle v_z \rangle$ is the cross-sectional mean axial velocity in the (modified) body. The last equation follows Meissner and Löffler (1978), while in Mothes and Löffler (1988) the argument of the arccos function has the opposite sign.

Finally, they obtain the tangential velocity inside the separation space $v_\theta(r)$ from the moment-of-momentum balance illustrated in Fig. 4.B.1, giving:

$$v_\theta(r) = \frac{v_{\theta w}}{\frac{r}{R}\left[1 + \frac{v_{\theta w}}{\langle v_z \rangle}\left(f_{lid} + \frac{f_{cone}}{\sin\varepsilon}\right)\left(1 - \frac{r}{R}\right)\right]} \tag{4.B.4}$$

where ε is the angle between the wall of the conical section and the cyclone axis. To calculate $v_{\theta CS}$, insert $r = R_x$ in this equation. In the original work, Meissner and Löffler differentiated between the friction factors at the cylindrical wall, conical wall and lid, f_{cyl}, f_{cone} and f_{lid}, respectively, but in the later publication of Mothes and Löffler (1988) they are all given as being equal and lying in the range: 0.0065 to 0.0075.

Obviously this model has some restrictions in its range of applications. As the model stands, it is only suitable for cyclones with slot inlet and a low loading. This is because the effect of the dust on the wall on the friction factors is 'not reliably quantified' as the authors state. If the effect of the solids is to be accounted for, the friction factors at the different walls are likely to differ. Another restriction is that it is only applicable to the conventional cylinder-on-cone cyclone design, and therefore not to cylindrical swirl tubes.

5

Cyclone Separation Efficiency

In the previous chapter we have examined various models for predicting the velocity distributions in cyclones. In this chapter we wish to first present a brief discussion of the issues, and to then present some of the literature models available for computing cyclone separation efficiency.

5.1 Discussion

There are basically two modeling concepts for cyclone separation efficiency in the literature: the 'equilibrium-orbit' models and 'time-of-flight' models.

Figure 5.1.1a illustrates the concept behind the equilibrium-orbit models. They consider the imagined cylindrical surface CS that is formed by continuing the vortex finder wall to the bottom of the cyclone. These models are based on *a force balance on a particle that is rotating in CS at radius* $R_x = \frac{1}{2}D_x$. In this balance the outwardly directed centrifugal force[1] is balanced against the inward drag caused by the gas flowing through, and normal to, surface CS and into the inner part of the vortex. The centrifugal force is proportional to the particle mass and therefore to x^3, while the (Stokesian) drag is proportional to x (Chap. 2). Large particles are therefore "centrifuged" out to the cyclone wall, and small particles are dragged in and escape out the vortex tube. The particle size for which the two forces balance (the size that 'orbits in equilibrium' in CS) is taken as the cyclone's x_{50} or cut size. As such, it is the particle size that stands a 50-50 chance of being captured. This particle size is of fundamental importance and is a measure of the intrinsic separation capability of the cyclone. As discussed in the previous chapter, all the gas velocity components are assumed constant over CS for the computation of the equilibrium-orbit size.

Figure 5.1.1b illustrates the other modeling approach: time-of-flight modeling. Here, the particle's migration to the wall is considered, neglecting the

[1] See discussion pertaining to the use of the term "centrifugal force" in Sect. 2.1

inward gas velocity. In the original time-of-flight model, the question was posed *whether a particle, injected at some lateral position in the inlet, had the time to reach the cyclone wall and be collected before reaching the cyclone bottom.*

Some later models have been hybrids between these two concepts, considering *both an interchange of particles across CS* (due to centrifugation and turbulent dispersion) *and particle migration to the cyclone wall.*

In the following sections, we will give an account of some of the models. Worked examples will be given in Appendix 5.A.

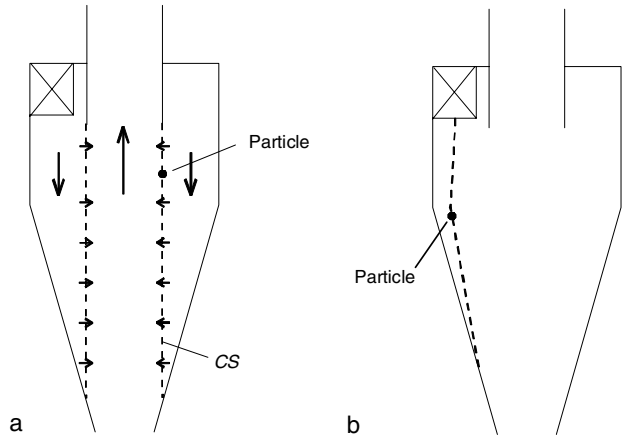

Fig. 5.1.1. Sketches showing the concept behind **a**, the 'equilibrium-orbit' models, and **b**, the 'time-of-flight' models

5.2 Models

5.2.1 Equilibrium-orbit Models: the Model of Barth

The model of Barth (1956) (see also Muschelknautz (1972)) is the original equilibrium-orbit model.

The forces acting on a particle rotating in CS are:

- the centrifugal force acting outward with a magnitude of: $\frac{\pi x^3}{6}\rho_p\left(\frac{v_{\theta CS}^2}{R_x}\right)$ and
- the (Stokesian) drag acting inward: $3\pi x\mu v_{rCS}$.

We are neglecting the gas density in comparison to the solid density in the centrifugal force term (Chap. 2). Equating these forces to find the cut size x_{50} gives:

$$x_{50} = \sqrt{\frac{v_{rCS} 9 \mu D_x}{\rho_p v_{\theta CS}^2}} \tag{5.2.1}$$

We calculate v_{rCS} and $v_{\theta CS}$ from Eqs. (4.2.1) and (4.2.6).

Once we have the cut size, we can fit a grade-efficiency curve through it. Barth determined a 'universal curve' by experiment, and gave it graphically in his paper. Dirgo and Leith (1985) have fitted a functional form to this curve (see also Overcamp and Mantha (1998)) to obtain:

$$\eta(x) = \frac{1}{1 + \left(\frac{x_{50}}{x}\right)^{6.4}} \tag{5.2.2}$$

Figure 5.2.1 shows this function.

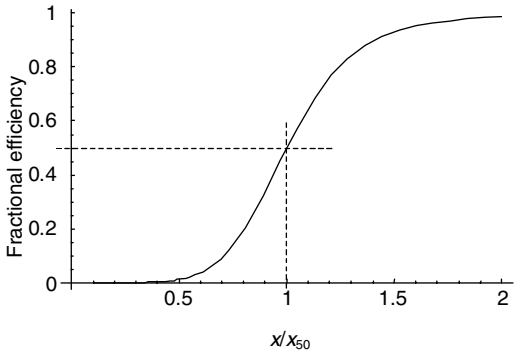

Fig. 5.2.1. Fitted grade-efficiency curve (Eq. 5.2.2) around the cut size of Barth

Equation (5.2.2) represents one functional form for representing the grade-efficiency curve (GEC). The writers' own analysis on numerous commercial and laboratory cyclones reveals that the form of Eq. (5.2.2) describes some cyclone geometries quite well, especially smooth, well-designed laboratory cyclones. The exponent 6.4 is, however, a little larger than the values typically observed in some large-scale, refractory-lined, commercial cyclones and in some poorly designed small-scale cyclones. In these latter cases, the exponent typically lies between 2 and 4.

If one has generated GEC data on a given cyclone type, one can then plot $\ln(\frac{1}{\eta(x)} - 1)$ versus $\ln(\frac{x}{x_{50}})$ using linear coordinates or simply $(\frac{1}{\eta(x)} - 1)$ versus $(\frac{x}{x_{50}})$ using log-log coordinates. If the majority of the data defines a straight line, then the functional form of Eq. (5.2.2) correctly describes the cyclone's GEC. If not, then some other function may be tried (see below). Assuming that the data do define, within reason, a straight line, then the slope of the line thus plotted, m, is the coefficient to be used (in place of 6.4) in Eq. (5.2.2). This slope is a measure of the 'sharpness' of the GEC. The greater m is, the steeper is the curve, and the GEC begins to conform to a 'stair-step' or 'sieve'

type of separator—collecting all particles greater than the x_{50} cut-point and rejecting or losing those that are smaller.

As indicated above, a poorly designed cyclone or one that is in poor mechanical condition will tend to exhibit low values for m. This is often evidence of excessive backmixing occurring within the cyclone. It can also be caused by gas leakage up the bottom of the cyclone or by excessive wall roughness or wall deposits.

Another useful functional form for the GEC is:

$$\eta\,(x) = 1 - \exp\left[\ln(0.5)\left(\frac{x}{x_{50}}\right)^{m}\right]. \tag{5.2.3}$$

Cyclones which are very 'clean' aerodynamically (minimum mixing, good mechanical condition, good 'seal' on the underflow, etc.) often have GEC's that conform to this exponential form. In this case, if one were to plot $\ln(1 - \eta(x))$ versus x on a log-log chart and find that the data defined a reasonably straight line, then Eq. (5.2.3) would correctly describe the cyclone's GEC. Typically, m will take on a value between 2 and 4 for this functional form with the higher values being associated with well designed, smooth-walled cyclones that are in good mechanical condition.

Using a rather idealized model of gas and particle behavior within a cyclone, Licht (1980) showed that, if the mixing is such that all the uncollected particles within a cyclone are subject to complete backmixing, then equation (5.2.2) correctly describes the GEC for the process. Likewise, it can be shown that if the uncollected particles are subject to only radial backmixing (and not axial as well), then Equation (5.2.3) correctly describes the GEC.

In the limiting case where no backmixing of any kind occurs, then the functional form of the GEC becomes:

$$\eta\,(x) = 0.5\left(\frac{x}{x_{50}}\right)^{m} \qquad \text{for } \eta(x) \le 1 \tag{5.2.4}$$

and a plot of GEC data using log-log coordinates would define a straight line having slope m. It turns out that if the particles were all small enough to settle under Stoke's law, the value of m would be 2 and the GEC would have the shape of a parabola up to the point where $\eta(x)$=1.

We note that in all three of the GEC's presented above, $\eta(x) \to 0$ as $x \to 0$, $\eta(x) = 0.5$ for $x = x_{50}$, and $\eta(x) \to 1$ as $x \to \infty$ (except for the 'no mix' case wherein $\eta(x) \to 1$ at some finite value of x. Unlike the other two functions, the parabolic, no-mix, function does not posess an asymptopic limit of 1 as $x \to \infty$, which, from a physical point of view, it must.)

Muschelknautz improved the model of Barth in a number of ways. As we discussed in the previous chapter, he measured friction factors in both cylindrical and conical bodied cyclones and, on basis of this work, accounted for the effects of wall roughness and solids loading upon the cut-point and the pressure drop. We will discuss the latest version of his model for cyclone

efficiency in Chap. 6. In Chap. 9 we will be dealing with the effect of solids loading on the cyclone separation performance and pressure drop.

5.2.2 Time-of-Flight Models

The original time-of-flight model was proposed by Rosin et al. (1932), who compared the time required for a particle injected though the inlet at some radial position to reach the cyclone wall, to the time available for this. They considered the smallest particle size that can traverse the entire width of the inlet jet before reaching the bottom of the cyclone as a critical particle size, which we will call x_{50}. The total path length for a particle swirling close to the wall (assumed cylindrical) is: $\pi D N_s$, where N_s is the number of spiral turns the particle takes on its way toward the bottom of the cyclone. We have here neglected to multiply by the cosine of the angle to the horizontal of the spiral path, this angle will normally lie between 15 and 30 degrees. Assuming the inlet velocity to prevail at the cyclone wall, the time the particle takes to reach the bottom is:

$$\frac{\pi D N_s}{v_{in}}. \tag{5.2.5}$$

The terminal velocity of a particle in the radial direction in the centrifugal field is given by Eq. (2.2.9). Taking here v_θ as v_{in}, r as $D/2$, and including the density of the gas, we obtain:

$$U_r' = \frac{x^2 \left(\rho_p - \rho_g\right)}{18\mu} \left(\frac{v_{in}^2}{r}\right). \tag{5.2.6}$$

Neglecting any radial gas velocity, the time required for the particle to reach the wall is b/U_r'. Equating this to the time available (we are looking for the critical particle that just manages to reach the wall), and solving for x, the critical particle size is obtained:

$$x_{50} = \sqrt{\frac{9b\mu}{\pi N_s v_{in} \left(\rho_p - \rho\right)}}. \tag{5.2.7}$$

To use this equation we need to determine N_s. Zenz (2001) gave a graph for N_s as a function of inlet velocity, based on experience. Fitting this graph by a simple function gives:

$$N_s = 6.1 \ \left(\ 1 - e^{-0.066 v_{in}}\right) \tag{5.2.8}$$

with v_{in} in m/s.

Rietema (1959) considered the migration of a particle to the wall as shown in Fig. 5.1.1b, using the idealized geometry of a purely conical cyclone. He assumed that the tangential gas velocity profile (i.e. v_θ as a function of r) does not change with axial position at constant r (the tangential velocity at

a given distance from the wall is therefore increasing as we move down the conical cyclone body). He also assumed that the axial velocity in which the particle moves, v_{zw}, is constant. With these assumptions he derived a cut size, which is the size of particle that is just captured when injected in the middle of a slot-type inlet:

$$\frac{1}{2}b = \frac{x_{50}^2\,(\rho_p - \rho)}{18\mu}\frac{H}{v_{zw}R}\int_0^R \frac{v_\theta^2}{r}dr \tag{5.2.9}$$

Rather than trying to model v_θ as a function of r, Rietema noted that the gas density times the integral in (5.2.9) equals the static pressure difference between the wall and the centre (see Chap. 2). He considered this to be the largest contribution to the total pressure drop over the cyclone, and therefore almost equal to it. This suggests that hardly any of the loss in static pressure in the vortex is recovered in the vortex finder, in line with the discussion in Chap. 4. Inserting the static pressure in (5.2.9) gives:

$$\frac{1}{2}b = \frac{x_{50}^2\,(\rho_p - \rho)}{18\mu}\frac{H}{v_{zw}R}\frac{\Delta p}{\rho} \Rightarrow \frac{x_{50}^2\,(\rho_p - \rho)}{\mu}H\frac{\Delta p}{\rho Q} = \frac{3}{2}\frac{R}{a} \tag{5.2.10}$$

where $Q = abv_{in}$. This equation incorporates Rietema's observation that v_{in}/v_{zw} has the constant value of 6[2].

Rietema found empirically that the left-hand side of the latter part of (5.2.10) is a characteristic cyclone number only dependent on geometry, and called this number Cy_{50}. By experiment he determines that $Cy_{50} = 3.5$ for a cyclone of optimal design.

The Rietema model for determining x_{50} in a cyclone is therefore:

$$Cy_{50} \equiv \frac{x_{50}^2\,(\rho_p - \rho)}{\mu}H\frac{\Delta p}{\rho Q} = 3.5. \tag{5.2.11}$$

Thus, although this model was derived by considering the gas flow pattern in the cyclone, it relates, in its final form, the separation cut-point diameter, x_{50}, to the pressure drop. Hence, the pressure drop needs to be predicted to use the model. A good pressure drop model for this purpose is that of Shepherd and Lapple, Eq. (4.3.18).

As we shall see in the following chapter, the empirical models of Svarovsky and Karpov/Saburov, like that of Rietema, also relate efficiency to pressure drop.

The strong influence of the vortex finder diameter, D_x, on the efficiency of cyclones is not directly evident in the reasoning behind the time-of-flight models. For the Rosin-Rammler-Intelmann model, Zenz (2001) argued that

[2] Rietema's original derivation assumed an inlet of circular cross section. The expressions have been rederived for a rectangular inlet.

reducing D_x prolongs the vortex in the cyclone[3] (that is, it pushes the 'natural end' of the vortex down; the issue of the natural end will be discussed later), increasing N_s and the time available for a particle to reach the cyclone wall. Such a dependency is not yet built into the expression for N_s, Eq. (5.2.8). Turning to the Rietema model, we saw in the previous chapter that the pressure drop depends rather strongly on D_x, and, thus, so does x_{50}. Therefore we could say that the effect of D_x on cyclone efficiency is brought in by 'the back door' in this model.

One more model should be mentioned when considering the time-of-flight modeling approach: the model of Leith and Licht (1972). Like the pure time-of-flight models mentioned above, this also considers the particle migration to the cyclone wall neglecting the radial gas velocity. The Leith and Licht model, however, considers not a *single* particle, but rather the *flux* of particles to the wall, which is calculated assuming complete radial, but no axial, particle mixing.

We shall not give the equations for this model. Clift et al. (1991) pointed out that for the derivation of the model to be consistent with the underlying concept, the equation for the particle flux to the wall should be different than that reported in the original paper. After changing this, and another aspect, the resulting expression gave grade-efficiency curves of a sigmoidal shape, consistent with practice as we discuss later in this chapter. But the model then shares the weakness of the time-of-flight models, in that it does not easily account for the effect of D_x on the efficiency. To remedy this, the same argument as Zenz made for the Rosin-Rammler-Intelmann model (longer vortex for smaller D_x) may be applied here, but these authors find the behavior of a cyclone vortex is not so simple. As we shall show later in this book, decreasing D_x increases the vortex core spin velocity and tends to reduce the stability of the vortex. Depending on how the bottom of the cyclone is designed, and other factors, such as the cyclone geometry, wall roughness, solids loading, etc., the vortex (bottom) "end" can "short circuit" by attaching itself to, and precessing around, the lower cone (or hopper walls). If sufficient height is available, this induces a *secondary vortex* of weaker intenstity *below* the main or *primary vortex*. Such short circuiting and precession disturbs the particle that have reached the wall and reduces particle collection performance. It is not known, however, how effective the secondary vortex is in collecting solids in cyclones that are long enough to accommodate a secondary vortex. This is a poorly understood area and is in need of additional investigation.

In conclusion, we can say that the time-of-flight modeling concept is entirely different in nature from the equilibrium-orbit concept. It is peculiar that these two very different concepts should result in efficiency models that agree well, both absolutely and in trends, over a wide range of cyclone designs

[3] We note that such an effect of D_x on the vortex length is contrary to a well-known correlation for the vortex length, and also contrary to a number of experimental observations, as will be discussed later

and operating conditions. Except for the Rietema model, the time-of-flight models predict somewhat larger cut sizes than the equilibrium-orbit models. Although we are using equilibrium-orbit models mostly in this book, we have to say that the time-of-flight concept is very consistent with what one sees in CFD simulations, for instance, those shown in Fig. 3.1.4. It is also very likely that the time-of-flight concept is the most promising for formulating models for the performance of cylindrical swirl tubes.

5.2.3 Hybrid Models: the Models of Dietz and of Mothes and Löffler

In Appendix 5.B, we give the model equations for one more cyclone performance model: that of *Mothes and Löffler*. This model is built on the approach of *Dietz*, and is hybrid between the equilibrium-orbit and the time-of-flight models.

This type of model considers both particle interchange between the outer and the inner vortices across CS and particle migration to the wall. It is in this sense that these models can be said to be hybrids between the other two types. In practice the x_{50} predicted by these models often lie close to the x_{50} predicted by the equilibrium-orbit models.

We have stated that the models agree quite well in spite of the very different underlying concepts. In the next sections, some quantitative comparisons between the model predictions and between predictions and experiment will be given.

5.2.4 Comparing the Models

So how do the predictions of these models compare? In Fig. 5.2.2, the predictions are plotted for a standard case: a Stairmand High Efficiency cyclone with a diameter of 0.2 m, separating solids of density 2730 kg/m^3 at an inlet velocity of 15 m/s.

The models agree well in terms of critical particle diameter or cut size. The grade-efficiency curve of Mothes-Löffler is obviously much flatter than that of Barth. We refer to our discussion above, where we state that Barth's index of 6.4 in Eq. (5.2.2) is in the high end of the range, and best suited for smooth, well-designed cyclones. In our experience the index for many older units of poorer design often lies between 2 and 4, which gives a slope much more in line with the model of Mothes and Löffler.

The performance predictions in Fig. 5.2.2 are for a standard cyclone geometry with a typical inlet velocity used in laboratory testing. In Appendix 5.A we shall be looking at a case involving a much larger inlet velocity, namely the one for which we predicted the pressure drop in Chap. 4.

This completes our treatment of some of the models proposed in the literature for cyclone separation performance. Although we have not been able to derive the models in detail, we trust that we have discussed the principles on

which they are based and have presented the governing equations in sufficient detail so that the reader can now use them to predict the performance of a given cyclone. In Appendix 5.A we shall be using them in a worked example. In Chap. 6 we will give the latest model equations for the Muschelknautz model.

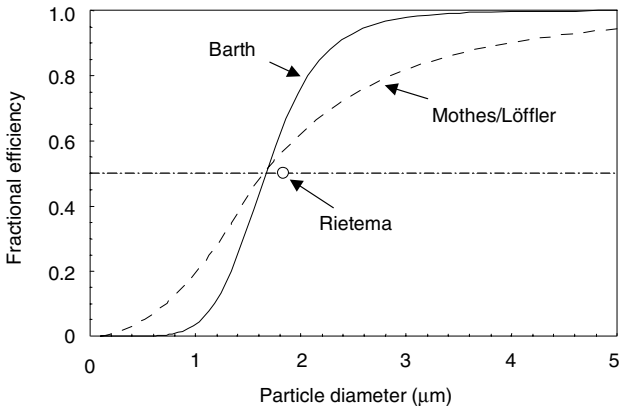

Fig. 5.2.2. Comparison of the model predictions for a Stairmand HE cyclone with $D = 0.2$ m, $D_x = 0.1$ m, $D_d = 0.075$ m, $S = 0.1$ m, $a = 0.1$ m, $b = 0.04$ m, $H = 0.8$ m and $H_c = 0.5$ m. Operating conditions: ambient air, inlet velocity: 15 m/s, solids density: 2730 kg/m^3, and low solids loading

We now wish to compare the predictions of cut size with a large body of experimental data, and we will put the models for pressure drop and separation to a special test. We will do this by seeing how well they can predict the effect of increasing the body length of the cyclone, and discuss the reasons for their successes and failures. We shall see that, although some models are successful in predicting the trends in cut-diameter and pressure drop with length up to a certain limit. Albeit, as briefly discussed above, a phenomenon known as the 'natural turning length', which none of the models account for, either limits the length of cyclones in practice, or makes performance predictions very uncertain if a double vortex occurs.

5.3 Comparison of Model Predictions with Experiment.

5.3.1 Agreement with Experiment in General

Abrahamsen and Allen (1986) compiled a large number of experimental grade-efficiency data, and plotted them against the square root of a parameter S_{AA}, defined as:

$$S_{AA} \equiv \frac{U'_{tCS}}{v_{rCS}} \tag{5.3.1}$$

They evaluated the particle terminal slip velocity in CS, U'_{tCS}, using the flow model of Meissner and Löffler in combination with Stokes' law, and v_{rCS} by the normal assumption of uniform flow. Their plot is shown in schematic form in Fig. 5.3.1. The range of experimental data, which stem from a multitude of sources, is shown as a gray area. The curves corresponding to the model prediction of Barth and Mothes-Löffler for the case described in the caption of Fig. 5.2.2 are also shown.

This plot shows that the equilibrium-orbit concept is, in general, quite successful, since the data are grouped around $S_{AA} = 1$. In principle, $S_{AA} = 1$ corresponds to the cut-diameter of Barth, although Barth used his own flow model rather than the model of Meissner and Löffler to calculate U'_{tCS}. $S_{AA} = 1$ does not, however, necessarily correspond to the cut-diameter of Mothes and Löffler, since they also considered collection of particles in the near-wall region. In most cases, however, including the case described in the caption of Fig. 5.2.2, Mothes and Löffler's cut-diameter is close to the diameter for which $S_{AA} = 1$. In Fig. 5.3.1 the shape of the Mothes-Löffler curve appears to agree very well with that of the gray area which represents experimental data. This again illustrates what we mentioned above, that the index value of 6.4 in Eq. (5.2.2) is in the high end, reflecting cyclones in good condition and of good design, and that this index can vary considerably in practice. Using an index of 3 in that equation gives almost the same slope as that of the model predictions of Mothes and Löffler. We should mention here that a lot of the actual grade-efficiency curves in the band are steeper than the shape of the area would seem to indicate.

The points in Fig. 5.3.1 are experimental G-E (grade efficiency) data for the system described in the caption of Fig. 5.2.2. These data were generated in the laboratory of one of the authors. The 'tail' at very fine particle sizes, where the efficiency increases with decreasing particle size, has nothing to do with the separation characteristics of the cyclone. Such a tail is a fairly common observation. In this case the tail exists for particle sizes less than about 0.5 to 0.6 μm, and is probably due to insufficient dispersion of the very fine particles of the feed solids.

5.3.2 A Case Study: the Effect of Cyclone Length

The effects on performance of some cyclone dimensions, such as gas inlet and outlet dimensions, have been extensively studied. An effect that is less well researched, and less well understood, is that of cyclone body length. We can therefore see it as a decisive test for the quality of the performance models, namely, whether they can predict this effect correctly, at least up to the point at which we reach the 'natural turning length'.

Having discussed the flow in cyclones, and the principles behind some models, we are able to anticipate to an extent the effects of increasing cyclone

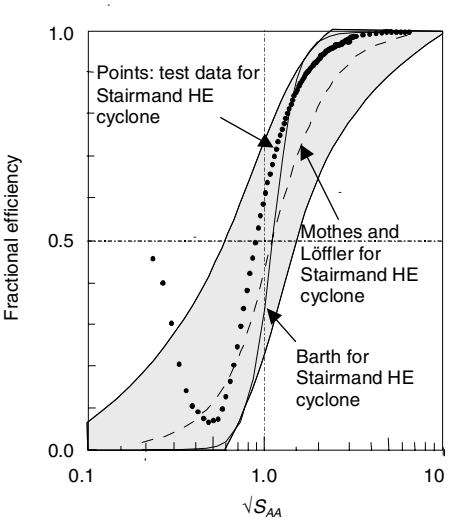

Fig. 5.3.1. Plot of Abrahamson and Allen showing the range of experimental grade-efficiency data in the literature. The curves corresponding to the Barth and Mothes-Löffler predictions shown in Fig. 5.2.2 are also included, together with experimental results

length. So what would we expect? We would expect the pressure drop to decrease. This is so because, as the length increases, so does the wall surface area and this imposes an additional friction on the flow. From our moment-of-momentum balance, this increase in friction decreases the spin in the inner vortex. As we discussed in Chap. 4, we would expect this to cause a decrease in pressure drop.

We cannot be sure about the effect that an increase in length would have on separation efficiency. According to the Barth and Mothes-Löffler models, a less intensive vortex means less centrifugal force on the particles in CS. Conversely, the radial velocity across a longer CS will be less, so that the inward drag on a particle in CS is also reduced. We cannot predict in advance what the net effect will be. We are in the same boat when turning to the time-of-flight models: they predict a smaller radial particle migration to the wall in the weaker vortex, but longer time for the particle to reach the wall.

In a recent study (Hoffmann, Groot, Peng, Dries and Kater, 2001) the effect of increasing the cyclone body length considerably on the performance was tested. The cyclone had dimensions: D= 0.200 m, D_x = 0.065 m, D_d = 0.110 m, S= 0.140 m, a= 0.114 m, b= 0.050 m and H_c = 0.410 m. It was equipped with extra cylindrical sections so that the length of the body could be varied between 0.260 m and 0.960 m. The cyclone feed was a chalk powder with density 2730 kg/m^3 dispersed in ambient air entering with an inlet velocity of 19 m/s. The dust loading was low at approximately 1.6 or

1.7 g dust/m^3 gas. The range of cyclone lengths and the effect on separation efficiency and pressure drop are shown in Fig. 5.3.2.

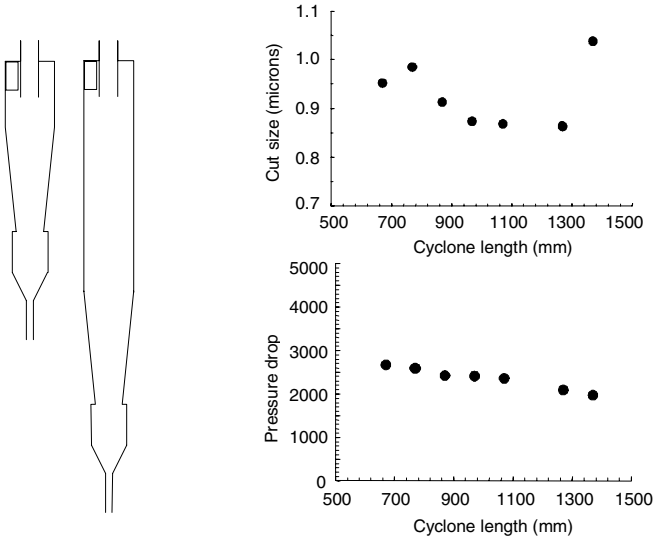

Fig. 5.3.2. The range of cyclone lengths tested, and the effect of length on cut size and pressure drop

The cut size x_{50} is seen to decrease slightly with increasing cyclone length, although the last result is atypical (and we will return to this issue below). The pressure drop decreases with increasing cyclone length as we anticipated.

Considering first the pressure drop model predictions, it is obvious that the purely empirical models of Shepherd-Lapple and Casal-Martinez (Eqs. 4.3.18 and 4.3.19) are not able to capture the effect of cyclone length, since they contain only the inlet and outlet dimensions. The models of Stairmand and Barth, however, which are based on considerations of the physical phenomena, both predict a decrease in cyclone pressure drop with increasing length. This is shown in Fig. 5.3.3 together with predictions from a CFD program (Boysan et al., 1986). These models predict the trend quite well, although the Barth model predicts higher pressure drops. We should note, however, that the outlet pressure was measured at a point close to the cyclone. If this pressure measuring point had been further from the cyclone, at a point where most of the swirl is attenuated, the experimental pressure drop would have been even higher (see the discussion in the previous chapter).

Researchers in Germany often let their laboratory cyclones exhaust to the atmosphere and, thus, their pressure drop is simply the inlet static pressure above atmospheric. Barth may have done the same when developing his pressure loss model as this is a good way to 'get around' the problem of interpreting

the cyclone outlet pressure when no solids are charged to the system during testing. Pressure loss models based on such experiments therefore have built into them a complete loss of velocity head or dynamic pressure.

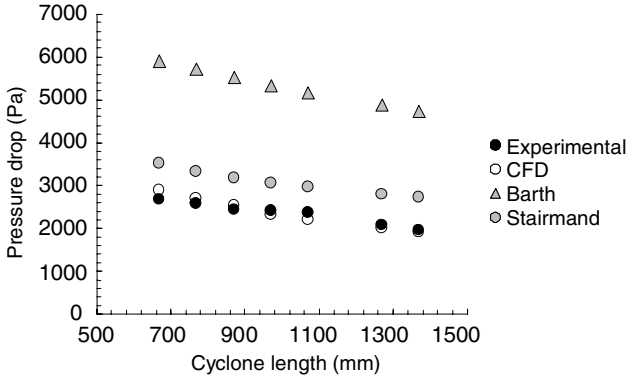

Fig. 5.3.3. Comparison of the measured pressure drop with the predictions of some models

As far as the separation performance is concerned, we cannot, as mentioned, tell *a priori* what the models will predict for the effect of cyclone length. Figure 5.3.4 shows that they, in general, predict a decrease in the cut size with increasing length, and therefore an increase in the separation efficiency. The models are generally successful for this low solids loading case. The CFD program is known to predict the performance of a Stairmand HE cyclone very well, so its relatively poor ability to predict the performance for this cyclone is somewhat surprising; the combination of the numerical procedure and the geometry of this particular cyclone may be unfortunate.

We could use the experimental Δp's to evaluate the Rietema model rather than the Δp's computed from the Shepherd and Lapple model. This would raise the Rietema points somewhat, causing them to lie almost on top of the Mothes-Löffler points. The trend in the Rietema predictions of a decreasing cut size with increasing cyclone length would be maintained in spite of the decreasing Δp.

In conclusion, we can say that the models based on considerations of the physical phenomena occurring within a cyclone are reasonably successful in predicting pressure drop and separation performance as a function of cyclone body length. The CFD model was found, in this case, to under-predict cyclone separation performance, while successfully reflecting the trend as a function of length.

The reason that the x_{50} cut size diameter of the longest cyclone lies well above those for the shorter cyclones—indeed, even a slightly shorter cyclone—(see Fig. 5.3.2) is that this particular cyclone's length exceeded the cyclone's

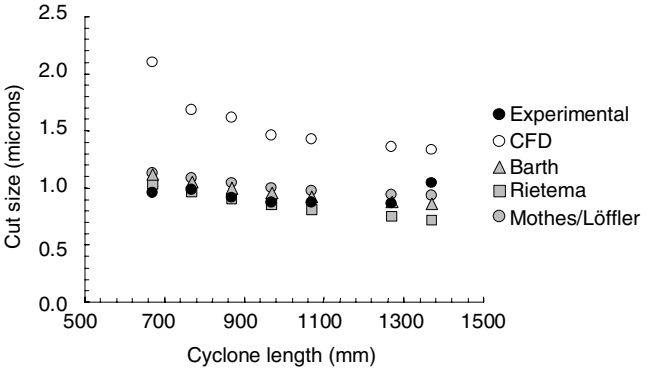

Fig. 5.3.4. Comparison of the experimentally measured cut size with the predictions of some models

'natural turning length'. This is a most interesting phenomenon *very relevant to cyclone design*, and we shall return to this key topic in a Chap. 9.

5.4 Overview

As in the previous chapter, we finish with a tabular overview of the models we have discussed.

Table 5.4.1. Models for cyclone separation efficiency at low solids loadings

Model	Range of application	Comments
Barth	Efficiency model valid for all cyclones and swirl tubes (but see Table 4.5.1).	Equilibrium-orbit model. Calculates the cut size, then fits an empirical grade-efficiency curve through it.
Rietema	Cylinder-on-cone cyclones with slot inlets.	Time-of-flight model. Derivation considers particle motion, but the final model relates cut size to pressure drop.
Mothes-Löffler	All centrifugal separators.	Combines migration to wall with interchange between inner and outer part of the vortex. Based on concept introduced by Dietz
Muschelknautz	Efficiency model valid for all cyclones and swirl tubes	Comprehensive model based on Barth's approach, will be covered in Chap. 6.

5.A Worked Example for the Prediction of Cyclone Separation Performance

Let us predict the separation efficiency of the cyclone reported in Appendix 4.A. As for the pressure drop, we have different models at our disposal and this is advantageous in that we are not dependent upon just one model for our predictions. If, for the case of x_{50}, various model predictions were to differ by, say, 50%, we would want to allow for this variation and interpret the results accordingly—not becoming overly attached to any one model's predictions.

In order to predict separation performance we require information about the solids feeding the cyclone, in addition to the geometrical data given in Fig. 4.A.1, information about the solids feeding the cyclone. Let us say we are feeding the cyclone a cement powder of density 2730 kg/m^3, at a relatively light load of 2.5 g per kg of gas. The feed has a volume (or mass) mean size of 27.5 μm and follows a log-normal volume or mass size distribution for which $\langle \ln x \rangle = 3.32$ and σ (the spread) $= 1.2$. $F(x)$ is then given by Eq. (2.B.5) shown in Fig. 5.A.1.

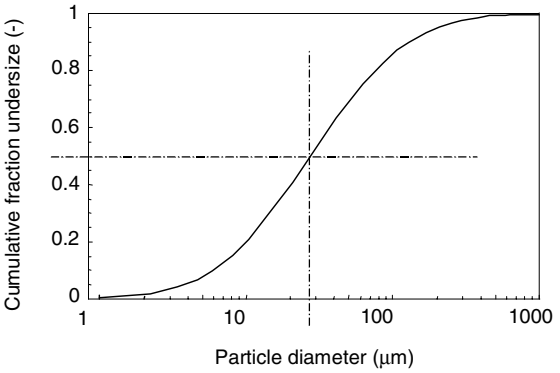

Fig. 5.A.1. Cumulative volume size distribution of the feed solids

The cyclone to which we are feeding the solids is quite large. We would therefore expect it to have a relatively large cut size.

Finally, we need the inlet velocity, which we take as 30 m/s, like in the previous chapter.

Solution

Let us start with the Barth model. We wish to use Eq. (5.2.1). First we need v_{rCS} and $v_{\theta CS}$, which we get from Eqs. (4.2.1) and (4.2.6), respectively. Filling in (4.2.1):

$$v_{rCS} = \frac{Q}{\pi D_x H_{CS}} = \frac{v_{in} ab}{\pi D_x H_{CS}} = \frac{30 \times 1.36 \times 0.96}{\pi \times 1.72 \times 5.03} = 1.44 \text{ m/s}.$$

Since the dust outlet is smaller than the gas outlet, CS intersects the physical cone near its lower end, and H_{CS} is shorter than the physical height $(H - S)$. It can be shown from simple geometric considerations that:

$$H_{CS} = (H - S) - H_c(R_x - R_d)/(R - R_d).$$

To find $v_{\theta CS}$ in (4.2.6) we first need to use Eqs. (4.2.4) and (4.2.5) to compute $v_{\theta w}$:

$$\alpha = 1{-}0.4\left(\frac{b}{R}\right)^{0.5} = 1{-}0.4\left(\frac{0.96}{2}\right)^{0.5} = 0.723 = \frac{v_{in}R_{in}}{v_{\theta w}R} = \frac{30 \times (2 - 0.96/2)}{2 \times v_{\theta w}},$$

which gives $v_{\theta w} = 31.5$, which is slightly higher than v_{in} due to the constriction of the inlet jet. Filling in (4.7) gives:

$$v_{\theta CS} = \frac{v_{\theta w}\left(\frac{R}{R_x}\right)}{\left(1 + \frac{H_{CS}R\pi f v_{\theta w}}{Q}\right)} = \frac{31.5\left(\frac{2}{0.86}\right)}{\left(1 + \frac{5.03 \times 2 \times \pi \times 0.00568 \times 31.5}{39.2}\right)} = 64.0 \text{ m/s}$$

where we have calculated the wall friction factor, f, from Eq. (4.2.9) using c_o = 0.0025, as given in the problem.

We can now fill in Eq. (5.2.1):

$$x_{50} = \sqrt{\frac{v_{r.CS} 9\mu D_x}{\rho_p v_{\theta CS}^2}} = \sqrt{\frac{1.44 \times 9 \times 1.81 \times 10^{-5} \times 1.72}{2730 \times 64.0^2}}$$
$$= 6.01 \times 10^{-6} \text{ m} = 6\mu\text{m}.$$

Thus, we are predicting the cut-diameter of the cyclone to be around 6 μm. We could now use Eq. (5.2.2) to construct a grade-efficiency curve around this cut size, if necessary.

We turn now to the Rietema model in combination with the Shepherd and Lapple model for the cyclone pressure drop. In the previous chapter, we found a pressure drop Δp of 3810 Pa from the Shepherd and Lapple model. Filling in Eq. (5.2.11):

$$\frac{x_{50}^2(\rho_p - \rho)}{\mu} H \frac{\Delta p}{\rho Q} = \frac{x_{50}^2(2730 - 1.2)}{1.81 \times 10^{-5}} 8 \frac{3810}{1.2 \times 39.17} = 3.5 \Rightarrow$$
$$x_{50} = 5.98 \times 10^{-6} \text{ m} = 6 \ \mu\text{m}$$

which agrees with the prediction of Barth above, as it often does (though normally not this precisely).

Finally, we use the model of Mothes and Löffler as it is presented in Appendix 5.B below. To use their model equations we need the tangential velocities $v_{\theta w}$ and $v_{\theta CS}$ from the Meissner/Löffler model given by Eqs. (4.B.1)–(4.B.4).

Space does not allow us to present all the details of the calculations, but we can give the intermediate results. Using $f_{cyl} = f_{cone} = f_{lid}$ =0.007, and filling in the data, we get: $v^*_{\theta w} = 37.9$ m/s for the ('constricted') velocity just after the inlet. This is higher than v_{in} due to the contraction and acceleration of the inlet jet (4.B.1). Using $\langle v_z \rangle = Q/(\pi R^2) = 3.12$ m/s, we then obtain $v_{\theta w}$ = 34.9 m/s for the velocity at the cylindrical wall (4.B.4). Equation (4.B.4) with $r = R_x$ gives us the tangential velocity in the surface CS: $v_{\theta CS} = 65.4$ m/s.

We now need to calculate R_{eq} from Eq. (5.3.1), so we need the volume of the cyclone, which is:

$$V_{cyc} = \frac{\pi}{4} D^2 H_{cyl} + \frac{\pi}{3} H_c \left(\frac{D^2}{4} + \frac{D D_d}{4} + \frac{D_d^2}{4} \right)$$

giving $V_{cyc} = 64.7$ m^3. It follows that $R_{eq} = 1.604$ m, which is slightly less than $D/2$. In Mothes and Löffler's cylindrical cyclone, we can take H_{CS} as equal to $(H - S)$, giving $v_{rCS} = 1.267$ m/s, which is slightly lower than that found for the physical cyclone in the Barth model, where H_{CS} was smaller.

Finally, we calculate the grade-efficiency from Eq. (5.B.2), using the formulae (5.B.6)–(5.B.10) and, as mentioned, $\mathcal{D} = 0.0125$ m^2/s. This is a straightforward substitution, involving the calculation of U'_{tCS} and U'_{tw} from Eq. (5.B.3). The resulting grade-efficiency curve is shown in Fig. 5.A.2, together with that of Barth, the latter being calculated from the cut-point diameter we found above and Eq. (5.2.2). For this cyclone with a somewhat a-typical geometry and a relatively high inlet velocity[4], the model of Mothes and Löffler predicts a smaller cut size than the other two models. The plot also exposes a slight weakness in this model: if the particle size for which $U'_{tCS} = v_{rCS}$ (which in this case is 5.5 μm) differs significantly from the cut size (in this case 4.6 μm) the curve takes on a somewhat peculiar shape with a break in the curve at the particle size for which $U'_{tCS} = v_{rCS}$.

We have not yet used our knowledge of the size distribution of the solids going into the cyclone. We can use the method illustrated in Fig. 3.2.2 to estimate the overall efficiency from Fig. 5.A.1. A cut-diameter of 6 μm can be seen to correspond to an overall efficiency of about 90%.

[4] Most of the models agree with the performance of the Stairmand HE cyclone for inlet velocities in the region of 15 m/s. The geometry we are using here has a considerably shorter cone and higher inlet velocity.

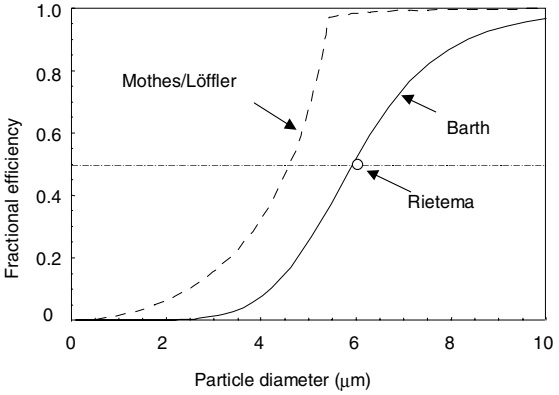

Fig. 5.A.2. Predicted grade-efficiency curves for the cyclone in Fig. 4.A.1. The cut size predicted by the Rietema model is also shown

5.B The Cyclone Efficiency Models of Dietz and of Mothes and Löffler

The models of Dietz (1981) and of Mothes and Löffler (1988) consider both the exchange of dust between the inner and outer part of the swirl and the migration of particles to the wall. They can therefore be considered as hybrids between the equilibrium-orbit and the time-of-flight models.

We shall be giving the model equations of Mothes and Löffler here, but we should credit Dietz with having pioneered this whole approach. Like the model of Mothes and Löffler, that of Dietz works quite well in practice, but Dietz's treatment of the particle exchange between inner and outer parts of the vortex raises some fundamental difficulties (Clift et al., 1991).

Mothes and Löffler simplified the cyclone geometry by making the cyclone cylindrical as shown in Fig. 5.B.1. They chose the radius of their cylindrical cyclone R_{eq} so that the volume of the cylindrical cyclone, and therefore the gas residence time, equals that of the physical one:

$$R_{eq} = \sqrt{\frac{V_{cyclone}}{\pi H}} \tag{5.B.1}$$

Particle mass balances are performed in the differential elements indicated in the figure under the assumption that the particles in each separate region (but not between the regions) are completely mixed in the radial direction. Particles reaching the cyclone wall in sections 1 and 2 are considered captured. Region 3 allows for reentrainment at the dust outlet, but this can often be neglected in practice.

The strategy is to calculate the axial particle concentration profiles of a given particle size in the three regions 1, 2 and 4, where the efficiency is computed from:

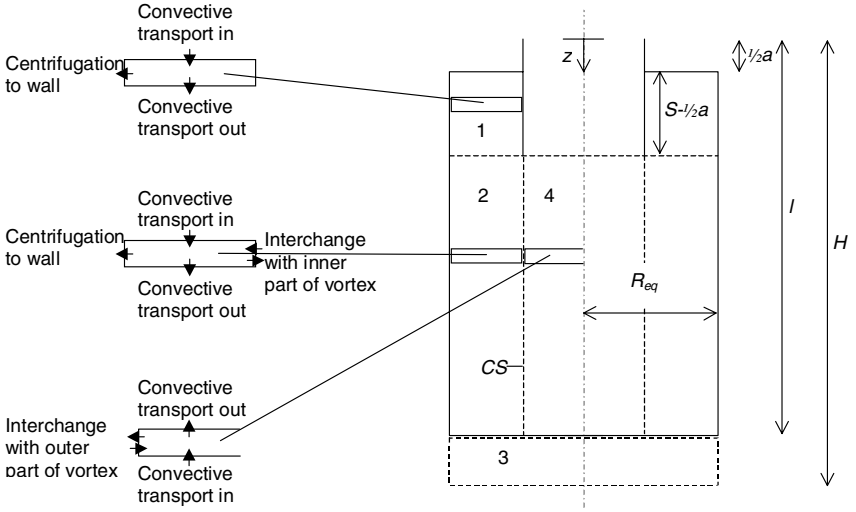

Fig. 5.B.1. Simplified cyclone geometry for the Dietz and Mothes-Löffler models. Dietz does not have Region 3

$$\eta\,(x) = 1 - \frac{c_4\,(z = S)}{c_0} \tag{5.B.2}$$

and where c_0 is the inlet concentration of particles of size x.

To calculate the particle fluxes to the wall and at the surface CS, Mothes and Löffler calculated the particle velocity relative to the gas at radius r from Eq. 2.2.7 using the centripetal acceleration v_θ^2/r for a:

$$U_t'\,(r) = \frac{x^2 \rho_p}{18\mu}\,\frac{v_\theta^2}{r} \tag{5.B.3}$$

At the wall the radial velocity was taken to be zero, while at CS it was assumed uniform:

$$v_{rCS} = \frac{Q}{\pi D_x (H - S)}. \tag{5.B.4}$$

We recognize this as Eq. 4.2.1 with H_{CS} taken as $(H - S)$ for this cylindrical cyclone.

If a particle is at CS, it will be collected if $U'_{tCS} > v_{rCS}$, otherwise it will be lost. This would give a jump in the grade-efficiency curve at the size for which $U'_{tCS} = v_{rCS}$. To avoid this difficulty, Mothes and Löffler also introduced a diffusive interchange, writing the flux $j_{2,4}$ of particles from Region 2 to Region 4 $j_{2,4}$ at CS as:

$$
\begin{aligned}
j_{2,4} &= -\mathcal{D}\frac{c_2 - c_4}{R_{eq} - R_x} + (U'_{tCS} - v_{rCS})\ c_4 \text{ for } U'_{tCS} \geq v_{rCS} \\
j_{2,4} &= -\mathcal{D}\frac{c_2 - c_4}{R_{eq} - R_x} + (U'_{tCS} - v_{rCS})\ c_2 \text{ for } U'_{tCS} \leq v_{rCS}
\end{aligned}
\tag{5.B.5}
$$

$\mathcal{D}$ is the particle diffusivity. Mothes and Löffler found that their predicted grade-efficiency curves agreed the best with experiment for $\mathcal{D} = 0.0125$ m^2/s.

The mass balances over the differential elements in the three regions resulted in three differential equations. The equation for Region 1 was solved directly starting at $z = 1/2\ a$, at which point the concentration is taken to be the inlet concentration c_o. The two differential equations for regions 2 and 4 are coupled, since both c_2 and c_4 appear in the interchange term (see Eq. 5.B.5) between the two regions at CS in both balances. In spite of this, these two equations are straightforward to solve (but very tedious unless one uses a mathematics package or other such tool with symbolic capabilities). By solving for c_4 in terms of c_2 in the equation for Region 2, and inserting the result in the equation for Region 4, Mothes and Löffler obtained an ordinary second order differential equation.

If they assumed no reentrainment at the dust outlet, the result for $c_4(z = S)$ was:

$$
c_4(S) = K_1 \left(\frac{m_1 - A}{B} \right) \tag{5.B.6}
$$

with:

$$
m_1 = \frac{A + D}{2} + \sqrt{\left(\frac{A + D}{2} \right)^2 - (AD - BC)}. \tag{5.B.7}
$$

Since the flux expressions (5.B.5) depend on the relative size of U'_{tCS} and v_{rCS}, so does the solution to the differential balance equations. The constants A, B, C and D are given by:

For $U'_{tCS} \geq v_{rCS}$:

$$
\begin{aligned}
A &= \frac{2\pi R_{eq} U'_{tw} (H - S)}{Q} + \frac{2\pi R_x D (H - S)}{Q (R_{eq} - R_x)} - 1 \\
B &= -\frac{2\pi R_x D (H - S)}{Q (R_{eq} - R_x)} - \frac{2\pi R_x (U'_{tCS} - v_{rCS})\ \ (H - S)}{Q} \\
C &= \frac{2\pi R_x D (H - S)}{Q (R_{eq} - R_x)} \\
D &= B - 1,
\end{aligned}
\tag{5.B.8}
$$

while for $U'_{tCS} \leq v_{rCS}$:

$$A = \frac{2\pi R_{eq} U'_{tw}\,(H-S)}{Q} - \frac{2\pi R_x\,(U'_{tCS} - v_{rCS})\,(H-S)}{Q} + \frac{2\pi R_x D\,(H-S)}{Q\,(R_{eq}-R_x)} - 1$$

$$B = -\frac{2\pi R_x D\,(H-S)}{Q\,(R_{eq}-R_x)} \tag{5.B.9}$$

$$C = \frac{2\pi R_x D\,(H-S)}{Q\,(R_{eq}-R_x)} - \frac{2\pi R_x\,(U'_{tCS} - v_{rCS})\;\;(H-S)}{Q}$$

$$D = B - 1.$$

Finally:

$$K_1 = c_o \exp\left(-\frac{2\pi R_{eq} U'_{tw}\left(S - \frac{a}{2}\right)}{Q}\right) \tag{5.B.10}$$

In these model equations, the subscript w signifies Mothes and Löffler's equivalent wall, so that by U'_{tw} we mean: $U'_t(R_{eq})$, while, as always, U'_{tCS} means $U'_t(R_x)$. Mothes and Löffler used the model of Meissner and Löffler (see Chap. 4) to calculate these velocities.

6

The Muschelknautz Method of Modeling

Over a period of more than 30 years, Professor Edgar Muschelknautz, along with his students and co-workers, working mostly at the University of Stuttgart, have developed what may be, overall, the most practical method for modeling cyclone separators at the present time.

The roots of the Muschelknautz method ('MM') extend back to the early work performed by Professor W. Barth (see Barth (1956), for example) of the University of Karlsruhe. Over the years, as understanding of the underlying phenomena and measuring techniques developed, Muschelknautz and co-workers, and those who have now followed him, have continued to refine the model. The reader of the literature will thus encounter many versions or improvements of the MM depending on the time of publication. It will also be noted that the more recent adaptations of the basic method are rather complex. We present some elements from simpler versions of the MM in other chapters (5 and 9); in this chapter and in Appendix 6.B we present what we believe to be a rather complete account of a later version of the model. Even here, however, we are obliged to strike a balance between covering all the details of the most recent versions of the MM, which would require another book in itself to do justice to all the details, and covering only the most basic elements of the model, which would limit its applicability or utility to the reader.

As a bit of a review, the most recent MM embodies three main features:

1. The ability to account for the effects of wall roughness due to both the physical roughness of the materials of construction and to the presence of collected solids.
2. The ability to account for solids 'saltation' or 'mass loading' effects, which we discuss in Chap. 9.
3. The ability to account for the change in particle size distribution (PSD) of the feed within the body of the cyclone.

In this chapter, we will focus mainly on the first two items above and will present our interpretation or implementation of item 3 in Appendix 6.B.

It is primarily the features listed above that distinguish the MM from other cyclone modeling methods, including the equilibrium-orbit models from which it springs. These features give the model its ability to simulate reality with reasonable precision in most cases of practical interest. Still, it not a perfect model and it continues to evolve and change with each new investigation of the assumptions and elements comprising this model.

Cyclone manufacturers are often required to give a legally binding, written guarantee of the performance of their equipment. If their equipment were to fail to meet this guarantee, they may have to absorb the total cost of the installation as well as the damage done to their company's reputation. Successful equipment manufacturers must make performance predictions with a very high level of confidence. Thus, they will normally perform extensive testing, analysis and correlation of a limited line of design geometries. They cannot afford to rely solely on a general purpose, 'utility' model developed independently of their particular product offering. Such correlations, if properly made, can predict performance better than any general purpose model that attempts to cover a broad range of dimensional ratios, body and hopper shapes, inlet configurations, loadings, surface conditions, physical properties, et cetera.

Thus, one hybrid approach to performance prediction is to perform extensive testing on a family of geometrically similar cyclones and to then apply certain equations, such as those presented in this chapter, to correlate the data.

Understandably, models developed in this manner for 'internal use' by cyclone manufacturers, or by organizations that use cyclones, are proprietary and not in the public domain. Hence, it is not possible for us to present or comment, herein, on their performance or applicability.

6.1 Basis of the Model

In this section we will present formulas required to design or evaluate a conventional cylinder-on-cone or a predominately cylindrical type of cyclone geometry. In doing so, we shall follow closely the methods of Muschelknautz (1970, for example) and, to some extent, those of Muschelknautz and Trefz (1990, 1991, 1992). Some departures from the MM will be worked into the development that follow the writers' own experiences and preferences.

We begin by computing the entrance 'constriction coefficient' α for a conventional 'slot-type' inlet from the empirical formula:

$$\alpha = \frac{1}{\xi}\left\{1 - \sqrt{1 + 4\left[\left(\frac{\xi}{2}\right)^2 - \frac{\xi}{2}\right]\sqrt{1 - \frac{(1-\xi^2)\,(2\xi - \xi^2)}{1 + c_o}}}\right\} \qquad (6.1.1)$$

where $\xi = b/(1/2D) = b/R$ (see Figs. 6.1.1 and 6.1.2 for symbol notation and definition) and c_o is the ratio of the mass of incoming solids to mass of incoming gas in the stream feeding the cyclone.

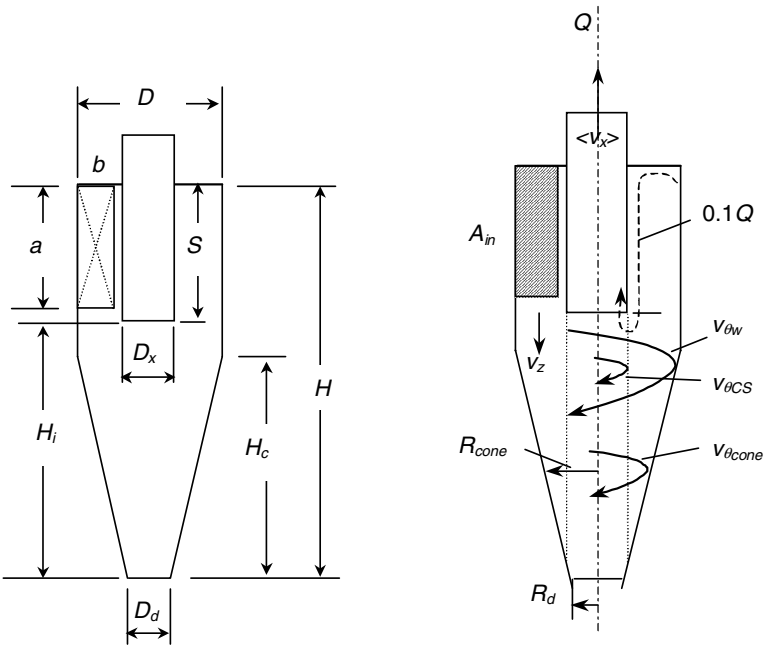

Fig. 6.1.1. Elevation views of a typical cylinder-on-cone cyclone showing various dimensional notations used herein

Knowing α, along with v_{in}, R_{in} and R, one computes the wall velocity $v_{\theta w}$.

$$v_{\theta w} = \frac{v_{in} R_{in}}{\alpha R} \tag{6.1.2}$$

where

$$v_{in} = \frac{Q}{A_{in}} = \frac{Q}{ab}. \tag{6.1.3}$$

We next compute the geometric mean radius:

$$R_m = \sqrt{R_x R}, \tag{6.1.4}$$

which we need in the computation of a 'wall axial velocity', v_{zw}

$$v_{zw} = \frac{0.9Q}{\pi\,(R^2 - R_m^2)}. \tag{6.1.5}$$

Trefz and Muschelknautz found that approximately 10% of the incoming gas 'short circuits' the cyclone and flows radially inward in a spiral-like manner along the roof and down the outside of the vortex tube (as sketched in

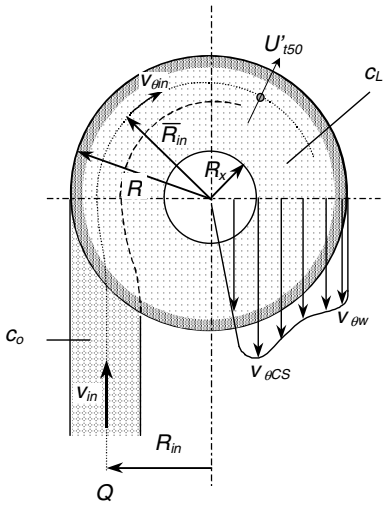

Fig. 6.1.2. Plan view of a typical cylinder-on-cone cyclone showing additional notation used in this chapter

Fig. 6.1.1). This boundary layer flow can vary from about 4% to 16% of Q but a good, average value for calculation purposes is 10%. As a consequence, approximately 90% of the incoming flow Q directly participates in the flow along the walls and in the formation of the inner vortex. This is the reason for the factor 0.9 in Eq. (6.1.5) and in Eqs. (6.2.3) and (6.4.2) below. As we will see below, the inner vortex flow has a major influence on the cut-point diameter, x_{50}.

In order to compute certain key cyclone characteristics, such as the internal spin velocity, $v_{\theta CS}$, or the particle cut size in the inner vortex core, x_{50}, it is necessary to first compute the gas-phase and total gas-plus-solids wall friction factors, f_{air} and f, respectively. Gas-phase wall friction factors for both cylindrical and conical cyclones as a function of body Reynolds number and relative wall roughness are presented in Fig. 6.1.3. Muschelknautz and Trefz define the *cyclone body Reynolds number* (compare with Eq. 4.2.8) as:

$$Re_R = \frac{R_{in} R_m v_{zw} \rho}{H \mu \left(1 + (v_{zw}/v_{\theta m})^2\right)} \tag{6.1.6}$$

with ρ and μ representing the gas phase density and absolute viscosity, respectively. $v_{\theta m}$ is a geometrical mean rotational velocity based on the spin velocity near the wall, $v_{\theta w}$, and that of the inner vortex $v_{\theta CS}$:

$$v_{\theta m} = \sqrt{v_{\theta w} v_{\theta CS}} \tag{6.1.7}$$

However, $v_{\theta CS}$ is, itself, a function of Re_R. Fortunately, in most applications, the term $(v_{zw}/v_{\theta m})^2$ in Eq. (6.1.6) is small in comparison to 1 and can be

neglected[1]. This is especially true in commercial units that operate at Re_R values greater than about 2000. In this industrially important range, in analogy to ordinary flow in a pipe, the wall friction factor is virtually independent of Re_R and thus, so are $v_{\theta CS}$ and $v_{\theta m}$ as well as all other quantities that are dependent upon this wall friction factor.

In order to read f_{air} off the chart in Fig. 6.1.3, we need, in addition to Re_R from Eq. (6.1.6), the wall relative roughness: k_s/R. The relative roughness is simply an estimate of the absolute roughness of the inside surface of the cyclone walls k_s, divided by the inside radius of the cyclone R, expressed in any consistent set of units. Here, k_s is normally taken to be about 0.046 mm or 0.0018 inches for commercial steel pipe. In some applications wherein brick or erosion protecting, refractory liners are installed, k_s may as high as 3 mm or 0.125 inches.

The relative roughness cannot be less than that for 'smooth' walls; that is, the lowermost curve shown in the upper and lower frames of Fig. 6.1.3. If the relative roughness is computed to be less than 6×10^{-4} it should be set equal to 6×10^{-4}.

We may note that, above a body Re_R of about 2000, the gas-phase wall friction factor is essentially independent of Re_R. In this region it depends primarily on the relative wall roughness k_s/R, as in ordinary flow through pipes. We can also observe that f_{air} becomes independent of k_s/R for $Re_R <\sim$ 1000, that is, in the 'laminar' flow regime. This too is analogous to ordinary flow in pipes.

Figure 6.1.3 is useful in showing thow the (solids free) gas friction factor in conical- and cylindrical-bodied cyclones varies with cyclone Reynolds number and relative wall roughness, that is $f_{air} = \mathrm{f}(k_s/R, Re_R)$. Even so, if we wish to incorporate it into a cyclone computer model, we need to express this functional relationship in equation form. Although the dependency between the variables shown in Fig. 6.1.3 is very nonlinear, and difficult to "fit", the authors have developed a set of equations that fit the entire range of f_{air}, k_s/R and Re_R values shown in Fig. 6.1.3 for both conical- and cylindrical-bodied cyclones. These empirical equations have a maximum error of about 20 to 22% relative to the data points shown in Fig. 6.1.3[2]. This error decreases, of course, with increasing solids loading. The gas phase friction factors computed with the empirical curve fits shown below have proven sufficiently accurate for most design applications.

For either conical or cylindrical-bodied cyclones, we can express the gas friction factor as the sum of two components—that for smooth wall, f_{sm}, plus

[1] If programming the computations, one could first compute Re_R by neglecting the squared term in Eq. (6.1.6), compute $v_{\theta CS}$ as described, and then use this value of $v_{\theta CS}$ to compute a new Re_R, repeating the procedure until no appreciable change occurred in the value of either Re_R or $v_{\theta CS}$.

[2] In a lightly loaded cyclone where in friction is dominated by the gas friction factor, a 22% error in the latter will typically correspond to an 8% error, approximately, in the cyclone's computed d_{50} cut size.

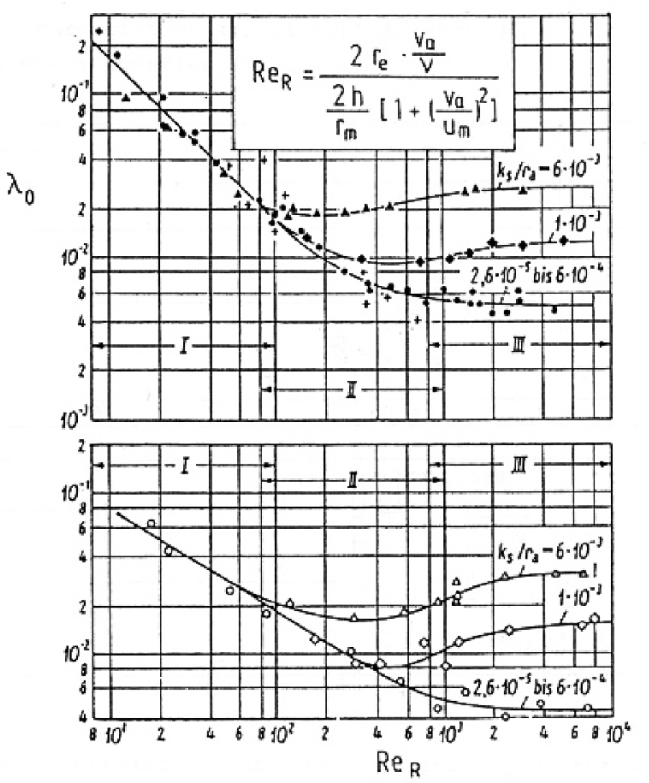

Fig. 6.1.3. Cyclone gas-phase wall friction factors for both cylindrical (top) and conical (bottom)-cyclones as a function of body Reynolds number and relative wall roughness. (Muschelknautz and Trefz, 1991). In the notation of this book: $\lambda_o = f_{air}$; $r_e = R_{in}$; $v_a = v_{zw}$; $h = H$; $u_m = v_{.\theta m}$; $r_m = R_m$; $r_a = R$

an added contribution due to wall roughness, f_r:

$$f_{air} = f_{sm} + f_r. \tag{6.1.8}$$

For conical-bodied cyclones:

$$f_{sm} = 0.323 Re_R^{-0.623}$$

$$f_r = \left(\log \left(\frac{1.60}{\frac{k_s}{r_a} - 0.000599} \right)^{2.38} \right)^{-2} \left(1 + \frac{2.25 \times 10^5}{Re_R^2 (\frac{k_s}{r_a} - 0.000599)^{0.213}} \right)^{-1}. \tag{6.1.9}$$

For cylindrical-bodied cyclones:

$$f_{sm} = 1.51 Re_R^{-1.0}$$

$$f_r = \left(\log \left(\frac{1.29}{\frac{k_s}{r_a} - 0.000599} \right)^{2.59} \right)^{-2} \left(1 + \frac{2.14 \times 10^5}{Re_R^{1.64}} \right)^{-1} . \tag{6.1.10}$$

When applying the above equations, if the computed relative wall roughness k_s/r_a turns out to be less than that for a smooth-walled cyclone (see lowermost curve for conical and cylindrical-bodied cyclones in Fig. 6.1.3), k_s/r_a should be set equal to that of a smooth-walled cyclone, i.e. 0.0006. Otherwise an error will occur during the computation of f_r when the logarithm of a negative number is attempted.

As mentioned in Chap. 4, the total frictional drag, f, within a cyclone consists of two components in the MM: that due to drag on the (pure) gas phase (f_{air} discussed above) and that due to an additional drag imposed by the moving strand of solids which is present at the walls. The expression for the total friction factor becomes:

$$f = f_{air} + 0.25 \left(\frac{R}{R_x} \right)^{-0.625} \sqrt{\frac{\eta c_o Fr_x \rho}{\rho_{str}}} \tag{6.1.11}$$

The second term in this equation is the frictional contribution due to the solids. This term depends on a number of geometrical and fluid flow variables, including a few which we have not introduced thus far. These include the density of the 'strand' of particles along the wall, rho_{str}, the cyclone's overall collection efficiency, η and the Froude number for the flow out the vortex tube, Fr_x. This expression for f can be compared with the earlier and simpler version, Eq. (4.2.9).

The quantity η is the overall efficiency, that is, the fraction of incoming solids collected by the cyclone. However, one does not know its value at this stage in the computations. Hence, we must assume a value for η initially and update it later in the computations, if necessary. Happily, this is seldom necessary or is a minor correction since most cyclones operate at overall efficiencies that are on the order of 0.9 to 0.99+ (or 90 to 99+%). This relatively high efficiency can be due to a number of factors including the processing of relatively large and/or dense particles or to the 'mass loading' effect (sometimes referred to as 'limit loading' or 'saltation' effect). In the MM this mass loading effect refers to the separation of that fraction of the incoming solids that exceed the 'limit loading' concentration, c_{oL}. We will discuss this 'limit loading' concept a bit more later.

In contrast to the high solids loading case, at low solids loadings the factor $c_o^{1/2}$ forces the entire term representing the solids contribution to the overall friction factor to small values. Under such conditions, it matters little what value one uses for η. But independently of how close our initial estimate of η is relative to the 'final' computed value, one can always repeat the computations with an updated value for η derived later from the computations. Moreover,

this procedure can be repeated, as necessary, until the change in η is less than some specified tolerance value such as $\pm 1\%$.

The ρ_{str} term, which represents the bulk density of the dust or strand layer at the walls, is approximately equal to 0.3 $\rho_{bulk}$to 0.5 ρ_{bulk}, where ρ_{bulk} is the bulk density of the solids at rest. Lacking better information, it is reasonable to assume a strand density equal to 0.4 ρ_{bulk}.

The last term we wish to define in Eq. (6.1.11) is the Froude number.

$$Fr_x = \frac{v_x}{\sqrt{2R_x g}} \tag{6.1.12}$$

where v_x is the superficial axial velocity through the inlet section[3] of the vortex tube.

6.2 Computation of the Inner Vortex Cut-Point, x_{50}

A very fundamental characteristic of any lightly-loaded cyclone is its cut-point diameter or cut size, x_{50}, produced by the spin of the inner vortex. This is the particle diameter that has a 50% probability of capture. As discussed elsewhere in this book, the cut size is analogous to the screen openings of an ordinary sieve or screen although, with a cyclone, the separation is not as sharp as that of a sieve.

In lightly-loading cyclones, x_{50} exercises a controlling influence on the cyclone's separation performance. It is the parameter that determines the horizontal position of the cyclone's grade-efficiency curve (fraction collected vs. particle size). However, under high solids-loading conditions ('high' can mean solids-to-gas inlet loadings, c_o, as small as about 0.01, or less, for smooth, small-scale units), mass loading effects within the entrance zone will dominate the cyclone's separation performance. When this occurs, any additional separation generated by the rotating *inner* vortex is normally small (in terms of mass of total feed solids collected) in comparison to that produced by the effect of mass loading.

In what follows, we will first present the MM for computing a cyclone's x_{50} cut-point which governs the performance under lightly loaded conditions (wherein the inlet loading c_o is less than the 'limit loading', c_{oL}, prior to describing the separation process experienced at higher loadings.

In order to compute x_{50}, we must first compute the tangential velocity of the gas at the 'inner core' radius R_{CS}. (See Figs. 6.1.1 and 6.1.2) This velocity follows from the expression

$$v_{\theta CS} = v_{\theta w} \frac{(R/R_x)}{\left[1 + \frac{f A_R v_{\theta w} \sqrt{R/R_x}}{2Q}\right]} \tag{6.2.1}$$

[3] Upstream of any flow expansion that may occur within the vortex tube.

where A_R is the total inside area of the cyclone contributing to frictional drag (as in the Stairmand model for cyclone pressure drop in Chap. 4). As shown in Fig. 6.A.1, it encompasses the inside area of the roof, the barrel cylinder, the cone, and the external surface of the vortex tube. Thus:

$$\begin{aligned} A_R &= A_{roof} + A_{barrel} + A_{cone} + A_{vt} \\ &= \pi \left[R^2 - R_x^2 + 2R\,(H - H_c) + (R + R_d) \sqrt{H_c^2 + (R - R_d)^2} + 2R_x S \right] \end{aligned} \tag{6.2.2}$$

This expression is also given in Appendix 4.A.

Knowing A_R, we are now in a position to compute $v_{\theta CS}$ from Eq. (6.2.1), which is needed in the computation of the cut-point diameter of the inner vortex:

$$x_{50} = x_{fact} \sqrt{\frac{18\mu\,(0.9Q)}{2\pi\,(\rho_p - \rho)\,v_{\theta CS}^2\,(H - S)}}. \tag{6.2.3}$$

This equation is a variation of Barth's famous expression for a cyclone's cut-size, Eq. (5.2.1). In fact, the two equations become identical if we neglect the roof 'leakage flow' and the gas density (relative to that of the solids), and set the x_{fact} term equal to 1. This x_{fact} term is simply a correction factor that *may* be applied, if desired, to force the computed cut point to match that observed in practice. It normally falls within the range of about 0.9 to 1.4. No such factor, however, has been applied in the example problems reported later in this chapter.

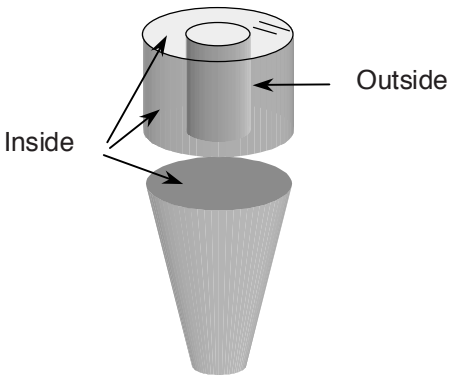

Fig. 6.2.1. Areas contributing to the area A_R term in Eq. (6.2.1)

Like the Barth equation, Eq. (6.2.3) is strictly valid only when the particle size being computed is settling in the Stokes law regime. One may check that this is the case by computing the particle Reynolds number:

$$Re_p = \frac{\rho U'_{t50} x_{50}}{\mu} \tag{6.2.4}$$

where U'_{t50} is the terminal velocity of the cut-sized particle rotating in CS (in Appendix 6.B and Fig. 6.1.2 U'_{t50} is used about a similar particle in the inlet region):

$$U'_{t50} = v_{rCS} = \frac{Q}{2\pi R_x H_{CS}}. \tag{6.2.5}$$

If $Re_p <\sim 0.5$, Stokes law applies. In the rare case that it does not, one may use:

$$x_{50} = 5.18 \frac{\mu^{0.375} \rho^{0.25} U'^{0.875}_{t50}}{\left[\frac{(\rho_p - \rho) v^2_{\theta CS}}{R_x}\right]^{0.625}} \tag{6.2.6}$$

which was derived from a simple, steady-state force balance relating the particle's drag to the centrifugal force at radius R_x. In this case, the drag coefficient used is the empirical relation,

$$C_D = \frac{18.5}{Re_p^{0.6}} \text{ valid for } 0.3 < Re_p < 1000. \tag{6.2.7}$$

Equation (6.2.6) may be used with any consistent set of units. Thus, if one selects the units of kilograms, meters and seconds for the dimensions of mass, length and time, the answer will be in meters. If one uses the lb-mass, foot and second set of units for mass, length and time, the answer will come out in feet.

6.3 Computation of Efficiency at Low Solids Loadings

In this section we will compute the grade-efficiency curve and overall separation efficiency at low inlet solids (classification only) loadings ($c_o < c_{oL}$). The grade-efficiency curve for a given cyclone expresses the functional dependence of separation performance upon particle diameter. As discussed in Chap. 3, it is normally an s-shaped function satisfying the limits:

$$\begin{aligned} &\eta \to 0 \text{ as } x \to 0 \\ &\eta \to 1 \text{ for } x \gg x_{50} \text{ (theoretically, as } x \to \infty) \\ &\eta = 0.5 \text{ for } x = x_{50} \text{ (the defining equation for} x_5 0) \end{aligned} \tag{6.3.1}$$

The grade-efficiency curve η is normally defined with the use of just the two parameters: the cut size, x_{50}, and a 'slope' m. A variety of equations have been proposed to represent $\eta(x_{50}, m)$ but, as pointed out in Chap. 5, one of the simplest and more practical forms is:

$$\eta_i = \frac{1}{1 + \left(\frac{x_{50}}{x_i}\right)^m}, \tag{6.3.2}$$

which is the discrete equivalent of Eq. (5.2.2), but with the exponent variable. If we have grade-efficiency data for a given cyclone we can test this equation to see how well it represents the cyclone's grade-efficiency performance. We do this by plotting $\ln(\frac{1}{\eta_i} - 1)$ vs. $\ln x_i$ and noting how well the plotted data define a straight line. The quantity m is the negative of the slope of the line that best fits the plotted data points.

Depending on the particular design, the slope thus found can vary anywhere from about 2 to 7 for this particular grade-efficiency function. If one is designing a new cyclone for which no grade-efficiency data is available, we suggest choosing a slope on the basis of experience with a similar design (similar size and operating environment), if possible. Lacking such information, we suggest using a 'typical' slope of about 3. For well-designed, smooth walled cyclones, one often observes slopes in the 4 to 6 range. We choose a value of 5 for the purpose of simulating two laboratory cyclones in the example calculations presented at the end of this chapter.

A large m (in the range 4 to 7) is characteristic of a cyclone having a sharp, nearly 'stair-step' shaped, grade-efficiency curve. Such a unit tends to behave like a sieve—collecting all particles greater than x_{50} but allowing smaller particles to pass through (out the overflow). Conversely, a cyclone that has a relatively small m has the opposite characteristics and is often evidence of an excessive amount of internal mixing stemming from poor aerodynamic design or poor mechanical condition. The latter would include rough walls, eroded walls, holes, leaking gaskets, upflow, wall depressions and/or protrusions, and the presence of wall deposits.

When one is designing a new cyclone system, it is customary to perform the calculations indicated above to find x_{50}, choose a slope—based on experience or otherwise – and then use Eq. (6.3.2) to compute points on the cyclone's grade-efficiency curve, η_i as a function of x_i, using the known x_{50} and m.

The overall collection efficiency is obtained by first dividing the feed into N size fractions, each fraction comprising a known fraction of the total mass of feed solids. Next, each of these mass fractions is multiplied by the efficiency of capture for the average particle size of each fraction. This efficiency of capture is that computed from the grade-efficiency curve. The sum of all N fractions thus computed is the overall collection efficiency. Mathematically, this may be expressed as,

$$\eta = \sum_{i=1}^{N} \eta_i \times \Delta MF_i \tag{6.3.3}$$

where ΔMF_i is the i^{th} mass fraction. This is the discrete equivalent of Eq. (3.2.8).

6.4 Determining if the Mass Loading Effect will Occur

Next we determine whether the mass loading effect (saltation) will occur. According to the MM, the amount of solids that the gas phase can hold in turbulent suspension upon its entrance into a cyclone depends on the mass average (the median) particle size of the feed, x_{med}, the cut-point of the inner vortex, x_{50}, and, to a lesser extent, on the inlet loading itself, c_o. This limiting or limit-loading is:

$$c_{oL} = 0.025 \left(\frac{x_{50}}{x_{med}} \right) (10c_o)^{0.15} \text{ for } c_o \geq 0.1 \tag{6.4.1}$$

and

$$c_{oL} = 0.025 \left(\frac{x_{50}}{x_{med}} \right) (10c_o)^{k} \text{ for } c_o < 0.1 \tag{6.4.2}$$

where

$$k = -0.11 - 0.10 \ln c_o \tag{6.4.3}$$

Now, *if $c_o < c_{oL}$, then saltation does not occur* upon entrance into the cyclone and the comparatively simple method for computing the cyclone's separation performance, as described in Sect. 6.3 above applies. Factors that may lead to this scenario include low solids loadings, c_o, a fine feed particle size distribution (i.e., small x_{med}), and a large inner vortex cut-point diameter, x_{50}. The latter is normally associated with large-diameter cyclones, cyclones incorporating rough, erosion-protecting liners, low volumetric flow rates, low density feed solids and/or high-density gases. It is also associated with poorly designed and/or damaged cyclones.

If $c_o > c_{oL}$, then saltation will occur and the MM asserts that the cyclone will, in effect, become a two-stage separator: the weight fraction of incoming solids exceeding the limit-loading will be centrifuged to the walls almost immediately upon entry. The fraction that remains in turbulent suspension will then be subject to separation within the inner vortex according to its particle size distribution. Accordingly we end up with both a 'mass loading' and a 'classification' type of cyclone separator operating in series with one another. This whole notion is also discussed in Chap. 9, where we discuss the effect of solids loading in light of experimental results.

6.5 Overall Separation Efficiency when $c_o > c_{oL}$

Here, we will determine the overall separation efficiency for saltation conditions, i.e. when $c_o > c_{oL}$. This efficiency includes the efficiency due to saltation in the inlet and the efficiency due to classification in the inner vortex. A portion of the incoming solids that is not collected by the former is collected by the latter, so that the total efficiency becomes (see also Chap. 9):

$$\eta = \left(1 - \frac{c_{oL}}{c_o}\right) + \left(\frac{c_{oL}}{c_o}\right) \sum_{i=1}^{N} \eta_i \times \Delta MF_i \tag{6.5.1}$$

where, again, ΔMF_i is the i^{th} mass fraction and η_i is the capture efficiency for the i^{th} size fraction computed via Eq. (6.3.1) with x_{50} obtained from Eq. (6.2.3).

Fig. 6.5.1 is presented to help visualize the mass loading ("saltation") and classification phenomenon that exists in the general case when the incoming mass loading exceeds the limit-loading. This illustration, which is a simple material balance, was created for a unit mass entering the cyclone over some arbitrary time interval. Note that the underflow solids quantity, divided by the feed solids quantity (unity), gives the overall collection efficiency as presented by Eq. (6.5.1).

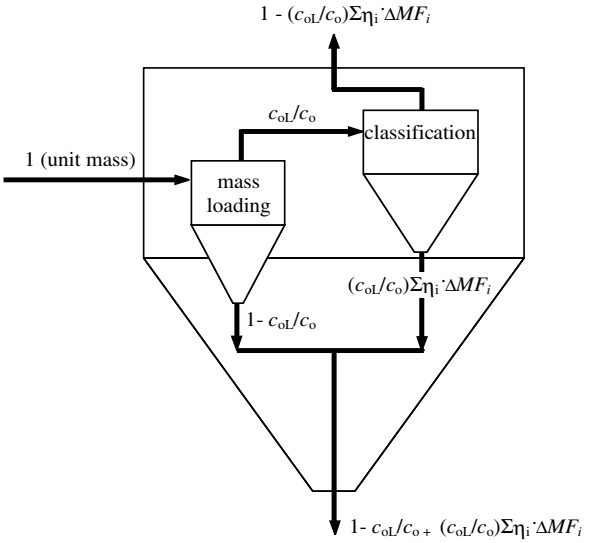

Fig. 6.5.1. General case illustrating both mass loading and classification phenomena that can transpire within a single cyclone

In addition to the normal feed particle size distribution that enters the cyclone, Muschelknautz and co-workers (Muschelknautz and Trefz, 1990, 1991; Trefz, 1992) have modified their earlier cyclone model (or models) to include an 'inner feed' or 'inner feed particle size distribution'. The concept here is that, if the inlet solids loading' exceeds the 'limit loading', some portion of the incoming feed solids will quickly separate out but those that don't will have a somewhat finer particle size than that feeding the cyclone. It is this

finer particle size distribution that actually reports to the inner vortex core for final separation based on particle size.

Although the concept of both an inlet and an inner feed particle size distribution has some appeal, and may even lead to some improvement in the basic model's overall predictive capabilities, its inclusion complicates the computations considerably. Moreover, test data show that the separation efficiency improves almost uniformly throughout the particle size range with increasing solids loading, indicating that the extra material separated in the inlet is largely unclassified. The notion of an inlet cut size does not agree with this evidence, unless the inlet cut is so shallow as to be of only secondary practical importance. For these reasons we will not include this part of the model in the main text. A description of our interpretation of the method is presented in Appendix 6.B where we also discuss the issue further, and show that the classification in the inlet is, indeed, not very strong. Trefz (1992) and Greif (1997) report further details of this part of the model.

6.6 Computation of Pressure Drop

We discussed the issue of pressure drop over a cyclone with tangential inlet in Chap. 4. The influence of solids loading on the pressure drop will be discussed qualitatively in Chap. 9. The effect can be explained simply as the consequence of increased wall friction caused by the solids on the wall.

According to the MM, pressure loss across a cyclone occurs, primarily, as a result of friction with the walls and irreversible losses within the vortex core, the latter often dominating the overall pressure loss. Inlet acceleration losses may also occur.

The wall loss, or the loss in the cyclone body, is given by,

$$\Delta p_{body} = \frac{f A_R \rho \left(v_{\theta w} v_{\theta CS}\right)^{1.5}}{2 \times 0.9 Q}. \tag{6.6.1}$$

The loss in the core and in the vortex finder is given by,

$$\Delta p_x = \left[2 + \left(\frac{v_{\theta CS}}{v_x}\right)^2 + 3\left(\frac{v_{\theta CS}}{v_x}\right)^{\frac{4}{3}}\right] \frac{1}{2}\rho v_x^2. \tag{6.6.2}$$

These two equations can be compared with Eqs. (4.3.3) and (4.3.4) from the model of Barth.

In some installations, the incoming gas-solid mixture must be accelerated from a region of low velocity to that which exists at the entrance of the cyclone. Such a condition would exist at the inlet to a highly-loaded primary cyclone above a fluidized bed, for example. If we apply the mechanical energy balance between a point located in the low velocity region (ahead of an inlet horn, for example) and a point in the high velocity region (within the horn) we obtain for the acceleration pressure loss,

$$\Delta p_{acc} = (1 + c_o) \frac{\rho \left(v_2^2 - v_1^2\right)}{2} \tag{6.6.3}$$

where $(1+c_o)\rho$ is the density of the gas-solid mixture undergoing acceleration from upstream velocity v_1 to downstream velocity v_2. We have assumed here that any 'slip' between the solids and the gas phases is negligible.

Thus, the total pressure loss is the sum of the wall and core/vortex finder loss as well as the acceleration loss, if any:

$$\Delta p = \Delta p_{body} + \Delta p_x + \Delta p_{acc}. \tag{6.6.4}$$

At low solid loadings, the core/vortex finder loss will generally dominate the other terms in Eq. (6.6.4), as we also mentioned in Chap. 4. At these loadings it may constitute 70 to 80% of the total loss. However, at high solid loadings, $c_o = 6$ kg/kg, for example, and typical of that which could occur at the inlet to a primary cyclone above a fluidized bed, the inlet acceleration loss could constitute over 50% of the total pressure loss across the cyclone.

The total loss shown above is that which occurs from inlet to (gas) overflow and represents also the loss in static pressure over the cyclone. As a rough estimate, the difference in static pressure between the inlet and the (solids) underflow, *under the point at which the vortex ends*, is the same as that computed by Eq (6.6.1) but without the core loss contribution. However, if the vortex core happens to extend or 'dip' down to the underflow pipe, the difference in *static* pressure between inlet and underflow can equal—or even exceed—the total pressure drop from inlet to overflow.

6.A Example Problems

In order to gain some understanding of how well the above model can predict reality, its predictions have been tested with the aid of three sets of carefully measured performance data collected on three different cyclone test installations. The test conditions and results are presented below.

6.A.1 Simulation of Data from Hoffmann, Peng and Postma (2001)

Hoffmann and co-workers have performed measurements on a cyclone having dimensions shown in Fig. 6.A.1. Physical property and flow data follow. These results will also be discussed in Chap. 9.

The test conditions were:

- Gas: air, atm. pressure; density, $\rho = 1.2$ kg/m^3; viscosity, $\mu = 1.8{\times}10^{-5}$ Pa s
- Gas volumetric flowrate, $Q = 0.04$ m^3/s and 0.08 m^3/s
- Particles: Snowcal 40 (chalk powder, Blue Circle Industries); particle density, $\rho_p = 2730$ kg/m^3; bulk density, $\rho_{bulk} \cong 0.5\rho_p = 1365$ kg/m^3
- Wall roughness, $k_s = 0.046$ mm (commercial steel)

Feed Particle Size Distribution (PSD)	
x (μm)	Wt. Fraction $< x$
0.3	0.000
1.0	0.135
2.0	0.300
3.0	0.440
3.4	0.500
5.0	0.630
8.0	0.750
15.0	0.850
30.0	0.940
40.0	0.975
60.0	1.000

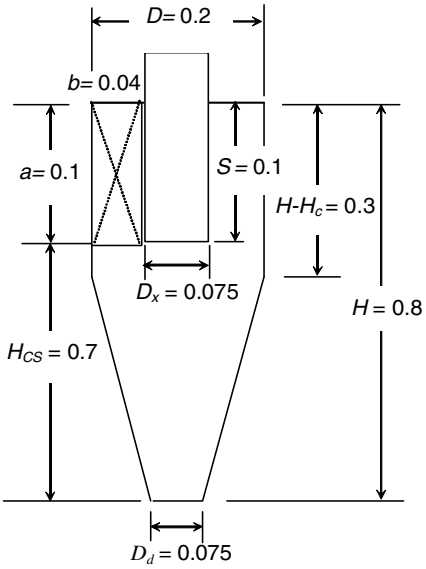

Fig. 6.A.1. Dimensions, in meters, of the Hoffmann cyclone simulated herein and the size distribution of the feed solids

Model Results

The following tabulated intermediate results were obtained on basis of the Muschelknautz method described in the sections above for an inlet velocity $v_{in} = 10$ m/s, a solids loading of 4.5 g/m^3, and a slope, m, for the grade-efficiency curve, equal to 5:

α	$= 0.623$	$v_{\theta CS}$	$= 18.6$ m/s
A_R	$= 0.46$ m^2	v_x	$= 9.05$ m/s
k_s/R	$= 0.00046 \rightarrow 0.0006$	v_{rCS}	$= U'_{t50} = 0.243$ m/s
Re_R	$\cong 749$	x_{50}	$= 1.68$ μm
v_{zw}	$= 1.83$ m/s	Re_p	$= 0.027$
Δp_{body}	$= 198$ Pa	c_{oL}	$= 0.00332$ kg/kg
Δp_x	$= 689$ Pa	f_{air}	$= 0.0058$
Δp	$= 887$ Pa	f	$= 0.0071$

The model predictions at 10 and 20 m/s inlet velocities, as a function of inlet solids loading, are shown in Fig. 6.A.2.

Figure 6.A.3 presents the model's predictions at 4.5 and 31.7 g/m^3 solids loadings corresponding to two of the four sets of experimental grade-efficiency data. Figure 6.A.4 presents the Muschelknautz predictions of the particle size distribution of the overhead dust fraction at two different solids loadings.

The results shown above are encouraging in that the model is observed to be reasonably capable of predicting both the trend and the absolute magnitude

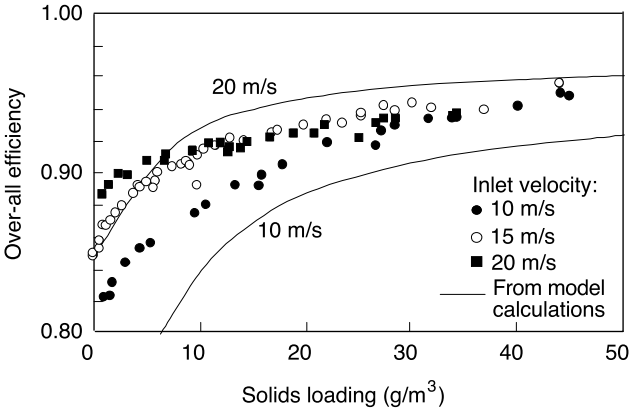

Fig. 6.A.2. The Muschelknautz model predictions as a function of inlet velocity and solids loading

of the experimental data. However, the model is not capable of predicting features like the minima or 'hooks' in the experimental data, seen around 4 to 7 microns in Fig. 6.A.3. One would, on basis of the MM, expect the measured efficiency data to asymptotically decrease to some limiting value of zero or some constant (depending on the mass loading effect) with decreasing particle size. These minima in the data are probably the result of fines agglomeration. They are commonly observed in cyclone installations that process very fine feed solids, as is the case at hand. Such agglomeration is most likely the result of the feed solids taking on an electrostatic charge in the inlet conveying piping. Humidity can also bring about agglomeration of very fine particles. It is well known, for example, that airborne dust levels sampled in manufacturing sites decreases as the ambient humidity level increases. But, independently of the cause, if fines agglomeration does occur, this would cause the fines fraction of the feed to be collected with a greater efficiency than would be possible otherwise.

The inner cut diameter, x_{50}, of 1.68μm predicted by the model is somewhat larger than the 1.2 μm seen experimentally (see the curve for 4.5 g/m^3 in Fig. 6.A.3). The MM shares this conservative efficiency estimate with some other models for this size of cyclone, for instance, the Barth model described in Chaps. 4 and 5 predicts an inner x_{50} of 1.56 μm for the same conditions. The result is the underestimation of the overall efficiency at conditions of low loading seen in Fig. 6.A.2. In large cyclones the picture is quite different, predictions are more in line with experiment as far as the x_{50} is concerned.

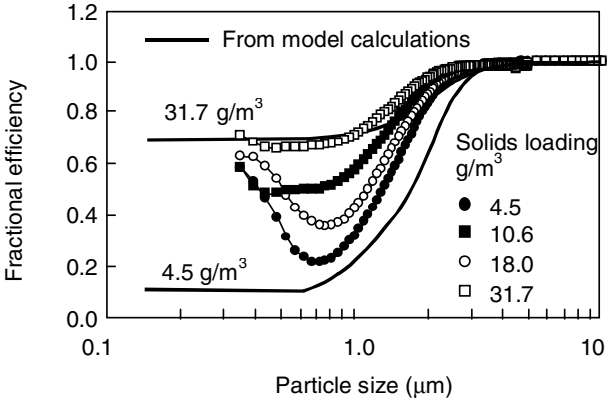

Fig. 6.A.3. The Muschelknautz model predictions of grade-efficiency at two different solids loadings, compared with experiment. Inlet velocity: 10 m/s

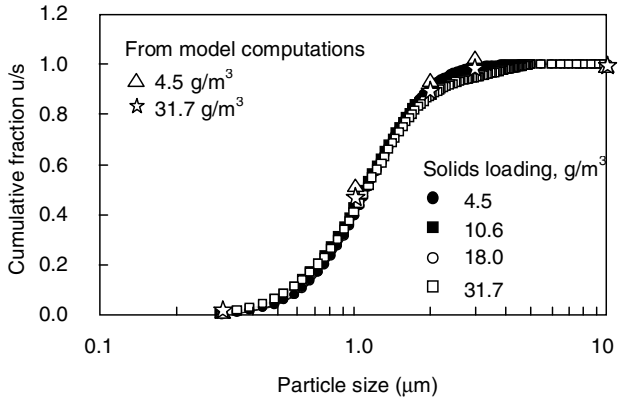

Fig. 6.A.4. The Muschelknautz model predictions of the particle size distribution of the overhead dust fraction at two different solids loadings. Inlet velocity: 10 m/s

6.A.2 Simulation of the Data from Obermair and Staudinger (2001)

Obermair and Staudinger have performed measurements on a cyclone having a variety of dust outlet configurations. For illustration purposes, one was selected for simulation herein and its geometry and dimensions are shown in Fig. 6.A.5. Physical property and flow data at test conditions follow.

The test conditions were:

- Gas: air at standard pressure and 20°C; density, $\rho = 1.21$ kg/m^3; viscosity, $\mu = 1.8{\times}10^{-5}$ Pa s
- Gas volumetric flowrate, $Q = 0.222$ m^3/s

- Particles: limestone dust; particle density, $\rho_p = 2770$ kg/m^3; bulk density, $\rho_{bulk} \cong 0.5\rho_p = 1385$ kg/m^3; solids loading, $c_o = 0.00531$ kg/kg
- Wall roughness, $k_s = 0.046$ mm (commercial steel)

Model Results

The Muschelknautz method provided the following results. As in the preceding example the slope of the grade-efficiency curve was set equal to 5.0.

α	$= 0.583$	$v_{\theta CS}$	$= 27.7$ m/s
A_R	$= 1.73$ m^2	v_{in}	$= 12.6$ m/s
k_s/R	$= 0.00046 \rightarrow 0.0006$	v_{rCS}	$= U'_{t50} = 0.360$ m/s
Re_R	$\cong 2110$	x_{50}	$= 1.92$ μm
v_{zw}	$= 2.55$ m/s	Re_p	$= 0.046$
Δp_{body}	$= 278$ Pa	c_{oL}	$= 0.00302$ kg/kg
Δp_x	$= 1481$ Pa	f_{air}	$= 0.0040$
Δp	$= 1759$ Pa	f	$= 0.0055$

The model predictions of the cyclone's grade-efficiency curve are shown in Fig. 6.A.6. The model is seen to predict actual performance quite well for particle sizes greater than about 2 μm but overpredicts actual performance for smaller sized particles. In this case, the model predicts a mass loading effect for the smaller sized particles that is larger than what was observed.

The measured total pressure drop in this particular study was 1297 Pa. The model predicts 1759. The measured overall collection efficiency was 83.1%. The model predicts 88.5%.

6.A.3 Simulation of the Data from Greif (1997)

Greif performed measurements on an experimental cyclone at various solids loadings and distributions and vortex tube immersion depths and diameters. Considerable attention was devoted to improving the limiting load at low to moderate levels of solids loadings. For illustration purposes, one data set was selected for simulation herein. Its geometry and dimension are shown in Fig. 6.A.7. Physical property and flow data at test conditions follow.

- Gas: air at standard conditions; density, $\rho = 1.20$ kg/m^3; viscosity, $\mu = 1.8\times10^{-5}$ Pa s
- Gas volumetric flowrate, $Q = 0.86$ m^3/s
- Particles: quartz dust; particle density, $\rho_p = 2650$ kg/m^3; bulk density, $\rho_{bulk} \cong 0.5\rho_p = 1325$ kg/m^3; solids loading, $c_o = 0.189$ kg/kg
- Wall roughness, $k_s = 0.1$ mm (commercial steel wall roughness)

Feed Particle Size Distribution (PSD)	
x (μm)	Wt Fract. $< x$
0.20	0.003
0.40	0.015
0.80	0.055
1.20	0.103
1.80	0.174
3.00	0.298
4.00	0.400
4.92	0.500
8.00	0.789
17.0	0.975
40.0	0.996
80.0	1.000

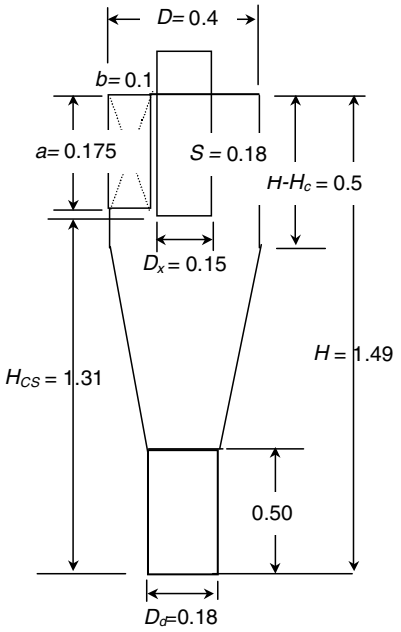

Fig. 6.A.5. Dimensions, in meters, of the Obermair and Staudinger cyclone simulated herein and the size distribution of the feed solids

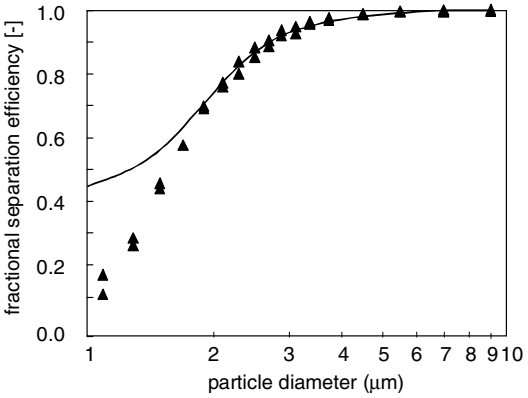

Fig. 6.A.6. Predicted and actual grade-efficiency peformance of the Obermair and Staudinger cyclone shown in Fig. 6.A.5

Feed Particle Size Distribution (PSD)	
x (μm)	Wt. Fraction $< x$
0.15	0.000
0.40	0.030
0.80	0.080
2.0	0.180
4.0	0.300
6.0	0.420
7.85	0.500
10.0	0.590
20.0	0.800
40.0	0.950
100.0	1.000

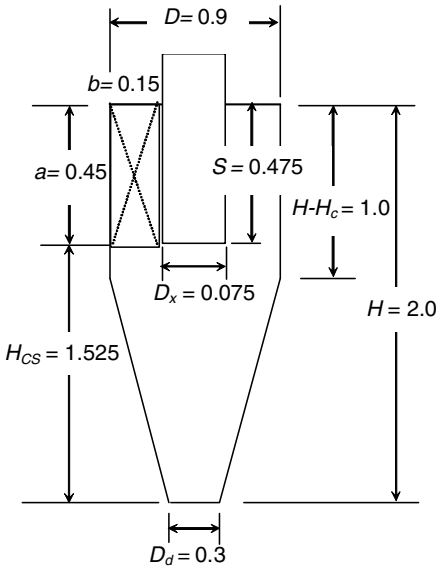

Fig. 6.A.7. Dimensions, in meters, of the Greif cyclone simulated herein and the cumulative size distribution of the feed solids

Model results

The Muschelknautz method provided the following results. As for the preceding example, the slope of the grade-efficiency curve was set equal to 5.0.

α	$= 0.725$	$v_{\theta CS}$	$= 22.2$ m/s
A_R	$= 5.82$ m^2	v_{in}	$= 12.7$ m/s
k_s/R	$= 0.000222 \rightarrow 0.0006$	v_{rCS}	$= U'_{t50} = 0.575$ m/s
Re_R	$\cong 6168$	x_{50}	$= 4.47$ μm
v_{zw}	$= 1.86$ m/s	Re_p	$= 0.171$
Δp_{body}	$= 284$ Pa	c_{oL}	$= 0.0157$ kg/kg
Δp_x	$= 1014$ Pa	f_{air}	$= 0.00403$
Δp	$= 1298$ Pa	f	$= 0.0107$

The model's prediction of the classification portion of the cyclone's grade-efficiency curve (i.e., that excluding the solids loading effect) is shown in Fig. 6.A.8. Here, efficiencies are plotted as a function of the dimensionless particle ratio x/x_{50}, where x is the particle diameter and x_{50} the cyclone's computed cut size. The model is seen to predict measurements reasonably well although the 'slope' of the predicted s-shaped grade-efficiency curve ($m = 5$) is greater than that of the experimental data.

Applying the model to the measured *total* separation curve, which includes the mass loading contribution, one obtains the results shown in Fig. 6.A.9. Here also, the model does a reasonably good job of predicting measured per-

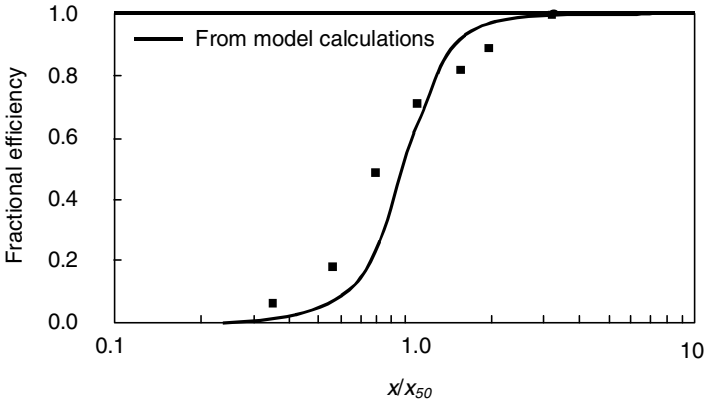

Fig. 6.A.8. Predicted and actual classification contribution to the total grade efficiency performance for the Greif cyclone shown in Fig. 6.A.7

formance. It is not able, however, to predict the shallow dip in the data for which a minimum is observed at an x/x_{50} value of about 1.0.

As above, the efficiencies in Fig. 6.A.9 are plotted versus the dimensionless particle diameter x/x_{50}, although it should be pointed out that Greif's original data were plotted as a function of the particle diameter divided by an 'inlet cut size', as described in Appendix 6.B below. This inlet cut size differs from x_{50} by only about 0.2 micron for the case at hand, and this difference has been neglected in Figure 6.A.9.

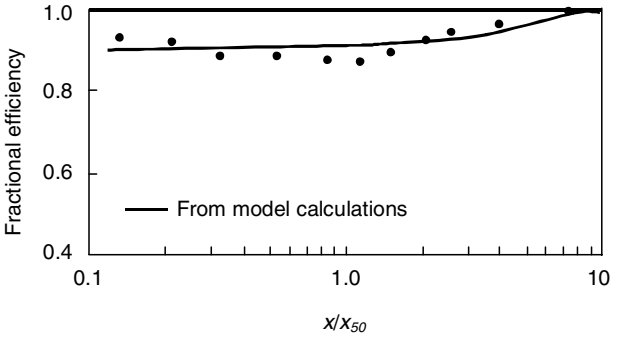

Fig. 6.A.9. Predicted and actual total grade-efficiency performance of the Greif cyclone shown in Figure 6.A.7

In summary, as we review the Muschelknautz model predictions presented in Sections 6.A.1 through 6.A.3, we observe that the model is capable of predicting actual performance reasonably well. This is especially encouraging

in light of the fact that no 'fine tuning' of the model was required to obtain the results.

6.B Incorporation of the 'Inner Feed'

As mentioned in the preceding section, Muschelknautz and coworkers have extended their earlier cyclone model to allow the incoming feed particle size distribution to change within the cyclone if the incoming solids concentration exceeds the limit loading. The concept here is that the solids that are not collected immediately upon entry, and which report on to the inner vortex core, will have a somewhat finer particle size than those entering the cyclone. This is another way of stating that any initial deposition of solids is selective with respect to incoming particle sizes.

According to the 'inner feed' concept, both the incoming feed and the inner feed have their own characteristic mass-averaged particle size (an 'x_{50}'). A grade-efficiency curve is applied to this inner feed in order to determine both the size distribution and the quantity of those solids that are reporting to the inner vortex that are captured. Under saltation conditions, the centrifugal force acting on the incoming solids produces its own cut-point, x_{50in} for the inlet wall region. This controls which particles come out of suspension ('salt out') and which ones remain in suspension and then enter the classification or inner-vortex zone. And even though the quantity or fraction of solids entering the cyclone that salt-out is already known (the weight fraction of incoming solids that exceed the limit loading), it is the inlet x_{50in} that will mostly determine the particle size distribution of the solids that report to the inner vortex.

We begin by first computing the tangential velocity of the constricted and somewhat accelerated incoming gas stream. This is an addition to the MM. Earlier in this chapter, we calculated the wall velocity, $v_{\theta w}$, from the constriction of the inlet jet using the 'constriction coefficient' α shown in Fig. 6.1.2, and then the inner tangential velocity $v_{\theta CS}$ from that. Now, to calculate the effect of solids loading in the inlet region, we calculate a velocity, $v_{\theta in}$, of the gas *in the region of the cyclone just after the inlet.* The equation for $v_{\theta in}$ is very similar to that for $v_{\theta CS}$ (Eq. 6.2.1):

$$v_{\theta in} = v_{\theta w} \frac{(R/R_{in})}{\left[1 + \frac{f A_W v_{\theta w} \sqrt{R/R_{in}}}{2Q}\right]} \tag{6.B.1}$$

where A_W, unlike A_R, is the inside area of the barrel and the upper half of the cone only. See Fig. 6.B.1.

Designating the area of the upper half of the cone $A_{cone,th}$,

$$A_W = A_{barrel} + A_{cone,th}$$
$$= \pi \left[2R\left(H - H_c\right) + \left(R + R_d\right)\sqrt{\left(H/2\right)^2 + \left[R - 0.5\left(R - R_d\right)\right]^2} \right]. \quad (6.B.2)$$

We also compute a similar rotational velocity midway down the cone at radius R_2,

$$v_{\theta 2} = v_{\theta w} \frac{\left(R/R_2\right)}{\left[1 + \frac{f A_W v_{\theta w}\sqrt{R/R_2}}{2Q}\right]}, \quad (6.B.3)$$

which is used to compute a height-averaged tangential or centripetal acceleration,

$$a_{in} = \frac{v_{\theta in} v_{\theta 2}}{\langle R_{in} \rangle}. \quad (6.B.4)$$

. Here,

$$\langle R_{in} \rangle = \sqrt{R_{in} R_2} = \sqrt{\left(R - 0.5\alpha b\right) R_2}. \quad (6.B.5)$$

An incoming particle will reach the wall of the cyclone with a 50% probability if it has a settling velocity of:

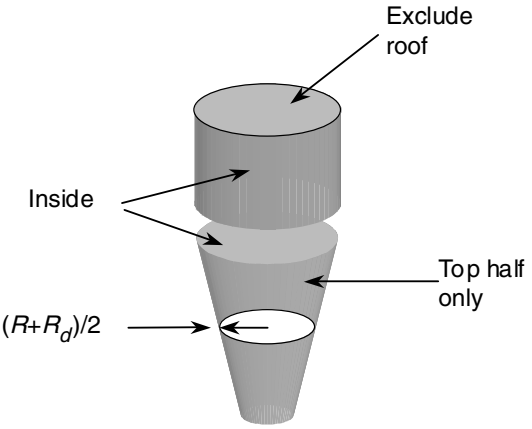

Fig. 6.B.1. Areas comprising the A_W term in Eq. (6.B.1)

$$U'_{t50} = \frac{0.9Q}{2A_W}. \quad (6.B.6)$$

Knowing the settling velocity of the entrance cut size particle, we can now compute its size using Stokes settling law (see Chap. 2) with the centripetal acceleration replacing the acceleration of gravity,

$$x_{50in} = \sqrt{\frac{U'_{t50} 18\mu}{\left(\rho_p - \rho\right) a_{in}}}. \quad (6.B.7)$$

The above equation is strictly valid only when the particle size being computed is settling in the Stokes law regime. One may check that this is the case by computing the particle Reynolds number:

$$Re_p = \frac{\rho U'_{t50} x_{50in}}{\mu}. \tag{6.B.8}$$

If $Re_p <\sim 0.5$, Stokes law applies. If not, one may use the equation,

$$x_{50in} = 5.18 \frac{\mu^{0.375} \rho^{0.25} U'^{0.875}_{t50}}{(\rho_p - \rho)^{0.625} a_{in}^{0.625}}, \tag{6.B.9}$$

which is valid for $0.3 < Re_p < 1000$.

The entrance cut-point, x_{50in}, establishes, or helps to establish, the inner feed particle size distribution which we will now compute.

As noted earlier, if the inlet loading c_o is less than the cyclone's limit-loading c_{oL}, then no saltation occurs and the calculations of the cyclone's performance is conducted according to Sect. 6.3. On the other hand, if

$$c_o > 4c_{oL} \tag{6.B.10}$$

then the average particle size of the inner feed equals the entrance cut-point diameter:

$$x_{medCS} = x_{50in}. \tag{6.B.11}$$

The functional form of this inner-feed particle size distribution cannot be rigorously computed at this time. Even so, it is reasonable to assume that it should resemble that of the particles entering the cyclone. Thus, if a Rosin-Rammler distribution described the feed size distribution, then the inner feed should have this same functional form. Many feeds can be represented by a distribution function that is identical in form to the grade-efficiency equation shown in Eq. (6.3.1):

$$MF_i = \frac{1}{1 + \left(\frac{x_{medCS}}{x_i}\right)^m} \tag{6.B.12}$$

where MF_i is the mass fraction of particles in inner feed < size x_i. If the functional form shown in Eq. (6.B.12) can reasonably describe the incoming feed then one should use its slope, m, in the above equation.

Independently of the equation selected to describe the inner-feed particle size distribution, all such equations can only be regarded as rough approximations to the true size distributions. Fortuitously, perhaps, in most practical situations wherein saltation or mass loading effects occur, the effect tends to dominate the overall collection process and so only a small portion of incoming solids ever report to the inner vortex. As a consequence, the overall collection efficiency is not highly sensitive to the choice of distribution function for the inner feed. If, however, one is only interested in the loss fraction, a difference in the total overall efficiency of 0.9992 and 0.9998, for example, can be significant since, in this case, the amount lost differs by a factor of 4.

If the inlet loading falls in the range,

$$c_{oL} < c_o < 4c_{oL} \tag{6.B.13}$$

the average particle size of the inner-feed particle size distribution becomes

$$x_{medCS} = x_{med} - \frac{1}{0.75}\left(x_{med} - x_{50in}\right)\left(1 - \frac{c_{oL}}{c_o}\right) \tag{6.B.14}$$

where, again, x_{med} is the mass average (median) particle size of the solids feeding the cyclone and x_{50in} is that for the inner feed.

As shown above, we may now substitute Eq. (6.B.14) into Eq. (6.B.12) to obtain a rough estimate of the inner feed particle size distribution for the intermediate case where Eq. (6.B.13) applies.

The overall or total efficiency under saltation or mass loading conditions includes the saltation efficiency and the classification efficiency. A portion of the incoming solids that is not collected by the former is collected by the latter according to:

$$\eta = \left(1 - \frac{c_{oL}}{c_o}\right) + \frac{c_{oL}}{c_o}\sum_{i=1}^{N}\eta_i \Delta MF_i \tag{6.B.15}$$

where, again, ΔMF_i is the i^{th} mass fraction and η_i is the capture efficiency for the i^{th} size fraction computed via Eq. (6.3.1) with x_{50} obtained from Eq. (6.2.3).

We wish to add that the concept of an inlet cut diameter leads one to expect grade-efficiency curves starting at, or close to, zero at higher loadings also (*i.e.*, under mass loading conditions). This, however, is not consistent with practice, where one finds that the entire grade-efficiency curve is displaced upward as the solids loading is increased, *i.e.* that there is a more or less uniform improvement in the collection of all particle sizes due to the effect of solids loading (see Appendix 6.A.1, Hoffmann et al. (1992) and Greif (1997)).

The author's experience is (and the second example in Appendix 6.A also indicates this) that the modeling of the effect of solids loading in some cases may improve by assuming *some* classification of the material separated in the inlet region due to the effect of loading. However, to be consistent with practice, the cut in the inlet region would have to be very shallow.

Greif (1997) has looked at the classification in the inlet, and his results, shown in Fig. 6.B.2, confirm that the 'cut' in the inlet is very shallow. In fact, it can be said that the large particles are removed completely, while the small ones are removed with a high, and almost uniform, efficiency. The ramifications of this will be discussed further in Chap. 9. Note that the results shown in Figs. 6.A.9 and 6.B.2 are not the same, although they look similar. Figure 6.A.9 shows results for the overall efficiency; 6.B.2 the classification in the inlet.

As mentioned, to be consistent with practice, the grade-efficiency curve describing the collection efficiency as a function of particle size in the inlet

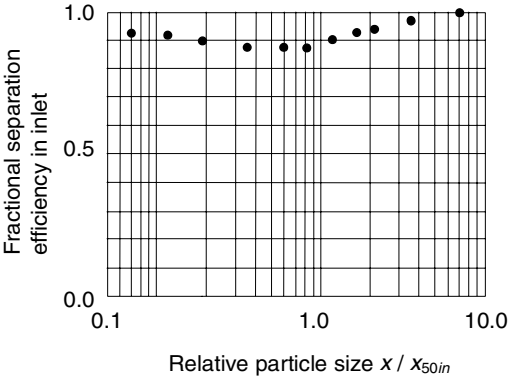

Fig. 6.B.2. Classification of the material salting out in the inlet region of a cyclone with $D = 90$ cm according to Greif (1997). The 'inlet cut size' x_{50in} was 4.2 μm, while the density of the test dust was 2650 kg/m^3

region would have to be very shallow or insensitive to particle size, precisely as Fig. 6.B.2 indicates.

7

Computational Fluid Dynamics

We have examined some of the most widely acclaimed and cited cyclone models. There is one more way of predicting the flow pattern, pressure drop and the separation efficiency in cyclones and swirl tubes, however: by Computational Fluid Dynamics, or 'CFD' for short.

In CFD, the equations governing the flow of the gas: the Navier-Stokes equations, are written in a 'finite difference' form, and solved with the aid of a computer on a grid of points spanning the body of the separator. The particles can either be treated as a sort of second fluid in the cyclone, or as individual particles, which can be tracked in the precalculated gas flow field.

The gas flow in the separator is turbulent, and this creates one problem when using CFD. In principle, if the computational grid could be made fine enough, CFD could be used to solve the Navier-Stokes equations directly, and the turbulence would automatically arise in the simulation. In 'direct turbulence modeling' such CFD simulations are already being carried out in small, simple geometries, and this field is advancing fast as the computational power increases. However, in real processing equipment, this is not possible yet. The number of grid points and time steps required is too high.

For this reason 'turbulence models' are required. These are meant to mimic the influence on the turbulence on the mean gas flow pattern. Correctly mimicking the effect of the turbulence is especially difficult in swirling flows, and we will, among other things, look more closely at this issue in this chapter.

We shall turn now from the gas flow to the flow of the particles. The particle flow can be modelled in two ways. One is the 'Eulerian' approach, where the particles are considered a second 'fluid' interpenetrating the gas and interacting with it, in accordance with the known interaction laws, normally Stokes' drag law. The advantage of this method is that, not only is it relatively easy to incorporate the effect of the gas on the flow of the particles, but it is also relatively easy to incorporate the effect of the particles on the flow of the gas (the 'coupling' between the two phases). The other approach is 'Lagrangian' particle tracking, where the movement of a single particle is followed, solving its equation of motion as it is tracked through the gas flow

field. Using this technique, therefore, the effect of the gas on the motion of the particle is calculated directly. On the other hand, the effect of the particles on the gas flow pattern is more difficult to account for in the simulation[1].

7.1 Simulating the Gas Flow Pattern

We first discuss simulation of the gas flow pattern. We will outline what it means to write finite difference equations for CFD simulations, and explain briefly the principle behind turbulence modeling. There exists an extensive literature on CFD, in general, and CFD in cyclones in particular. However, it is not possible to cover all the detail here, and so our discussion will have to be qualitative. The reader is referred to the literature for further information.

The CFD technique is introduced in the book of Patankar (1980). This book is now dated in terms of computational capabilities, and in some of the most recent methods used, but it is an excellent and very lucid introduction to the principles behind CFD. We can warmly recommend it. Another introduction is by Versteeg and Malalasekra (1996).

7.1.1 Setting up the Finite Difference Equations

In CFD, finite difference equivalents of the differential balance equations are solved in a 'computational grid'. The computational grid consists of 'node points' at which we wish to calculate the dependent variable, which can be the temperature, the concentration of some chemical component or, as it is in the Navier-Stokes equations, the momentum (mass times velocity). A one-dimensional finite difference grid is sketched in Fig. 7.1.1.

Differential balance equations for some quantity φ, which could be the concentration of some chemical species, or the x-, y- or z-momentum, are given in Appendix 7.A. We wish to give an idea of how finite difference equations are formulated by presenting a finite difference equivalent of the one-dimensional balance equation, Eq. (7.A.2), in its steady state form:

$$0 = S - v_x \frac{\partial \varphi}{\partial x} - D \frac{\partial^2 \varphi}{\partial x^2}. \tag{7.1.1}$$

There are different ways of doing this. One way is to take the differential equation, and substitute estimates for the first and the second derivatives in terms of the values of the dependent variable at the grid points. The definitions of the first and second derivatives indicate that we should take:

$$\frac{\partial \varphi}{\partial x} \rightarrow \frac{\varphi_{i+1} - \varphi_{i-1}}{2\Delta x} \text{ and: } \frac{\partial^2 \varphi}{\partial x^2} \rightarrow \frac{\varphi_{i+1} + \varphi_{i-1} - 2\varphi_i}{\Delta x^2}. \tag{7.1.2}$$

[1] Generally speaking, 'Eulerian' indicates that the frame of reference for the description of the flow field is stationary, while 'Lagrangian' indicates that the frame of reference is a material particle, *i.e.* following the flow.

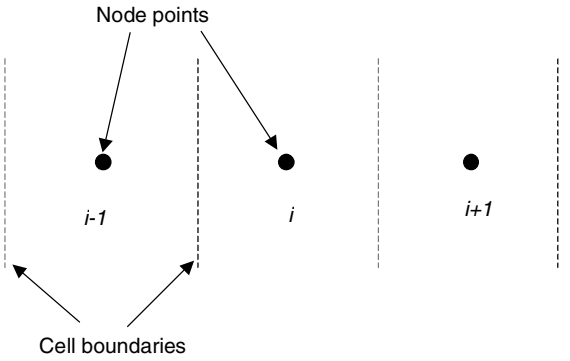

Fig. 7.1.1. Sketch of a one-dimensional computational grid

Inserting this in Eq. (7.1.1), we get the finite difference equation:

$$0 = S - v_x \frac{\varphi_{i+1} - \varphi_{i-1}}{2\Delta x} - D\frac{\varphi_{i+1} + \varphi_{i-1} - 2\varphi_i}{\Delta x^2}. \tag{7.1.3}$$

This can be rewritten as:

$$\frac{2D\varphi_i}{\Delta x^2} = S + \varphi_{i-1}\left(\frac{D}{\Delta x^2} - \frac{v_x}{2\Delta x}\right) + \varphi_{i+1}\left(\frac{D}{\Delta x^2} - \frac{v_x}{2\Delta x}\right). \tag{7.1.4}$$

We have thus obtained an algebraic equation for φ at node point i in terms of the values at the neighboring points. The set of equations for φ at all the node points can be solved iteratively to obtain the flow field. This is the principle of CFD.

Another way of formulating finite difference equations is to perform the balances in φ directly on the computational cells. Eq. (7.1.4) could have been derived by performing the same balance on the cell in Fig. 7.1.1 as that on the differential element in Appendix 7.A. To obtain Eq. (7.1.4), when performing the balance, we make the following choices for the values of φ and its gradient at the cell boundary between node i-1 and i[2]:

$$\varphi \to \frac{\varphi_{i-1} + \varphi_i}{2} \text{ and: } \frac{\partial \varphi}{\partial x} \to \frac{\varphi_i - \varphi_{i-1}}{\Delta x} \tag{7.1.5}$$

-and similarly for the boundary between i and i+1:

$$\varphi \to \frac{\varphi_i + \varphi_{i+1}}{2} \text{ and: } \frac{\partial \varphi}{\partial x} \to \frac{\varphi_{i+1} - \varphi_i}{\Delta x}. \tag{7.1.6}$$

[2] Obviously in this case we also need to assign values to v_x at the left and right cell boundaries in terms of its values at the grid-points. We only obtain the same equation as (7.1.4) if the value v_x at the central node point is assigned to both boundaries. One possible choice is to use the average between the two node-points surrounding the boundary in question.

We leave it to the interested reader to perform this balance. A third way of formulating finite difference equations is to integrate the differential balance equations over the computational cells. This is explained in the book of Patankar.

Finite difference schemes based on the principles above are called 'central differencing'. Central differencing schemes have stability problems in situations where convective transport is significant compared to the diffusive transport. Various methods have been devised to overcome this problem. The 'upwind scheme' assigns the value of φ at a cell boundary to be the value at the node point from which the fluid is flowing, rather than the mean as in Eqs. (7.1.5) and (7.1.6).

In addition to the central differencing and upwind differencing schemes, which are 'first-order' schemes, another popular finite difference scheme is the 'QUICK' scheme, a 'second-order' upwind differencing scheme. Higher order means that more node points are involved when estimating the values of the dependent variables and their derivatives for formulating the finite difference equations.

7.1.2 Turbulence Models

It was mentioned at the start of this chapter that direct turbulence modeling is not yet possible. It is therefore necessary to mimic the effect of the turbulence on the mean flow pattern by means of some model.

When the velocity components in the Navier-Stokes equations are split in two parts:

- a fluctuating part due to the turbulence with a mean of zero and
- a mean part,

and the equations are then time-averaged, the effect of the turbulence appears as extra stresses augmenting those caused by the molecular viscosity. These extra stresses are called the 'Reynolds stresses'. There are 9 Reynolds stresses, 3 in each of the three coordinate planes. It can be shown that the Reynolds stress tensor is symmetrical, so that only 6 of the stresses are independent. We have to refer to a text on fluid dynamics for a satisfactory discussion of these issues.

Reynolds stresses again give rise to the notion of a 'turbulent viscosity' augmenting the molecular one. In most practical situations, the turbulent viscosity turns out to be much higher than the molecular one. Contrary to the molecular viscosity, the turbulent viscosity needs neither to be homogeneous, *i.e.* the same at all points in the flow field, nor isotropic, *i.e.* the same in all directions.

For the reader's awareness, we briefly describe the most used turbulence models below.

In the 'k-ε turbulence model', balance equations are solved for the turbulence kinetic energy per unit mass, k, and the dissipation rate of the turbu-

lence per unit mass, ε, and a turbulent viscosity is calculated from these two parameters. The turbulent viscosity found is necessarily isotropic.

In the 'Reynolds stress model', or 'RSM' for short, transport equations (differential balance equations similar to the balance equations derived in Appendix 7.A), are solved for all 6 independent Reynolds stresses. These transport equations can be formulated by manipulating the time-averaged Navier-Stokes equations, but it is very time consuming to solve all these coupled equations.

In the 'algebraic stress model' or 'ASM', the transport equations for the Reynolds stresses are rewritten as algebraic expressions by assuming that the 'transport of the stresses' around the flow field is proportional to the transport of the turbulent kinetic energy, k.

The ASM gives conceptual problems in swirling flows, and for this reason Boysan et al. (1986) formulated a hybrid between ASM and RSM in which transport equations for some stress components are solved, while, for the rest, the algebraic expressions from the ASM are used.

The newest technique is 'Large Eddy Simulation' or LES, where the larger eddies, which are mostly responsible for anisotropy in the turbulence, are simulated directly, while the effect of the smaller eddies is accounted for in a simple turbulence model. Thus this is an intermediate step toward direct turbulence modeling.

7.1.3 Simulations

In this section some of the most recent CFD results are shown, illustrating how well CFD simulations match reality at the time of writing this book, and the sort of useful information CFD can give. Obviously, CFD is a very dynamic and rapidly changing field of research, as simulation software and hardware continue to improve at a rapid pace.

First we illustrate the significance of the turbulence model. It has long been known that the workhorse of turbulence modeling, the elegant k-ε model, does not suffice for strongly swirling, confined flows. Simulations based on the k-ε model will normally give tangential velocity profiles much like solid-body rotation, nothing like the measured near-Rankine type profiles (Chap. 3). Other, more sophisticated, turbulence models are therefore normally used for cyclone modeling. Figure 7.1.2 shows profiles of the tangential and axial gas velocities in a Stairmand HE cyclone using RSM and LES, respectively. The profiles are compared with profiles measured by LDA (see Sect. 10.1). It is clear that the simulations globally agree with the measurements, although there are significant differences in detail, as there is between the turbulence models mutually.

Not only can the turbulence model influence the simulated flow pattern significantly, but also the finite differencing scheme. In Fig. 7.1.3 profiles of axial velocity from simulations with a first order and a second order differencing scheme are compared (Phyfe, 1999). Two different turbulence models,

the 'Renormalization Group k-ε model' and the RSM are used. The simulations agree well between the turbulence models (for the first order schemes the two turbulence models agree precisely), but they are significantly different between the finite differencing schemes. Measured values of the axial velocity are also shown in the figure; they agree roughly with the second order schemes. This illustrates a danger in CFD: the profiles generated using the first order differencing schemes look quite plausible if one does not have the other data, and the two profiles even agree very well with each other. Nevertheless, the profiles are quite different from those measured. First order schemes are susceptible to 'numerical diffusion'. Numerical diffusion has an effect similar to viscosity when solving the Navier-Stokes equations, but is caused purely by numerical inaccuracy. Flows with a strong cross-grid component, such as in cyclones, are particularly sensitive to this.

It is probably fair to say that the main strength of CFD at the present time is that it can reveal features of the flow that are otherwise difficult to ascertain, rather than its power to predict cyclone and swirl tube performance from first principles. Figure 7.1.4 shows profile plots for the tangential velocity in the inlet region of a cyclone with a tangential inlet (McAuley and Dries, 2000). An area of low tangential velocity, visible as the smooth gray area in the left-hand figure, prevails around the 'back' of the vortex finder pointing away from the inlet. This area of low near-wall gas velocity is a problem in cyclones with a tangential inlet, since the particles are prone to depositing on the wall here, sometimes giving rise to operational problems. In certain fluid bed coking and FCCU operations, large deposits of slate-like coke will often form in this stagnant region of the cyclone.

Figure 7.1.5 shows isosurfaces of swirl velocity (surfaces in which the swirl velocity is constant) colored according to pressure, generated by a large eddy simulation incorporating a sub-grid Smagorinsky (mixing length) eddy viscosity. Also instantaneous streamlines for the gas flow are shown; in the left figure these are white, and in the right they are colored according to the pressure. In the gray-scale images, the most important colors are indicated. The outer isosurface is obviously one wherein the swirl velocity takes a low value, since it is near the wall. It therefore follows the outer contours of the cyclone. We showed in Sect. 4.4 that, within the cyclone body, the swirl velocity is almost constant in the axial direction. The isosurfaces should therefore be cylindrical within the body, and this can be seen vaguely in the left half of the left-hand figure.

The irregularity in the color of the outer isosurface appears to indicate wave-like fluctuations in the near-wall pressure, *i.e.* near-wall turbulent boundary layer structures, consistent with what has been stated about the instability of the near-wall flow in Sect. 3.1.1. The low pressure in the inner part of the vortex and in the vortex finder is clearly to be seen. A very low pressure can be seen also to exist in the apex of the cone. Its location is consistent with what is seen experimentally when the vortex extends to the bottom of the cyclone, not terminating upon a vortex stabilizer or due to the 'natural

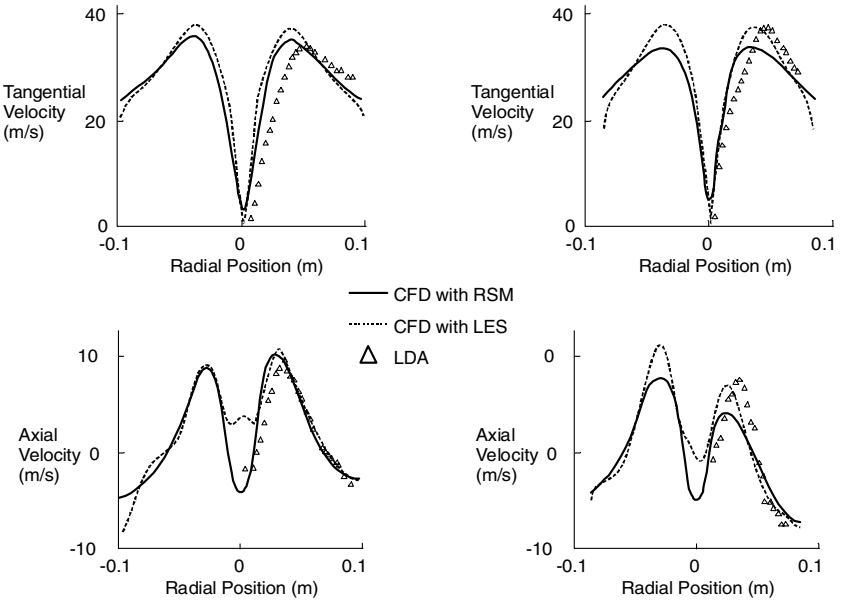

Fig. 7.1.2. Profiles for the tangential and axial velocity profiles at two axial stations in a Stairmand HE cyclone with CFD and LDA (Slack et al., 2000). The cyclone length is 0.82 m, and the axial stations are: left: 0.17 and right: 0.44 m under the lid of the cyclone

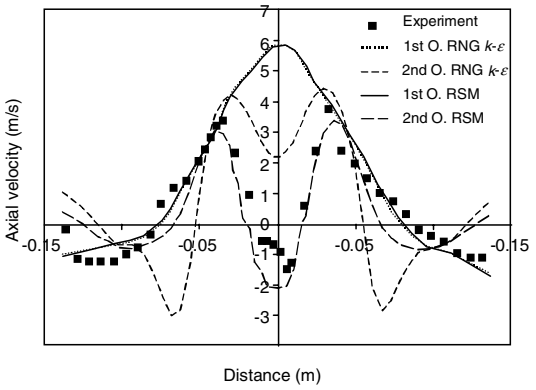

Fig. 7.1.3. Comparison of axial velocity profiles by CFD using first and second order finite differencing schemes and two different turbulence models (Phyfe, 1999)

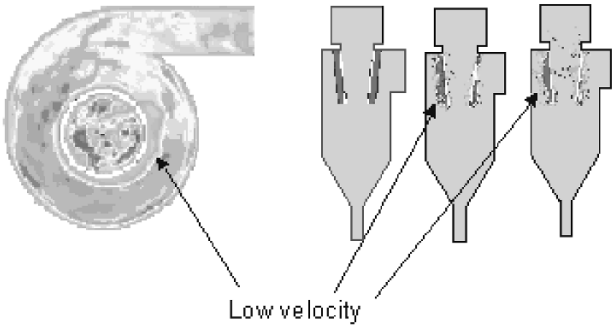

Fig. 7.1.4. Profile plots for the tangential velocity in a tangential inlet cyclone, with the area of low near-wall velocity on the back of the vortex finder indicated

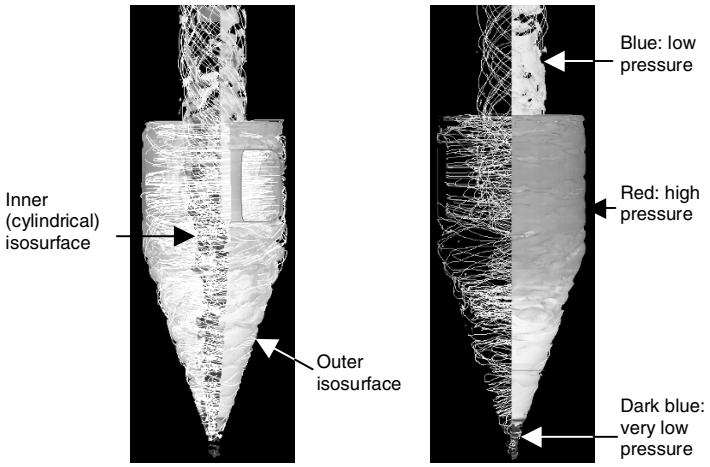

Fig. 7.1.5. Isosurfaces of swirl velocity colored according to the pressure. In the gray-scale figures the most important colors are indicated. The figures also show instantaneous streamlines for gas elements. These are white in the left figure and colored according to the pressure in the right figure. Courtesy CSIRO Thermal and Fluids Engineering, who developed the code in-house

end' phenomenon. This underpins the importance of a good underflow seal, as pointed out in Sect. 11.2 and the need to provide erosion protection in the lower cone when processing abrasive solids. The instantaneous streamlines clearly show the irregularity in the flow pattern due to the turbulent eddies.

Figure 7.1.6 shows another image illustrating the turbulent eddies in LES (Prasad and Bakker, 1999). To the left, the vectors represent the instantaneous velocity field, and to the right the velocity field averaged over a period of 0.25 seconds. The averaging clearly gives rise to a much more pat-

terned overall picture, although the vortex core can still be seen to be twisting around the axis of the cyclone.

We have presented some of the latest CFD simulations of cyclone gas flow, both from the reviewed and the nonreviewed literature. Many questions remain, and swirling flow remains very difficult to simulate correctly in all respects.

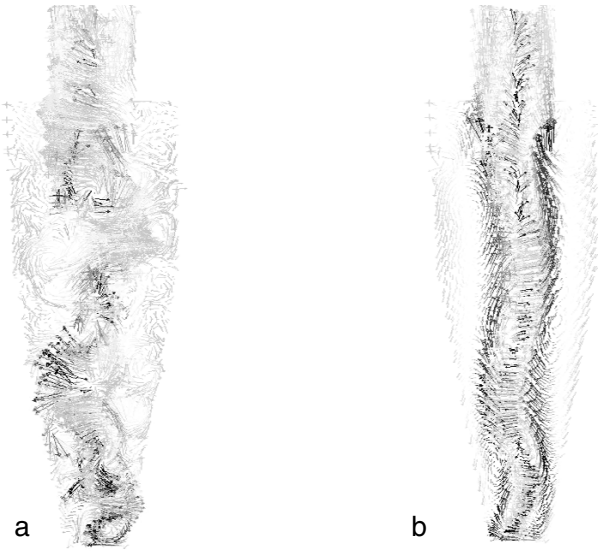

Fig. 7.1.6. LES simulations of the flow in cyclones (Prasad and Bakker, 1999). **a** is the intantaneous flow, and **b** the flow averaged over 0.25 s

7.2 Simulating the Particle Flow

We turn now to the particle flow. As mentioned, there are two ways of simulating the particle flow. In one of these the particle flow is regarded as a second phase interpenetrating and interacting with the gas phase. This is the Eulerian approach, wherein the modeling is performed relative to a stationary frame of reference. This makes the simulation of the influence of the particles on the gas flow relatively easy and this is one of the advantages of this method. On the other hand, it gives less insight into the flow of a given particle through the cyclone. The other approach involves tracking a single particle through the gas flow field. This is the Lagrangian approach and it uses a frame of reference that follows the particle under study. The influence of the particles on the gas can also be estimated using Lagrangian tracking, but it is more difficult and less reliable.

7.2.1 Eulerian Modeling

In Eulerian particle modeling, the particles are considered as a continuous fluid, just like the gas. This 'fluid' interpenetrates with the gas in the cyclone, and interacts with it, in accordance with the known laws of interaction, for instance, Stokes' law. Transport equations, which are coupled through the interaction terms, are solved for both fluid and particle phases.

7.2.2 Lagrangian Particle Tracking

In this approach, the particle equation of motion is solved, mostly in a precalculated gas flow field. The particle position and velocity are calculated after successive short time intervals, and in this way the particle is tracked through the cyclone or swirl tube.

Once the particle enters a particular cell with a given velocity relative to the gas ($U'_{i,0}$, for instance), its velocity after a short time interval Δt can be calculated from Eq. (2.2.5):

$$U'_i = \frac{x^2\,(\rho_p - \rho)\,a_i}{18\mu}\left(1 - \exp\left[-\frac{18\mu\Delta t}{x^2\rho_p}\right]\right) + U'_{i,0}\exp\left[-\frac{18\mu\Delta t}{x^2\rho_p}\right]. \quad (7.2.1)$$

Knowing the gas velocity in the cell, the absolute particle velocity can be calculated from its velocity relative to the gas. The position of the particle after Δt can also be calculated by integrating the absolute particle velocity over Δt, since the distance traveled equals $\int_{\Delta t} U\ \mathrm{d}t$.

Doing this for a series of time intervals gives the path of the particle through the cyclone. The mean value of the gas velocity is used for this since this is normally all we have available from the CFD simulations. If one wishes to take the fluctuation in the particle velocity due to turbulent eddies into account, the gas velocity can be augmented by a fluctuating part with a mean of zero and a spread and frequency of change that is consistent with the intensity and scale of the turbulent eddies. Sometimes one comes across codes where the particle velocity, rather than the gas velocity, is given a random component. This is incorrect and gives rise to a turbulent dispersion that does not decrease with increasing particle size, as it should.

7.2.3 3-D particle tracks

We have already shown some particle tracks in a 2-D CFD simulation in Chap. 3. The pictures show the effect of the turbulence in causing particle dispersion. This, in turn, has the effect of flattening the grade-efficiency curve. Figure 7.2.1 shows Lagrangian particle tracks in 3-D. Tracks of particles can be seen moving down the wall toward the dust exit and moving up the gas outlet pipe, having been lost from the cyclone.

CFD is obviously a field that changes rapidly. In the first place turbulence modeling is developing very fast. After a long period of increasing complexity

in turbulence modeling, we are now facing a phase where the simulations will probably become simpler, as more and more features of the turbulence can be simulated directly. However, demands on computing power, and on the finite differencing algorithms, are becoming more stringent at the same time.

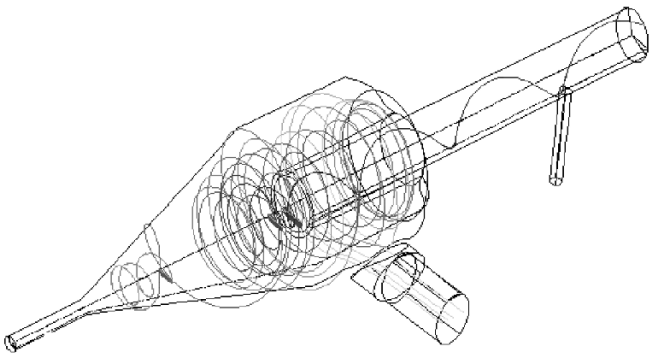

Fig. 7.2.1. Lagrangian particle tracks in 3-D. Courtesy of Fluent Inc.

Eulerian particle modeling has been somewhat less successful until now. Figure 7.2.2 shows tangential velocity profiles in a finite-volume, 2-D axisymmetric simulation of the tangential velocity profile in a cyclone with and without solids (Meier and Mori, 1998). Although the simulation correctly shows the tangential velocity decreases due to the presence of the solids, the quantitative comparison with experimental data still leaves a lot to be desired (as does the printing of Meier and Mori's article).

7.3 Some Simulations of the Gas and Particle Flow in Cyclones

We mention some of the latest developments in CFD modeling of the gas and particle flow in cyclones. Much of the research literature being published aims at modeling specific systems, often with commercial software and in many studies the RSM turbulence model is used. We limit this discussion to the publications of one group at Delft Technical University, in which significant strides forward have been taken in the numerical modeling techniques and in the understanding of the working of cyclones.

7.3.1 LES Simulations of Derksen and van den Akker

The simulations of the group of Jos Derksen and Harrie van den Akker at Delft Technical University (Derksen, 2003, 2005; Derksen et al., 2006) stand

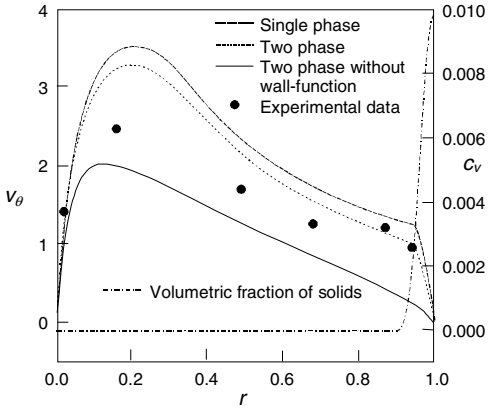

Fig. 7.2.2. The tangential velocity profiles in a cyclone with and without solids present modeled with Eulerian particle simulation (from Meier and Mori, 1998)

out in the recent literature as being cutting-edge both in terms of numerical techniques and providing insight into the working of cyclones.

These authors use the lattice-Boltzmann discretization method for solving the Navier-Stokes equations. In lattice-Boltzmann discretization, the motion of the fluid is represented by the motion and collision of discrete particles moving between the nodes of a fixed grid (the lattice). This discretization method, which has recently become more frequently used, but is still not standard, is thus completely different from the ones briefly discussed in Sect. 7.1.1. If the rules for the particle collisions and the morphology of the lattice upon which they move are set correctly, the dynamics of these particles will represent a numerical solution to the Navier-Stokes equations (Wolf-Gladrow, 2000; Chen and Doolen, 1998).

The turbulence modelling strategy used is large-eddy simulation, or LES, where, as mentioned in Sect. 7.1.2, the larger (or "resolved") eddies are allowed to form spontaneously in a time-progressing simulation, and the effect of those eddies that are smaller than the computational grid is modelled by a simple subgrid turbulence model, or "subgrid-scale" (SGS) model that yields a turbulent viscosity, which is added to the molecular viscosity.

In many ways LES is the most exciting development in CFD, since the sweeping assumptions and significant element of empiricism inherent in classical turbulence modeling is largely avoided, such that results for turbulent flows are more plausible. Moreover, as is also shown by Derksen (2003) the resolved turbulent eddies are, if the computational grid or lattice is reasonably refined, much more significant in influencing the flow of both the gas and the particles than is the subgrid-scale turbulence. Thus, as we have mentioned earlier in this chapter, with LES, turbulence modeling is becoming simpler and less crucial for the results.

The main draw-back of LES is the computational effort involved, primarily because an unsteady-state, time-progressing solution is necessary in contrast to classical turbulence modeling, which is aimed at finding a mean flow field, and often, but not always, seeks only a steady-state solution. A single-phase simulation on a Beowulf-cluster, consisting of Dual Pentium III 700 MHz PCs connected through Ethernet (100 Mbit/s), using six CPUs in parallel typically took 2.5 days of wall clock time to reach statistical convergence. Including particle tracking in the simulations did not increase the computational time per time step very much, but due to the long residence time of the particles in the separator, the total duration of a simulation became one order of magnitude larger than for the single-phase simulation.

Derksen (2003) studied the gas and particle flow pattern and the separation efficiency in a Stairmand HE cyclone (see Fig. 15.1.1 and Table 15.1.1). Important simplifying assumptions in the simulations were:

- one-way coupling, *i.e.* the effect of the gas flow on the particle flow is taken account of, but not the effect of the particles on the gas flow
- non-interacting particles, *i.e.* particle-particle collisions were not taken into account.

Also an obstruction was simulated in the downstream tubing to avoid non-physical flow phenomena to propagate back into the flow from the outlet boundary (see below).

The flow of the particles was studied by Lagrangian particle tracking as described in Sect. 7.2.2.

Figure 7.3.1 shows vector plots of the flow in the cyclone. In the figure to the left the time-average flow pattern is shown. The familiar pattern of downflow in the outer part and upflow in the inner, with a velocity deficit around the core is recognizable. However, it is also clear in this figure, as it was in Fig. 7.1.6b, that the time-mean position of the core of the vortex does not coincide with the cyclone axis, but deviates from it slightly. In addition to this, Derksen states that the core also precesses around its time-mean position. This latter feature gives rise to a strongly fluctuating fluid velocity near the core, a fluctuation that is, in contrast to the fluctuation in the rest of the cyclone, not due to random turbulent motion.

The top figure to the right is a vector plot showing the time-mean flow pattern, and the bottom-right figure is a snapshot of an instantaneous flow pattern. Note the strong turbulence in the latter.

As also pointed out by the authors of this book earlier (Hoffmann et al., 1996), Derksen states that the dust collection vessel needs to be included in the simulation.

Derksen also shows a series of comparisons of the gas velocity fields in his simulations and in measurements performed with LDA (see Sect. 10.1) by Hoekstra (2000). Some are redrawn in Fig. 7.3.2. We note that the agreement is quite impressive, even in case of the fluctuating velocity components, adding to the credibility of the LES turbulence simulations.

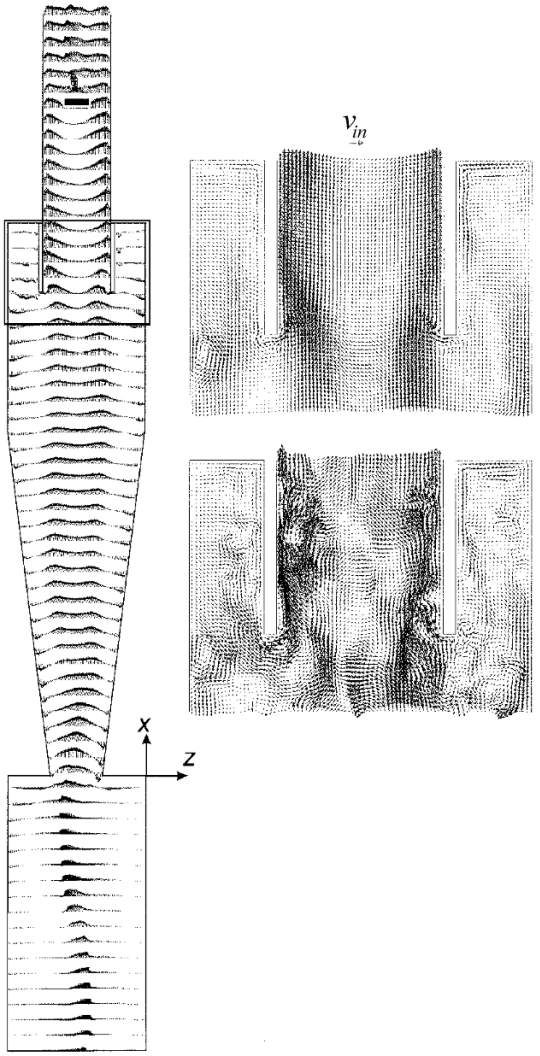

Fig. 7.3.1. Velocity vectors from the simulations of Derksen (2003), reproduced with permission from Elsevier Science. Left: the entire cyclone, top right: the time-mean flow pattern bottom right: an instantaneous flow pattern

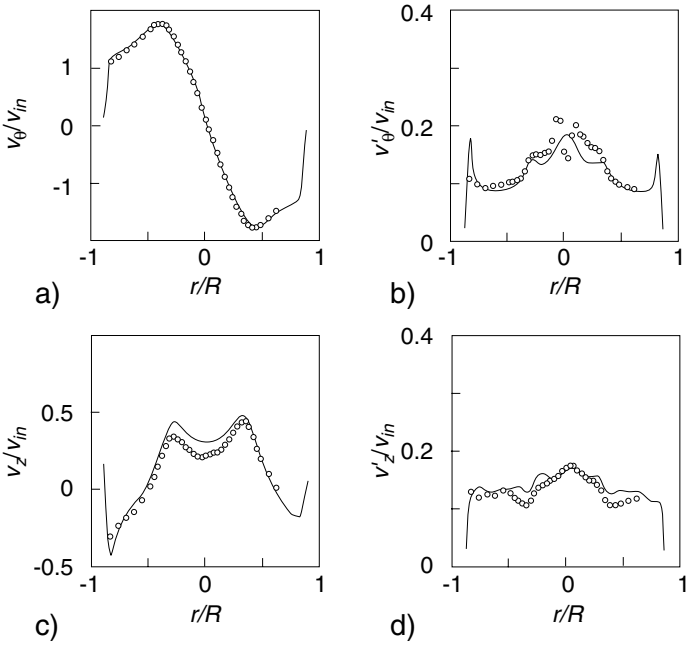

Fig. 7.3.2. Comparison of the mean and fluctuating gas velocity components between CFD (curves) and experiment (points) at an axial station 2.0D above the dust exit of the cyclone. a) and b), the mean and fluctuating tangential velocity. c) and d), the mean and fluctuating axial velocity. Drawn on basis of graphical data in Derksen (2003)

Derksen also performs particle tracking in parallel with calculating the flow field, which adds significantly to the computational effort. He calculates the separation efficiency of the cyclone by monitoring the particles collected and entering the dust collection hopper and those lost entering the vortex finder. Figure 7.3.3 shows two grade-efficiency curves at different points in time during the simulation of his cyclone working with an inlet gas velocity of 16.1 m/s.

As mentioned, performing simulations with particle tracking demands great computational effort, and Derksen tried different ways of reducing this. One was to inject the particles in a "frozen" instantaneous gas flow field, and thus tracking particles in a pre-calculated flow field. Another method was to allow the gas flow field to perform a loop through a set of precalculated flows while the particles are tracked. Both methods gave grade-efficiency curves in reasonable agreement with the curves shown in Fig. 7.3.3.

Although the simulations in this and the other papers from the same group, mentioned below, are very impressive, there is one contention that we do not entirely agree with, namely that the turbulent fluctuations in the gas velocity

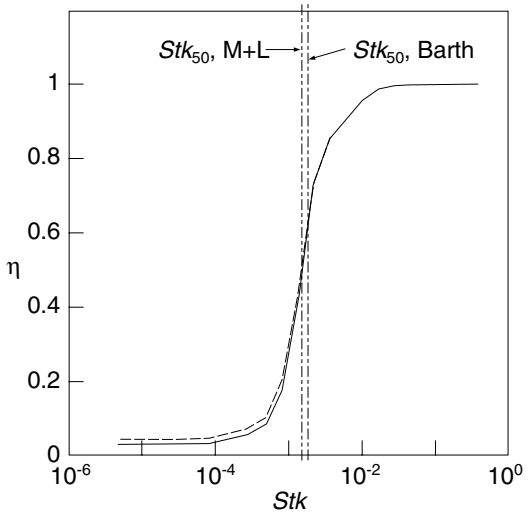

Fig. 7.3.3. Grade-efficiency curves from Derksen (2003) at different points in time. The predictions for Stk_{50} of the models of Barth and Mothes and Löffler (Chap. 5) are also indicated

are more important in bringing small particles into the inner vortex, and therefore be lost, than the mean inward gas flow from the outer to the inner vortex.

We agree that the turbulent fluctuations in the gas velocity seem far more significant than the mean inward flow from the outer to the inner vortex in an instantaneous snapshot, such as the one shown in Fig. 7.3.1. However, the concentration of particles of sizes close to x_{50} is almost uniform radially, and turbulent dispersion will therefore not have an important effect in causing a net radial transport of such particles, e.g. from the inner and outer vortices, while the mean inward gas flow will, however small it seems compared to the turbulent fluctuations. We do agree that the turbulent fluctuations will have an important effect in bringing larger particles into the inner vortex, and conceivably smaller particles out of it, and so widen the grade-efficiency curve.

As a further argument supporting what went before, we also remind the reader that, as shown in Fig. 7.3.3, the x_{50}, and therefore the Stk_{50} predicted by the models of Barth and of Mothes and Löffler, both described in Chap. 5, agree quite well with that determined by Derksen. This means that *in the idealized flow patterns envisaged by Barth and by Mothes and Löffler, which did not take into account turbulence at all, particles smaller than the cut size determined by the simulations of Derksen will be carried into the inner vortex and lost from the cyclone.* This ends our discussion of this issue.

A remark in the paper of Derksen (2003) about the flow in, or close to, the cyclone vortex finder is:

> Just upstream of the vortex finder entry vortex breakdown occurs, similar to the breakdown structures observed by Escudier et al. (2005) slightly upstream or inside a contraction.

In a subsequent paper Derksen (2005), the flow in a cyclone-like geometry is studied in more detail, with emphasis on the gas exit tube, using the same numerical techniques as above. This cyclone-like geometry is shown in Fig. 7.3.4. The flow in the same geometry had earlier been investigated experimentally by Escudier et al. (2005).

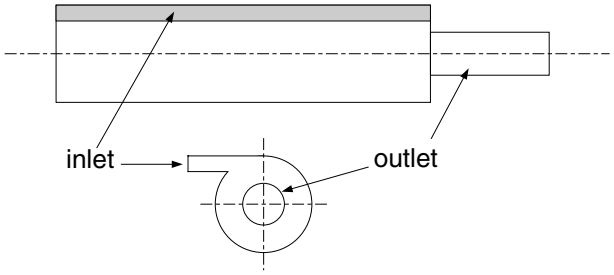

Fig. 7.3.4. Schematic drawing of the vortex tube configuration used in the simulations of Derksen (2005)

It adds credence to the simulations that Derksen (2005) compares many of the flow features in his simulations with the flow features experimentally determined by Escudier et al. and that he uses three different SGS models and three different grid resolutions to show the effects of both on the results of the simulations. In general he achieves very good agreement between simulation and experiment.

Obviously the vortex tube shown in Fig. 7.3.4 is very similar to a cyclone, and the exit tube very similar to the vortex finder in a cyclone. One very interesting feature found by Derksen is a vortex breakdown of type "0", according to the classification of types of vortex breakdown by Faler and Leibovich (1977), in the exit tube at certain flowrates and in certain geometrical configurations. In a type "0" breakdown, a "gas bubble" with recirculatory flow is formed at the point where the vortex breaks down, and the flow downstream is much more turbulent, and less intensely swirling. Derksen's simulations are shown in Fig. 7.3.5.

The existence of such a break-down is supported by the experiments of Escudier et al. (2005). It also appears to be present in a swirl tube, at least one with a conically shaped vortex finder (sketched in Fig. 15.1.12g). Figures 7.3.6 and 7.3.7 shows the flow pattern in the gas outlet and downstream tubing of a

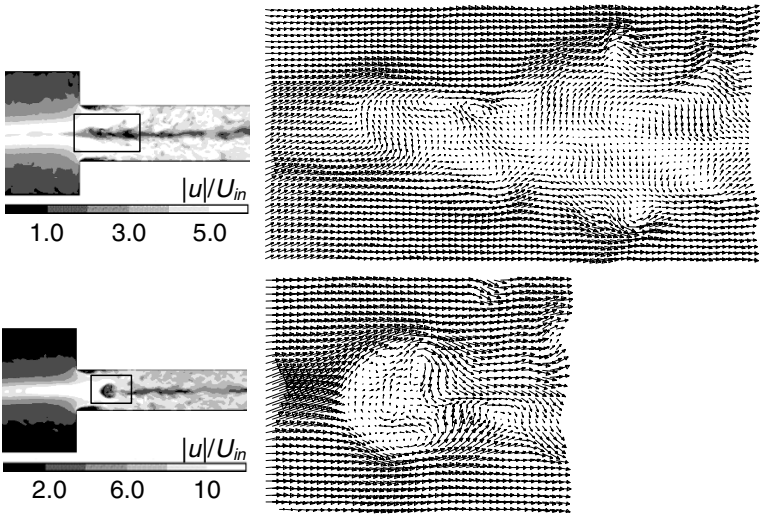

Fig. 7.3.5. CFD simulations of Derksen showing type "0" vortex breakdown in the gas outlet of a swirl-tube-like geometry, reprinted from Derksen (2005), copyright 2004, with permission from Elsevier

reverse-flow swirl tube with a conically shaped gas outlet visualized with helium bubbles Peng, Hoffmann, Dries, Regelink and Foo (2005). The streaklines of the neutral boyancy tracer are clearly diverging in the gas outlet, consistent with a type "0" vortex breakdown. The clear formation of a core—wherein the helium-filled tracer bubbles collect in this experiment—in the downstream tubing shows that there is still some vortex motion present there.

Obviously the existence of such a vortex breakdown in the vortex finder will have significant impact on our understanding of the very high pressure drop in the vortex finder (see Chap. 4), and the working of pressure-recovery vanes (see Hoffmann et al., 2005, Sect. 15.1.5).

We mentioned that one assumption in Derksen (2003) was one-way coupling between the gas and the solid phase. In Derksen et al. (2006), this assumption is relaxed, and the effect of the solids on the gas flow pattern, i.e. two-way coupling, is taken into account in simulations of the flow in the same cyclone geometry as in Derksen (2003). In order to do this without having to trace prohivitively many particles, each particle that is traced is considered to represent a whole assembly of like particles[3], the action of which on the gas flow is fed back into the gas equations to determine the effect of the particles on the gas flow field.

Figure 7.3.8 shows the distribution of particles of three values of Stk in the cyclone separation space. Each picture represents a view of a thin slice

[3] This is a standard technique in Lagrangian particle tracking in order to reduce the number of trackings necessary

Fig. 7.3.6. Visualization of the flow in the gas outlet of a swirl tube

(0.04D thick) of the cyclone, which was operated at $v_{in} = 16.1$ m/s, which is the same inlet velocity as in Fig. 7.3.3. The middle figure thus represents particles of a size close to the cut-size of the cyclone.

Unfortunately these simulations were too demanding on computer resources to allow simulations to reach a steady state.

One important effect of the particles on the gas flow was to suppress turbulence in the gas. Figure 7.3.9 shows profiles for the tangential velocity, the axial velocity and the kinetic energy in the turbulent eddies per unit of mass, all scaled by the inlet velocity, for three cases: without solids present and with solids in two different mass fractions in the inlet gas. Figure 7.3.9c shows the clear effect of the solids in suppressing the turbulence in the gas.

Consistent with our discussion in Chap. 4, Derksen et al. (2006) consider that the axial flow profile is a slave of the tangential flow profile, and its axial evolution.

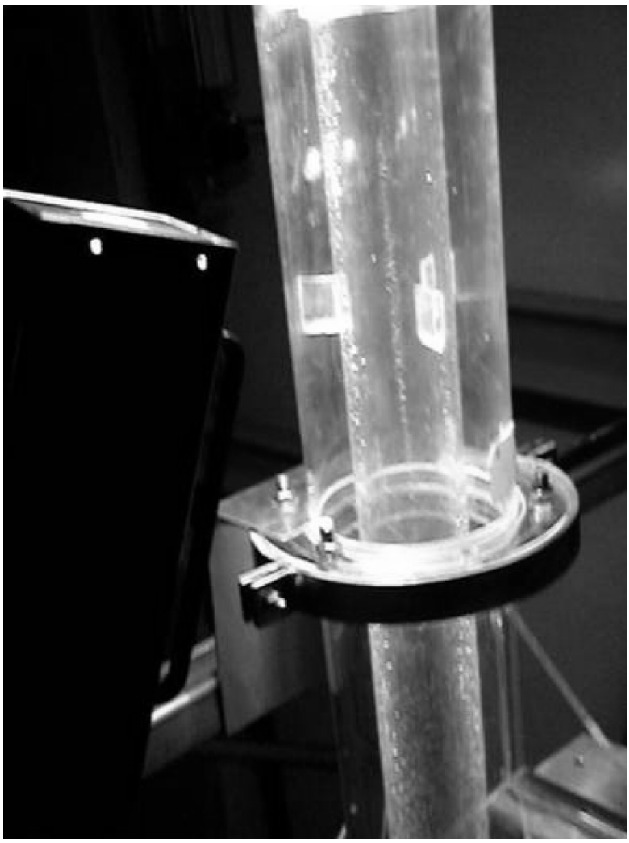

Fig. 7.3.7. Visualization of the flow in the tubing downstream of the gas outlet of a swirl tube

Derksen et al. (2006) also propose—consistent with the contention that turbulence is the most important reason for particle loss—that the effect of solids loading in improving cyclone separation efficiency (see Chap. 9) is due to the particles suppressing turbulence at high concentrations (in spite of the reduced vortex intensity). While we agree that turbulence is suppressed and that the vortex intensity is reduced, and also agree that turbulence may contribute to particle loss from a cyclone, we are of the opinion, as mentioned in Sec. 9.1.1, that the main effect of high solids loading is in bringing particles to the wall in the inlet jet due to particles shielding each other from the effects of the gas flow. This is supported by the fact, mentioned above, that in the idealized flow of, e.g., Barth particles below the approximate cut size found by Derksen (2003) will be lost from the cyclone even without any turbulence at all.

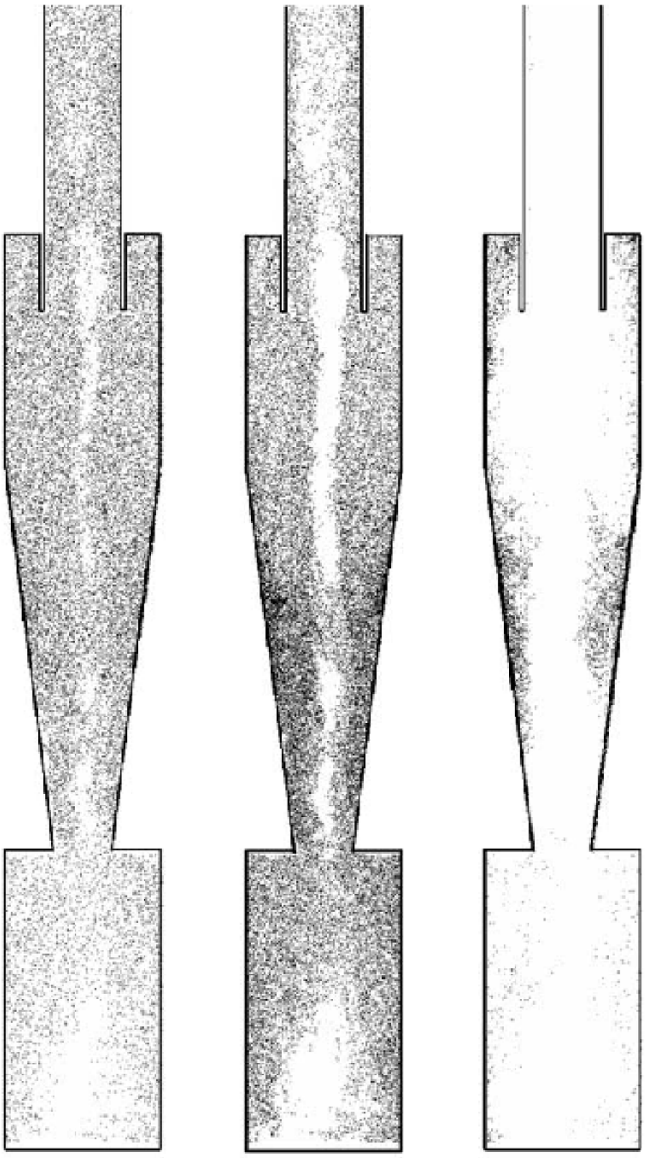

Fig. 7.3.8. Snapshots of the particle positions in a thin ($0.04D$) vertical slice in a 2-way coupled simulation. Particle mass fraction in the incoming stream: 0.1. a): $Stk = 3 \times 10^{-4}$, b): $Stk = 2.3 \times 10^{-3}$ and c): $Stk = 1.8 \times 10^{-2}$. Reproduced from Derksen et al. (2006) with permission from Elsevier.

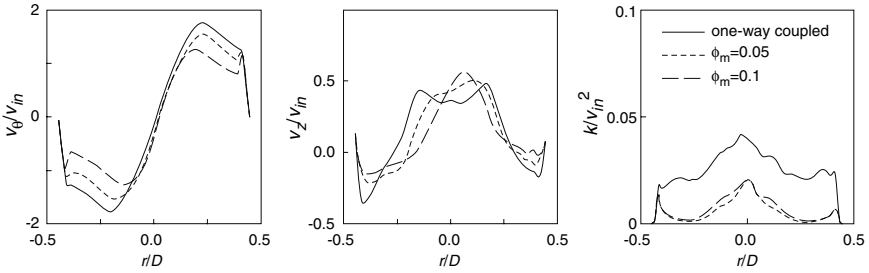

Fig. 7.3.9. The influence of solids on, from left to right: the tangential velocity, v_θ, the axial velocity, v_z and the turbulent kinetic energy per unit mass, k. Drawn on basis of graphical data in Derksen et al. (2006)

7.3.2 Some Remarks on CFD in Cyclones

As mentioned, LES seems to be a significant step forward, allowing not only direct simulation of the most important effects of turbulence, but also more direct[4] calculation of the effect of the particles on the turbulence intensity.

As increasing computer power makes finer spatial grids possible the SGS models will become less important and the simulations more direct. Increasing computer power is, at the time of writing, however, no longer a matter of course, since a limit on the clock frequency of conventional processors has been reached, and the way to higher computer power is envisaged through parallelization, something that most CFD packages are already making use of. The focus will therefore probably increasingly switch to developing more efficient software in the near future.

Significant strides still need to be made, however. Cyclone efficiency depends to a large extent on the behaviour of dense particle strands where the interaction between the particles becomes important, and this is a field where much research still needs to be done and one in which the authors of this book are active. Also, although interesting progess is being made, phenomena such as the vortex end are still not successfully simulated.

We have yet to see a CFD simulation that has been proven in the open, peer-reviewed research literature to outperform the efficiency models given in Chaps. 5 and 6 in terms of predicting the separation performance of cyclones in general, although we are encouraged to see the agreement between model and simulation in Fig. 7.3.3. Also, analytical cyclone models and scaling rules allow a degree of abstraction and generalization and gives an over-all understanding of the process that specific simulations cannot give.

We look forward to seeing the developments of CFD for cyclone modeling in the time to come.

[4] The drag force between the gas and the particles must still be evaluated by using a model, *e.g.* by assuming Stokes drag law

7.A Transport Equations

To refresh the reader's memory, we briefly consider transport, or balance, equations in this appendix. (If the variable is being conserved in the flow field we can call them conservation equations). The 'Navier-Stokes equations' we mentioned in Chap. 2 are a particular type of transport equation. Transport equations can be derived by balancing a certain quantity, let us call it φ, over a differential volume element. The balance is:

$$\text{Accumulation of } \varphi = \text{Generation of } \varphi + \text{Transport of } \varphi \text{ in} - \text{Transport of } \varphi \text{ out.} \tag{7.A.1}$$

φ is transported in and out of the differential element both by convection: flow with the fluid flowing in and out of the box, and by diffusion, molecular transport in the down-gradient direction across the box boundaries, which is proportional to the concentration gradient in φ.

We perform the balance in the simple case of one-dimensional flow, on a differential element that has unit width and height (the y and z directions), see Fig. 7.A.1

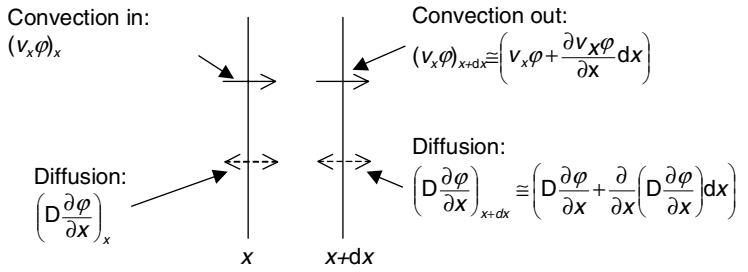

Fig. 7.A.1. Sketch of a one-dimensional element, showing the transport in and out

This figure shows the transport of φ in and out of the element. The rate of accumulation of φ in the element is $(\partial\varphi/\partial t)\,\mathrm{d}x$ and, if S denotes the rate of generation of φ (for instance by chemical reaction, S may be positive or negative) per unit volume, the rate of generation of φ in the element is: $S\mathrm{d}x$.

Applying the balance from Eq. 7.A.1 and simplifying gives the one-dimensional differential balance equation, the steady version of which is used in the main text:

$$\frac{\partial\varphi}{\partial t} = S - v_x\frac{\partial\varphi}{\partial x} - \mathcal{D}\frac{\partial^2\varphi}{\partial x^2}. \tag{7.A.2}$$

Here we have made two assumptions. The first is that the fluid is incompressible, which means that the derivative of the velocity is zero (same volume flow in and out of the element):

$$\frac{\partial v_x \varphi}{\partial x} = v_x \frac{\partial \varphi}{\partial x} + \varphi \frac{\partial v_x}{\partial x} = v_x \frac{\partial \varphi}{\partial x}.$$

The second is that the diffusion coefficient $\mathcal{D}$ is constant, so that

$$\frac{\partial}{\partial x}\left(\mathcal{D}\frac{\partial \varphi}{\partial x}\right) = \mathcal{D}\frac{\partial^2 \varphi}{\partial x^2}.$$

When performing the balance in three dimensions, the differential element takes the form of a box, as sketched in Fig. 7.A.2.

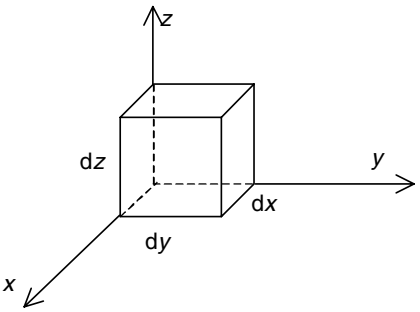

Fig. 7.A.2. A sketch of a differential box over which φ is balanced

The balance is a straightforward extension of the one-dimensional balance; we refer to the standard texts on transport phenomena and just write the balance equation for an incompressible fluid with a constant $\mathcal{D}$:

$$\frac{\partial \varphi}{\partial t} = S - v_x \frac{\partial \varphi}{\partial x} - v_y \frac{\partial \varphi}{\partial y} - v_z \frac{\partial \varphi}{\partial z} - \mathcal{D}\left(\frac{\partial^2 \varphi}{\partial x^2} + \frac{\partial^2 \varphi}{\partial y^2} + \frac{\partial^2 \varphi}{\partial z^2}\right). \qquad (7.A.3)$$

In order to formulate the flow equations for a fluid, for instance, for the gas in the cyclone or swirl tube, we must balance both mass and momentum. The mass balance leads to the 'equation of continuity'; the momentum balance to the 'Navier-Stokes equations' for an incompressible Newtonian fluid. When balancing momentum, we have to balance the x-, y- and z-momentum separately. The fluid viscosity plays the role of the diffusivity. Books on transport phenomena (e.g. Bird et al., 2002; Slattery, 1999) will give the full flow equations both in Cartesian, cylindrical and spherical coordinates.

8

Dimensional Analysis and Scaling Rules

One might ask, here at the outset, "Why bother with 'scaling rules' when one can simulate practically any size and type cyclone of interest with a good model?" While the latter is generally true, scaling—when based on the performance of a sufficiently large, geometrically similar laboratory model—can predict the performance of an industrial cyclone installation considerably more accurately than the models. It is also the writers' experience that scaling rules are important for two additional reasons:

- Certain simplified scaling rules and dimensionless quantities allow the designer or practitioner to make quick, 'back-of-the-envelope' type calculations and decisions pertaining to cyclone design and performance.
- The scaling formulae allow one to better 'see' the effects of changes in one variable upon another—both qualitatively and quantitatively.

In this chapter we shall derive and present relationships or formulae that will allow us to predict a cyclone's cut-point diameter, grade-efficiency curve, overall or 'gross' efficiency, and pressure drop on the basis of measurements taken on a geometrically similar cyclone. These formulae should also allow us to evaluate the performance of an operating cyclone and, if necessary, assist us in troubleshooting its design, mechanical condition, or mode of operation.

When scaling cyclones we have to consider not only the fluid but also the particle dynamics. This might lead us to expect complicated scaling laws, but in the end we shall find that simple rules can provide a wealth of useful information.

In scaling we wish to predict the performance of one unit, which we will call the 'prototype', from that of another, the 'model'. We do this by identifying all parameters determining the unit's performance. We may not know the effect of each parameter, but we do know that the equations expressing the performance in terms of the parameters must be *dimensionally consistent*. This allows us to reduce the number of parameters by bundling them in dimensionless groups. Making these groups the same between model and pro-

totype, we know that their dimensionless performance will also be the same (Perry, 1997).

To derive the dimensionless groups for cyclones, we can proceed along two lines of inquiry:

a) classical dimensional analysis, or
b) inspection of the equations of motion for gas and particles.

In a) we list the variables influencing the cyclone performance, and arrange them in dimensionless groups. In b) we arrive at the groups by making the equations of motion for the gas and the particles dimensionless. Both lines of enquiry are enlightening in their own way, so we shall follow both, the latter in Appendix 8.A.

8.1 Classical Dimensional Analysis

8.1.1 Separation Efficiency

The separation efficiency in a cyclone depends on a series of physical and operational parameters, which we can subdivide as follows:

- Parameters related to the individual particle
  - the particle size x,
  - the particle density ρ_p. We see in the equation of motion for the particle, Eq. (2.2.1), that both ρ_p itself and the density difference with the gas $(\rho_p - \rho)$ can be included, the former for the unsteady terms, the latter for the steady terms.
  - the particle shape, which we express as Wadell's sphericity ψ, defined as *the surface area of a volume equivalent sphere divided by the surface area of the actual particle.*
- Parameters related to the feed solids as a whole
  - the solids loading at the inlet, c_o.
  - the particle size distribution (PSD) of the feed solids, which can influence the grade-efficiency of the cyclone. In reality, these authors cannot confirm that the PSD influences the cyclone cut-point or grade-efficiency, but it has been claimed in the literature that large particles in the feed will 'sweep' smaller ones to the wall in the inlet region, so we include this parameter initially. If a mathematical distribution function is fitted to the feed, the size distribution can be characterized by a mean size $\langle x \rangle$, and a spread σ.
- Parameters related to the gas
  - the gas density ρ,
  - the gas viscosity μ,
  - a characteristic velocity v_{ch}. In practice, the inlet velocity v_{in} or the mean velocity in the vortex finder v_x are often preferred; some prefer the mean axial velocity in the cyclone body $\langle v_z \rangle$.

  - the gas relative humidity, RH. Components such as water vapour or ammonia can influence particle agglomeration or dispersion and, hence, grade and overall collection efficiency.
- Parameters related to the configuration of the cyclone
  - the cyclone size, which we can represent by the body diameter D,
  - geometry of the cyclone (H, a, b, D_x etc.),
  - roughness of the cyclone wall, k_s.
- Parameters related to conservative force fields
  - the gravitational acceleration g,
  - the Coulomb potential of an electrical field ϕ,
  - parameter giving the strength of other fields present; we assume there are none.

This is a large number of parameters, the full list is:

$$\eta(x) = \mathrm{f}(x, \rho_p, \Delta\rho, \psi, c_o, \langle x \rangle, \sigma, \rho, \mu, v_{ch}, g, RH, \phi, D, H, a, b, D_x, \text{more geometrical parameters}). \tag{8.1.1}$$

In order to render the process more tractable, we must make some simplifications and assumptions:

The simplifications:

- We ignore the effects arising from particle agglomeration, and, therefore, also the effects of the composition (humidity) of the gas.
- As is standard in scaling, we assume that the model and the prototype are geometrically similar. This means that all dimensionless numbers describing the cyclone geometry, for example the ratio of the vortex finder diameter to the body diameter: D_x/D, are the same between model and prototype.
- The particle sphericity ψ mainly enters the analysis because it influences the particle terminal velocity. We can account for its effect if we use the Stokesian diameter as a measure of particle size x rather than, for instance, a volume or mass equivalent diameter. We recall from Chap. 2 that the Stokesian (or "dynamically equivalent") diameter is the diameter of a sphere having the same terminal settling velocity and density as the particle under consideration.

The assumptions:

- The gravitational field represented by g is so small compared to the centrifugal field that its effect can be ignored. We need to qualify this: at higher solids loadings, the motion of the strands formed on the cyclone wall can be influenced by gravitational forces. This influence may or may not be beneficial depending upon cyclone orientation in the gravitational field.

- The particles are always at their terminal velocity (Chap. 2). In this case, ρ_p need not be included explicitly, but only the density difference: $\rho_p - \rho \equiv \Delta\rho$.

These simplifications and assumptions do not significantly limit the range of application of our analysis. We now make some additional assumptions, however, that do limit the range of systems to which our analysis can be applied. The reader confronted with a specific scaling problem should check which, if any, of the assumptions below are warranted for his or her system.

- We assume that no electrostatic field is present. So our analysis is not valid for electrostatically-enhanced cyclone separators.
- We assume that the solid loading is no more than 2–3 g dust per kg feed gas (*i.e.*, mass loading ratio of less than about 0.003 kg solids/kg gas). Then we can ignore the effect of the particles on the gas flow pattern, which is determined mainly by c_o, and, to a much lesser extent, by $\langle x \rangle$ and σ. This limits the range of validity of this analysis in practice to lightly-loaded cyclones and/or to second and third-stage units. Many first-stage or 'rough-cut' cyclones work at elevated solids loadings.
- Finally, we ignore the effect of the wall roughness, k_s. Wall roughness is due not only to the material of construction (e.g. metal, refractory lining) but also to the solids loading. Solids rolling and sliding along the wall give rise to an 'equivalent' wall roughness of their own (see Chaps. 4 and 6). Thus, in this chapter, we shall limit our discussion to cyclones with smooth walls and low solids loadings. Note that *cyclone wall roughness is important in many practical situations.* We look at the effect of wall friction in Chaps. 4, 5, 6 and 9. As a final comment on roughness, it is actually the difference in *relative* roughness between the model and the prototype that we are ignoring here. This relative roughness is defined as the absolute surface roughness k_s divided by the radius of the cyclone body (upper cylindrical section), $D/2$. A large commercial-scale cyclone with some wall deposits or surface erosion, for example, may have a relative roughness no larger than a small, 'smooth walled', laboratory cyclone. If this is the case, then the wall friction and, hence, wall shear stress, imposed on the gas flow is the same in both model and prototype at comparable cyclone Reynolds numbers or in the fully developed turbulent flow regime of the friction factor versus Reynolds number chart (described in Chap. 6). This is exactly analogous to ordinary flow in pipes. Recalling that the Reynolds number is the ratio of inertial to viscous forces, at high Reynolds numbers the flow within a cyclone becomes turbulent because the viscosity of the fluid is unable to dampen out the effects of any local disturbance.

Making all these simplifications, we state that the cyclone's separation efficiency, $\eta(x)$ is:

$$\eta\,(x) = \mathrm{f}(x, \Delta\rho, \rho, \mu, v_{ch}, D), \tag{8.1.2}$$

and by the classical techniques for dimensional analysis, for instance the *Buckingham Pi method* (Perry, 1997), we obtain:

$$\eta(x) = \mathrm{f}\left(\underset{\mathrm{I}}{\frac{\mu}{D\rho\, v_{ch}}}, \underset{\mathrm{II}}{\frac{x}{D}}, \underset{\mathrm{III}}{\frac{\Delta\rho}{\rho}}\right). \tag{8.1.3}$$

Group I is $1/Re$. It is a classical result in fluid mechanics that the Reynolds number Re determines the gas flow pattern.

One thing missing from Eq. (8.1.3) is a dimensionless group that relates directly to the movement or separation of the particles. This can be achieved by introducing the well-known 'Stokes number', Stk. We can create this new dimensionless number by multiplying together powers of the existing numbers as follows:

$$\frac{1}{18} \times \mathrm{III} \times \mathrm{II}^2 \times \mathrm{I}^{-1} = \frac{\Delta\rho\, x^2 v_{ch}}{18\mu D} \equiv Stk. \tag{8.1.4}$$

This new number can replace any one of the numbers from which it was made without loss of information. If we replace group II with Stk, we obtain:

$$\eta(x) = \mathrm{f}\left(Re, Stk, \frac{\Delta\rho}{\rho}\right). \tag{8.1.5}$$

This is as far as classical dimensional analysis can take us. However, in Appendix 8.A we obtain more physical insight by inspecting the equations of motion for the gas and the particles. One important result of this is that the density ratio in (8.1.5) need not appear separately, as the effect of the particle density is accounted for in Stk. This fact allows us to simplify (8.1.5) even further so that it becomes:

$$\eta(x) = \mathrm{f}(Re, Stk). \tag{8.1.6}$$

Often the designer or investigator is interested only in the cut size x_{50}, when applying scaling rules to cyclones. Then $\eta(x)$ in (8.1.6) can be set equal to 0.5 and, denoting the Stokes number corresponding to x_{50} by Stk_{50}, Eq. (8.1.6) gives:

$$Stk_{50} = \mathrm{f}(Re). \tag{8.1.7}$$

8.1.2 Pressure Drop

A similar analysis can be made for the cyclone pressure drop Δp. If we include all the variables influencing Δp we obtain:

$$\Delta p = \mathrm{f}(\langle x\rangle, \sigma, c_o, \rho, \mu, v_{ch}, D, k_s, g, \text{geometrical parameters}). \tag{8.1.8}$$

Here also we assume geometrical similarity and a low solids loading, so that the effect of the geometrical variables, $\langle x\rangle$, σ and c_o can be neglected. We also

neglect k_s. After these simplifications, performing the dimensional analysis gives:

$$\frac{\Delta p}{\rho v_{ch}^2} = \mathrm{f}\left(\frac{\rho v_{ch} D}{\mu}, \frac{gD}{v_{ch}^2}\right). \tag{8.1.9}$$

The group on the left-hand side we recognize as one half of the Euler number, Eu. The groups on the RHS are the Reynolds number Re, and the Froude number Fr, respectively. Thus:

$$Eu = \mathrm{f}(Re, Fr). \tag{8.1.10}$$

Fr describes the influence of gravity on the flow field. This can be dismissed directly, referring to the classical result that there is no effect of gravity in the absence of free fluid surfaces or stratification in the system. Thus:

$$Eu = \mathrm{f}(Re). \tag{8.1.11}$$

We may note that this result is identical to that which we would have obtained had we applied the above analysis to the flow of a fluid through a smooth-walled pipe.

We should reiterate that the dimensional analyses in these sections only apply to cyclones operating at low solid loading, where the effect of the particles on the gas flow can be ignored.

This completes our treatment of dimensional analysis in cyclones. In the following section we look at applying it in practice.

8.2 Scaling Cyclones in Practice

The formal rules for scaling of cyclones have thus provided us with some fairly simple scaling rules. In practice, even further simplification is possible, and we shall discuss this below.

8.2.1 Approximately Constant Stk_{50} over a Wide Range of Re

Equations (8.1.7) and (8.1.11) suggest that if we arrange experiments in a geometrically similar model to have the same Re as the prototype, then Stk_{50} and Eu will be the same as well. From Stk_{50} and Eu we can then calculate the cut size and the pressure drop in the prototype. Thus, although the pressure drop or the cut size for the prototype and the model are different in general, one can use the pressure drop and cut size obtained from model tests to predict these same quantities for the prototype.

Still, there is a practical problem. Due mainly to their difference in the characteristic size (D), it is not always easy to obtain Reynolds number similarity in a laboratory model with an industrial-scale cyclone without operating the model at very high velocities or constructing a very large 'model'. The first example presented in Appendix 8.B is included to help illustrate this point.

To avoid the problem of having to deal with extremely high velocities in the model experiments, it is possible to perform such studies with water as the carrier fluid, rather than a gas.

An additional problem in achieving Reynolds-number similarity is that, when comparing the performance of one industrial cyclone with that of another, obtaining data at the same Re for the two is often not possible.

But is it really necessary to scale-up cyclones on the basis of Re similarity? A redeeming feature is that, in many cases, *Reynolds number similarity is not very critical*. This has long been known, but the issue has only been studied quantitatively recently, by Overcamp and Scarlett (1993), among others. They defined Re and Stk in terms of the inlet velocity. We shall use the symbols Re_{in} and Stk_{in}, respectively. Figure 8.2.1 shows a plot of the square root of Stk_{in50} against Re_{in} for a wide range of cyclones, taken from their paper.

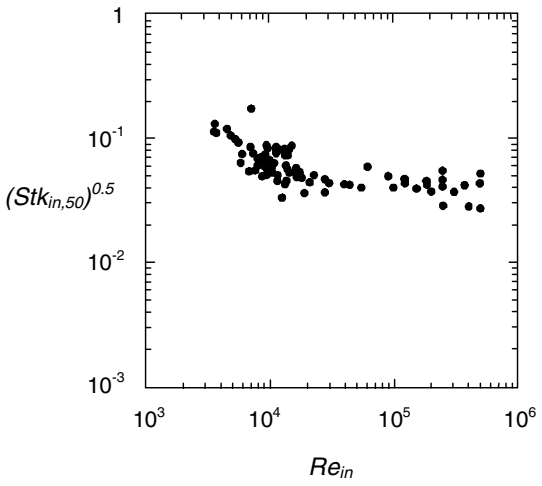

Fig. 8.2.1. Stk_{in50} vs. Re_{in} for a range of cyclones, taken from Overcamp and Scarlett (1993)

Most commercial-sized cyclones operate at Re_{in} values between 10^5 and 10^6. Thus, for the commercially important range of Re_{in} greater than $2{\times}10^4$, Stk_{in50} is seen to be reasonably independent of Re_{in}. This lack of, or weak, dependency of Stk_{50} (or Stk corresponding to some other efficiency) upon Re is the basis for the widely used 'Stokesian scaling' of cyclones. We therefore arrive at the important conclusion that, in Stokesian scaling, the same separation efficiency is assumed for the same value of Stk in geometrically similar cyclones. We can see this more clearly if we examine the equation for the 50% collection efficiency point as computed by means of our equilibrium-orbit model from Chap. 5. Therein, we recall, we performed a simple force balance (centrifugal force in equilibrium with Stokes' drag force) on a particle

orbiting on an imaginary cylinder of diameter D_x. This led to the following expression for the cut size (here we include the gas density via the $\Delta\rho$ term)

$$x_{50} = \sqrt{\frac{9\mu v_{rCS} D_x}{\Delta\rho v_{\theta CS}^2}}, \tag{8.2.1}$$

which can be written as,

$$\frac{x_{50}^2 v_{\theta CS}\Delta\rho}{9\mu D_x} \equiv Stk_{50} = \frac{v_{rCS}}{v_{\theta CS}} \tag{8.2.2}$$

where we here have chosen $2 \times v_{\theta CS}$ as the characteristic velocity v_{ch} in Stk_{50}. Thus, from the equilibrium orbit model point of view, when we apply Stokesian scaling for the computation of x_{50}, this is equialvent to stating that the ratio of radial to tangential velocity,

$$\frac{v_{rCS}}{v_{\theta CS}}$$

at the equilibrium orbit position is the same for both of our geometrically similar cyclones. From our general knowledge of fluid flow in various equipment types, a constant velocity ratio is what we would expect for fully developed, gas phase turbulent flow conditions.

It is interesting to note that the Stokes number that we present above, and which we can readily derive from an elementary force balance on an equilibrium orbiting particle, multiplied by the velocity ratio $\frac{v_{\theta CS}}{v_{rCS}}$ is simply equal to the ratio of drag to inertial forces acting upon the particle.

In a stricter sense, however, Stk is also the ratio of the response or relaxation time of the particle, $\Delta\rho/18\mu$ (see Chap. 2), to a characteristic time scale of the fluid, D/v_{ch}. In addition the Stokes number shown in Eq. (8.2.2) can also be expressed in the form:

$$Stk_{50} = \frac{x_{50}^2 v_{\theta CS}\Delta\rho}{9\mu D_x} = \frac{\frac{x_{50}^2 v_{\theta CS}\Delta\rho}{9\mu}}{D_x} \equiv \frac{d_s}{D_x}, \tag{8.2.3}$$

which is the ratio of the x_{50} particle's "*stopping distance*" to some characteristic cyclone dimension, in this case, the diameter of the vortex finder, D_x. This stopping distance is the distance that particle of size x_{50} would travel against fluid drag if the fluid surrounding the particle was to suddenly stop its motion. Thus when we apply Stokesian scaling, we are also implicity stating that the dimensionaless stopping distance ratio, d_s/D_x, reamins constant between model and prototype. If, for example, we were to increase the size of a cyclone so that D_x increases, in order for the Stokes number to remain constant, the equilbrium particle's stopping distance, d_s, would also have to increase. If we hold $v_{\theta CS}$, $\Delta\rho$ and μ constant and double D_x, then x_{50}^2 would have to double, causing x_{50} to increase by the square root of 2. Thus, scaling-up a cyclone always results in an increase in cut size if the other variables (comprising the

stopping distance) are fixed. It is for this reason, and from this perspective, that one sometimes encounters the statement "cyclones do not scale-up".

For $Re_{in} < 2 \times 10^4$, Stk_{in50} can be seen to increase, showing that small cyclones are less efficient than one would expect from Stokesian scaling. Our defining equation, (8.1.4), for the Stokes number,

$$\frac{\Delta\rho x^2 v_{ch}}{18\mu D} \equiv Stk \tag{8.2.4}$$

shows that an increasing Stk_{50} means an increasing x_{50}.

We can give an idea of the scale where this becomes a consideration. In a cyclone with a tangential inlet of circular cross section working with ambient air at an inlet velocity of 15 m/s, $Re_{in} = 2 \times 10^4$ would correspond to an inlet diameter of 2 cm. The reduced efficiency is therefore only a feature in small sampling cyclones or in very small 'multicyclone' banks. Cyclones in 'small' industrial units comprising multicyclone installations are seldom less than 15 cm in diameter.

We should mention that Lidén and Gudmundsson (1997) found some variation in Stk_{50} with Re, even at larger Re. Their study mostly concentrated on small cyclones, typically a few centimeters in diameter.

Figure 8.2.1 includes data from cyclones of different geometries. Although we can clearly see the trend in the figure, there is considerable scatter. For $Re_{in} > 2 \times 10^4$, $(Stk_{in50})^{0.5}$ varies by a factor of 4, and so does the cut-point diameter. Trying to predict the performance of all cyclones, irrespective of the geometry, from a Stk_{50}-Re plot is therefore not a worthwhile exercise. Even so, the plot does give a 'ball-park' estimate of the Stk_{in50} of cyclones.

Since separation performance, as measured by Stk or Stk_{in50}, is virtually independent of Re it is not necessary to maintain a constant Re between the model and the prototype when attempting cyclone scale-up. In most such laboratory studies, it is far preferable to use air rather than water. This also makes it easier to find a test dust, since many dusts give problems with solubilization or swelling or incomplete particle wetting, among other things, when dispersed in water.

8.2.2 *Eu* Only Weakly Dependent on *Re*

As we found for separation performance described above, Re-similarity is not critical for the pressure drop, either. In Chap. 4 we found that many of the empirical models for cyclone pressure drop only contain the ratio of inlet to outlet areas, implying that Eu will be the same between geometrically similar cyclones, irrespective of Re-similarity. Obviously, as was the case for separation efficiency, this is only valid when Re is high enough that the friction factor is essentially independent of Re. This should come as no real surprise since the same situation holds true for most flow devices (such as pipes, elbows, orifices, contractions and expansions, etc.) that operate in fully developed turbulent flow. In such cases, pressure loss can be characterized by the formula:

$$\Delta p = K\frac{1}{2}\rho v^2 \tag{8.2.5}$$

where K is recognized as the familiar Eu number which we defined earlier. For such devices it is well known that K is very weakly dependent upon Re and can generally be treated as a constant in matters of practical interest.

This principle does have its limitation. The scaling rule of constant Eu and the models in Chap. 4 have, in the authors' experience, significantly overpredicted pressure loss in very large-scale cyclones. There is a weak but definite Re-number effect on the pressure loss coefficient Eu. This variation in Eu is only with Re to the power of -0.17 to -0.2 but, when scaling up small scale lab data by a factor of 10 or more, one can easily overpredict pressure loss by 50% or more.

In most cases, such an error on the conservative side in predicting pressure drop is perfectly acceptable since, if anything, the plant will experience less pressure drop through the cyclone installation and this seldom creates an operational problem. However, if there is some delicate pressure balance across a slide valve, for example, which relies on an accurate knowledge of the cyclone's pressure drop, then one should try to acquire the most accurate estimate possible.

8.2.3 Some other Considerations

The above scaling rules have been found by experience to be valid in cyclones of somewhat conventional designs operating at low solids loadings and normal inlet velocities.

But cut size, grade-efficiency and pressure drop in such conventional designs are not the only items one must consider when designing a cyclone or evaluating its performance. Other factors will often play a crucial role; these may include:

- the design configuration and operating environment at the gas outlet and the solids discharge,
- the position and action of the vortex natural turning point,
- the effectiveness of the underflow seal in preventing gas upflow,
- the effect of solids loading upon overall separation efficiency and pressure loss,
- the effect of wall roughness upon separation performance and pressure loss,
- the effects of physical damage, poor construction, wall deposits, wall flow disturbances and other such nonideal conditions.

Most of these factors are discussed elsewhere in this book. The effects of the natural turning point and solids loading are discussed in Chap. 9.

In geometries where the position of the end of the vortex is known to affect performance (for instance if the cyclone length is near the 'critical length'), one would require Re-similarity between the model and the prototype if one were to have confidence in the scale-up.

8.2.4 *Stk*-*Eu* Relationships

In process engineering work the viewpoint is often taken that an improved quality of separation or purification is achieved at a correspondingly higher cost. Empirical relationships are developed which relate the quality of separation achieved to the cost. Not surprisingly this includes both cyclones and swirl tube separators. The measure of the quality of separation is the cut size, x_{50} or the dimensionless cut size, Stk_{50}, and the 'cost' is the pressure drop required to achieve this, or its dimensionless measure: Eu.

It follows from Eqs. (8.1.7) and (8.1.11):

$$Stk_{50} = \mathrm{f}\,(Eu)\,. \tag{8.2.6}$$

Svarovsky (1984) found that for all 'reasonable' cyclone designs:

$$Eu_b \sqrt{Stk_{b,50}} = \sqrt{12}. \tag{8.2.7}$$

The mean axial velocity in the cyclone body $\langle v_z \rangle$ was used to evaluate the Reynolds and Euler numbers. This is signified with the subscript b. His plot, featuring the line representing Eq. (8.2.7) and his supporting data, is shown in Fig. 8.2.2.

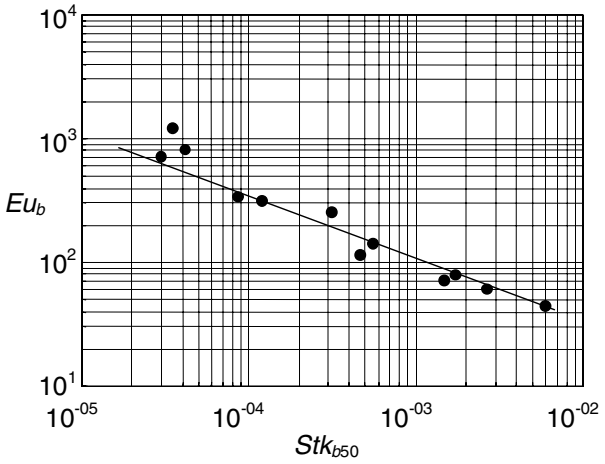

Fig. 8.2.2. Eu_b vs. Stk_{b50} for a variety of cyclones according to Svarovsky (1984). The line represents Eq. (8.2.7)

Others have presented similar correlations. Karpov and Saburov (1998) give:

$$Eu_b \; Stk_{b50} = 0.8, \tag{8.2.8}$$

which lies considerably above the line of Svarovsky, and thus gives a more pessimistic view of cyclone performance.

It is noteworthy that if one makes the reasonable assumption: $H \cong 3D$, then Rietema's criterion $Cy_{50} = 3.5$ (see Chap. 5) can be written $Eu_b Stk_{b50} = 0.92$, which is very close to Eq. (8.2.8). However, as we saw in Chap. 5, Rietema's model predicts the effect of cyclone length correctly, while Eqs. (8.2.7) and (8.2.8) do not.

We should also mention the work of Bürkholz (1989), who, by a variant of dimensional analysis, derived a general separation parameter applicable to various types of separation equipment based on impaction, including cyclones, mist-mats, lamellar fibre filters and packed beds. Bürkholz' derivation begins with a dimensional analysis including, in addition to the variables in Eq. (8.1.2), a height H[1], the gravitational acceleration, g, and *the pressure drop,* Δp. The two former variables are quickly eliminated, while inclusion of the latter is an important aspect of the analysis, and allows Bürkholz to arrive directly at a relationship between Stk_{in50} and Eu_{in}. We note that including Δp in the analysis is not quite *kosher* in terms of dimensional analysis, since Δp is not an independent, but a dependent, variable.

This procedure initially leads Bürkholz to a relation:

$$\eta(x) = f(Stk_{in}, Re_{in}, Eu_{in}) \tag{8.2.9}$$

where the subscript *in* signifies that Bürkholz used v_{in} as a characteristic velocity. Note that Bürkholz' definitions of Eu_{in} and Stk_{in} miss the factors 1/2 and 18, respectively, in the numerators relative to our definitions.

Various further simplifications, partly based on experimental evidence and similar in nature to the simplification that earlier allowed us to eliminate the density ratio $\Delta\rho/\rho$ before, allow Bürkholz to reduce these three dimensionless groups to one:

$$\eta(x) = f(\psi_A), \qquad \psi_A \equiv \frac{1}{4}\frac{\rho_s \Delta p^{\frac{2}{3}} x}{\rho^{\frac{1}{3}}\mu^{\frac{4}{3}}D^{\frac{2}{3}}} = Stk_{in} Re_{in}^{\frac{1}{3}} Eu_{in}^{\frac{2}{3}} \frac{1}{4}\frac{18}{2^{\frac{2}{3}}} \tag{8.2.10}$$

where the last numerical factor on the right-hand-side arises from the different definitions of Stk_{in} and Eu_{in}. Some of the simplifications leading to Eq. (8.2.10) are easy to follow, while the reasoning behind one of them remains obscure, at least to these authors.

Bürkholz found by experiment that in cyclones $\sqrt{\psi_A} \approx 1.7$ for $\eta(x) = 0.5$, i.e. by the cutsize of the cyclone. Substituting this in (8.2.10), and solving for Eu_{in} gives:

$$Eu_{in} = 2\left(\frac{1.7^2}{\frac{1}{4}18 Stk_{in50} Re_{in}^{\frac{1}{3}}}\right)^{\frac{2}{3}}. \tag{8.2.11}$$

which is also a *Stk-Eu* relation.

[1] This is a geometrical variable. Bürkholz' initial derivation relates to a mist mat, and H is its thickness

These authors' experience is that Svarovsky's relation, Fig. 8.2.2 or Eq. (8.2.7) works very well. We have presented the other relations for completeness, and for the reader to recognize them should he or she encounter them in other contexts. It is possible that the difference between the various relations to some extent reflects a difference in the experimental methods on which they are based, namely a difference in the method of measuring the outlet pressure, as discussed in Chap. 4.

The line fitting the experimental results by Svarovsky (see Fig. 8.2.2 or Eq. (8.2.7)) tells us that the Stokes number varies as the reciprocal of the square of the Euler number. Furthermore, since the Stokes number varies as the square of the cut size, x_{50}, and the Euler number varies directly with pressure loss, Δp, it follows that the cut size is inversely proportional to pressure loss. Thus, other factors unchanged, any attempt to decrease the cut size will be accompanied by an increase in pressure loss.

Figure 8.2.2 also serves as a sort of benchmark for comparing cyclone designs or for evaluating the performance of a working cyclone. For example, if we were to gather test data on a lightly loaded cyclone system and plot its Stokes number versus Euler number on Figure 8.2.2, the resulting line *should* lie close to or below Svarovsky's line. If, on the other hand, the point were to lie significantly above his line, this would be a good indication that something is hampering the cyclone's performance. This could include any number of factors: physical damage, poor constuction, wall deposits, wall flow disturbances, blockage, gas upflow and even poor design practice. For cyclones operating in parallel, connected by common plenums, an operating point significantly above Svarovsky's line may indicate problems arising from cross-talk (see Chap. 16).

We may also use Svarovsky's graph or equation to get a rough estimate of the cut size that we could expect at some maximum allowable pressure loss. In this case, we would first compute the Euler number knowing the allowable pressure loss, the gas density and the superficial axial velocity (based on the cyclone's cross sectional area). We would then use Fig. 8.2.2 or Eq. (8.2.7) to compute the corresponding Stokes number and, from this, the cyclone's cut size (knowing the gas properties, cyclone diameter and, again, the superficial axial velocity). Clearly, we could reverse this process and obtain an estimate of pressure loss corresponding to a given cut size.

The relationships derived in this chapter allow us to predict a cyclone's cut-point diameter, grade-efficiency curve, overall or 'gross' efficiency, and pressure drop on the basis of measurements taken on another, geometrically similar, cyclone. They also allow us to assess the performance of an operating cyclone and determine whether or not there is something wrong with its design, or with its physical/mechanical condition, or in the way in which it is operated. We will look at an example in Appendix 8.B.

8.A Inspecting the Equations of Motion

In this appendix we make the equations of motion for gas and particles dimensionless, so that the parameters form dimensionless groups. If these groups are equal for model and prototype, the governing equations are identical in the two.

8.A.1 Equation of Motion for the Gas

The flow pattern of the gas can be determined by solving the Navier-Stokes equations if there is no influence from the particles. If we assume a Newtonian viscosity in Eq. (2.A.2), it becomes:

$$\rho \frac{D\mathbf{v}}{Dt} = -\nabla p - \mu \nabla^2 \mathbf{v} + \rho \mathbf{g}. \tag{8.A.1}$$

Using a characteristic velocity v_{ch}, along with D and ρ as scaling parameters, we get the following dimensionless parameters:

$$\mathbf{v}^* \equiv \frac{\mathbf{v}}{v_{ch}};\ p^* \equiv \frac{(p - p_o)}{\rho v_{ch}^2};\ t^* \equiv \frac{t v_{ch}}{D};\ \nabla^* \equiv D\nabla;\ \nabla^{*2} \equiv D^2\nabla^2;$$
$$\frac{D}{Dt^*} \equiv \frac{D}{v_{ch}} \frac{D}{Dt}.$$

Introducing these in Eq. (8.A.1), we get, after some work (Bird et al., 2002)

$$\frac{D\mathbf{v}^*}{Dt^*} = -\nabla^* p^* + \left(\frac{1}{Re}\right) \nabla^{*2} \mathbf{v}^* + \left(\frac{1}{Fr}\right) \frac{\mathbf{g}}{g}. \tag{8.A.2}$$

The dimensionless velocity and pressure of the gas are thus determined by Re and Fr. As mentioned in the main text, gravity only affects a flow pattern if the system contains free surfaces or stratification layers. Thus, Reynolds number similarity with geometric similarity is enough to ensure dynamic similarity for a gas cyclone with low solids loading.

This is the formal requirement for dynamic similarity, and is consistent with the results of the classical dimensional analysis in the main text. As we mentioned there, experience teaches us that over a wide range of operating conditions Reynolds number similarity is not all that critical for Stokes number similarity between cyclones, and this indicates that, in this range, it is not all that critical for dynamic similarity.

8.A.2 Equation of Motion for a Particle

The Lagrangian equation of motion of a particle rotating at the radial position r in a centrifugal field with circumferential velocity v_θ is (Eq. 2.2.4 resolved in the radial direction)

$$\left(\frac{\pi x^3}{6}\right)\rho_p\frac{dU_r'}{dt} = -3\pi x\mu U_r' + \left(\frac{\pi x^3}{6}\right)\Delta\rho\frac{v_\theta^2}{r} \tag{8.A.3}$$

where we have assumed that the particle is sufficiently small for Stokes drag law to apply. Making this equation dimensionless, using the same scaling parameters as above, v_{ch}, D and ρ, gives:

$$Stk\frac{\rho_p}{\Delta\rho}\frac{dU_r'^*}{dt} = -U_r'^* + Stk\frac{v_\theta^{*2}}{r^*}. \tag{8.A.4}$$

If the motion is steady, the left-hand side is zero. The steady motion of the particle is therefore determined by Stk, and ρ_p does not need to be included explicitly in the analysis, as mentioned in the discussion following Eq. (8.1.4). Also the density ratio $\Delta\rho/\rho$ does not occur in the equations when the added mass and Basset terms are neglected.

Inspection of the equations of motion of the gas and particle phases has thus confirmed the results of classical dimensional analysis, simplified the results of the analysis further, and has, we trust, increased our understanding of the physical significance of the dimensionless groups.

8.B Sample Cyclone Scaling Calculations

8.B.1 Calculating the Inlet Velocity in a Scale Model Required for *Re* Similarity

Determine the velocity at which we would have to operate a 6" (152 mm) diameter model cyclone to obtain Reynolds number similarity to a 48" (1220 mm) industrial cyclone.

Operating Conditions:

Model: $\rho_m = 1.19$ kg/m^3
$D_m = 0.152$ m (ID)
$\mu_m = 1.8\ 10^{-5}$ Pa s
$v_{in,m}$= (to be determined)

Prototype: $\rho = 1.30$ kg/m^3
$D = 1.22$ m
$\mu = 3.710^{-5}$ Pa s
$v_{in} = 22.4$ m/s

Herein, the subscript m refers to the model, no subscript to the prototype.

Solution

Since $Re_{in,m} = Re_{in}$, it follows that,

$$v_{in,m} = \rho v_{in} D \mu_m / (\rho_m D_m \mu)$$

and, upon substitution, we find that,

$$v_{inm} = 82.4\text{m/s!}$$

This is an extremely high velocity and, for an inlet area of 5×10^{-3} m^2 (8 in^2) for the model (corresponding to 0.33 m^2 or 512 in^2 for the prototype), the model cyclone would require 0.42 m^3/s or 15 ft^3/sec of blower capacity (at a considerable pressure loss). Such a flow condition would normally exceed the limits of most laboratory facilities. Additionally, a laboratory-sized cyclone operating at such high inlet velocities would exhibit such a small cut-point diameter that it *could* prove difficult to collect sufficient overhead solids to permit an accurate determination of the cut size and the grade-efficiency curve. Static charge effects created at such high velocities, along with particle agglomeration, could also complicate the analysis.

Although the 1.2 m diameter cyclone used in the preceding example may seem rather large, many industrially important processes utilize cyclones of at least this size. Some are as large as 4 m or 13 feet.

8.B.2 Predicting Full-Scale Cyclone Performance using a Scale Model

A model cyclone of diameter $D = 0.2$ m operating at an inlet velocity $v_{in} = 15$ m/s at ambient conditions on a chalk powder of density 2700 kg/m^3, at low solids loading, is by testing found to have the grade-efficiency curve shown in Fig. 8.B.1. The cyclone pressure drop was found to be 950 Pa.

We wish to predict the performance of a geometrically similar cyclone of diameter $D = 1.5$ m operating with an inlet velocity v_{in} of 20 m/s, separating catalyst particles from a gas consisting of light hydrocarbons at elevated temperature and pressure in an FCC reactor installation.

Solution

We note from the experimental data reported above that the model's cut-point diameter, x_{50}, is 0.98 μm. We do not have data at the same Re for model and prototype, so we will make use of the approximations mentioned in the main text. Re_{in} is large enough in both model and prototype to assume that the grade-efficiency is about the same in the two cyclones for the same value of Stk, and that their Eu values are the same.

We look up the physical properties of gas and particles in the industrial unit. They are summarized together with the relevant geometrical data in Table 8.B.1

We begin by scaling the entire grade-efficiency curve. We calculate Stk corresponding to the particle sizes in the model data. These values of Stk

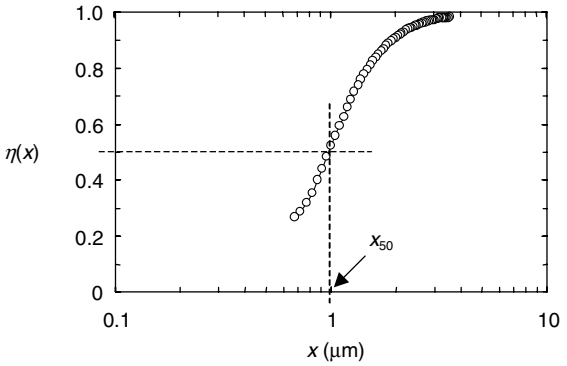

Fig. 8.B.1. Experimental grade-efficiency data for a laboratory model cyclone

Table 8.B.1. Relevant physical and operational data for model and prototype

	Model	Industrial unit
$\Delta\rho$	2700 kg/m^3	1500 kg/m^3
v_{in}	15 m/s	20 m/s
μ	1.8.$\times 10^{-5}$ kg/ms	1.5.$\times 10^{-5}$ kg/ms
ρ	1.2 kg/m^3	1.0 kg/m^3
D	0.2 m	1.5 m
a	0.1 m	0.75 m
b	0.04 m	0.3 m

must correspond to the same efficiencies in the prototype, and we can back-calculate the corresponding particle sizes. Using subscript i as an index for the experimental points on the grade-efficiency curve, the scheme can be written:

$$\text{Given } (x_i, \eta_i)_{\text{model}} \rightarrow \text{ calculate } (Stk_i, \eta_i)_{\text{model}} = (Stk_i, \eta_i)_{\text{prototype}} \rightarrow \text{calculate } (x_i, \eta_i)_{\text{prototype}}.$$

For instance, one of the points on the curve in Fig. 8.B.1 is: (x_i, η_i) = (1.15, 0.637). Since we are assuming approximate dynamic similarity between the model and prototype we can use Stk based on any characteristic velocity, such as v_{in}, which is the velocity we have been given. We then calculate:

$$Stk_{in,i} = \frac{\Delta\rho x_i^2 v_{in}}{18\mu D} = \frac{2700 \times \left(1.15 \times 10^{-6}\right)^2 \times 15}{18 \times (1.8 \times 10^{-5}) \times 0.2} = 8.27 \times 10^{-4}.$$

This is also the value of $Stk_{in,i}$ for the same η_i in the prototype, so we can back-calculate the corresponding value of x_i in the prototype by solving for x_i in:

$$8.27 \times 10^{-4} = \frac{1500 \times x_i^2 \times 20}{18 \times (1.5 \times 10^{-5}) \times 1.5} \text{ giving: } x_i = 3.34 \times 10^{-6}\text{m} = 3.3\ \mu\text{m}.$$

Repeating this for all the points gives the data for the prototype shown by the solid black points in Fig. 8.B.2.

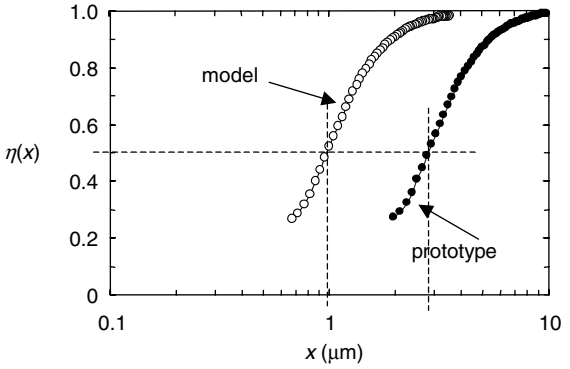

Fig. 8.B.2. G-E data for the model, with the calculated G-E data for the prototype

We can read off the cut size of the prototype in the figure, or we can calculate it directly by setting Stk_{in50} equal in the two cyclones:

$$\left(\frac{\Delta\rho x_{50}^2 v_{in}}{18\mu D}\right)_{\text{model}} = \left(\frac{\Delta\rho x_{50}^2 v_{in}}{18\mu D}\right)_{\text{prototype}},$$

and solve for x_{50} in the prototype. The result is:

$$x_{50} = 2.85 \times 10^{-6}\text{m} = 2.8\mu\text{m}.$$

We see from the figure that we can expect all catalyst particles greater than about 10 μm to be completely captured in the industrial unit. We also see that the grade-efficiency curve for the prototype has the same s-shape form as that of the model on the logarithmic scale.

One may quickly obtain a rough 'back of the envelope' estimate of the overall or gross separation performance of a lightly-loaded cyclone as follows (see also Sect. 3.2.3):

First, we 'fit' the experimental G-E data with a simple step function or stair-step curve, as shown in Fig. 8.B.3, for example. This step function representation of the s-shaped G-E curve has the properties:

$$\eta(x) = 0 \quad \text{for} \quad x < x_{50} \quad \text{and} \quad \eta(x) = 1 \quad \text{for} \quad x > x_{50}.$$

Next, we note the weight percent of the feed particles $> x_{50}$. This is our estimate of the overall or gross collection efficiency. The weight percent $< x_{50}$ comprises the losses.

The authors have found this technique to be quite useful in practice, especially in situations where one is anticipating the effect a change in cut-point

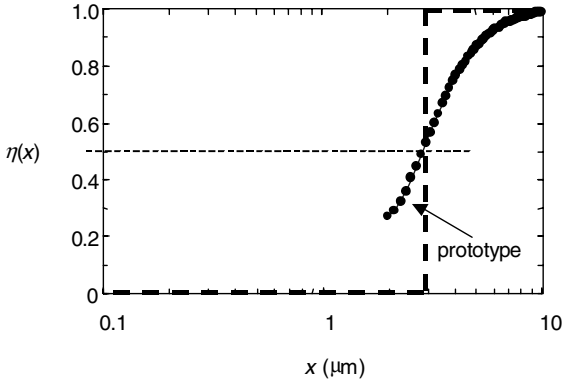

Fig. 8.B.3. Grade-efficiency data for the prototype showing a stair-step type of approximation

diameter may have upon total collection performance, namely, the loss fraction.

When viewed from this 'step function' perspective the cyclone behaves in a manner that is completely analogous to a perfect sieve: all particles entering the 'sieve' (the cyclone) that are greater than the sieve openings (the cyclone cut-point) are retained (captured). Likewise, all particles that enter but are less than the sieve openings (cut-point) pass on though (exit with the overhead gases). Even for the particle that may become 'stuck' in the sieve openings there is an analogy—this is the cyclone's cut size or, as it is sometimes called, its cut-point.

Let us now try to estimate the overall pressure drop in the commercial reactor cyclone. The discussion in the main text of this chapter and in Chap. 4 leads us to expect the Eu number to be the same for the two. In addition, we can calculate Eu on basis of the inlet velocity:

$$(Eu_{in})_{\text{model}} = \left(\frac{\Delta p}{\frac{1}{2}\rho v_{in}^2}\right)_{\text{model}} = \frac{950}{\frac{1}{2}\times 1.2\times 15^2} = 7.03$$
$$= (Eu_{in})_{\text{prototype}} = \frac{(\Delta p)_{\text{prototype}}}{\frac{1}{2}\times 1.0\times 20^2}\,.$$

Solving for the pressure drop over the industrial prototype, we obtain a value of 1400 Pa. We note that, even though the gas density was lower in the commercial unit, the overall pressure drop for the commercial unit increased, relative to the model, due the increase in inlet velocity.

It should also be pointed out that the Eu number of the commercial cyclone is essentially constant and independent of variations in any of the variables comprising this dimensionless number, such as gas density or inlet velocity. Thus, if we were to know its pressure drop for any operating condition then, knowing also the gas density and its inlet velocity, we could quite easily

compute its Euler number. From this, we could then compute its pressure drop at any gas density and/or inlet velocity of interest. In the above example, if the inlet velocity were to be increased to 30 m/sec, the pressure drop would increase to $(30/20)^2 \times 1410 = 3170$ Pa. Such simple scaling methods can be of very practical value to the plant or support engineer.

We will leave it to the reader to locate the point corresponding to Stk and Eu on the plot of Svarovsky, to see how well this cyclone works. Remember to change the scale velocity from v_{in} to $\langle v_z \rangle$. You will find the necessary information for this in Table 8.B.1.

9

Other Factors Influencing Performance

In this chapter we will look at two special factors that strongly influence cyclone performance. These are solids loading and the 'natural turning length', both of which affect cyclone separation performance, wear and pressure drop, especially in cyclones with a tangential inlet. The natural turning length may also correlate with clogging.

9.1 The Effect of Solids Loading

Contrary to what one might expect intuitively, cyclone performance improves with increasing solids loading up to quite high loadings: the overall efficiency increases, and the pressure drop decreases with increasing solids loading.

9.1.1 Effect on Separation Efficiency of Cyclones

Cyclone designers have long known that the separation efficiency of tangential inlet cyclones improves with increasing solids loading. Even so, the exact mechanism for this improvement is still not established beyond doubt, in spite of many investigations of the topic.

Figure 9.1.1 shows the overall efficiency as a function of loading for a cyclone with a tangential inlet. The overall efficiency can be seen to increase substantially with increasing solids loading. It increases so much that, at a moderate solids loading of 40 g solids per m^3 of air, the fractional emission from the cyclone is only about one third of what it is at low loading. Thus, the fraction, or percentage, of incoming solids that is lost decreases with increasing solids loading even though the *absolute* magnitude of the losses still increases[1]. This is clearly an effect to be aware of, since problems can arise with a plant cyclone design based on testing in a model at an unknown (high) solids loading.

[1] For 15 m/s in Fig. 9.1.1, the absolute emission at a loading of 44 g/m^3 is 15 times that at 1 g/m^3.

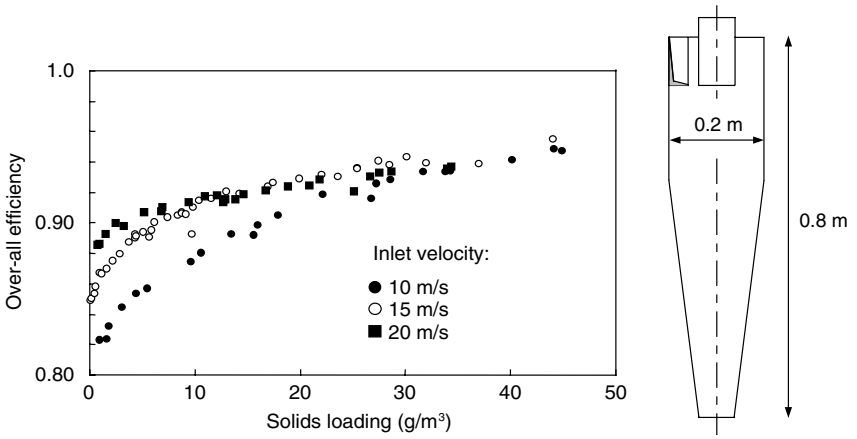

Fig. 9.1.1. Overall efficiency of a cyclone acting on a chalk powder with a median particle diameter of 3.7 μm as a function of solids loading (Hoffmann et al., 1991). Dimensions of the cyclone: $D = 0.2$ m; $D_x = 0.075$ m; $S = 0.1$; $a = 0.1$; $b = 0.04$; $H_c = 0.5$ m; $H = 0.8$ m; $D_d = 0.075$. Scale drawing of the cyclone also shown.

Figure 9.1.2a and b show grade-efficiency data and size distributions of the overhead fraction corresponding to some of the points shown in Fig. 9.1.1. Three features in Fig. 9.1.2 are noteworthy:

- Moving in the direction of decreasing particle size, the efficiency decreases, goes through a minimum, and again increases for the very small particles
- the increase in solids loading pushes the grade-efficiency curve upwards as a whole, and
- the size distribution of the overhead solids remains essentially unchanged with solids loading, despite the dramatic increase in separation efficiency.

The two latter features are consistent with the following picture of the effect of solids loading on efficiency: an 'extra' amount of solids ('extra' compared to what would normally be separated in the cyclone body in accordance with the cyclone grade-efficiency curve) separates or 'salts out' more or less unclassified in the cyclone inlet region, i.e. that for each size class about the same weight or volume fraction separates out in the inlet. The remaining solids continue to the 'inner' vortex, where they are classified roughly the same as they would be at low loading. We say "roughly the same" since the extra solids on the wall at high loading will attenuate the vortex somewhat.

We will be returning briefly to the topic of solids loading in swirl tube separators later. Here, we wish to note that a difference exists between the behavior of cyclones with tangential inlets and swirl tubes equipped with inlet vane assemblies, so that the results shown in these figures cannot be applied to swirl tubes.

9.1.2 Models for the Effect on Separation Efficiency of Cyclones

The reason for the effect of loading on separation efficiency is not established beyond doubt, but the data and observations in the previous section can help us evaluate the merits of the explanations forwarded in the literature. A number of mechanisms and models have been proposed.

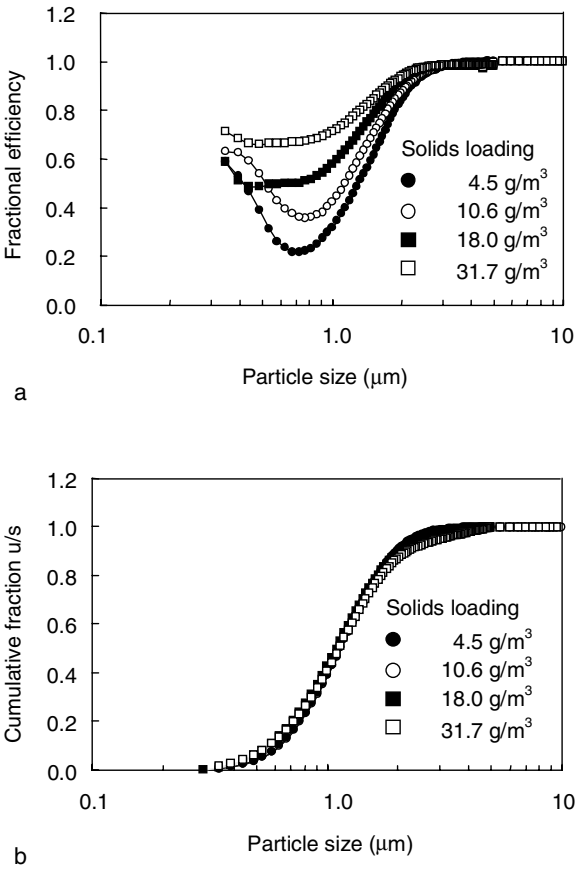

Fig. 9.1.2. a, b Grade-efficiency and overhead size distributions for some of the experiments in Fig. 9.1.1. Inlet velocity: 10 m/s. The size distributions of the feed and overhead fractions were measured by an optical disc centrifuge using a line-start technique

One explanation for the effect is the critical loading concept of Muschelknautz. We refer to our discussion of the Muschelknautz method in Chap. 6, and give here only a brief outline of the hypothesis. This concept sprang from a model for horizontal pneumatic conveying of powders. The idea is that the

turbulence in the carrier gas can support only so much powder (the 'critical load') in a horizontal conveying tube against the force of gravity. The excess powder beyond this critical load will settle out of the gas stream to the bottom of the tube spontaneously and, according to the early work of Muschelknautz, essentially unclassified (see below and Chap. 6 for more discussion of the issue of classification in the inlet region). The extension of this notion to cyclones is straight-forward: the solid-laden inlet jet is considered as a sort of conveying tube, and the centrifugal force is substituted for the gravitational force.

In his earlier papers, Muschelknautz arrived at the following expression for the critical load or 'limit load' in terms of kg dust (that the gas could keep in turbulent suspension) per kg of gas:

$$c_{oL} = \frac{f D_m \mu}{2\,(1 - D_x/D)\,\rho_p x_{med}^2 v_{\theta m}} \tag{9.1.1}$$

where $D_m = (D D_x)^{1/2}$ and $v_{\theta m} = (v_{\theta w} v_{\theta x})^{1/2}$, and x_{med} is the median size of the inlet dust. An example of how to use this equation is included in Appendix 9.A. Another, more recently developed expression for the critical load is given in Eqs. (6.4.1) and (6.4.2). The expression in Chap. 6 is of a different type, and is not based on a direct analogy with pneumatic conveying in a gravitational field.

As mentioned, the upwards shifting and flattening of the grade-efficiency curve with increasing solids loading seen by Hoffmann et al. (1992), and also exhibited by the data in Fig. 9.1.2 strongly supports the idea that the 'extra' material separating out in the inlet due to the solids-loading effect is essentially unclassified. However, in the more recent work, Muschelknautz and Trefz introduced the notion of a cut size in the inlet region of a highly-loaded cyclone in addition to the cut size in the inner vortex. This was discussed in detail in Chap. 6. We note that the observed change in shape of the grade-efficiency curve with loading is not consistent with the notion of a sharp 'cut' in the inlet region.

The upward shifting and flattening of the curve may, however, be consistent with a *certain* classification in the inlet. Greif (1997) found that at high loadings the large particles are completely removed in the inlet region, while the smaller particles are separated in the inlet with a high (but < 1), almost uniform, efficiency (see Fig. 6.B.2). Greif looked at this as a very shallow 'cut' in the inlet, meaning that the 's-shaped' GEC is rather 'flat' and reflects an efficiency which is significantly greater than zero for all particle sizes. In this way Greif could reconcile the change in shape of his grade-efficiency curves as a function of increased loading (Greif found much the same solids loading effect as Hoffmann et al. (1992)) with the observation of his predecessors that the material continuing to the inner vortex at high loadings is finer than the feed.

As an alternative to the critical loading concept, Mothes and Löffler (1984) put forward the idea that the improvement of cyclone efficiency with solids

loading is due to particle agglomeration. They proposed a model for particle agglomeration, based on calculating

- the impaction probability and
- the sticking probability

of a small particle moving toward a large one. As the size of the small particle increases, the impaction probability increases while the sticking probability decreases. They found that the product of the two probabilities, which gives the probability that the small particle will actually agglomerate with the larger 'cleaning' particle, is a maximum for a particle size of about 2 μm, if the large particle is 15 μm. In this concept the larger particles are thus held to 'sweep up' smaller particles as the large particles move to the wall in the cyclone inlet region. According to the Mothes and Löffler model the separation of small particles due to solids loading should therefore increase with the concentration of larger 'cleaning' particles. We refer the reader to their paper for further information.

Empirical relations without any mechanistic explanation have also been proposed. Smolik, as quoted by Svarovsky (1981), proposed:

$$\eta\left(c_2\right) = 1 - \left(1 - \eta\left(c_1\right)\right)\left(\frac{c_1}{c_2}\right)^{0.18} \tag{9.1.2}$$

where c_1 and c_2 denote two different solids loadings in the inlet stream expressed in any concentration unit. $\eta(c_i)$ is the corresponding overall, fractional efficiency.

Another purely empirical model was proposed by Zenz. This is a graphical method. The chart of Zenz, which is based on years of practical experience, is shown in Fig. 9.1.3.

Both the models of Smolik and Zenz predict cyclone separation efficiency as a function of loading purely from knowledge of the efficiency at low loading and the loading itself. Physical and operational factors, such as cyclone geometry and size, solids size distribution and density, inlet velocity and other operating conditions, are not included in these models, and the effect of these parameters is thus not thought to be of primary importance. In the Muschelknautz model, on the other hand, the inlet velocity, the cyclone dimensions, and the mean size and density of the inlet solids all feature.

When trying to weigh up the relative merits of the mechanistic explanations for the effect of loading on cyclone separation, we observe that the results in Figs. 9.1.1 and 9.1.2 are consistent with the notion of the extra material being largely unclassified, and they are in this sense more consistent with the Muschelknautz concept than the concept of Mothes and Löffler. However, the Muschelknautz concept, as given in Eq. (9.1.1), leads us to expect a range of low loadings—under the 'critical load'—where there is no effect of solids loading on the fractional separation. We, nonetheless, do not see such a range in Fig. 9.1.1, the effect of solids loading starts from zero loading, as the models of

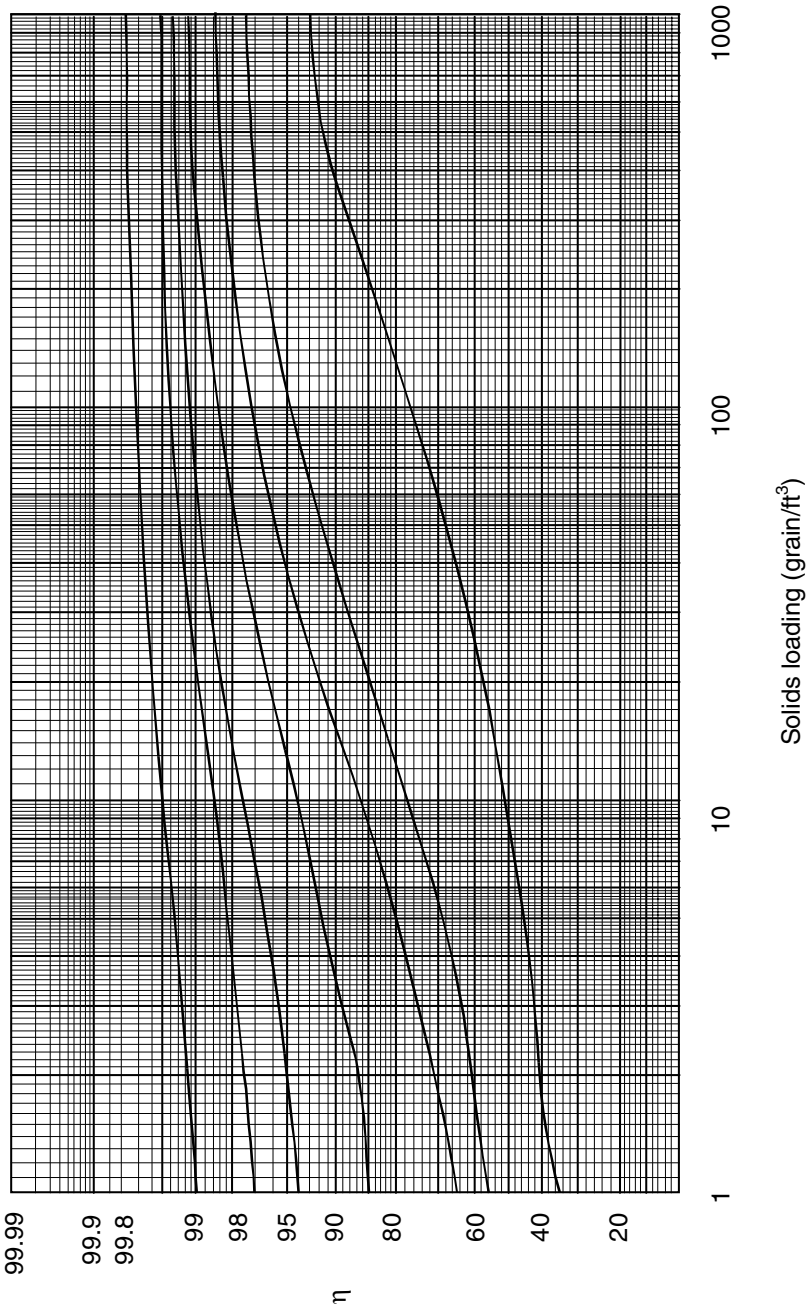

Fig. 9.1.3. The graphical model of Zenz for estimating the effect of solids loading on cyclone separation efficiency. 1 grain/ft^3 = 2.29 g/m^3

Smolik and Zenz also predict (see also Appendix 9.A). In the later revisions of his theory, on which revisions Chap. 6 is based, Muschelknautz has overcome this problem, and calculations based on the equations in that chapter show an effect of solids loading at virtually all loadings, more consistent with the experimental evidence. On the other hand he has there introduced the inlet cut diameter which, as we mentioned above, is not easily reconciled with the experimental evidence.

Parenthetically, we mention that if the solids that drop out in the inlet are unclassified, we can estimate the grade-efficiency curve of a cyclone working at high loading from one working at low loading. If a fraction η_{sl} is removed unclassified in the inlet, and the rest goes through to the inner separation space, where it is classified according to the grade-efficiency $\eta_i(x)$, then the grade-efficiency curve at high loading becomes:

$$\eta\left(x,c\right)=1-\left(1-\eta_{sl}\right)\left(1-\eta_i\left(x\right)\right). \tag{9.1.3}$$

When we consider the merits of the agglomeration hypothesis in light of the experimental evidence, solids loading test results do not show a clear preference for a particular particle size in the extra material that is separated on account of the loading effect, although we would expect such a preference. In addition, a rough calculation shows that the volume 'swept' by the large particles on their way to the wall just after the tangential inlet is much too little to explain the magnitude of the effect seen in practice. Nevertheless, the theory that agglomeration is responsible for the effect of solids loading on cyclone efficiency still has its followers.

One could try to resolve the second problem mentioned above and explain the magnitude of the effect of loading on efficiency by taking into account also agglomeration in the upstream tubing leading to the cyclone, in addition to the agglomeration in the inlet region of the cyclone itself. However, it then emerges as curious that the effect of solids loading is so consistent between different industrial and laboratory installations, which presumably comprise very dissimilar piping arrangements upstream of the cyclone. High humidity levels may reduce repulsion forces among particles that are electrically charged, and may enhance the cohesion forces between particles in contact. If so, high humidity levels with some types of dust could cause the smaller particles to form agglomerates and, hence, separate as though they were much larger particles. Various cyclone vendors state that humidity affects cyclone collection performance although the writers are not aware of any published data quantifying the effect. We are aware of one cyclone vendor, however, that uses a proprietary method that specifically accounts for the effect of humidity when predicting cyclone collection performance.

At this point, the reader may be wondering what to conclude regarding the mechanism for the entrance solids-loading effect. It is our judgment that the solids-loading effect is due to a reduction in the drag force that the individual solids experience upon entering the cyclone. Our own interpretation of the

features of Fig. 9.1.2 is as follows: the data in the figure exhibit three somewhat independent effects:

1. Below about 0.6 to 0.7 microns, we see the probable effects of particle agglomeration. We believe that these very fine particles entered the cyclone as agglomerates and this is why they were collected with such high efficiency. The smallest particles had the greatest ability to stay bound in agglomerates, since for them the surface forces tending to bind them were stronger compared with the intertial forces tending to break them free. Thus they may either have agglomerated in the inlet piping, or failed to have been dispersed in the particle dispersion system. For example, the 0.3 μm particles incorporated in agglomerates behaved, from an aerodynamic point of view, as though they were larger particles in their passage through the cyclone. This 'fines agglomeration effect', as expected, occurred at all incoming solids loadings.
2. Superimposed on the above effect is the expected sharp increase in efficiency with increasing particle size. This effect becomes most apparent in the data shown in Fig. 9.1.2 a for particle sizes above about 0.6 to 0.7 μm.
3. Upon comparing the GEC at 4.5 g/m^3 loading with that for the 31.7 g/m^3 loading, it is very clear that the efficiency of all particle sizes increases with increases in loading. The intermediate loading data points, or GECs, lie between the 4.7 and 31.7 g/m^3 loadings, as expected.

We are interested in the effect mentioned under item 3 above, and it seems likely that this is due to some effect of the solids on the two-phase flow pattern in the inlet region of the cyclone. Aside from the energy considerations which lead to the Muschelknautz' solids-loading or 'critical loading' concept, one can understand the basic mechanism by keeping in mind that, as the concentration of particles increases, they shield one another from the drag that they would have experienced as individual particles. The individual particles thus move as an ensemble, and behave as though they were much larger 'particles', thus making them relatively easy to separate within the entry section of the the cyclone. As a simple example, one may find that it is difficult to throw a few grains of ordinary flour particles very far across a room. Drag rapidly decelerates them and decreases their forward momentum. However, if one grabs a handful of flour (a concentrated ensemble), one can easily toss the particles a meter or more from the point of release, since nearby particles shield their neighbors from the full impact of the air's drag force. The same principle applies to racecars and even to birds in flight, which take advantage of the shielding provided by the lead car, or lead bird, by 'drafting' behind it. Developing an accurate, quantitative model of this phenomenon may not be a simple task but the concept is relatively easy to understand.

We mention that Hoffmann et al. (1991) found that all their results for the separation efficiency as a function of solids loading could be perfectly fitted with the expression:

$$\eta\left(c_o\right) = \frac{k_1 c_o^{k_2} + \eta_0}{k_1 c_o^{k_2} + 1}. \tag{9.1.4}$$

This reasonably simple expression may form a good basis for an empirical model, if the constants k_1 and k_2 can be related to the relevant parameters. η_0 is the efficiency at very low loading.

Figure 9.1.4 shows photos from Trefz (1992) of a cyclone with a tangential inlet, working with low and high loadings. The photos give an interesting insight into the flow in the inlet region of the cyclone. Unfortunately, the inlet jet cannot be distinguished in the left picture with the low loading to determine whether its shape is different from that in the right picture with the high loading.

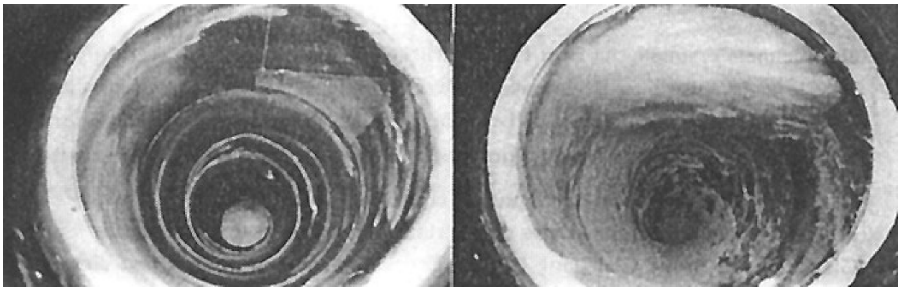

Fig. 9.1.4. Photographs of a cyclone with a tangential inlet (top right in the photos) working with a low solids loading (left) and a high loading (right). At the low loading, the solids dispersed in the inlet gas are not visible, only the characteristic strands on the wall are seen. At the high loading, the solids in the inlet gas are visible, and are seen to move directly to the wall

9.1.3 Effect on the Separation Efficiency of Swirl Tubes

Much less experimental data are available on the effect of solids loading on the separation efficiency of swirl tubes with swirl vanes. If the effect of solids loading is indeed one taking place in the inlet region of tangential inlet cyclones, we might expect it to be quite different in devices with swirl vanes.

This turns out to be so. Experimental data obtained in the laboratories of the writers show a clear difference between the effect of loading in the two types of device. The evidence is scant, however, and will not be reported at this stage.

There are no models in the open literature for computing the effect of solids loading on swirl tube efficiency. The best approach for doing this in the first instance may be to fit the exponent a in a relationship of the Smolik type:

$$\eta\left(c_2\right) = 1 - \left(1 - \eta\left(c_1\right)\right)\left(\frac{c_1}{c_2}\right)^a, \tag{9.1.5}$$

or to fit k_1 and k_2 in Eq. (9.1.4) to results from testing by expressing a in terms of the relevant operational and physical parameters.

9.1.4 Effect on the Pressure Drop of Cyclones

While there are several schools of thought regarding the exact mechanism behind the effect of solids loading on separation efficiency, the effect of loading on cyclone pressure drop is somewhat less contentious.

Figure 9.1.5 shows experimental results for the effect of solids loading on pressure drop for the cyclone described in Fig. 9.1.1.

It was shown in Chap. 4 that one effect of wall friction was to decrease the swirl intensity in the cyclone body, and that this in turn had the effect of lowering the cyclone pressure drop. It was also shown that only the pressure drop models based on a moment-of-momentum balance, and therefore taking into account the effect of wall friction, could account for the change of pressure drop with cyclone length and/or an increase in cyclone surface area. Wall friction increases not only with the cyclone surface area and the roughness of the wall material itself, however, but also with the solids loading. The attenuating effect such friction has on the inner core spin velocity is the reason why the pressure drop across cyclones decreases with increased solids loading.

As shown in Chap. 4, the Barth-Muschelknautz approach takes into account the effect of wall friction through a wall friction factor, f, which depends on the physical roughness of the (usually metal) walls, as well as the additional, 'effective' wall roughness created by the solids spiraling down the walls. The procedure for using the Barth-Muschelknautz model to predict the effect of solids loading on pressure drop is as follows: calculate $v_{\theta CS}$ from Eq. (4.2.6), using Eqs. (4.2.4) and (4.2.5), find the friction factor from Eq. (4.2.9), and then use Eq. (4.3.4) to calculate the pressure drop.

Smolik proposed an empirical model for the effect of loading on cyclone pressure drop, in addition to his above-mentioned model for the effect of solids loading on efficiency (see Svarovsky, 1981):

$$\frac{\Delta p\,(c)}{\Delta p_0} = (1 - \alpha \cdot c^{\beta}) \tag{9.1.6}$$

where Δp_0 is the pressure drop for zero load. In this equation the constants α and β are dimensional and take on the values 0.02 and 0.6, respectively, if the units[2] of the solids loading c are g/m^3.

[2] Solids loading in this book and in the literature is often expressed in terms of mass of dust per volume of gas, such as g/m^3 or grain/ft^3. While this is intuitively appealing in text and graphics, it is not optimal in mathematical expressions, where the loading may occur in exponents or as arguments of logarithms and/or together with empirical constants, such as in Eq. (9.1.6). In mathematical expressions the loading can best be expressed as a dimensionless ratio, for instance as a mass fraction. In SI units this may be done by expressing the loading in kg dust per kg of gas, denoted by c_o in this book.

Worked examples for using these two models to predict the effect of loading on pressure drop are given in Appendix 9.B, where the predictions of the models are also compared with the experimental results in Fig. 9.1.5.

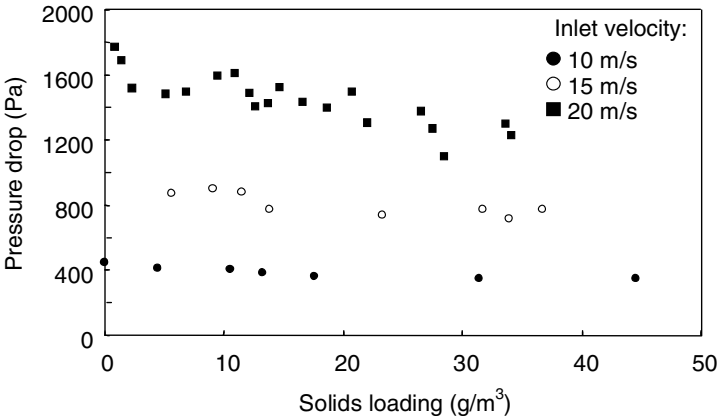

Fig. 9.1.5. The influence of solids loading on the pressure drop at three different inlet velocities over the cyclone reported in Fig. 9.1.1

In a series of recent papers, Gil and co-workers (Gil et al., 2001; Gil, Romeo and Cortés, 2002; Gil, Cortés, Romeo and Vellila, 2002) investigated the working of a pressurized fluidized combustion cyclone equipped with provisions for pneumatic extraction of solids from a dipleg under the cyclone. Among other things, they investigated the effect of solids loading on the cyclone separation efficiency and pressure drop (Gil, Romeo and Cortés, 2002). Their solids loading varied from 0.03 to 0.230 kg solid per kg of air, the inlet velocity, v_{in} was 14 m/s, and the operating pressure was 2.2 bar.

Gil et al. compared a number of relations for predicting the effect of solids loading on cyclone efficiency and pressure drop. For the efficiency they found that the model of Muschelknautz (MM, see Chap. 6) predicted the effect exceptionally well.

For the pressure drop they compared not only the models of Smolik and Muschelknautz with their experimental results, but also the empirical models of Briggs (1946):

$$\frac{\Delta p(c)}{\Delta p_0} = \frac{1}{1 + 0.0086c^{0.5}} \tag{9.1.7}$$

and of Baskakov et al. (1990):

$$\frac{\Delta p(c_o)}{\Delta p_0} = \frac{1}{1 + 3.1c_o^{0.7}} + 0.67c_o. \tag{9.1.8}$$

The model equation of Briggs is in terms of c, the solids concentration in g/m^3, while the model of Baskakov et al. is in terms of c_o, the solids concentration expressed as a mass fraction. The latter is, as mentioned, better.

They found that the Muschelknautz model described their results for pressure drop exceedingly well. In Appendix 9.B we replot their results and compare them with the three empirical models for the effect of solids loading on pressure drop given above.

The improvement (i.e. decrease) in pressure drop with increasing solids load does not continue indefinitely: Zenz (2001), quoting Dry et al. (1993), shows that at a solids charge of about 7 kg/s m^2, which for an inlet velocity of 15 m/s of ambient air translates to about 0.5 kg solids per kg air, the pressure drop reaches a minimum of about 0.4 of its value at low loading, but then rises with any further increase in solids loading.

9.1.5 Effect on the Pressure Drop Across Swirl Tubes

The effect of solids loading in swirl tubes is quite different from that in tangential inlet cyclones, although the reason for this is not immediately evident: one might expect that the solids would affect both types of separators in the same manner. Nevertheless, limited data available indicate that the effect of solids loading on pressure drop—although qualitatively the same—is less pronounced in swirl tubes than in conventional, slotted entry cyclones, at least in the range of relatively low loadings.

9.1.6 Computing the Performance of a Cyclone with High Loading

We wish to conclude this discussion on the entrance solids-loading effect by simply stating that the effects of solids loading cannot be ignored if performance is to be accurately predicted. This applies not only to cyclone simulation models, but also to the use of the scaling laws developed in Chap. 8.

There are two possible strategies for predicting the performance of a cyclone at elevated solids loading. One is to:

- first predict the performance of the device at low loading either by using a model for low solids loading, such as Barth or Mothes and Löffler for the efficiency, and Shepherd and Lapple for the pressure drop (Chaps. 4 and 5) or by using the scaling criteria in Chap. 8) with results of laboratory testing or plant data, and
- subsequently account for the effect of solids loading using perhaps the methods of Smolik or Zenz.

The other is to use a comprehensive model that accounts for the effect of solids loading directly, such as the Muschelknautz model given in Chap. 6.

If one uses test data taken on a model cyclone to help predict the performance of a full-sized unit, it is important not to use a higher solids loading in the model than that, which the full-sized unit is expected to experience. It is best to test the model over a range of known solids loadings.

9.2 The Effect of the Natural Vortex Length

In addition to the effect of solids loading, another effect that the cyclone designer ignores at his or her peril is the natural turning length of the vortex.

Most of the models developed in Chaps. 4 and 5 predict that longer cyclones perform better, at least that the optimal length is considerably longer than the lengths of most commercially available cyclones. See also the discussion of this issue in Sect. 5.3.2. However, since the inception of the cyclone it has been known that the cyclone or swirl tube cannot be made arbitrarily long. If it is too long, the vortex will spontaneously 'end' at some point within the body of the separator. The point at which this occurs is called the 'natural turning point', or the 'end' or 'tip' or 'tail end' of the vortex, and the distance from the entrance of the vortex finder to the end of the vortex is called the 'natural vortex length'. The pioneering work in this field was done by Alexander (1949).

Below, we will look at the nature of the turning point, and consider why and how the cyclone designer should account for its behavior.

9.2.1 The Nature of the Vortex End

If, in a transparent cyclone, there is some mobile dust or liquid on the cyclone wall, the end of the vortex can clearly be seen as a ring. Until now, it has not been possible to ascertain the exact nature of the vortex end. Two possible explanations circulate in the literature and among cyclone experts.

One is that the end of the vortex is an axisymmetric phenomenon, that the end represents a sort of recirculating 'gas bubble'. Such a vortex end is observed in the research field of vortex breakdown in 'vortex tubes', tubes in which a flowing liquid is caused to swirl with swirl vanes. A difference between a vortex tube and a cyclone or swirl tube is that the flow reverses in the latter, while in the vortex tube it continues past the vortex end, and discharges from the bottom of the tube. Another difference is that this type of experiment is usually (but not always, see Sarpkaya, 1995) performed under laminar flow conditions, while the flow in a cyclone is turbulent.

Another explanation is that the end of the vortex attaches to the side wall (i.e. the vortex core bends), and turns around or 'precesses' around the wall at a high rate; see Fig. 9.2.1. Such a phenomenon, known as 'vortex precession' can be observed, perhaps most easily, in liquid cyclones, where the core can be visualized with air bubbles; see Fig. 9.2.2.

The second type of phenomenon has been demonstrated to exist at least under some conditions in the laboratories of the authors. Under proper dust and lighting conditions, it was possible to 'freeze' the motion of the precessing vortex with a stroboscope and see the vortex core bend and attach to the wall. By adjusting the strobe's frequency so that it is slightly faster or slower than the precessing vortex 'tail', the vortex end could be made to give the illusion of rotating backwards or forwards. If the vortex is 'frozen' on the wall in such

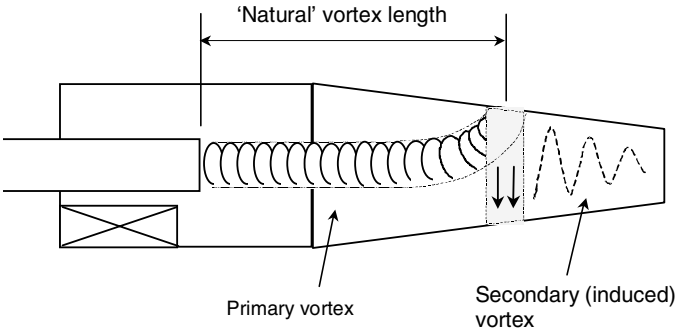

Fig. 9.2.1. Illustration of the natural vortex length

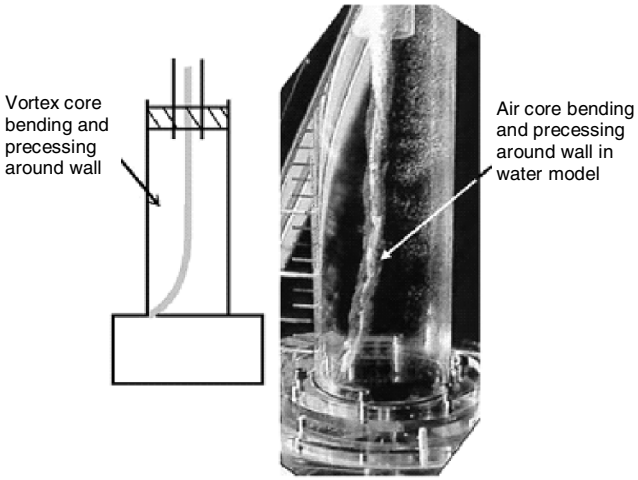

Fig. 9.2.2. Water model exibiting vortex core precession

a manner, one can even observe a rotating 'eye' attached to the inner wall of the cyclone. See Fig 9.2.3. See also our discussion of cyclone erosion in Chap. 12.

Although the vortex may attach to, and precess around, the lower walls of the cyclone as in Fig. 9.2.1, vortex motion does not completely cease in the axial direction at this point or, more correctly, plane of attachment. This 'primary' vortex induces a 'secondary' vortex just downstream of it. This is a type of fluid 'coupling'. The induction of the secondary vortex is probably related to the precession of the primary vortex. This precession is always in the same rotational sense as the swirl in the bulk of the vortex, as sketched in Fig. 9.2.1.

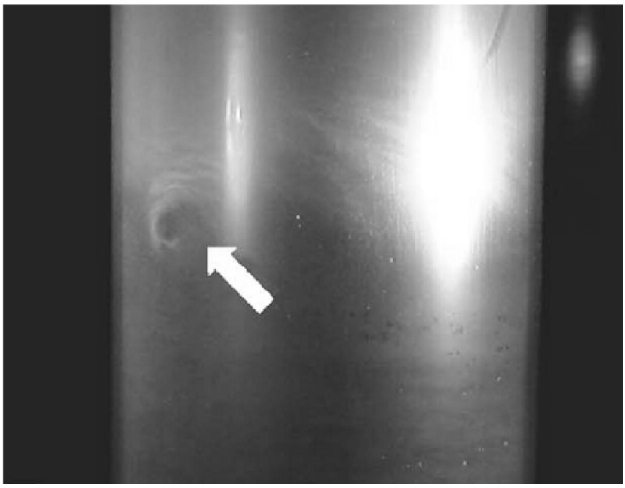

Fig. 9.2.3. A stroboscopic image of the "eye" of the vortex core precessing along the cyclone wall

The following sections will show that the vortex end significantly influences the behavior of cyclones and swirl tubes. Its nature, and the factors governing its position, should therefore be well understood by anyone who designs such cyclonic type separators, and this topic should be given high priority in cyclone research at this time.

9.2.2 Asymmetric Wall Velocity Resulting from Precession of the Vortex Core

If we perform a simplified analysis of the gas velocity near the wall in a cyclone operating with the vortex end precessing around the wall, an interesting result emerges with respect to the near-wall velocities. The illustration below attempts to show the vortex end precessing around the entire inner wall of a cyclone while, at the same time, displaying a snapshot of its characteristic rotational "imprint" ("eye" of the hurricane) at any given point in time.

We notice first that the end of the vortex is precessing around the inner wall of the separator at some precessional frequency f and precessional velocity vector $\mathbf{v}_p$. For the case illustrated, this motion is counterclockwise (ccw) as viewed from above. However, superimposed on this motion is the vortex core spin or rotational velocity vector, $\mathbf{v}_{CS}$. This core spin velocity adds to the precessional velocity $\mathbf{v}_p$ at its top-most position (position A in illustration) producing the resultant velocity $\mathbf{v}_A$. On the other hand, the core spin vector opposes the precessional velocity at the bottom-most position (position B).

Thus, at positions A or B, the net or resultant velocity is:

$$\mathbf{v} = \mathbf{v}_p + \mathbf{v}_{CS}$$

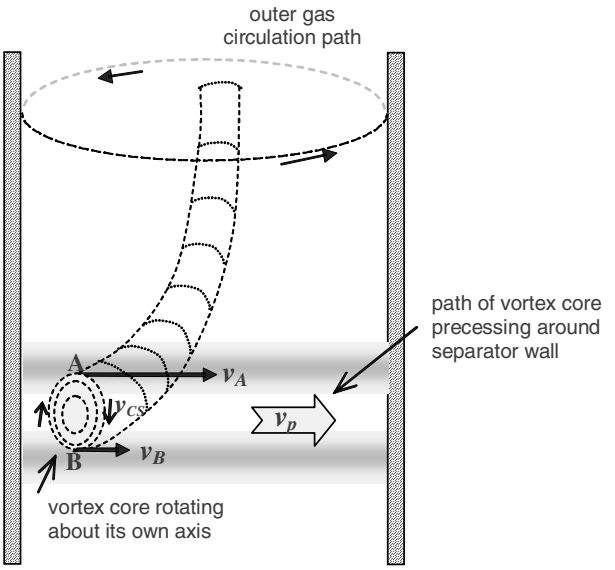

Fig. 9.2.4. Vortex end in contact with, and precessing around, inner wall

Example calculation

Let us now substitute some values for the purpose of computing **v** at positions A and B.

For a 200 mm diameter laboratory cyclone operating at a gas flow rate of 200 m^3/hr, and an inlet velocity magnitude v_{in}= 9.75 m/s, we find, basis simple calculations from actual measurements (Peng, Hoffmann, Dries, Regelink and Stein, 2005) that,

$$\mathbf{v}_p = 25 \text{ m/s}$$

and compute (basis the approximation, $v_\theta = const/r^n$ with $n = 0.8$, $v_{in} = 9.75$ m/s, $r_{cs} = 37$ mm and $r_{in} = 100 - 25 = 75$ mm)

$$\mathbf{v}_{CS} = 17 \text{ m/s}.$$

Thus, at position A,

$$\mathbf{v} = \mathbf{v}_A = 25 + 17 = 42 \text{ m/s}$$

and, at position B,

$$\mathbf{v} = \mathbf{v}_B = 25 - 17 = 8 \text{ m/s}$$

For this case, the resultant velocity at the bottom of "imprint" of the vortex core on the wall is slightly less than the inlet velocity. However, that at the top is about *4.3 times* the inlet velocity.

Similar calculations at an inlet flow rate of 400 m^3/hr (inlet velocity magnitude, $v_{in} = 19.5$ m/s) lead to $\mathbf{v}_A = 93.3$ m/s and $\mathbf{v}_B = 24.7$ m/s. For this case, the velocity at the bottom of the "imprint" $\mathbf{v}_B$ is about 27% greater than the inlet velocity. The velocity at the top of the imprint, $\mathbf{v}_A$, is *4.8 times* the inlet velocity.

Thus, not only can one expect an asymmetric velocity distribution near the wall but the velocity at the top of the vortex "imprint" can greatly exceed the inlet velocity, as the above example illustrates. This, we believe, has some far-reaching implications in regards to the design and operation of commercial cyclone systems.

Potential consequences of a precessing vortex

In light of what is reported above, if the end of the vortex is allowed to attach to, and precess around, the inner walls of the cyclone, such action can lead to severe localized erosion in the form of an acute erosion ring. This ring effectively defines the path of the precessing vortex end.

The intense velocity resulting from the aforementioned precessional motion also can be expected to significantly impair separation performance as some fraction of the "collected" dust spiraling down the walls becomes abruptly re-entrained by the action of the precessing vortex. Furthermore, particles of dust in this region of the cyclone may attrite at a rate greater than what one might expect from considerations of inlet velocity or even the core spin velocity alone.

Since the orderly helical flow of solids (or liquid) down the walls of the cyclone can be expected to be abruptly disturbed as it enters (and becomes momentarily entrapped in) the precessing "ring", tacky or sticky particles may tend accumulate on the wall in the vicinity of ring.

In addition to the above, we wish to point out that, in our judgment, not *all* of the physical height available in the cyclone is utilized if the vortex tail "short-circuits" the cyclone in the manner described above.

9.2.3 The Significance of the Vortex End

Once one is aware of the fact that a vortex has a 'natural length', one may think it is permissible to simply substitute this length for the physically available length of the cyclone or swirl tube. The assumption being that the end of the vortex simply limits the useful length of the separation space.

Although this seems to be approximately true in swirl tubes with a cylindrical body, experimental results indicate that the separation performance of cylinder-on-cone cyclones is reduced more than would be expected from the reduction of their effective length when the vortex ends within the conical section. One example is the dramatic reduction in separation efficiency (corresponding to an increase in cut diameter) for the longest cyclone length

reported in Sect. 5.3.2. Here, the vortex ends on a conical wall in the hopper under the cyclone.

There are, as the discussion in the two previous sections indicate, reasons, other than efficiency considerations, for designing cyclones to avoid the vortex ending in the separation space. The 'collected' dust that would normally experience an orderly downward transport along the wall will encounter a gross disturbance at the point (actually a plane) where the vortex ends. This usually occurs near the lower cone wall.

It has furthermore been claimed that the position of the vortex end is related to the sharpness of the cyclone cut (Abrahamsen and Allen, 1986). In support of this, the writers have observed considerable mixing of the solids originating in the plane where the precessing vortex 'tail' attaches to the lower walls of model cyclones. This has been observed in both dedusting and demisting cyclones.

But aside from the harmful effects upon separation performance, cyclones in which the vortex ends in the separation space are also prone to fouling and clogging, since the transport of dust (or liquid) along the wall toward the dust (or liquid) exit is less efficient below the vortex end. The position of the end of the vortex can often be determined upon inspection of the cyclone. If the vortex has been ending on the wall one can, as mentioned, usually observe a sharply defined ring-like zone of wall deposits or, depending on the abrasiveness of the solids, a burnished or eroded ring-like pattern along the lower cone or cylindrical wall. Sometimes the wear is so severe that the walls in the lower section of the cyclone completely fail. The erosion problem is discussed in some detail in the section on cyclone erosion in Chap. 12.

The position of the end of the vortex is likely to complicate the problem of 'crossflow' or 'cross-talk' between cyclones working in parallel that are fed from and discharge into common plenums.

Figure 9.2.5 shows the wall pressure profile along the entire length of a tangential-inlet cyclone. The remarkable thing about this data is the very sharp decrease in static pressure that occurs in the vicinity of the plane where the end of the vortex attaches to, and precesses around, the walls of the hopper. This sharp dip in static pressure is, of course, a direct result of the low-pressure vortex core contacting the hopper wall.

As one might expect, the frequency of rotation of the vortex core around the inner walls of the cyclone (or swirl tube) has been observed to be directly proportional to the gas flow rate. Interestingly, for any given gas flow rate, this precession frequency is also found to be approximately equal to the core's maximum spin velocity divided by the circumference of the inner wall at the plane of attachment. We will illustrate this below.

We begin by using the empirically determined "n-law" (see Appendix 2.A) to compute, for any given flow rate, the maximum core spin velocity from the measurements (Peng, Hoffmann, Dries, Regelink and Stein, 2005) shown in Fig. 9.2.6:

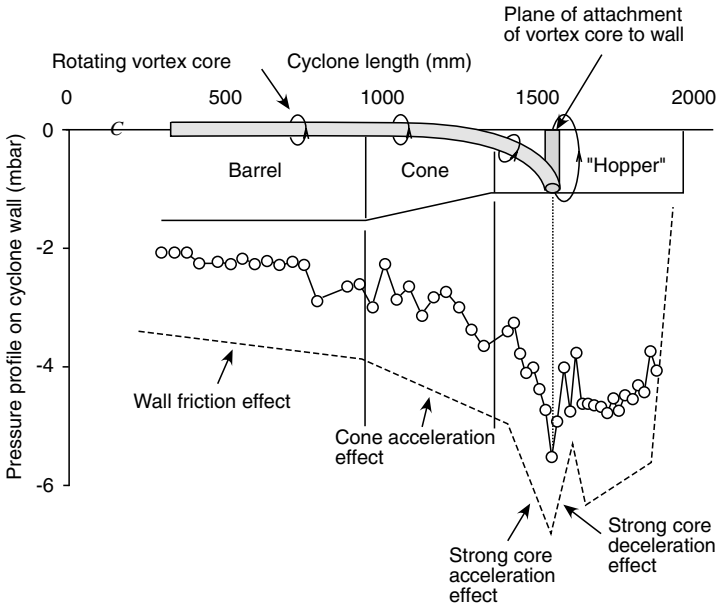

Fig. 9.2.5. Wall pressure profile showing sharp decrease in pressure in plane where vortex attaches to hopper wall. Basis Peng, Hoffmann, Dries, Regelink and Stein (2005)

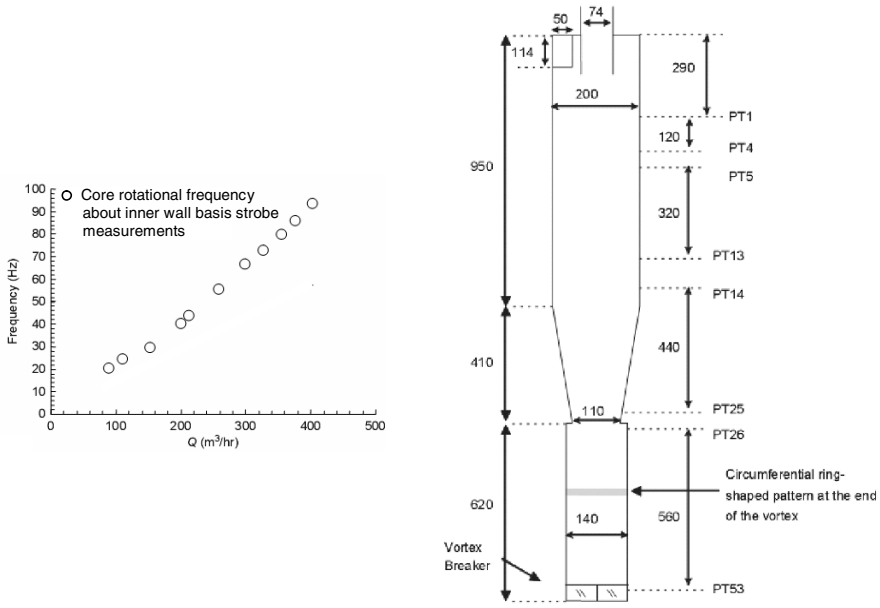

Fig. 9.2.6. Stroboscopic measurements of core precessional frequency for cyclone illustrated

$$v_{\theta\ max} = \left(\frac{r_e}{r_{\theta\ max}}\right)^n v_{in} \tag{9.2.1}$$

where,

$v_{\theta\ max}$ = maximum core spin velocity, m/s
r_e = average radius of entry gas = $(D - b)/2$, m
$r_{\theta\ max}$ = radius where $v_{\theta\ max}$ occurs $\approx (0.8d_x)/2$, m
n = empirical coefficient ≈ 0.8
v_{in} = inlet velocity Q/A_{in}, m/s
Q = volumetric flow rate, m^3/s
A_{in} = inlet area, m^2

In this study $r_e = (0.200 - 0.050)/2 = 0.075$ m, $r_{\theta\ max} \approx (0.8 \times 0.074)/2 = 0.030$ m, $n \approx 0.8$, and $A_{in} = 0.050 \times 0.114 = 0.0057$ m^2.

After computing $v_{\theta\ max}$ for each value of Q, we then compute the velocity at which the precessing core travels around the inside walls:

$$v_p = \pi f d_{hop} \tag{9.2.2}$$

where f is the measured frequency (reported in Fig. 9.2.6) and d_{hop} is the inside diameter of the cyclone where the vortex end attaches and precesses which, in this case, is the inside diameter of the hopper, having diameter 0.140 m.

In Fig. 9.2.7 we plot the velocity at which the "vortex end" or core transverses around the inside wall of the hopper (from Eq. 9.2.1) versus the estimated maximum tangential velocity of the vortex core (from Eq. 9.2.2). This plot strongly suggests that the precessional velocity is directly related to the maximum spin velocity. Thus, as stated earlier, precession frequency can be estimated by simply dividing the core's maximum spin velocity by the circumference of the inner wall to which it is attached. If this is true, then the end of the vortex acts much like a rubber wheel that rotates around the inner walls at a velocity equal to the maximum spin velocity of the vortex core.

Understandably, the "calculated velocities" reported in Fig. 9.2.7 depend upon the choice of values for both n and the radius where the maximum spin velocity occurs. For this work, we selected what we believe are reasonable values based on data reported in the literature ($n = 0.8$ and $r_{\theta\ max} = 0.8d_x/2$). No attempt was made to "curve-fit" the data by varying the value of n or the "0.8" coefficient in the equation for $r_{\theta\ max}$. Ideally, one should measure the maximum spin velocities (as a function of Q) and plot these versus the velocities obtained basis frequency measurements.

Where the vortex ends can have a significant bearing on cyclone performance. We'll try to illustrate this by examining two scenarios for vortex attachment, as shown in Fig. 9.2.8. The frame on the left has the vortex ending, and precessing around, the lower cone walls. Here, the pressure at the bottom of the cyclone (or top of the dipleg) can be expected to equal the inlet pressure minus the pressure loss due, primarily, to wall friction. (The latter typically

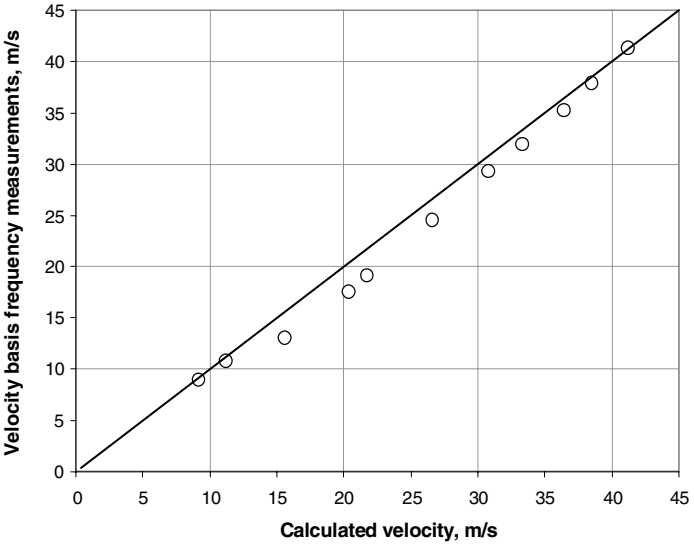

Fig. 9.2.7. Calculated vs. measured core velocity at wall

represents only 25% to 50% of the total pressure loss across the cyclone.) The frame on the right, however, has the vortex ending at the top of the dipleg. When this occurs, the pressure at the bottom of the cyclone (top of the dipleg) can be expected to be equal to the inlet pressure minus the *total* pressure loss across the cyclone. In this case, the bottom of the cyclone behaves much like an aspirator and the resulting low static pressure may cause solids to backup and "flood" both the dipleg and bottom portion of the cyclone. This, obviously, can lead to a host of problems including a sharp increase in emissions, erosion or fouling of the bottom section of the cyclone, and a sharp increase in particle attrition. As a rule, one normally wants to design a cyclone so that the vortex end does not terminate at the bottom of the cyclone.

9.2.4 Models for the Natural Vortex Length

The position of the vortex end is difficult to model. The first and, by far, the best known relation for the natural vortex length (*i.e.* the length from the lip of the vortex finder to the position of the end of the vortex) was proposed by Alexander (1949):

$$\frac{L_n}{D} = 2.3 \frac{D_x}{D} \left(\frac{D^2}{ab} \right)^{\frac{1}{3}} . \tag{9.2.3}$$

Zhongli et al. (1991) also proposed an expression for L_n involving the same groups, but the variation in L_n with *both* of the groups D_x/D and D^2/ab was qualitatively opposite to that in Eq. (9.2.3).

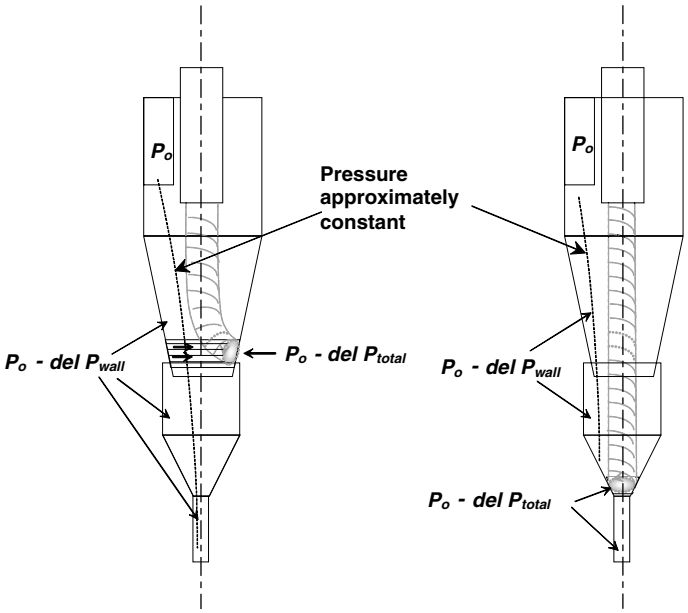

Fig. 9.2.8. Vortex end terminating on cone wall (left) and at bottom of cyclone (right)

Büttner (1999) wrote that Alexander had mainly used very small cyclones for his study, and, based on a review of some of the data in the literature, Büttner suggested that L_n increases with the cyclone Reynolds number. In fact, the increase should be so strong that problems with the natural vortex length should not occur at all in cyclones with an Re_{in} of more than 10000, which includes all cyclones larger than a few centimeters in diameter. Although the equation of Alexander often underestimates the vortex length in normal-sized cyclones, and Büttner therefore may have a point with the Re dependency, this dependency is in our experience not nearly as strong as Büttner claims. Real problems with the end of the vortex phenomenon are encountered in cyclones having diameters of several meters, and operating over a wide range of Reynolds numbers.

The authors' own experience with vortex behavior has resulted in the following observations:

- The vortex is destabilized, *i.e.* the vortex length decreases with increasing wall roughness (rough liner, eroded walls, or wall deposits) in both conventional cyclones and swirl tubes. The vortex is also destabilized at intermediate solids loadings (tens of grams of dust per cubic meter of gas) compared to very light loadings (a few grams of dust per cubic meter of gas). At very high loadings, where it appears that the vortex core is weak-

ened to the point where the whole concept of a high velocity 'inner core' breaks down, this effect disappears again.

- The vortex can be destabilized, *i.e.* L_n decreased, by too small a vortex finder diameter.
- The vortex length can be influenced by the presence of a vortex stabilizing plate or cone.
- The vortex length is increased by underflow (a bleed flow drawn from the dust hopper), and is shortened by gas backflow from the dust hopper (due to leakage, for instance).
- In general, anything that reduces the angular momentum of the spinning vortex core will tend to destabilize (shorten) the vortex. In this regard, the vortex behaves very much like a spinning top. Both are rotating masses subjected to frictional drag and both can become unstable and undergo precessional motion. The top's angular momentum vector precesses about the earth's gravitation line of force. The angular momentum vector at the end of the vortex precesses about its low pressure axial core.

All these factors obviously complicate matters if we are trying to construct a universal expression for the natural vortex length. The cyclone designer has to be especially aware of the natural vortex length when designing a cyclone. Things such as installing a refractory versus a metal liner, or decreasing the lower cone diameter can change the effective length of the vortex. Under these conditions, especially, the true length of the vortex may be much less than the physical length shown 'on the drawing board'.

Obviously, there are still a number of unanswered questions concerning vortex stability. There is much to understand regarding the unstable nature of the end of the vortex, in predicting its position based on the physical and operational variables, in controlling its erratic behavior, and in determining how all this affects cyclone design and performance. It is an area where significant progress can, and needs, to be made.

9.A Predicting the Effect of Solids Loading on Cyclone Efficiency

As mentioned in the main text, one strategy for calculating the performance of a cyclone at elevated loading is to calculate the working of the cyclone or swirl tube at low loading, and then calculate the effect of solids loading afterwards.

Let us try to predict the effect of loading on the efficiency of the cyclone in Fig. 9.1.1. All the data we need are in the figure legend. We start by calculating the Muschelknautz critical load, Eq. (9.1.1):

$$c_{oL} = \frac{f D_m \mu}{2\,(1 - D_x/D)\,\rho_p \langle x \rangle^2 v_{\theta m}}.$$

First we have to calculate $D_m = (D_x D)^{1/2} = (0.075 \times 0.2)^{1/2} = 0.122$ m.

We also need $v_{\theta m} = (v_{\theta w} v_{\theta x})^{1/2}$. This is more of a problem. To be consistent and adhere to the Barth-Muschelknautz approach, we should use Eq. (4.2.4) to calculate $v_{\theta w}$ and Eq. (4.2.6) to find $v_{\theta x}$, which is the same as v_{CS}. However, this seems quite cumbersome if we only want to estimate the effect of loading on efficiency[3].

To speed up the process we can take $v_{\theta w}$ as being roughly equal to the inlet velocity, v_{in}, and we can obtain $v_{\theta x}$ from the n-law, Eq. (4.2.2) using a reasonable value for n of 0.8. Doing this for the inlet velocity of 15 m/s, and first substituting the known value of v_θ at $r = (D/2)$ to find the constant C, we get:

$$v_{\theta w} = v_{in} = 15 = \frac{C}{(D/2)^n} = \frac{C}{(0.2/2)^{0.8}} \;\Rightarrow\; C = 2.377$$
$$\Rightarrow\; v_{\theta x} = \frac{2.377}{(D_x/2)^n} = \frac{2.377}{(0.075/2)^{0.8}} = 32.9 \text{ m/s}$$

This procedure gives us a value of $v_{\theta m}$ of 22.2 m/s. Finally we need the value of f. This is complicated by the fact that f is a function of the load itself (Eq. 4.2.9), and thus c_{oL} is a function of loading. This makes sense: a higher f leads to more turbulence, which is able to support a higher load. It is cumbersome, though, to take this into account, and we can take a short-cut if we are working with a cyclone with reasonably clean, smooth walls. In that situation, Muschelknautz suggests using the value of f corresponding to a clean wall, which is about 0.005.

Finally we insert this in Eq. (9.1.1):

$$c_{oL} = \frac{f D_m \mu}{2\,(1 - D_x/D)\,\rho_p \langle x \rangle^2 v_{\theta m}} = \frac{0.005 \times 0.122 \times 1.81 \times 10^{-5}}{2\,(1 - 0.075/0.2)\,2730 \times (3.7 \times 10^{-6})^2\, 22.2}.$$
$$= 0.0106$$

Thus, up to a loading of 0.0106 kg solids per kg gas (about 13 g/m^3) we should expect no effect of solids loading on efficiency. Actually, a slight decrease in efficiency can be expected as the increased load increases the wall friction and, therefore, attenuates the vortex. Once c_{oL} is exceeded we would expect the overall efficiency to increase according to:

$$\eta\,(c) = \frac{(c - c_{oL}) + \eta_i c_{oL}}{c} = 1 - \frac{c_{oL}}{c}\,(1 - \eta_i)\,.$$

Here, c represents the quantity of material that enters the cyclone, $(c - c_{oL})$ is the quantity separated in the inlet due to loading (*i.e.* a fraction of $(c - c_{oL})/c$, which was also called η_{sl} in the main text), c_{oL} is the quantity reporting to the

[3] The values for $v_{\theta w}$ and $v_{\theta x}$ when using this precise and cumbersome method are 16.1 m/s and 33.1 m/s, respectively, very close to what we find below.

inner vortex, and $c_{oL}\eta_i$ of that is separated there. Strictly speaking, also η_i is a function of the load, since the load influences the intensity of the vortex, but as an approximation we take η_i as constant and equal to its value at low loading.

Note that Muschelknautz' later formulae for the critical load, Eqs. (6.4.1) and (6.4.2)), result in the much lower critical load of 0.0026 kg solids per kg gas.

The model of Smolik is easier to use. The efficiency at any loading can be calculated from a known efficiency at a particular loading. Looking at the data used to create Fig. 9.1.1, we find, for instance, that the efficiency at a 10 m/s inlet velocity is 0.832 at a loading of 1.87 g/m^3. Thus, for the inlet velocity of 10 m/s:

$$\eta\left(c_2\right) = 1 - \left(1 - \eta\left(c_1\right)\right)\left(\frac{c_1}{c_2}\right)^{0.07} = 1 - \left(1 - 0.832\right)\left(\frac{1.87}{c_2}\right)^{0.07}.$$

Using the chart of Zenz is also relatively simple, but more time consuming. By interpolating between the data in Fig. 9.1.1, one finds for an inlet velocity of 10 m/s and inlet concentration of 1 grain/ft^3 (= 2.29 g/m^3) that the efficiency is 0.838. This falls very close to one of the curves in the Zenz chart, and the efficiencies for higher loadings can, for this particular case, be read rather easily off the chart. For the other two inlet velocities it is necessary to interpolate between the curves in Zenz' chart. Obviously, the results are limited to the precision of the chart.

Figure 9.A.1 shows a comparison between the Smolik model, the Zenz graphical method and the experimental results.

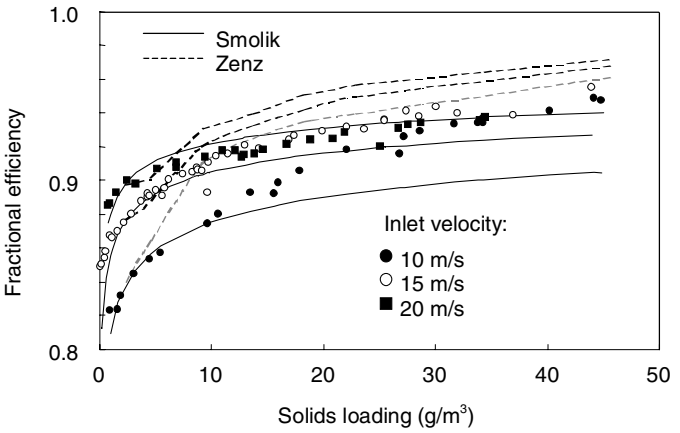

Fig. 9.A.1. The predictions of Smolik and Zenz compared with the experimental data from Fig. 9.1.1 in the main text

The spread in the Zenz predictions are due to the limitations in reading the chart. We see that both methods predict the effect of solids loading on efficiency reasonably well, the Zenz method slightly overpredicts the effect, and Smolik's slightly underpredicts it. It is also evident that there are variations in the effect of solids loading with inlet velocity that are not accounted for by these two models. For instance, the effect of loading upon separation efficiency decreases as the inlet velocity increases.

The predictions of Muschelknautz are not shown in the figure. The critical loading of 13 g/m^3 found above for an inlet velocity of 15 m/s means that the Muschelknautz model predicts a break in the curve at this value of loading, as mentioned above. Such a break is not seen in the data. This break would still exist even if we used the more recent Muschelknautz model reported in Chap. 6, only here the threshold may be as low as about 3 g/m^3, which is more consistent with the results. The predictions of the Muschelknautz model for the improvement of efficiency with loading around 40 g/m^3 are of the right order of magnitude.

9.B Predicting the Effect of Loading on Cyclone Pressure Drop

Four models predicting the effect of loading on pressure drop were mentioned in the main text: the empirical relations of Smolik, Briggs and Baskakov, and the Muschelknautz model.

We first apply the Smolik equation to the results shown in Fig. 9.1.5 in the main text. This relation can be applied directly. For instance, we find that the pressure drop at zero load, Δp_0, is about 430 Pa for an inlet velocity of 10 m/s, so at this inlet velocity:

$$\frac{\Delta p\,(c)}{\Delta p_0} = (1 - \alpha \cdot c^{\beta}) \;\Rightarrow\; \Delta p\,(c) = 430(1 - 0.02 \cdot c^{0.6}).$$

Figure 9.B.1 shows the experimental results from Fig. 9.1.5 together with the predictions of the Smolik Equation. Obviously this model describes the effect of loading on pressure drop very well. The equation of Smolik takes the pressure drop at zero loading as input, and it would not be fair to include the Barth-Muschelknautz model, which *predicts* the pressure drop at zero loading, in this figure. Moreover, as mentioned in Chap. 4, the Barth-Muschelknautz model predicts higher pressure drops than those measured here, probably due to a difference in experimental method when measuring pressure drops.

Also included in Fig. 9.B.1 is a curve fit of the form:

$$\Delta p(c) = \delta(1 - \alpha \cdot c^{\beta}) v_{in}^{\gamma}.$$

The optimal values of the four constants turned out to be: $\alpha = 0.0446$, $\beta = 0.506$, $\delta = 5.829$ and $\gamma = 1.905$. This equation, shown as broken curves in

the figure, fits the results quite well. The dependency of pressure drop upon inlet velocity is seen to be slightly less than a square or pure parabolic dependency, *i.e.*, $v^{1.90}$ rather than v^2. The writers believe that this is related to the fact that, at any given solids loading, an increase in the inlet velocity results in an enhanced centrifugal field and therefore in the gas and solids exchanging (losing) more of its momentum through interaction with the outer wall. Thus the gas moment-of-momentum is reduced somewhat compared to what would be expected and this manifests itself as a slightly weaker dependency of pressure loss upon inlet velocity.

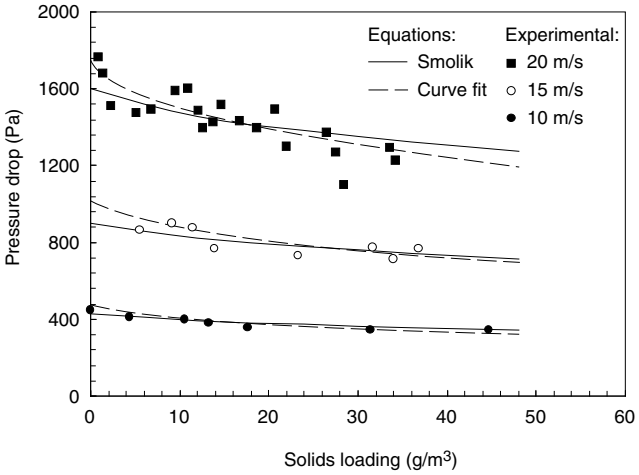

Fig. 9.B.1. The predictions of Smolik for the effect of solids loading on pressure drop at three different inlet velocities compared with the experimental results from Fig. 9.1.5. A curve-fit to the experimental results is also shown

Admittedly, simply curve-fitting the data provides little insight into the underlying mechanisms relating pressure drop to inlet velocity or solids concentration. Even so, such a data regression allows us to express the data in a very efficient equation format suitable for machine computations and for interpolation purposes.

In Fig. 9.B.2 we have replotted the experimental results of Gil, Romeo and Cortés (2002) together with the models of Smolik (9.1.6), Briggs (9.1.7) and Baskakov et al. (9.1.8). It is possible to plot the model equations of Smolik and Briggs directly on an x-axis of c_o, by rewriting them, substituting for c by realizing that $c = c_o[\text{kg/kg}] \times \rho[\text{kg/m}^3] \times 1000[\text{g/kg}]$.

As Gil, Romeo and Cortés (2002) also conclude, the Baskakov model appears to describe their results the best. The Smolik equation seems to overestimate the effect of the solids loading quite a lot. Gil, Romeo and Cortéz suspect, and we agree, that the problem may lie in the fact that their ex-

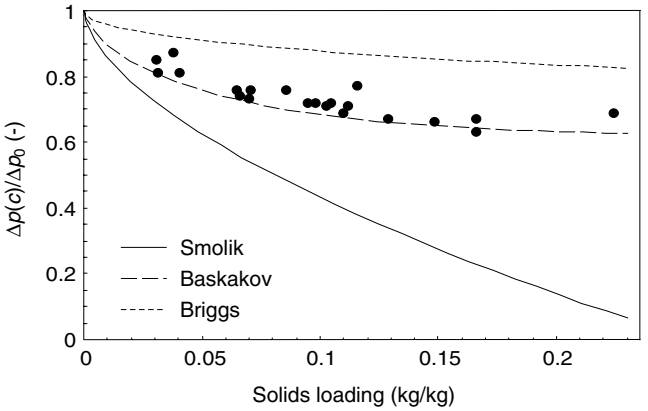

Fig. 9.B.2. The experimental results for the pressure drop in the pressurized fluidized bed combustion cyclone of Gil, Romeo and Cortés plotted together with the model predictions of Smolik, Briggs and Baskakov, respectively

periments were performed at elevated pressures. When rewriting the Smolik equation in terms of c_o rather than c, as shown above, a dependence on the gas density, which is inherent in expressing the solids loading in g solids per m^3 of gas, becomes more evident; a rather significant dependency that may not be warranted physically.

In spite of the difficulties mentioned earlier in this appendix with comparing the absolute predictions of the empirical models and the Muschelknautz model, it is nevertheless possible to compare the *trend* between the models, for instance between the Smolik model and the Muschelknautz model. Using the data from Fig. 9.1.1, and following the procedure for the Barth-Muschelknautz model outlined in the main text gives $v_{\theta w} = 21.4$ m/s, and:

$$v_{\theta CS}\,(c) = \frac{57.1}{1 + 0.294\,(1 + 3\sqrt{c})}$$

whereby $H_{CS} = 0.7$. Finding v_x from:

$$v_x = \frac{abv_{in}}{\frac{\pi}{4}D_x^2} = \frac{0.1 \times 0.04 \times 20}{\frac{\pi}{4}0.075^2} = 18.1 \text{ m/s},$$

and substituting these two velocities in (4.3.4) gives the cyclone pressure drop as a function of the inlet concentration c (at least the part of the pressure drop generated in the vortex finder, which is by far the greatest). Substituting $c = 0$ gives a pressure drop of 3370 Pa for zero loading, obviously higher than the measured pressure drop.

In order to compare the trend predictions of the two models, we can set the value of Δp_0 in the Smolik model to the same as the Muschelknautz prediction, namely 3370 Pa. Figure 9.B.3 shows the result. The agreement between

the two predictions is very good, particularly when taking into account that the Barth-Muschelknautz prediction is not directly empirical, but takes into account the reason for the reduction in pressure drop: the reduction of the swirl velocity in the centre of the separation space and in the vortex finder.

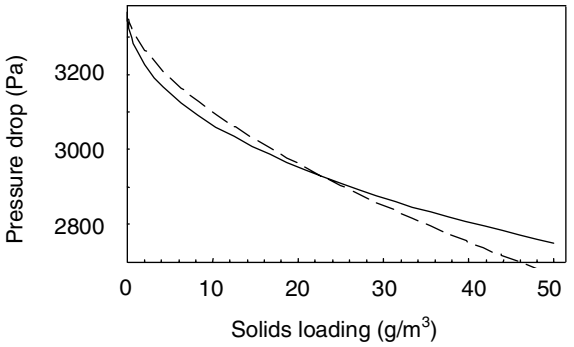

Fig. 9.B.3. Comparison of the trends in pressure drop with solids loading predicted by the Barth-Muschelknautz and Smolik (broken curve) models

10

Measurement Techniques

A range of experimental or measurement techniques is available for determining the functioning of gas cyclones and swirl tubes. The choice of technique depends on the situation: the techniques giving the best results in the laboratory on relatively small-scale equipment under controlled conditions, may be quite different from those giving the best results in industrial equipment.

In the laboratory, the goal of most measurement campaigns is to further ones understanding of the basic phenomena that govern the performance of cyclone and related centrifugal separation apparatus. Such things as:

- detailed velocity and pressure profiles,
- specific erosion patterns and rates,
- dust concentration profiles,
- particle paths/trajectories,
- particle attrition rates,
- the effect of design modifications,
- the effect of upflow or hopper crossflow for flow maldistribution,
- dust discharge configuration or hardware,
- agglomeration effects,
- the effect of changes in operating conditions (flow rate, operating pressure, solids loading, and particle size, shape and density, etc.)

are often the target of the investigation, aside from more traditional measurements of grade and overall efficiency and overall pressure loss. Laboratory cyclone equipment is designed 'from the ground up' to facilitate accurate measurement of such effects.

In an industrial cyclone system, the goal of measurements has related but somewhat different objectives. Here, one is more interested in ascertaining the overall performance of the cyclone under plant operating conditions. This may be done to so that plant personnel can:

- check out the general state of the equipment,
- compare performance with design targets,

- verify vendor guarantees or warranties,
- check on compliance with air quality standards,
- check on the effectiveness of certain process or design features or changes,
- help determine the remaining service life of the equipment, that is, when the equipment needs to 'come down' for repair.

Depending on the specifics of the plant, other measurement objectives could be added to the above list. However, in virtually all cases, one can be certain that the commercial unit was not built to facilitate accurate measurement or testing.

Plant measurements pose some very special challenges. They must often be performed outdoors under very hot, cold, or inclement weather conditions, on windblown platforms or on stacks that may be many stories tall, with inlet and outlet ducting geometries that are far removed from ideal, and with systems that have few, if any, working sample ports. In some cases, an accurate knowledge of even some basic operating conditions, such as volumetric flow rate, operating pressure and temperature, or gas composition, may not be known or it must be estimated in a rather crude fashion. Alternatively, if such information is available, it may not be known at the point in the system where the cyclones are installed. In some cases, one may not even have up-to-date drawings of the cyclones and any inspection records that may assist in the interpretation of the measurements may be lost or woefully lacking in information.

Commercial cyclone installations are usually subject to a performance evaluation after they are brought on-line and process conditions have stabilized. Such "Start-of-run" measurements may be performed to verify vendor performance predictions or, a closely related objective, to determine if the cyclone(s) are performing their intended process duty. Aside from these important reasons, early in-the-run performance measurements also provide a benchmark with which to compare preformance later in the run. cyclone performance will usually deteriorate with run time in commercial systems since they are normally required to run for months or even years between turnarounds. Such deterioration may be due to a number of factors: erosion (increased wall roughness or holes in walls), corrosion, weld cracking, deposit formation, distortion, seal problems, etc. (see related discussion in Chap. 12). Periodic performance measurements allow plant personnel to detect and monitor the rate of performance degradation and thereby estimate its useful remaining run life.

Cyclones in commercial service are often installed in parallel arrays or in series with other cyclones. Under such conditions, it is rarely possible to determine the performance of the individual cyclones. Thus, even after the data is collected, it is often a challenge to interpret it correctly.

In some parallel cyclone arrays, wherein it is suspected or known that the cyclone system is not performing up to design expectations, it may be possible to inject a tracer, such as helium gas, in a common header upstream of the cyclones and measure the time required for the tracer to exit out the

overflow line from each cyclone[1]. Such measurements can provide clues as to the cause of the sub-par performance. The technique may tell us, for example, if gas is short-circuiting one or more cyclones, or whether one or more cyclones are running with plugged, or partially plugged, underflow pipes, or if one or more cyclones are filled or partially filled with solids. It may also tell us how uniformly the gas is being distributed among the individual cyclone units. This latter problem may be the result of an inlet gas or solids distribution problem. The same applies to a gas/liquid cyclone installation.

Even after one obtains performance data, correctly interpreting it can be quite challenging when the results are not what we are expecting. In some situations, we might even *expect* a certain outcome (such as poor separation performance) but determining the root cause from the performance data is anything but straight forward. When two or more cyclone sets are arranged in series, for example, it may be very difficult to determine which stage is malfunctioning. It is in situations like this where an in-depth understanding of cyclone behavior and experience comes most into play. Because cyclone systems vary so widely from one industry to the next, and from one service to another, it is not possible to prepare a detailed troubleshooting guide that would cover all of the various cyclone failure modes that are possible for every industry or application. On the basis of the authors' experience in analyzing and troubleshooting various cyclone installations, however, we do want to point out that *the majority of cyclone problems relate, in some way or the other, to the inability of the solids to properly discharge out the cyclone(s) underflow chute or pipe.* This certainly includes such things as gas leakage up the solids discharge opening, plugging of the underflow piping or hopper, or an unstable solids discharge. We'll have more to say about cyclone underflow sealing in the next chapter but, an example of a plugged or unstable discharge would be poor aeration of one or more cyclone underflow pipes (i.e., "diplegs") in applications wherein they are required to be "sealed" in a fluidized bed. Thus, as we can glean from the above discussion, measurement and analysis go hand-in-hand.

It is often only possible to obtain relative measurements of performance. One may be 'stuck' with a very poorly located sample point or tap, for example, yet this particular sample tap may reveal *changes* in performance that are still very meaningful to plant personnel.

Measurements are very costly to undertake, whether in the laboratory or in the plant. Plant measurement errors are almost always greater than those one can obtain under a controlled, laboratory environment, although meaningful laboratory measurements present their own, unique set of challenges.

With this in mind, we wish to present some of the most commonly employed cyclone measurement techniques. While all of the following techniques

[1] In some installations it may be possible to also measure the time it takes for the tracer to exit out the underflow line from each cyclone, but this is not very common

can be applied in a laboratory research environment, a number of them can be usefully applied in a commercial plant facility also. In particular, this would include the procedures for pressure drop, on-line and off-line sampling, and methods for particle size analysis.

10.1 Gas Flow Pattern

Since the flow in a cyclone or swirl tube is complex, the direction of the axial and radial velocity components are not known in advance. This has to be borne in mind when considering how to measure the flow field.

A 'hot-wire anemometer' measures the gas velocity at a given point from the cooling of an electrically heated wire stretched out in a fork. The faster the gas flows over the wire, the stronger the cooling. A traditional hot wire anemometer will measure the absolute gas velocity (the speed), but not the direction. 3-D anemometers have been developed, which will also measure direction by comparing the cooling of wires stretched out in different directions. Although much has been done to develop the theory, hot wire anemometers still require calibration.

The traditional 'pitot tube' (see Figure 10.1.1a) has the advantage that, if properly configured, it needs no calibration. When pointed against the direction of the gas velocity, it will measure the dynamic pressure directly as $(p_1 - p_2)$ (see the figure). From this the velocity can be calculated using the formula[2]:

$$v = \sqrt{\frac{2\,(p_1 - p_2)}{\rho}}. \tag{10.1.1}$$

The error in using this formula without a calibration will be normally only a couple of percent. If the pitot tube is of the elliptical type, the error will drop to a fraction of a percentage point.

It is possible to use a conventional pitot tube to ascertain the direction of a velocity within a cyclone. It is far easier, however, to use a '5-bore pitot tube' (Figure 10.1.1b) rather than try to glean the direction by tilting a traditional pitot tube. After calibration, a 5-bore pitot tube will give information about the magnitude and direction of the gas velocity from the pressure differences between orifices located at various points on the spherical measuring head, as indicated in the figure.

A major problem with both the hot wire anemometer and the pitot tube is that the measurements are intrusive. A probe is inserted, and this may well disturb the flow pattern. Obviously, the smaller the probe is relative to the vessel, the less the disturbance.

In 'laser-Doppler anemometry' (LDA), the velocity of the gas is measured as the speed of small seed particles that follow the gas flow faithfully. In the

[2] This formula is valid up to about 60 m/s, at higher velocities the compressibility of the gas has to be taken into account

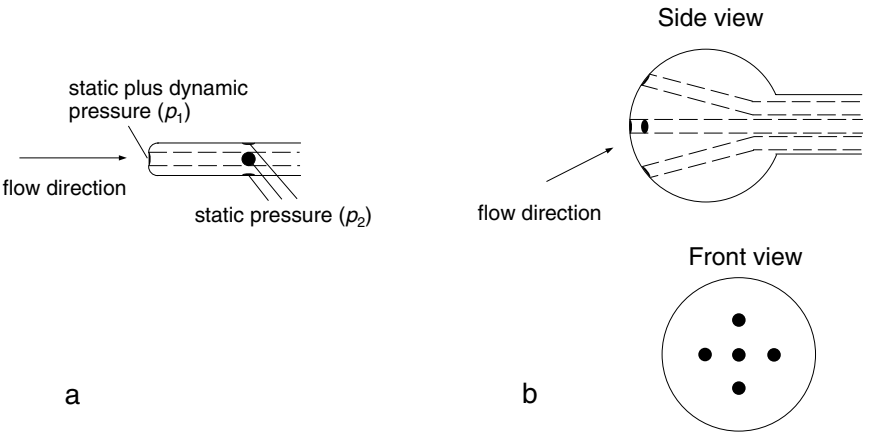

Fig. 10.1.1. Diagrams showing the principles of **a** a traditional Prandtl-type pitot tube, and **b** a 5-bore pitot tube

'fringe anemometer' two laser light beams are caused to cross, which creates an interference pattern (the measuring volume) through which the seed particles fly (a visualization of this is shown in Figure 10.1.2[3]). The light scattered by the particles as they pass through the measuring volume is detected as a 'Doppler burst', and the frequency of this is a measure of the speed with which the particles traverse the measuring volume. In classical LDA each of the components of the gas velocity are measured consecutively. In newer systems, different velocity components can be measured in the same volume simultaneously using different colored laser light, which can be detected separately.

The main advantage of LDA is that it is nonintrusive. Problems can be caused by the seed particles not faithfully following the gas in a strongly swirling region of gas flow, and by the optical breaking of the laser beams in the cylindrical wall of the cyclone or swirl tube.

The three methods discussed above are all suitable for determining the mean gas velocity. If we wish to determine also the fluctuating velocity component due to turbulence, a meter with a short response time is needed. Both hot-wire anemometry and LDA can be used for this. The response time of hot-wire anemometers is being reduced by equipment miniaturization, but LDA is the most widely used technique for turbulence characterization.

[3] Although the picture is a good way of visualizing the interference pattern, it does not quite reflect the situation correctly. If, for instance, the intensity peaks in the incoming radiation are the black lines, then the intensity peaks in the interference pattern will be where the black lines cross, which should then be the location of the darker bands in the interference pattern, and not, as they are in the picture, the location of the lighter bands.

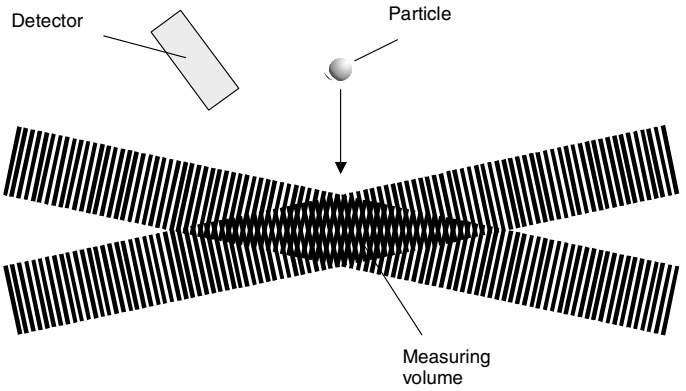

Fig. 10.1.2. Visualization of a seed particle flying through an interference pattern created by two crossing laser beams

10.2 Pressure Drop

When deciding how best to measure the pressure drop over centrifugal separation equipment, we first have to decide what we mean by the term 'pressure drop'.

As discussed in Chap. 4, the swirl in cyclones and swirl tubes means that the static and dynamic contributions to the total pressure vary strongly throughout the equipment. It is therefore not sufficient to measure the static pressure at a given position, subtract the static pressure at the inlet, and call this the 'pressure drop'. We take 'pressure drop' to mean *the drop in total pressure*, dynamic plus static. The drop in total pressure is equal to the dissipative loss of mechanical energy per unit volume in the flowing gas[4].

Measuring the pressure at the inlet of a cyclone is not a problem: there is no swirl there, and the static pressure is uniform over the cross section, so we can measure the pressure with a standard pressure tapping at the wall.

At the gas outlet, on the other hand, residual swirl is the problem: a significant dynamic pressure is stored in the swirling motion, and the static pressure is not uniform over the cross section. Some researchers studying the pressure drop in cyclones have solved this by letting the cyclones discharge directly to the atmosphere, taking the outlet pressure as atmospheric. This is a good solution if solids are not used in the system. Others have placed rectifying or 'straightening' vanes in the outlet pipe from the cyclone or swirl tube, and measured the static pressure after the rectifier (the axial velocity in inlet and outlet is about the same for normal cyclones and swirl tube designs).

[4] Note that in most other process equipment not involving swirling flow, we are not confronted with this problem in defining pressure drop, since the drop in *static* pressure is proportional to the dissipative mechanical energy loss, as long as the inlet and outlet fluid velocities are approximately the same.

Others, fearing that rectifiers would influence the flow in the separator body, measured the static pressure by a conventional pressure tapping at the wall in the outlet of a cyclone. Because the static pressure happens to vary in an approximately linear manner with radius in the cyclone outlet, this wall static pressure is approximately equal to what the cross-sectional average static pressure would have been after an ideal rectifier. This is discussed in Chap. 4. If the two latter methods are used one should keep in mind that, without rectification of the outgoing stream, more dissipative loss will occur in the downstream tubing as the swirl energy is dissipated. If one does use wall pressure taps to measure static pressure, the taps should be gas purged so that they do not plug while in service. A purge velocity of 0.2 to 0.5 m/s will usually suffice in keeping particles from entering the pressure taps. To avoid flow disturbances from the pressure taps, they should be small, of the order of 1 mm in diameter for laboratory-scale units, but may be as large as 4 to 5 mm on large commercial-scale installations. The inside edge of the taps should be smooth and flush with the inner surface of the pipe or duct into which they are inserted.

The differences in measured pressure drops and in model predictions of pressure drop in the research literature, particularly the difference between the Barth model predictions and the experimental results in Fig. 5.3.2, can probably be traced back to different cultures in measuring the outlet pressure.

It is difficult to give general recommendations for the method of measuring the outlet pressure when solids are being used in the system. The most important thing is to interpret the measurements correctly.

10.3 Particle Flow

Tracing an individual particle as it moves through the separator body is not yet possible. Several research groups are developing methods for tracing of radioactive particles in 3-D based on the detection and cross-triangulation of γ-rays emitted back-to-back. However, the tracer particles still have to be relatively large and the method is at present only suitable for particle velocities up to a few meters per second. Both of these limitations are being pushed back rapidly, though, and experimental particle tracking in cyclones and swirl tubes should become possible in the near future.

Phase Doppler anemometry (PDA) is a technique akin to LDA. In PDA the laser light scattered in the measuring volume by a particle is detected at two angles, making it possible to gain information not only about the velocity of a particle but also its size. Mothes and Löffler (1985) report a study wherein they used this technique to gain information about the distribution of particle sizes within the body of a gas cyclone.

10.4 Overall Separation Efficiency

When determining the efficiency of cyclones and swirl tubes, samples can be taken at three positions: the inlet, the gas outlet and the dust outlet (see Figure 10.4.1).

Inspecting Eq. (3.2.2) shows that the overall separation efficiency, η, can be calculated from the mass flows of solids at any two of the three sampling points. If also the solids mass flow at the third is determined, one can check on the 'material balance' by way of Eq. (3.2.1).

If there is no net flow of gas out the cyclone underflow, the captured solids fraction is a pure solids stream, and it may be possible to determine the mass flow of this fraction by collecting the underflow solids for a known time, and weighing. This method can often be applied in both an industrial and a laboratory installation.

In other cases, the underflow rate is not available but a sample of the underflow can be taken. Providing the sample is representative of the underflow, the underflow particle size distribution (PSD) can be ascertained. This PSD may also be independently computed from measured PSDs of the feed and the overflow streams and compared with the measured underflow PSD. The two underflow PSDs thus determined should agree. If not, there is something wrong with one or more of the measurements. This technique has been used in practice as a means of checking the accuracy of the feed and overflow measurements. See also the discussion around Eqs. (3.2.3) and (3.2.4).

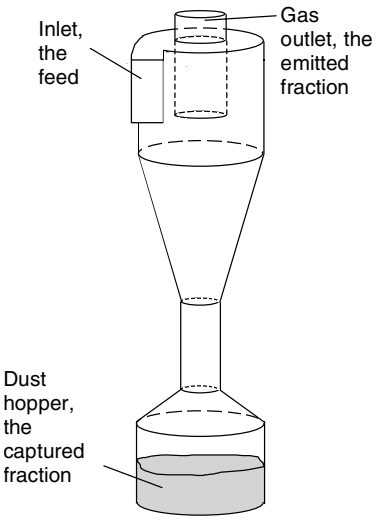

Fig. 10.4.1. Sketch indicating the sampling points for determining cyclone separation efficiency

The mass flow of the feed solids is sometimes known in an industrial installation from measurements taken elsewhere in the plant. In an experimental laboratory rig, a test is often of a limited duration, and the mass of feed solids can be determined accurately by weighing the entire charge. If these options are not workable, the inlet solids flow has to be determined by on-line sampling from the piping upstream of the cyclone or swirl tube, or inferred from measurements or information regarding the solids flow rate in the overflow and underflow streams.

The mass flow of the overflow fraction normally has to be determined in an industrial installation by on-line sampling downstream of the cyclone, while in a laboratory test rig total capture of the overhead fraction by filtering may be feasible.

Once the mass flowrates of solids at two of the three points shown in Fig. 10.4.1 have been determined with sufficient accuracy, the efficiency of the cyclone or swirl tube can be determined from Eq. (3.2.2).

The error in a measurement is often roughly proportional to the absolute value of the measured variable. This is used in Appendix 10A to show that the error in the value of η calculated from the three mass flows is by far the lowest if the overflow fraction is one of the two mass flows measured.

10.4.1 On-line Sampling of Solids

Sampling for determining solids concentrations in gas streams and for size analysis needs to be done carefully. Below we highlight some of the intricacies of sampling on-line in the piping both upstream and downstream of a cyclone or swirl tube.

Sampling on-line involves drawing off a small stream of the solids-laden gas by means of the sampling probe. The small stream of dust-laden gas is led through a filter in which the solids are captured, and from which they can be removed for subsequent analysis.

The first rule of on-line sampling is that it has to be done 'isokinetically', that is, the gas velocity at the mouth of the sampling probe has to be the same as that of the flowing gas at that point. Figure 10.4.2 illustrates this principle.

We note two extreme cases where isokinetic sampling may be less critical for measuring particle size distribution:

- at high gas velocities, and when the smallest particles or droplets are rather large and the particles have a high density relative to the fluid, all particles approaching the nozzle will travel in a more or less straight line "ignoring" any curvature of the fluid streamlines caused by deviations from isokineticity. Note, however, that although isokinecitity is not crucial for measuring the particle size distribution in this extreme case, it is still a prerequisite for measuring the true particle concentration.

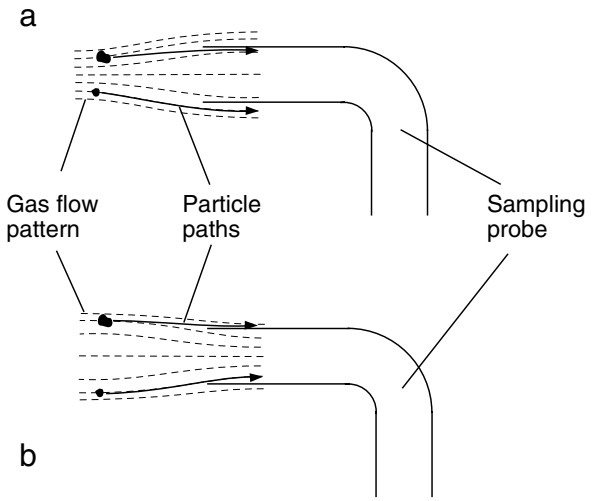

Fig. 10.4.2. Sketches showing the consequence of not sampling isokinetically. In **a** the sampling velocity is too low, and the gas flows around the probe in the pattern indicated. Small particles manage to flow around the probe, while larger ones at the same position relative to the probe mouth enter the probe by their inertia. The sampling will overestimate the solids concentration in the gas, and the size distribution of the captured material will be biased toward large particles. In **b**, the sampling velocity is too high, and the converse takes place, the solids concentration is underestimated, and fraction of fine particles is overrepresented in the captured material

- at low gas velocities, and when the largest particles are relatively small and have a low density, all the particles may follow the gas streamlines faithfully, the measured size distribution will therefore not depend on isokineticity.

The former of these two cases may well arise in cyclone research. If the maximum and/or minimum particle size and the particle density are not known *a priori*, however, it is impossible to tell whether one of these conditions apply, and in general it is advisable to sample isokinetically whereever possible. Hangal and Willeke (1990) discuss the issue of sampling from a gas stream, and present a model for the capture efficiency of particles as a function of the particle's Stokes number, the ratio of gas to sampler inlet velocities and the angle of the sampler relative to the gas flow.

The second important point is that the sampling should be representative of the entire cross-sectional area of the pipe. This means that in most cases sampling has to be done at a number of cross-sectional positions. Ensuring representative sampling can be difficult if sampling is done too close to an upstream flow disturbance, such as a bend. The gas velocity profile will then

be skewed, making isokinetic sampling more difficult. But, more importantly, the solids concentration is likely to be nonuniform over the cross section of the pipe. The former of these two problems can be overcome by determining the cross-sectional gas velocity profile and making sure that sampling is isokinetic, but there is really no acceptable way of overcoming the latter problem.

In order to minimize errors arising from such effects, a number of guidelines have been laid down in industry norms or specifications. It is useful to consult such a norm or specification when faced with the task of determining solids concentration and size distribution by on-line sampling. We mention some of the most important points below, enough to carry out a reasonably accurate sampling, and refer to, for example, the norm ISO 9096 for more information.

The mouth of the sampling probe should be at least 4 mm in diameter and be sharp edged and tapered to avoid turbulence around the inlet to the probe. If the process stream is at elevated temperature, and contains moisture or 'condensables', the part of the sampling system outside the process piping may need to be heated to avoid condensation. If there is moisture or condensables in the system, one has to be careful to account for this when working out the flows, for instance, if the gas is dried before it is metered in the sampling train.

The gas velocity can best be measured using a (Prandtl type) pitot tube. Either this can be done in a separate measurement, or the sampling system can incorporate a separate probe for velocity measurement.

The sampling position should be at least 5 diameters downstream and 2 diameters upstream of a flow disturbance, such as a bend or a valve. Some vendors or users of sampling or flow measurement equipment demand much larger undisturbed sections. If the undisturbed section cannot be made long enough, where feasible, a half-area mixing baffle (a transverse plate having half the cross-sectional area of the pipe) can help in distributing the gas and solids flow uniformly over the pipe cross section. It is better to sample in a vertical than in a horizontal pipe section. The ISO norm recommends sampling at a series of specified cross-sectional positions in the pipe to obtain a more representative sample. Each of these positions represents an equal fraction of the pipe cross section.

A sampling time of at least 3 minutes is recommended, although the sampling time obviously has to be adjusted in accordance with the solids concentration.

Before closing this section on sampling we wish to point out that, once a plant is built, it is normally too late to think about accurate sampling if this was not considered in the original design phase. In such instances, one may not be able to get accurate measurements of a particular feed or overflow stream. However, even a less-than-ideal sample point may still prove very useful for monitoring *trends* in the cyclone system's performance, such as a sudden increase in the coarse fraction of solids reporting overhead or a steady increase in pressure drop. A trend of increasing pressure drop over time could be indicative of material depositing or growing on the inside of the gas outlet

pipe. A steady decrease in cyclone pressure drop over time could be a sign of increased wall roughness brought about by wall deposits or wall erosion and/or corrosion. Recall that an increase in effective wall roughness will result in an attenuation of the core spin velocity and this, in turn, will reduce the cyclone's overall pressure loss.

10.5 Grade-Efficiency

There are two ways of determining the grade-efficiency $\eta(x)$ of cyclones:

1. In the case of a laboratory cyclone unit, inject monosized particles in the cyclone, and measure the overall efficiency to obtain one point on the grade-efficiency curve.
2. Inject a feed of a wide size distribution into a laboratory cyclone or, in the case of an commercial installation, utilizing the solids already reporting to and from the cyclone, collect samples and perform size analyses on any two of: the feed, the overflow and the captured (underflow) fractions. Then use Eq. (3.2.6) to calculate $\eta(x)$. To obtain reasonably accurate results, the overflow fraction should be one of the fractions analysed.

The first method eliminates a host of potential sources of error. The measurement is very direct, and if the cyclone is run properly with a reasonably low solids loading, not much can go wrong. The drawback of using this method is that it is obviously a very time-consuming and cumbersome procedure, and it will not normally be practical in an industrial context, not to mention the problems of finding fine, monodisperse particles at a reasonable price. We will therefore concentrate on the second method in this section.

The main issues of concern in this second method are:

- obtaining and preparing samples for size analysis in the case of a laboratory cyclone
- choosing the method for size analysis

These two issues will be considered together in what follows, since the sample preparation depends on the method used for size analysis.

10.5.1 On-Line *vs.* Off-Line Size Analysis

Two main options exist for the measurement of particle size distributions: on-line and off-line.

Off-line analyses involve collecting samples of the solids fractions, dispersing them and analyzing them off-line, often using a liquid-borne technique. This method is more accurate than 'real time' on-line methods and it is often the most user friendly. Still, it has one important drawback. When collecting a particle sample from the process stream and re-dispersing it in liquid, one

loses the information of its state of dispersion in the cyclone or swirl tube. For instance, a small particle may have been traveling through the system as part of an agglomerate which, due to its large size, was captured in the separator. But when a sample of the captured fraction is dispersed in a liquid, it will normally disperse into its constituent or elementary particles so that our particle will appear in the size analysis as a small particle. Thus, the calculated grade-efficiency would show an anomalously high efficiency for such small particles. This is probably the reason for the typical 'tail' seen at the fine end of many experimental grade-efficiency curves, as mentioned in Chap. 5.

On-line analysis, which measures the particle size distribution in 'real time' while the particles are still dispersed in the carrier gas, avoids this problem. These methods characterize the particles as they appear in the gas stream, whether they are present as agglomerates or as dispersed particles. This can be an important advantage, especially in industrial situations, where the state of dispersion of the particles in the system is not always known. However, on-line analysis of particle sizes is normally far less accurate than off-line analysis and some serious errors can be introduced in the process of conveying the solids-bearing bleed stream through the size analyzer.

In summary: if the state of dispersion of the particles in the process is known or can be discovered (perhaps by comparing an on- and an off-line size analysis), off-line sizing gives the best results. Otherwise, on-line methods should be used, if feasible. In some situations, a relatively minor degree of particle agglomeration is known to occur but may be ignored if it does not significantly affect the purpose of the measurements.

10.5.2 Sample Capture and Preparation

We have already discussed the problems of isokinetic sampling. The issues are the same whether one wishes to measure only the solids concentration to determine the overall efficiency, or to subject the collected sample to size analysis either off-line or on-line by leading the bleed stream through some on-line size analyzer. In the latter case, the analyzer may be calibrated only for certain fixed gas flow rates passing through it, making it necessary to vary the opening of the sampling tube (or the number of parallel sampling tubes), to achieve isokinetic sampling.

When preparing a sample for off-line size analysis, one needs to ensure that the particles are dispersed in the suspension. This mostly means adding some surface tension reducing agent and dispersing agent to the suspension to make sure that the particles are fully wetted and dispersed (examples of such agents are Teepol and Calgon). The surface tension reducing agent ensures wetting of the particle surfaces, so that no gas is trapped between them. The dispersing agent avoids particle agglomeration in the suspension, often by imparting an electrical charge to the surface of the particles, so that they

repel each other. Vendors of sizing equipment normally list dispersing agents suitable for different types of particles.

The particles also have to be dispersed mechanically in the liquid. This can be done by stirring the suspension and/or by treating it in an ultrasonic bath to break up particle agglomerates. If the particles have a relatively high settling velocity, one needs to ensure that the large particles do not settle out. If the particles are soluble in the liquid one may be able to circumvent solubility concerns by ensuring that the liquid is first saturated in the material of which the particles consist.

10.5.3 Methods for Size Analysis

It goes beyond the scope of this book to give a full account of the methods available for particle size analysis. For a further study of this, we refer to the book of Allen (1990). The principles behind the methods differ widely, and they yield different measures of the particle size.

The size that determines the behavior of the particle in cyclones and swirl tubes is the dynamically equivalent size. Using methods that measure this size avoids errors arising from such things as a varying particle density or particle shape and, for this reason, are considerably preferable to others. Unfortunately, these methods are also rather labour intensive. Below we mention the most used sizing techniques, and discuss briefly their usefulness for grade-efficiency analysis. We start with on-line methods.

The 'cascade impactor' measures the particle size by leading the particle-bearing gas through a series of stages, each consisting of a jet and an impaction plate. When the particle-bearing gas, accelerated in the jet, impacts the plate, the particles that are below the 'cut size' for that stage will flow around the plate with the gas, while the coarser ones will impact the plate and stick to it. Each subsequent stage is configured such that it will have a lower cut size. If the cut size for each stage is known, or determined by testing, the particle size distribution can be found by weighing the material collected on each impaction plate. This method thus measures a dynamically equivalent particle size on-line.

A 'cyclone train' consists of a series of small cyclones (a few cm in diameter) with a progressively lower cut size. Like the cascade impactor, the cyclone train permits on-line measurement of the dynamically equivalent particle size distribution. The advantage of the cyclone train is that the cyclones can collect more particles than a cascade impactor.

A 'laser diffraction particle analyzer' can measure, in principle, the size distribution of particles suspended in a gas. However, if one attempts to determine the size distribution of agglomerates, laser diffraction may not give a very accurate result due to the nonsphericity of agglomerates. See also the discussion of this method below. Laser diffraction does not give a dynamically equivalent particle size.

Turning now to off-line methods

The 'disc centrifuge' classifies particles off-line in a liquid suspension in a centrifugal field. A suspension of particles is injected onto the surface (at radius R_o) of a 'spin fluid', housed in a disc-shaped cavity and spun at a precisely known rate (angular velocity Ω). The centrifugal force field propels the particles radially outward. The concentration of particles is measured as a function of time, t, at a fixed radial position. This can be done either by sampling or, as in the 'photosedimentometer', optically (see Figure 10.5.1). A light source/photocell couple located close to the edge of the disc-shaped cavity (at R_{dc}) measures the level of light obscuration. The velocity of the particles is a function of the diameter, density and shape. A force balance on a particle (treated as a sphere of diameter x) gives the following expression:

$$x^2 = \frac{18\mu \ln\left(\frac{R_{dc}}{R_o}\right)}{(\rho_p - \rho)\ \Omega^2\,(t - t_o)}, \tag{10.5.1}$$

where μ is the viscosity of the spin fluid and t_o the time at which the suspension is injected.

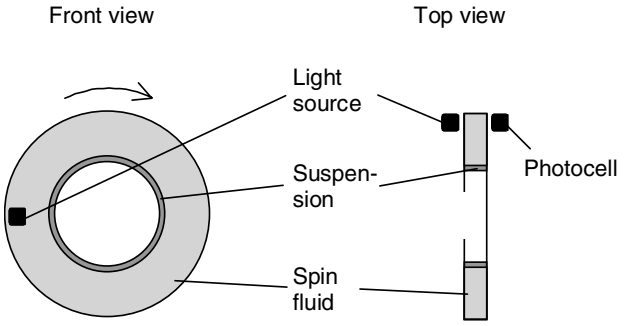

Fig. 10.5.1. Sketch showing the working principle of the disc centrifuge

The output from disc centrifuges has the form of turbidity versus time. The turbidity of a uniform dispersion is given by Lambert-Beer law (Devon et al., 1991):

$$\frac{I}{I_o} = \exp\left(-\tau\ l\right), \tag{10.5.2}$$

where I_o is the incident intensity, I the transmitted intensity, τ the turbidity and l the path length of the light. The theory behind the disc centrifuge has been set out by Allen (1987), although his treatment needs to be corrected on a couple of points of detail. Centrifugal sedimentometers measure dynamically equivalent particle sizes down to a fraction of a micron. They are therefore eminently suitable for cyclones and swirl tubes. Nevertheless, they are very labour intensive, and the technique can be difficult. If one is not careful,

instabilities can occur wherein a whole pocket of the suspension will settle out rather than the individual particles separately ('streaming', a phenomenon similar in nature to the effect of solids loading in cyclones as discussed in the Chap. 9), thereby spoiling the results. Streaming can be revealed by a stroboscopic light, but can also be recognized in the shape of the output curve by a trained operator.

Gravitational, as opposed to centrifugal, sedimentometers are also used to measure particle size distributions. In these, an initially homogeneous suspension is allowed to settle under the influence of gravity in a column. Particle sizes are determined either by sampling or by optical detection.

In the 'Andreasen settling bottle', samples are taken at fixed time intervals at a given level in the suspension. At any given time, particles with a 'critical' size have just settled from the surface of the suspension past the detection level. Particles finer than this are still present at the detection level at their original concentration, while particles coarser than the critical size are not present. The critical size corresponding to each sampling time can be found using Stokes law, and in this way the cumulative size distribution can be calculated directly from the particle concentrations in the samples.

As an alternative to sampling, optical detection of the turbidity of the suspension as a function of height and time is sometimes practiced. This is much less labor intensive than sampling, but, in contrast to the Andreasen settling bottle, a calibration is necessary.

Contrary to the belief of many, these methods are, in principle, suitable down to sub-micron particle sizes. Brownian motion is not a problem, since the displacement due to diffusion is proportional to the *square root* of time, not to time itself (it therefore makes no sense to derive a criterion for whether the method is suitable by comparing the mean displacements due to Brownian motion and due to settling after one second). The biggest problem is convective currents, which can be induced by a nonuniform suspension temperature during the process of settling.

In the 'electrical sensing zone' technique, a current flows between two electrodes placed on each side of an orifice. The particles are suspended in an electrolyte, and are made to travel through the orifice by drawing the electrolyte into the tube through the orifice (Figure 10.5.2). When a particle flows through the orifice, a jump in the current, proportional to the volume of the particle, is registered. This is a standard method for size analysis and is the principle underlying the operation of the popular Coulter Counter, which has been a standard for particle size analysis for the past 30 years. It measures a volume equivalent particle size, and therefore does not take into account the effects of variations in density or shape upon the particle's behavior in a centrifugal separator. This instrument is capable of measuring particle sizes in the 1 to 120 micron range. The range of particle sizes that can be measured in one analysis is limited, since the particle/orifice size ratio needs to be within certain limits. If the distribution is too wide, the solids have to be fractionated

by filtering before analysis. Below a particle size of 1 or 2 microns electrical noise becomes too disturbing and the method becomes difficult to use.

Particle sizing in liquid suspension by 'laser scattering' is becoming very popular. The method is extremely user friendly and reproducible. A suspension of the particles is irradiated with a laser beam, the particles in the suspension scatter the light and their size can be inferred from the scattering pattern, which is detected by ring-shaped detectors. The authors have had mixed success with off-line laser scattering analysis for cyclone characterization. For very large cyclones working with light particles, where the cut size is large, say 20 μm, laser-scattering analyses has resulted in reasonable grade-efficiency curves. For a small cyclone, however, working on a chalk powder and having a cut size of around 1.2 μm, laser scattering gave results that appeared to be inferior to centrifugal sizing. Laser scattering does not give a dynamically equivalent size. The method is less suitable for nonspherical particles, and uncertainly is still high in the sub-micron range.

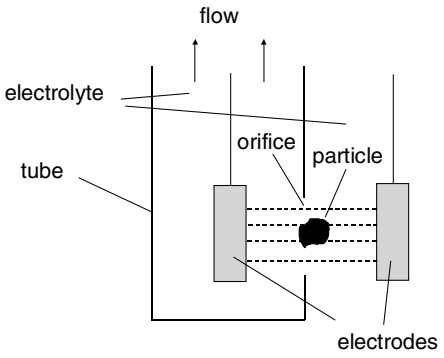

Fig. 10.5.2. Illustration of the electrical sensing zone principle for particle sizing

With any of the methods described above wherein the particles are suspended in a liquid medium, it is important that the medium itself does not significantly interact with the particles, thereby changing their size and/or density. Certain natural organic particles, such as grain flours or wood dust generated from sanding operations, will gneerally swell when suspended in water. They also become "water-logged" over time as a result of water filling up their cellular air pockets. The investigator just needs to be aware of such interactions and choose a suspension medium that is appropriate for the particle under investigation.

We have now looked at some of the different sizing techniques, the issue of off-line *vs.* on-line sizing, and the issue of which measure of particle size we obtain from the different methods. Before closing this section with some recommendations we need to consider one more issue: which type of distribu-

tion do the different methods give us—number, surface or volume—and which type do we actually want?

Let us answer the last question first. We saw in the early chapters that the distribution that gives us the most direct information about cyclone performance and that allows us to convert between cut size and overall separation efficiency is the mass distribution. If the particle density is independent of particle size, this mass distribution is the same as the volume distribution. This distribution is of overriding importance to our cyclone studies.

One question which then arises is, "What do the various particle analyzers measure?" From the electrical sensing zone technique, we get a number distribution, in spite of the fact that the method measures the volume of the individual particles. From the particle volume the instrument computes a volume equivalent particle diameter (see Chap. 2). The instrument then counts and reports the particles within a series of narrow (volume equivalent) diameter ranges.

This method can therefore be characterized as a 'counting technique', as can microscopy and those laser scattering techniques that measure one particle at a time. Although such methods are very precise, it can be difficult to obtain a good volume distribution from them. One has to count 1 million particles of 5 μm for every one particle of 500 μm to get the same volume. In other words: if the size distribution is wide it takes a lot of counting to get enough large particles included for a statistically good result in the coarse end.

Other methods, 'look at' the entire particle assembly together, such that a reading representing the the entire particle assembly has to be deconvoluted to obtain the size distribution. For light scattering methods the scattering pattern from nonspherical particles can give rise to the appearance of 'ghost peaks' in size ranges where no particles are actually present. Experience also shows that laser scattering tends to give wider size distributions than other methods.

The settling methods give us what we want: the Andreasen settling bottle yields a cumulative volume size distribution according to a dynamically equivalent diameter directly, since at any given time particles larger than the critical particle size are no longer detected. The disc centrifuge gives us a differential volume distribution: the turbidity can be shown to be proportional to the volume of the particles in a given band. Another advantage of the disc centrifuge is that it 'sees' only one particle size at a time.

The cascade impactor and cyclone train also give us the appropriate distribution: each captured fraction represents the volume (or actually mass) fraction of solids in the band between the cut diameters of two successive stages. This method also provides us with the dynamically equivalent particle size.

In conclusion, we can say that generating grade-efficiency data places some rather stringent demands on the accuracy of the particle sizing. We saw in Chap. 3 that relatively minor errors in the size data can lead to considerable deviation in grade-efficiency data. In an industrial context, on-line methods

may be best in some situations, while in a laboratory—where the state of dispersion of the test solids is known and controlled—off-line, liquid-borne methods give the best results. For true, accurate results, one should use a sizing technique that gives the dynamically equivalent particle size. The techniques that can do this, however, are cumbersome and labour intensive. If the particles involved are relatively large, a sizing technique based on laser scattering may yield acceptable grade-efficiency data. Electrical sensing zone techniques probably give better results than laser scattering, but may be impractical if the size distribution of the particles is wide. All the same, one should be careful with both laser scattering and electrical sensing zone methods—many industrial solids contain different types of particles, such as pulp and sand particles, with very different shapes and densities. These two techniques will not distinguish between them.

10.A Estimate of Errors

For a series of equivalent and independent observations y_i (i=1...N), the mean or average value is:

$$\langle y \rangle = \frac{1}{N} \sum_{i=1}^{N} y_i. \tag{10.A.1}$$

The variance can be estimated as:

$$s^2 = \frac{1}{N-1} \sum_{i=1}^{N} \left(y_i - \langle y \rangle \right)^2 = \frac{N}{N-1} \left(\langle y^2 \rangle - \langle y \rangle^2 \right), \tag{10.A.2}$$

where the advantage of using the second formula in the equation above is that it is computationally simpler. The estimated standard deviation is simply the square root of the estimated variance:

$$s = \sqrt{s^2}. \tag{10.A.3}$$

If N tests have been made, one would not, of course, just pick out one measurement and regard this as the best estimate of the quantity being measured. Rather, one would report the mean value. If a *series* of such mean values were generated, these would also have a certain standard deviation, which would be smaller than the standard deviation of the individual results. *The standard deviation in the mean values* can be found directly from the standard deviation of the individual results:

$$s_{mean} = \frac{s}{\sqrt{N}}. \tag{10.A.4}$$

We refer to a basic book on statistics for derivation of these results (e.g. Kreyszig, 1970).

If one wishes to estimate the variance (or standard deviation) in a *result* calculated from a number of data $f(x, y, z \ldots)$, each of which have certain standard deviations themselves, we can use *Gauss' formula for error propagation*:

$$s_f^2 = \left(\frac{\partial f}{\partial x}\right)^2 s_x^2 + \left(\frac{\partial f}{\partial y}\right)^2 s_y^2 + \left(\frac{\partial f}{\partial z}\right)^2 s_z^2 \ldots \tag{10.A.5}$$

Let us apply this to the issue of cyclone or swirl tube efficiency. We stated in the main text that including the overhead fraction when calculating the efficiency would result in lower errors.

Let us call the errors in determining each of the three mass flows M_f, M_c and M_e s_f, s_c and s_e, where, again the subscripts f, c and e refer to the feed, the collected, and the emitted particles, respectively. As stated in Chap. 3, we can estimate the efficiency in three ways (Eq. 3.2.2):

$$\begin{aligned} &\text{a)}\ \eta = \frac{M_c}{M_f}, \\ &\text{b)}\ \eta = 1 - \frac{M_e}{M_f}, \\ &\text{c)}\ \eta = \frac{M_c}{M_c + M_e}. \end{aligned} \tag{10.A.6}$$

The two last expressions incorporate the mass flow of the overhead solids, the first does not. Using Gauss' formula with the first expression (10.A.6a) for η gives:

$$s_\eta^2 = \left(\frac{\partial \eta}{\partial M_f}\right)^2 s_f^2 + \left(\frac{\partial \eta}{\partial M_c}\right)^2 s_c^2 + \left(\frac{\partial \eta}{\partial M_e}\right)^2 s_e^2 = \frac{M_c^2}{M_f^4} s_f^2 + \frac{1}{M_f^2} s_c^2 + 0 s_e^2. \tag{10.A.7}$$

We apply the same procedure for the two other expressions for η.

We now assume, as suggested in the text, that the error in each of the measurements of mass flow is simply proportional to the measurement itself, so that:

$$s_f = CM_f,\ s_c = CM_c,\ s_e = CM_e,$$

where C is a constant. This gives, after some simplification, the following three expressions in (10.A.6) for the variance in the calculated value of η:

$$\begin{aligned} &\text{a)}\ s_\eta^2 = \frac{2\left(CM_c\right)^2}{M_f^2}, \\ &\text{b)}\ s_\eta^2 = \frac{2\left(CM_e\right)^2}{M_f^2}, \\ &\text{c)}\ s_\eta^2 = \frac{2\left(CM_cM_e\right)^2}{\left(M_c + M_e\right)^4}. \end{aligned} \tag{10.A.8}$$

For illustration purposes, let us now assume that the cyclone or swirl tube is operating at 95% efficiency and, accordingly, take the values of 1.0, 0.95 and 0.05 for M_f, M_c and M_e, respectively. We then obtain for the three variances the expressions:

$$\text{a) } s_\eta^2 = 1.805C^2,$$
$$\text{b) } s_\eta^2 = 0.005C^2,$$
$$\text{c) } s_\eta^2 = 0.0045C^2.$$

Thus, the estimated variance in the calculated efficiency will be about 400 times greater—and the standard deviation 20 times greater—than the one we would have obtained if we had included the overflow fraction in the calculations. A similar principle is applicable for the calculation of grade-efficiency data.

We have to qualify this discussion, however. If the feed and collected fractions can be determined a lot more precisely than the overflow fraction, we might come to different conclusion when using Gauss' formula with the new estimates of measurement errors. This could result, for instance, if we were able to accurately weigh the feed and the captured solids, while being forced to perform on-line sampling of the overflow fraction.

11

Underflow Configurations and Considerations

The design, operation and mechanical condition of the underflow configuration can, and usually does, strongly impact the separation performance of a cyclone. In reality, the cyclone's performance is just as good as its underflow design. It is the writers' observation that about 90% of all cyclone related problems are due to problems associated with the inability of the 'collected' solids to properly discharge out the underflow. This can be due to a blockage or bridge of some sort or, more often, gas leakage into the cyclone via the underflow piping because of a poor underflow seal.

In this chapter we shall examine a number of issues pertaining to underflow design, including some commonly used geometries, the problem of gas leakage into the bottom of the cyclone, evidence of an improper underflow seal, means of eliminating underflow related problems and how to prevent them in the first place.

11.1 Underflow Configurations

Figure 11.1.1 illustrates six common industrial underflow or 'seal' configurations. Most industrial cyclone systems utilize one of these seal designs or some variant thereof. The primary purpose of these underflow sealing devices is to isolate, more or less, the cyclone from the conditions that exist downstream of the sealing device. Without such a seal, either gas would blow out the bottom of the cyclone or it would flow up the cyclone. Neither of these conditions is normally desirable although a controlled amount of gas 'blowdown' may be specified in some instances for solids conveying purposes.

The rotary lock, 'star' or 'feeder' valve and the screw conveying discharge device, shown in Figs. 11.1.1a and 11.1.1b and 11.1.2, are two devices often used to seal against high differential pressures existing between the cyclone and the underflow. These devices are very suitable for some cyclone applications such as the flour mill application shown in Fig. 11.1.3. However, rotary valves do require motors that render them unsuitable for use inside of vessels

that operate at high temperatures or in situations where the cyclones within such vessels must operate unattended over an extended period—3 to 4 years in some applications.

Blade tips and surfaces, and the inner surfaces of their housings, are subject to erosive wear if the cyclone's discharge solids are abrasive. Rotary feeders are often equipped with bronze or other types of replaceable blade tips for better wear protection or with flexible tips for improved sealing. Both design types are used in applications involving organic materials such as plastics or polymeric solids.

'Flapper' type valves, such as those shown in Fig. 11.1.1c and Fig. 11.1.4 are used to prevent gas in-leakage under discharge pressures only slightly higher than that within the bottom of the cyclone (difference typically less than about 0.3 bar or 4 psi). This valve may be located in a solids receiving vessel whose contents may or may not be fluidized. If the solids are fluidized, the valve is often submerged about a meter below the surface of the fluidized bed. If the solids within the receiving vessel are not fluidized, the valve must be located in the 'freeboard' region above the surface of the bed.

Flapper valves are normally subjected to a somewhat higher pressure outside the valve than that inside the valve. This tends to hold the hinged flapper plate closed. Solids raining down the dipleg, however, will eventually create sufficient static pressure head to force the flapper plate to open. This allows some or all of the solids in the dipleg to 'dump' out the valve and, when this happens, the valve closes and the fill and dump cycle repeats. This assumes that the solids remain freely flowing and do not defluidize within the dipleg. An excessively long solids residence time within the dipleg can lead to solids compaction and the inability of the solids to discharge properly. This, in turn, can lead to "dipleg flooding" and a significant decrease in cyclone collection performance.

The flapper plate is usually hung with a positive closing tilt of about 3°. This is not done for the purpose of building up a solids level above the valve since the back-force created by such a small tilt for normal flapper valves is negligible. Rather, the tilt is provided to prevent the valve from hanging open, and losing its seal, should the dipleg itself be installed slightly off true vertical or should the dipleg tilt so as to open the flapper valve during operation. The latter can occur particularly in vessels containing cyclones that experience a large thermal change upon startup. Such startups can subject the cyclone and diplegs to temperature increases of 800°C or more.

The flapper valve shown on the right-hand side of Fig. 11.1.4 is normally installed where it is readily accessible for routine inspection through an easily opened access door, as shown.

Flapper valves are used to seal both high and low solids-loaded cyclone underflows although the valve type shown on the left hand side of Fig. 11.1.4 is more commonly used with lightly-loaded, 'second-stage' cyclones operating in a fluid bed environment.

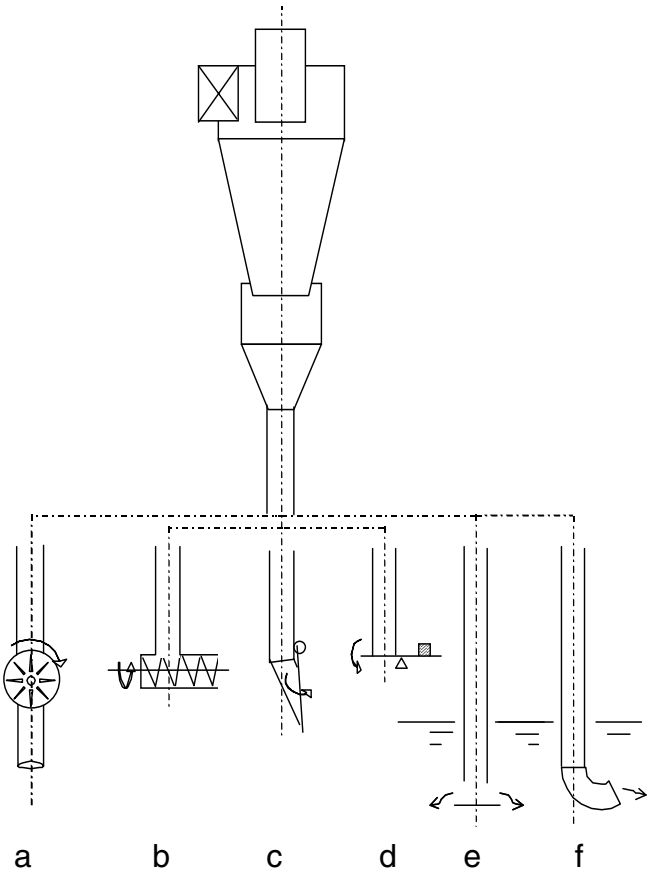

Fig. 11.1.1. Conventional cyclone featuring six common types of underflow 'seal' configurations:
a) Rotary lock (star) valve (working principle much like a revolving door)
b) Screw (extruder) discharge
c) Flapper valve (flap fixed with a hinge above the dust discharge orifice)
d) Counter-weighted valve (should not be submerged within a fluid bed)
e) Submerged dipleg
f) Submerged 'J-bend'

The counter-weighted 'flapper valve' depicted in Fig. 11.1.1d is very similar to the flapper valves described above but it has a counter-weight whose mass and moment arm can be adjusted to control the closing force or, equivalently, the force the dipleg solids must overcome to open the valve. These valves are somewhat more complex than their simple flapper valve counterparts but they are capable of generating a more positive seal. Unlike the flapper valve,

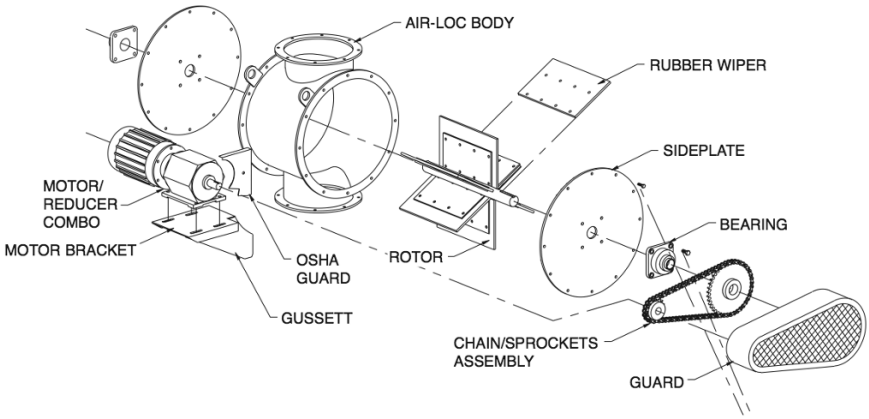

Fig. 11.1.2. Rotary Valve/Feeder components. Courtesy Koger Air

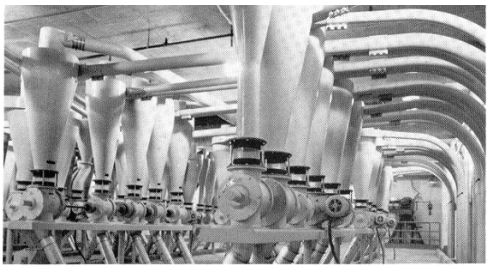

Fig. 11.1.3. A flour mill plant featuring a multiple arrangement of cyclones equipped with bench-mounted rotary air lock valves, and sight-glasses above the valves. Courtesy Kice Industries

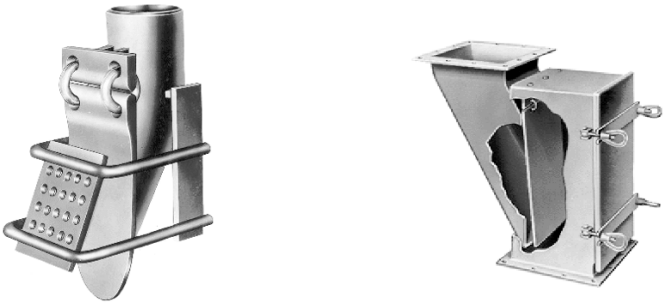

Fig. 11.1.4. Flapper-type underflow sealing valves featuring free-swinging hinged seal plates. Ducon type CA Trickle Valve (left) and type FA Trickle Valve (right). Courtesy Ducon Technologies Inc.

however, and because of their hinge mechanism, they are not submerged in fluidized solids.

Figs. 11.1.1e and 11.1.1f illustrate a fluid-type of underflow seal wherein the underflow piping or dipleg is partly submerged within a fluidized bed. In Fig. 11.1.1e, a circular 'splash' or 'dollar' plate, located about 1 to 1.5 pipe diameters below the dipleg opening, is used to both prevent rising gas bubbles within the bed from flowing up the dipleg and to help spread out the solids exiting the bottom of the dipleg. In Fig. 11.1.1f, a section of curved pipe, known as a 'J-bend', is used to prevent rising gas bubbles from entering the dipleg opening. J-bends, unlike conventional dollar plate closures, tend to direct their solids in a specific direction. This can, in some circumstances, be a desirable factor when one is contemplating which direction the solids should be discharging. Furthermore, since the J-bend is directly welded to the dipleg, there is no need for bars or angle iron supports to position and hold a bottom plate, as is the case with the dollar-plate design.

Submerged seals are very commonly employed to seal the underflow piping in highly-loaded primary or rough-cut cyclone systems. In such cases, the intent of the seal is to help minimize the amount of entrained gas exiting out the bottom of the cyclone. By discharging the solids 1.5 to 2 meters below the bed surface, this type of underflow seal prevents solids from being immediately reentrained were they simply dumped above the bed.

A cyclone installed to separate liquid from a carrier gas is normally equipped with a liquid drain pipe that is submerged at its bottom end in a pool of liquid. This type of seal is very similar to that shown in Fig. 11.1.1e. The drain pipe must be of sufficient height above the gas-liquid interface level to overcome the suction created by the cyclone. In systems where foaming is possible, such an underflow seal must also take into consideration the decrease in liquid density brought about by foaming.

11.2 Importance of a Good Underflow Seal

As a rule, it is vitally important that a cyclone be operated at all times with a good underflow seal. All underflow seals in gas-cyclone systems allow some gas in-leakage, however, if the discharge pressure is greater than that which exists at the bottom of the cyclone.

Rotary lock valves allow gas to leak around the flat circular side plates and through the space between the tips of their rotating blades and the mating surface of their housing. They also 'pump' gas from the high-pressure side to the low-pressure side due to the conveying action of their rotating pockets. Screw conveyors also leak around the tips of their conveying flights. Their rotating screws can also act as gas 'pumps'. Flapper valves will normally permit gas to leak inwards over the entire perimeter of their elliptical openings. This occurs to some extent even when the valve is closed, depending on the physical condition of their mating surfaces. The valve loses even more of its

sealing capability when the discharging solids force it to open (even though it normally opens less than 10 degrees).

Counter-weighted flapper valves generally do not leak as much gas as flapper valves. This is because, unlike the flapper valve, the discharging solids tend to spread out around the entire perimeter of the circular opening when the valve opens (normally only slightly) and because the circular opening has a smaller perimeter compared to the elliptical flapper valve.

Leakage out of 'open' diplegs submerged within a fluidized bed takes place due to entrained gas being conveyed out with the solids. Because of their relatively high solids flow rate, this outgoing gas leakage is more pronounced in highly-loaded primary cyclone diplegs (those likely to be equipped with dollar plates or J-bend type 'seals'). It is reduced with increasing dipleg submergence. Increased submergence provides the solids more time to deaerate before they exit the dipleg. It also produces greater static pressure at the bottom of the dipleg. This, in turn, creates a higher column of solids and more solids compaction at the bottom of the dipleg.

Although gas leaking out the underflow of a cyclone can pose an operating problem, it is normally far more important to limit in-leakage or gas flowing up the solids discharge opening. From a separations point of view, a little positive gas 'blow-down' can be slightly beneficial. Negative 'blow-down' or upflow, is potentially disastrous from a separations viewpoint.

If gas flow up the solids discharge opening is not adequately restricted, such upflow will reentrain some fraction of the solids attempting to make their way out the underflow. This will produce a degradation in overall separation performance as solids that otherwise would have been collected will be conveyed out the gas overflow pipe. In addition, upflow will set up a gas and solids recirculating flow pattern within the cyclone. These two effects are illustrated in Fig. 11.2.1.

Gas upflow and solids recirculation are not independent phenomena. Some portion of the solids that are reentrained (namely, the coarser fraction) will be centrifuged back to the wall of the cyclone where they will have the effect of generating an increase in effective wall roughness. This, in itself, will weaken the spin intensity within the inner vortex and thereby increase the cut-point diameter and the solids loss rate. If the solids are abrasive, the resultant increase in solids circulating on the walls will also increase the wall erosion rate thereby shortening the life of the unit. If the solids happen to be sticky or tacky, the increase in solids traffic at the walls will tend to promote the formation of wall deposits. This also acts as an additional wall roughness and, it too, reduces overall separation performance. Moreover, solids caught up in such an internal recirculation pattern will be subjected to what may be described as a 'closed-circuit grinding machine' and this will bring about an increase in their attrition rate. In addition, any coarse/abrasive solids that are entrained out the overflow as a result of gas upflow will increase the rate of erosion of the inside walls of the vortex finder and all downstream piping.

If they happen to be sticky solids, they will increase the rate of fouling of the downstream piping.

Obviously, cyclones should be designed, operated and maintained to minimize gas leaking up their solids discharge openings as this can bring about a host of process and operational problems. In practice inleakage can often be controlled by:

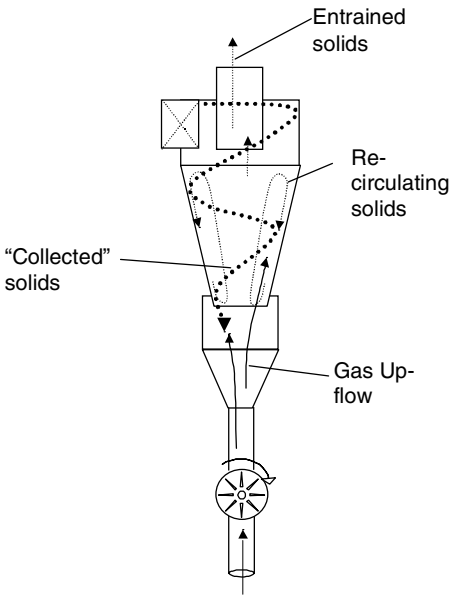

Fig. 11.2.1. Gas upflow illustrating solids entrainment and recirculation

1. maintaining as small a clearance as possible with rotary lock and screw discharge devices.
2. maintaining an adequate seal on the mating surfaces of flapper valves and counter-weighted valves.
3. ensuring that flapper valves and open-ended diplegs are adequately sealed (submerged) if they terminate within fluidized beds.
4. avoiding excessive aeration of any diplegs or the hopper into which the solids discharge.

One also has to inspect any access or inspection hatches, light and sight ports, and any flanges for the possibility of gas leaking into the cyclone. This is especially true if such features are located in the lower cone, hopper or dipleg regions. Obviously, holes resulting from erosion or corrosion should be repaired as soon as conditions permit.

If the above were not sufficient reason to do whatever is necessary to minimize excessive gas upflow, it's worth pointing out that gas upflow, if sufficient, will affect the stability of the inner vortex and may shorten its 'effective length', thus reducing separation performance and possibly increasing erosion in the cone area as well as solids entrainment.

The amount of upflow a cyclone can tolerate without serious impairment of its performance is not something one can calculate from first principles or predict from models. The answer depends on a number of complex factors—not the least of which is the settling velocity of the solids (*i.e.*, their mass and size). Fortunately, most cyclones can tolerate a small amount of upflow (of the order of 2 or 3% of its inlet volumetric flow rate) without incurring a serious performance degradation. Rather, the problems caused by upflow most often occur in the underflow piping. Here the solids that were separated in the main cyclone body are concentrated and must travel downwards against any rising gas 'leakage' flow.

11.2.1 Inleakage Example

In the simple example shown in Fig. 11.2.2, we find two cyclones of identical design but with differing solids discharge diameters. Let us assume that both cyclones are operating in a plastics processing plant under identical conditions, and are subjected to the same rate of upflow gas, Q. The only difference between the two operating cyclones is that the one on the LHS is equipped with a solids discharge pipe of inside diameter D_t; that on the right with one having discharge diameter $D_t/3$.

It follows that the gas rise velocity for the dipleg on the RHS will be 9 times greater than that on the LHS.

Let us now assume that the solids loading is rather low and that the upward gas rise velocity in the smaller dipleg is 1.4 m/s. Let us also assume that we know from laboratory testing that this is sufficient to entrain all particles smaller than about 720 μm in diameter or 95% of all the solids attempting to exit the cyclone.

Obviously, this situation could pose a problem as most of the solids attempting to exit the dust hopper would find it difficult to enter the dipleg. We could expect that many of the solids—especially the finer fractions—would become reentrained in the rising vortex core and exit out the overflow piping. This situation also could be expected to lead to gross solids recirculation with the hopper.

On the other hand, the gas velocity in the larger dipleg would be only 0.16 m/s, which, from entrainment tests, is conservatively estimated not to entrain particles larger than about 200 microns, or about 0.2% of the collected particles. Of the two designs, it is clear that a larger diameter dipleg is far less likely to cause underflow problems.

The above example is a simplified description of a situation that existed and was successfully remedied in an actual operating plant. The leakage was

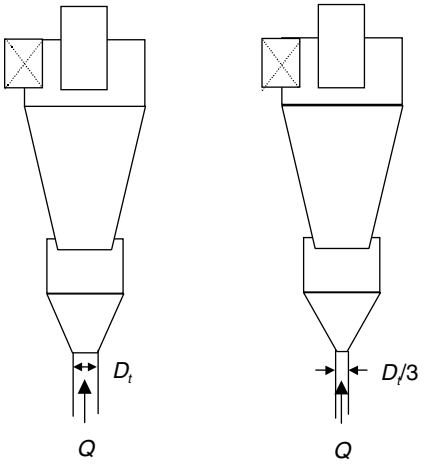

Fig. 11.2.2. Gas leakage in two cyclones of differing solids discharge pipe diameter

produced by the suction created from the inlet-to-underflow pressure drop across the cyclone. A rotary lock valve of excellent design was installed in the underflow piping. Still leakage through this valve resulted in the situation described above. This example again only emphasis the need for designers to take the 'systems approach' to the design of a cyclone installation.

11.3 Upsets Caused by 'Too Good' an Underflow Seal

Flapper valve seal. Under some unique operating and design conditions it is possible for the underflow seal to be so effective that the solids within a cyclone dipleg defluidize due to a lack of aeration. If this were to occur, solids would back up into the cyclone and produce a condition known as 'flooding'. The solids would build up to some equilibrium level within the cyclone and, after this, the cyclone would behave like a 'tee' in the line and exhibit no separation ability. This condition, though rare, is most likely to occur in the start-up phase of cyclones equipped with flapper valves. The mating surfaces of such valves are often machined (thinking that this makes them 'better valves') and are therefore able to form a very 'good' seal. If such valves are operated in an environment wherein the pressure outside the valve exceeds that within the valve (which is almost always the case for such valves), the solids collected by the cyclone may simply collect within the valve and in the lower section of the dipleg and defluidize. Having defluidized, the solids will be unable to exert static pressure head upon the inside surface of the flapper plate; rather, they will 'bridge' and exert a radially directed pressure upon the dipleg walls.

It is possible to avoid such solids bridging by modifying the flapper valve assembly so that a small amount of gas can leak into the valve and maintain some fluidization of the dipleg solids. This can be achieved by suitable modification of the flapper valve assembly. Once the flapper valve assembly has been in service for some time, normal erosive wear of the mating surfaces will automatically permit sufficient leakage to prevent solids compaction.

Active aeration of diplegs is normally undesirable since the aeration piping will generally not hold up over an extended period in the rather severe operating environment in which they normally operate.

Defluidized Bed. Another cause of upsets is that resulting from a dipleg that terminates in a poorly aerated region of a fluidized bed. This can apply to flapper valves and to 'open-ended' diplegs, such as those that terminate with dollar plates or J-bends. The way to avoid such an upset is to design for sufficient aeration in the region where the dipleg or diplegs will terminate within the bed. Related to this is the special case of a dipleg being submerged too deeply within a fluidized bed.

Wang et al. (2000) studied the flow in a dipleg, 80 mm diameter by 4.6 m long, returning solids to a fluidized bed in a dedicated experimental setup. They distinguished four different flow regimes that may exist. They are, navigating down the dipleg:

1. rotating gas flow with the solids concentrated at the wall ('inlet region')
2. 'dilute' solids-gas flow with an overall solids volume fraction of 0.05-0.1. Here, the solids travel in 'strands', having a slip velocity with the gas an order of magnitude higher than the terminal velocity of an individual particle
3. 'dense' particle-gas flow low in the dipleg wherein the solids volume fraction is about 1/3, and the solids are in a fluidized state
4. 'packed' bed, where the solids are supported, in part, on the side wall, as in hoppers, and the solids flow is intermittent

Wang et al. studied the velocity distribution and the solids volume fraction by optical probes, and the axial pressure profile in the dipleg. They found that flow types 3 or 4, listed above, might or might not be present, depending on how the rig was operated. When only types 1 and 2 were present, the gas underflow or 'blowdown' out the dipleg was excessively high. In the other extreme, if a packed bed was present (flow type 4), the solids flow would be disrupted, possibly leading to 'flooding' of the cyclone as mentioned above. The optimal regime is thus when type 3 flow, a dense flow of aerated solids, prevails low in the dipleg.

Which flow regimes were present in the dipleg during a given experiment depended on the solids circulation rate and on the submergence depth of the dipleg end in the fluidized bed: if the submergence depth was insufficient for a given solids circulation rate, only flow types 1 and 2 would be present, while if it was too deep, a packed bed could develop. An increase in the solids circulation rate led to a smaller optimal submergence depth.

Figure 11.3.1 shows typical pressure profiles from the paper. For the case where flow types 1, 2 and 3 prevail, the pressure profiles in the two lower sections (where there is negligible rotation, and on the average a uniform distribution of solids over the cross section) represent a 'hydrostatic' pressure increase, which more or less agrees with what one would calculate from the bulk density of the solids and gas in the section. On the other hand, when a packed bed develops in the lower part of the dipleg, the material is supported off the side wall, like in a silo, and the pressure profile is no longer described by a 'hydrostatic' type of linear pressure increase with depth.

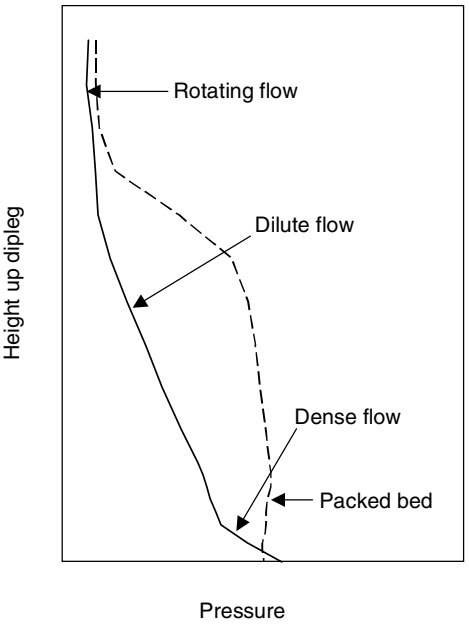

Fig. 11.3.1. Pressure profiles from the paper of Wang et al. (2000). The fully drawn curve is for a case where flow types 1, 2 and 3 are present, the broken one for a case where a packed bed (flow type 4) has developed

As we reflect back on the material above, it should be clear that there is much more to cyclone design than just the cyclone itself. Good cyclone design practice and operation accounts for all those components of the system of which it is a part and with which it interacts. One cannot design or specify a flapper valve, for instance, without thinking about how it will affect the cyclone—both during normal operation and upon startup. One cannot design a fluid-bed aeration system without thinking about where the cyclone diplegs will terminate and the need for adequate aeration. Components cannot be designed in isolation of one another. Design disciplines interrelate and, when things go wrong, they often do at the discipline interfaces.

11.4 Second-Stage Dipleg Solids 'Backup'

Figure 11.4.1 is a simple illustration of an internal, two-stage cyclone system contained within a fluidized bed vessel (typically a reactor or regenerator). We wish to compute the 'backup' h of the solids within the second-stage dipleg above the fluid bed level, which is at the vessel's lower cylindrical/conical transition.

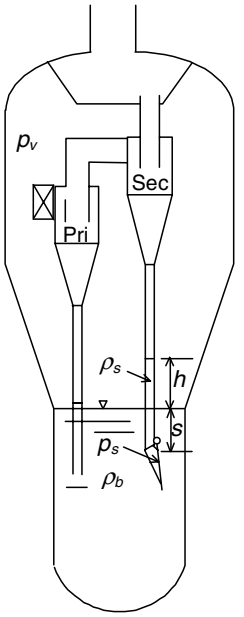

Fig. 11.4.1. Sketch of a fluidized bed vessel with primary and secondary stage cyclones with diplegs

If p_v is the pressure in the vessel's 'dilute' phase (above the fluid bed) then:

$$p_v - \Delta p_{pr} - \Delta p_s + \rho_s g h + \rho_s g s = p_s. \tag{11.4.1}$$

In addition, for equilibrium between the pressures on the two sides of the flapper valve, which occurs when it is just about to open:

$$p_v + \rho_b g s = p_s. \tag{11.4.2}$$

Here, p_s is the pressure within and near the bottom of the second-stage dipleg; Δp_{pr}, Δp_s are the pressure drops across the primary and second-stage cyclones, respectively, ρ_s and ρ_b are the bulk densities of the dense-phase

solids in lower section of the second-stage cyclone diplegs and in the vessel bed, respectively; h and s are the height of the solids 'backup' in the second-stage diplegs above the bed interface, and the second-stage dipleg submergence ('seal'), respectively.

Substituting Eq. (11.4.1) into Eq. (11.4.2) and solving for h gives:

$$h = s\left(\frac{\rho_b}{\rho_s} - 1\right) + \frac{\Delta p_{pr} + \Delta p_s}{\rho_s g}, \tag{11.4.3}$$

which is the 'backup' height of solids above the 'dilute-phase/dense-phase' fluidized bed interface. We observe that this backup height depends on the specific weight of both the fluid bed solids and the dense-phase bed within the second-stage cyclone's dipleg, as well as the submergence height s and the pressure drop across both cyclone stages. This pressure drop includes losses across the primary cyclone (including any inlet 'acceleration' loss), that across the primary-to-secondary transition or connecting ducting, and the pressure loss from the inlet of the second-stage cyclone to bottom of the second-stage cyclone. Lacking better information, this latter inlet-to-bottom or inlet-to-underflow pressure loss may be assumed to be approximately 30% of the inlet-to-overflow pressure loss across the second-stage cyclone. In Chaps. 4 and 6 we have examined cyclone models that permit us to compute the 'wall' pressure loss. This 'wall loss' is normally a good estimate of the inlet-to-underflow pressure loss. Note that these statements are only true if the vortex does not penetrate to the bottom of the cyclone, for instance when a vortex stabilizer installed. If the vortex is allowed to reach the bottom of the cyclone, the static pressure there is very close to—or may even be lower than—the static pressure in the vortex finder.

The interaction of the variables affecting the backup height h shown in Eq. (11.4.3) has some very significant consequences for both the designer of such systems and for operating personnel. If, for instance, the dipleg is submerged too deeply (large s), or if the overall pressure loss is too large or the specific weight of the second-stage dipleg solids too low, h may increase to the point where the solids back up into the second-stage cyclone(s). This can happen, and has happened, in commercial units when the distance from the bottom of the second-stage cyclone to the bed level was too small. If the diplegs do 'flood' due to excessive solids backup the separation performance of the second-stage cyclone will be adversely affected as previously collected solids become reentrained out the second-stage cyclone's gas outlet pipe. Although not always directly observable, such a problem will normally result in a cyclic type of 'puffing' of solids out the overflow.

A worked example for the calculation of solids back-up in diplegs is included in Appendix 11.A. In addition, a quantitative estimation of the different contributions to the solid back-up in diplegs on basis of a moment balance on flapper valves is included in Appendix 11.B.

One may wonder why the flapper valve is ever used if the second-stage cyclone's dipleg is submerged (and therefore, sealed) below the surface of the

fluidized bed? There are two reasons—both intended to prevent the destructive effects of gas upflow:

1. flapper valves are generally needed to seal the second-stage cyclone diplegs upon startup when bed solids are being fed to the vessel during which time the bed level is below the bottom of the diplegs
2. flapper valves prevent gas upflow into the diplegs if the vessel's bed level were to drop and unseal the diplegs.

In the discussion above, very little has been said about the primary cyclone. This is because primary cyclones typically have a low pressure loss and normally seal very well against upflow if their diplegs are submerged in the fluid bed. Secondary cyclones, on the other hand, normally operate at a substantial pressure loss and, hence, 'vacuum' relative to the vessel pressure. This is because the 'suction' in the lower part of the second-stage units includes a number of pressure losses, namely:

1. primary inlets (inlet gas and solids 'acceleration' losses),
2. primary cyclones themselves, particularly the vortex finder,
3. second-stage cyclones' inlet chutes and,
4. secondary cyclones.

Primary cyclones can, however, allow considerable amounts of entrained and educted gas to flow out the bottom of their diplegs.

11.5 Hopper 'Crossflow'

When a parallel arrangement of two or more cyclones share a common dust hopper or underflow chamber the potential exists for hopper 'crossflow' or 'cross-talk'. It occurs when the following two conditions are present:

1. The inlet flow is not evenly divided among the cyclones.
2. The cyclone underflows are not isolated (sealed) from one another.

In reality, some crossflow occurs in all cyclones that share a common hopper or underflow chamber. (It also occurs in a similar separator, known as a hydrocyclone that is widely used to separate or classify solids from a carrier liquid). A nonuniform flow to the cyclones produces a variation in pressure within the solids discharge piping of the individual cyclones. This imbalance results in some 'blow-down' of gas out of one or more of the cyclones and a compensating upflow of gas in one or more of the remaining cyclones. As a general observation, the 'blow-down' does not negatively affect separation performance and actually improves the solids collection performance of those cyclones experiencing blow-down. Unfortunately, the separation performance of those cyclones that experience gas upflow may be seriously impacted. The extent of the impact relates to both the extent of the inlet maldistribution and the 'tolerance' of the cyclones to upflow as established by the design.

The best way to avert hopper crossflow is to design the cyclone system so that the incoming gas splits evenly among the various cyclones operating in parallel. In analogy to an electrical circuit, if the gas flow or, its analog, *current* is to be evenly divided, the *resistance* that the incoming gas must experience from inlet-to-overflow and from inlet-to-underflow must also be identical for each of the cyclones operating in parallel. Thus, a parallel arrangement of cyclones is analogous to an electrical circuit, as shown here in the two-cyclone configuration of Fig. 11.5.1.

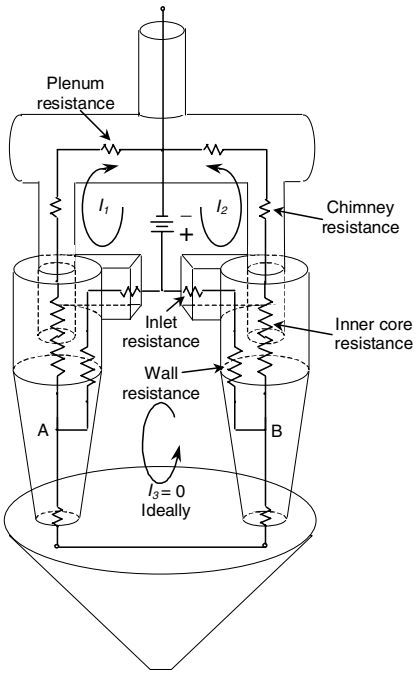

Fig. 11.5.1. An electrical analog of a parallel arrangement of two cyclones sharing common overflow and underflow plenums

From this simple electrical analog representation, it can be observed that, in order to avoid hopper crossflow (*current*), the pressure or *voltage* at points A and B must be equal. That is,

$$V_A = V_B. \tag{11.5.1}$$

For this to occur, all *resistances* in current loops 1, 2 and 3 for the cyclone on the left side of the figure must be equal to their counterparts on the right side of the figure. These *resistances* include that of the inlet chute, the wall, the vortex core, the chimney, the plenum chimney and that of the cone discharge opening, for the case illustrated in Fig. 11.5.1. If this conditions is met then,

$$I_3 = 0 \tag{11.5.2}$$

and no *current* (gas) will flow in the I_3 current loop connecting points A and B. Thus, no hopper crossflow will occur. If the condition mentioned above is not met, then a gas *current* (flow) will occur within the hopper or bottom plenum chamber. Although it may not be obvious at first, even a small *potential* (pressure) difference between points A and B can lead to significant hopper *current* since the *resistance* (associated with the cone discharge openings) is normally very small.

If the underflow or solids discharge openings are designed so that they cannot 'communicate' with one another, such as their being sealed in a fluid bed or their isolation through the use of rotary lock or flapper valves, then the two resistances shown at the solids discharge opening in Fig. 11.5.1 take on the ideal value of infinity. This prevents hopper crossflow even if the other resistances associated with current loop I_1 do not equal those in current loop I_2. If these resistances are different, the gas flow to each of the two cyclones will differ. Even so, this is seldom a problem in practice since the flow imbalance is normally less than a few percent and the effect this has on the overall performance of most commercial units is negligible. In contrast, any gas flow through the hopper can be a cause of considerable concern.

An electrical circuit analogue can be very useful for visualizing a flow configuration qualitatively. Still, it has its limitations. When the flow is turbulent, as it mostly is, it is proportional to the square root of its driving force, the pressure drop, while an electrical *current* is directly proportional to its driving force—the *potential difference* to the first power. In the case of cyclones, where swirling flows are involved, the 'pressure' we are referring to is the total pressure: static and dynamic together. Our losses due to the resistances are the dissipative or frictional losses.

11.6 Hopper Venting Options

It is frequently necessary to install a cyclone atop a solids receiving vessel or hopper. Often the solids within the hopper must be 'aerated' so that they will freely flow out the bottom of the hopper and not compact. The issue which then arises is, "How does one handle the vent gas?" As shown in Fig. 11.6.1, several options exist, and we shall briefly enumerate and discuss these below.

Option A.—Here the solids discharge pipe or 'dipleg' empties directly into the aerated hopper and aeration gas is forced to flow up the dipleg. As discussed above, such a design may lead to a significant deterioration in cyclone performance because of vent gases flowing up the same pipe through which the solids are attempting to discharge. This would be the case, especially, if the superficial rise velocity of the gas in the dipleg were significantly greater than the settling velocity of the solids.

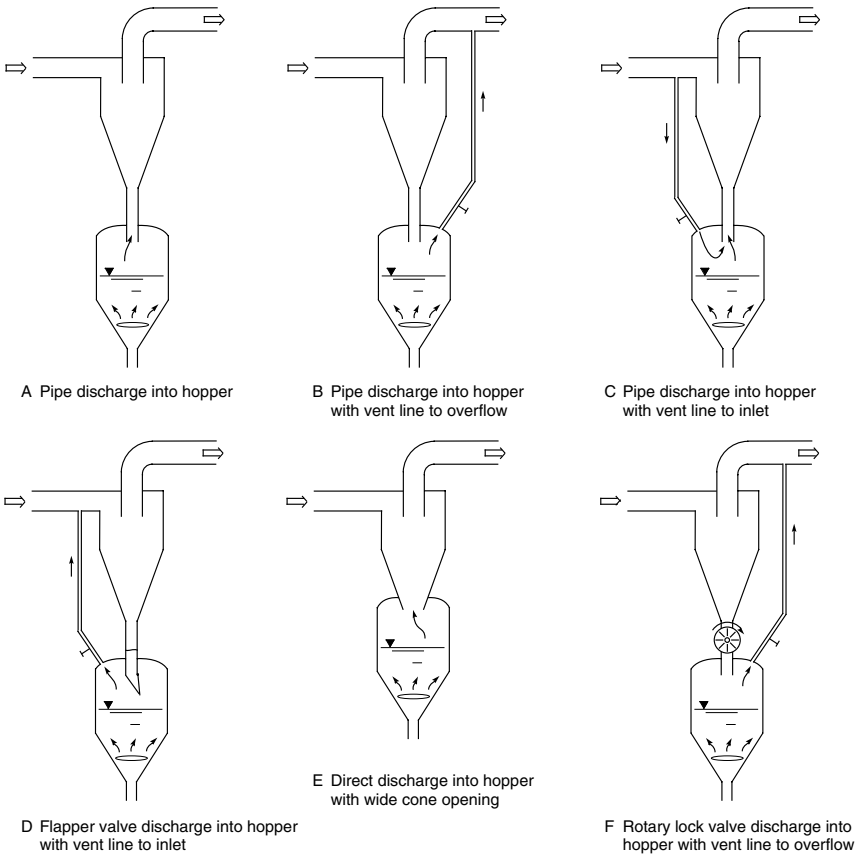

Fig. 11.6.1. Options for hopper venting

Option B.—In this configuration the vent gases are routed to the cyclone overflow piping. Since the pressure within the overflow pipe is normally significantly less than that within the bottom of the cyclone (and hopper), there exists a natural tendency for the vent gases to escape the hopper and flow up the vent line. Some vapors exiting the cyclone underflow line, and a portion of the solids entrained within these vapors, will also ?ow up the vent pipe as well. Still, this arrangement generally avoids the problem described in Option A above. This configuration, however, may not perform satisfactorily if the vortex extends down into the hopper since this would set up a competing low pressure path for the hopper vent gases.

Option C.—If one attempts to vent the hopper back to the cyclone's inlet pipe or duct two problems can occur. First, the higher pressure in the inlet piping will force some of the inlet gases and solids to flow down into the hopper. This gas, along with some fraction of the solids conveyed downwards

with this gas, will then be forced to flow up the cyclone's solids discharge pipe. Secondly, hopper aeration gas will also escape by flowing up the cyclone discharge pipe, as it would in Option A above. Such a vent design is not recommended without some sort of sealing device on the dipleg. Although rarely done, the section of the inlet where the vent pipe connects to the inlet ducting may be converted into a venturi type eductor. This configuration, if properly designed, would ensure that all hopper vent gases (along with some gas and entrained solids exiting the cyclone underflow) would be routed back to the cyclone inlet.

Option D.—This option is very similar to Option C except that it uses a flapper valve to seal the solids discharge pipe. Vent gases, along with any solids that this gas may contain, are routed back to the cyclone's inlet. This arrangement has the advantage of forcing solids entrained by the hopper aeration gas back into the cyclone where they are subject to capture. However, in order for this configuration to properly work, the hopper must operate at a somewhat greater pressure than the pressure at the inlet to the cyclone. This also means that, in practice, it will operate at a pressure greater than that at the bottom of the cyclone and that existing within the dipleg. This will tend to cause solids to build up in the dipleg to whatever height is necessary to force the flapper plate to open against the differential pressure existing between the top of the dipleg and the dilute phase of the hopper. Because of this backup of dipleg solids, one must allow adequate dipleg height to avoid solids backing up into the cyclone itself. The reader may note that this arrangement is, from a fluid flow point of view, no different from that in a conventional fluidized vessel containing overhead cyclones whose diplegs terminate in flapper valves above the bed.

Option E.— This simple option is very similar to that shown in Option A. Here, hopper vent gases are forced to flow up the cyclone, as is the case for Option A. However, unlike Option A, the area available for upflow is much larger. Under these conditions, it is possible for the solids to spiral out the bottom cone opening along the cone walls while the vent gas flows (via a separate path) upwards through the middle of the cone opening. The vortex within the cyclone will impart some spin to this upwards flowing gas and solids mixture and this can be expected to separate out some of the solids entrained by the hopper aeration gases. With this design it is recommended that the hopper aeration be limited to the minimum amount required to prevent solids compaction within the hopper and that the superficial velocity up the cyclone discharge opening be maintained less than about 1 m/s. Field or laboratory tests may need to be performed to establish the maximum amount of aeration gas permissible. If the hopper is subject to periodic dumping of its contents, it may be acceptable to increase the hopper aeration rate during the actual dumping operation.

Option F.— This last option, which utilizes a rotary lock valve on the cyclone underflow line is a very effective way of preventing hopper aeration gas and entrained solids from flowing back up the cyclone. Like Option B, the

relative low pressure that exists in the cyclone overflow line helps to withdraw hopper vent gases out the overflow. Of course, some portion of the solids entrained in the vent gas will also be conveyed into the overflow line. Even so, this is a very widely used configuration, especially in applications where the solids are not too abrasive and where the valve is readily accessible for routine inspection and repair. Also, as mentioned in Option C above, if the inlet were to be equipped with an eductor section, the vent line could be routed back to it.

In those configurations shown above requiring a vent line, it is almost always necessary to install one or more block valves so as to help set the vent gas flow and for isolation purposes. If the solids are erosive, one must limit the velocity within the vent line to acceptable levels (generally under 30 m/s) so as not to erode the vent line piping. Vent line elbows, valves and any flow restriction orifice that may be present are especially vulnerable to erosive attack. Special erosion resistant, double-block valves may be necessary under highly erosive conditions.

11.A Dipleg Calculation

A fluid-bed cyclone system is designed with a 1.52 m submergence of the second-stage diplegs. The pressure drop from inlet of the primary cyclones to bottom of the secondary cyclones is estimated to be 11 kPa at maximum flow conditions. Solids 'bulk' densities under operating conditions are estimated to be 640 kg/m^3 for the bed and only 320 kg/m^3 for the second-stage diplegs. We wish to compute the second-stage cyclones' dipleg 'backup' height, h.

Solution

Substituting the above numbers into Eq. (11.4.3) we find:

$$h = 1.52 \text{ m} \left(\frac{640 \text{ kg/m}^3}{320 \text{ kg/m}^3} - 1 \right) + \frac{11000 \text{ Pa}}{320 \text{ kg/m}^3 \times 9.81 \text{ m/s}^2} = 5.0 \text{ m}$$

In this case, one would want to make certain that the bottom elevation of the second-stage cyclones (top of diplegs) is located at least 5 m above the bed surface. In practice, this design would call for a 6 m, or greater, elevation difference.

11.B Moment Balance on Flapper Valve Plate

If we perform a moment balance about the hinge rings of a typical flapper valve plate, we can quantitatively predict the effect that the flapper plate

weight and tilt has on the solids 'backup' within the dipleg. We shall make our analysis sufficiently general so that it also includes the more customary effects of flapper valve submergence and the suction pressure imposed by the cyclone.

We begin by performing a basic moment balance using the forces and moment arms shown in Fig. 11.B.1. This moment balance is taken about the hinge rings located at the top end of the flapper plate. At the point where the solids level in the dipleg is just sufficient to begin opening the valve the moment balance becomes:

$$(W_{fp} - B_{fp})\ r_e + r_i A_i\,(p_e - p_i) = 0 \tag{11.B.1}$$

where W_{fp} and B_{fp} are the weight of the flapper plate and boyancy force acting on the flapper plate; r_e is the projection of the radius vector normal to the forces W_{fp} and B_{fp}; r_i is the radius vector projection normal to the (resultant) force $A_i(p_e - p_i)$; p_e and p_i are the pressures inside and outside the flapper valve, respectively, at bed submergence level s; and A_i is the elliptical area of the flapper plate exposed to inside flapper valve pressure p_i.

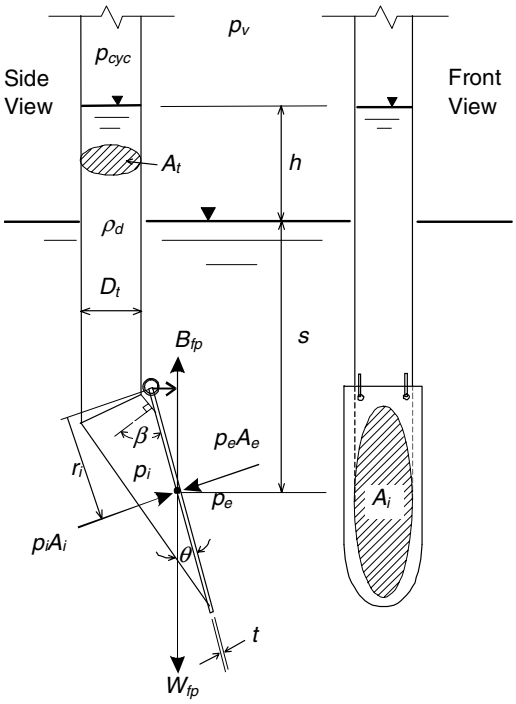

Fig. 11.B.1. Forces acting on a flapper valve plate submerged in a fluidized bed

Now,

$$A_i = \frac{A_t}{\cos\beta} = \frac{\pi D_t^2}{4\cos\beta} \tag{11.B.2}$$

$$p_i = \rho_d g\,(h+s) + p_{cyc} \tag{11.B.3}$$

$$p_e = \rho_{bed} g s + p_v \tag{11.B.4}$$

$$W_{fp} = lwt\rho_{fp} g \tag{11.B.5}$$

$$B_{fp} = lwt\rho_{bed} g \tag{11.B.6}$$

$$r_e = r_i \sin\theta \tag{11.B.7}$$

where D_t andA_t are the inside diameter and cross-sectional area of the dipleg, respectively; β is the angle between the flapper plate and a line drawn normal to the lower, mitered pipe section of the flapper valve (as shown in Fig. 11.B.1); θ is the angle between the flapper plate and true vertical; ρ_d, ρ_{bed} and ρ_{fp} are the densities of the dipleg solids, bed solids, and of the flapper plate; p_{cyc}, $p_v$are the pressures within the dilute phase of dipleg (at bottom of cyclone) and vessel; s is the vertical distance from bed surface to mid-height of flapper plate (defined herein as the flapper valve 'submergence'); h is the vertical distance from bed surface to bed level within dipleg; and finally, l, w, t are the length, width and thickness of the flapper plate, respectively.

Substituting Eqs. (11.B.2) through (11.B.7) in Eq. (11.B.1) and solving for h leads to the expression:

$$h = \frac{4lwtg\,(\rho_{fp} - \rho_{bed})\sin\theta\cos\beta}{\pi g \rho_d D_t^2} + \frac{g\,(\rho_{bed} - \rho_d)\,s}{g\rho_d} + \frac{\Delta p_{cyc}}{g\rho_d} \tag{11.B.8}$$

which tells us that the solids backup above the bed level is due to three separate influences as represented by the three terms in Eq. (11.B.8).

The first term accounts for the height the catalyst must back up above the bed in order to overcome the weight (more precisely, 'torque') imposed by the flapper plate.

The second term is the 'manometer effect' and accounts for the difference in solids densities in the bed outside the flapper valve and that inside the valve. If there is no difference in these densities, or if the dipleg is not submerged, this term vanishes. In lightly-loaded (that is, second or third-stage) cyclones for which Eq. (11.B.8) mainly applies, the dipleg solids density is normally less than that of the bed. This results in a positive contribution to the solids backup, h. We may note that the backup increases as the submergence increases and with a decrease in dipleg solids density.

Finally, the last term accounts for the additional backup imposed by the suction of the cyclone to which the flapper valve is attached, relative to the pressure in the vessel itself. Here, Δp_{cyc} is the pressure difference between the dilute phase of the vessel and the dilute phase of the dipleg. As such, it accounts for the total pressure loss resulting from the pressure drop across any primary cyclone that may exist and the pressure drop from the inlet to the underflow of the cyclone for which h is being calculated. For the latter, if one

does not know the pressure loss from the inlet to the underflow piping, one should use the full, inlet-to-overflow pressure loss across the cyclone. As mentioned earlier, the pressure at the bottom of the cyclone can vary significantly depending on where and how the end of the vortex terminates.

11.B.1 Example

Given: A flapper valve of 41 cm is submerged 1.5 m in a fluidized bed of catalyst. The existing 1 cm thick flapper plate is experiencing erosion and a proposal has been made to replace the plate with a special hardened-steel plate having double the thickness.

Determine the additional backup of dipleg catalyst that the much thicker and heavier flapper plate will produce.

Additional information:

l = 94 cm, w = 46 cm , t = 1 cm (present design)
t = 2 cm (proposed design)
D_t = 39 cm
θ = 5°
β = 60°
ρ_{fp} = 7830 kg/m^3
ρ_d = 400 kg/m^3
ρ_{bed} = 560 kg/m^3
s = 1.52 m
Δp_{cyc} = 0.30×10^5 Pa (total pressure loss from vessel dilute phase to cyclone bottom)

Substituting the above values into Eq. (11.B.8), we obtain for the backup:

$$h = 0.029\text{m} + 0.61\text{m} + 7.64\text{m} = 8.28 \text{ m} \tag{11.B.9}$$

From this we see that the cyclone suction term dominates the catalyst backup level.

If we now recompute the submergence for the 2 cm thick flapper plate our new value for h becomes:

$$h = 0.057\text{m} + 0.61\text{m} + 7.64\text{m} = 8.30 \text{ m} \tag{11.B.10}$$

Obviously, the thickness of the flapper plate has a negligible impact on catalyst backup above within the dipleg. This is true despite the fact that the 2 cm flapper plate is computed to have a mass of 64 kg (141 pounds)! Thus, irrespective of other influences, the pressure difference between the dilute phase of the vessel and the dilute phase of the dipleg almost always governs the distance that the dipleg solids back up above the bed level. This is one reason why we want to constrain the pressure drop across the cyclone system. Other reasons relate to erosion concerns that are associated with excessive cyclone velocities—hence, pressure drop—and the desire, in some operating units, not to reduce the pressure of the gas exiting the vessel any more than necessary.

12

Some Special Topics

This chapter presents information about three diverse topics relevant to cyclone technology; thus the title, "Some special topics". Two of the topics are related to the gas velocity in the separator: cyclone erosion and the critical deposition velocity. The last topic is the working of cyclones or swirl tubes under conditions of high vacuum.

12.1 Cyclone Erosion

In many cyclone installations abrasive wear or erosion is of major concern to plant operating and maintenance departments. It is one of the major causes of unscheduled unit shutdowns in units that process abrasive particles such as coal, sand, fly-ash, coke and alumina-based catalyst. Even natural grains, such as the hard tips of rice grains can, and do, erode holes in metal-walled conveying lines and in cyclones which process them. The same is true of certain plastic particles or pellets and of some wood products.

As shown in Figs. 12.1.1 and 12.1.2 later in this section, several zones within a typical cyclone are especially vulnerable to erosive attack. These include the inlet 'target area', the lower cone and the dust hopper and/or upper dipleg (if present). We will discuss each of these areas separately below.

12.1.1 Inlet 'Target Zone'

As the name implies the inlet 'target zone' refers to that section of the cyclone barrel which is, more or less, in the direct line-of-sight of the incoming particles. In the case of an inlet scroll, the 'target zone' would be that area of the scroll that is in the line-of-sight of the straight duct feeding the scroll. In either case, erosion occurs much as it would within a conventional pipe bend in a pneumatic conveying system. In this region of the cyclone the solids (especially the larger ones) do not all follow the curve of the gas streamlines but cross these streamlines and impact upon the cylindrically shaped barrel

of the cyclone (see also Fig. 9.1.4). Greatest wear typically occurs at the point where the particles' angle of incidence with the curved, cylindrically shaped wall is about 20 degrees. This region of peak wear can vary from about 15 degrees up to about 35 degrees for common ductile materials of construction (MOC) such as mild steel or aluminum plate.

Mills and Mason (1979) conducted an experimental study on erosion of 50 mm ID mild steel pipe bends (bend radius of curvature to pipe diameter ratio = 2.8) by air-conveyed sand particles. A number of very interesting and useful findings were reported by these two investigators pertaining to the effects of gas velocity, particle size and solids loading upon the erosion and penetration of pipe bends. Due to the similarity between the flow entering—and within—a bend, and that within the curved entrance section of a typical cyclone, we believe the results should be of interest to anyone working with or designing cyclones that handle abrasive solids.

Mills and Mason found, for instance, that for a solids-to-air mass ratio, c_o, of 2 and for sand particles having an average size of 70 μm, the run time, T, before a bend would fail due to wall penetration is strongly and inversely dependent upon the gas conveying velocity. They found:

$$T = Cv^{-3.5} \tag{12.1.1}$$

where C is a proportionality constant.

We wish to point out that Mills and Mason's time-to-failure studies reveal a dependency of bend failure upon velocity that is not the same as the dependency of 'specific erosion' (mass or volume of material eroded per unit mass or volume of impacting solids) upon velocity. The specific erosion typically varies only as the 2^{nd} to 3^{rd} power of velocity. Thus Mills and Mason's results indicate that the mass eroded from the bends *at the point of failure* is more sensitive to velocity than that found in more commonly reported specific erosion tests.

Mills and Mason also report some rather interesting and, we believe, relevant results involving the dependency of time-to-failure of bends upon mean particle size and mass ratio. Without going into the details of their investigation, it was found that the time-to-failure, T, is very nearly proportional to the square root of particle size,

$$T = C_1 x^{0.45} \tag{12.1.2}$$

where C_1 is a proportionality constant. Upon first inspection, this result appears to run counter to our general belief that larger particles are more erosive than smaller particles, hence, T should decrease with increasing x. Studies clearly show that specific erosion rates do increase with particle size. However, this is true only up to a certain size (typically about 40 to 50 μm for particles such as fly ash or sand), beyond which erosion remains essentially constant. (See for instance, Kotwal and Tabakoff, 1981). Mills and Mason's study pertained to sand particle sizes in the 70 to 280 μm size range and,

thus, the specific erosion rate is not expected to vary in their study. But, unlike specific erosion rate, the time-to-failure was observed to increase with increasing particle size as given by Eq. (12.1.2) above. Mills and Mason report that, "the finer particles are more likely to be affected by the swirling and secondary flows induced by the bends than are larger particles, and so in certain circumstances are capable of causing very much more wear". (See also Mills, 1977).

Underlying much of what is reported here lies the fact that, from a wall penetration and failure point of view, it is not how much total material that is eroded from an elbow or bend that is always important, but how rapidly wall *penetration* occurs. Under some conditions (of particle size, velocity or mass loading) eroding solids may remove a significant quantity of material from a test target specimen or bend but not cause a localized failure. Under other conditions less total material may be removed but the specimen fails in service due to the ability of the impacting solids to penetrate deeply in a localized area of the specimen target. Another manifestation of this behavior is Mills' and Mason's findings regarding the dependence of time-to-failure of a bend upon solids mass loading, c_o, which they report as,

$$T = C_2 c_o^{-1.58}. \tag{12.1.3}$$

Like the effect of particle diameter reported above, this also seems to run counter to conventional 'pneumatic conveying' belief in that it predicts a decrease in time-to-failure with increasing solids loading or concentration. As Mills and Mason point out, a large number of tests show that the amount of erosion does decrease with increased solids loading. However, this is overshadowed by the fact that, at least for the bend erosion tests conducted by Mills and Mason, the *local depth* of wear increased with an increase in solids loading. Thus, instead of a protective 'cushioning' effect due to the interference of neighboring particles, it appears that, as the concentration of particles increases, the erosive action is concentrated in a localized area of bends, causing them to fail sooner.

Storch and Pojar (1970) performed an interesting and rare study of erosive wear within a variety of steel cylinder-on-cone cyclones with tangential inlets. Erosion rates in each cyclone's cylinder and cone sections were measured as a function of gas inlet velocity and solids concentration for two different types of abrasive dust. The experimental results are illustrated in Fig. 12.1.1, frames a through d. The wear reported is that after exposing the cyclone to a fixed total quantity of dust.

As shown, erosion is very pronounced in the inlet 'target zone'. It drops off rather rapidly with axial position below this zone and continues to drop, levelling off at some minimum value with increasing distance away from the inlet as long as there is no decrease in cross-sectional area of the cyclone body. Each of the erosion curves thereby assumes some minimum value above the cone section.

12.1.2 Lower Cone Section

As shown in frames a through d of Fig. 12.1.1, however, erosion increases rather strongly with axial distance down the cone section and reaches its maximum value in the lower or lowermost section of the cone. It is even observed to form a strong lower cone erosion peak (actually an erosion 'ring')

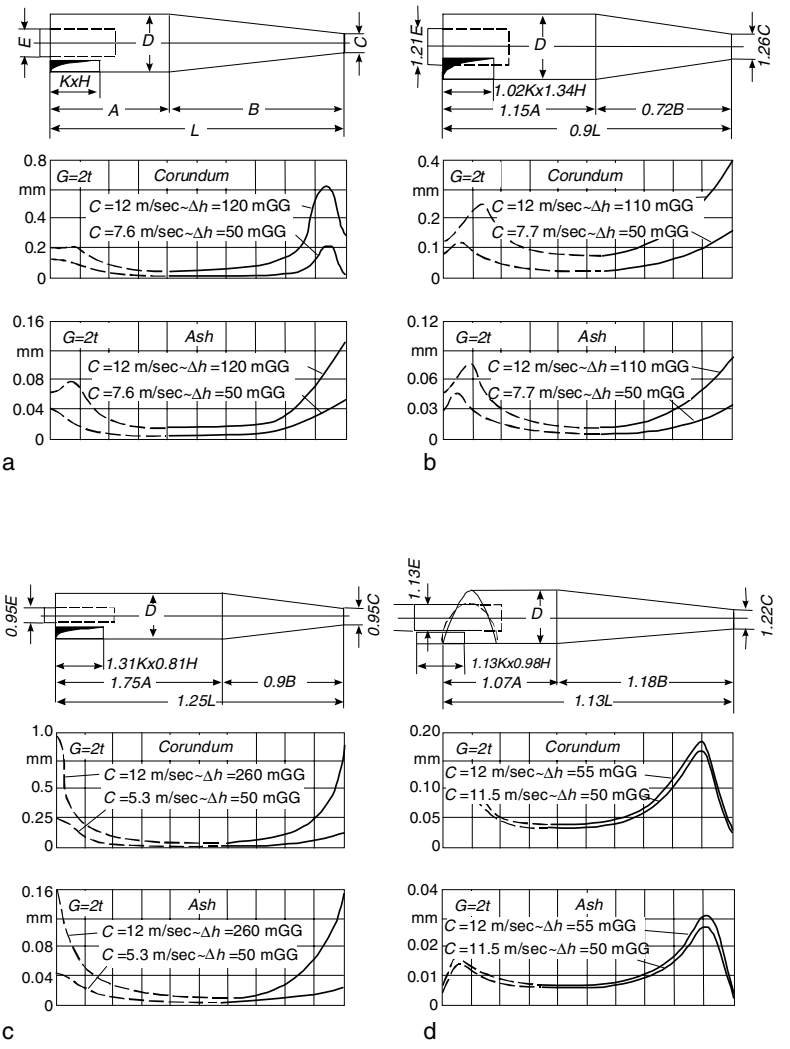

Fig. 12.1.1. a, b, c, d Erosion as a function of axial position, particle type and velocity for four different cyclone geometries

With appropriate replotting of the 16 curves shown in these figures one finds that the amount of erosion at a given axial position in the conical section of these cyclones is a strong, inverse function of the cone diameter at that position:

$$e = C_3 D_c^{-2.8} \tag{12.1.4}$$

where e is the erosive wear reported in Fig. 12.1.1, D_c is the cone diameter at any axial position within the cone, and C_3 is an unknown proportionality constant.

The exponent varies over the range 2.3 to 3.2, with 2.8 being the average value. This value was obtained by replotting all the erosion data leading up to the point of maximum erosion but excluding the data immediately upstream of the two 'corundum' peaks for cyclone a. The rate of erosion leading up to these two peaks increased remarkably rapidly and was approximately proportional to the inverse 8^{th} power of the cone diameter.

If the variation in the amount of erosive wear for the cone sections is proportional to the flux of solids (solids rate per unit surface area) one would expect wear to be inversely proportional to cone diameter since cone diameter times a unit height is the local unit cone area. Such is obviously not the case.

If, for the cone section of a given cyclone we assume that the rate of erosive wear (wall material removed per unit time per unit area) is proportional to the total kinetic energy of the particles that impact the wall per unit time and area, then,

$$e = \alpha \frac{v_\theta^2}{a} \tag{12.1.5}$$

$$a = \pi D_c \tag{12.1.6}$$

and,

$$U_\theta \propto v_\theta = \frac{\beta}{R_c} = \frac{\beta'}{D_c} \tag{12.1.7}$$

where α, β, β' are proportionality constants (note that they are dimensional); a is the wall area per unit height of a cone section of radius R_c and diameter D_c; and U_θ, v_θ, are the tangential particle and gas velocities near the wall, respectively.

Substituting Eqs. (12.1.6) and (12.1.7) into Eq. (12.1.5) we obtain,

$$e = \gamma D_c^{-3} \tag{12.1.8}$$

This suggests, for this very simple kinetic energy model, that the local erosion rate within the cone section is inversely proportional to the 3^{rd} power of the local cone diameter. In deriving Eq. (12.1.8), the local particle velocity near the wall (shown in Eq. 12.1.7) was assumed proportional to the local gas velocity. This local gas velocity near the wall is, in turn, assumed to be that of a free vortex and, thus, inversely proportional to the cone radius, as in Eq. (12.1.7).

Equation (12.1.8), though quite elementary, is interesting in that its prediction of the dependency of cone erosion upon local cone diameter is very close to that found from the experimental data represented by Eq. (12.1.4).

This also has ramifications for the effect of solids loading on cyclone erosion: we would, based on this, expect wear to be directly proportional to solids loading. This is not incompatible with Eq. (12.1.3), where the variation in the time to failure is qualitatively consistent with this simple model, but a bit stronger (to the power of -1.58 rather than -1.0). As explained above, the wear may become more localized with increasing loading.

The results of the erosion study with cyclone a, when processing corundum particles, and with cyclone d, processing both the ash and corundum, are very interesting in that the erosion is observed to peak within the lower cones and to then fall off abruptly below these peaks. In the writers' judgment these peaks were created by a type of vortex instability that caused the 'end' of the inner vortex to attach to, and precess around, the lower cone walls. Such behavior is schematically illustrated in Fig. 12.1.2, and is often referred to as the 'natural end of the vortex'. This phenomenon is discussed in Chap. 9[1]. Thus, *the physical length of a cyclone does not necessarily represent its active or effective length if it were to 'short circuit'* as described above.

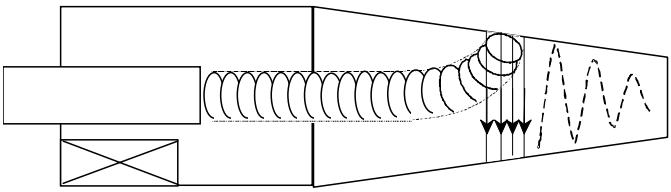

Fig. 12.1.2. Vortex 'tail' attached to and precessing along lower cone wall

At the point of attachment, the high velocity vortex core is therefore in direct contact with the lower cyclone walls, which, in the presence of solids, produces the observed erosion peak.

A vortex, being a spinning mass itself, is much like a spinning top and any phenomena which weakens its spin can render it unstable. Such instability within a cyclonic type separator can cause the lower tip or tail end of the vortex core to attach to the lower walls of the cyclone (the position of the natural end of the vortex moves up into the conical section of the cyclone). Thus, the physical length of a cyclone does not necessarily represent its active or effective length if it were to 'short circuit' as described above.

[1] In general, a vortex created within a cyclone has two options: it may dissipate in free space or it may attach to a surface. Normally, the vortex will attach to a surface such as the lower conical or cylindrical walls of a cyclone or dust hopper or even to the top of a dipleg. In short bodied cyclones it may, however, extend down into an open space below the cyclone and dissipate or terminate therein.

One phenomenon that can weaken the spin is increased wall roughness that decreases the angular momentum of the rotating gas core. It is not an easy task to predict, beforehand, the conditions under which a vortex will become unstable, nor to predict precisely at which axial position it will end. This is still an area under active investigation, see also the discussion of this in Chap. 9. We recall, for example, that, for cyclone a shown in Fig. 12.1.1, when the cyclone was fed corundum solids a localized erosion peak (erosion band) occurred in the lower cone. On the other hand, when it was fed fly ash particles, no such localized peak developed. The probable explanation for this is that, relative to the ash particles, the corundum particles used by Pojar and Storch were much more dense and much larger than the ash particles. (The density of the ash and corundum particles was 2178 kg/m^3 and 4091 kg/m^3, respectively, while the average particle size was about 27 μm and 80 μm, respectively.) The larger corundum particles can be expected to have increased the effective wall roughness due to their size alone. Furthermore, the corundum particles were able to erode and roughen the walls to a much greater extent than that for the ash particles. These factors, along with the corundum's greater mass, can be expected to have weakened the angular momentum of the vortex relative to that of the ash particles. We believe that this, in turn, caused the vortex tail to become unstable, attach to the lower cone wall, and produce the observed peak in the erosion profile. We note that the resulting peak wear created in the corundum study (Fig. 12.1.1a) is approximately 10 times that for the ash study for which no erosion 'peak' was observed.

As mentioned, the end of the vortex phenomenon is discussed further in Chap. 9, and the importance of determining the exact nature of this phenomenon under different conditions and in different geometries is emphasized.

12.1.3 Vortex Tube Outer Surface

Erosion of the outer surface of the gas outlet tube or vortex finder can occur from several possible causes and we will briefly discuss each of these below. Perhaps the most obvious cause is direct impaction, which can occur if any part of the vortex finder lies in the projected path of the particles entering the cyclone. See Fig. 12.1.3a. As shown in Fig. 12.1.3b, the incoming gas can be expected to constrict, either due to the geometry or due to the effect of the gas already rotating in the cyclone and flow around the gas outlet tube. But this is not always the case for the solids.

Equipping the cyclone with an inlet scroll or decreasing the width of the inlet duct, as shown in Figs. 12.1.3c and 12.1.3d, are two common ways of preventing the particular problem shown in Fig. 12.1.3a. In the latter case, the height of the inlet may be increased in proportion to the decrease in inlet width if one wishes to maintain the same inlet velocity. In some instances, it may be possible to decrease the diameter of the vortex tube or increase the barrel diameter to avoid the interference. It may even be possible to install two smaller inlets, spaced 180° apart, as per Fig. 12.1.3e. Helical roof designs

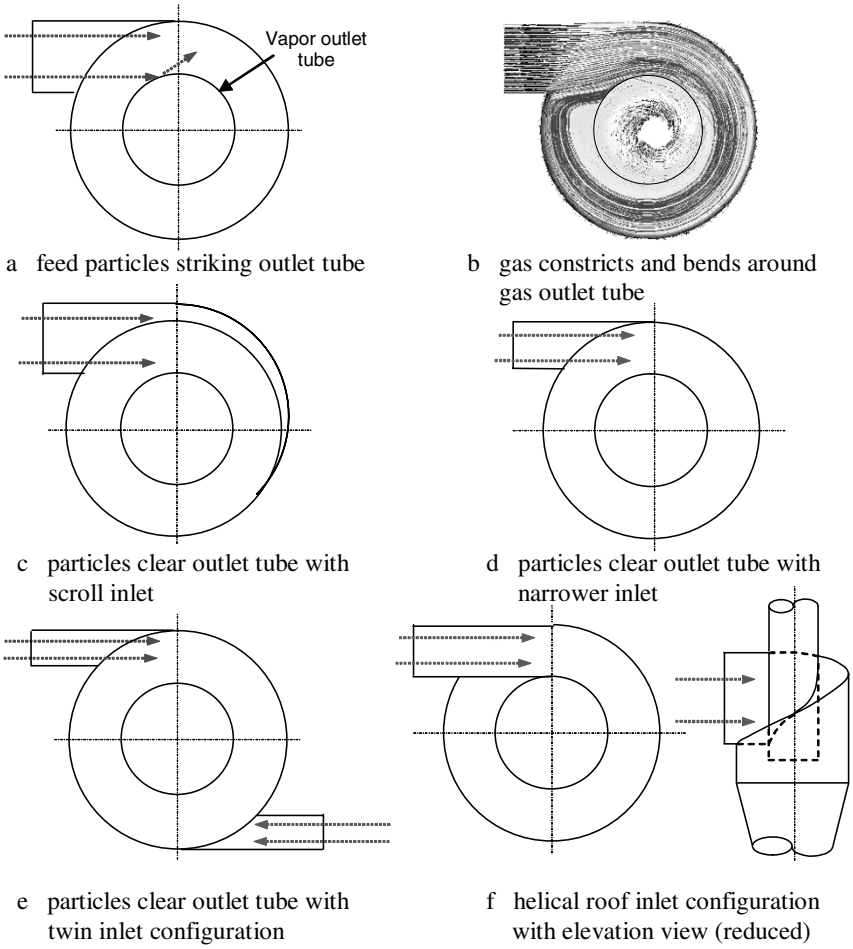

Fig. 12.1.3. Vortex finder in line-of-sight of incoming gas/solids mixture and design techiques to avoid this condition. CFX image courtesy of USDA Agricultural Research Service, Southwestern Cotton Ginning Research Laboratory and New Mexico State University

avoid the issue of incoming solids striking the vortex finder since they are constructed so that the width of the inlet duct matches the annular space surrounding the vortex finder, as shown in Fig. 12.1.3f.

One of the most interesting aspects of the flow shown in Fig. 12.1.3b, and another potiential cause of vortex tube erosion, is the very abrupt change in flow direction at the location where gas that has already entered the cyclone circles around and encounters the incoming gas stream. In the detailed plan view shown in Fig. 12.1.4, this is seen to occur at about the 2:30 clock position. It is here that the gas that is about to complete its first revolution within the

barrel section collides with the incoming gas and is abruptly deflected inward, forcing it (in this particular example) to then collide with the outer surface of the vortex finder. It is also deflected downwards, as shown by the flow streamlines and arrows in Fig. 12.1.5. We believe that such a flow deflection *could* cause some portion of the dust entrained in the abruptly deflected gas stream to strike and erode the outer wall of the vortex tube in a vertical region that lies below the white dots shown in Fig. 12.1.4. The "angle of attack" in this region varies from 0° up to a maximum of about 40° for this particular geometry. We recall that the region of peak wear varies from about 15° up to about 35° for common ductile materials of construction.

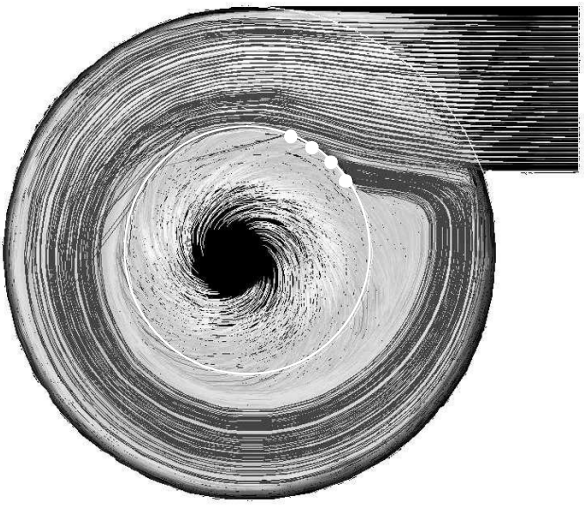

Fig. 12.1.4. Detailed view of flow pattern shown in Fig. 12.1.3b showing abrupt change in flow pattern at the 2:30 clock position. CFX image courtesy of USDA Agricultural Research Service, Southwestern Cotton Ginning Research Laboratory and New Mexico State University

One might also expect that any such abrupt collision and deflection of the solids-bearing gas stream would have a negative impact on separation performance. However, according to Funk and Hughs (2000), just the opposite may be true. They report,

> In the plan view of the cyclone streamlines, air makes one revolution in the barrel of the cyclone, then makes an abrupt change in direction near the entrance (where it collides with incoming air). This forces the dust-laden air to make a tight turn inward and downward. The fact that the air is leaving the dust behind at that point appears to be more important to cyclone efficiency than the fact that the dust

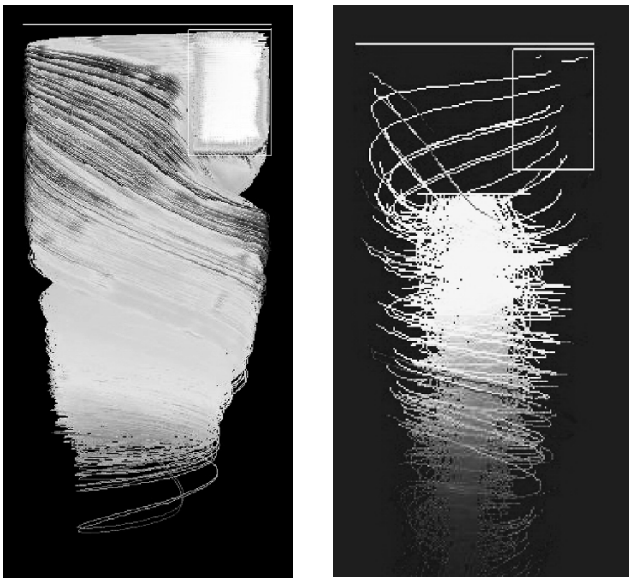

Fig. 12.1.5. Elevation views of flow pattern showing abrupt change in flow as gas in barrel section encounters incoming gas. CFX image courtesy of USDA Agricultural Research Service, Southwestern Cotton Ginning Research Laboratory and New Mexico State University

> is reintroduced into incoming air. This alternate approach to understanding cyclone dynamics was thought to possibly explain the results of an earlier experiment attempting to prevent such reintroduction.

Funk (2005) also reports that, on the basis of laboratory experiments utilizing cyclones with internals that eliminated the "collision" described above,

> The modified cyclones prevented the re-entrainment of particles after one revolution, but they had much higher emissions than the conventional flat roofed (standard) cyclones

Funk furthermore reported that the tight turn inward and downward "might also contribute to separation" (*i.e.*, improve separation performance). On the other hand, the writers are aware of at least two separate commercial fluid bed primary cyclone installations that have experienced serious erosive wear at the location of the white dots shown in Fig. 12.1.4 and which have exhibited rather poor separation performance. In both cases the height of the vortex finder below the roof line, i.e., its penetration, was substantially less than the height of the inlet chute, allowing particles that were deflected inwards to short-circuit the cyclone. Obviously, this is an area deserving of further investigation.

Thus, it is the writers' opinion that the external surfaces of vortex finders within fluidized vessel cyclones can also become the target of high levels of

erosive wear, even if these surfaces are *not* in the "line-of-sight" of the incoming solids. Here we are referring to what is normally called the "first-stage" or "primary cyclones".

Still another possible cause of this rather unique mode of vortex finder wear—at least in first-stage cyclones operating above a fluidized bed—relates to the design of the inlet horns and chutes. As shown in Fig. 12.1.6, gas and solids enter the cyclone through the inlet horn over a rather wide arc. A portion of the solids enter the horn along a path that directs them toward the center of the cyclone. Unlike the incoming gas, some of these incoming solids may be too large and/or dense to follow the gas streamlines and, under certain design and flow conditions, they could end up striking the outside surface of the vortex finder, as shown by the two curved, dashed lines in Fig. 12.1.6.

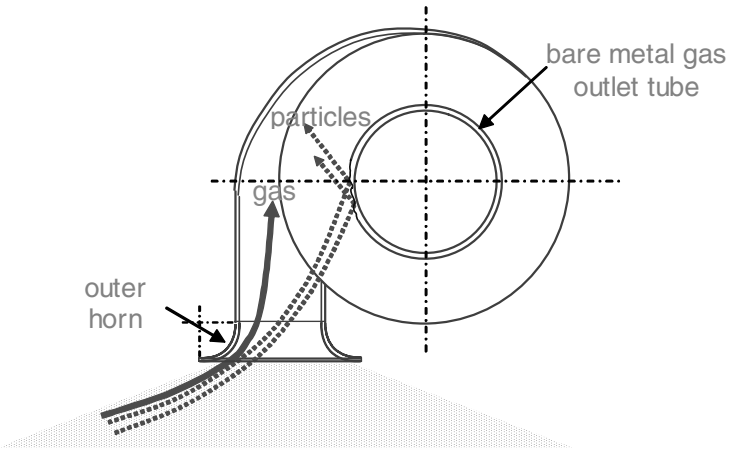

Fig. 12.1.6. Gas outlet tube erosion caused by high velocity particles entering cyclone by path shown

Aside from the purely inertia effect just described, it is also possible for incoming solids to strike the outer horn segment, deflect, and then impinge upon the outside surface of the vortex tube. To the extent that this occurs it should be possible to eliminate or greatly reduce this erosion mechanism by eliminating the outer horn segment and replacing it with a straight section of inlet duct, as shown in Fig. 12.1.7.

Conditions that can be expected to increase the rate of wear by any of the above erosion mechanisms are the same conditions that tend to cause particles to not follow the gas path when the latter undergoes any type of curved motion: high inlet velocities (20 to 25 m/s or more), high solids loading, and a high concentration of coarse particles in the feed. In fluidized bed operations all three of these conditions can be brought about by operating the bed at excessively high velocities. The latter two can result even at normal air rates

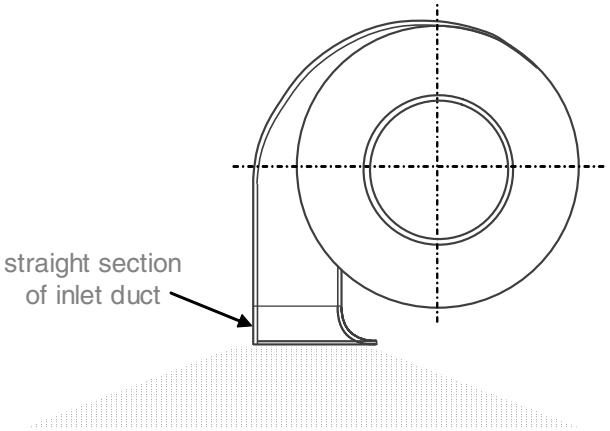

Fig. 12.1.7. Outermost horn segment replaced by straight section of inlet duct

if the bed level is too high bed or if the air grid is damaged. Short inlet ducts are thought to contribute to the problem. Over time, particle impaction of the vortex finder can lead to its complete penetration (unless it is protected by a dense, erosion protective, refractory liner) and a serious loss in separation performance, especially if the vortex finder penetration is smaller than the height of the inlet chute. The erosion mechanism shown in Fig.12.1.3 a and b are not unique to fluid bed cyclone installations; rather, they can occur in any cyclone system whose geometry and mode of operation favor such behavior.

Before leaving this section we wish to point out that the outer horn deflection mechanism described above also applies to the innermost horn segment, as one might expect. Hence, solids may also impact the inside wall of the inlet scroll or barrel, depending on the design. However, as mentioned above, these surfaces are almost always covered with erosion resistant, protective liners and, for this reason, their wear rates may not be noticeable or significant. What may be significant, however, and what may not be fully appreciated, is the effect that the particle behavior described above has on cyclone separation performance. This is another area that appears to have received virtually no attention by the research community.

12.1.4 Erosion Protection

Given sufficient time, most cyclones will experience sufficient erosive wear that they must either be replaced or repaired. If the service life of the cyclone is deemed unacceptable, one has two basic options for ameliorated erosive wear: one is to reduce the velocities within the cyclone; the other is to render the cyclone less vulnerable to erosive attack through 'hardware' modifications. Reducing velocities, namely by increasing the inlet and/or gas outlet areas, is seldom a viable option, at least not after the unit has been built since,

aside from the cost involved and the impact this may have on production, this also normally results in some decrease in separation performance. The time to think about 'velocities' is when the cyclones are being designed. Normally, cyclones are designed for inlet velocities between 18 to 26 m/s (60 to 85 ft/s), with outlet velocities somewhat higher. However, if pressure drop permits and the solids (due to their hardness or size) are not especially erosive, velocities far in excess of this range may be specified in special cases, such as in 'third-stage' cyclones handling catalyst 'fines'. Thus, as a practical matter, one is normally required to make 'hardware' changes to the cyclone only if erosion becomes a concern to operations. (We are excluding here modifications resulting from temperature excursions, spray water damage, coke or other accumulations, poor gas and/or solids distribution, solids underflow/discharge problems, corrosion, etc.) Erosion related hardware modifications typically involve the:

1. installation of 'wear plates' ('permanent' or removable, internal or external)
2. replacement, in-kind, of worn sections of the cyclone
3. replacement of worn sections with heavier gauge metal or thicker plate
4. replacement of eroded sections of the cyclone with harder, more abrasion resistant materials of construction (MOC)
5. repair or replacement of any eroded metal, refractory, ceramic, brick or other type of liner that may have been previously installed
6. modification of the cyclone to fix any design or construction flaws such as:
   - raised seams or dents that may cause particles to skip then strike downstream at an unfavorable angle of attack. This applies equally well to the inlet piping/ducting and any overflow or underflow piping or ducting such as headers, chutes or diplegs.
   - gaskets that protrude into the flow field that detrimentally affect the particles' otherwise smooth flow path down the walls
   - sight or light ports or access ports or hatches or protruding wall probes that are not smooth and flush with the inside walls
   - rotary valves or underflow seals that may be allowing gas to leak up the cyclone, causing solids to 'hang up' and erode the lower section of the cyclone and to attrit themselves. This is especially true of 'pull through' systems that tend to suck air or gas up the bottom of the cyclone if the underflow seal is not adequate.

It is possible, though rare, to install one or more cyclones in parallel with an existing cyclone, or cyclones, in order to reduce velocities and, hence, the rate of wear. However, unless the velocities in the existing design are higher than they need to be in order to achieve the desired separation, this is not normally an option.

The path one follows to combat erosive wear will be strongly affected by considerations of costs and downtime to do the work versus future savings from repairing the unit so that such repairs do not become a frequent occurrence.

Cyclones are utilized in a bewildering array of industries and operations. Erosion, for some of these processes, is of little or no concern. Such may be the situation for cyclones that process natural flours, soft rubbery products, mists, paper and fabric/fiber dust, leather fibers and pharmaceuticals, among others. In other processes, erosion can range from mild to severe, depending on the velocities involved, and the feed particles' loading, size, hardness and sharpness. In this category, we can include cyclones that process sawdust, certain plastic or polymer fines and pellets, coffee, cereal/grain, soybean fines, sugar, most food products and particleboard fines. Cyclone installations that, due to the size, hardness, sharpness and concentration of the feed solids are subject to high levels of erosive wear (or potential wear) include those that process: metal dust, cement fines, foundry dust, various oxides, scale, pulverized coal, crushed rock and brick fines, salts or crystals, sand fines, tar sand, carbide grit, swarf and shavings (metallic chips or turnings), petroleum coke, catalytic cracking and other alumina-based catalysts particles.

In low erosion applications, and in low pressure rating applications, cyclones are most commonly fabricated from sheet metal; 10 or 12 gauge. Mild or galvanized steel is common for units smaller than about 1 meter in diameter. These units may have replaceable, flush mounted, metal wear plates affixed in areas that are prone to erosion. These areas normally include the inlet 'target zone' and the lower cone section.

Cyclones that must process particulates that are more aggressive are normally fabricated from thicker, 3 to 6 mm (about $1/8^{\text{th}}$ to $1/4^{\text{th}}$ inch) metal plate. Wear plates are a common feature of these units. Some may have specially hardened, internal, metal liners, as illustrated in Figs. 12.1.8 and 12.1.9.

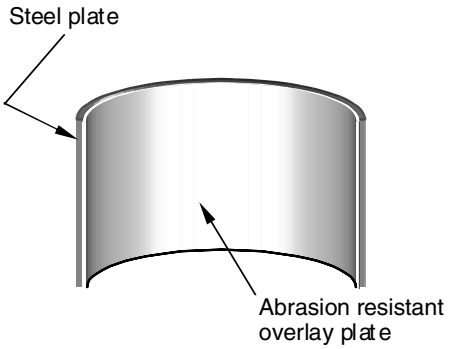

Fig. 12.1.8. Cyclone wear plate consisting of a mild steel plate with an abrasion resistant metal overlay such as chromium carbide. Such a plate is typical of that which may be installed in the cyclone's inlet 'target zone' (just downstream, and in the line of sight, of the inlet duct)

If it is prudent to provide erosion protection for the cyclone, it is often necessary to also protect any bends in the ducting or piping feeding the cyclone. The cyclone shown in the foreground back in Fig. 1.3.4 is observed to have an erosion protective, replaceable liner installed on the outermost face of the rectangular inlet bend located just ahead of the cyclone. This technique of protecting the piping feeding the cyclone is also clearly visible in Fig. 12.1.10.

The cyclone bodies or the wear plates may be fabricated from chromium carbide overlay plate, hard metals such as heat-treated alloy steel, 11-14% manganese austenitic steel, Ni-hard, high-chrome, ordinary or heat-treated carbon steel, weld hard-facing/overlay, manganese steel and aluminum, or from various chromium carbide alloys such as those made from molybdenum, manganese and tungsten.

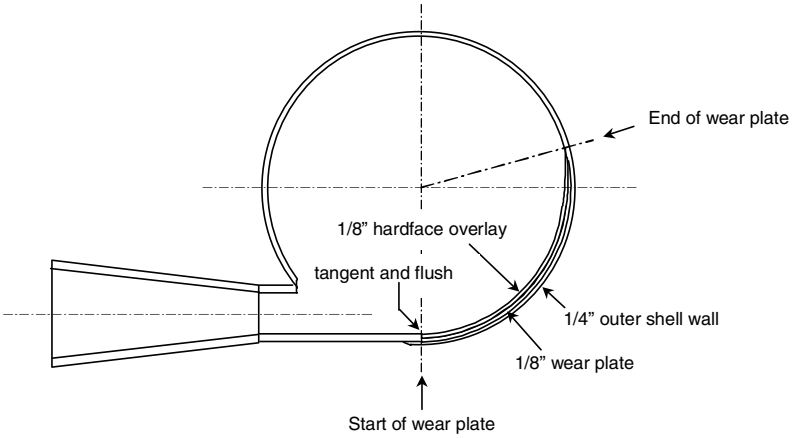

Fig. 12.1.9. Cyclone with a entrance 'target zone' wear plate consisting of a $1/8^{\text{th}}$ inch thick 'wear plate' with a $1/8^{\text{th}}$ thick hardface overlay metal. Finished wear plate is designed to be tangent and flush with inside surface of cyclone at leading edge

When the tendency for erosive attack is high, more aggressive erosion protection measures must be taken. An example would be a cyclone processing ordinary silica sand, which has been observed to erode through a 6 mm thick steel cyclone wall in less than 4 weeks. Although metal liners of the type mentioned above may be quite effective in many applications, some unit operations, such as fluid catalytic cracking and certain coal or coke processing units require the use of a high temperature, high density alumina-based refractory or ceramic liner.

'Castable' and 'plastic' refractories are the two types of liners most commonly used. The 'plastic' varieties incorporate phosphate as a chemical bond-

Fig. 12.1.10. A commercial installation consisting of a parallel arrangement of two cyclones sharing a common underflow hopper and overflow plenum (or 'header'). Note blower in bottom left-hand side of image 'pulls' gas through the cyclones. Also note the specially designed erosion-resistant elbow just ahead of the cyclones. Courtesy Fisher-Klosterman Inc.

ing agent and are typically identified as 85 or 90 RAM where the number refers to the weight percent alumina comprising their mix. These substances have a density of about 2600 kg/m^3 (160 lb/ft^3), an ASTM C-704 erosion loss rating of between 2 and 10 cc, and a permanent linear shrinkage upon heating to 815°C (1500°F) typically less than −0.6%. They consist mostly of the Al_2O_3 (approx. 80–85%) and lesser amounts of other oxides, such as SiO_2. Aluminium oxide (99.5%) has a Moh's hardness of 9 (diamond being 10 on this scale) and a Vicker's hardness of about 2500. These hardness ratings are similar to that of sintered silicon carbide and approach that of reaction-bonded silicon carbide. As such, the material is very resistant to abrasion and erosion.

The refractory material is normally installed 25 mm thick over a 25 mm thick metal liner in the form of a mesh, which acts as an anchoring system, that is first securely welded to all internal surfaces of the cyclone exposed to erosive wear. This generally includes all inside surfaces except, in some cases, all or part of the inside or outside surface of the vortex tube. If the cyclones are equipped with diplegs, such as those in FCCU service, the re-

fractory lining will usually extend about 1 meter down into the dipleg. In some applications, the lining in the 'first stage' diplegs will extend the entire length of the diplegs. Inlet horns and any crossover chutes reporting to second and third-stage cyclones will generally require refractory lining as well. Somewhat thinner liners are occasionally used. Liners much thicker than 25 mm would normally increase the weight and cost of most cyclones, and their hanger support systems, to the point of being prohibitive.

Refractory liners in cyclones are in general too thin to vibration cast. Rather, they are first carefully mixed by adding very clean water to the dry refractory mix, according to the manufacturer's instructions, and the resulting mixture is then hand-packed or rammed into and behind the metal anchoring matrix. The selection, anchoring and workmanship are critical to the longevity of the refractory lining.

The metal anchoring system is usually a cellular mesh grating designed for holding the refractory liner in place. See the examples in Figs. 12.1.11 and 12.1.13. Some metal anchoring materials are designed to be more flexible, so that they can be rolled to fit diameters as small as 150 mm, making them suitable for use in small diameter cyclones and in cyclone diplegs and ducting.

To the extent that 'the devil is in the details', it certainly applies to cyclone refractory installations. Such matters as the purity and exact quantity of the water used in the refractory mix, the weld pattern selected to fix the metal anchoring system, the manner in which the refractory is cured, and even the metallurgy in the welding rods can and will significantly affect the service life that the refractory will provide. For instance, a little too much water will result in 'slumping' of the refractory and a significant loss in its erosion resistance. Special attention to welding is necessary in a 'coking environment' since coke tends to diffuse into, and grow behind, metal anchoring mesh, breaking the welds. However, with proper procedure, all the refractory manufactures' products presently produced for high temperature severe erosion service can provide a good quality refractory lining. This attention to detail becomes somewhat easier to understand when one considers that a typical FCCU cyclone, for example, is expected to run efficiently for up to 4 years between turnarounds and, in the process, handle over 5 billion kilograms (approximately 10 billion pounds) of very abrasive catalyst without any serious loss in its mechanical integrity.

Unfortunately, in highly erosive environments, the initial surface smoothness of the refractory will soon give way to a much rougher surface. This can occur after only a few months of service as the softer binder near the surface erodes away, exposing the very hard aggregate particles that comprise the refractory mix. From this time on, the effective roughness of the refractory can be expected to remain fairly constant even though its thickness will, on average, decrease over time. Figure 12.1.12 shows a sample of a very dense refractory liner removed from an FCCU reactor cyclone after many years of service. This refractory was worn down to about half of its original 25 mm thickness prior to its replacement.

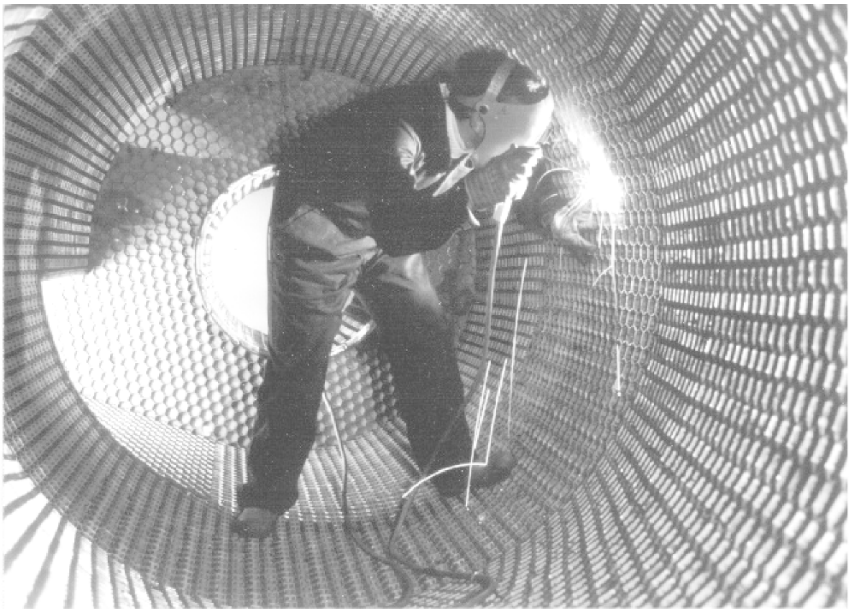

Fig. 12.1.11. 25 mm thick Hexmetal refractory anchoring grid being spot-welded to all internal surfaces of the cyclone. Note rectangular inlet chute starting in lower left-hand corner of image. Courtesy of Causeway Steel Products

Aside from the localized roughness depicted in Fig. 12.1.12, any surface exposed to erosive wear within cyclones will usually develop helical-shaped grooves. These grooved areas correspond to the path or paths that the bulk of the solids take as they spiral down the cyclone walls. To understand their cause, we have to go back to our discussion of the pressure profile set up by the swirling flow, as described in Chaps. 2 and 3. Here we learned that the static pressure within a cyclone increases with increasing radius. Furthermore, the tangential velocity of a region of gas swirling near the walls is, due to frictional drag, relatively low. The relatively low velocity of this 'high pressure wall gas' coupled with its relatively large radius of curvature, causes the gas near the wall to experience much less centrifugal force than higher velocity gas layers rotating at a smaller radii and which are at a lower pressure. This sets up a very unstable flow situation. The result is that solids-laden gas layers near the walls 'break away' from the wall and are replaced, or displaced, by rotating gas layers from the inner regions of the cyclone. This effect tends to occur in one or more parallel spiral-like bands that extend from the gas entrance region all the way down to the dust discharge opening of the cone or hopper.

As a general observation—and something that has been noticed by various researchers—all flow spiraling or rotating near a concave surface is inherently unstable and tends to break away from the wall in localized areas. Such activity will occur irrespective of the 'aerodynamic cleanliness' or smoothness

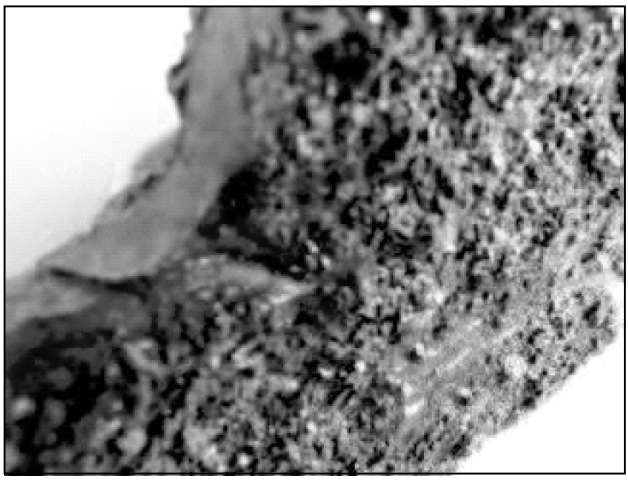

Fig. 12.1.12. A section of a very dense alumina-based refractory liner removed from an FCCU reactor cyclone. Liner was worn to approximately half of its original 25 mm thickness. Surface grain roughness is approximately 2 mm

of the wall. Rough walls or wall disturbances magnify, enhance or trigger the effect. The physical reason for this instability is the same as for the secondary flows along the cyclone roof and cone sections discussed in Sect. 3.1.1.

In those regions where the solids-rich gas near the walls breaks away, nearby wall solids are swept laterally into the region and this action tends to concentrate them into helical-shaped bands or 'strands' of solids. These bands of moving dust produce the helical-shaped erosion bands that are observed in most cyclones after they have been in service for a while.

In regards to refractory-lined cyclones, we therefore can observe two types of surface roughness. One is a localized roughness of the type shown in Fig. 12.1.12, and another is that represented by the long spiral-like grooves that can extend over the entire length of the cyclone and which follow or define the flow path of the spiraling bands of dust.

Localized wall roughness is detrimental to separation performance in cyclones (operating at Reynolds numbers exceeding 2000, approximately) only if it results in a relative roughness (absolute roughness divided by cyclone radius) greater than 6×10^{-4}, approximately. Above this value, the wall friction factor increases with increasing relative roughness and this, in turn, decreases the vortex spin and overall separation performance (see the cyclone friction factor charts in Fig. 6.1.3). For the refractory sample shown in Fig. 12.1.12, the cyclone diameter would had to have exceeded 6 m for the 2 mm roughness *not* to have aversely affected separation performance. Since FCCU (and most other) cyclone diameters are normally far less than 6 meters, one can be certain that a refractory roughness comparable to that shown in Fig. 12.1.12 will negatively affect separation performance.

Refractory work should be inspected and tested while the work is being done. Refractory should be smooth, hard, evenly applied and should just cover the top surface of the metal anchoring grating as shown, for example, in the photograph of the refractory liner installed on the roof of the cyclone shown in Fig. 12.1.13.

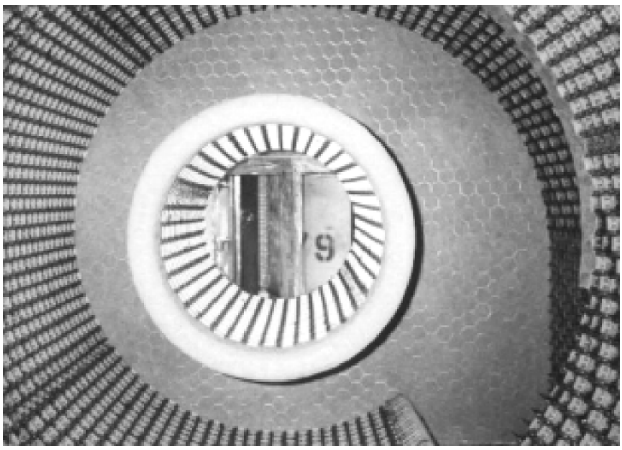

Fig. 12.1.13. Roof, barrel and vortex tube sections of an FCCU cyclone lined with ACTCHEM high temperature erosion protective refractory over Hexmetal. Note inlet scroll starting in lower right-hand corner of image. Courtesy of Actchem, Inc.

Ceramic liners are also used quite successfully to protect cyclones and ancillary equipment from erosive damage. Like refractories, ceramic liners come in many different grades and compositions. Silicon carbides, such as alumina-bonded silicon carbide, nitride-bonded silicon carbide, and reaction-bonded silicon carbide are used, as well as 85% to 99.5% alumina materials. Alumina-bonded silicon carbide ceramic is often used in high temperature, high erosion environments. The wear resistance of most ceramic material is about 60 times greater than ordinary steel and about 10 times greater than ni-hard (a nickel-chromium alloy iron casting) and hard-faced metal plate. Ceramic lined cyclones have been found to last more than 100 times longer than unlined cyclones made from mild carbon steel. When considering a ceramic liner, one should be careful not to focus on a 'percentage' grading of the material and assume there is some sort of industry standard, or 'grade' of material similar to steels. This can lead to confusion, as no such standards exist for these materials.

Ceramic liners have performed well in a wide variety of erosive environments including rotary dryer, cement, coal and ash handling facilities. This material provides a very high degree of both abrasion and corrosion resistance and is highly resistant to thermal shock. It can be cast directly onto a weld mesh support frame welded to the inside walls of a cyclone. Alternatively,

precast annular tiles can be grouted into the cyclone as the final stage in their fabrication. See Figs. 12.1.14, 12.1.15 and 12.1.16.

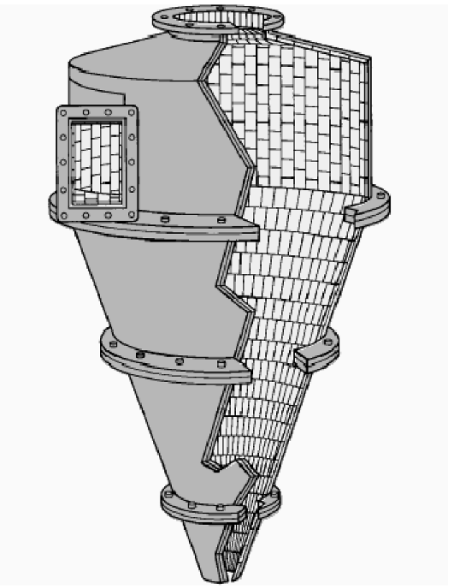

Fig. 12.1.14. Illustration of a cyclone lined with a CoorsTek liner consisting of standard and preengineered alumina or silicon carbide brink liners. Courtesy of CoorsTek

Ceramic liners vary in thickness from about 6 to 25 millimeters, depending on the type of installation and the severity of service. In some large-scale cyclones, silicon carbide bricks have been installed. Most ceramics have a density of about 3800 kg/m^3 (240 lb/ft^3) and can withstand temperatures up to about 1500°C.

Ceramics tend to have a much smoother surface than refractory liners and this can result in improved cyclone efficiency. This statement is qualified somewhat, however, by the fact that some ceramic cyclone installations consist of flat pieces of tile that produces a surface finish which only approximates a smooth, continuous surface. From a cyclone design point of view, a surface that only approximates a smooth cylindrical or conical inner surface is difficult to simulate in any computer model of separation performance. The difficulty lies in establishing a reasonable estimate of the 'effective' wall roughness of the tiled surface. This effect, however, is less of a concern as the cyclone diameter increases. This is because cyclone performance is affected by the 'relative' roughness (roughness divided by the radius or diameter of the cyclone) and not the absolute roughness, *per se*. The tile effect is also of less concern in units greater than about 2 meters in diameter. If the tile surface is curved

Fig. 12.1.15. Two 2.5 meter diameter industrial cyclones with 6 mm thick ceramic linings installed for erosion protection. Courtesy Omegaslate (UK) Limited

to match the inside curvature of the cyclone body sections, then the overall relative surface roughness of the resulting installation can be significantly less than hand-packed refractory. The latter will typically have a surface roughness of 2 mm, approximately. The manner in which the tiles are anchored can vary widely but, to avoid preferential wear at joints between the individual tiles, angled tile patterns have been used which allows the erosive solids to skip over the joints. The metal anchoring can be designed so that it is not, itself, eroded until the ceramic liner has worn down to at least 75% of its original thickness.

Cast Basalt is also used in various high erosion situations. This is a volcanic rock that has been crushed and cast at about 1250°C, either in moulds or by centrifuging, to obtain the desired shape, and then given a special heat treatment where it recrystallizes into a very hard material (720 Vickers, 8-9 on the Mohs scale). It is used to protect pipes, cyclones and other equipment from erosive attack.

Independently of the type of erosion-protective liner installed, premature failure of the cyclone or cyclone system can occur. There are numerous causes for this. Most are unit or task specific. However, as a rule, cyclone system failure is often attributable to an increase in the feed flow rate, the particle size, the solids loading, or some combination of the three. In the case of refractory and ceramic lined cyclones, a poor refractory or ceramic liner installation can also significantly shorten a unit's run time. In addition, thermal cycling can

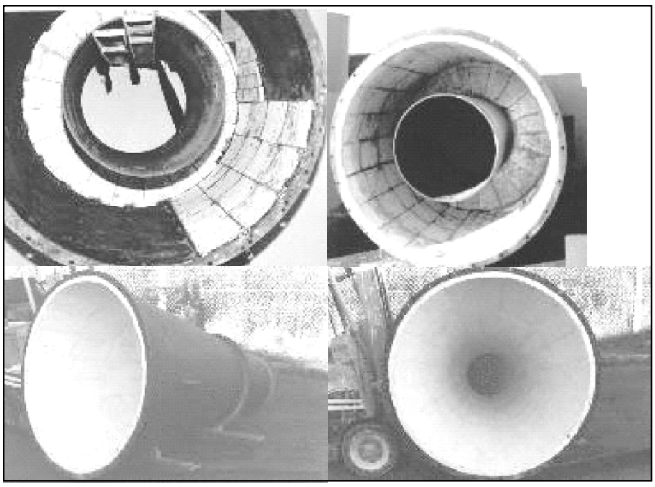

Fig. 12.1.16. A 25 mm thick, 95% alumina ceramic liner during and after installation in a 1800 mm diameter cyclone that will be used to remove silica sand from a pneumatic conveying system. Tiles are secured with a welded metal anchoring system and set with a refractory cement mixture. Upper pictures show cyclone barrel, inner roof and vortex tube. Lower pictures are of finished cone section. Courtesy Omegaslate (UK) Limited

cause the liner to fail. In some refractory installations, a change in temperature of less than 50 degrees can pop refractory 'biscuits' out of their supporting anchors. In the special case of FCCU regenerator cyclones, 'afterburning' can result in temperatures in excess of the cyclones' metallurgical limits and cause severe damage to the entire cyclone system, including plenum, interbracing and diplegs. In addition, water spray nozzles, often used to control regenerator temperatures, can thermally shock and damage the cyclones and other system components that the water contacts if the spray nozzles fail to properly atomize the water. Finally, any seams or wall disturbances (even things like coke growth) can disrupt the solids flow pattern and produce localized erosion and premature failure.

12.2 Critical Deposition Velocity

In the operation of cyclones, we generally wish to avoid particles settling out in the horizontal piping or ducting feeding or exiting the cyclones. Thus, we wish to know the minimum gas velocity required to prevent solid particles from settling and accumulating on the bottom of the piping. Wicks (1971) examined the forces acting on a particle resting at the bottom of a horizontal pipe (lift, drag, boyancy and gravity, similar to the principles outlined by White, 1940, see Fig. 12.2.1) and developed a very useful correlation for

computing the minimum superficial pipe velocity V_S required to prevent a particle from stagnating along the bottom of the pipe. His equation may be expressed in the form,

$$1 = \alpha V_S + \beta V_S^{2.5} \tag{12.2.1}$$

where:

$$\alpha \equiv \frac{10\mu}{(\rho_p - \rho)\, g x D_t} \quad \text{and} \quad \beta \equiv \frac{\rho^{1.5}}{100\,(\rho_p - \rho)\, g \mu^{0.5} D_t^{0.5}}$$

While Wicks' technique was originally derived for liquid-solid systems, it has been found to apply to 'fluids' in general and is recommended herein for gas-solids systems in addition to liquid-solid systems.

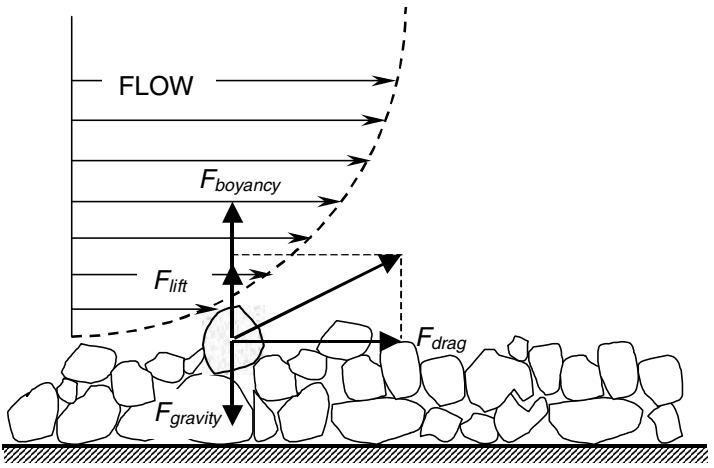

Fig. 12.2.1. Gravitation and fluid-flow forces acting on a particle located near the bottom of a horizontal pipe

Since Eq. (12.2.1) is implicit in the unknown variable, V_S, it must be solved by an iterative (trial-and-error) technique if we wish to obtain a rigorous solution. If one wishes to avoid trial-and-error calculations, the writers have found[2] that the following, explicit equation

$$V_S = \left(\frac{1}{\beta} - \frac{\alpha}{\beta^{1.4}} \right)^{0.4} \tag{12.2.2}$$

normally provides excellent approximate answers (typically within 1% of the rigorous solution) providing,

$$\frac{\alpha}{\beta^{1.4}} < 1. \tag{12.2.3}$$

[2] Method used is that given by Mansour (1990) but with "average" value of V_S set equal to zero

In many applications of industrial interest, the $\alpha/\beta^{1.4}$ term is small compared to the $1/\beta$ term. This permits an even further simplification of Eq. (12.2.1), namely,

$$V_S = \frac{1}{\beta^{0.4}} \tag{12.2.4}$$

In the event that the piping or ducting is not circular, the equivalent diameter,

$$D_{eq} = 4\frac{A}{P_{wet}} \tag{12.2.5}$$

should be used in place of D_t wherein, D_{eq} is the equivalent diameter of the flow region, A is the cross-sectional area of the duct, and P_{wet} is the 'wetted' perimeter. For gas-solids flow of interest herein, the wetted perimeter is the same as the true inner perimeter of the duct.

A worked example, illustrating the use of this method is included in Appendix 12.A.

12.3 High Vacuum Case

In most applications of interest absolute pressure is of sufficient magnitude to cause the mean free path of the gas molecules to be much smaller than the particles feeding the cyclone. This mean free path is the average distance a gas molecule travels between collisions with another molecule. Under such conditions the gas behaves as a continuum and, if the particle Reynolds number is sufficiently small (less than 1 in any case), the familiar Stokes law may, as discussed in Chap. 2, express the drag force acting on a particle moving through the gas

$$F = 3\pi\mu x U' \tag{12.3.1}$$

As we also mentioned in Chap. 2, if the particles and/or the absolute pressure is sufficiently small, a factor called the slip or *Cunningham correction factor*, C_c, is introduced into Eq. (12.3.1):

$$F = 3\pi\mu x U'/C_c \qquad C_c > 1 \tag{12.3.2}$$

Note that we have here divided the Stokes' drag by the Cunningham correction factor, while in Chap. 2 we multiplied the terminal velocity with it; both give the same result. In Chap. 2 we gave the simple relation quoted in Allen (1990) for C_c:

$$U' = U'_{Stk}C_c = U'_{Stk}\left(1 + \frac{2\lambda}{x}\right) \tag{12.3.3}$$

A more sophisticated expression for C_c is given by Davies (1945),

$$C_c = 1 + \frac{2\lambda}{x}\left(A_1 + A_2 \exp\frac{-A_3 x}{\lambda}\right) \tag{12.3.4}$$

λ is the mean free path of the gas, and A_1, $A_2$and A_3 are constants based on experimental measurements. These constants have the values,

$$A_1 = 1.257,\ A_2 = 0.400 \,\text{and}\, A_3 = 0.55.$$

The two alternative expressions (12.2.3) and (12.3.3) give somewhat similar values for C_c.

From elementary kinetic theory of gases, the mean free path can be expressed in the form (Friedlander, 1977)

$$\lambda = \frac{\mu}{\rho}\sqrt{\frac{\pi MW}{2RT}}. \tag{12.3.5}$$

Inspecting the foregoing equations we see that, as pressure decreases and the gas density decreases, the mean free path of the gas phase increases. This, in turn, increases the correction factor, C_c and, hence, decreases the drag force acting on the particle. The practical effect of this is that particles are separated with greater efficiency under vacuum conditions than under ambient or elevated pressures.

12.3.1 Application to Cyclone or Swirl Tube Simulation

When computing the x_{50} cut size of a cyclone operating under high vacuum conditions, one should account for its decrease resulting from the influence of the slip correction factor. However, the slip correction factor depends upon the x_{50} cut size and thus we recommend the following iterative procedure for computing x_{50}:

1. Compute λ from Eq. (12.3.5).
2. Let $C_c = 1$ initially.
3. Let $C_{co} = C_c$
4. Compute the cyclone cut size from Eq. (5.2.1) which has been modified by the introduction of the slip correction factor:

$$x_{50} = \sqrt{\frac{9v_{rCS}\mu D_x}{C_c\rho_p v_{\theta CS}^2}}. \tag{12.3.6}$$

5. Let $x = x_{50}$ and compute a 'new' C_c from Eq. (12.3.4).
6. Compare this 'new' C_c with previous estimate as follows: If ABS$[C_c - C_{co}]/C_c \leq N_\varepsilon$ (0.01, typically), then go to Step 7. Else let $C_{co} = C_c$. Go to Step 4.
7. x_{50} computed in Step 4 is the desired cut size under prevailing vacuum conditions.

A worked example showing how to use this calculation scheme is included in Appendix 12.B.

12.A Worked Example for Calculation of the Critical Deposition Velocity

Given: $D_t = 0.300$ m (0.984 ft)
ρ_p=1.600 × 10^3 kg/m^3 (99.9 lb_m/ft^3)
ρ= 12.2 kg/m^3 (0.762 lb_m/ft^3)
$\mu = 0.04$cp → 4.00 × 10^{-5} kg/ms (2.69 × 10^{-5} lb_m/ft s)
x= 200 μm → 2.00 × 10^{-4} m (6.56 × 10^{-4} ft)
g= 9.81 m/s^2 (32.2 ft/s^2)

Find: V_s

Solution

$$\alpha \equiv \frac{10\mu}{(\rho_p - \rho)\, g x D_t} = \frac{10 \times 4.0 \times 10^{-5}}{(1600 - 12.2)\ \ 9.81 \times 2.0 \times 10^{-4} \times 0.3} = 4.28{\times}10^{-4}\text{s/m}$$

$$\beta \equiv \frac{\rho^{1.5}}{100\,(\rho_p - \rho)\, g \mu^{0.5} D_t^{0.5}} = \frac{12.2^{1.5}}{100\,(1600 - 12.2)\ \ 9.81\,(4.0 \times 10^{-4})^{0.5}\, 0.3^{0.5}}$$
$$= 7.90 \times 10^{-3}\text{s}^{2.5}/\text{m}^{2.5}$$

$$V_S = \left(\frac{1}{7.9 \times 10^{-3}} - \frac{4.28 \times 10^{-4}}{(7.9 \times 10^{-3})^{1.4}} \right)^{0.4} = 6.93 \text{ m/s}\,(22.7 \text{ ft/s})$$

This solution is identical to the rigorous (trial and error) solution of Eq. (12.2.1) to within three significant figures. It may be noted that the second term enclosed in parenthesis above is negligible in comparison to the first. Accordingly in this particular example, Eq. (12.2.4) also provides an excellent approximation to Eq. (12.2.1):

$$V_S = \frac{1}{(7.9 \times 10^{-3})^{0.4}} = 6.93 \text{ m/s}\,(22.7 \text{ ft/s})$$

12.B Worked Example Taking Into Account Slip in Calculation of the Cut Size

The 1.72 m diameter cyclone described in Appendices 4.A and 5.A is to be operated at an absolute pressure of 0.1 atmosphere. We wish to compute the x_{50} cut-point diameter. We shall assume, for the sake of simplicity, that there is no change in the total friction factor as a result of the decrease in operating pressure.

Solution

At the reduced pressure of interest the gas density is 0.1 times that at ambient conditions. Thus, $\rho = 0.1 \times 1.2\text{kg/m}^3 = 0.12\ \text{kg/m}^3$.

Step 1:

$$\lambda = \frac{1.81 \times 10^{-5}}{0.12}\sqrt{\frac{\pi 29}{2 \times 8.31 \times 103 \times 294}} = 6.51 \times 10^{-7}\ \text{m} = 0.65\ \mu\text{m}$$

Note—due to the ten-fold reduction in pressure, our mean free path is ten times that of air at standard conditions.

Step 2:

$$C_c = 1$$

Step 3:

$$C_{co} = C_c = 1$$

Step 4:

$$x_{50} = \sqrt{\frac{9 \times 1.44 \times 1.81 \times 10^{-5} \times 1.72}{1 \times 2700 \times 64.7^2}}\ 5.97 \times 10^{-6}\ \text{m}\ = 6.0\ \mu\text{m}$$

Step 5:

$$C_c = 1 + \frac{2 \times 6.51 \times 10^{-7} l}{5.97 \times 10^{-6}}\left(1.257 + 0.400 \exp\left(\frac{-.55 \times 5.97 \times 10^{-6}}{6.51 \times 10^{-7}}\right)\right) = 1.27$$

Step 6:

$$\frac{|1.27 - 1|}{1.27} = 0.213\ \text{not}\ \leq 0.01 \Rightarrow C_{co} = 1.27$$

Repeat steps 4, 5 & 6:

Step 4:

$$x_{50} = \sqrt{\frac{9 \times 1.44 \times 1.81 \times 10^{-5} \times 1.72}{1.27 \times 2700 \times 64.7^2}} = 5.30 \times 10^{-6}\ \text{m}\ = 5.3\ \mu\text{m}$$

Step 5:

$$C_c = 1 + \frac{2 \times 6.51 \times 10^{-7} l}{5.30 \times 10^{-6}}\left(1.257 + 0.400 \exp\left(\frac{-.55 \times 5.30 \times 10^{-6}}{6.51 \times 10^{-7}}\right)\right) = 1.31$$

Step 6:

$$\frac{|1.31 - 1.27|}{1.31} = 0.031\ \text{not}\ \leq 0.01 \Rightarrow C_{co} = 1.31$$

Repeat steps 4, 5 & 6:

Step 4:

$$x_{50} = \sqrt{\frac{9 \times 1.44 \times 1.81 \times 10^{-5} \times 1.72}{1.31 \times 2700 \times 64.7^2}} = 5.22 \times 10^{-6} \text{ m} = 5.2 \ \mu\text{m}$$

Step 5:

$$C_c = 1 + \frac{2 \times 6.51 \times 10^{-7} l}{5.22 \times 10^{-6}} \left(1.257 + 0.400 \exp\left(\frac{-.55 \times 5.22 \times 10^{-6}}{6.51 \times 10^{-7}}\right)\right) = 1.315$$

Step 6:

$$\frac{|1.315 - 1.310|}{1.315} = 0.0038 \leq 0.01$$

Go to Step7:
Step 7:

$$x_{50} = 5.2 \ \mu\text{m}$$

Consequently, as a result of the reduction in operating pressure, the x_{50} cut-point of the cyclone is reduced from 6.0 (at 760 mm Hg) to 5.2 μm (at 76 mm Hg). This is illustrated schematically in Fig. 12.B.1.

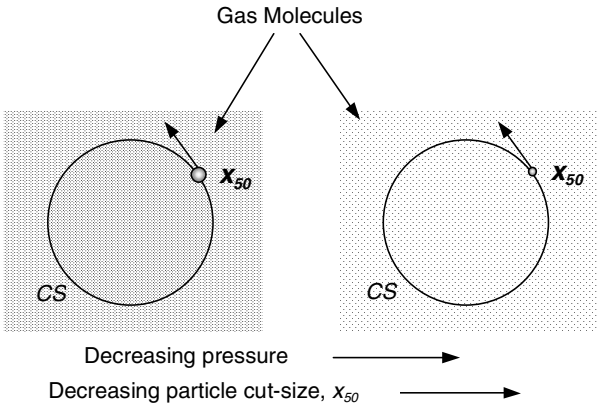

Fig. 12.B.1. Effect of decreasing pressure on equilibrium 'cut size' x_{50} orbiting in a cross-sectional plane of cylindrical surface *CS*

As this example tends to suggest, one does not normally have to account for the suppression of the x_{50} cut-point unless the cyclone is to be operated under 'high' vacuum conditions (typically less than about 100 mm Hg) or with a high molecular weight gas. The influence of such variables is revealed by inspecting Eqs. (12.3.5), (12.3.4) and (12.3.6).

Note: For simplicity sake it has been assumed above that the dust-to-air *mass* loading is the same as that reported for the 'reference' cyclone described in Appendices 4.A and 5.A. This implies that the dust mass flow rate is 10 times less than that for the reference cyclone. This follows from the fact that

the absolute pressure, the gas density and *mass* flow rate of the gas was reduced by a factor of 10. The inlet gas *volumetric* flow rate and inlet gas velocity, however, remained unchanged relative to the reference cyclone.

If we had operated our vacuum cyclone with the same absolute mass flow rate of dust that reported to our reference cyclone, then the dust concentration term, c_o in Eq. (4.2.9), would have increased 10-fold, and f_{dust} by a factor of $\sqrt{10}$. A comparison with the variation in the friction factor for flow in a reasonably rough pipe at the same two pressures (and comparable values of Re) shows that Eq. (4.2.9) predicts an unrealistically large increase in f because of this increase in f_{dust}. Equation (6.1.11) represents an improvement over Eq. (4.2.9) in this respect. In Eq. (6.1.11) the increase in c_o is compensated due to the inclusion of the factor ρ (the gas density).

13

Demisting Cyclones

Until now we have been concerned with the separation of solid particles from gas streams. However, cyclones may be also utilized quite effectively to separate liquids contained in a carrier gas stream. The principles are the same but liquids pose some unique problems and some advantages relative to solids-collecting cyclones.

We wish to point out at the outset here that, by far, the majority of vapor-liquid separation tasks are performed using either conventional gravity settling or 'knock-out' drums or demisting meshes or pads. Knock-out drums or pots are very robust and are almost always used to separate liquid from carrier gas stream if the incoming stream contains a high volumetric fraction of liquid (greater than several percent). With proper design they can generally be depended upon to separate the majority of droplets greater than about 500 μm but are not suitable for collecting finer droplets. Demisting mats, on the other hand, exhibit relatively low pressure drops (typically less than a few centimeters of water column) and can capture drops as small as a few microns. They are not suitable for high liquid loading conditions such as that which may exists under two-phase slug flow conditions, nor in applications where the demisting mat could be exposed to foam. They are also subject to fouling from any solids or waxy, gummy or coke-forming material in the feed stream.

In between these two separator types are vapor-liquid cyclone separators. Cyclonic type separators have been gaining in importance during the past decade and are now playing a major role in the oil and gas industries, especially in offshore applications where large and expensive gravity separators are being replaced by much more compact, and much more efficient gas-liquid separation equipment. In gas transmission installations cyclones are also well suited to protect gas compressors and turbines from fouling and erosion. In such service they are capable of removing essentially 100% of the solid and liquid particles 6 to 8 microns and larger.

Cyclones, like gravity separators, can be designed to handle large volumetric concentrations of incoming liquid if they are equipped with or set atop

a liquid hold-up drum. As with a gravity separator, such a drum is used to provide liquid level control and, normally, several minutes of liquid surge capacity. Our focus, herein, however, will be on what we shall call 'demisting' cyclones.

Unlike the particles feeding conventional gas-solids cyclones, liquid particles feeding a gas-liquid cyclone are normally greater in size and are not porous. These two factors tend to make for an easier separation. In many systems the gas/liquid mixture feeding the cyclone enters through some upstream piping wherein small droplets coalesce into larger drops, the driving force for the coalescence of colliding droplets being provided by surface tension. We'll present an example of this below. In addition, unlike gas-solids cyclones, once the incoming liquid droplets are centrifuged to the wall of the cyclone, they merge with the liquid wall film to form a much larger mass which is not easily removed or re-entrained back into the gas phase. In gas-solids cyclones, fine dust particles are much more easily re-entrained off the walls. The droplets entering a gas-liquid cyclone are also not likely to plug the cyclone as sometimes occurs with statically charged or tacky solids in a gas-solids cyclone.

In some applications, deposits may form on the roof or outside area of the vortex tube if these surfaces are not sufficiently wetted by the incoming liquid. In these cases, the affected surfaces normally can be kept clean with spray nozzles. Gas-liquid cyclones do not normally pose the same erosion concerns experienced with certain solids handling cyclones. The factors mentioned above – the formation of wall films and their relative immunity to both plugging and erosion – have given their designers more latitude with respect to their construction and design details than that commonly observed with gas-solids cyclones. Thus, demisting cyclones can be found with a wide variety of internal features including relatively thin, close-fitting vanes, narrow slits or shave-offs, anti-creep skirts, isolation disks, coalescing mats, relatively small liquid discharge openings, recirculation slots or slits and attendant piping, and other intricate internals.

13.1 Liquid Creep and 'Layer Loss'

Notwithstanding their many advantages, demisting cyclones also pose a few problems relative to dedusting cyclones. Unlike gas-solids cyclones, some portion of the incoming liquid tends to deposit along the upper walls of the cyclone in the form of a wall film. This wall film is not static or stationary but is driven by the secondary gas flow dragging it up the walls, then radially inwards across the roof, and down the vortex tube. If not redirected, this liquid will simply 'short circuit' the cyclone and exit along with the gas phase. Such behavior, known as 'layer loss', is clearly detrimental to overall separation performance but can be avoided through the use of appropriate 'roof skimmers', vortex-tube 'anti-creep skirts', or inlet 'raceways'. A few such devices are illustrated in Fig. 13.1.1. The raceway functions very much like

the roof-skimming cylinder but attempts to prevent liquid from reaching the upper areas of the cyclone in the first place. The anti-creep skirt often has a serrated or 'saw-toothed' trailing edge to facilitate the dislodging of the liquid film. At high liquid loadings (greater than about 1 kg liquid/kg of gas), both roof skimmer or raceway and an anti-creep skirt should be installed.

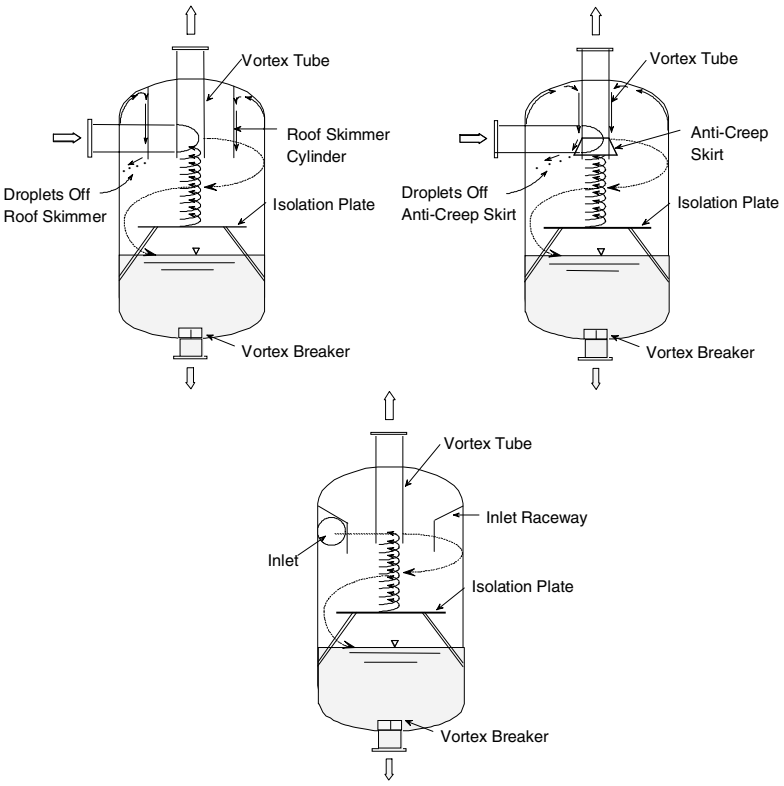

Fig. 13.1.1. Illustration of three vapor-liquid cyclone devices for preventing liquid losses due to secondary flow behavior: roof skimmer, vortex tube anti-creep device and inlet raceway

Unlike their gas-solids cousins, the inlet pipe feeding a vapor-liquid cyclone should not be inserted in very close proximity to the cyclone roof. Nor should it be designed with a 'helical' roof design for gas-liquid cyclones. Both of these configurations tend to encourage the 'layer loss' described above. If possible, the top of the inlet piping should be located at least one inlet pipe diameter below the outside edge of the roof. In principle, at least, it is possible to reduce 'layer losses' by directing the inlet pipe slightly downward (e.g. 10°) although this is rarely observed in practice.

Wherever possible, the inlet piping to a gas-liquid cyclone should consist of a straight section of pipe having a length-to-inside diameter (L/D) ratio not less than 10 following any upstream bends, tees or other flow disturbances. In no case should the L/D ratio drop below 5. Any upstream bend should also cause the two-phase mixture reporting to the cyclone to turn in the same rotational direction as that within the cyclone. For example, if the gas-liquid mixture enters the cyclone in a clockwise manner in plan view, then the nearest upstream bend that lies in a horizontal plane should also make a clockwise turn.

13.2 Demisting Cyclone Design Considerations

Demisting type cyclones are sized following the same general design guidelines reported elsewhere in this book. Unlike gas-solids cyclones, however, the drop size distribution feeding demisting cyclones is generally not very well known. Still, unless the droplets are less than about 10 μm in size, droplets contained in most process streams can be separated with conventional cyclone type separators. This is simply because most cyclones will exhibit a d-50 cut-point diameter between about 3 to 15 μm and the vast majority of droplets contained in process streams (except for 'fogs') are much greater than this. In fact, it is rather difficult to design a cyclone that cannot capture or separate most of the liquid in the majority of applications of commercial interest. The main challenge in such designs lies less with the inherent ability of the cyclone to separate incoming droplets from the gas phase but more with the proper handling of the liquid phase once it is 'centrifuged' to the walls of the separator.

As mentioned above, a vapor-liquid cyclone of the conventional reverse-flow variety must be designed to handle liquid films attempting to make their way out the vortex tube (*i.e.*, 'layer losses'). Additionally, the cyclone must be designed so that the vortex 'tail' (the end of the vortex) is isolated or decoupled from any liquid that is allowed to collect in the lower section of the separator or from the liquid already flowing down the walls. See, for example, Fig. 13.1.1. Furthermore, proper underflow sealing is just as important with vapor-liquid cyclones as it is for gas-solids cyclones.

As an illustration of an underflow seal problem (and related problems), a cyclonic type of droplet separator was once installed on the outlet flange of a very large knock-out drum ahead of a wet-gas compressor (WGC). The separator was equipped with drainpipes that reported down to a pool of liquid and which sealed the drainpipes under normal or design flow conditions. Despite the existence of the knock-out drum and the separator, liquid carry-over from this two-stage separation arrangement led to a major failure of the downstream WGC. Calculations of the separation performance of the cyclonic separator showed that only an insignificant trace of liquid should have escaped the separator for the flow conditions that were in effect at the time of the fail-

ure. In fact, the vapor flow rate was more than double the flow for which the separator was originally designed. This led to a very low computed cut-point diameter for the separator and from this, alone, it appeared as though it was impossible for any significant quantity of liquid to have escaped capture by the separator. Unfortunately, not only was the gas flow through the separator much higher than design conditions originally specified for this service, there was a serious mismatch between the cyclonic separator's gas outlet diameter and the diameter of the gas outlet flange located atop the vessel and to which the separator was directly flanged and in close contact. This smaller diameter outlet flange intensified the swirl and had the same effect that a reduction in vortex tube diameter would have on a conventional cyclone. This produced a pressure loss across the separator that greatly exceeded design expectations. This excessive pressure loss created a suction on the separator's drain pipes sufficient to 'suck' or educt liquid out the bottom of the knock-out drum, through the separator located atop the drum, and into the WGC. Once the true cause of the liquid carryover problem was understood, the limitations with the upstream separation equipment were addressed with the result that not a trace of liquid could be detected at the inlet to the newly rebuilt WGC.

A point we wish to make here is that the ultimate performance of an operating cyclone installation is not just a function of the cyclone design. Rather, the entire 'system' must be examined beyond considerations pertaining solely to droplet aerodynamics and forces acting upon individual droplets. The failure described above was a classic case of what can happen when one limits one's attention to just 'the separator'. There was nothing 'wrong' with the separator, per se, even though it was being operated beyond its design velocities. Likewise, there was nothing 'wrong' with the diameter of the outlet pipe/flange, located atop the vessel, as far as its ability to handle the gas flow through the vessel. But the two, in combination, created the problem described above. The vessel outlet pipe became, in effect, a part of the separator. It's been said that, "Things tend to go wrong at the discipline interfaces." This is true also in the physical 'interfaces' connecting different pieces of equipment; in this case, the separator and the vessel flange.

In two-phase mist-annular flow through ordinary piping, it is observed that the pressure drop through a given section of pipe is greater than that for the gas flow alone. The increase in pressure drop increases very rapidly with increases in liquid loading up to about 0.1 kg liquid per kg of gas. After this, the increase tends to level off rapidly. A film of liquid gives rise to most of the increase in pressure drop. In such cases, the primary reason for the increase in pressure drop is the increased wall roughness created by waves on the surface of the pipe walls. Such is also the case with vapor-liquid cyclones, which may be viewed as operating in a swirling type of 'mist-annular' flow state. In Sect. 13.5 below, we will present an equation for estimating the effect that the liquid phase has on the wall friction factor for gas-liquid cyclones.

13.3 Some Vapor-Liquid Cyclone Design Geometries and Features

Vapor-liquid cyclones come in a bewildering array of design geometries and configurations. The basic design shown in Fig. 13.1.1, and variants thereof, is perhaps the closest thing one can envision as a 'standard' design. Interestingly, most vapor-liquid or demisting cyclones do not feature a conical lower section but tend to be of the cylindrical variety. As shown, it is quite common for vapor-liquid cyclone vessels to function as both a separator and as a liquid holdup vessel. In this capacity, it is quite important – from a separations point of view – that the 'end' of the vortex not be allowed to come in contact with the surface of the liquid pool which exists in the lower part of the cyclone vessel. Hence, an 'isolation' plate (also know as a 'stilling plate' or 'vortex stabilizer plate') is used to provide a surface upon which the end of the vortex can 'lite' and spin like a top. Obviously then the purpose of this plate is not to 'break' or interfere with the vortex but to prevent it from contacting the surface of the liquid phase. Under no conditions should a 'cross' type of device be used to 'break' the main (gas-phase) vortex as these create extreme levels of turbulence and greatly weaken the vortex.

A true 'vortex breaker' is normally inserted just ahead of the vessel's liquid exit nozzle as shown in Fig. 13.1.1. This is a very important feature in the geometry at hand since the angular momentum of the incoming gas-liquid mixture will produce bulk rotation of the liquid pool. If a vortex is allowed to form, some of the incoming gas may exit out the underflow and create pump cavitation or other problems downstream. The vortex will also act as a type of fluidic 'choke' and restrict the flow rate out the bottom liquid exit nozzle.

Vortex breakers normally consist of simple crosses of flat plate metal or a flat circular plate located about 1 outlet pipe diameter above the exit pipe. The plate diameter is normally 2 to 4 times the diameter of the exit pipe. The writers prefer to use both a cross and a wide circular plate in order to prevent a vapor core vortex 'finger' from dipping down and exiting through only one of the 4 open quadrants comprising the vortex cross. Some vortex breakers are "seat of the pants" designs which may, or may not, work. Although there is no one universal standard governing their design, most engineering companies and engineering contractors have "in house" design rules or specifications that cover most design situations one is likely to encounter in practice. This includes vortex breakers for both bottom and side exiting pipes. Pump manufactures are another good source for design assistance.

Aside from installing a vortex breaker on the exiting liquid phase, it is good practice to limit the liquid velocity out the underflow nozzle to a maximum value of about 1 m/s. Downsteam of this nozzle the line size may be reduced to comply with normal pipe sizing criteria or, if solids are present, to prevent their setting out in any horizontal sections of the piping. Consideration should also be given to installing perforated, vertical wall baffles in the liquid phase as these serve to retard bulk rotation of the liquid pool.

Figs. 13.3.1 through 13.3.6 depict several other vapor-liquid cyclone geometries and are somewhat illustrative of the great variety of designs in commercial service. These illustrations are indicative and not exhaustive.

Figure 13.3.1 shows the 'Gasunie' cyclone separator. Note the anti-creep skirts on the vortex finder and the large vortex breaker. The cyclone is of the reverse-flow type and the vanes imparting the swirl to the incoming liquid-laden gas form a fairly shallow angle to the horizontal.

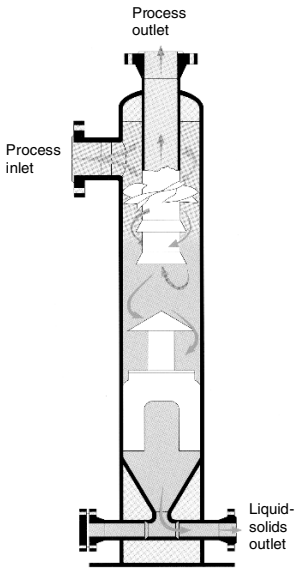

Fig. 13.3.1. Gasunie cyclone separator courtesy of Gasunie Engineering B.V.

Figure 13.3.2 illustrates an 'inline' flange-to-flange reverse-flow cyclone using a stilling plate to isolate the collected liquid from the active vortex. This plate is supported directly off the vessel walls and contains slot-like openings for the liquid to pass through. The vessel's length and/or diameter below the stilling plate may be increased, as necessary, to provide liquid surge or holdup capacity and level control.

Figure 13.3.3 shows a flow-through cyclone that uses a vane type inlet (very common in such flow-through designs) to impart the necessary spin to the incoming gas-liquid mixture. This particular design is very interesting in that it features a demisting mat to first coalesce very fine incoming droplets into larger drops ahead of the cyclone section. We note that the mat does not 'collect' or separate any of the incoming droplets but simply acts to physically enlarge the drop-size distribution. A large ring is attached to the lower end of the vortex tube to help isolate the swirling gas flow from the exiting liquid

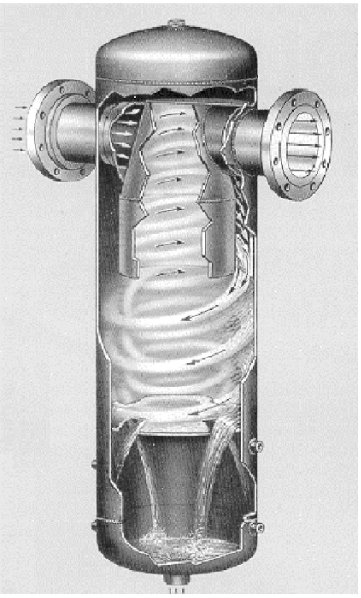

Fig. 13.3.2. Wright-Austin type TS vapor/liquid cyclone separator. Courtesy Hayward Industrial Products, Inc.

phase and to thus facilitate removal of the liquid. A smaller diameter ring is attached near the leading edge of the vortex tube to reduce any 'layer loss' of the type described above. Flow-through cyclones such as this one, or the generic design shown on the right of Fig. 13.3.3 may be designed to operate in either the horizontal or vertical direction. However, it is the writers' opinion that such cyclones perform better in the vertical (down) direction since the arrangement better accommodates gravitational removal of the liquid phase.

As we observed when studying the equilibrium-orbit model of Sect. 5.2, a cyclone's cut size and overall efficiency are dependent upon its diameter. We found that the centrifugal force acting to separate a particle (or droplet, for the case at hand) to the inner walls of the separator is inversely proportional to the radius of the gas outlet pipe, and that the cut size is proportional to the square root of this radius, other factors being equal. Thus, rather than having all the flow report to just one relatively large cyclone, one can achieve an improvement in separation performance by dividing and evenly distributing the flow over a number of small diameter cyclones. A 'multicyclone' (or 'multiclone'), such as that shown in the left-hand side of Fig. 13.3.4, illustrates such an arrangement. It consists of a number of relatively small diameter, cylindrical-bodied cyclones housed in a single pressure-retaining vessel. Two tube sheets are used to isolate the inlet chamber from the upper clean-gas plenum chamber and the lower liquid receiving chamber. The cyclone assembly shown is equipped with liquid level control or sensing taps and a flanged

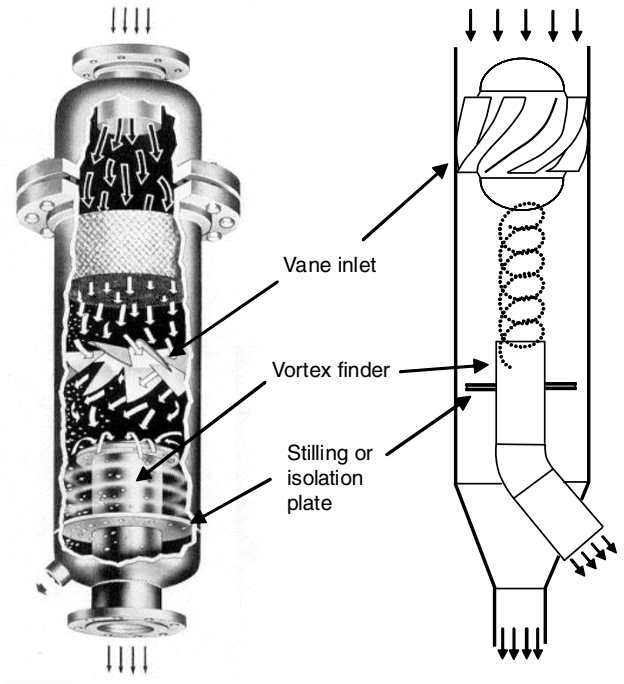

Fig. 13.3.3. Left: Wright-Austin type 31L CLC vapor/liquid cyclone separator. Courtesy Hayward Industrial Products, Inc. Right: A generic flow-through cyclone design

top head for inspection and maintenance access. The three frames to the right of the multiclone vessel illustrate three different designs of the individual cyclone units:

The first features a twin-scroll inlet design, spaced 180 degrees apart, for imparting spin to the incoming gas-liquid mixture. Such twin inlet designs result in a more symmetrical inlet flow pattern relative to the 'slotted inlet' design commonly used in gas-solids separators. They also allow the designer to reduce the overall height of the cyclone body since, for the same total volumetric flow rate, the inlet (a scroll in this case) height is half that of a single inlet design.

The second cyclone body shown in Figure 13.3.4 illustrate a vane-type inlet design that we refer to herein as a swirl tube separator. Vane inlets are the most symmetrical of all inlet designs but are somewhat more complicated to design and fabricate or, in some cases, to cast. Both the twin inlet and vane inlet cyclone designs described thus far are of the conventional reverse-flow variety.

The separator on the far right of Fig. 13.3.4 and in Fig. 13.3.5 is a rather sophisticated cylindrical-bodied flow-through or straight-through type cyclone.

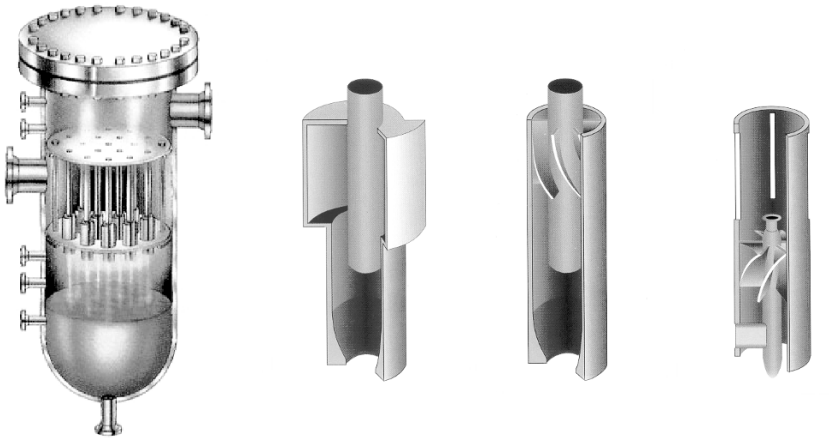

Fig. 13.3.4. A Burgess-Manning multicyclone vapor/liquid separator unit (left-most frame) and three different cyclone body designs: Burgess-Manning type R-T, R-A and A-X, respectively. Courtesy Burgess-Manning, Inc.

Like the aforementioned design, it uses an inlet vane assembly for generating the spin required to separate the incoming liquid (and solids that may be present) to the walls. This separated material is then forced to exit out of a symmetrical array of vertical slots by a purge flow amounting to 15–20% of the incoming gas flow. This purge stream is recycled back into the separator though a hollow pipe, which also supports the inlet vane, see Fig. 13.3.5. The relatively low static pressure that exists in the vortex core is what drives this recirculating gas flow. The liquid (and solids, if present) that exits the slots with the purge flow report to the liquid pool at the bottom of the vessel. Figure 13.3.5 also illustrates the use of a 'half-pipe' vessel inlet design often used to remove any large drops or incoming liquid slugs ahead of the multicyclone assembly.

Because they can more effectively separate smaller droplets relative to a conventional, large, single-stage cyclone, multiclones are reported to have 'turn-down ratios' (maximum-to-minimum volumetric feed rate that still meets performance targets) as high as 4:1.

Strong similarities exist between gas-solid and gas-liquid cyclones and, thus, the reader may wish to review the related discussion presented in Sect. 16.2 pertaining to gas-solid multiclone separators.

Scrubbing type cyclones use features of both a dry cyclone and a spray chamber to remove pollutants[1] or particulates from a gas stream. This type

[1] In this text, we distinguish "pollutants" from "particulates", recognizing that not all particles (liquid or solids) are "pollutants". In most industrially important operations particles are captured for recycling back to the process from which

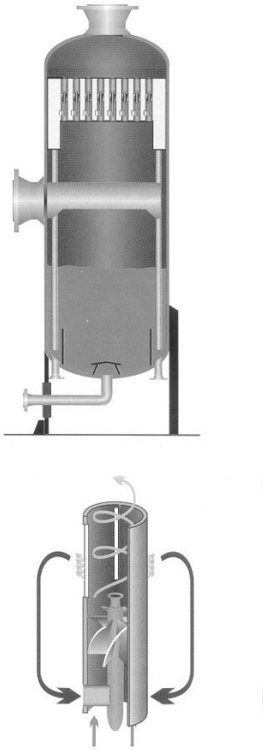

Fig. 13.3.5. A Burgess-Manning separator vessel (top frame) equipped with type A-X recycling type multicyclones (bottom frame). Courtesy Burgess-Manning, Inc.

of technology is a part of the group of air pollution or particulate collection devices collectively referred to as wet scrubbers.

Figure 13.3.6 is a photograph of a skid-mounted venturi-scrubber/cyclone separator system. Spray water injected (see far left-hand side in the photograph) is captured by the rather short cylindrical-bodied cyclone separator located immediately downstream of the scrubber. We note that the cyclone has a scroll-type rectangular inlet and that the downstream blower makes this a pull-through type system. Scrubber water collected by the cyclone reports to a receiving tank located below the cyclone. From here, it is pumped back up through the scrubber's spray nozzles.

The two cyclonic scrubbers shown in Fig. 13.3.7 are capable of removing particulates as small as 2 to 3 microns as well as any gaseous components that are soluble in water. They typically operate at liquid-to-gas (L/G) ratios of 0.3 to 1.3 l/m^3 (2 to 10 gal/1000 ft^3) and at pressure drops of 4 to 25 cm

they came or they are the product or byproduct themselves. In some situations both definitions fit.

Fig. 13.3.6. A skid-mounted venturi scrubber/cyclone ensemble by Fisher-Klosterman, Inc.

of water (1.5 to 10 in. of water). They are often utilized in mining, drying, foundries, and food processing industries.

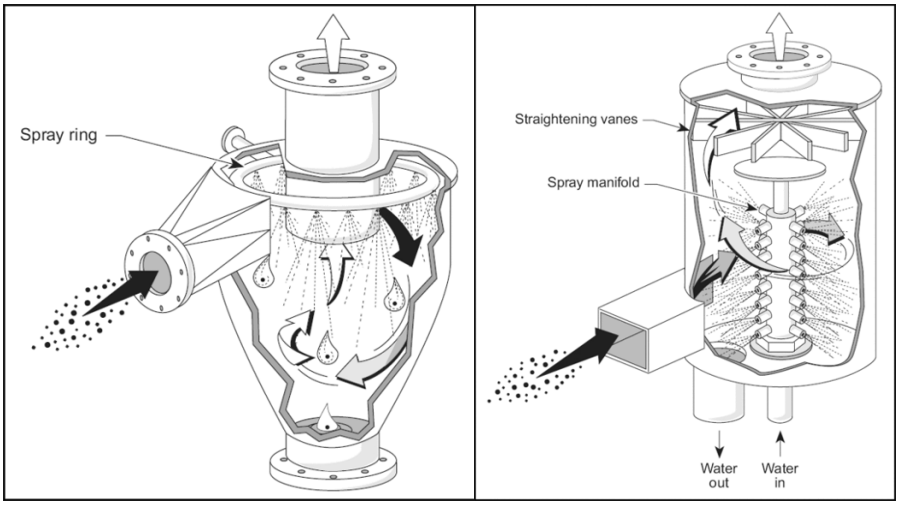

Fig. 13.3.7. Left: an irrigated cyclone scrubber. Right: a cyclonic spray scrubber. Source: US Environmental Protection Agency

Unlike simple spray towers that operate at gas velocities on the order of 0.6 to 1.5 m/s (2 to 5 ft/s), cyclonic scrubbers are designed to operate at gas velocities of 60 to 180 m/s (200 to 600 ft/s). This makes cyclonic scrubbers much more efficient than spray towers in removing particulates due to the much greater particle-to-liquid relative velocity and turbulence. However, cyclonic type scrubbers are still not as efficient as venturi scrubbers.

Although cyclonic scrubbers are relatively compact and quite robust, due to their high gas velocities, they must sometimes be equipped with special abrasion-resistant liners to control the rate of erosion, especially in their inlet target zones. Aside from erosion, corrosion can also be a concern since most structural alloys corrode from exposure to moisture in the air or gas stream. Corrosion is of special concern if the gas contains agressive constituents such as acids, caustics, dehydrating agents, halogens and halogen salts, organic halides, carbolic acid, etc.

Spray nozzle plugging is another concern. Nozzles have a tendency to plug either due to particles in the water recycle stream or in the gas stream. Nozzles can also erode internally due to particles in the recycle water. They can also corrode. Strainers are usually required to protect the nozzles from such internal erosion. In any case, the design of the spray header should be such that the nozzles are accessible for routine cleaning or replacement.

The design of cyclonic scrubbers is usually based on pilot tests, experience with units in similar service and empirical correlations rather than any fundamental model of absorption or particle collection performance. A skid mounted test unit, similar to that shown in Fig.13.3.6, can give plant personnel a very good indication of the expected performance of a commercial scale unit.

13.4 Estimating Inlet Drop Size for Two-Phase Mist-Annular Flow

Unlike a solids collecting cyclone, the performance of a demisting cyclone is much more dependent upon the flow conditions that exist in the upstream piping. This, of course, is because the 'particle' or drop size distribution feeding the cyclone is strongly dependent upon such factors as shear rate and surface tension. The shear rate is, itself, a function of the upstream pipe diameter, the superficial gas velocity and the physical properties (namely densities and viscosities) of the gas and liquid phases.

Under mist or mist-annular flow conditions, such as that illustrated in Fig. 13.4.1, one can use the 'Harwell' technique to get a rough estimate of the average drop size (UKAEA, 1980).

The Harwell procedure applies to steady-state flow conditions and to the flow pattern existing downstream of any flow disturbances (such as orifice plates, valves, expanders, bends, tees, etc.). It is only one of several correlations available for computing drop sizes. Nonetheless, it was developed on

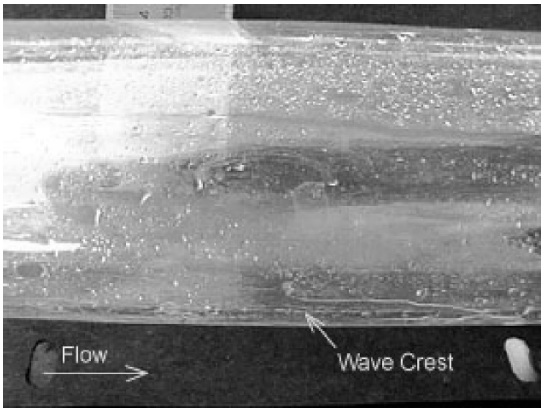

Fig. 13.4.1. Mist flow in a horizontal 2 inch ID pipe. Note small wave crest at bottom center of pipe

basis of many steam-water, air-water and other fluid data and, because of this, it is considered by the writers to be one of the more accurate and robust correlations available.

Harwell's method for predicting average drop size contains two additive terms. One is dependent upon the volumetric concentration of droplets in the gas phase and the other is independent of the droplet concentration. However, the concentration dependent term is rather difficult to estimate a priori and we will not include it here. When this term is neglected, the average drop size computed will tend to be somewhat smaller than that which we would expect to experience in practice. This approach is normally quite acceptable from a separator sizing or evaluation point of view since any droplets larger than what we may compute are those that are most easily separated.

The Harwell equation predicts that the 'Sauter mean' (the mean of the surface distribution rather than the volume distribution, see Chap. 2) droplet diameter is:

$$\langle x \rangle_{Sa} = 1.91 D_t \frac{Re^{0.1}}{We^{0.6}} \left(\frac{\rho}{\rho_l} \right)^{0.6} \tag{13.4.1}$$

where Re and We are the Reynolds and Weber number, respectively. They are defined as,

$$Re = \frac{\rho v_t D_t}{\mu}, \quad We = \frac{\rho v_t^2 D_t}{\sigma}$$

and where $\langle x \rangle_{Sa}$ is the Sauter mean droplet diameter. D_t is the internal diameter of the pipe, ρ and ρ_l are the gas and liquid densities, μ is the gas viscosity, v_t is the mean gas velocity within the pipe and σ is the interfacial surface tension ('IFT')

The Weber number can be understood as the ratio of inertial forces, which tend to break a droplet apart, and surface tension forces, which tend to hold it together.

In certain mass-transfer operations, such as spray columns, the Sauter mean diameter is a useful quantity to know. However, in studies of droplet erosion or droplet separation, the volume or mass median diameter is more physically meaningful. This volume-average (median) drop diameter is related to the Sauter-mean diameter through the following approximation (AIChE, 1978).

$$\langle x \rangle_{med} = 1.42 x_{Sa}. \tag{13.4.2}$$

An example calculation for estimating the Sauter mean droplet size in pipelines is included in Appendix 13.A.

13.4.1 Estimating Drop Size Distribution

The preceding section provides us with a technique for estimating the volume-averaged drop size of a collection of droplets flowing within a pipe under mist-annular flow conditions. And while this is often all that one may wish to know about the droplet distribution, it is sometimes of interest to know, or at least estimate, the entire drop size distribution. Such would be the case if one wished to perform a cyclone simulation study which required, as input, an estimate of the inlet drop size distribution which may exist within the upstream pipe feeding the cyclone.

Fortunately, it turns out (AIChE, 1978) that the width of the drop size distribution is strongly dependent upon the volume or mass average droplet size, x_{med}, as previously computed. Furthermore, if the drop size distribution [*i.e.*, $F(x)$] is normalized by dividing each x by x_{med}, then, as a rough approximation, all droplet distributions are identical and can be represented as shown in Table 13.4.1 and 13.4.2:

Table 13.4.1. Points on the standard size distribution for droplets

x/x_{med}	0	0.3	0.62	1	1.5	2.9
$F(x/x_{med})$	0	0.05	0.25	0.5	0.75	1.0

For this distribution the mean size $\langle x \rangle$ is almost equal to the median size x_{med}.

We may note that:

- only about 5% of the droplets will be of size $x/x_{med} = 0.30$ or less
- 100% will be less than $x/x_{med} = 2.9$

In Appendix 13.A, an example calculation showing how to use this standard droplet distribution is given.

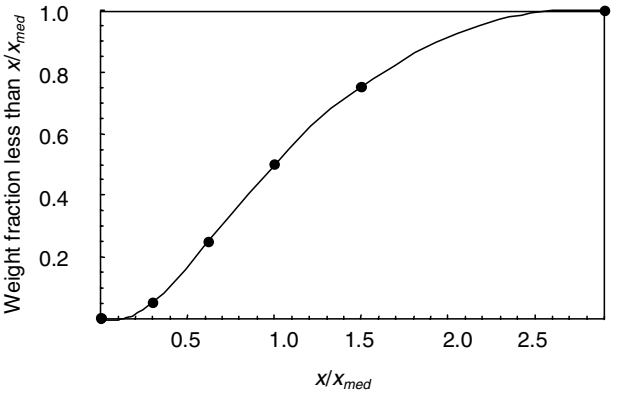

Fig. 13.4.2. Standard size distribution for droplets in pipelines

13.5 Modeling the Performance of Vapor-Liquid Cyclones

The method we wish to present here for modeling the performance of vapor-liquid ('demisting') cyclones follows closely the method presented by Muschelknautz and Dahl (1994) and that presented for gas-solids cyclones previously reported in Chap. 6. All the same, to avoid repetition of the formulism, here we shall focus on pointing out differences in the two methods. The reader is encouraged to refer back to Chap. 6 while reading the discussion below.

The calculation method reported below is rather rudimentary in comparison to that which we have reported earlier for gas-solids cyclones. There is still substantial room for further refinement in the modeling of vapor-liquid cyclones.

Unlike their gas-solids counterparts, one almost never knows from measurement the droplet size distribution feeding vapor liquid cyclones and, quite often, one is often not certain of the quantity of liquid feeding the cyclone. Still, the method presented below should provide some help as it provides a rough method for estimating the cyclone's cut size and, if the liquid loading and its approximate distribution is known, the overall collection efficiency.

The equations assume that the cyclone is constructed with a roof skimmer or raceway and a vortex tube anti-creep skirt to minimize the detrimental effects of liquid creep, as well as a vortex stabilizing plate to prevent collected liquid from becoming re-entrained.

13.5.1 Computation of Cut Size

As was the case for gas-solids cyclones, we begin by computing the entrance 'constriction' coefficient, α, from Eq. (6.1.1). If, as is often the case for vapor-liquid cyclones, the entrance duct is a circular pipe, the 'width' variable, b,

appearing in the formula $\xi = b/(\frac{1}{2}D) = b/R$, is to be interpreted as the inside diameter of the cyclone's inlet pipe, d_e. In addition, the inlet loading variable, c_o, is now defined as the ratio of the mass of incoming *liquid* to mass of incoming gas in the feed stream.

We compute the tangential velocity of the gas at the 'inner core' radius, R_{CS}, by following the calculation procedure leading up to Eq. (6.2.1) and by using the same equation reported therein for the frictional area term,A_R. However, for the computation of the total friction factor, f, we do not use Eq. (6.1.11) but the simpler, approximate expression geared to liquids:

$$f = f_{air}\left(1 + 0.4c_o^{0.1}\right) \tag{13.5.1}$$

where, as before, f_{air} is the gas-only friction factor computed from Fig. 6.1.3. The term in parenthesis above is a liquid-loading correction factor to the gas-only friction factor. It varies in magnitude from 1, at negligible loadings, to 1.4 at a inlet loading of 1.0. Its dependency upon loading is very weak beyond a loading of about 0.1. That is, a thicker film of liquid on the wall does not offer much more resistance to flow than a thinner film.

The all-important cut size or cut-point diameter of the inner vortex may now be computed directly from Eq. (6.2.3) or, if necessary, Eq. (6.2.6) where the particle density, ρ_p, now refers to the density of the liquid phase.

13.5.2 Computation of Efficiency at Low Inlet Loadings

In this section we will compute the grade-efficiency curve and overall separation efficiency at low inlet loadings ($c_o < c_{oL}$)—the classification-only case.

The grade-efficiency curve one uses to quantify separation efficiency as a function of particle (drop) size should be based on experimental data or plant measurements taken on a cyclone of similar design and operation. However, lacking such information, we suggest, as before, using Eq. (6.3.2) with a 'slope', m, of about 3.

Overall collection efficiency is again computed from Eq. (6.3.3) by summing up the efficiencies of the individual size fractions, weighted by their mass fraction in the incoming feed.

13.6 Criteria for Determining if 'Mass loading' ('Saltation') Occurs

In analogy to our gas-solids cyclones, the amount of liquid that the gas phase can hold in turbulent suspension upon its entrance into a cyclone depends on the mass average drop size of the feed, $\langle x \rangle$, the cut-point of the 'inlet wall region', x_{50in}, and, to a lesser extent, the inlet loading itself, c_o. For gas-liquid cyclones, Muschelknautz and Dahl (1994) report for the limit-loading concentration:

$$c_{oL} = 0.0078 \left(\frac{x_{50in}}{\langle x \rangle} \right) (10 c_{ok})^k \qquad \text{for } 0.01 < c_{ok} > 0.5 \qquad (13.6.1)$$

where

$$k = 0.07 - 0.16 \ln c_{ok} \qquad (13.6.2)$$

and where c_{ok} is the mass of liquid *suspended* in the incoming gas stream per unit mass of gas. However, introducing the quantity x_{50in} complicates the analysis considerably. Furthermore, our calculations show that x_{50in} is typically only about 25% greater than the cut size of the inner vortex, x_{50}, calculated by Eq. (6.2.3). For these reasons, we will substitute $x_{50}$for x_{50in} and rewrite Eq. (13.6.1) as,

$$c_{oL} = 0.0078 \left(\frac{x_{50}}{\langle x \rangle} \right) (10 c_{ok})^k \qquad \text{for } 0.01 < c_{ok} > 0.5. \qquad (13.6.3)$$

As mentioned above, c_{ok} is the mass of liquid *suspended* in the incoming gas stream per unit mass of gas. As such, it will always be less than the total liquid loading since some portion of the incoming liquid will always enter the cyclone as 'wall flow'. Yet, in most practical applications, we do not know c_{ok} since it is difficult or impractical to either measure in an operating plant or to predict, in general, from fluid flow considerations. However, if we use the total incoming liquid loading, c_o, in place of the suspension loading,c_{ok}, in Eq. (13.6.3), the result will be 'conservative' as far as overall separation efficiency is concerned. This is because the actual limit-loading will, in reality, be less than that computed using the total entrance liquid loading, c_o, and any liquid entering the cyclone in excess of c_{oL} will be captured immediately upon entrance. Thus, we shall use the total liquid loading, c_o, in Eq. (13.6.3) knowing that our estimate of the amount of liquid that may be captured because it exceeds the limit-loading will be a conservative one. In the event that the incoming liquid loading exceeds 0.5, we recommend using 0.5 for c_{ok} in Eq. (13.6.3).

If $c_o < c_{oL}$, then there is no 'mass loading' effect and the comparatively simple method for computing the cyclone's separation performance, as described in Sects. 13.5.1 and 13.5.2, applies. Conditions that may lead to this scenario include a low liquid loading, c_o, a very fine feed drop size distribution, and a large inner vortex cut-point diameter, x_{50}.

If $c_o > c_{oL}$, then 'mass loading' will occur and the cyclone will, in effect, become a two-stage separator: separating a portion of the incoming liquid immediately upon its entrance into the cyclone and a portion of the remaining liquid via classification in the spinning inner core.

13.6.1 Overall Separation Efficiency when $c_o > c_{oL}$

As we reported for gas-solids cyclones, the overall or total efficiency for gas-liquid cyclones under mass loading or saltation conditions also includes a

'saltation' and a 'classification' contribution. A portion of the incoming liquid that is not collected by the former is collected by the latter, so that the total efficiency becomes:

$$\eta = \left(1 - \frac{c_{oL}}{c_o}\right) + \left(\frac{c_{oL}}{c_o}\right) \sum_{i=1}^{N} \eta_i \times \Delta MF_i \tag{13.6.4}$$

where, again, ΔMF_i is the i^{th} mass fraction and η_i is the capture efficiency for the i^{th} size fraction computed via Eq. (6.3.2) with x_{50} obtained from Eq. (6.2.3).

13.7 Re-entrainment From Demisting Cyclones

Although re-entrainment, as mentioned in the beginning of this chapter, is much less of a problem in demisting than in dedusting cyclones, demisting cyclones are in some practical applications operated at such severe conditions that re-entrainment does, nevertheless, become the limiting factor for separation. For example, with the push to process natural gas under high gas and liquid loads and at high pressure, the physical properties of the gas and liquid are becoming more challenging in terms of separation efficiency. Also for gas processing off-shore and sub-sea the accuracy and robustness of models predicting the separation efficiency is more crucial, since the consequences of equipment failure are more severe in such applications.

13.7.1 Re-entrainment Mechanisms and Governing Parameters

Only little work focusing on high liquid loading in, and re-entrainment from, demisting cyclones has been published, although some is beginning to emerge in the research literature. Ng et al. (2006) studied flooding phenomena in, and entrainment from, once-through swirl tubes with upflow. They installed and tested radical design improvements to the swirl vanes, using vanes with peripheral rather than axial inflow, to significantly delay the onset of flooding and entrainment.

Below we give a short account of some work that has been done in one of the author's (Hoffmann) own research group (Austrheim, 2005) in the framework of the HiPGaS (High Pressure Gas Separation) project, which sheds some light on the nature of the phenomenon of re-entrainment, and points the way to the formulation of predictive models.

Re-entrainment from cyclones may take place due to droplet entrainment from the film of separated liquid on the cyclone wall close to the exit from the cyclone, or from some edge at the outlet. We focus on the former, and assume that if re-entrainment takes place from an edge rather than a wall, the parameters governing the process will be the same or similar.

Different mechanisms of entrainment from a liquid film on a wall dominate in different film flow regimes. In a classic paper, Ishii and Grolmes (1975) summarize four basic mechanisms for entrainment from a liquid film into a gas flowing co-currently above it. The two that are likely to be relevant in demisting cyclones are illustrated in Fig. 13.7.1.

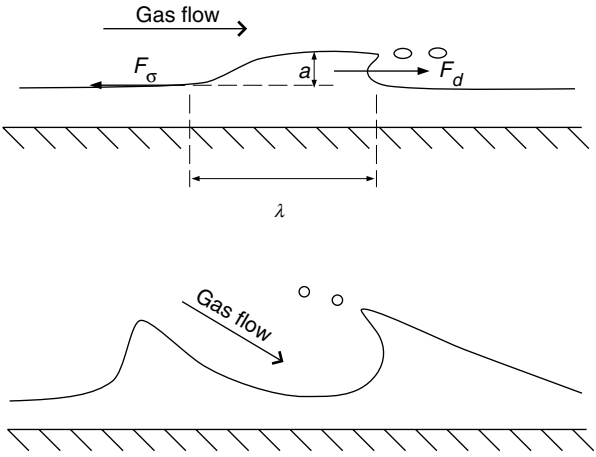

Fig. 13.7.1. Two mechanisms Ishii and Grolmes (1975) report for entrainment from a liquid film into a gas flowing over it. Top: entrainment by droplets being sheared from the surface of a roll wave, which is dominant at higher film Reynolds numbers. Bottom: entrainment by the gas undercutting a wave crest, which dominates at low film Reynolds numbers

The flow regime in the film depends on the film Reynolds number:

$$Re_l \equiv \frac{\rho_l u_l \delta}{\mu_l} = \frac{\rho_l \Gamma}{\mu_l} \tag{13.7.1}$$

where δ is the thickness of the film, u_l its mean velocity and ρ_l and μ_l the density and viscocity of the liquid, respectively. Γ is the liquid flow in the film per unit wetted perimeter, P_w, and is sometimes called the "liquid loading", but in this book we reserve that term for the volumetric liquid concentration in the droplet-laden gas flow.

The film flow regime relevant in the work of Austrheim (2005) is the regime corresponding to intermediate or high Re_l, where the so-called "roll-wave" entrainment dominates: waves on the liquid film are sheared as shown in the top plate of Fig. 13.7.1. The figure also illustrates the strategy of Ishii and Grolmes for modeling this process. They considered a force balance between the drag force F_d , from the gas acting on a wave crest on the film, and the retaining force of the surface tension F_σ as indicated in Fig. 13.7.1. They

considered that roll wave entrainment would take place when the drag force exceeds the retaining force:

$$F_d \geq F_\sigma. \tag{13.7.2}$$

We have to refer to their paper for the details of the derivation, but their criterion for the onset of entrainment is:

$$\begin{aligned} \frac{\mu_l u_g}{\sigma}\sqrt{\frac{\rho_g}{\rho_l}} &\geq 11.78 N_\mu^{0.8} Re_l^{-1/3} \qquad \text{for} \quad N_\mu \leq \frac{1}{15} \\ \frac{\mu_l u_g}{\sigma}\sqrt{\frac{\rho_g}{\rho_l}} &\geq 1.35 Re_l^{-1/3} \qquad \text{for} \quad N_\mu \geq \frac{1}{15} \end{aligned}. \tag{13.7.3}$$

We mention that at high values of Re_l, the criterion becomes independent of Re_l, and therefore simpler. In Eq. (13.7.3), N_μ is a "viscosity number", which measures the ratio of the viscous force due to the internal flow in the wave to the force due to surface tension:

$$N_\mu \equiv \frac{\mu_l}{\sqrt{\rho_l \sigma \sqrt{\frac{\sigma}{g\Delta\rho}}}}, \tag{13.7.4}$$

where $\Delta\rho$ is the difference between the liquid and gas densities.

In applying this to cyclone demisters, Austrheim (2005) assumed that the cyclone efficiency, *when limited by re-entrainment*, is a function of the *ratio* of F_d and F_σ, such that the efficiency can be written:

$$\eta_{entr}(a) = \mathrm{f}\left(\frac{\frac{\mu_l u_g}{\sigma}\sqrt{\frac{\rho_g}{\rho_l}}}{N_\mu^a Re_l^{-1/3}}\right), \tag{13.7.5}$$

calling the group on the right-hand-side the *re-entrainment number*. Ishii and Grolmes (1975) and Austrheim (2005) adjusted the value of the exponent a to optimize the performance of their models, Austrheim finding the optimal value to be 0.4.

The Reynolds number of the film, which is swirling around the wall of a cyclone, was calculated as:

$$Re_l = \frac{\rho_l u_l \delta}{\mu_l} = \frac{\dot{Q}\eta\rho_l}{P_w \mu_l} \tag{13.7.6}$$

where P_w is taken as $\pi D/\cos\alpha$. $\dot{Q}$ is the total liquid flow to the cyclone, η is the fraction separated to the wall and α is the angle to the horizontal of the liquid flow. The latter is taken as equal to the angle to the horizontal at which the *gas* flows, which again, in the vaned swirl tube used by Austrheim, is taken as equal to the exit angle, β, of the vanes.

Since the liquid film in cyclones is swirling around the wall rather than running along the wall in a gravity field, g in Eq. (13.7.4) needs to be replaced

by the centripetal acceleration of the film, which is the square of the tangential film velocity divided by the radius of the cyclone wall, $u_{\theta,l}^2/R$.

This makes it necessary to determine $u_{\theta,l} = u_l \cos\alpha$, where u_l is the absolute velocity in the liquid film. By a procedure similar to that used by Ishii and Grolmes (1975), Austrheim (2005) derives the following expression for $u_{l,\theta}$:

$$u_{l,\theta} = \sqrt{\frac{f_{g,i}\rho_g u_{g,\theta}}{f_{l,w}\rho_l}}, \tag{13.7.7}$$

where $f_{g,i}$ and $f_{l,w}$ are the friction factors between the gas and the liquid film surface and the liquid film and the wall, respectively, found from:

$$f_{g,i} = 0.005\left(1 + 300\frac{\delta}{R}\right)$$
$$\sqrt{f_{l,w}} = K \cdot Re_l^m \text{ where: } \begin{cases} K = 3.73; m = -0.47 & \text{for } 2 < Re_l < 100 \\ K = 1.96; m = -1/3 & \text{for } 100 < Re_l < 1000 \end{cases} \tag{13.7.8}$$

Finally, to calculate $f_{g,i}$, we need δ, the thickness of the liquid film, which is calculated as:

$$\delta = \frac{\dot{Q}}{P_w u_l} = \frac{\dot{Q}\cos\alpha}{P_w u_{l,\theta}} = \frac{\dot{Q}\cos^2\alpha}{\pi D u_{l,\theta}} \tag{13.7.9}$$

$u_{\theta,l}^2/R$ should thus replace g in Eq. (13.7.4) when calculating N_μ for use in Eq. (13.7.5).

As an aside, we can mention at this point that, as an alternative to the dimensionless parameters of Ishii and Grolmes (1975), van Rossum (1959) used the *Weber number* for the liquid film, with the film thickness as length scale, and a *"correlation parameter"*, S:

$$We \equiv \frac{\rho_g v_g^2 \delta}{\sigma} \qquad S \equiv \frac{u_g \mu_l}{\sigma} \tag{13.7.10}$$

to correlate data for the inception of entrainment from a liquid film. For velocities higher than 25 m/s he found that the critical Weber number for inception of entrainment was practically independent of S for $S > 5$, while it became dependent on S for lower S-values.

13.7.2 Data for Re-entrainment

Data for the efficiency of a cyclone bank were obtained in an experimental model of a gas scrubber, incorporating also an inlet vane and a mist mat or demisting mesh under the cyclone "bank", which consisted of two cyclones operating in parallel. A simple diagram of the scrubber is shown in Figure 13.7.2.

The model (called the"high-pressure rig") could be operated at pressures up to 100 bar. The fluids used in the rig were:

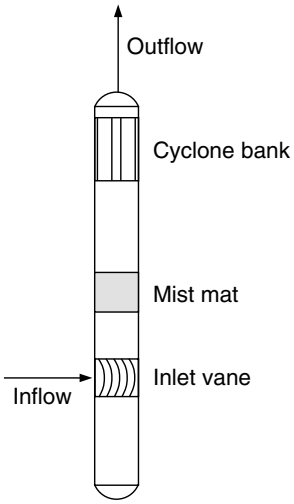

Fig. 13.7.2. Diagram of the scrubber tested by Austrheim (2005)

- air/Exxsol D60, Exxsol D60 is a commercial hydrocarbon liquid
- a synthetic "live" natural gas system, the gas being synthesized from methane, ethane and N-pentane.

Figure 13.7.3 shows the raw efficiency data plotted against superficial air velocity in the cyclones. The fact that the efficiency reduces with increasing gas velocity confirms that re-entrainment, and not separation efficiency of the incoming droplets, is the factor limiting the cyclone separation efficiency.

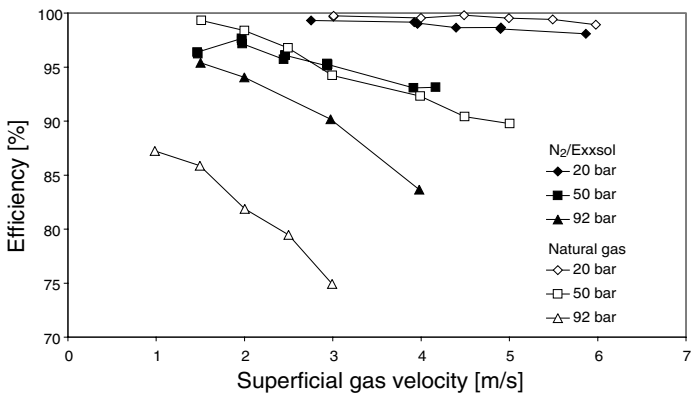

Fig. 13.7.3. Cyclone efficiency in the high-pressure rig with a constant liquid flowrate to the cyclones of 45 l/hr per cyclone

Figure 13.7.4 shows the same data as in Fig. 13.7.3 plus some additional ones at other liquid loadings (the liquid loadings were in the range 9–73 l/hr per cyclone) plotted against the re-entrainment number. In fact, to optimize this plot not only the exponent a was optimized but also the power of (ρ_g/ρ_l), which was made 0.8 rather than the 0.5 of the original model of Ishii and Grolmes (1975).

Plotting the data against this modified re-entrainment number clearly brings all the results onto one line, giving hope that the re-entrainment number can form the basis for a model of re-entrainment in cyclones.

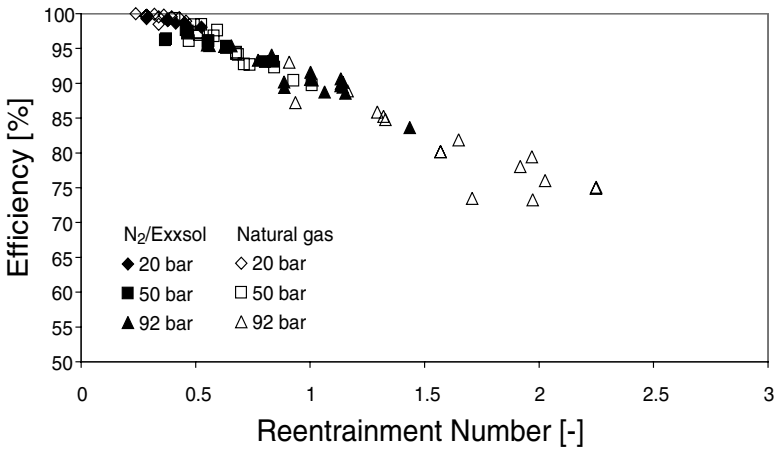

Fig. 13.7.4. The cyclone efficiency plotted agianst the modified re-entrainment number $([\mu_l u_g/\sigma][\rho_g/\rho_l]^{0.8})/(N_\mu^{0.4} Re_l^{-1/3})$

We stress, however, that this is still in the research stage. Figure 13.7.5 incorporate also results obtained from another rig ("low-pressure rig") operating from 1–7 bar on two fluid systems: air/water and air/Exxsol. These new results were also very scattered when plotted against the superficial gas velocity, but are also clearly brought onto one line by plotting against the re-entrainment number. However, the two lines representing the two rigs do not coincide, although perhaps the onset of re-entrainment does take place at the same value of the re-entrainment number in both rigs.

It turns out that also the film Weber number, Eq. (13.7.10), is successful in bringing some of the results onto one line.

It thus seems that these parameters are promising for the formulation of a model for re-entrainment in demisting cyclones. We are of the opinion that the formulation of such a comprehensive model should be an important research priority for the near future, particularly in light of the intensifying interest in off-shore, subsea natural gas processing.

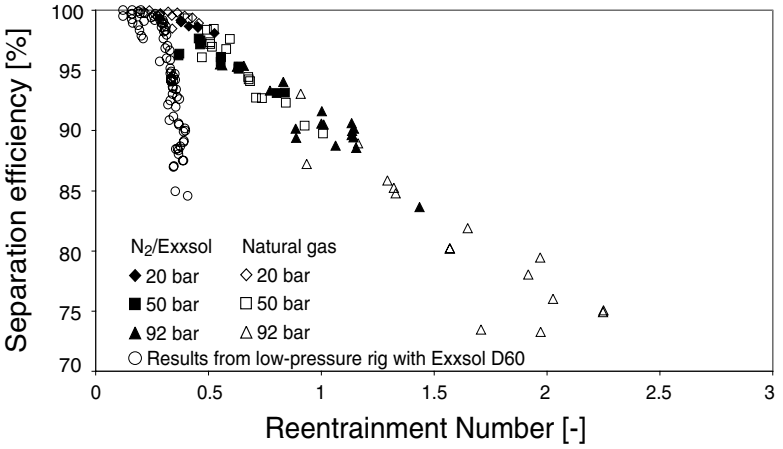

Fig. 13.7.5. A comparison between the cyclone efficiency in the high-pressure and the low-pressure rigs in terms of the modified re-entrainment number $([\mu_l u_g/\sigma][\rho_g/\rho_l]^{0.8})/(N_\mu^{0.4} Re_l^{-1/3})$. The data from the low-pressure rig include cyclone superficial gas velocities in the range 6–30 m/s and liquid loads in the range 0.002–0.09 vol%

13.A Example Calculations of Droplet Sizes in Pipe Flow

13.A.1 Finding the Mean Droplet Size

A gas having a density of 13 kg/m^3 and a dynamic viscosity of 0.006 cp flows through a pipe of 30 cm internal diameter at 6.7 m/s. Entrained in this gas is a liquid hydrocarbon having a density of 930 kg/m^3. A two-phase flow map indicates mist-annular flow. The interfacial tension (or 'IFT') = 20 dynes/cm.

Compute the Sauter-mean and volume-mean droplet diameters.

Solution

To convert to a consistent set of units, we elect to express the IFT and the gas viscosity in SI units:

$$\sigma = 20 \text{ dynes/cm} \times 0.001(\text{N/m})/(\text{dyne/cm}) = 0.02 \text{ N/m}$$

$$\mu = 0.006 \text{ cp} \times 0.001(\text{Pa s})/(\text{cp}) = 6 \times 10^{-6} \text{ Pa s}$$

Thus,

$$Re = \frac{\rho v_t D_t}{\mu} = \frac{13 \times 6.7 \times 0.3}{6 \times 10^{-6}} = 4.4 \times 10^6$$

and

$$We = \frac{\rho v_t^2 D_t}{\sigma} = \frac{13 \times 6.7^2 \times 0.3}{0.02} = 8.87 \times 10^3.$$

Substituting the above two dimensionless ratios, along with the pipe diameter and density values into Eq. 13.4.1, we obtain,

$$\langle x\rangle_{Sa} = 1.91 d_t \frac{Re^{0.1}}{We^{0.6}} \left(\frac{\rho_g}{\rho_l}\right)^{0.6} = 1.91 \times 0.3 \times \frac{\left(4.4 \times 10^6\right)^{0.1}}{\left(8.87 \times 10^3\right)^{0.6}} \left(\frac{13}{930}\right)^{0.6}$$
$$= 8.7 \times 10^{-4} \text{ m} = 870 \ \mu\text{m}$$

and, from Eq. (13.4.2), the volume or mass average droplet size is estimated to be,

$$x_{med} = 1.42 \times 870 \cong 1300 \ \mu\text{m}.$$

Thus, by weight or by volume, approximately 50% of the droplets flowing in the pipe will be smaller than, and 50% larger than, 1300 μm or 1.3 mm.

13.A.2 Finding the Droplet Size Distribution

In the above example we found that $x_{med} = 1300$ μm. Knowing x_{med}, we can therefore compute x for various x/x_{med} ratios for which the various weight fractions smaller than x are known.

$$x = \frac{x}{x_{med}} x_{med}.$$

Values of the droplet diameter computed by the above equation are reported in the second row of Table 13.A.1 and shown in Fig. 13.A.1.

For this computed drop size distribution only about 5% of the drops will be less than 390 μm in diameter and virtually all will be less than 4 mm (4000 μm).

Table 13.A.1. Points on the size distribution of the droplets in the pipe

x/x_{med}	0	0.3	0.62	1	1.5	2.9
x, μm	0	390	806	1300	1950	3770
F(x/x_{med})	0	0.05	0.25	0.5	0.75	1.0

13.B Flow Distribution in Parallel Demisting Cyclones

Figure 13.B.1 depicts a parallel ('multicyclone') arrangement of six demisting cyclones, with each cyclone discharging its overhead vapors into a common attic chamber and its underflow liquid into a common pool of liquid. The two 'front' cyclones take their feed from the near-wall regions of the inlet duct. The two 'back' cyclones take their feed from the centermost section of the inlet ducting. The 'middle' cyclones take their feed from that section of the inlet

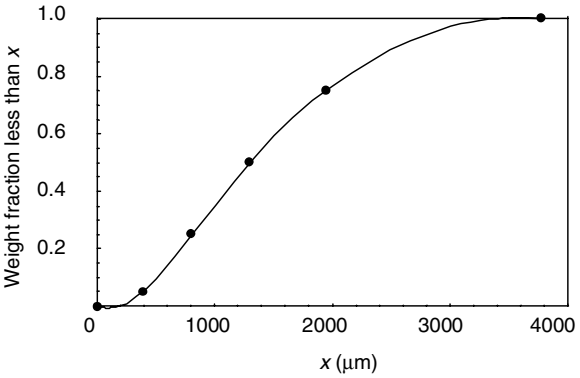

Fig. 13.A.1. Estimated drop size distribution for the example problem on basis of the AIChE design technique

ducting that lies between the wall and the middle of the entrance duct. Since wall friction retards the flow near the two sidewalls of the inlet ducting, the two front cyclones experience a slightly lower impact pressure than either the middle or back cyclones. This forces more vapor to flow into the back cyclones than to the two front cyclones. (Note, in this analysis, and for simplicity sake, we will focus attention on the two 'front' and 'back' cyclones.) This somewhat greater vapor flow to the two back cyclones produces, in turn, a greater vortex spin and an attendant reduction in static pressure in the back cyclones relative to the two front cyclones. This will manifest itself as a difference in liquid level within the bottoms of the cyclones. We can perform some basic fluid flow analysis on the configuration shown in Fig. 13.B.1 and thereby gain some insight into the flow behavior therein.

We begin by regarding the inlet ducting feeding the six cyclones as being divided into six equal-area rectangular openings each of height h and width s, as shown in Fig. 13.B.2 below. For estimation purposes, we will use an equation describing the velocity profile in a circular duct to describe the lateral velocity profile in the rectangular ducting feeding the cyclones. Thus, the velocity v at a distance y from a sidewall is (Hinze, 1975).

$$\frac{v}{v_{max}} = \left(\frac{y}{3s}\right)^{\frac{1}{n}} \tag{13.B.1}$$

where v is the axial velocity a distance y from the side wall, v_{max} is the maximal axial velocity (at the entrance duct centerline), s is the width of each of the six entrance ducts, and

$$n = \frac{1}{\sqrt{f}} \tag{13.B.2}$$

where f is the Moody friction factor for the inlet duct.

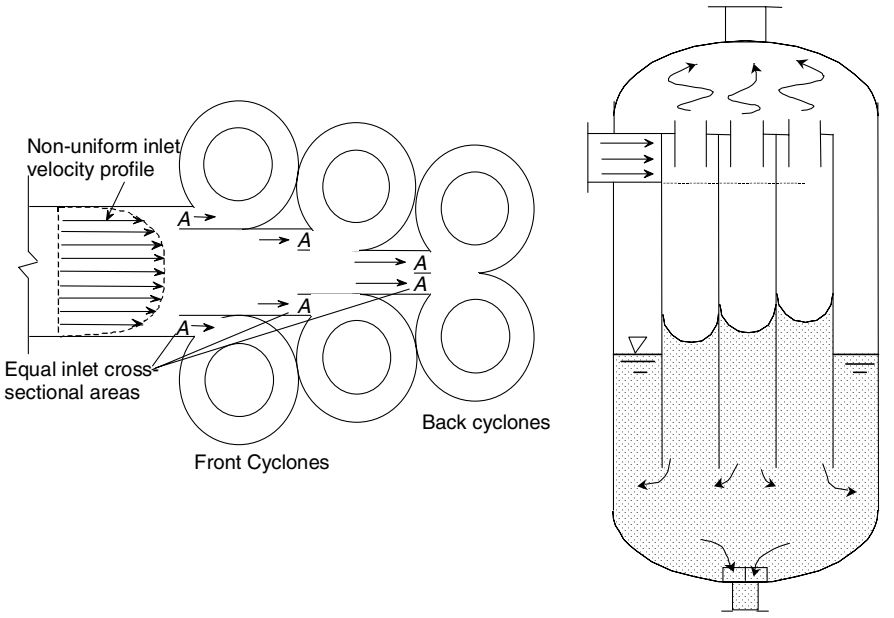

Fig. 13.B.1. Nonuniform entrance velocity profile (left frame) and associated static pressure difference (right frame) within a set of demisting cyclones

The flow to one 'front' cyclone is:

$$Q_F = \int_0^s vhdy = hv_{max} \int_0^s \left(\frac{y}{3s}\right)^{\frac{1}{n}} dy = \frac{hv_{max}}{3^{\frac{1}{n}} s^{\frac{1}{n}}} \left[\frac{y^{\frac{1}{n}+1}}{\frac{1}{n}+1}\right]_0^s = \frac{hsv_{max}}{3^{\frac{1}{n}}\left(\frac{1}{n}+1\right)}, \tag{13.B.3}$$

while the flow to one 'back' cyclone is:

$$Q_B = \int_{2s}^{3s} vhdy = 2hv_{max} \int_{2s}^{3s} \left(\frac{y}{3s}\right)^{\frac{1}{n}} dy = \frac{hv_{max}}{3^{\frac{1}{n}} s^{\frac{1}{n}}} \left[\frac{y^{\frac{1}{n}+1}}{\frac{1}{n}+1}\right]_s^{3s} = \frac{hsv_{max}}{3^{\frac{1}{n}}\left(\frac{1}{n}+1\right)} \left[3^{\frac{1}{n}+1} - 2^{\frac{1}{n}+1}\right]. \tag{13.B.4}$$

It is apparent from an inspection of Eqs. (13.B.3) and (13.B.4) that a back cyclone experiences a different volumetric flow rate than either of the two front cyclones. Since the inlet duct areas are the same for each cyclone, the ratio of these flow rates is also the same as the ratio of the average inlet velocities:

$$\frac{Q_B}{Q_F} = \frac{\langle v_B \rangle}{\langle v_F \rangle} = 3^{\frac{1}{n}+1} - 2^{\frac{1}{n}+1}. \tag{13.B.5}$$

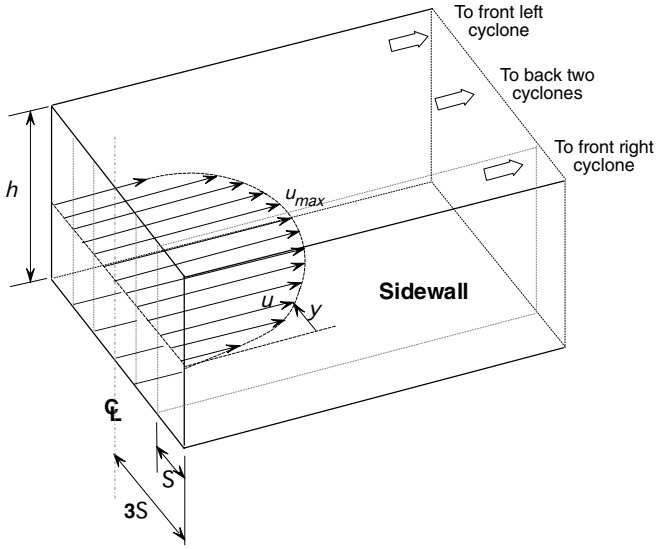

Fig. 13.B.2. Sketch illustrating the flow distribution upstream of a parallel array of demisting cyclones

And so we find that the imbalance is a function of the coefficient n or, according to Eq. (13.B.2), the friction factor, f. If the gas were not retarded by wall friction at all, then $f = 0$, n goes to infinity and the RHS of Eq. (13.B.5) becomes unity. This would correspond to an absolutedly flat velocity profile within the main inlet duct, and, hence, no inlet flow maldistribution.

The total pressure of the gas phase near the liquid surface, *i.e.*, the 'underflow' of either the front cyclones (subscript F) is:

$$p_{F,tot} = p_{F,static,duct} + p_{F,dynamic} - \Delta p_{F,in-uf}. \tag{13.B.6}$$

Likewise, the total pressure at the underflow of either back cyclone is:

$$p_{B,tot} = p_{B,static,duct} + p_{B,dynamic} - \Delta p_{B,in-uf} \tag{13.B.7}$$

where Δp_{in-uf} refers to the difference between cyclone inlet and underflow.

Subtracting Eq. (13.B.6) from (13.B.7) and canceling out the two static pressure terms gives the difference in pressure at the bottom (gas/liquid interface) between the front and back cyclone(s):

$$\Delta p = p_{B,dynamic} - p_{F,dynamic} - \Delta p_{B,in-uf} + \Delta p_{F,in-uf} \tag{13.B.8}$$

or,

$$\Delta p = \frac{1}{2}\rho\langle v_B\rangle^2 - \frac{1}{2}\rho\langle v_F\rangle^2 - \frac{1}{2}\rho K_{in-uf}\langle v_B\rangle^2 + \frac{1}{2}\rho K_{in-uf}\langle v_F\rangle^2 \tag{13.B.9}$$

with K_{in-uf} = inlet-to-underflow pressure loss coefficient. This coefficient must be computed from either a cyclone model or calculated on basis of measurements on an operating unit or on a laboratory model of the operating unit. The computation of K_{in-uf} requires one to measure or compute the inlet-to-underflow pressure difference, along with the gas density and average velocity in the upstream duct feeding one of the cyclones. Like the Euler number, it is a constant and has the same value for each of the cyclones, assumed herein to be physically identical in their construction.

Equation (13.B.9) can be simplified to give:

$$\Delta p = \frac{1}{2}\rho\,(1 + K_{in-uf})\ \left(\langle v_F\rangle^2 - \langle v_B\rangle^2\right). \tag{13.B.10}$$

Equation 13.B.10 will give a positive number if the pressure at the bottom of the back cyclone(s) is greater than that at the bottom of the front cyclone(s), and vice versa. The equation shows clearly that the difference in pressure between the bottoms of the front and back cyclones is dependent upon the difference in the square of the average velocity reporting to these cyclones. The two average inlet duct velocities in Eq. 13.B.10 are obtained by dividing the inlet volumetric flow rates from Eqs. (13.B.3) and (13.B.4) by the cross-sectional area of their inlet ducts, A. Doing so and substituting the results into Eq. 13.B.10 we obtain, after simplification:

$$\Delta p = \frac{\rho\,(\,1 + K_{in-uf})}{2}\left[\left(3^{\frac{1}{n}+1} - 2^{\frac{1}{n}+1}\right) - 1\right]^2 \left[\frac{v_{max}}{3^{\frac{1}{n}}\left(\frac{1}{n}+1\right)}\right]^2. \tag{13.B.11}$$

As before, the pressure difference shown here vanishes if there is no friction such that $n \to \infty$.

Obviously, the same sort of analysis and observations apply to any number of cyclone pairs whose underflows discharge into a common liquid seal pool. One just needs to work through the detailed computations on a case-by-case basis along the lines presented above.

In addition to vapor maldistribution, liquid maldistribution in the inlet piping will also give rise to a pressure imbalance within the bodies of front and back cyclones. This occurs because of the reduction in spin in the cyclone(s) that receive the greatest share of the liquid. This may not be a concern at the low liquid loadings typically associated with demisting type cyclones. At heavier loadings, however, one may need to modify the inlet piping to minimize liquid segregation ahead of the individual cyclones.

A worked example for estimation of the static pressure difference between demisting cyclones arising from inlet maldistribution is presented next.

13.B.1 Calculation of Flow Distribution

Given: An industrial demisting cyclone system consists of three pairs of identical cyclones which share a common hopper, as shown in Fig. 13.B.1. It is estimated that the wall friction factor in the ducting leading up to the cyclone is 0.019 or about 30% greater than that for gas-only.

Compute: The flow imbalance ratio according to Eq. (13.B.5).

Solution

Substituting our Moody friction factor into Eq. (13.B.2), we find that $n = 7.5$. This leads to the flow ratio: $Q_B/Q_F = \langle v_B \rangle / \langle v_F \rangle = 1.28$. Thus, due to the nonuniform velocity gradient in the inlet ducting, the back cyclones will experience about 30% more vapor flow than the two front cyclones. It is interesting to note that the computed value of the coefficient n, 7.5, is not too different from the 'Law of the Wall' coefficient of 7 often used to describe the velocity profile in fully developed turbulent flow within pipes.

13.B.2 Calculation of the Liquid Level Difference between the Front and Back Cyclones

Data for the cyclone system shown in Figs. 13.B.1 and 13.B.2 is as follows:

$\rho = 11.9$ kg/m^3
$K_{in-uf} = 2.6$ (based on a cyclone simulation study)
$f = 0.018$ (*i.e.*, $\cong$1.3 times f_{air})
$n = 7.5$
$v_{max} = \langle v \rangle / 0.80 = 18.2/0.80 = 22.8$ m/s (approximately)

Substituting these values into Eq. 13.B.11, we obtain a pressure difference between the back and front cyclones of about -0.224 kPa (about -23 mm or -1 inch of water column). Since this pressure differential (back - front) is negative, the liquid level in the two back cyclones will be 23 mm of water column higher than that for the two front cyclones. The level in the two middle cyclones can be expected to lie between that of the front and back cyclones.

Despite the rather large flow imbalance we found leading up to the entrance of the cyclones, this did not result in a significant difference in 'bottom' pressure among the cyclone pairs. However, as Eq. 13.B.11 shows, an increase in the gas density (as in high pressure separators) and/or the flow rate through the main inlet duct would increase the pressure and elevation differences reported above. Furthermore, if the liquid phase reporting to the bottom of the cyclones were to be a low-density foam or froth, the difference in their elevations would increase inversely with the decrease in the 'liquid's' effective density. If this foam column grew too high, it would become entrained overhead by the vortex and exit with the exiting gas phase.

Before closing this discussion we wish to call attention to the fact that the liquid seal at the bottom of each cyclone causes their performance to be rather unaffected by flow imbalances of the type we just observed. This would not be the case had the cyclone underflows not been isolated from one another. In this case, any pressure imbalance that would exist between the cyclone underflows will cause gas to flow down some of the underflow openings and up other underflow openings. This, in turn can lead to a serious degradation of separation performance and is the reason why most multiclone systems do not perform as well as one of its individual cyclones tested in isolation.

When faced with a cyclone performance problem it is almost always advisable to focus attention on the underflow configuration. The majority of performance problems are due, for one reason or the other, to the inability of particulates to properly discharge out the underflow openings.

13.C Method for Estimating Wall Film Thickness and Velocity

In some special applications it is of value to be able to estimate certain physical characteristics of the film of liquid that is flowing down the walls of a gas/liquid cyclone. This includes the fraction of the cross-sectional area occupied by the gas and by the liquid wall film, the film velocity, residence time, and film thickness. Such information is of interest, for example, in performing heat transfer computations wherein the wall film is heated by an external steam jacket, or the film is cooled by an external chilled water enclosure. Knowledge of the film characteristics is also of value if one is interested in ensuring that a sufficient film velocity or thickness is maintained to keep solids from depositing upon the walls. Herein, we shall present a technique that is intended to provide an estimate of the wall film's flow characteristics.

We saw in Sect. 13.7.1 that the tangential liquid film velocity and the liquid film thickness were required to calculate the reentrainment number. In that section these parameters were estimated by a method similar to that of Ishii and Grolmes (1975) by considering a force balance on the film resolved in the tangential direction. That model was geared to situations where reentrainment from a liquid may be important: high gas and liquid film velocities. Also the liquid film in that example was being transported upward against gravity, although the effect of gravity was not accounted for in the model. In this appendix we will derive an expression for the vertical velocity of a liquid film moving downward and the thickness of this film using a similar principle, but considering a force balance on the film resolved in the vertical direction. We will use different empirical expressions for the film-wall and gas-film friction factors, $f_{l,w}$ and $f_{g,i}$ to those used in Sect. 13.7.1, Eq. (13.7.8), and we will take into account the effect of gravity.

The model we develop in this appendix is thus based on a two-phase, cocurrent flow force balance that relates the cross-sectional liquid void fraction

(and, hence, the gas fraction) to the gas and liquid mass flow rates, physical properties, cyclone diameter, wall and interfacial friction factors, and the acceleration of gravity. We assume that all of the liquid entering the cyclone is spun to the walls immediately upon entry and flows down as a *uniformly* thick film[2], see Fig. 13.C.1.

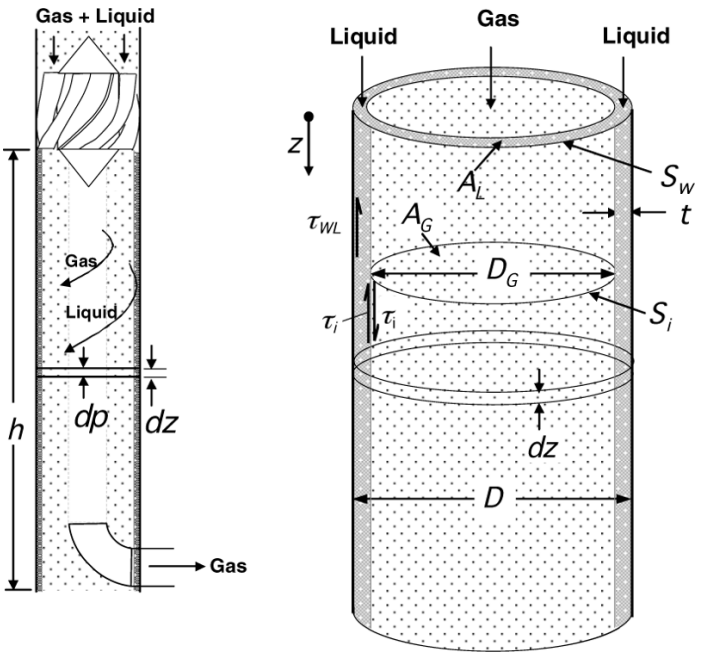

Fig. 13.C.1. Simplified view of cyclone with liquid film of thickness t along wall with gas comprising the core flow. Left image: cyclone overview. Right image: detail of a vertical segment of the cyclone

In *most* gas-liquid cyclone installations, the majority of all incoming liquid is deposited upon the walls immediately upon entry into the cyclone as a result of the "mass loading" effect alone. This is due to the relatively large size of the incoming liquid drops and also to the "mass loading effect" discussed in Sect. 13.6 above.

In this model, the primary purpose of the centrifugal force field generated by the rotational motion imparted to the incoming feed stream is to convey and keep the liquid on the walls of the cyclone. Herein we shall assume that the gas and liquid phases spiral down the walls of the cyclone in a helical

[2] A uniformly thick wall film is an idealized condition that is difficult to achieve in practice. A vane-type inlet with multiple openings (distribution points) generally provides a much more uniform distribution of the liquid than that of a slot or pipe type inlet.

fashion at a common, constant angle relative to the horizontal. We may view the flow as that over a flat plate created by unfolding the cylindrical walls of the cyclone. In this case, the gas and liquid flow paths are simply straight lines making a constant angle to the horizontal.

The force balance model equation that we shall derive below must be solved in an iterative manner for the vapor void fraction. Knowing this void fraction and the cyclone diameter, the wall film thickness can be computed. It is then possible to compute the average gas and wall film velocity, as well as the "slip velocity", the ratio of the average gas velocity to the average liquid film velocity.

13.C.1 Two-Phase, Co-current, Annular Force Balance, Resolved in the Axial Direction

We begin by performing a force balance in the axial z direction over a cross section of the cyclone of height dz. See Fig. 13.C.1. We shall assume that, for all practical purposes, all of the liquid is spiraling down the inner walls of the cyclone as a wall film with the gas phase comprising the core flow. A force balance on the gas phase gives (note that dp is itself negative),

$$-A_g dp - \tau_{g,i} \sin\alpha S_i dz + \rho_g A_g g dz = 0. \tag{13.C.1}$$

And that on the liquid phase,

$$-A_l dp - \tau_{l,w} \sin\alpha S_w dz + \tau_{g,i} \sin\alpha S_i dz + \rho_l g A_l dz = 0 \tag{13.C.2}$$

where A_g, A_l are the horizontal cross-sectional areas of gas and liquid wall film, respectively, dp is the axial pressure difference[3] across dz, $\tau_{g,i}$ and $\tau_{l,w}$ are the gas/liquid and wall/liquid shear stresses, respectively, α is the angle of the gas and liquid film flows (assumed here to be equal) relative to the horizontal, ρ_g, and ρ_l are the gas and liquid densities, S_i, S_w are the perimeters of gas core flow and the outer liquid film (the latter being the same as the inner wall perimeter), and g is the acceleration due to gravity.

Eliminating dp between Eqs. (13.C.1) and (13.C.2) and simplifying gives:

$$\frac{\tau_{l,w} \sin\alpha S_w}{A_l} - \tau_{g,i} \sin\alpha S_i \left(\frac{1}{A_g} + \frac{1}{A_l}\right) - (\rho_l - \rho_g) g = 0. \tag{13.C.3}$$

Now, if we name the fraction of the total cross-sectional area, $A = \pi D^2/4$, taken up by gas the "void fraction", ε, then $A_g = \varepsilon A$, $A_l = (1-\varepsilon)A$. Furthermore, we take the wetted wall perimeter, S_w, and the interface perimeter, S_i as $S_w = \pi D$ and $S_i = \pi D_g = \pi \varepsilon^{1/2} D$, respectively. Substituting this into Eq. (13.C.3) and simplifying gives:

$$\frac{4\tau_{l,w} \sin\alpha}{(1-\varepsilon) D} - \frac{4\tau_{g,i} \sin\alpha}{D\varepsilon^{1/2}(1-\varepsilon)} - (\rho_l - \rho_g) g = 0. \tag{13.C.4}$$

[3] We assume, as is normal, that the pressure in the gas permeates the liquid film

13.C.2 Friction Factors and Shear Stresses

In this section we give expressions for the wall and interfacial friction factors and corresponding shear stresses, starting with the wall friction factor and shear stress.

Wall Friction Factor and Shear Stress

By definition,

$$\tau_{l,w} \equiv \frac{1}{2}\rho_l \langle v_l \rangle^2 f_{l,w} \tag{13.C.5}$$

where $f_{l,w}$ can be computed by any number of correlations, among others those given in Eq (13.7.8). Herein we report two such correlations for $f_{w,l}$—that of Liang-Biao and Aziz (1996)—and that obtained using a conventional Moody type friction factor correlation (Swamee and Jain, 1976), with the Reynolds number defined in terms of an equivalent hydraulic diameter.

The correlation of Liang-Biao and Kaziz is:

$$f_{w,l} = \frac{1.629}{Re_l^{0.516}} \left(\frac{v_{s,g}}{v_{s,l}} \right)^{0.0926} . \tag{13.C.6}$$

We can rewrite the parameters in this equation as follows:

$$\begin{aligned}
v_{s,g} &= \text{superficial gas velocity } = \frac{\dot{m}_g}{\rho_g A} \\
v_{s,l} &= \text{superficial liquid velocity } = \frac{\dot{m}_l}{\rho_l A} \\
Re_l &= \text{liquid film Reynolds number} = \frac{\rho_l \langle v_l \rangle d_{Hl}}{\mu_l} \\
d_{Hl} &= \text{film hydraulic diameter} = \frac{4A_l}{S_w} = \frac{4\,(1-\varepsilon)\,A}{\pi D} = (1-\varepsilon)\,D
\end{aligned} \tag{13.C.7}$$

Furthermore the mean liquid velocity, $\langle v_l \rangle$ can be written:

$$\langle v_l \rangle = \frac{\dot{m}_l}{\rho_l A_l} = \frac{\dot{m}_l}{\rho_l\,(1-\varepsilon)\,A} = \frac{4\dot{m}_l}{\rho_l\,(1-\varepsilon)\,\pi D^2} \tag{13.C.8}$$

with $\dot{m}_l$ and $\dot{m}_g$ the liquid and gas mass flowrates.

Substituting these expressions into eq. (13.C.6) gives:

$$f_{l,w} = \frac{1.629}{\left(\frac{4\dot{m}_l}{\pi D \mu_l}\right)^{0.516}} \left(\frac{\rho_l \dot{m}_g}{\rho_g \dot{m}_l} \right)^{0.0926} \tag{13.C.9}$$

An alternative method for estimating the wall friction factor is to use a standard pipe friction factor equation, such as the explicit formula of Swamee and Jain, using the equivalent diameter of the film in Re_l. Thus,

$$f_{l,w} = \frac{0.25}{\left[Log_{10}\left(\frac{e}{3.7D} + \frac{5.74}{Re_l^{0.9}}\right)\right]^2} \tag{13.C.10}$$

where e is the conventional absolute wall roughness. Re_l, and the equivalent diameter comprising part of Re_l, are given in Eq. (13.C.7) above.

Using the expression for $\langle v_l \rangle$ in Eq. (13.C.7) in the definition for the wall shear stress, $\tau_{l,w}$, Eq. (13.C.5), gives:

$$\tau_{l,w} = \frac{8\dot{m}_l^2}{\pi^2 D^4 \rho_l \left(1-\varepsilon\right)^2} f_{l,w} \tag{13.C.11}$$

where $f_{l,w}$ is computed by either Eq. (13.C.9) or (13.C.10).

Interfacial Friction Factor and Shear Stress

Similar to the wall shear stress, the interfacial shear stress is defined as:

$$\tau_{g,i} \equiv \frac{1}{2}\rho_g \langle v_g \rangle^2 f_{g,i} \tag{13.C.12}$$

For turbulent gas flow $f_{g,i}$ may be computed from some empirical function of the gas Reynolds number, as outlined below.

Zhao and Liao (2002) proposed the following formula for computing the gas/liquid interfacial friction factor for annular flow:

$$f_{g,i} = 0.046 Re_g^{-0.2} \tag{13.C.13}$$

where Re_g, the gas Reynolds number, is defined as:

$$Re_g \equiv \frac{\rho_g \langle v_g \rangle D_g}{\mu_g}. \tag{13.C.14}$$

$\langle v_g \rangle$, the mean gas velocity, can be written:

$$\langle v_g \rangle = \frac{\dot{m}_g}{\rho_g A_g} = \frac{\dot{m}_g}{\rho_g \varepsilon A} = \frac{4\dot{m}_g}{\rho_g \varepsilon \pi D^2} \tag{13.C.15}$$

Substituting Eq. (13.C.15) into Eq. (13.C.14), and noting that the diameter of the region available for gas flow, $D_g = \varepsilon^{1/2} D$:

$$Re_l = \frac{4\dot{m}_g}{\pi \mu_g \varepsilon^{1/2} D} \tag{13.C.16}$$

Thus, Eq. (13.C.13) becomes,

$$f_{g,i} = 0.046 \left(\frac{4\dot{m}_g}{\pi \mu_g \varepsilon^{1/2} D}\right)^{-0.2} \tag{13.C.17}$$

Filling the expression in Eq. (13.C.15) for the mean gas velocity, $\langle v_g \rangle$, into Eq. (13.C.12) gives:

$$\tau_{g,i} = \frac{8\dot{m}_g^2}{\rho_g \varepsilon^2 \pi^2 D^4} f_{g,i} \tag{13.C.18}$$

where $f_{g,i}$ is computed from Eq. (13.C.17). We note that Eq. (13.C.18) is very similar to Eq. (13.C.11).

13.C.3 Final Form of Void Fraction Equation

Substituting the shear stresses, $\tau_{g,i}$ and $\tau_{l,w}$, from Eqs.(13.C.11) and (13.C.18) into the force balance equation, Eq. (13.C.4), and simplifying, we obtain an implicit expression relating void fraction to known quantities such as cyclone diameter, gas and liquid mass flow rates, gas and liquid densities and viscosities, and the acceleration of gravity:

$$\frac{32 \sin\alpha}{\pi^2 D^5 (1-\varepsilon)} \left[\frac{\dot{m}_l^2}{\rho_l (1-\varepsilon)^2} f_{l,w} - \frac{\dot{m}_g^2}{\rho_g \varepsilon^{5/2}} f_{g,i} \right] - (\rho_l - \rho_g) g = 0 \tag{13.C.19}$$

where $f_{l,w}$ and $f_{g,i}$ are given by Eqs. (13.C.9) or (13.C.10), and (13.C.17).

Equation (29) must be solved iteratively for the void fraction, ε, as a function of the independent quantities:

$$\dot{m}_l,\ \dot{m}_g,\ \rho_l,\ \rho_g,\ \mu_l,\ \mu_g,\ D,\ f_{l,w},\ f_{g,i} \text{ and } g\ .$$

Once ε is known for a given set of local conditions, it is then possible to compute the liquid phase fraction $(1-\varepsilon)$, the film thickness, t, the film and gas phase velocities, v_l and v_g, and the slip velocity, v_{slip}.

Knowing ε and the cyclone diameter, D, the film thickness, t, for any value of ε can now be computed,

$$t = \frac{D(1-\sqrt{\varepsilon})}{2}, \tag{13.C.20}$$

which follows from the fact that

$$1 - \varepsilon = \frac{A_l}{A} = \frac{\frac{\pi}{4}D^2 - \frac{\pi}{4}(D-2t)^2}{\frac{\pi}{4}D^2}$$

An estimate of the residence time of the liquid film over cyclone height H can be obtained by dividing its helical path length, $H/\sin\alpha$, by the film velocity v_l,

$$\theta_{l\_res} \cong \frac{H}{v_l \sin\alpha}.$$

Due to friction and the effects of gravity, the angle at which the liquid film flow relative to the horizontal, α_l, will increase somewhat over the length of the cyclone. Lacking direct measurements an average value of 45° to 55°

is suggested, basis observation. If the feed enters the cyclone through a vane assembly, the initial or starting angle will be fixed by the angle of the trailing section of the vanes (typically $\sim 20°$ to $30°$). If the feed enters through a tangential inlet (slot or round pipe), the starting angle will be approximately $30°$. Near the bottom of the cyclone, the angle typically increases to $45°$ to $60°$ as a result of wall friction and the effects of gravity.

The vertical "slip velocity", defined as the ratio

$$v_{slip} \equiv \frac{\langle v_g \rangle}{\langle v_l \rangle} \tag{13.C.21}$$

becomes, with the help of Eqs.(13.C.8) and (13.C.15),

$$v_{slip} \equiv \frac{\langle v_g \rangle}{\langle v_l \rangle} = \frac{\rho_l}{\rho_g} \times \frac{\dot{m}_g}{\dot{m}_l} \times \frac{(1-\varepsilon)}{\varepsilon A} \tag{13.C.22}$$

Although the two mean velocities differ, there is no discontinuity (no "slip") at their interface.

13.D Example calculation

For the purpose of illustrating the use of the above formulas, we'll go through the calculations for computing the wall film thickness, velocity, residence time and slip velocity for a commercial scale cyclone designed to separate an aqueous phase from an air stream.

$\dot{m}_l$	= 30,000 lb/hr	= 3.78 kg/s
$\dot{m}_g$	= 150,000 lb/hr	= 18.9 kg/s
α_l	$\cong 40°$	
D	= 30.0 in	= 0.762 m
H	= 48.0 in	= 1.219 m
ρ_l	= 62.4 lb/ft^3	= 1000 kg/m^3
ρ_g	= 0.150 lb/ft^3	= 2.40 kg/m^3
μ_l	= 1.00 cp	= 0.001 Pa·s
μ_g	= 0.040 cp	= 4.0×10^{-5} Pa·s

Wall friction factor according to Liang-Biao and Kaziz:

$$f_{l,w} = \frac{1.629}{\left(\frac{4\dot{m}_l}{\pi d \mu_l}\right)^{0.516}} \left(\frac{\rho_l \dot{m}_g}{\rho_g \dot{m}_l}\right)^{0.0926}$$

$$= \frac{1.629}{\left(\frac{4 \cdot 3.78}{\pi 0.762 \cdot .001}\right)^{0.516}} \left(\frac{1000 \cdot 18.9}{2.40 \cdot 3.78}\right)^{0.0926} = 0.0362$$

Wall friction factor according to Swamee and Jain:

$$d_{Hl} = (1-\varepsilon)D = (1-\varepsilon)0.762$$

$$\langle v_l \rangle = \frac{4\dot{m}_l}{\rho_l(1-\varepsilon)\pi D^2} = \frac{4 \times 3.78}{\pi 1000(1-\varepsilon)0.762^2} = \frac{0.00829}{1-\varepsilon}$$

$$Re_l = \frac{\rho_l \langle v_l \rangle d_{Hl}}{\mu_l} = \frac{1000 \times 0.00829 \times 0.762}{0.001} = 6317$$

e = wall roughness = 0.0018 in. = 0.000046 m

$$f_{l,w} = \frac{0.25}{\left[\log_{10}\left(\frac{e}{3.7D} + \frac{5.74}{Re_l^{0.9}}\right)\right]^2} = \frac{0.25}{\left[\log_{10}\left(\frac{0.000046}{3.7 \times 0.762} + \frac{5.74}{6317^{0.9}}\right)\right]^2} = 0.0354$$

Interfacial friction factor according to Zhao and Liao:

$$f_{g,i} = 0.046\left(\frac{4\dot{m}_g}{\pi\mu_g\varepsilon^{1/2}D}\right)^{-0.2}$$

$$= 0.046\left(\frac{4 \times 18.9}{\pi\, 4.0 \times 10^{-5}\varepsilon^{1/2}0.762}\right)^{-0.2} = 0.00304\varepsilon^{0.1}$$

Substituting into our force balance equation (using only the Swamee and Jain value for $f_{l,w}$):

$$\frac{32\sin\alpha}{\pi^2 D^5(1-\varepsilon)}\left(\frac{\dot{m}_l^2}{\rho_l(1-\varepsilon)^2}f_{l,w} - \frac{\dot{m}_g^2}{\rho_g\varepsilon^{5/2}}f_{g,i}\right) - (\rho_l - \rho_g)g = 0$$

$$\frac{32\sin 40}{\pi^2 0.762^5(1-\varepsilon)}\left(\frac{3.78^2}{1000(1-\varepsilon)^2}0.0354 - \frac{18.9^2}{2.40\varepsilon^{5/2}}0.00304\varepsilon^{0.1}\right)$$

$$- (1000 - 2.40)9.81 = 0$$

or

$$\frac{0.004104}{(1-\varepsilon)^3} - \frac{3.670}{(1-\varepsilon)\varepsilon^{2.4}} - 9786 = 0$$

By trial and error,

$$\varepsilon = 0.99264$$

In this particular example, wall friction and gravity are controlling; interfacial friction has a relatively minor effect on the film's thickness, velocity and residence time (computed below).

The wall film thickness is therefore,

$$t = \frac{d\,(1-\sqrt{\varepsilon})}{2} = \frac{0.762\left(1-\sqrt{0.99264}\right)}{2} = 0.00140 \text{ m } = 1.40 \text{ mm}$$

The vertical wall film velocity is,

$$\langle v_l \rangle = \frac{4\dot{m}_l}{\rho_l (1-\varepsilon)\pi D^2} = \frac{4 \times 3.78}{1000\,(1-0.99264)\,\pi 0.762^2} = \text{ 1.13 m/s (3.71 ft/s)}$$

The slip velocity is,

$$v_{slip} \equiv \frac{\langle v_g \rangle}{\langle v_l \rangle} = \frac{\rho_l}{\rho_g} \times \frac{\dot{m}_g}{\dot{m}_l} \times \frac{(1-\varepsilon)}{\varepsilon A} = \frac{1000}{2.40} \times \frac{18.9}{3.78} \times \frac{(1-0.99264)}{0.99264 \times \frac{\pi}{4} 0.762^2} \text{ = 33.9}$$

The liquid film residence time is,

$$\theta_{l\_res} \cong \frac{H/\sin 40}{v_L} = \frac{1.219}{1.13} = 1.68 \text{ s}$$

As a final note, we must bear in mind that the wall film within a gas-liquid cyclone does not normally spread out as a uniformly thick film. Instead, the liquid tends to segregate somewhat even though all areas of the walls may still be wetted. In order to achieve even a reasonable approach to uniform wall wetting, it is necessary for the feed stream to pass through a vane type inlet assembly having a multitude of vane openings (8 to 12, for example). It is also necessary that the liquid be distributed uniformly upstream of the vane. In general, the liquid film's average velocity will be greater than, and its actual residence time less than, that computed by the above method due to segregation.

14

Foam-Breaking Cyclones

14.1 Introduction

Foams consist of cellular liquid structures, or lamellas, that are filled with gas. Some type of surfactant is required in order for foams to form—they cannot occur in pure liquids. If a gas, such as air, is sparged into a liquid containing a surfactant, the surfactant will form a double layer around the gas bubble, creating a collection of spherical foam bubbles. Such foams tend to be unstable and readily coalesce or break due to their high liquid content. More stable polyhedral foam, of most interest to us, is formed as a result of mechanical stresses, and is much more stable or difficult to break. Breaking of foam occurs in three stages: drainage of the cellular liquid comprising the walls, breakage of the foam walls, and diffusion of the gas out of the foam cells.

At the consumer level, most of us enjoy or find useful products that produce foams. This includes, for example, saving foams, bubble bath products, kitchen detergents, carpet cleaners, cappuccino, beer and other beverages, whipped cream toppings, foam insulation, and many others. At the industrial level, some foams are also useful—indeed essential—to the process. Froth flotation, wherein a foam is artificially created to remove organic pollutants, is one such example. Another is the use of foams to recover valuable minerals from ore. In both of these cases, the process takes advantage of the tendency of certain substances to migrate preferentially into foam. Foams are also used to help prevent fuel fires on airport runways during certain emergency landings. Such foams are created deliberately. In many industrial or processing units, however, foams are often unwanted and troublesome to operations.

Various types of equipment and techniques have been employed to suppress foam formation in biological and process equipment. These include both chemical and mechanical methods. Chemical methods include various defoaming chemicals (silicone oils, non-ionic surfactants, etc.) Mechanical methods employ sprays, wire mesh elements, heat, live steam injection, air or steam-operated ejectors, sonic horns, vacuums, centrifuges, and the use of large re-

tention time vessels. Defoaming chemicals enjoy widespread industrial use but they have the disadvantage of changing the chemical and physical properties of the system. They can also be quite expensive. Thermal methods can damage the product. Centrifuges, though costly, can be effective but most have narrow passages spread out over a large area. Such passages can plug and are difficult to clean. It turns out that one of the most effective ways of breaking many types of process foams is through the application of centrifugal force, and the shear associated with the use of such force. Thus, what we wish to describe herein is the use of cyclonic type devices for suppressing or breaking process foams. This type of equipment that has become quite popular in recent years although the concept of using a cyclone to break foams dates back to at least 1951, Fraser (1951).

Relatively little fundamental information on the design and performance of foam-breaking cyclones appears in the literature. What little is known about them, at least from the user's point of view, is more descriptive than quantitative. This chapter reflects the state of affairs. Even so, it is the writers' hope that the information contained herein will provide the reader who is unfamiliar with these, most interesting separators, with a basic understanding of the art and practice underlying their application and performance.

We shall begin by noting that, if a cyclone is fed a fluid mixture consisting of a heavy phase and a light phase, the light phase will tend to be displaced radially inward by the heavier phase as the latter attempts to make its way to the outer walls in the centrifugal field. If the incoming mixture happens to be a 'foam' or 'froth' (mixtures consisting of less than about 20 volume percent liquid) the gas bubbles will tend to concentrate and form a continuous gas phase along the central axis of the cyclone. In addition to concentrating the less dense foam phase along the cyclone axis, the shear stresses created within the cyclone leads to a distortion of the cellular structure of the foam which appears to result in an increase in the liquid drainage rate. Thus, the combined effects of centrifugal force and shear can be used to separate an incoming foam into its component vapor and liquid phases so that, in principle, only liquid reports out the bottom of the cyclone and only gas out the top.

Such cyclones are known as 'foam-breaking' or 'defoaming' cyclones or separators. A simple illustration of a defoaming cyclone installation is presented in Fig. 14.1.1. The separator itself is seen to consist of a tangentially fed cylindrical tube mounted vertically within a vapor/liquid separator. The cyclone's underflow opening is sealed in the vessel's liquid phase. Vapor reports out the top of the cyclone and liquid out its underflow. The separator may or may not feature a conventional vortex tube. If not, the roof plate will usually have a circular opening that is somewhat smaller than the inside diameter of the body tube. The resulting roof 'ring' serves to help prevent liquid from exiting out the top. The individual separator tubes are typically fabricated from 150 to 250 mm (6 to 10 inch) pipe.

Since the design of defoaming cyclones is based largely on tests and experience, it is difficult to provide any firm design guidelines herein. However,

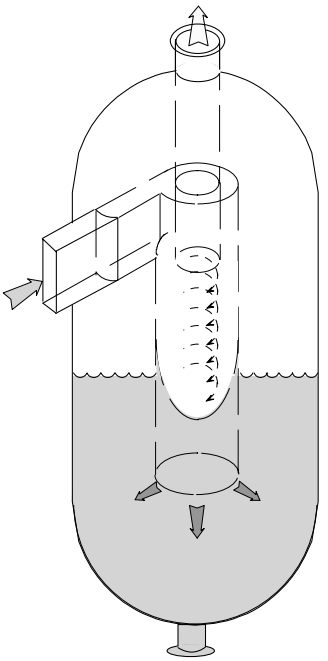

Fig. 14.1.1. A simplified illustration of a defoaming cyclone system

Mohan and Shoham (2002) report that their cylindrical-bodied three-phase gas/water/oil cyclone separator (CLCC separator, see Fig. 14.1.2) was able to break foams at gas entrance velocities in excess of 40 ft/s (12 m/s). Foam breaking was not effective at low gas velocities, i.e., 10 ft/s.

As mentioned earlier, foam-breaking or defoaming type of cyclone separators have enjoyed considerable commercial success in recent years, especially in refinery and drilling/wellhead installations handling dirty and/or heavy crudes. This is largely due to:

1. their demonstrated effectiveness in this application area,
2. their relatively low initial and operating cost,
3. the fact that they normally can be built off-site then retrofitted relatively quickly within existing gravity separators and secured in place without hot-welding and,
4. their simple construction and lack of moving parts or small openings that could plug during service.

To the industrialist faced with a production-limiting foaming problem defoaming cyclones can be a very attractive solution. Any process-related downside risks with these devices are normally deemed minor. When it comes to "selling" their use to management, their relatively low cost and potential to solve the foaming problem will normally offset any process risk concerns. They may

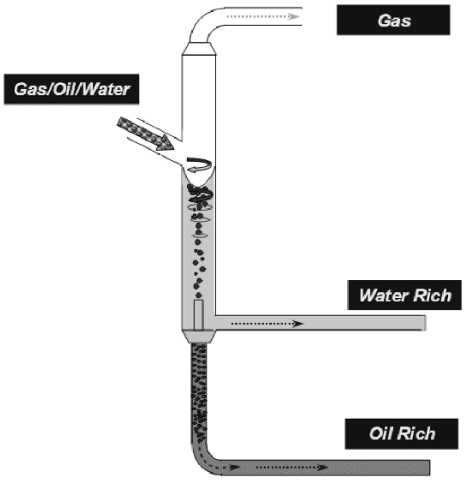

Fig. 14.1.2. A three-phase "GLCC" cyclone separator (adapted from Mohan and Shoham, 2002)

even be viewed as an improved version of an inlet distributor—something which is needed anyway.

Excessive amounts of foam in a vessel can result in a host of operating and production problems, including reduced product throughput, level control problems, excessive liquid entrainment out the vapor outlet piping, excessive vapor out the liquid underflow piping, and underflow pump cavitation problems. If foaming occurs in a compressor knockout drum it can easily flood a mesh pad or vane (chevron) separator. When this occurs, the foam carryover from the drum can severely damage the gas compressor downstream.

The traditional approach to handling foam problems involves the use of one or more commercially available antifoam chemicals. This, however, requires one to install and maintain a special chemical injection system and the on-going purchase of chemicals, which can significantly increase production costs. Foam-breaking cyclones can often significantly reduce, if not altogether eliminate, the dependency upon such chemical injection. In one Gulf of Mexico platform for which the writers are familiar, a defoaming cyclone separator eliminated the use of chemicals for an annual cost saving of about 400,000 USD.

14.2 Some Design Considerations and Factors Influencing Behavior

One of the problems in applying foam-breaking cyclones is that it is difficult to quantitatively predict, a priori, just how well they will perform in practice.

If the liquid phase viscosity is too high (greater than approximately 50 cp, for example), the dispersed foam bubbles may not respond well to the applied centrifugal field within the cyclone. Likewise, if the bubbles are too small or form a 'micro-dispersion', the separation will be ineffective.

On the other hand, the production or process engineer often is only interested in knowing if his or her unit is going to have a foaming problem or not—"yes or no?" Whether the separation efficiency is 99% or 99.8% is of less consequence. Under these conditions, experience with similar processes can be extremely valuable and, if such experience is not available 'in-house', the equipment vendor's experience may prove very helpful.

As with all foam-related problems, surface tension and surface chemistry play an important role with defoaming cyclone-type separators. Yet, in most cases of practical interest, our understanding of the coalescence process is poor. This is because many industrially important processes for which foam is a problem are characterized by heavy, 'dirty' feeds consisting of a complex heterogeneous blend of gas, oil, water, dissolved salts and, often, solids. Operating pressures and temperature may also be far removed from ambient conditions or from that which can be readily studied in a laboratory setting.

In many situations, it is not even clear if the foam is entering the feed line or if it is being generated in the receiving vessel that is having a 'foaming problem', or both. Independently of how it arises, cyclonic type separators can, in many applications, either coalesce an incoming foam or degas the incoming liquid phase so that it cannot produce a rate-limiting foaming problem downstream. In addition, since defoaming cyclones eliminate conventional "splash plates", they also eliminate this common cause of foam formation.

In certain applications, an incoming liquid stream is saturated with gas, and any decrease in static pressure will result in the liberation of gas bubbles. If this liquid is injected in a cyclonic type separator, the drop in static pressure within the core of the separator will tend to release or 'liberate' the dissolved gas so that a gaseous core is formed. A similar air core is also observed to occur in traditional hydrocyclone installations in the minerals industry. The creation of this gas core is similar to popping the cork on a bottle of one's favorite champagne or other carbonated drink. The static pressure within the core of a defoaming type cyclone type separator can easily drop to 700 mm of water column (1 psi) below inlet pressure in low or moderate pressure applications. At high gas densities, the drop in static pressure can exceed 10 times this value. The point we wish to make is that the cyclone, itself, has the potential of 'degassing' the incoming feed by reducing its static pressure. If the liquid phase is not too viscous (less than about 50 cp), the gas bubbles thus liberated may then be separated from the liquid phase.

As the liquid spirals down the walls of the cyclone and travels deeper into the liquid pool, the static pressure increases. This pressure increase is due to the increased hydrostatic head and to the loss of spin. This tends to halt the liberation of gas and helps to explain, at least in part, the workings of defoaming cyclones.

A spontaneous production of foam may be triggered by simply injecting a stream that has a propensity to foam into a conventional liquid knock-out vessel. This is likely to happen if the feed stream experiences an abrupt pressure decrease upon entering the vessel. It is also likely to occur if the feed stream's incoming kinetic energy is abruptly dissipated through impact with a 'splash' or 'deflector' plate or some other device (a dished-head, for example) that is capable of generating a large amount of surface area. Ideally, one wishes to avoid splash plates and utilize the incoming momentum of the feed in a more productive way. Such cyclones can serve one of two functions. They can:

1. act as excellent inlet diffusers by eliminating the splashing that can produce a foaming problem or
2. utilize the feed stream's incoming momentum to generate high G-forces (100 to 200 G's, or more, in some applications) which act to separate any gas bubbles from the liquid phase. These same G-forces may also be helpful in separating two incoming liquid phases that may also be present in the feed stream. If the feed stream is comprised of a gas and two immiscible liquid phases, the inlet velocity may be limited by the need to prevent the formation of a liquid/liquid emulsion.

The designer has the task of sizing a foam-breaking cyclone system so that it can physically handle the combined vapor and liquid volumetric throughput without excessive liquid 'carryover' and excessive gas 'carryunder'. For example, the gas-phase vortex (shown in Fig. 14.1.1 above) must not be allowed to dip below the bottom opening of the cyclone—a condition known as gas 'blow out'. Gas blow out is most likely to occur at maximum gas rates and low liquid rates.

The designer must also be able to estimate overall gas phase pressure loss as a function of gas and liquid throughput at operating conditions. The defoaming cyclone system must sometimes be designed to handle incoming slugs of liquid so that they neither upset the process nor physically harm the equipment.

As with all such centrifugal separators, one would not normally scale up a foam-breaking cyclone by simply increasing its diameter to accommodate an increase in flow rate. From a pressure drop point of view it may be acceptable to increase (or decrease) the cross-sectional area of the cyclone body in proportion to any increase (or decrease) in feed volumetric flow rate, as discussed in Chap. 4. However, other factors being equal, the separation performance will decrease with increasing diameter and, for this reason, body tube diameter is normally held reasonably constant and the number of tubes is chosen to accommodate the total flow rate. Thus, one large 480-mm diameter separator would not be installed in place of ten 150-mm diameter separators running in parallel unless one was only interested in capturing 'slugs'. Most commercial designs appear to consist of a parallel arrangement of 2 to 6 defoaming cyclones symmetrically arranged off a common, centrally located header.

When one views the inlet configuration of some of the commercially available designs, one may question the uniformity of the gas and liquid distribution to the individual separator tubes. The gas and liquid cannot be expected to divide perfectly uniformly among the various separator tubes when injected through the feed header. However, unless there is reason to suspect some gross maldistribution, one does not have to be overly concerned about this. As we found in the previous chapter, maldistribution stemming from a nonsymmetrical inlet velocity profile in the inlet manifold leads to a rather small pressure differential at the bottom (gas-liquid interface) of the individual separators. In addition, the individual tubes are effectively isolated from one another because their underflow openings are independently sealed in the vessel's liquid pool. Hence, they do not 'communicate' with one another. This does not mean that the gas distributes itself uniformly, only that the nonuniformity does not significantly affect the liquid level within the individual separator tubes. This would not be the case if the underflow seal were lost, however. The other rather obvious factor that bears mentioning is that experience with hundreds of commercial installations has proven that the feed headers that are typically used, actually work in practice.

An even more challenging task facing the designer is the prediction of separation or defoaming performance. Here, manufacturers of defoaming cyclones must rely heavily on experience with processes similar to that under consideration. By comparing 'oil-to-gas' ratios, operating temperature and pressure, liquid phase viscosities, gravities, interfacial tensions and other such properties and operating conditions, equipment vendors are usually able to design a 'new' system that will meet the customer's process needs. In some cases, however, the vendor may not have a good reference point for comparison and a unit will be installed as a test case. This is often appropriate since the cost of equipping a separator vessel with foam-suppressing or degassing cyclones is generally not a major expenditure compared to the potential benefit.

Foam-breaking cyclones can be installed in either vertical or horizontal vessels. In some offshore drilling operations, certain vapor-liquid separation vessels are routinely retrofitted with defoaming separators if there is a known or suspected foaming problem. This is usually possible since the individual tubes can pass through existing manways and be assembled inside the main separator vessel. If necessary, the separator assembly can be supported off the inside walls of the main vessel, as well as the vessel's inlet, thereby avoiding 'hotwork'.

In tall, vertical vessels, the distance from the vessel inlet to the liquid level may far exceed the height required by the foam-breaking cyclones. This is especially true at low liquid levels within the main separator vessel. Under these conditions the cyclone body tubes may need to be extended so that their bottom openings are always submerged and sealed.

In critical applications, where one must minimize entrained liquid carryover, wave-plate or chevron type separators can be inserted ahead of the gas outlet pipe to capture any mist that may escape capture by the foam-breaking

cyclones. Demisting pads, though highly effective from a separations point of view, may only be used if the system is sufficient 'clean' so that there is little or no possibility of their plugging by solids or from wax or coke deposits.

Before startup, the foam-breaking separator assembly should be thoroughly inspected for alignment, gasketing/sealing, bracing, bolting, flow obstructions, et cetera, by an inspector familiar with the design and purpose of this type of equipment.

14.3 Applications

Some typical applications for defoaming cyclones include:

- Onshore and offshore platforms
- 2 and 3-phase production separators
- Geothermal separators
- Test separators
- Flash drums
- Flare/vent scrubbers
- Free-water knock-out drums (FWKO) or slug-catching drums
- Overhead accumulators
- Underbalanced drilling separators
- Produced water degasser separators
- Recycle hydrogen vessels
- Atmospheric separators
- Gas diverter vessels
- Certain chemical processes

Manufacturers of foam-breaking or foam-suppressing separators each have their own special experience, preferred design methods, and specialized equipment offerings. Some of the equipment offered by several manufacturers is presented in Figs. 14.3.1 through 14.3.7. Hopefully, these illustrations will help reveal some of the many design details and configurations that are possible.

14.4 Estimating Submergence Required to Prevent Gas 'Blow Out'

In this section we shall present a simple method for estimating the submergence required to prevent incoming vapor from escaping out the bottom opening of a defoaming cyclone. From fluid statics, we know that the hydrostatic pressure at the bottom opening of the cyclone, at elevation $z = 0$ (see Fig. 14.4.1), must equal the hydrostatic pressure at this same elevation outside the cyclone. This leads directly to the relationship:

$$p_{uf} + \rho g h = p_{of} + \rho g H \tag{14.4.1}$$

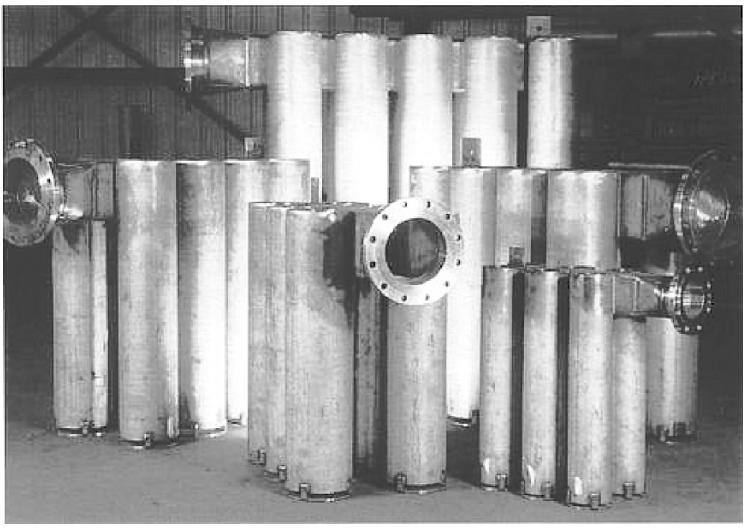

Fig. 14.3.1. A collection of Porta-Test Revolution 'defoaming' separators of various size and capacity. Courtesy Natco Group

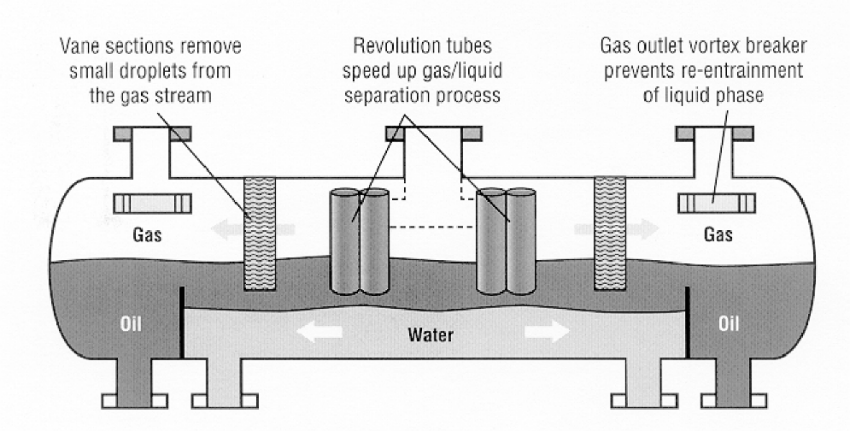

Fig. 14.3.2. A high-capacity horizontal separator featuring 'foam-breaking' Porta-Test Revolution separators as the first stage separator. Courtesy Natco Group

where p_{uf} is the gas phase pressure at the bottom of the cyclone directly above the cyclone's liquid level; p_{of} is the gas phase pressure upon exiting out the top of the cyclone (equal to the gas pressure in the vessel); ρ is the liquid phase density, and H, h are the elevations above the $z = 0$ reference plane as indicated in Fig. 14.4.1.

The cyclone's underflow and overflow pressures can be expressed as:

$$p_{uf} = p_{in} - \Delta p_{in-uf} \tag{14.4.2}$$

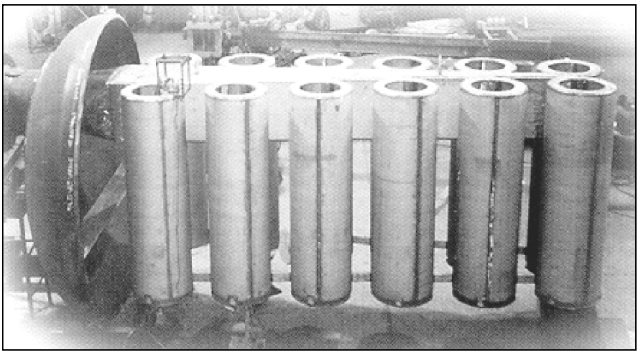

Fig. 14.3.3. A twelve-tube cluster of Porta-Test Revolution separators being installed in a horizontal vessel. Courtesy Natco Group

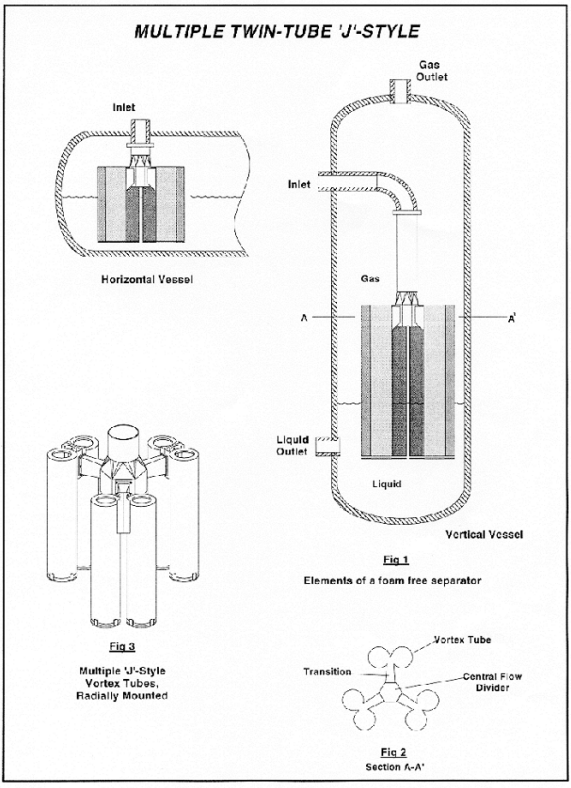

Fig. 14.3.4. A top-fed, multiple 'J' style 'Foam-Free' vortex tube assembly shown mounted in a horizontal and vertical vessel housing. Courtesy EGS Systems, Inc.

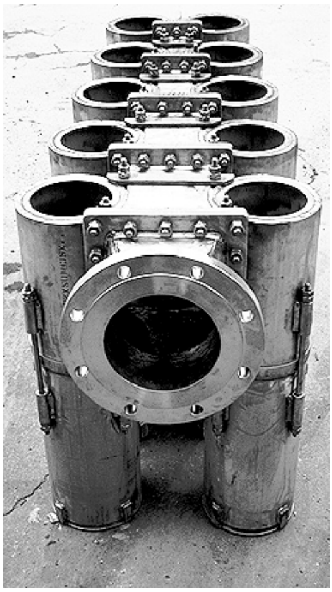

Fig. 14.3.5. A 10-tube parallel assembly of 'Foam-Free' vortex tubes shown bolted together off a central manifold inlet duct. Courtesy EGS Systems, Inc.

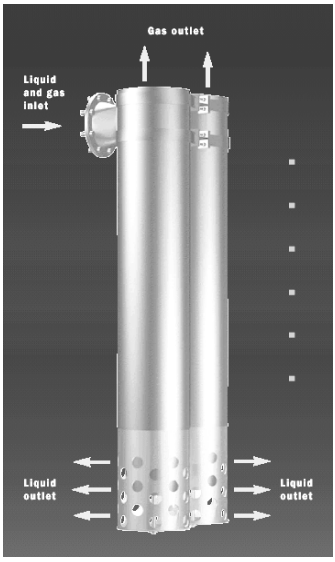

Fig. 14.3.6. A twin-tube G-Sep CCI foam-breaking cyclone cluster. Courtesy Kvaerner Process Systems

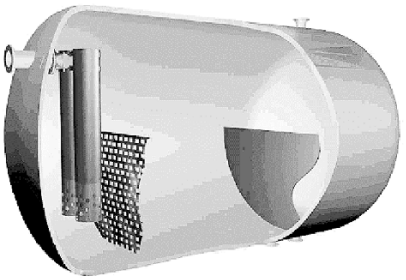

Fig. 14.3.7. A three-dimensional illustration of a twin-tube G-Sep CCI foam-breaking cyclone within a horizontal vessel. Shown also is a perforated vertical plate for improved distribution of the liquid phase(s) and a downstream, light-phase 'spill-over' baffle. Courtesy Kvaerner Process Systems

$$p_{of} = p_{in} - \Delta p_{in-of} \tag{14.4.3}$$

where p_{in} is the pressure at the cyclone inlet, and Δp_{in-of}, Δp_{in-uf} are the pressure drops from inlet to overflow and inlet-to-underflow, respectively.

Substituting Eqs. (14.4.2) and (14.4.3) into Eq. (14.4.1) and simplifying:

$$\rho g\,(H - h) = \Delta p_{in-of} - \Delta p_{in-uf}. \tag{14.4.4}$$

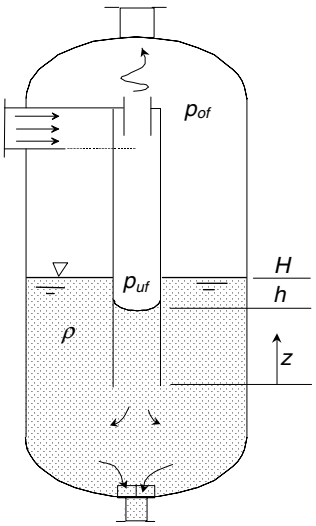

Fig. 14.4.1. A cyclonic type separator with liquid sealed underflow

This equation relates the elevation of the liquid level in the cyclone, h, to the submergence, H, and the inlet-to-overflow and inlet-to-underflow pressure

drops across the cyclone. If conditions are such that h (measured upwards from the reference elevation $z = 0$) becomes 0, gas will begin to blow out the bottom opening of the cyclone. Setting $h = 0$ and solving for H, Eq. (14.4.4) becomes

$$H = \frac{\Delta p_{in-of} - \Delta p_{in-uf}}{\rho g} \tag{14.4.5}$$

This equation provides a relatively simple method for computing the minimum submergence, H, required to prevent gas from blowing out the bottom of the cyclone. An example calculation is presented in Appendix 14.A.

'Blow out' is to be avoided since it can lead to several problems, including:

- product gas exiting out the vessel's liquid underflow pipe
- cavitation of the underflow pump
- liquid entrainment out the top of the vessel (as the result of rising bubbles)
- foam generation, and
- disturbance of any hydrocarbon/water separation that may be occurring in the liquid phase of the main vessel.

The pressure drops appearing in Eq. (14.4.5) should be computed on basis of gas-liquid cyclone pressure loss correlations developed for the particular design geometry and operating conditions that apply. Lacking such data, one may use a more 'generic' pressure drop correlation—at least for the computation of the inlet-to-overflow pressure loss.

Very few correlations are available for predicting the inlet-to-underflow pressure loss. This is also the case for gas-solids cyclones but is especially true of gas-liquid cyclones. The Muschelknautz method described in Chap. 6 for gas-solids cyclones may be used for rough estimation purposes if one substitutes the friction factor for gas-liquid cyclones (see Chap. 13) in place of the gas-solids friction factor. However, as a word of caution, the writers have observed that this correlation tends to overpredict actual pressure losses. Clearly, neglecting the inlet-to-underflow pressure loss altogether in Eq. (14.4.5) will lead to a conservative estimate of the minimum submergence, H.

If the separator under consideration is a commercially available design, one should consult the manufacturer regarding expected pressure losses. Manufacturers normally develop their own correlations for pressure loss and other key system performance measures—applicable to their particular line of equipment. This information, understandably, is not generally reported in the open literature.

One should normally submerge the bottom opening of the cyclone (or cyclones) sufficiently to handle a gas flow rate 50% greater than 'design' operating conditions—more in some applications. In addition, the cyclone bodies may have to be extended (beyond that required for separation or normal sealing purposes) if the liquid level in the vessel housing the cyclones is likely to drop significantly during operation.

14.A Example Computation of Submergence Required to Prevent Underflow Gas 'Blow Out'

A defoaming cyclone-type separator is to be installed to prevent excessive foam-related problems in a commercial high-pressure 'test separator' handling a heavy crude feed. We wish to use Eq. (14.4.5) to estimate the submergence required to prevent gas from blowing out the separator's underflow opening. The cyclone's pressure drops and the liquid density at design conditions are:

ρ = 750 kg/m^3
Δp_{in-of} = 5200 Pa
Δp_{in-uf} = 1200 Pa

Solution

Substituting into Eq. (14.4.5):

$$H = \frac{\Delta p_{in-of} - \Delta p_{in-uf}}{\rho g}$$

$$H = \frac{(5200 - 1200)\ \text{Pa} \frac{\text{N}}{\text{m}^2\text{Pa}} \frac{\text{kg m}}{\text{N s}^2}}{750 \frac{kg}{m^3} 9.81 \frac{m}{s^2}} = 0.54m(1.8ft)$$

Thus, at 'design' conditions, the bottom opening of the separator should be submerged no less than 0.54 m below the vessel's normal liquid level. In practice, we would want to apply a safety factor of 1.5 (or more) and increase the submergence to 0.8 m or 2.6 ft.

15

Design Aspects

The modeling equations in the previous chapters are not enough to design a cyclone or swirl tube from scratch. The models do not perform well for uncommon designs, and they are not complete enough to be used to find an optimal design for a given duty directly. To assist those who may have the task of actually designing and constructing a cyclone or swirl tube we include some guidelines here. Although the majority of the discussion that follows directly pertains to "dedusting" cyclones and swirl tubes, most of it also applies equally well to demisting cyclones. Regarding the latter, see also Chap 13.

15.1 Cylinder-on-Cone Cyclones with Tangential Inlet

In this section we concentrate on cylinder-on-cone cyclones with tangential inlets. To give a feel for the range of 'viable' designs we list some frequently used designs. We then proceed to give some specific design and construction advice.

15.1.1 Some Standard Cyclone Designs

There is a wide range of cyclone geometries in use. We have already mentioned the Stairmand High Efficiency geometry (Stairmand HE). Stairmand also designed a compact High Flow (HF) geometry. Abrahamsen and Allen (1986) collected a number of geometries, some of which are listed in Table 15.1.1. Also the Lapple cyclone, taken from the list of geometries in Svarovsky (1981), is included.

The dimensions of the cyclones in Table 15.1.1 have been recalculated so that they all have the same inlet area of 0.01 m^2. They are drawn to scale in Fig. 15.1.1, where they are presented from left to right in the same order as in Table 15.1.1. Symbol notation is defined in Fig. 15.1.2. Comparing the cyclones on basis of equal inlet area means that they have the same capacity

Table 15.1.1. Cyclone geometries from Abrahamsen and Allen (1986), one from Svarovsky (1981)

Name	D	D_x	S	H	$H-H_c$	a	b	D_d
Muschelknautz E	680	170	311	934	173	173	58	228
Muschelknautz D	357	119	318	863	262	187	54	195
Storch 4	260	117	176	1616	909	260	38	91
Storch 3	192	107	200	821	462	167	60	92
Storch 2	225	108	239	1097	464	188	53	84
Storch 1	365	123	142	1943	548	100	100	64
Tengbergen C	337	112	145	930	187	100	100	112
Tengbergen B	210	112	224	604	324	179	56	112
Tengbergen A	277	112	157	647	180	135	74	202
TSN-11	348	136	242	959	219	184	54	154
TSN-15	266	158	350	1124	589	166	60	119
Stairmand HE	316	158	158	1265	474	158	63	119
Stairmand HF	190	141	165	755	283	141	71	71
Van Tongeren AC	325	100	325	1231	436	149	67	130
Vibco	286	111	124	720	228	111	90	66
Lapple GP	283	141	177	1131	566	141	71	71

in terms of volumetric gas flow, if they are operated at the same inlet velocity. The figure shows considerable variation in design. Noteworthy are the couple of very long Storch designs, and the wide variation in dust outlet and vortex finder diameters. The Stairmand HF and Tengbergen B designs can be very handy if a given flowrate is to be handled with a compact cyclone. In the Vibco design, the scrolled inlet spirals down to the level of the cyclone lid. This is commonly referred to as a 'helical roof' design.

15.1.2 Design of the Inlet

The cross section of a tangential inlet tube to a cyclone is often rectangular. Inlets with circular cross sections ('pipe-type' inlets) are mostly used only in small sampling cyclones and in some applications where a simple circular inlet can achieve the desired separation and/or simplicity of construction and low cost are prime considerations. Certain 'shop' and grain-processing cyclones fall into this category.

A rectangular type inlet joins the cyclone body in a natural way, but requires a circular-to-rectangular transition piece (see the sketch in Fig. 15.1.3). This transition piece is often located quite close to the cyclone and, thus, the flow transition occurs rather abruptly. This type of transition is not recommended since it leads to boundary layer separation and extra turbulence in the incoming flow. Ideally, one should design a cyclone's inlet transition chute like venturi type flow meters: confining angles should be no more than 21 degrees and expanding angles no more than 15 degrees (Perry, 1997).

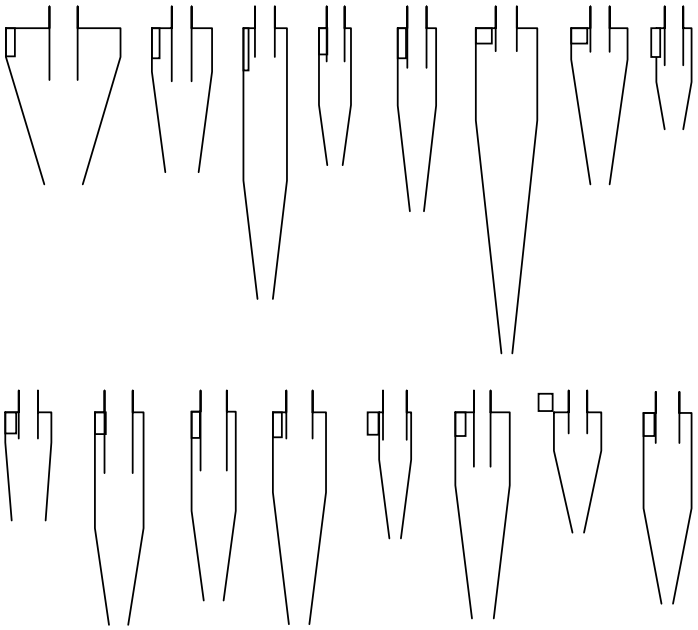

Fig. 15.1.1. Scale drawings of the cyclone designs in Table 15.1.1, listed in the order shown in the table and, as in the table, based on the same inlet area

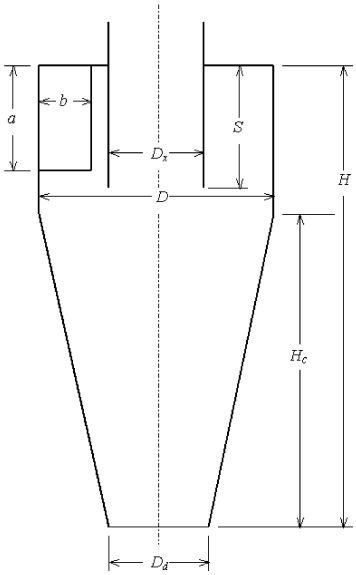

Fig. 15.1.2. Definition of dimensional symbols reported in Table 15.1.1

Aside from generating turbulence, a poorly designed inlet transition section, namely one that is too short, can lead to particle fouling and to rapid erosion of the cyclone's inlet 'target zone' (see Chap. 12). This is particularly true if the transition piece was installed, in part, to decelerate the incoming flow ahead of its entrance into the cyclone.

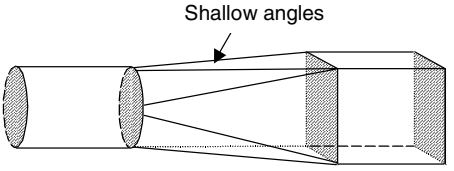

Fig. 15.1.3. Sketch of a circular to rectangular transition piece

As we mentioned in Chap. 1, the simplest inlet configuration for a cyclone is the so-called 'slot' inlet[1], where the inlet simply joins the cyclone body flush with the outer wall. However, if the inlet is relatively large (as it is in the high capacity cyclones, see the previous section) or the solids loading is high, it is better to offset its position radially. In this way, it joins the cyclone outside the body (see, for example, Fig. 15.1.4) and is gradually restricted so that its outside radius matches that of the cyclone. This is the 'scroll' or 'wrap-around' type of inlet.

In compact, high flow cyclones a scroll type inlet is often used to prevent the inner portion of the inlet jet from impacting the vortex finder and thereby disturbing the flow and possibly causing erosion problems. As indicated above, scroll type inlet designs are a common feature of 'primary' or first-stage cyclones, although some manufacturers include them as a standard feature independently of the solids loading. Additionally, since the inlet scroll reduces the angle of attack of the incoming particles with the cyclone barrel wall, such inlets may be utilized to reduce bouncing of rubbery or elastic-type feed particles. Some equipment designers prefer scroll type inlets since they provide a somewhat smoother aerodynamic transition into the barrel region of the cyclone. They also provide some degree of 'pre-separation' of the bulk of the incoming solids in heavily-loaded installations. In fact, at solids loadings greater than about 1 kg solids per kg gas (or 1 lb solids per lb gas) the majority of the incoming solids will be "centrifuged" to the inner surface of the scroll before exiting the scroll section.

Equipping a cyclone with an inlet scroll, as depicted in Fig. 15.1.4, produces an effect upon cyclone performance that is similar to that produced by increasing the body diameter, while keeping the vortex finder diameter constant. This is so because the scroll increases the inlet radius relative to a

[1] This configuration is also sometimes called a 'tangential' inlet, but we reserve this term to distinguish from axial inlets with swirl vanes

conventional slot, pipe or vane-type inlet. This increase in inlet radius brings about an increase in incoming angular momentum and this, in turn, generally leads to an increase in the core spin velocity, a decrease in cut-point diameter, and an attendant increase in overall pressure loss. This is taken into account in the Barth model: Eq. (4.2.4) calculates a higher spin velocity in the vortex core due to the higher value of R_{in} in a scroll inlet. This is generally true even though the variable R_{in} appears in both the numerator and the denominator of Eq. (4.2.4) since the second term in the denominator is usually small in comparison with the first term.

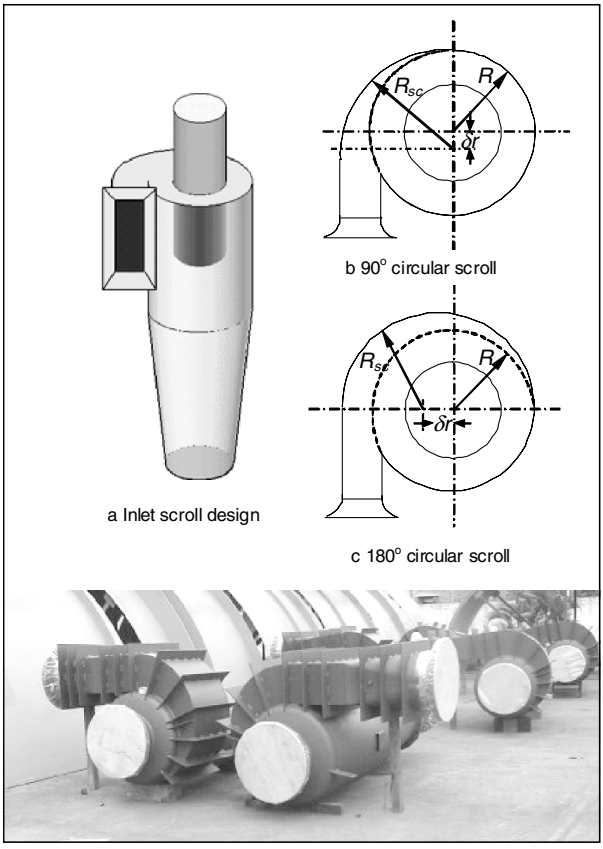

Fig. 15.1.4. a, b, c Circular scroll-type inlet geometries together with a commercial example of a wide-bodied, 180° inlet scroll, courtesy Fisher-Klosterman Inc.

One type of scroll inlet is the *circular scroll*. Figs. 15.1.4 b and c illustrate simple 90° and 180° circular scrolls. These, along with 270° and 360° scrolls (not illustrated here), are the four most commonly encountered in practice. We note that, unlike 'logarithmic' scrolls (see below), the radius of curvature

of these circular scrolls does not change with scroll angle, θ. This makes them relatively simple to fabricate. All such scrolls are designed so that their leading edge is tangent to the outside wall of the inlet duct and their trailing edge is tangent to the cyclone barrel section. For the 90° and 180° scrolls shown in Figs. 15.1.4 b and c, this can be assured by designing the scroll so that the 'offset' distance δr is:

$$\delta r = R_{sc} - R \tag{15.1.1}$$

where R_{sc} and R are the radii of the scroll and cyclone barrel sections, respectively.

An example calculation pertaining to design of a circular 135° scroll is presented below presented in Fig. 15.1.5. Here L is the distance from the start of the scroll to the center of the cyclone. In this example we will let $L = 41.625$ cm and $R = 32.5$ cm.

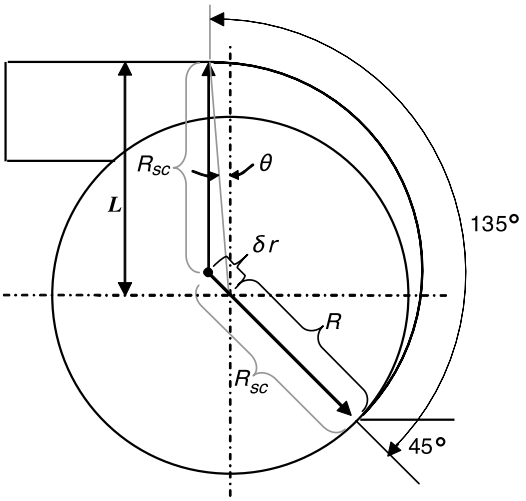

Fig. 15.1.5. Illustration of a circular 135° scroll used in the example scroll calculation

From basic geometric considerations,

$$L = R_{sc} + \delta r \sin 45^\circ$$
$$R_{sc} = R + \delta r$$

Thus,

$$\delta r = \frac{L - R}{1 + \sin 45^\circ} = \frac{41.625 - 32.5}{1 + \sin 45^\circ} = 5.35 \text{ cm}$$
$$\theta = \tan^{-1}(\delta r \frac{\sin 45^\circ}{L}) = 5.19^\circ$$

Scroll "wrap-around" angle = 135° + θ = 140.2° (relative to center of *cyclone*) or 135° (relative to *scroll*).

Another type is the *logarithmic scroll*. This configuration is characterized by a constantly changing radius of curvature, R_{sc}, as a function of scroll angle, θ, as illustrated in Fig. 15.1.6. In general, a logarithmic scroll of this type may be represented by the expression:

$$\ln\left(\frac{R_{sc}}{R_{ini}}\right) = \left[\frac{1}{\theta_{fin}} \ln\left(\frac{R_{fin}}{R_{ini}}\right)\right] \theta \tag{15.1.2}$$

or by:

$$R_{sc} = R_{ini}\left(\frac{R_{fin}}{R_{ini}}\right)^{\frac{\theta}{\theta_{fin}}} \tag{15.1.3}$$

where θ is the scroll's angular coordinate in radians, R_{sc} is the scroll radius at angle θ, R_{ini} is the scroll radius at the start of the scroll ($\theta_{ini} = 0°$), and R_{fin} is the scroll radius at the end of the scroll ($\theta = \theta_{fin}$).

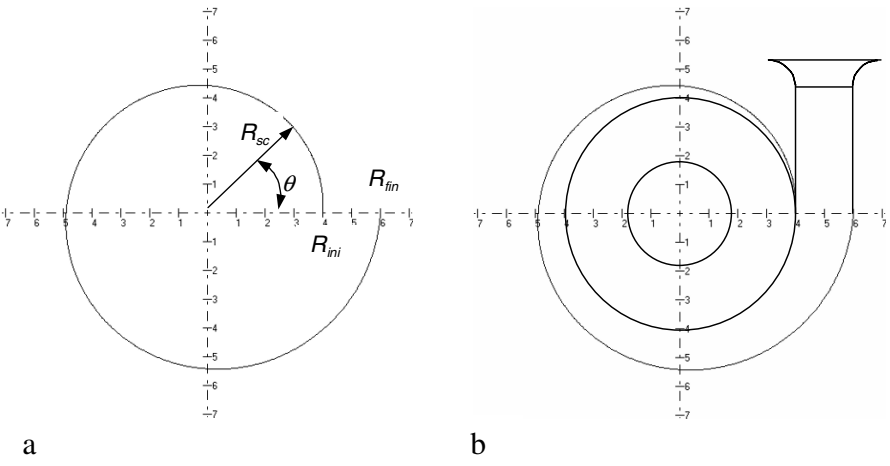

Fig. 15.1.6. a—360° logarithmic scroll pattern, b—Integration of scroll with cyclone

Figure 15.1.6a was created by plotting Eq. (15.1.3) for the special case of $R_{ini} = 4$ (at $\theta_{ini} = 0°$) and $R_{fin} = 6$ (at $\theta_{fin} = 360°$). Figure 15.1.6b is included to show how the logarithmic scroll shown in Fig. 15.1.6a could be integrated into a cyclone design.

Figure 15.1.7 illustrates a cyclone equipped with internal scrolls. Here, in the elevation view and sectional views it can be seen that opposite walls of the barrel section curve radially inward to form the outer walls of the scroll segments. Once the flow enters one of the inlet openings it is forced (by the

outer scroll wall) to flow along a smoothly decreasing radius for 180° (for the twin scroll) or 120° (for the tri-scroll) before joining the flow entering from the other scroll(s). Such an internal scroll design offers some advantages in situations where plot or layout area is limited. All the same, since the particle-bearing gas streams entering the cyclone do so on a somewhat smaller radius than that which they would for an external scroll, the spin velocity in the inner core will also be smaller, other factors being equal. This will result in a somewhat larger x_{50} cut-size but also a somewhat smaller overall pressure loss. Somewhat offsetting the effect of the smaller radius, however, is the decrease in wall-induced frictional drag relative to an external scroll, such as that shown in Fig. 15.1.6b. Inlet horns can be added at the entrance to each scroll (as shown in the bottom right image of Fig. 15.1.7) in order to provide a somewhat smoother flow entry into the outer region of the rectangular inlet slots.

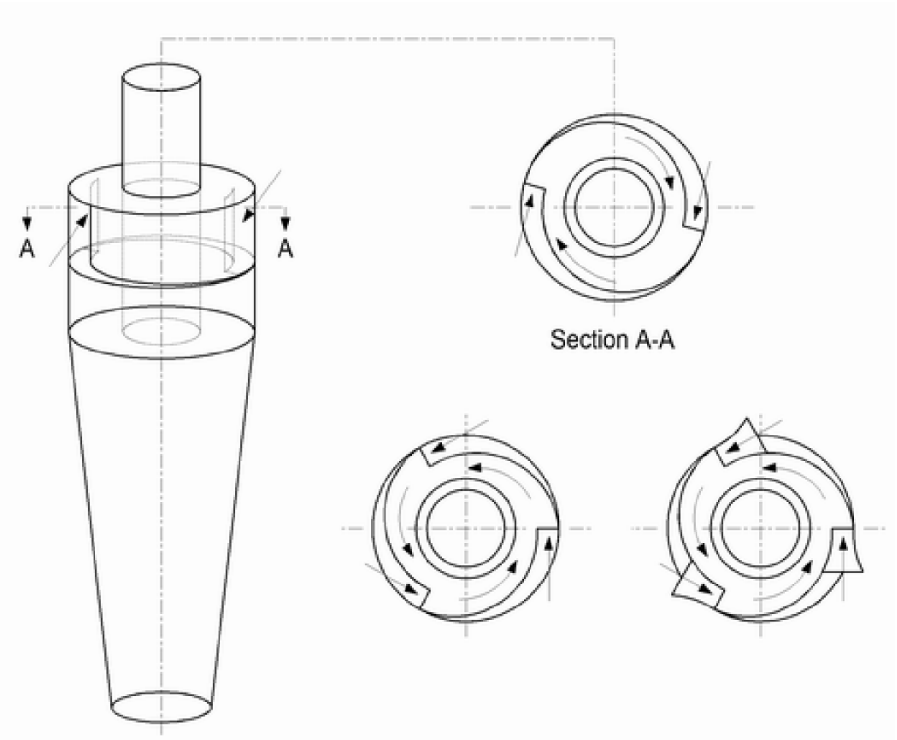

Fig. 15.1.7. Illustration of a cyclone with internal scrolls. Twin internal scroll unit shown in elevation (left) and in sectional view (top right); a tri-scroll inlet shown in plan view (bottom middle) and with trumpet-shaped inlet "horns" (bottom right)

15.1.3 Design of the Cone Section

This section presents the geometry of construction of a 3-dimensional cone or, more specifically, that of a frustum of such a cone. Applications include:

- the main conical section of the cyclone proper
- the conical-shaped sections of the hopper—hopper cone and, possibly, hopper roof
- some vortex finder designs
- any reduction or expansion sections of circular pipe such as that found in the ducting feeding or exiting the cyclone.

When one designs cyclones, the cone diameters, D_{c1} and D_{c2}, and the height of the cone, H_c, or cone angle, β, are normally known. Given these, one can then compute the cone lengths or radii l_1 and l_1+l_2 (shown in Fig. 15.1.8) and the 2-dimensional pattern angle θ. The values for l_1 and l_1+l_2, are given by the equations:

$$l_1 = D_{c1}\sqrt{\frac{1}{4}+\left(\frac{H_c}{D_{c2}-D_{c1}}\right)^2} = \frac{D_{c1}}{2\sin\beta} \tag{15.1.4}$$

$$l_1 + l_2 = D_{c2}\sqrt{\frac{1}{4}+\left(\frac{H_c}{D_{c2}-D_{c1}}\right)^2} = \frac{D_{c2}}{2\sin\beta}. \tag{15.1.5}$$

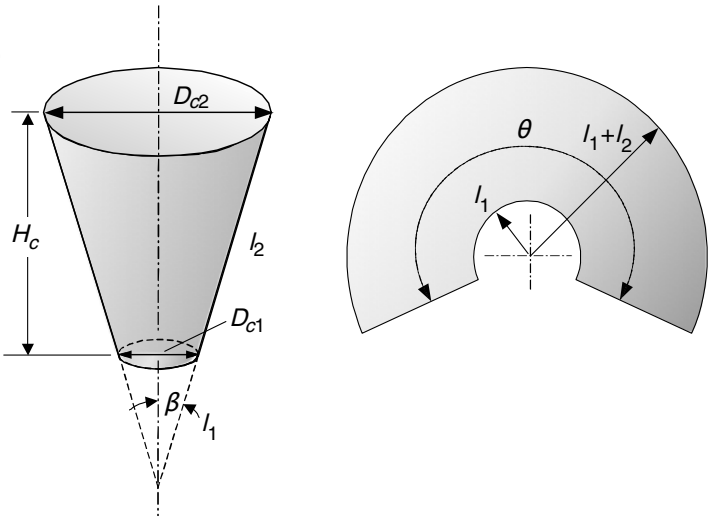

Fig. 15.1.8. Cyclone cone geometry and its construction pattern

The pattern angle θ is given by:

$$\theta = \frac{360^\circ}{\sqrt{1 + \left(\frac{2H_c}{D_{c2} - D_{c1}}\right)^2}} \tag{15.1.6}$$

or simply:

$$\theta = 360^\circ \sin\beta \tag{15.1.7}$$

where θ is in degrees, and β is the half-angle shown in Fig. 15.1.8. Angle θ will be $\leq 180^\circ$ if:

$$\frac{2H_c}{D_{c2} - D_{c1}} = \frac{1}{\tan\beta} \geq \sqrt{3}$$

or if

$$\beta \leq 30^\circ.$$

15.1.4 Solids Outlet Configurations

Careful design of the dust outlet section of the cyclone can mean the difference between a cyclone working satisfactorily and one emitting coarse particles re-entrained into the vortex from the material already separated. Figure 15.1.9 shows four possible configurations of the dust outlet.

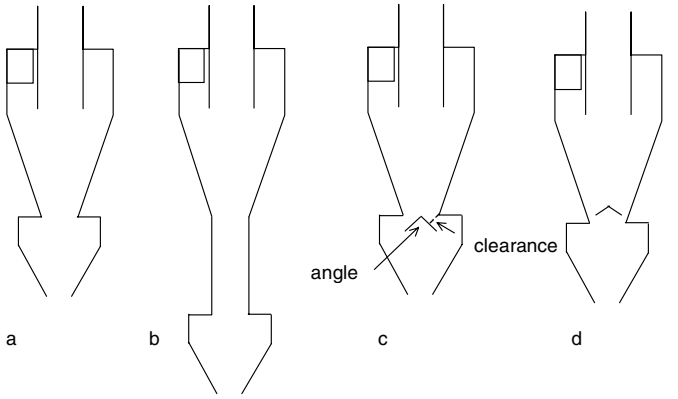

Fig. 15.1.9. Some possible dust outlet configurations

In configuration a the solids hopper is simply attached to the solids outlet of the cyclone. This can often lead to the end of the vortex (sometimes referred to as the 'vortex tail') extending downward to the free surface of the solids in the hopper and to the entrainment of some portion of these solids. This is avoided in different ways in the other three configurations. In configuration b a cylindrically-shaped section is attached to the dust exit. As a rule this section is at least half of the height of the cyclone itself. The vortex may terminate in the tube section, or it may extend down into the hopper, especially in

smooth-walled cyclones. However, if it does, solids that may be entrained from the hopper in the rising gas core will then have an opportunity to become centrifuged back to the (cylinder) wall. For this reason configuration b is regarded as an excellent design geometry where sufficient vertical space exists for its insertion.

In c and d 'vortex stabilizers' (of the simple 'Chinese hat' type) are installed, either just under (c) or just above (d) the dust exit itself. The purpose of the stabilizer is to provide the vortex end with a smooth surface upon which it can attach and center itself. A well-designed vortex stabilizer will improve separation efficiency by preventing the bottom end of the vortex from "wandering around" in the lower section of the cyclone; thereby preventing it from entraining dust off the walls. Furthermore, the stabilizer also provides an unambiguous height upon which to base cyclone calculations since the stabilizer terminates the vortex on its top surface. In so doing, the low-pressure vortex core is not allowed to dip down into the dust receiver or, if so equipped, the rotary air lock, screw conveyor, or dipleg. This has the effect of increasing the static pressure below the stabilizer, which is normally desirable. A stabilizer can also be very useful if one is lacking vertical height in which to install the cyclone.

A vortex stabilizer should not be mistaken for a 'vortex breaker'. See Fig. 15.1.10. Such 'breakers' usually consists of a single metal plate or a metal 'cross plate' which is inserted in the hopper or upper section of a dipleg. Their primary intent is to halt the vortex spin that causes erosion in the hopper and upper regions of the dipleg (if so equipped). Unfortunately, such a 'breaker' also produces intense mixing in the lower regions of the cyclone and hopper, as well as a significant reduction in the core spin velocity. Because these two effects lead, in turn, to a significant reduction in overall separation performance, we do not recommend their use. The fact that a vortex breaker (unlike a vortex stabilizer) may lead to a reduction in the cyclone's overall pressure loss should not be construed as a positive aspect of their behavior. The reason for the lower pressure loss is the vortex breaker significantly reduces the spin in the vortex core, which is normally responsible for the majority of the overall pressure loss as we discussed in Chap. 4, and this, together with the mixing it produces, impairs separation performance.

At high solids or liquid loadings (> 10 vol.%, approximately) one must be careful not to unduly restrict the cone discharge opening or the annular space surrounding the vortex stabilizer, if the later are employed in the design. In some cases it may be necessary to eliminate the "cone" altogether and install a purely cylindrical-bodied cyclone.

Obermair and Staudinger (2001) studied the gas flow, pressure drop and separation efficiency in cyclones with the dust outlet configurations shown in Fig. 15.1.9. The corresponding performance data is presented in Table 15.1.2. Upon comparison, we see that configuration a is not as efficient a design as the others. This is probably due to re-entrainment from the solids hopper. It does exhibit a comparatively low pressure drop, however. Its two vortex-stabilized

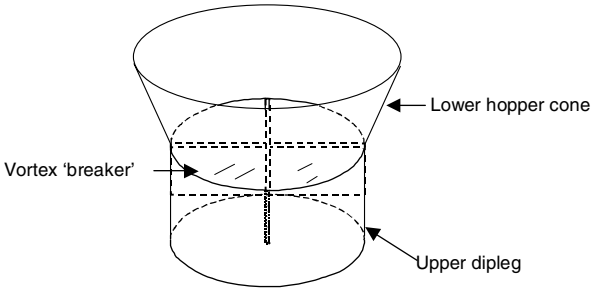

Fig. 15.1.10. A cross type of 'vortex breaker' located in the upper part of a cyclone dipleg

counterparts, configurations c and d, display significantly improved efficiencies although at somewhat higher pressure drops. The latter is especially true of configuration d. The cylindrically extended cone design, configuration b, exhibits the best separation performance at a pressure drop intermediate between c and d.

Table 15.1.2. Results of Obermair and Staudinger (2001)

Configuration	Separation efficiency [%]	Pressure drop [Pa]
a (top images, Fig. 15.1.11)	69.9	942
b (bottom images, Fig. 15.1.11)	approx. 82	approx. 1300

Figure 15.1.11 shows Obermair and Staudinger's LDA measurements of the flow pattern that exists in the lower sections of cyclone configurations a and b.

The vortex can be seen to penetrate to the dust hopper in both cases. Note that this represents the mean flow pattern. The axis of the vortex is seen to spiral slightly around the cyclone axis, less strongly, but not unlike, the CFD simulations shown in Fig. 7.1.6b.

In configurations with vortex stabilizers, sufficient room should be left around the stabilizer shields or cones for the gas and solids that must flow around them (Mothes and Löffler, 1985). In configuration c, if the solids outlet is about 3/4 D_x, the clearance indicated in the figure should be about 1/3 D_x. The angle of the Chinese hat, also indicated in the figure, can be between 90° and 120°. This angle can be somewhat greater in the c type configuration.

As a final comment on the above, it is the writers' opinion that, if the vortex extends through the cyclone into the hopper, which it did in the above-mentioned work, results similar to those presented here for configuration b would have been obtained had the cone and cylinder sections in this configuration been replaced by a one-piece cone section connecting the bottom of the barrel section with the top of the hopper. Here, the inside diameter of the

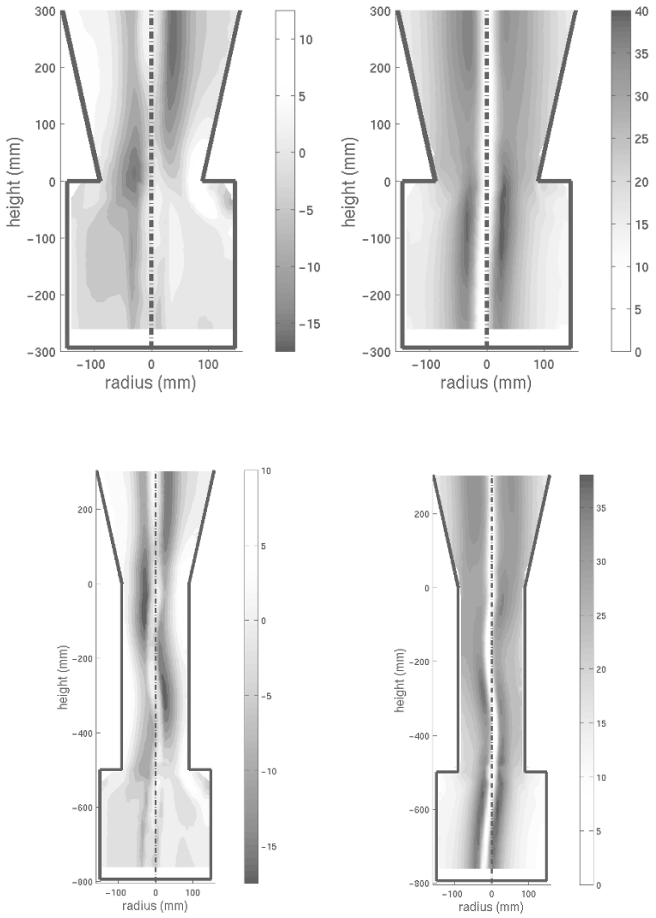

Fig. 15.1.11. Axial (left) and tangential (right) velocities that exist in the lower sections of cyclone configurations a and b measured with LDA (Obermair and Staudinger, 2001). The gray-scale versions of the figures were kindly supplied to us by the authors of that paper. Velocities in m/s

bottom of the cone would be the same as the inside diameter of the cylindrical extension pipe.

15.1.5 Vortex Finder Geometries

A vortex finder—or 'vortex 'tube'—normally consists of a simple hollow cylinder centered within the cyclone and extending down to the approximate level of the bottom of the inlet duct. It serves several important functions including that of defining (or controlling) the diameter of the inner vortex 'core'—at

least, as we have shown in Sect. 4.4, immediately below the lip of the vortex finder wall. It also centers the vortex within the body of the cyclone and conducts the incoming gas out the top of the cyclone[2]. As we've seen earlier, both separation cut-point diameter, pressure loss and "natural length" of the vortex are strongly dependent upon the diameter of the vortex tube. Because of its importance, it is often regarded as the 'heart' of the cyclone.

As shown in Fig. 15.1.12 (and Fig. 15.1.1), vortex tubes come in a variety of shapes and sizes, depending primarily on design objectives and, not the least, on tradition, preferences, or experiences of the designer or design organization. We will briefly introduce and discuss some of their geometries below.

Frames a, b and c of Fig. 15.1.12 show three typical cylindrical-bodied vortex tubes differing only by their lengths. These are, by far, the most common geometries in commercial use. From the standpoint of minimizing emissions, it is normally good design practice to extend the vortex tube somewhat below the level of the inlet floor, as shown in frame c. Measurements by Heumann (1991), shown in Fig. 15.1.13, suggest that the optimum vortex tube length is about 1.25 times greater than the height of the inlet duct. In this particular study, the emission loss for the vortex finder having a relative penetration (t/a) of 0.5 was about 50% greater than that for a t/a value of about 1.25. These measurements were taken on a "second-stage" type cyclone (as shown) processing fine calcined alumina (AlO_2). The pressure drop remained essentially unchanged at 11 inches of water column for these measurements.

A shorter vortex tube, such as that shown in frame b, offers some advantages and disadvantages relative to what we shall call herein the "optimum" length shown in frame c. It is less costly to fabricate, weighs less, provides somewhat improved accessibility through the tangential inlet chute for inspection and repair, imposes less stress (due to radial buffeting) on the weld joints where the vortex tube attaches to the cyclone roof and, in some "short" design geometries, may lead to some reduction in overall pressure loss.

However, if the vortex tube is too short (on the order of half that of the inlet height, or less), some fraction of the incoming gas-solids mixture will tend to pass directly from the inlet to the vortex tube, thereby 'short circuiting' the cyclone and decreasing separation performance, as exemplified by the performance data shown in Fig. 15.1.13. On the other hand, extending the vortex tube tends to bring about the opposite set of results in regards to costs/weight, accessibility/inspection, stress and pressure loss. The point about 'stress' can be easily overlooked since this part of the cyclone may not always receive the attention it deserves in the mechanical design stage. In some situations, flow around the vortex tube can cause buffeting and lateral vibration of the vortex tube. This motion can lead—and has led—to fatigue cracking at its circular junction to the cyclone roof. Such cracks will result in 'short circuiting' of incoming particles out the top of the cyclone and, if the

[2] Note that even in horizontal arrangements, the "top" is used herein to refer to the gas outlet end of the cyclone

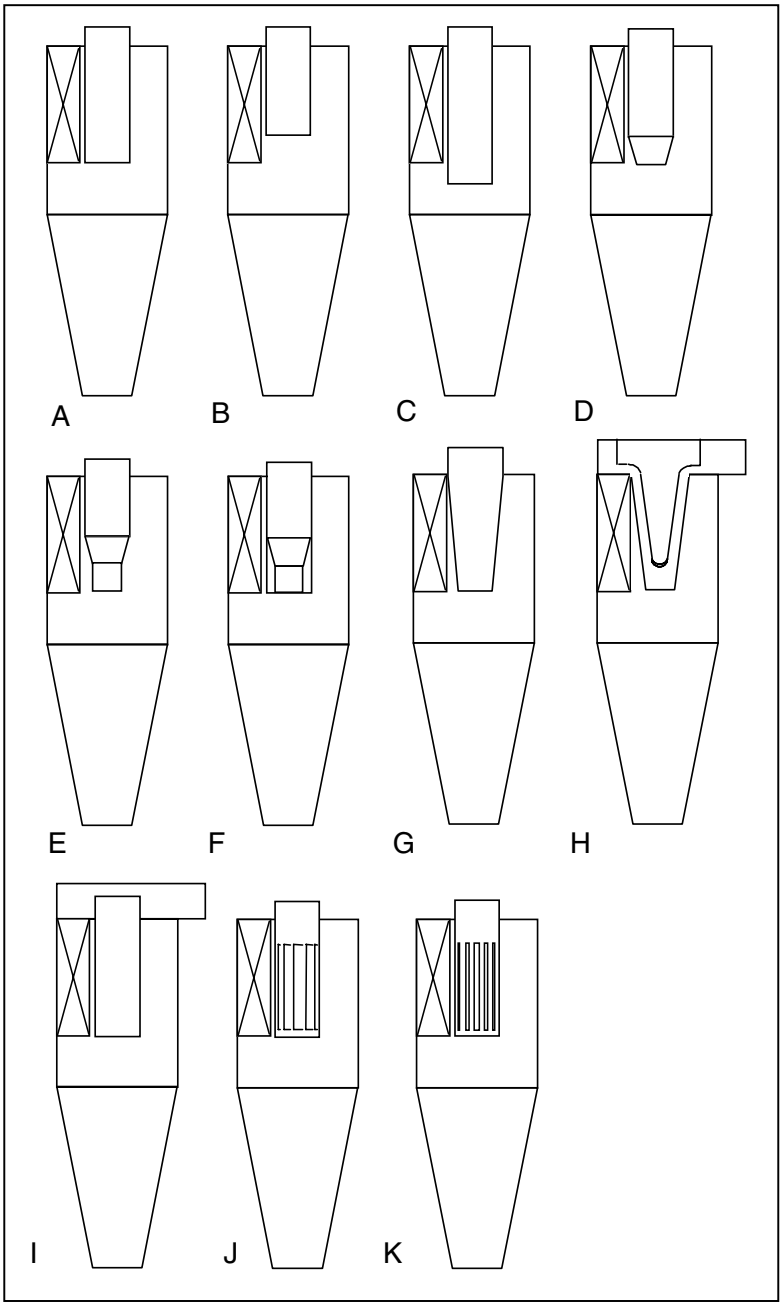

Fig. 15.1.12. Vortex tube geometries

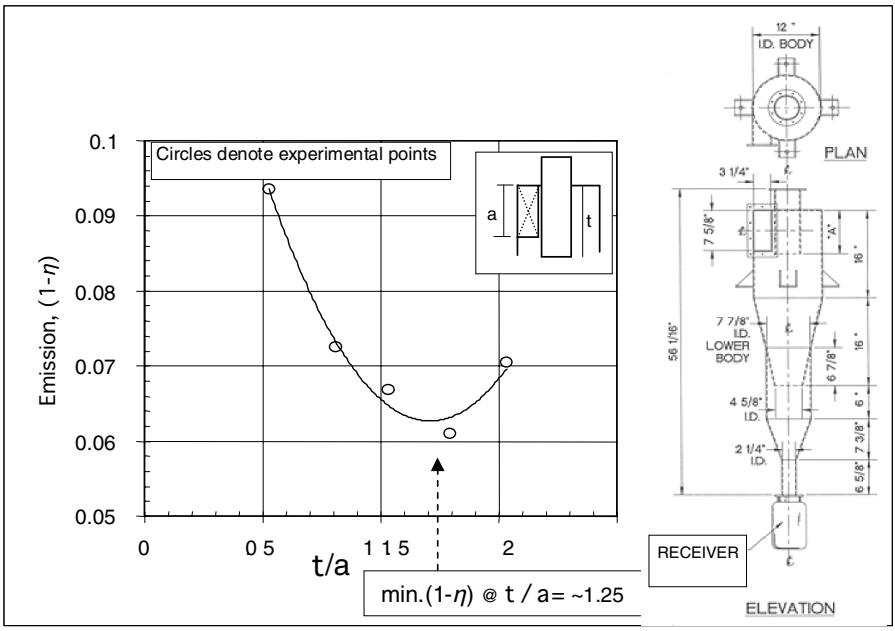

Fig. 15.1.13. Effect of vortex tube penetration (t/a) on emissions $(1 - \eta)$ for cyclone shown on basis of data by Heumann (1991)

problem is not corrected in time, to complete detachment of the vortex tube from the roof.

The 'restricted' vortex tube designs shown in frames d, e and f each feature some sort of reducing cone or cone-and-cylinder at their inlet openings. They can usually be found in cyclones that have been modified to improve separation performance by reducing the effective vortex tube diameter. However, they may also be included as part of the original design in situations where there is an expectation of a significant future increase in gas volumetric flow rate. In this case, the restriction section can be removed and, if necessary, replaced with a more open cylindrical section.

Pressure-recovery type vortex tubes, along with pressure-recovery type diffusers set atop the roof of the cyclone, are occasionally used to convert some of the rotational energy of the exiting gas back into static pressure. Based on data presented by Muschelknautz and Brunner (1967), a modest amount of pressure recovery (15 to 20% reduction in vortex core pressure loss) can be achieved with a simple conically shaped vortex tube, such as that shown in frame g. More efficient recovery (35 to 40% loss reduction) is possible with a well-designed internal conical insert, such as that shown in frame h. Normally, such a vortex tube is directly connected to a wide-bodied outlet diffuser or 'exit scroll' which sits atop the cyclone roof.

It is also possible to insert a specially designed vane assembly into the vortex tube for pressure-recovery purposes. Such a design is illustrated in Fig. 15.1.14. It may, as indicated in the figure, be placed in various axial positions in the vortex finder or above it in the downstream tubing. The leading edge of such a vane, if used, should not materially alter the angle of attack of the gas entering the vane so as not to produce gross mixing and turbulence or retardation of the spin. Rather, it should gradually straighten-out the swirl and convert it into, ideally, pure axial flow.

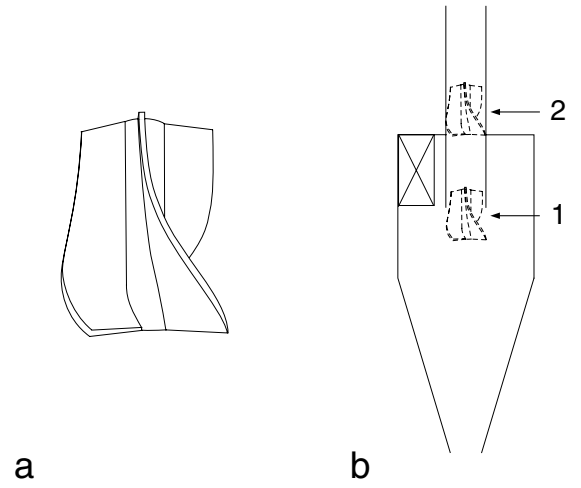

Fig. 15.1.14. Sketch of a simple rectifying vane and two possible positions in, or downstream of, a cyclone vortex finder

Shepherd and Lapple (1939) were among the first to examine systematically the working of various pressure-recovery devices. Among them were a helical-shaped cyclone roof (see the discussion of this below), straightening vanes in or above the vortex finder, and even a straightening vane mounted on baffles below the vortex finder. They found that mounting vanes in the vortex finder gave rise to 30–50% reduction in cyclone pressure drop. Vanes curved to meet the angle of the on-coming gas performed better than simple straight vanes. Mounting vanes above the vortex finder in the down-stream tubing had little effect.

Muschelknautz (1980) investigated the effect of a number of pressure-recovery configurations including an exit scroll, a simple diffuser, an annular diffuser with exit scroll, and a central body mounted with its bottom flush with the vortex finder lip without and with rectifying vanes. The last four configurations were combined with a smoothing of the vortex finder lip. He found that these modifications reduced the pressure drop by 12, 31, 40, 44 and

62% of the pressure drop with a conventional cylindrical, sharp-edged vortex finder, respectively.

Browne and Strauss (1978) carefully designed a vaned flow-straightener with a central body that upstream diverges and is equipped with straightening vanes such that the resultant gas velocity remains constant during the flow straightening, and then converges so that it—together with the pipe wall—forms a diffuser section reducing the gas velocity to the pipe velocity. This would seem to be the most ideal vaned straightening configuration proposed in the literature. The authors mount the device downstream of the vortex finder (5 duct diameters from the lip of the vortex finder) in a Stairmand HE cyclone (see Tab. 15.1.1 and Fig. 15.1.1) in order not to disturb the flow and reduce the separation efficiency. With this configuration they obtained a pressure drop reduction of 22.2%. In a short later paper (Olszewski and Strauss, 1978), the same group reported that insertion of the rectifying vane reduced the separation efficiency little or none. However, the flow through their cyclone with the rectifying vane inserted was higher than without it, so that one would have expected a higher efficiency with the vane if the vane had no detrimental effect on the efficiency at all.

These authors (Hoffmann et al., 2005) mounted rectifying vanes in two positions:

a) the position marked 1 in Fig. 15.1.14, and
b) with the lower edge of the rectifier almost flush with the vortex finder lip,

and found pressure drop reductions of 30% and 21% for positions a) and b), respectively. However, mounting the vanes also gave rise to reductions in the separation efficiency, most for position a). We also used velocity profiles measured earlier with LDA (see Chap. 10) in a tangential-inlet cyclone and in a swirl tube to calculate the dynamic pressure stored in the swirling motion of the gas as it enters the vortex finder, which is also the maximal recoverable pressure. We found this maximal recoverable pressure to be about 51% for the tangential inlet cyclone, and 40% for the swirl tube.

The decision to use or not use such sophisticated pressure-recovery types of vortex tube assemblies hinges on the projected savings in operating cost it provides versus the added expense of construction and the impact that such a device may have on access for routine inspection and maintenance. It is not shown beyond doubt whether or not the installation of vanes for pressure recovery always impacts negatively on the flow pattern in the cyclone body, and therefore the separation efficiency.

Frame I of Fig. 15.1.12 illustrates a pressure recovery diffuser that forces the spiraling gas exiting the vortex finder to expand radially outward through an annular gap. According to Dehne (2006) it is important that the distance between the discharge of the vortex finder tube and the upper cover plate be calculated correctly, a smaller vertical gap at high circular exit gas velocities and *vice versa*. According to Dehne, the average reduction in pressure loss is approximately 16%–17%, but only if the gap space has been correctly calcu-

lated and implemented. Otherwise, there may even be an increase in pressure loss.

In a simple cyclone diffuser performance test conducted by the writers, however, a much larger decrease in cyclone pressure loss was observed. The apparatus tested was a 6-inch (153 mm) cylindrical bodied cyclone shown in Fig. 15.1.15. The cyclone Reynolds number for these tests were in the 800 to 1000 range (per Eq. 4.2.8) which, for cyclones, makes the Eu value very insensitive to the Reynolds number. (See gas phase friction factor charts in Ch. 6, for example.)

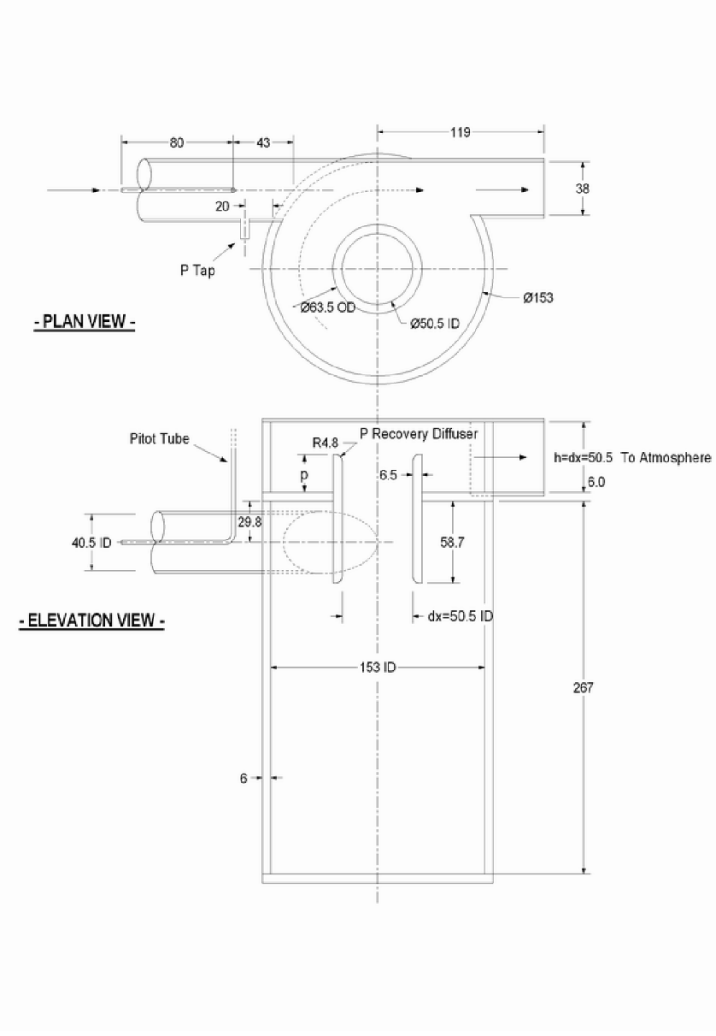

Fig. 15.1.15. Simple diffuser assembly tested by the authors

Here, the pressure drop across the cyclone was measured as a function of the distance the vortex finder extended upwards into the diffuser chamber, the latter normalized by dividing by the inside height of the chamber, or vortex finder (since, for this study, the height of the diffuser was chosen to be equal to the inside diameter of the vortex finder). The pressure loss coefficient, i.e., the Euler number, Eu, was then computed using the superficial velocity out the vortex finder as the reference velocity. The penetration of the vortex finder within the cyclone proper remained constant in these tests (at 58.7 mm). The results are shown in Fig. 15.1.16. We note that, at 0% penetration, a Eu of about 19 was found. As the penetration increased, Eu steadily decreased (the volumetric flow rate from the blower actually increased) and reached a minimum at a penetration of about 80%. At penetrations greater than about 90%, Eu became very sensitive to the penetration and increased in exponential fashion as the area available for flow decreased. Clearly, there are two competing mechanisms underlying the results shown in Fig. 15.1.16: one associated with the reduction in pressure loss brought about by the expansion of the jet (the downward sloping line shown); the other associated with the increase in pressure loss arising from the restriction between the vortex finder and the top plate. This latter mechanism dominates at penetrations exceeding about 80%.

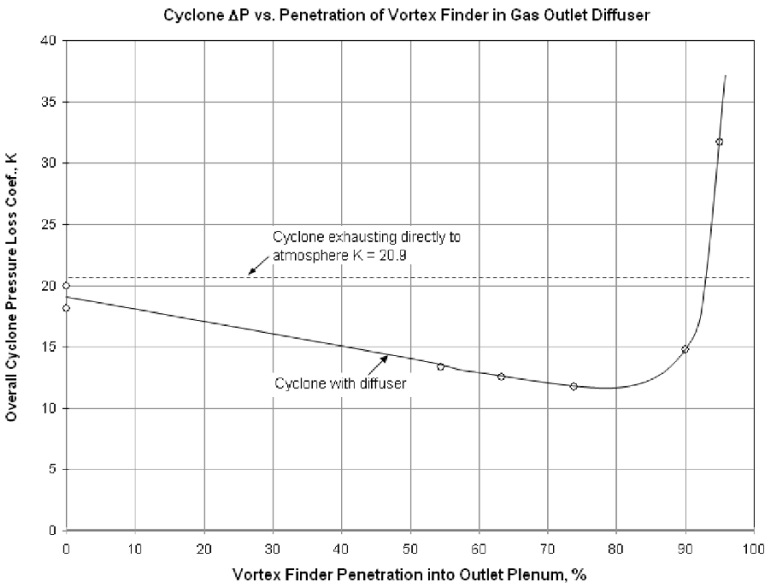

Fig. 15.1.16. Pressure loss coefficient as a function of vortex finder penetration intor outlet diffuser for apparatus shown in Fig. 15.1.15

The dashed line in Fig. 15.1.16 represents the measured value of Eu when the diffuser was removed and the gas was allowed to exhaust directly to the atmosphere. We note that this value was found to be slightly greater that that observed for the diffuser test at a penetration of 0%.

Most significantly, the overall pressure loss across the cyclone was found to decrease by 40% at a penetration of about 75% relative to 0% penetration of the vortex finder into the diffuser chamber. Compared to the case where the gas exhausted directly out the vortex finder (the dashed line), the pressure loss decreased by about 44%. These are very significant reductions, especially in light of the simplicity of the diffuser geometry employed in this study. These results support Dehne's earlier comments, only they indicate a far larger pressure drop reduction. They are also very similar to those reported by Idelchik (1986) for the pressure loss coefficient for linear (irrotational) flow of a jet exiting a pipe and impacting a flat baffle plate. See Fig. 15.1.17.

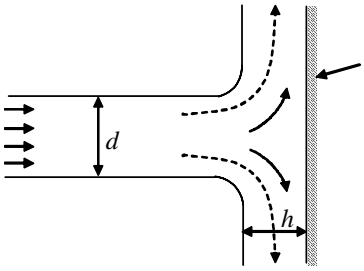

Fig. 15.1.17. Simple pressure recovery diffuser for a non-rotating jet impinging upon a nearby baffle plate. After Idelchik

Here, the pressure loss coefficient was reduced by about 40% when the separation space between the outlet of the pipe, normalized by the inside diameter of the pipe, was reduced from 1 (roughly analogous to our 0% penetration reported above) down to 0.2 (corresponding to our 80% penetration). Note that our cyclone tests showed a minimum at around 75 to 80% penetration. Thus, independently of whether the flow is rotating or not, deflecting it onto a flat plate results in a pressure loss reduction having a minimum at a separation distance between the exiting gas and the target plate of approximately 20% of the pipe or vortex finder diameter. There is no doubt that an outlet scroll or volute will convert some of the rotational kinetic energy back into static pressure when the flow entering the diffuser is rotating. This, however, does not, in the authors' experience, constitute a very significant part of the the pressure recovery brough about by a diffuser.

Before leaving this topic we wish to report that gas impacting the flat roof of the plenum or diffuser section atop our test cyclone resulted in a noticeable drum-like vibration and hum. Thus, before one would construct such a cyclone, it is recommended that a check on the vibration characteristics

of the roof plate be performed so as to ensure that the plate is sufficiently rigid or damped so that it does not resonate at some excitation frequency prevailing in the gas phase.

Frames j and k of Fig. 15.1.12 illustrate two extended-length vortex tubes with closed bottoms but with vertical slits or louvres through which the gas must enter in order to exit the cyclone. Slits and louvres may take on a wide variety of configurations including single or multiple louvres or slits in addition to spiral-like slits or louvres, among others. Such design geometries force the gas to make a sharp flow reversal upon entering the openings of the louvers or slits. Particles that are too large to follow the gas streamlines are thereby separated from the gas prior to entering the openings. Schmidt (1993) designed and investigated an interesting variety of such devices and found that they are capable of producing a 25 to 50% reduction in pressure loss and a 3-fold reduction in x_{99} (that particle size which is collected with 99% efficiency). Nevertheless, such vortex tube designs are not commonly encountered in practice. This may change in the future as experience with such 'unconventional' designs accumulates. Mechanical designers must be aware, however, that special provision may have to be made to support such long-bodied vortex tubes against lateral or radial movement. Additionally, inspection, access and wear issues have to be given due consideration.

When two or more cyclones are connected in series, an outlet scroll is normally installed directly atop the first stage cyclone. See, for example, Figure 15.1.18. It serves, or may serve, two useful purposes: First, it functions as a type of 90° bend, redirecting the gas from its vertical flow pattern within the vortex tube back into a horizontal flow pattern prior to it's entry into the second or third-stage cyclone downstream. Additionally, the scroll may be used as a type of preseparator by helping to centrifuge some of the solids to the outer wall of the scroll and, hence, to the outer wall of the inlet chute feeding the downstream cyclone. It may therefore be viewed as a type of 'inlet scroll' feeding the downstream cyclone, serving a function similar to the inlet scroll one often finds on highly loaded first-stage cyclones.

In regards to the two outlet scrolls shown in Fig. 15.1.18, the scroll on the left mostly serves the function of a 90° elbow since it offers little time or distance for solids to segregate to the outer walls. Even so, it is relatively simple to design and construct, and adds little to the overall weight of the system. Since these factors affect overall cost, it is by far the design most commonly found in practice. However, if achieving the highest possible degree of separation performance is a design priority, the 'full' scroll shown on the right-hand side of Fig. 15.1.18 should be given careful consideration. Regrettably, there appears to be no published studies that would help one to even estimate the improvement in separation efficiency of a cyclone equipped with an upstream scroll of the type shown on the right-hand side of Fig. 15.1.18. Lacking such information, most designers are reluctant to install them, a situation most understandable given that they have no way of assessing their process benefits.

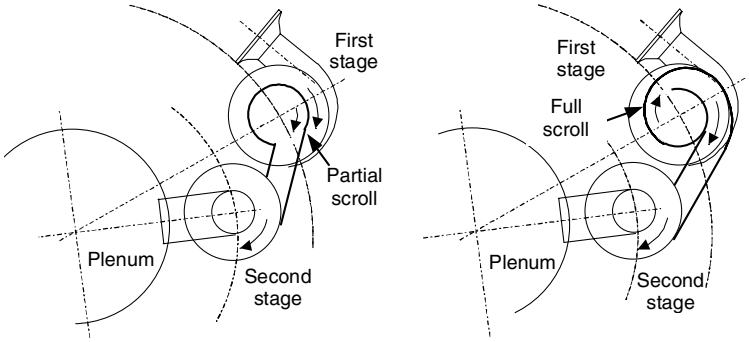

Fig. 15.1.18. A top view of two types of gas outlet scrolls

Outlet scrolls may also be installed on any cyclone wherein the exhaust gas is to undergo a significant reduction in velocity—namely, its expansion to the atmosphere. Independently of whether or not the cyclone is the final stage of a two or three-stage system, or the only stage, a well designed outlet scroll, such as that shown on the right-hand side of Fig. 15.1.18 or in Fig. 15.1.19, will produce some pressure recovery. The smooth expansion of the gas as it negotiates its way through the scroll reduces the gas rotational velocity and converts a portion of its energy into an increase in static pressure. Without such a scroll, the gas would undergo an abrupt expansion with an attendant loss of kinetic energy. A simple application of the mechanical energy balance (in the form of Bernoulli's equation) shows, for example, that if a scroll were to smoothly expand an atmospheric air stream from 47 m/s to only 23 m/s, recovering the dynamic pressure as static pressure rather than having it dissipated into heat by turbulence, a pressure recovery of about 100 mm of water column (approximately 4 inches) would be realized.

15.1.6 Cyclone Length

The issue of overall cyclone length was already discussed in Chaps. 5 and 9 in connection with the effect of length on pressure drop/efficiency and the natural vortex end.

It is not possible to give definitive guidelines as to what constitutes a 'correct' cyclone length. Table 15.1.1 and Fig. 15.1.1 give some idea as to the range of lengths commonly used in practice. The choice of the cyclone length is a compromise between safety—in the sense that the vortex should not end in the cyclone body—and costs; the latter being strongly impacted by the length of the cyclone. All else being equal, increasing the length of a cyclone (within reason) will generally improve separation performance and

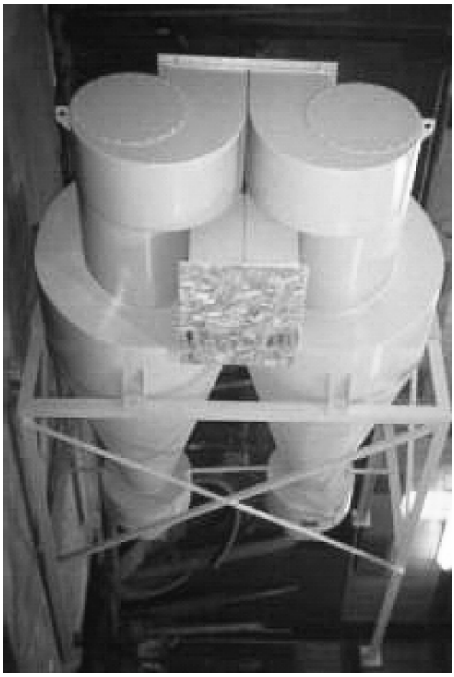

Fig. 15.1.19. A Beckert and Hiester twin cyclone dust collector featuring scroll inlets and gas outlets and helical roofs

lower pressure drop. We note that a patent application of MacLean et al. (1978) claims a design of cyclone with an optimal body length of:

$$\frac{(H-S)}{D} = -1.09\left(\frac{A_x}{A_{in}}\right) + 4.49 \tag{15.1.8}$$

where A_x and A_{in} are the cross-sectional areas of the outlet and inlet, respectively. The patent claims the advantages of using this length as better separation and less wear, but it is not stated how this optimal cyclone length was found.

15.1.7 Cyclone Roof

Most cyclones are designed with flat roofs. Under high pressure or high vacuum conditions, however, it is sometimes necessary to fabricate a cyclone with a domed roof. Typically, such a roof is either elliptical or hemispherical—depending on such factors as the differential pressure across the roof, wall thickness, the size of the cyclone, and the relative vortex finder-to-barrel diameter. In such instances, it is recommended that a flat "false" or "inner" roof be installed (and properly vented if necessary) so that the flow pattern is the same as that of a conventional flat-headed cyclone.

Literature data comparing roof or head designs is scarce. However, a study by Heumann indicates that both separation performance and pressure loss are negatively impacted if, on otherwise identical cyclones (see Fig. 15.1.20), a flat-headed roof is replaced by a domed-roof. The performance data reported in Table 15.1.3 is based on the results of numerous tests using mixed samples of coal fly ash under virtually identical operating conditions. At least for the conditions under which the test were performed, it is clear that the domed-roof design significantly impairs separation performance, as measured by the emission rates reported.

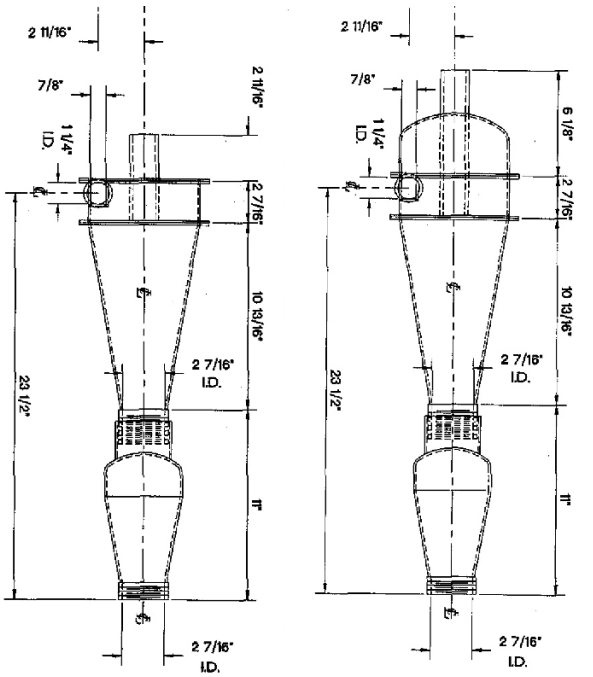

Fig. 15.1.20. Two cyclones used by Heumann to compare roof designs

Table 15.1.3. Flat versus domed roof performance from Heumann

Roof Geometry	ΔP, in water	$(1-\eta)$, loss fraction
Flat	10.65	0.0126
Domed	11.05	0.0191 (52% increase)

As suggested by Heumann, and on basis the writers' own observations, any void or attic space *above* the inlet plane tends to cause incoming solids to

hang-up in this region. Some poorly designed inlets can have the same effect. This produces extra frictional and accelerational drag on the rotating gas and an attendant decrease in separation performance. Such behavior can also lead to more rapid erosion of the attic space and increased particle attrition given that such activity creates, in effect, as closed-circuit grinding machine for the incoming solids. See also the inlet flow "interference" discussion in Sec. 12.1.3.

Although most cyclones are constructed with flat heads, some manufacturers prefer to construct classic "helical head" or "helical roof" cyclones. Such a roof design is made by forming the head into the shape of a downwardly spiraling helical ribbon (approximately 15° pitch), starting at the point where the top plate of the rectangular inlet chute ends and ending after one complete revolution within the annular space between the vortex finder and barrel section. The design is very similar to that described in Appendix 15.B for helical inlet vane assemblies. Examples of helical roof cyclones include one of the authors' test cyclones shown in Fig. 15.1.21 and a commercial unit presented earlier in Fig. 15.1.19.

Fig. 15.1.21. Illustration of a helical-roof cyclone. Cyclone shown features one of the author's (Stein) custom built versions of a Mini CV06 cyclone designed by Bill Pentz (http://billpentz.com/woodworking/cyclone/index.cfm) and built in clear PETG plastic (similar to Lexan® but bendable) by Ed Morgano of Clear Vue Cyclones (http://www.clearvuecyclones.com)

When the gas and solids enter a helical roof cyclone, the roof forces it to assume a helical downward spiral in the barrel section of the cyclone. With

a flat roof design, (and a horizontal entry chute) the entering gas and solids mixture tends to collide with itself after making nearly one complete revolution in the upper barrel section. The resulting static pressure buildup that is thereby produced as these two streams meet forces the gas-solids mixture that has completed nearly one revolution to then assume a downwardly spiraling path. Depending on the particulars of the design, this downwardly directed flow can occur rather abruptly, especially in situations where the width of the inlet chute is as wide (or wider) than the width of the annular space between the outer surface of the vortex finder and the inner surface of the barrel.

To the writers' knowledge, no side-by-side comparative study of helical versus flat head cyclones has been published and, thus, it is difficult to state which design is "better" from a separations point of view. Commercial experience, however, clearly shows that both designs are capable of performing their intended separation duty. From a construction point of view, the flat roof design is certainly less complicated of the two; however, the latter provides considerably more mechanical support to the vortex finder and its extension above the roof. In some applications this is very desirable since vortex finders tend to be buffeted and the resulting vibration has been known to crack the welds where the vortex finders join the roof in flat head designs. The helical roof design eliminates (or lessens) the need for gussets or other such reinforcing members atop the roof.

One would have to exercise care in any side-by-side comparative study of the two roof designs to ensure that the only significant difference between the flat head and helical head designs is the roof itself. This would require that:

1. the vertical distance from the start of the helical roof to the bottom opening of the vortex finder is the same as the distance from the flat head roof to the bottom opening of the vortex finder,
2. the vertical distance from the bottom opening of the vortex finder to the bottom of the cone (i.e., the ostensible height of the inner vortex) is the same in both designs,
3. the cyclone barrel and vortex finder diameters, cone height, solids discharge opening, and inlet height and width are the same in both designs,
4. the two cyclones operate at the same: gas rate, solids type and loading, particle size distribution, humidity, etc.

15.1.8 Cyclone Operating Conditions

The inlet velocity in commercial cyclone installations is typically between 15 to 18 m/s (50 to 60 ft/s) for heavily loaded cyclones. This increases to 23 to 26 m/s (75 to 85 ft/s) for most lightly-loaded or second-stage units. Even higher velocities may be found in some tertiary installations. Even so, at inlet velocities of more than about 30 m/s, the danger of erosion, especially in the lower part of the cone, or cyclone body, rises sharply when processing abrasive solids.

Cyclones are quite 'forgiving' for changes in the inlet velocity. Depending on the particular application, they will often operate reasonably well even if the inlet velocity drops to 5 m/s. If the incoming solids are being pneumatically conveyed into the cyclone, one has to be watchful that they do not 'salt out' in the ducting upstream of the cyclone. This can lead to unstable flow and poor overall collection performance. Also, some products deteriorate if allowed to 'sit around' in the inlet ducting.

Svarovsky (1981) gives a recommended range of inlet velocities in terms of the cyclone pressure drop. Noting that experience shows cyclone separation efficiency can drop off at excessively high pressure drops (or inlet velocities), he recommends operating within the pressure drop range of 40-100 m *gas* column. This converts to an inlet velocity range of 25-40 m/s using the Shepherd and Lapple model (Eq. 4.3.18) to find the inlet velocity from the pressure drop. The corresponding values are 15–25 m/s using the Casal/Martinez-Benet model (Eq. 4.3.19). Svarovsky notes that a factor, in addition to that of separation efficiency, limiting the inlet velocity is cyclone wear. He reports cyclone wear as being proportional to the fourth power of the gas velocity. We refer to the discussion of cyclone wear in Chap. 12.

This completes our look at the design of cylinder-on-cone cyclones with tangential inlets. In the following section we discuss the design of cylindrical swirl tubes with swirl vanes. In this discussion, we concentrate on the aspects that are specific to swirl tubes. For the aspects shared between swirl tubes and tangential entry cyclones, much of the discussion above is equally valid for swirl tubes, such as the discussion pertaining to vortex finder configurations.

15.2 Design of Swirl Tubes with Swirl Vanes

The design of swirl tubes features much less prominently in the literature than cylinder-on-cone cyclones. The main design features specific to swirl tubes are the inlet vanes, the length of the swirl tube body and the configuration of the solids outlet region.

15.2.1 Design of the Inlet Vanes

Figure 15.2.1 shows a cylindrical swirl tube with swirl vanes. We will look at the effects of two aspects of vane design: the shape of the vanes—in particular the entrance and exit angles—and their thickness and number, which determines the area available for flow and, therefore, the velocity in the vane-pack. In this discussion we will often refer to the individual vane elements comprising the vane assembly as a "blade element", "vane element", or simply "blade" or "vane".

In conventional tangential inlet cyclones the swirl velocity near the wall is determined by the entrance duct velocity v_{in}, and an entrance constriction coefficient. In swirl tubes, it is mostly determined by the velocity exiting the

throat of the vane openings along with the exit angle of the vanes. We will discuss this further in Sect. 15.2.2.

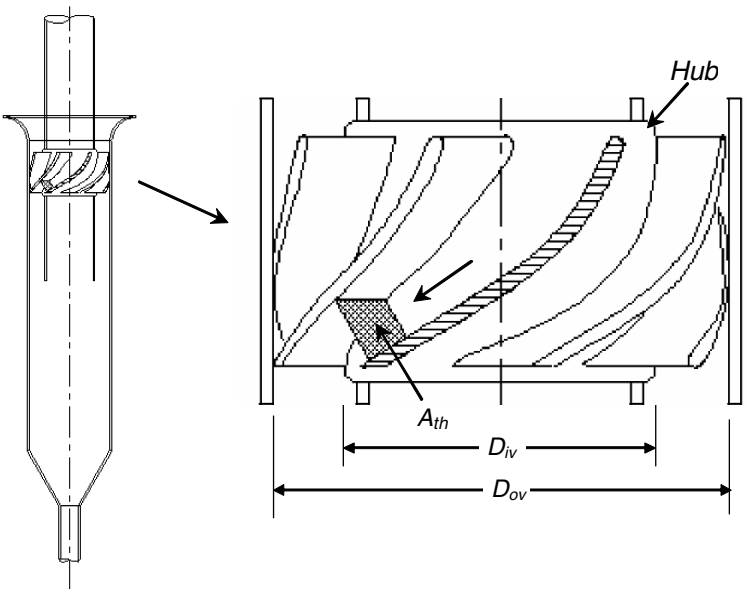

Fig. 15.2.1. A cylindrical-bodied swirl-tube type cyclone with an axi-symmetric vane-type inlet

Fig. 15.2.2 shows sketches of vane arrangements.

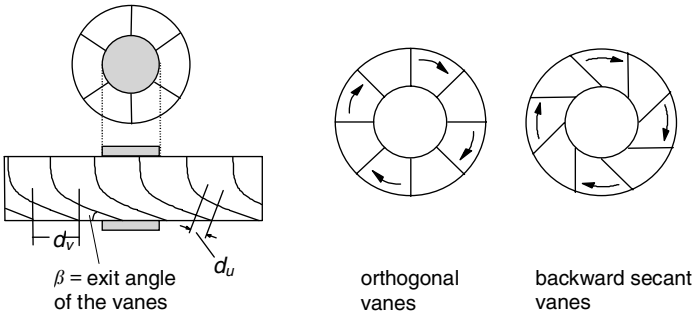

Fig. 15.2.2. Sketches of vane arrangements (Postma et al., 1998). To the left a top view of a vane pack above an 'unfolded' sideview of the pack. To the right top views of two vane arrangements. The backward secant arrangement is meant to concentrate the solids at the outer wall in the pack

For a given flowrate decreasing the exit angle β decreases the cross-sectional flow area (normal to flow) and increases the swirl intensity, the separation efficiency, and the pressure drop. If β is made too small, boundary layer separation and turbulence generation may occur within the vanepack (Nieuwstadt and Dirkzwager, 1995). Muschelknautz and Trefz (1991) recommend a β within the range 15–30°. They also recommend that the vanes are spaced so that the ratio d_u/d_v (see the figure) is about 1/4. The two lines defining the distance d_u are drawn orthogonally through the vane tip and the bent-to-straight transition point on the subsequent vane, respectively.

Only sporadic work has been done to optimise the shape of the vanes for maximal swirl generation with minimal pressure drop. Simple vanes are '2-D', which are only bent in one direction, while '3-D' vanes are also twisted so that a line drawn in the plane perpendicular to the cyclone axis along the surface of the vane will always cut the swirl tube axis.

If the vanes were infinitely thin, the exit axial and tangential velocity components could be calculated from the volumetric gas flow, the vane exit angle and its inner and outer diameters. However, the vanes are often quite thick and may occupy a non-negligible fraction of the flow area. In this case the gas exits more or less as jets from each of the rectangular or trapezoidal-shaped gaps at the bottom of the vane pack. The tangential velocity in these jets determine the tangential velocity in the swirl tube body, much as the velocity of the inlet jet determines the tangential velocity in the body of a cyclone with a tangential inlet. In the following section we give a method of estimating this exit velocity from the vane pack.

15.2.2 Calculation of Inlet 'Throat' Area For a Vane-Type Inlet Device

Figure 15.2.1 and the right-most plate of Fig. 15.2.2 shows sketches of inlet vane assemblies having eight vane elements or blades. The thickness of the vanes is comparable to the other dimensions. The space available for flow between the vanes for these particular "backward secant" geometries is of trapezoidal shape. We find that the available *horizontal* flow area (that in the plane of the page in the right-most plate of Fig. 15.2.1) remains constant in the upper part of the vane pack, but decreases as the angle β decreases when we move down the lower part of the vane pack. What we are ultimately interested in, however, is the flow area *normal to the flow direction in the exit region of the vane*, since this determines the velocity of the gas entering the body of the swirl tube.

We use the following notation: D_{ov}, D_{iv} for the outer and inner diameter of the vane assembly, respectively; D_{mid} for the geometric mean diameter of vane equals $(D_{ov}D_{iv})^{1/2}$; l for the horizontal separation between two adjacent vane elements; l' for the horizontal width of a vane element; N_v for the number of vane elements (also equals number of vane openings); t for the vane thickness; β for the vane angle relative to the horizontal; and a_v, b_v for the length and

width, respectively, of the trapezoidally shaped area normal to the direction of flow. D_{iv} is also the outside diameter (OD) of the cylindrical tube or "hub" from which the vane elements radiate.

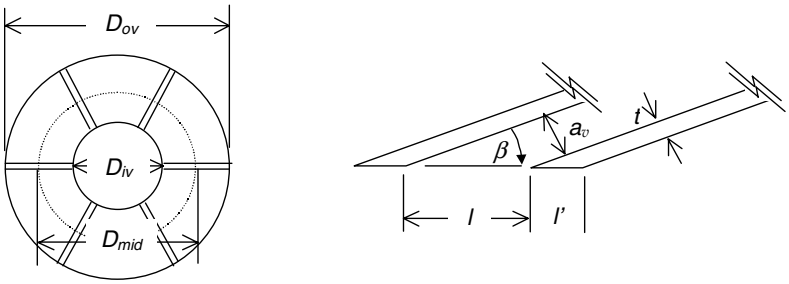

Fig. 15.2.3. Top and side view of an inlet vane assembly. The figure on the left shows characteristic vane diameters for a 6-element vane; that on the right, characteristic dimensions of the trailing-edge section of two adjacent vane elements located at mean vane diameter D_{mid}

The circumference at diameter D_{mid} is very closely approximated by the expression:

$$\pi D_{mid} = N_v \, (l + l') \tag{15.2.1}$$

so,

$$l = \frac{\pi D_{mid}}{N_v} - l' = \frac{\pi D_{mid}}{N_v} - \frac{t}{\sin\beta}. \tag{15.2.2}$$

The 'height' and 'width' of each of the N_v trapezoidally shaped flow areas normal to the flow direction is:

$$a_v = l \sin\beta = \left(\frac{\pi D_{mid}}{N_v} - \frac{t}{\sin\beta} \right) \sin\beta \tag{15.2.3}$$

$$b_v = \frac{D_{ov} - D_{iv}}{2}. \tag{15.2.4}$$

And, since $A_{th} = a_v b_v N_v$, the total vane throat area normal to the flow direction is:

$$A_{th} = N_v \left(\frac{\pi D_{mid}}{N_v} - \frac{t}{\sin\beta} \right) \left(\frac{D_{ov} - D_{iv}}{2} \right) \sin\beta, \tag{15.2.5}$$

which may also be expressed somewhat more simply as,

$$A_{th} = \frac{1}{2} (\pi D_{mid} \sin\beta - N_v t)(D_{ov} - D_{iv}) \tag{15.2.6}$$

An example calculation of the throat area and the resulting tangential velocity of the gas entering the body of the swirl tube is included in Appendix 15.A for the secant type vane illustrated in Fig. 15.2.1 or 15.2.2.

For an "orthogonal" type vane geometry of the type shown in Figs. 15.2.2, 15.B.1 and 15.B.2, the cross-sectional area of the vane passages or "pockets" normal to flow are rectangular and not trapezoidal, as was the case above. For orthogonal vanes the height of the individual flow passages remains constant with radial distance away from the hub. For this case, the formulas reported above still apply but the variable D_{iv} replaces the variable D_{mid}. The total vane throat area then becomes,

$$A_{th} = \frac{1}{2}(\pi D_{iv} \sin\beta - N_v t)(D_{ov} - D_{iv}) \text{ for orthogonal vanes.} \qquad (15.2.7)$$

Appendix 15.B presents a detailed example of how to construct the "cut-out" pattern of one of the vane elements comprising a six-bladed orthogonal vane assembly.

15.2.3 Length of the Swirl Tube Body and the Solids Exit

In cylinder-on-cone cyclones, indications are that the separation performance becomes erratic if the vortex terminates within the conical section. Our experience is that this is less so with cylindrical swirl tubes. It appears that the main effect of the vortex ending in the tube is simply to shorten the effective length of the tube.

If the body tube length is increased so that it is greater than the 'natural vortex length', the vortex end or 'tail' will 'pop' up into the tube body, and take up a position on the wall at some distance from the solids (or liquid) discharge opening. It is likely that a drop in efficiency and a rise in pressure drop will be observed at the length at which this first takes place, since the effective tube length will decrease quite considerably at this point.

A tube length of between $2D$ and $3D$ is most often recommended in the literature. Alexander's expression for the natural length of the vortex may be applied to swirl tubes if a good equivalent for the inlet area can be identified.

The solids exit is often an annular slot around the periphery of a base plate. Yaodong et al. (1991) examined three different solids exit configurations for reverse-flow swirl tubes: a) a conventional flat base plate, b) a plate with a central orifice and c) an open bottom configuration. A central orifice caused the vortex motion to extend into the dust bunker. It nevertheless had a beneficial effect on separation efficiency, stabilizing the vortex motion. The reentrained dust from the bunker was separated again in the separation space above the plate anyway. The separation efficiency was not as good without the base plate. A few comments are in order here, however: First, if underflow "blowdown" is practiced, so that the underflow openings are effectively decoupled from one another, gas is not permitted to flow back up any slot or hole in the base plate. Such blowdown is known to improve separation performance. Secondly, if multiple swirl tubes are arranged in parallel to form a multiclone, one should not include any plates or other obstacles or paraphernalia in the

bottom of the tubes that could interfere with the ever-present upflow that will occur within some of the cyclones as a result of a lack of perfect flow distribution to each of the individual swirl tubes. The more open the underflow, the more tolerate the swirl tubes will be to any flow maldistribution feeding them. The same applies to cyclones. Finally, slots or small openings in the bottom plate have been found to plug with foreign debris (such as welding rods, refractory, insulation, deposits, etc.)

As with more conventional cyclones, a vortex stabilizer may also be installed in swirl tube type cyclones. Nevertheless, for reasons given above, one has to be most careful if the swirl tube is to be installed in a multicyclone configuration. One has to ensure that the underflow configuration can handle the flow maldistribution that always accompanies multicyclone configurations. Some examples of vortex stabilizers can be found in Chap. 13, which discusses demisting cyclones.

15.A Example Calculation of the Throat Area

A swirl tube equipped with a 6-element inlet vane of 5 mm thickness is to be used to separate entrained droplets from a carrier gas. The vane will be fitted into a 150 mm ID cyclone and will have an inner diameter of 100 mm. The vanes' trailing edge will be 30° off the horizontal.

Find the vane's cross-sectional area normal to flow and the corresponding throat velocity for a gas rate of 0.20 m^3/sec. Also compute the tangential component of this velocity.

Solution

Substituting into our equations for D_{mid} and A_{th}:

$$D_{mid} = (D_{ov}D_{iv})^{\frac{1}{2}} = (150 \times 100)^{\frac{1}{2}} = 122 \text{ mm} \tag{15.A.1}$$

$$A_{th} = N_v \left(\frac{\pi D_{mid}}{N_v} - \frac{t}{\sin\beta}\right)\left(\frac{D_{ov} - D_{iv}}{2}\right)\sin\beta$$

$$= 6\left(\frac{\pi 122}{6} - \frac{5}{\sin 30°}\right)\left(\frac{150 - 100}{2}\right)\sin 30° = 4041 \text{ mm}^2 = 0.00404 \text{ m}^2 \tag{15.A.2}$$

Therefore, the velocity of the jets emerging from the vane pack is: $v_{th} = Q/A_{th} = 0.20/0.00404 = \underline{49.5 \text{ m/s}}$

The tangential component is: $v_o = v_{th}\cos\beta = 49.5\cos 30° = \underline{42.9 \text{ m/s}}$

It is this tangential component of the inlet velocity that generates the force that separates the droplets from the gas. On the other hand, it is the axial component of the inlet throat velocity that most affects the downward velocity component of the liquid spiraling down the cyclone walls.

In Fig. 15.A.1, A_{th} according to Eq. (15.2.5) has been plotted against the angle β.

The area decreases with β until it becomes zero at some positive value of β, whereby the vanes are touching each other[3]. The results for vane thickness $t = 0$ are also shown in the figure. Here, as expected, we do not reach zero area until at zero β. It is seen that at small β the fractional error in the calculated area incurred by neglecting the vane thickness becomes quite substantial.

The figure also illustrates that even if t is zero, the area for flow in the flow direction decreases with β. The mistake is often made to think that the *resultant* velocity of the gas as it emerges from a vane pack (with infinitely thin vanes) is equal to the vertical velocity with which it enters the vanes. This is not so, since, as the conservation of mass over the vane pack demands, the superficial *vertical* velocity of the gas is the same before and after the vane pack.

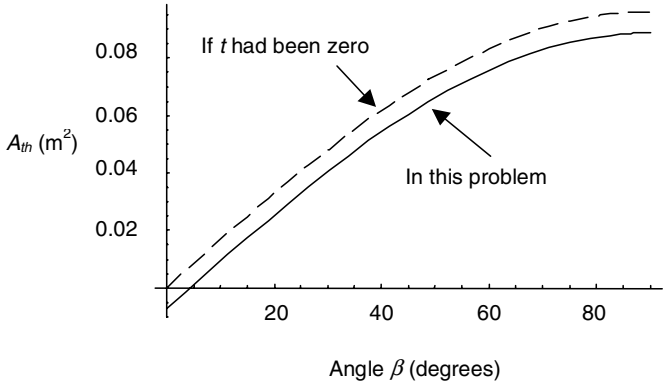

Fig. 15.A.1. A_{th} as a function of the angle β according to Eq. (15.2.5)

15.B Construction of a Vane "Cut-out" Pattern of an Orthogonal Vane Assembly

Here we shall give the procedure for constructing the 2-D "cut-out" pattern for the 6-bladed orthogonal vane assembly shown "unfolded" in Fig. 15.B.1 and in the photographs of Fig. 15.B.5. The vane assembly is to have an outside diameter of 145 mm OD vane to fit around a 72.5 mm OD cylindrical pipe "hub". We have selected a discharge angle, β, of 20°. Each vane element consists of a curved inlet section and a "straight" discharge section. The term "straight" refers to the profile of (the bottom section of) the vane when

[3] The negative values of A_{th} means that the vanes overlap.

unfolded and projected onto a 2-dimensional plane, as shown in Fig. 15.B.2. This "straight" section of the vane will form a perfect 20° helix once it is bent to conform to the circular curvature of the central hub. It follows that the shortest path between two points on the surface of the hub lies on this helix. This hold true at any radius for the purely helical section of the vane.

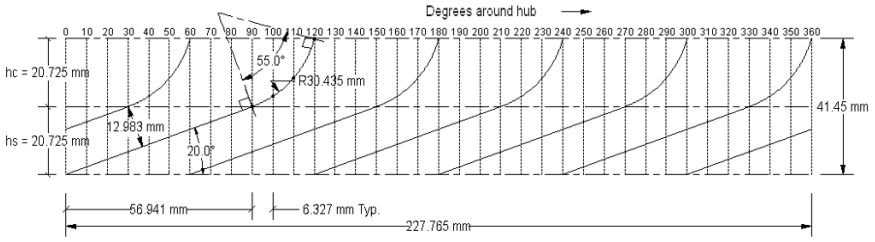

Fig. 15.B.1. Desired vane pattern surrounding central hub

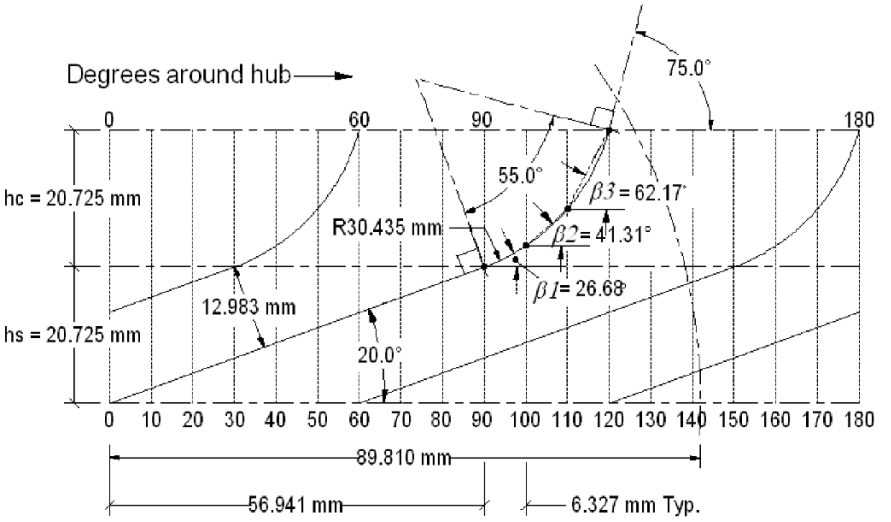

Fig. 15.B.2. Detailed view of 2-D vane pattern surrounding hub

The upper, curved section of the vane complicates the design somewhat but provides for a much smoother entrance flow transition (compared to a completely "straight" vane element). The height of the curved section was selected to be half the total vane height. The overall height of the vane depends

on the angle β, the degree of vane "overlap", and the height of the curved and straight sections. A detailed design procedure follows:

- First, we "unfold" the cylindrical hub surface to form a rectangle having an overall length of $D_{iv}\pi = 72.5\pi = 227.76$ mm. This length represents, of course, the circumference of the central hub.
- We next draw the lower ("straight") section of the six, upwards-sloping 20-degree vane sections, each spaced exactly 60° apart. See Fig. 15.B.2. We choose to allow these straight sections to overlap one another by exactly 30°. This, then, fixes the angular extent of the straight sections at 60° + 30° or 90°. It also fixes the height of the straight sections at $(90°/360°)227.765 \tan 20° = 20.725$ mm, and the perpendicular distance between the straight sections at $(60°/360°)227.765 \sin 20° = 12.983$ mm. This would also be the height of the available flow passage between adjacent vanes *if* the vanes had no thickness.
- The design of the curved section of the vane elements is a bit more complicated. Designing it so that its inner and outer edges match the ID of the hub and cylindrical housing can be an arduous task at first. We will present one method to accomplish this task, although the reader may devise other methods.
  We recall that this section of the vane is to be of the same height as the straight section (20.725 mm). Thus, our rectangular pattern shown in Figs. 15.B.1 and 15.B.2 has a total height of 41.45 mm. We also wish for the curved sections to extend 30° around the hub, so that the total angular extent of each *complete* blade element is 90° + 30° or 120°. Thus, each complete vane element will overlap an adjacent element by 60°.
- We construct the leading, curved section of the vane by drawing a simple circular arc starting at, and tangent to, the top end of the straight section of a given vane element, and ending 20.725 mm above this point at an angle of 75° relative to the horizontal. See Fig. 15.B.2. We want to point out that 75° is somewhat arbitrary, and is up to the designer, but it typically lies between 70° and 90°. The center or focus of this arc is the point of intersection between a line drawn perpendicular to the top end of the *straight* section of the vane and another line drawn perpendicular to the 75°-line where the latter crosses the 120° division on the rectangular pattern. The radius of the thus-drawn arc turns out to be 60.871 mm, and the arc is found to subtend an angle of 55.0°, as shown.
- The above work should provide us with a good grasp of how the vanes will look in elevation view. It clearly illustrates the leading and trailing angles that will dictate the gas flow path. It also defines the overall height of the vanes along with their "overlap" and spacing.
  With this, we are now in a position to create the "cut-out" pattern for each vane in plan view. The "straight" or bottom half of the cutout pattern is very similar to what engineers sometimes design and attach to tall smokestacks to reduce flow-induced vibration at high wind loadings. The

pattern is cut from its two-dimensional plane and bent around the cylindrical surface of the stack to form the desired helical-shaped ribbon. Instead of a "stack", we will bend our helix around a cylindrical hub.

- The cut-out pattern for each vane or blade will consist of four segments: a bottom, 20° sloping section and three straight line segments – each 10° in circumferential measure, that approximate the curvature of the upper half of the vane, as shown in Fig. 15.B.2. Thus, for pattern construction purposes, the upper curved section will be treated as though it is comprised of three "straight" vane segments having β angles of 26.68°, 41.31°, and 62.17°, as shown. This, then, is the key to the design of the upper curved segment. Each of the four segments comprising the vane will therefore form *its own helix* about the central hub. Below, we shall use the β*'s* to compute the inside radius of the corresponding four segments of the *cut-out pattern*, R_{ivp}.
- For a helix, R_{ivp} is the reciprocal of its *radius of curvature*, κ, which is known (Rieger and van Vliet, 2002) to be a function of R_{iv} and the height of the segment, h_s,

$$\kappa \equiv \frac{1}{R_{ivp}} = \frac{R_{iv}}{R_{iv}^2 + h_s^2}. \tag{15.B.1}$$

Although h_s is shown in Fig. 15.B.2 to be the height of the bottom half of a complete vane element, it is also taken, herein, to be the variable representing the height of *each* of the three *curved* vane segments above it.

From simple geometric considerations, Eq. (15.B.1) can also be expressed in a form that is somewhat more relevant to our purposes,

$$R_{ivp} = R_{iv}\left(1 + \tan^2\beta\right). \tag{15.B.2}$$

Using the above equation with $R_{iv} = D_{iv}/2 = 36.25$ mm, we compute R_{ivp} for our four β values. The results are presented in Table 15.B.1.

Table 15.B.1. R_{ivp} as a function of β for the four vane segments shown in Fig. 15.B.2

β, degrees	R_{ivp}, mm
20	41.05
26.68	45.40
41.31	64.25
62.17	166.32

- Now, the circumferential pattern length of each of these four segments must be identical to the "unfolded" straight-line segments shown in Fig. 15.B.2. Knowing these, we can compute their angular extent. Hence, for the (bottom) 20° vane segment, its circumferential length is:

$$\frac{20.725 \text{ mm}}{\sin 20^\circ} = 60.60 \text{ mm} \tag{15.B.3}$$

and its angular extent is,

$$\frac{60.60 \text{ mm} \cdot 360^\circ}{2\pi \cdot 41.05 \text{ mm}} = 84.58^\circ. \tag{15.B.4}$$

Repeating the above procedure for the other entries in Table 15.B.1, we obtain the circumferential lengths and corresponding angular extents shown in Fig. 15.B.3 Here we note, for example, that the bottom vane segment occupies a circular arc of 84.58° and has an inside radius of 41.05mm when laid-out on a flat 2-D surface. Attached to this is the first curved segment, which is seen to extend over 7.98°, and has a radius of 45.40 mm. Similar arcs and radii are shown for the two remaining segments comprising the upwardly curved section of the vane. We may note that, in this pattern view, the outer radius of the "straight" or 20° vane segment must equal R_{ivp} plus the width of the vane, or $41.05 + 36.25 = 77.30$ mm. (A similar relation holds for the remaining three segments.) We also observe that the steepest (leading) vane segment has the greatest radius. In the limit, if this leading vane element were to be vertical, it would become a straight line with an infinite radius and a zero radius of curvature.

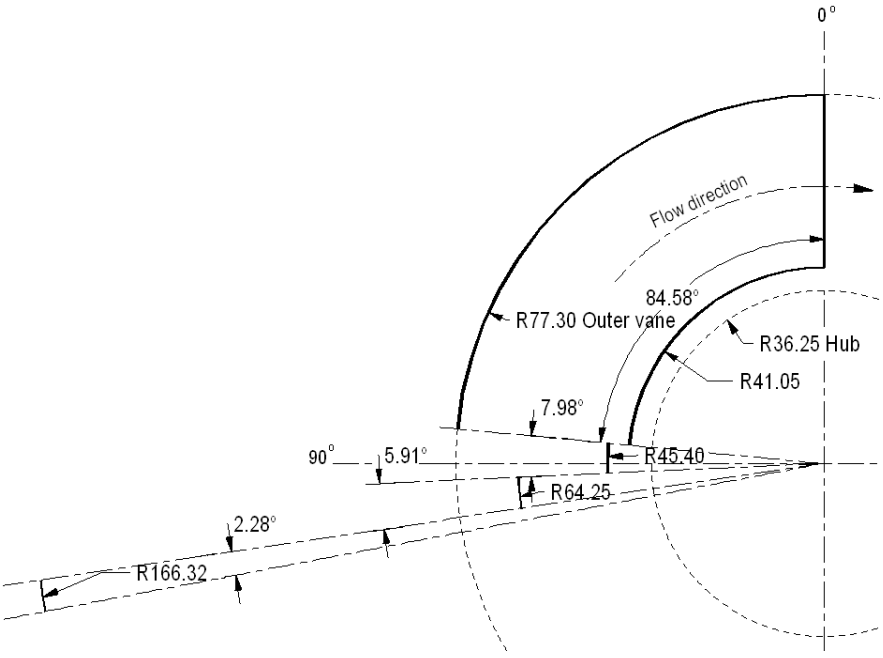

Fig. 15.B.3. Initial construction of 2-D vane pattern surrounding hub

- Although the above work completes the 2-D pattern for the bottom "straight" half of the vane element, we must now complete the upper curved section. We do this by first joining each curved segment to the end of the prior segment. For example, the segment having a 45.40 mm radius is joined to the end of the preceding 41.05 mm radius segment. The same procedure is applied to the remaining two segments in order to complete the inside curvature of the complete vane element. Once this step is complete, the inside curvature will appear as shown in Fig. 15.B.4.

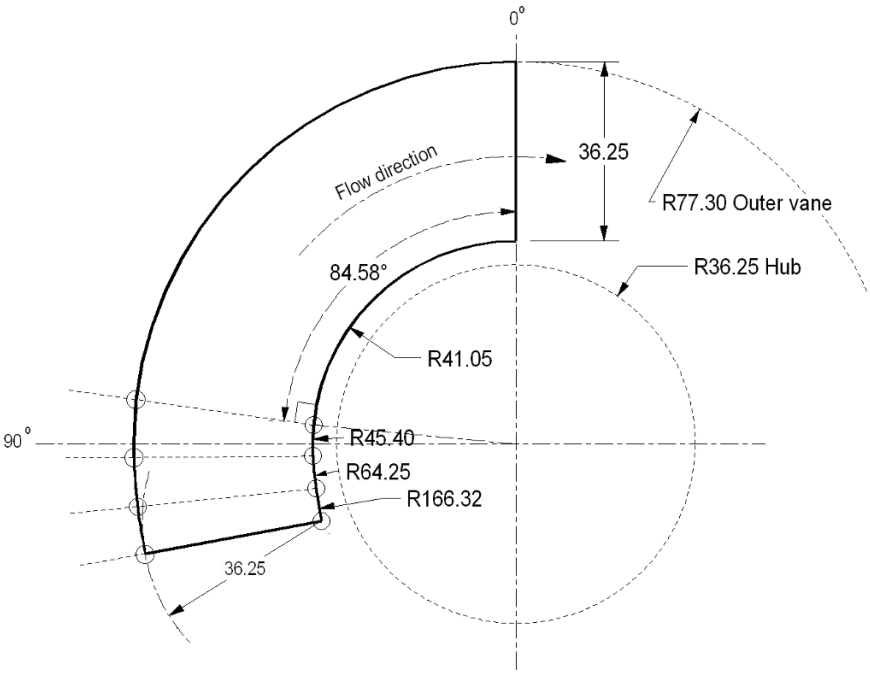

Fig. 15.B.4. Final construction of 2-D vane pattern surrounding hub

- To complete the vane construction pattern, we draw outward radiating lines from the end of each inner segment perpendicular to the end of the segment. These are shown as dashed lines on the left-hand-side of Fig. 15.B.4. The small circles on the heavy inner curve are their starting points. We next draw radial arcs of length 36.25mm from each of these inner circles. Where these arcs intersect the dashed radials defines the *outer edge* of the leading curved section of the vane element.
- To construct the physical vane assembly, we first must transfer the pattern shown in Fig. 15.B.1 onto the central hub. Next, we transfer the vane pattern shown in Fig. 15.B.4 (six in this example) onto a flat sheet of suitable metal or plastic, cut-out the flat vane elements, and wrap them

around the hub—conforming to the pattern marked on the hub. Only the leading, curved section of each vane has to be bent into a curved shape. The "straight", 20° vane segments need only be affixed to the hub at a 20° angle.

Some pointers on vane construction that may prove helpful:

- Before finalizing the design, one may wish to construct a prototype or model from stiff card stock, plastic, or thin aluminum sheet metal. One such model is shown in Fig. 15.B.5. This model was constructed from 0.2 mm thick card stock using the technique and dimensions reported above. Such a model will assist us in evaluating the final fit-up. It may tell us, for example, if there are any distortions due to bending of the leading curved section of the vanes.
- The leading curved section may be divided into as many segments as one desires. In our example, three were used but, for larger vane assemblies, this may be increased to six or more. The more segments used in the design of the curved section of the vane, the closer the ID of the vane will conform to the OD of the hub, and the closer the OD of the vane will conform to the ID of the cylindrical housing that encloses the vane assembly.
- Thick vanes can be difficult to bend and fabricate into a final vane assembly. Vanes should be kept as thin as is practical consistent with their intended service. The reduction in flow area coupled with competing considerations of corrosion, erosion and intended service life are the main factors affecting choice of vane thickness. Most vanes in commercial service will have a thickness of 2 to 10mm. If the vanes are cast, and erosion is a concern, the vane thickness may be intentionally increased in some areas to better withstand erosive attack.
- Except for very thin vanes, the leading edge of each vane element should be radiused to reduce turbulence.

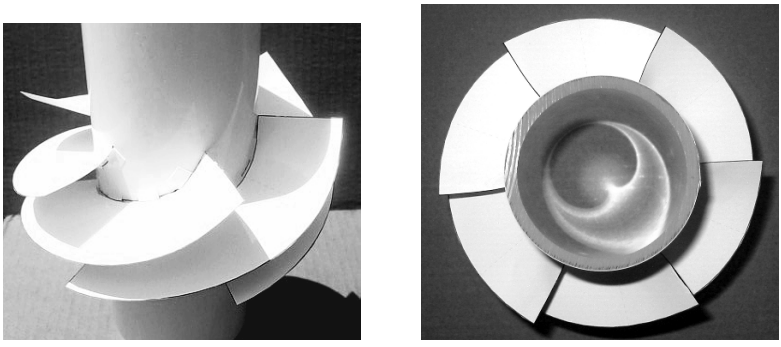

Fig. 15.B.5. A model six-bladed, 20° vane constructed per method and dimensions described in text. Design and photo by L. E. Stein

16

Multicyclone Arrangements

In this chapter we wish to briefly discuss two types of multi-unit arrangements used in cyclone and swirl tube installations in industry. We also give some guidelines for the choice of arrangement in a given application including a worked example given in Appendix 16A. In addition, we briefly describe how to apply the modeling equations outlined in previous chapters to multicyclone arrangements.

There are many situations wherein one cyclone or swirl tube is inadequate for the separation task at hand. In such situations, it is often feasible to use multiple units either in *series* or in *parallel* or both.

16.1 Cyclones in Series

When the solids concentration is high, and the emission from just one separator stage would be too high, a second – or even a third – separator can be added in series with the first stage separator to collect additional solids. Such an arrangement is sketched in Fig. 16.1.1. It is customary to refer to the individual stages as the 'primary', 'secondary', and 'tertiary' stages or as the 'first', 'second', and 'third' stage. In some industries, the primary cyclone is also called a 'rough-cut' cyclone despite the fact that its overall efficiency (mainly arising from high inlet mass loading) will normally greatly exceed the efficiency of subsequent stages.

As seen in the figure, the overflow from the first cyclone (stage I) is charged to the second one (stage II) and so on. Cyclones working in series can be modeled using the same equations as for a single cyclone. To predict the separation efficiency of stage II or stage III, it is necessary to know the concentration and the size distribution of the feed solids, which is the concentration and size distribution in the overflow from the cyclone stage immediately preceding it. In addition, any significant decrease in pressure or change in temperature across a prior stage requires a recomputation of the gas flow rate, viscosity and density reporting to the following stage. If any additional 'outside' streams are

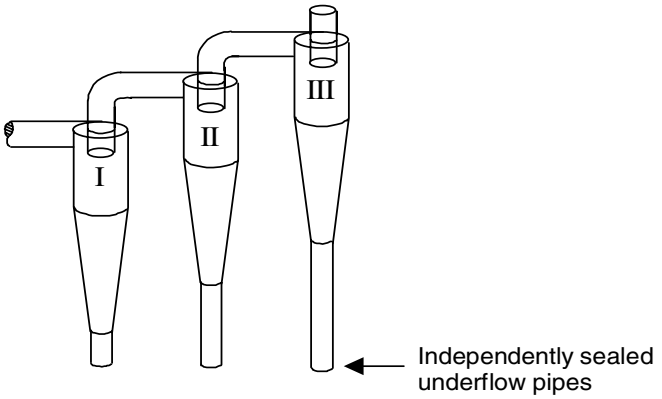

Fig. 16.1.1. Cyclones working in series

introduced into stage II or stage III, the gas and solids stream properties will have to be recomputed accordingly.

The size distribution of the overflow solids from stage I can be found by solving Eq. (3.2.6) for $f_e(x)$:

$$f_e\,(x) = [1 - \eta\,(x)]\,\frac{f_f\,(x)}{(1-\eta)}. \tag{16.1.1}$$

However, with a series arrangement, there will almost always be a 'mass loading' effect in the first stage or primary cyclone. In fact, the main purpose of installing a primary cyclone in the first place is to separate out the bulk of the solids in the carrier gas stream. We saw in Chap. 9 that the mass loading effect significantly influences the shape of the grade-efficiency curve, $\eta(x)$. The question arises: how can this be accounted for when calculating the feed to the secondary cyclone? The answer lies in the fact, that, since the extra material separated in the inlet due to the mass loading effect is more or less unclassified, mass loading does not significantly affect the size distribution of the overhead material from the primary cyclone (Fig. 9.1.2). Accordingly, as a first approximation we can ignore the effect of solids loading when using Eq. (16.1.1) to calculate the overhead size distribution from the primary cyclone. The dust loading to the secondary cyclone will normally be much less than that to the primary cyclone—often less than 1%.

An example showing how to calculate the efficiency of two cyclone stages in series is included in Appendix 16.A.

16.2 Cyclones in Parallel

There are two common reasons for choosing to install more than one cyclone or swirl tube in parallel. One is that one device handling the whole gas stream

would become too large for practical purposes. The other is that the cut size obtained with one large cyclone or swirl tube would be too large to achieve the required separation efficiency. This latter consideration can be understood as follows.

Consider Eq. (5.2.1):

$$x_{50} = \sqrt{\frac{v_{rCS} 9 \mu D_x}{\rho_p v_{\theta CS}^2}}.$$

If geometrically similar cyclones or swirl tubes of different sizes are operated at the same inlet velocity, v_{rCS} and $v_{\theta CS}$ will also be similar. The equation therefore shows that the cut size is roughly proportional to the square root of the vortex finder diameter. Thus, in geometrically similar cyclones, the cut size will be proportional to the square root of the characteristic cyclone dimension, say D. Incidentally, since $v_{\theta CS}$ and v_{rCS} are proportional to the inlet and outlet velocities, it can be also observed from inspection of Equation (5.2.1) that the cut size for geometrically similar cyclones is inversely proportional to the square root of any characteristic velocity such as the gas superficial inlet or outlet velocity.

Additionally, Eqs. (4.3.18) and (4.3.19) indicate that the Euler number and, therefore, the pressure drop, are independent of the cyclone size for geometrically similar cyclones or swirl tubes if the inlet velocity is kept constant. We can thus gain in efficiency without increasing pressure drop by splitting up the solid-laden process stream over two or more cyclones or swirl tubes and operating them in parallel.

When designing parallel cyclones, the overriding concern is that the gas and solids be distributed evenly between the various units. One way of achieving this is to design and arrange the cyclones or swirl tubes in such a manner that each individual unit experiences the same total pressure (dynamic and static) and that the gas exiting each gas outlet pipe experiences the same flow resistance. These two criteria normally can be met by rendering both the inlet and overflow piping as symmetrical as possible. Since it is often impractical to design perfectly symmetrical overflow piping or ducting, the piping should be large enough so that its resistance is negligible compared to the pressure drop across the cyclones, even if the piping is not identical (in length or number of bends, for example).

Under high solids or liquid loading, special attention also must be directed towards achieving uniform solids or liquid distribution. At some point in the upstream piping the incoming gas/solids mixture will usually encounter a bend which will tend to segregate the incoming solids to its outer wall. This can lead to solids maldistribution in the inlet piping and, in turn, hopper 'crossflow' as discussed in Chap. 11. For this reason, bends should be located well ahead of any parallel bank of cyclones – preferably 10 pipe diameters or its equivalent.

Parallel arrangements of cyclones come in a wide variety of configurations. Their inlet distributor geometry is normally comprised of either:

1. a segmented section of rectangular ducting, such as that shown in top portion of Fig. 16.2.1, or
2. a common casing or chamber into which the inlet gas-solids enters prior to dividing and flowing to the individual cyclones. Examples are shown in Figs. 16.2.2 and 16.2.3. Cyclones whose feed consists of gas-solids entrainment off a fluidized bed also fall into this category.

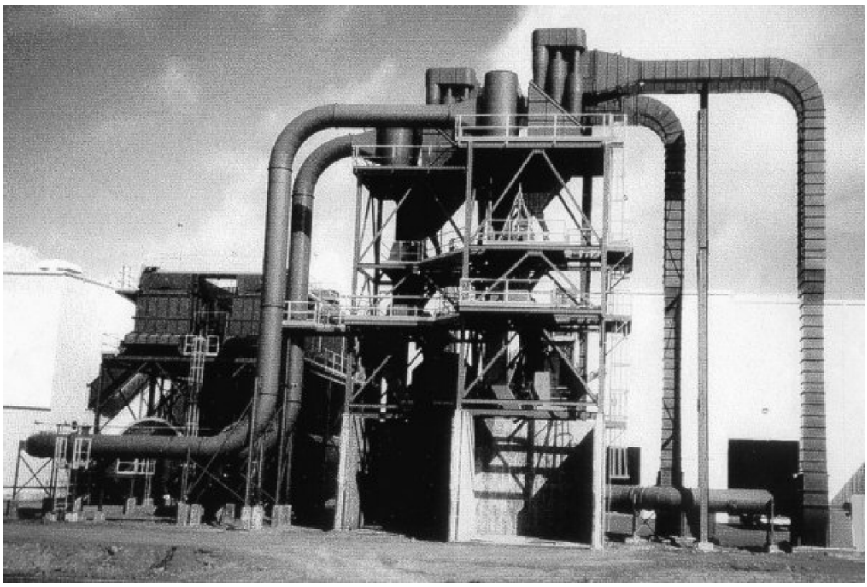

Fig. 16.2.1. A series and parallel arrangement of cyclones in a USA particleboard clean-up facility. Courtesy of Polutrol-Europe

One commercially available system comprising a parallel arrangement of cyclones, called 'swirl tubes', is the multicyclone unit illustrated in Fig. 16.2.2. The solids-bearing feed stream enters the separator vessel via a centrally located pipe at the top of the vessel. The feed exits this inlet pipe near its bottom end from where it flows radially outwards – between two tube sheets - and into the feed chamber or plenum. The solids-bearing gas then enters the individual 'swirl tubes' wherein it is split into a solids-laden underflow stream and a 'clean-gas' overflow stream.

Figure 16.2.3 shows another commercial multicyclone featuring closely spaced individual 'swirl tubes' arranged on a tube sheet but fed from one side of the tube array.

The three installations shown in Figs. 16.2.2 and 16.2.3 illustrate only a few of many possible multicyclone arrangements. Each equipment designer

or manufacturer has his own preferred design geometry or geometries and experiences regarding cyclone design, tube layout, plenum design and manner of addressing the flow distribution issue. The various arrays offered by the equipment manufactures differ mostly in their inlet arrangements and the geometry of the cyclone layout.

A true 'multicyclone' is not only a parallel arrangement of cyclones, but also one wherein the individual cyclones are housed within a common casing that constitutes the inlet chamber. Furthermore, the dust (or liquid) discharge and the gas outlet pipes also report to their own common outlet plenum and hopper, respectively. Multicyclone systems of the type shown in Figs. 16.2.2 and 16.2.3 are usually comprised of numerous small diameter cyclones (typically under 250 mm in diameter) and this normally leads to excellent separation performance relative to fewer, larger units handling the same total volumetric flow.

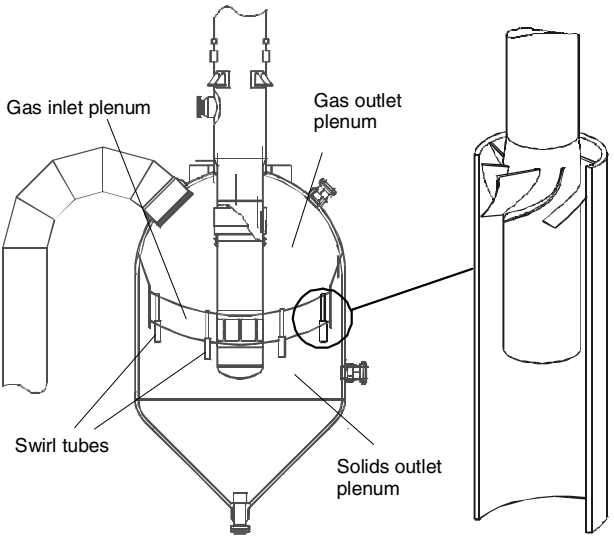

Fig. 16.2.2. Shell third-stage separator with swirl tubes working in parallel. Courtesy Shell Global Solutions International

Another way of arranging cyclones in parallel is shown in Figs. 16.2.4 and 16.2.5. Unlike multicyclones, these cyclones are not enclosed inside a separate housing, are not arranged on a common tube-sheet, are external, and are usually larger than the cyclones comprising a multicyclone installation. They still, however, take their feed from a common inlet duct and their overflow pipes and solids discharge openings report to common collection chambers.

Some inlet headers or distributors are in-line; others are circular. The circular arrangement usually provides the most uniform flow distribution but

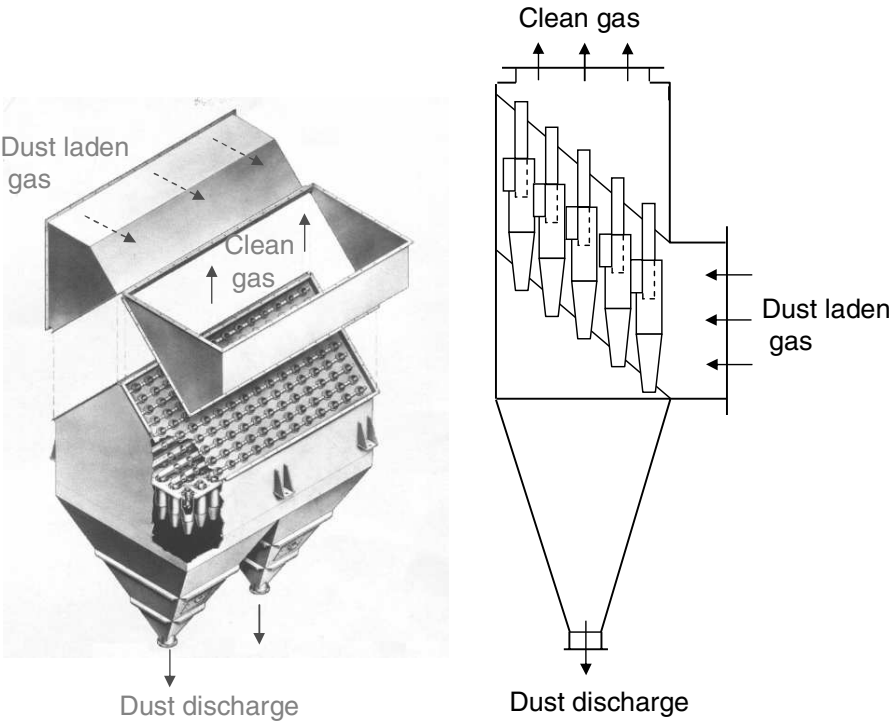

Fig. 16.2.3. Left: a 'Cyclo-Trell' Multicyclone unit featuring a closely packed arrangement of parallel swirl tube type cyclones. Courtesy Hamon Research Cottrell. Right: Simplified view of a multicyclone showing upper and lower tubesheets

their inlet and gas outlet designs tend to be more complex than in-line configurations. An example of a circular inlet layout is shown in Fig. 16.2.6.

A simplified vessel plan view of two parallel sets of three-stage cyclones is presented in Fig. 16.2.7. Such parallel and series arrangements are very commonly found in fluid bed processing units including catalytic cracking units (FCCU), acrylnitrile (ACN), wood and sludge burning, and similar fluid bed processing units. Figure 16.2.8 is a photograph of 10 parallel cyclones for service in a fluid-bed application. Here we note that the cyclones are attached to and suspended off the underside of the vessel head. Clearly visible are the vertical standpipes or 'diplegs' that return the collected catalyst back to the fluidized bed. Figure 16.2.9 presents a rather remarkable view of a large, newly constructed, two-stage cyclone system being lifted by a huge crane. Such designs are rather typical of those found in the regenerator vessel of a FCCU unit. This picture illustrates many important and interesting features including primary cyclone inlet horns and scrolls, diplegs with 'flapper' valves at their bottom openings, and three levels of interbracing. Such bracing is utilized for improved lateral stability of the entire cyclone system. The reader

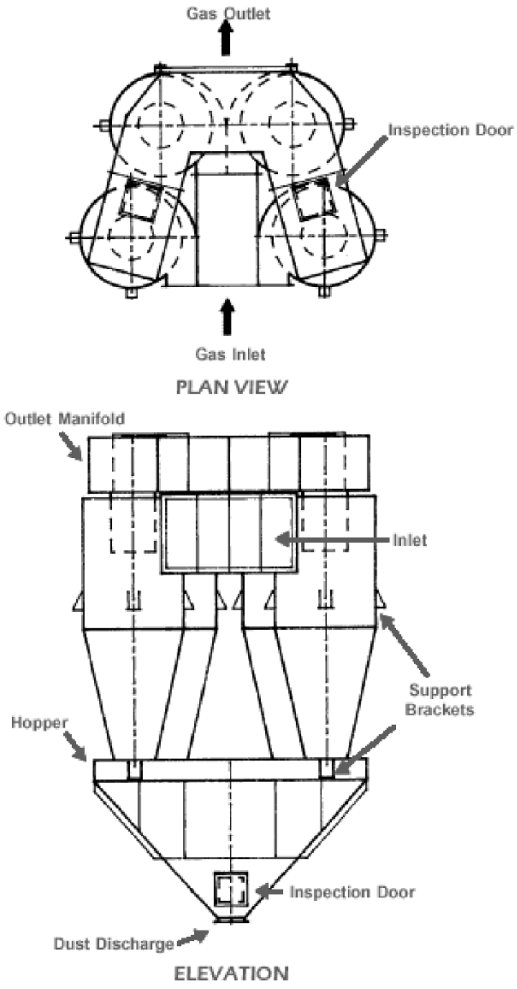

Fig. 16.2.4. Plan and elevation views of a parallel arrangement of four cyclones sharing a common inlet duct, dust hopper, and clean gas outlet plenum. Courtesy Emtrol LLC

may also discern that two of the first-stage diplegs are slanted off true vertical. This is a fairly common feature of such systems and is a design technique used to prevent interference between the discharge end of one or more diplegs and some other vessel component, such as a 'spent cat distributor'. The extent to which diplegs may be slanted and still avoid flow problems depends on the application. However, as a general guide, their angular departure from true vertical should not exceed about 15°.

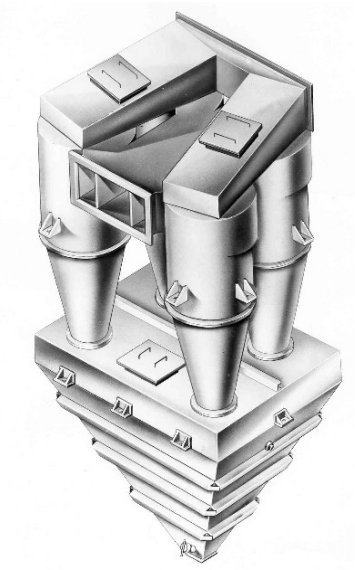

Fig. 16.2.5. A parallel arrangement of four cyclones sharing a common inlet duct and a common overhead and underflow plemum. Courtesy Ducon Technologies Inc.

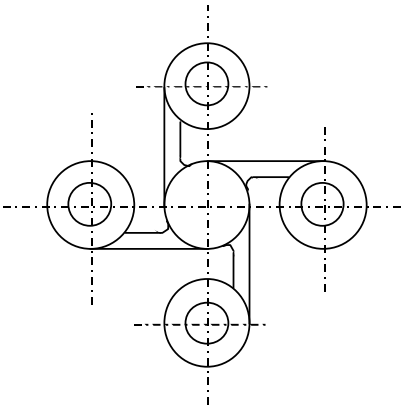

Fig. 16.2.6. Plan view of four cyclones with a circular inlet distributor

Returning now to the much smaller sized cyclones comprising most multicyclone installations, one of their advantages over an external array of parallel cyclones is that the individual cyclones do not have to be equipped with their own individual inlet pipes or ducts. A disadvantage is that, because the individual cyclones are fully enclosed, it is not normally possible to perform diagnostic or repair work on the *individual* cyclones while they are in service. On the other hand, it is sometimes possible to repair or 'patch up' an

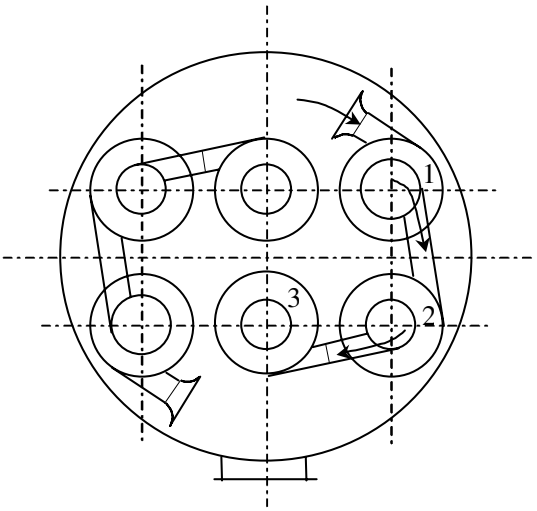

Fig. 16.2.7. Vessel plan arrangement view of two parallel sets of three-stage cyclones

external cyclone that may be eroding or to unplug it with blasting jets, if necessary, while on-stream. In short, external cyclones are more accessible. Cyclones comprising a multicyclone installation are usually replaced when they become worn, whereas most other cyclones (such as those illustrated in the figures below), are usually repaired, often in-place.

Because of their small size, some multicyclone installations experience operational problems as a result of plugging of their inlet ducts, bodies, or exit pipes. This can happen when dust agglomerates due to the presence of moisture, particularly when the temperature falls below the gas dew point. Plugging of cyclone bodies can occur if the hopper plugs and the dust level is allowed to rise to the level of the cyclones.

Pressure taps should be installed on multicyclone installations as an aid in determining how well they are performing. If the pressure drop across the system is less than their design value then there is a good chance that the dust collection efficiency will be lower than it should be. There are several reasons why the pressure drop across a multicyclone can be lower than expected: First, the gas flow through the unit may be less than that for which it was designed. In this case, if the lower flow is expected to be the normal operating value then a portion of cyclones can be blocked off (in some symmetrical manner). Second, there may be holes in the upper tube sheet or in the collectors themselves that allow the dust laden gas to bypass the collectors. Thirdly, the inner walls of the individual cyclones may have become coated with deposits. Such deposits tend to increase the effective wall roughness which, in turn, decreases the spin, causing the pressure drop to decrease. The latter is especially true If the pressure drop is observed to be slowly decreasing over time (and which cannot be explained on the basis of some change in operating conditions). The

presence of holes in the tube sheet or cyclone bodies, or deposit formations, can normally be verified only by inspection.

Fig. 16.2.8. A parallel set of 10 first-stage cyclones attached to the underside of the vessel head. Courtesy Fisher-Klosterman Inc.

Parallel arrangements of cyclones can be modelled using the same model equations as for single units. The solids-bearing gas stream is simply divided evenly between the parallel-working units. However, units working in parallel will generally under-perform single, isolated units due to the problems associated with nonuniform gas (and sometimes, solids) distribution, as discussed in Chaps. 11 and 15.

There is no good way of estimating the difference in performance between a single unit and the same unit working in parallel with others. Some workers claim that this difference is significant. Our own experience is that units working in parallel can perform almost as well as single units *if* uniform gas and solids distribution is achieved in the inlet manifolding. One must be especially attentive of the inlet manifolding in configurations where the cyclones' underflow openings are free to communicate with one another. And, as indicated back in Fig. 16.1.1, under no conditions should series-connected cyclones dis-

charge their solids into a common solids receiving vessel or hopper without proper isolation of their underflow pipes.

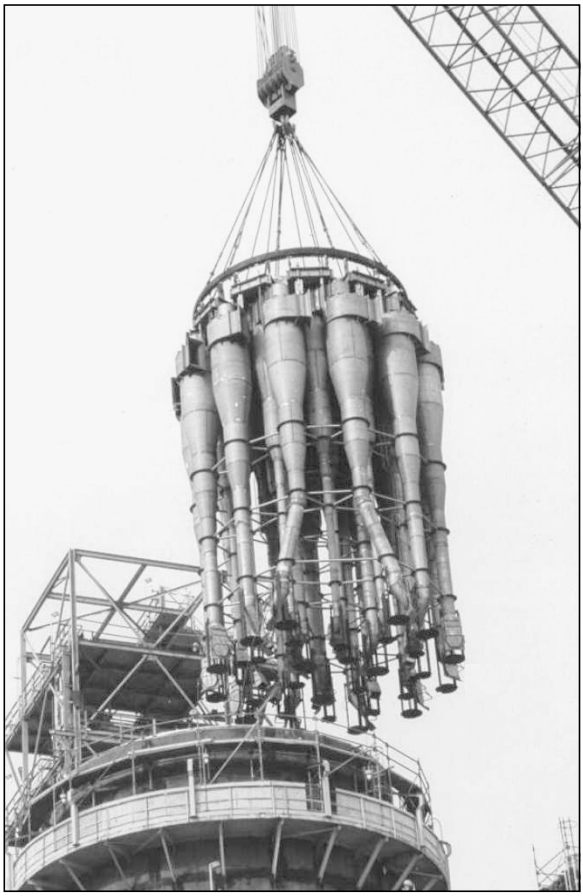

Fig. 16.2.9. A large 2-stage cyclone system typical of that used to collect catalyst entrained off of the fluidized bed of a fluid catalytic cracking unit (FCCU). Courtesy Emtrol LLC

16.A Example Calculation for Multicyclone Arrangements

Let us assume that the separation of the large cyclone in Appendix 5.A is insufficient to meet emission standards. Specifically the loss from that cyclone

of[1] 300 mg/Nm^3 has become unacceptable as we are faced with a new 70 mg/Nm^3 limit on emissions.

At the initial stage in the decision process, and before any measurements are made, we wish to estimate on paper whether this target can be achieved using cyclone technology, and if it can, what sort of cyclone arrangement must be installed downstream of the large cyclone.

Solution

The *first* step is to estimate the cut size needed to achieve the target emission. The required overall efficiency for the new cyclone stage is:

$$\eta_{req} = \frac{(300 - 70)}{300} = 0.77.$$

If we know the size distribution of the solids lost from the large, first-stage cyclone we can determine the approximate cut size needed to achieve this. The strategy is as follows:

- Use the data from Appendix 5.A: the feed solids properties, the overall efficiency, the grade-efficiency curve and Eq. (16.1.1) to calculate the differential size distribution of the overflow fraction from the first-stage cyclone.
- Convert this differential size distribution to a cumulative one
- Use the method illustrated in Fig. 3.2.2 on this size distribution to convert η_{req} for the new cyclone installation to a required cut size.

Let us use the simple model of Barth for this first calculation. If we find that cyclones are a feasible option, we can use more sophisticated calculation models, or scale experimental results for model cyclones later.

In Appendix 5.A we computed the first-stage cyclone's cut size (6 μm), overall efficiency (90 %) and grade-efficiency curve by the method of Barth. As we have mentioned elsewhere, the experience of these authors is that most commercial cyclones separate with a somewhat shallower cut (lower exponent than 6.4), but for this calculation, we use the Barth grade-efficiency curve.

We arrive at $f_e(x)$ by inserting the log-normal distribution (Eq. 2.B.6) with $\ln \langle x \rangle = 3.32$ and $\sigma = 1.2$ for $f_f(x)$, Eq. (5.2.2) with 6 μm for x_{50} for $\eta(x)$, and 0.9 for η in Eq. (16.1.1).

Actually, it is possible to obtain an analytical expression for $f_e(x)$ in this particular case, but in most cases we need to split the x-axis up in a series of intervals, Δx_i, and then read or calculate values at the interval midpoints: $f_f(x_i)$ and $\eta(x_i)$, and calculate points on the overhead size distribution: $f_e(x_i)$ by Eq. (16.1.1).

[1] mg/Nm^3 = a milligram solids per normal cubic meter of gas. A normal cubic meter is a cubic meter under conditions of normal temperature and pressure: 0°C and 1.013 bar.

The second step is to convert this differential size distribution to a cumulative one. This is straightforward. We use Eq. (2.3.3) or its finite equivalent:

$$F\left(x_i + \frac{1}{2}\Delta x_i\right) = \sum_{j=1}^{i} f\left(x_j\right)\Delta x_j$$

The resulting cumulative size distribution of the overhead solids from the large cyclone is shown in Fig. 16.A.1; the points on the distribution calculated by the above procedure are connected with lines in the figure.

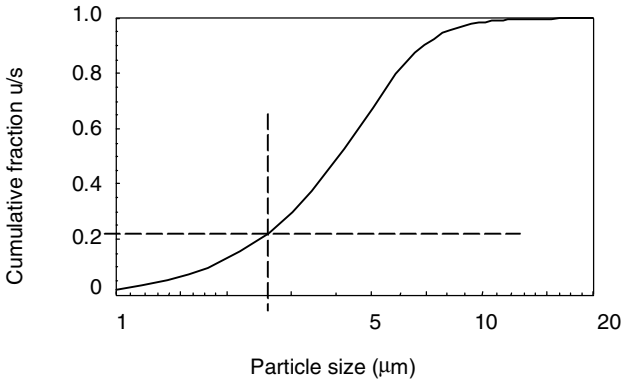

Fig. 16.A.1. Size distribution of the overhead solids from the large cyclone

Finally we use this size distribution to convert the required overall efficiency of 0.77 to a required cut size, using the method illustrated by Fig. 3.2.2. This process is shown in Fig. 16.A.1, and the required cut size can be seen to be approximately 2.6 μm.

In regards to the cyclone's cut size, we again utilize Eq. (5.2.1):

$$x_{50} = \sqrt{\frac{v_{rCS} 9\mu D_x}{\rho_p v_{\theta CS}^2}},$$

which, as mentioned, shows that the cyclone cut size x_{50} is proportional to the square root of the diameter of the vortex finder, D_x. For a fixed cyclone geometry, therefore, the cut size is proportional to the characteristic cyclone dimension, which we shall take to be the body diameter, D. Thus, the smaller the cyclone, the smaller the cut diameter, so the more cyclones we split the total flow over, the smaller will be the cut size of the installation.

Knowing the required cut size, the *second* step is to determine what sort of cyclone installation would be required to achieve this. The strategy is now:

- Choose a standard cyclone geometry from Table 15.1.1

- Calculate the cut size as a function of the cyclone size
- Choose the cyclone size giving the required cut size
- Calculate the number of cyclones in parallel required to accomodate the total flow

We choose a standard cyclone geometry from Table 15.1.1. The choice can be indicated by considerations specific to the plant in question. In this example, we shall select the Lapple geometry, and a somewhat conservative inlet velocity of 20 m/s.

To use Eq. (5.2.1), we need to calculate the velocities v_{rCS} and $v_{\theta CS}$ from Eqs. (4.2.4)–(4.2.6), following the procedure outlined in Appendix 5A. In doing this, we note that the velocities we calculate are only functions of *dimensional ratios*[2]. In other words, for a constant inlet velocity the internal velocities we calculate are independent of the scale of the cyclone.

Upon substituting the operational, physical and geometrical data in (4.5)-(4.7), along with values for v_{rCS} and $v_{\theta CS}$ and D_x with (141/283) D (see Table 15.1.1) in (5.2.1), we obtain the desired expression for the cut size. This cut size is observed to be a function of the cyclone diameter. Thus, for the Lapple cyclone with an inlet velocity of 20 m/s we find:

$$x_{50} = 3.75 \times 10^{-6}\sqrt{D}. \tag{16.A.1}$$

By repeating this exact same procedure for the first-stage cyclone we obtain the result:

$$x_{50} = 3.00 \times 10^{-6}\sqrt{D}, \tag{16.A.2}$$

which, for a 4 m diameter cyclone, gives a cut size of 6 μm. This is consistent with our result in Chap. 5. The Lapple geometry is relatively longer than the first-stage cyclone, which makes it more efficient, but the lower inlet velocity and the relatively larger vortex finder makes for a larger cut size for a given D.

From (16.A.1) we find that the value of D required to obtain a cut size of 2.6 μm is 0.48 m. Moreover, using the data in Table 15.1.1, the inlet height and width of such a cyclone are 0.24 m and 0.12 m, respectively.

With an inlet velocity of 20 m/s, the volumetric flow rate to each cyclone becomes $0.24 \times 0.12 \times 20 = 0.576$ m^3/s. The total flow is $(0.34\times4) \times (0.24\times4) \times 30 = 39.2$ m^3/s, so we need $39.2/0.576 = 68$ cyclones in parallel to accommodate the total flow.

This is a lot of cyclones and would very likely be deemed impractical from a cost point of view (including the cost of plot space!), not to mention the problems one would encounter in trying to design a system this size and still provide uniform flow to each cyclone.

In a case like this, we would try to reduce the number of second-stage cyclones by increasing their inlet velocity and seeing if the resulting pressure loss is still acceptable. Increasing the inlet velocity allows us to increase the

[2] To see this more clearly substitute $v_{in}ab$ for Q in Eq. (4.2.6).

size of the second-stage cyclones (higher inlet velocity – smaller cut size) and this, in turn, increases their gas handling capacity. Thus, fewer cyclones are required to handle the flow. The price for this is an increase in pressure drop. Table 16.A.1 shows four possibilities in addition to our 68-unit, 20 m/s case.

Table 16.A.1. Four different inlet velocities to the second stage cyclones

v_{in} [m/s]	Cyclone diameter [m]	N_o cyclones	Pressure drop [Pa]
20	0.48	68	1934
25	0.60	35	3021
30	0.72	20	4351
35	0.84	13	5922
40	0.96	8	7735

Obviously, if pressure drops on the order of 6 to 8 kPa are acceptable from a process point of view, an 8 or 13-unit multicyclone (or some number in between) could prove to be a viable option for the task at hand. If not, other types of separation equipment may have to be considered such as a baghouse, an electrostatic precipitator, or a wet scrubber. Nevertheless, even if the pressure drop across the cyclones were acceptable, one would still need to consider the long-term wear implications associated with operating the cyclones at velocities in the range of 35 to 40 m/s. If the solids being processed are not especially abrasive and/or if they are sufficiently fine in size, it may be possible to operate at these velocities. If not, erosion-protective liners may need to be installed. Some bare-metal multicyclone systems have been observed to operate for many years at velocities of 70 to 85 m/s while processing several tons per day of rather abrasive sand-like particles that were under about 25 μm in size.

Multicyclone installations which must exhibit a relatively low cut size (such as that shown in the example above) are not normally suitable in processes that can tolerate only a very limited amount of pressure drop across the separator, such as 100 mm of water column, or less. If this is not a constraint, however, the fact that they operate dry and with no moving parts endows them with some distinct advantages over other separator types, such as wet scrubbers or bag houses. This is especially true if selling or using the product in dry form is advantageous to operations or if, for personnel protection or from a maintenance point of view, one does not wish to handle and maintain bag filters.

17

List of Symbols

A	Cross-sectional area	m^2
A	a constant in the Mothes and Löffler model	
A_R	total inside surface area of the cylone	m^2
A_W	inside area of the cyclone inlet region (MM)	m^2
A_1,A_2,A_3	constants in Cunningham corr'n equation	
$\mathbf{a}$	acceleration vector; components: a_i; size: a	m s^{-2}
a	height of the cyclone inlet or of vane open area	m
a	area	m^2
B	buoyancy force	N
B	a constant in the Mothes and Löffler model	
b	width of the cyclone inlet or of vane open area	m
C,C_1,C_2	constants	varies
C	a constant in the Mothes and Löffler model	
C_c	Cunningham correction factor	
C_D	drag coefficient	
Cy_{50}	characteristic cyclone number of Rietema	
c	solids loading of inlet gas	g m^{-3}
c_o	mass fraction of dust in the incoming gas	
c_{ok}	mass fraction of liquid in the incoming gas	
c_{oL}	limiting loading (as mass fraction) in the MM	
c_V	volume concentration of particles	
c_0–c_4	vol. concn. of particles of size x (Mothes-Löffler)	
D	diameter	m
D	a constant in the Mothes and Löffler model	
$\mathcal{D}$	particle diffusivity (Mothes-Löffler)	m^2 s^{-1}
d	distance	m
d_v, d_u	dimensions for the design of vane packs	m
Eu	Euler number, $\Delta p/(1/2\rho v^2)$	
e	rate of erosion	kg $m^{-2}s^{-1}$
F, F'	cumulative undersize distribution function	
$\mathbf{F}$	force vector; components F_i; absolute value F	N

Fr	Froude number, gD/v^2	
f	friction factor	
f	frequency	s^{1-}
$f(\cdot)$	differential density distribution function	m^{-1}
G	friction factor in Stairmand equation $= f/2$	
g	gravitational acceleration (abs. value g)	m s^{-2}
H	height, total height of cyclone, submergence	m
H_i	height of the inner vortex	m
$H_{cyl}*$	dimensionless height in the M-L model	
h	height	m
I, I_o	transmitted, incident light intensity	W m^{-2}
I	electrical current	A
j	volume flux of particles	m s^{-1}
K	constant in Barth's pressure drop model	
K	constant $(= Eu)$	
K_1	constant in the Mothes and Löffler model	
k	parameter in the Rosin-Rammler distribution	m^{-n}
k	turbulent kinetic energy per unit mass	J kg^{-1}
k	exponent in empirical relations for	c_{oL}
k_s	absolute wall roughness	m
L	diameter of a cylindrically shaped particle	m
L_n	natural vortex length	m
l	length	m
l'	horizontal thickness of vane	m
M	mass of solids	kg
M	mass flow of solids	kg s^{-1}
MF	mass fraction	
MW	gas molecular weight	kg $kgmol^{-1}$
m	exponent in GEC or PSD curve expressions	
m	mass	kg
N	number	
K	constant in Barth's pressure drop model	
n	exponent in tangential velocity model	
P	perimeter	m
p	pressure	Pa
q	term in Stairmand's pressure drop model	
Q	volumetric flow rate	m^3 s^{-1}
R	$D/2$	m
R	gas constant	J K^{-1} $kgmol^{-1}$
R_{cx}	ratio of vortex core to vortex finder radii	
Re	Reynolds number, $(\rho v D)/\mu$	
Re_R	'cyclone body Reynolds number' (MM)	
R_o, R_{dc}	radii in disc centrifuge	m
r	radial coordinate	m
S	length of vortex finder within cyclone	m

S	source term	varies
S_{AA}	velocity ratio of Abrahamsen and Allen	
Stk	Stokes number, $(\Delta\rho x^2 v)/(18\mu D)$	
s	height, width	m
s	estimate of standard deviation	varies
T	run time *or* time-to-failure	s
T	temperature	°C
t	time	s
t	thickness	m
t	vortex tube penetration in Fig. 15.1.13	m
$\mathbf{U}'$	particle velocity rel. to gas; components U'	m s^{-1}
$\mathbf{U}$	particle velocity; components: U	m s^{-1}
V	volume	m^3
V	superficial gas velocity	m s^{-1}
V	electrical voltage	V
$\mathbf{v}$	gas velocity; abs. value v; components: v_i	m s^{-1}
v_{in}, v_x	mean gas velocity in inlet and vortex finder	m s^{-1}
$v_{\theta w}*$	wall velocity just after inlet (M-L model)	m s^{-1}
W	weight	N
We	Weber number, $(\rho v^2 D)/\sigma$	
w	width	m
x	particle diameter	m
$\langle x\rangle_{Sa}$	'Sauter mean' particle diameter	m
x_{fact}	empirical correction factor	
y	an independent observation	
y	distance from side wall	m
z	axial coordinate	m

Greek and other:

α,β,β',γ	proportionality constants	varies
α	entrance constriction coefficient	
β	angle	
β	ratio of velocities in the M-L model	
$\Delta\cdot$	difference in	
δr	'offset' distance for scroll design	m
ε	angle between conical wall and cyclone axis	
ε	turbulent energy dissipation rate per unit mass	J $kg^{-1}s^{-1}$
Γ	Gamma function	
φ	conserved quantity	varies
γ	specific weight (density relative to water)	
η	overall fractional separation efficiency	
$\eta(\cdot)$	grade-efficiency	

λ	mean free path	m
μ	viscosity	kg m^{-1} s^{-1}
θ	tangential coordinate	
ρ	density (without subscript: gas density)	kg m^{-3}
ϕ	Coulomb potential of an electrical field	C m^{-1}
σ	standard deviation, or spread	varies
σ	surface tension	N m^{-1}
τ	particle relaxation time	s
τ	turbidity	
$\boldsymbol{\tau}$	shear stress tensor with components τ_{ij}	Pa
ξ	$= b/R$	
Ω	angular velocity	s^{-1}
ψ	Wadell's sphericity	
∇	del operator	m^{-1}
$\langle\cdot\rangle$	mean	
$\|\cdot\|$	absolute value	

Subscripts:

1,2	indicating spatial points or solids loadings
2	in the cyclone inlet region
50	cut size
25,75	reference to 0.25, 0.75 fractional efficiency, respectively
A	resultant at position A
a	annular
air	in a clean (air only) cyclone
acc	due to acceleration into the cyclone inlet
B	back or resultant at position B
b	bed
b	bulk
$body$	in the cyclone body
c	captured (or underflow) fraction
c	cone, conical wall
c	vortex core
ch	characteristic
$comm$	commercial
cyc	cyclone
cyl	cylindrical wall
CS	in the surface CS
D	drag
d	dust outlet
d	dipleg solids
$dust$	due to the dust
e	overflow (or emitted or lost) fraction

e	external
eq	equivalent
F	front
f	feed
$fact$	factor
fin	final
fp	flapper plate
i	index *or* internal
in	inlet
ini	initial
l	liquid
lid	top surface
N	number
m, mid	geometric mean
m	model
med	median
o	start or reference or gas-only
of	overflow
ov, iv, mid	pertaining to vane pack geometry
p	particle or precessional
pr	primary
r	radial
rCS	radial gas velocity component in the surface CS
req	required
S	stagnation
s	secondary
s	spiral
s	submerged
sc	scroll
sv	surface-to-volume
$sepspace$	in the separation space
sl	due to solids loading
Stk	when Stokes' law applies
str	of a strand of solids
t	tube
t	terminal velocity
th	throat
tot	total
uf	underflow
V	volume
v	vessel
v, u	pertaining to vane pack geometry
vol	volume
vt	vortex tube
w	wall

wet	wetted
x	gas exit tube or vortex finder
z	axial
θ	tangential
θ	CS tangential velocity component in the surface CS

Superscripts

$^\circ$	angular or temperature degrees
*	dimensionless parameters

List of Tradenames

- Mathematica—Wolfram Research, Inc.
- MathGV—Greg VanMullem
- MATLAB—The MathWorks, Inc.
- Mathcad—MathSoft Engineering & Education, Inc.
- FLUENT—Fluent Inc.
- TEEPOL—Royal Dutch/Shell Group
- Trickle Valve—Ducon Technologies Inc.
- Calgon—Calgon Corporation
- Hexmetal, Flexmetal, Hexmesh—Causeway Steel Products, Ltd.
- CoorsTek—CoorsTek Incorporated
- Porta-Test Revolution—Natco, Canada
- G-Sep—Kvaerner Group
- Cyclo-Trell—Hamon Research-Cottrell
- Teflon—DuPont
- Lexan—GEC

References

Abrahamsen J and Allen R W K 1986 *IChemE Symp Ser* **99**, 31–43.

AIChE 1978 'Drop sizes in annular gas-liquid flows'.

Alexander R M 1949 *Proceedings Aus. I.M.M.* **152–153**, 203–228.

Allen T 1987 *Powder Technol.* **50**, 193–200.

Allen T 1990 *Particle size measurement* 4 edn Chapman and Hall London.

Austrheim T 2005 Experimental characterization of high-pressure natural gas scrubbers PhD thesis University of Bergen Dept. of Physics and Technology.

Barth W 1956 *Brennstoff-Wärme-Kraft* **8, Heft 1**, 1–9. (in German).

Baskakov A P, Dolgov V N and Goldovin Y M 1990 *Exp. Therm. Fluid Sci.* **3**, 597–602.

Binnie A M and Hooking G A 1948 *Proceedings of the Royal Society, series A* pp. 194–398.

Bird R B, Stewart W E and Lightfoot E N 2002 *Transport phenomena* 2 edn John Wiley & Sons New York.

Blevins R D 1984 *Applied fluid dynamics handbook* Van Nostrand Reinhold Company New York.

Boysan F, Swithenbank J and Ayers W H 1986 *in* Cheremisinof, ed., 'Encyclopedia of Fluid Mechanics' Vol. 4 Gulf Publ. Co., Book Division Houston pp. 1307–1329.

Briggs L W 1946 *Trans. Am. Inst. Chem. Eng.* **42**, 511–526.

Browne J M and Strauss W 1978 *Atmos. Env.* **12**, 1213–1221.

Bürkholz A 1989 *Droplet Separation* VCH Publishers Weinheim.

Butcher T 2001 Cracow clean fossil fuels and energy efficiency program, formal report Technical Report BNL-52632 Office of Fossil Energy, US Department of Energy.

Büttner H 1999 *J. Aerosol Sci.* **30**, 1291–1302.

Casal J and Martinez-Benet J M 1983 *Chemical Engineering* **Jan. issue**, 99–100.

Chen S and Doolen D 1998 *Annu. Rev. Fluid Mech.* **30**, 329–364.

Clift R, Ghadiri M and Hoffmann A C 1991 *AIChE Journal* **37**, 285–289.

Clift R, Grace J R and Weber M E 2005 *Bubbles, Drops and Particles* Dover Publications.
Davies C N 1945 *Proc. Phys. Soc.* **57**, 259.
Dehne M F 2006 'Private communication'.
Derksen J J 2003 *AIChE Journal* **49**, 1359–1371.
Derksen J J 2005 *Computers & Fluids* **34**, 301–318.
Derksen J J, Sundaresan S and van den Akker H E A 2006 *Powder Technology* **163**, 59–68.
Devon M J, Provder T and Rudin A 1991 *in* T Provder, ed., 'Particle Size Distribution II, ACS Symposium Series' ACS Washington DC.
Dietz P W 1981 *AIChE Journal* **27**, 888–892.
Dirgo J and Leith D 1985 *Filtration and Separation* **March/April issue**, 119–125.
Dry R J, White R W and Joyce T 1993 *in* '4th Int. CFB Conference, preprint volume' pp. 732–737.
Escudier M P, Bornstein J and Zehnder N 2005 *J. Fluid Mech* **98**, 84–95.
Faler J H and Leibovich S 1977 *Physics of Fluids* **20**, 1385–1400.
Fraser D 1951 *J. Bacteriology* **61**, 115–119.
Friedlander S K 1977 *Smoke, dust and haze* John Wiley & Sons New York.
Funk P A 2005 'Private communication to L. E. Stein'.
Funk P and Hughs S 2000 *in* 'Proceedings of the ASAE Annual International Meeting' number ASAE004026.
Gil A, Cortés C, Romeo L M and Vellila J 2002 *Powder Technol.* **128**, 78–91.
Gil A, Romeo L M and Cortés C 2001 *Powder Technol.* **117**, 207–220.
Gil A, Romeo L M and Cortés C 2002 *Chem. Eng. Technol.* **25**, 407–415.
Greif V 1997 *Fortschr.-Ber. VDI* **Reihe 3 Nr. 470**. (in German).
Hangal S and Willeke K 1990 *Environ. Sci. Technol.* **24**, 688–691.
Heumann W L 1991 *Chemical Engineering* **98**, 118–120.
Hinze J O 1975 *Turbulence* McGraw-Hill New York.
Hoekstra A J 2000 Gas Flow Field and Collection Efficiency of Cyclone Separators PhD thesis Delft University of Technology.
Hoffmann A C, Arends H and Sie H 1991 *Filtration and Separation* **28**, 188–193.
Hoffmann A C, de Groot M and Hospers A 1996 *Can. J. Chem. Eng.* **74**, 464–470.
Hoffmann A C, Groot M, Peng W, Dries H W A and Kater J J 2001 *AIChE Journal* **47**, 2452–2460.
Hoffmann A C, Peng W, Dries H, Regelink M and Foo K 2005 *Energy & Fuels* **20**, 1691–1697.
Hoffmann A C, Peng W and Postma R 2001 Experimental results.
Hoffmann A C, van Santen A, Allen R W K and Clift R 1992 *Powder Technol.* **70**, 83–91.
Idelchik I E 1986 *Handbook of hydraulic resistance* Hemisphere Publishing Corp New York.

Ignatowitz E 1994 *Chemietecknik* Vollmer GmbH & Co. Haan-Gruiten. (in German).

Iozia D L and Leith D 1989 *Aerosol Sci. and Technol.* **10**, 491–500.

Ishii M and Grolmes M A 1975 *AIChE Journal* **21**, 308–318.

Karpov S V and Saburov E N 1998 *Theoretical Foundations of Chemical Engineering* **32**, 7–12.

Kaye B H 1995 *Chaos, Solitons & Fractals* **6**, 245–253.

Kotwal R and Tabakoff W 1981 *Journal of Engineering for Power* **103**, 265–270.

Kreyszig E 1970 *Introductory mathematical statistics; principles and methods* John Wiley & Sons New York.

Leith D and Licht W 1972 *AIChE Symp. Ser.* **68, No 126**, 196–206.

Lewellen W S 1971 *A review of confined vortex flows* NASA CR-1772.

Liang-Biao Q and Aziz K 1996 *in* 'Proceedings of the SPE Western Regional Meeting' Anchorage, Alaska.

Licht W 1980 *Air pollution control engineering* Marcel Dekker Inc. New York.

Lidén G and Gudmundsson A 1997 *J. Aerosol Sci.* **28**, 853–874.

MacLean J P, Brown J D, Hoy H D and Cantwell J E 1978 'Uk patent application gb 2011285a'.

Mansour A R 1990 *Chem. Eng. Comm.* **89**, 49–53.

Meier H F and Mori M 1998 *Computers Chem. Eng.* **22 suppl**, S641–S644.

Meissner P and Löffler F 1978 *Chemie-Ing.-Techn.* **50**, 471. (in German).

Mills D 1977 The erosion of pipe bends by pneumatically conveyed suspensions of sand PhD thesis Thames Polytechnic.

Mills E D and Mason J S 1979 *J. of Powder & Bulk solids Technology* **3**, 13–20.

Mohan R S and Shoham O 2002 Design and development of gas-liquid cylindrical cyclone compact separators for three-phase flow Semi-annual technical progress report University of Tulsa.

Mothes H and Löffler F 1984 *Staub-Reinhalt Luft.* **44**, 9–14. (in German).

Mothes H and Löffler F 1985 *Ger. Chem. Eng.* **8**, 223–233.

Mothes H and Löffler F 1988 *Int. Chem. Eng.* **28**, 231–240.

Muschelknautz E 1972 *Chemie-Ing.-Techn.* **44**, 63–71. (in German).

Muschelknautz E 1980 *VDI-Berichte.* **363**, 49–60. (in German).

Muschelknautz E and Brunner K 1967 *Chem.-Ing.-Techn.* **39, nr.9**, 531–538. (in German).

Muschelknautz E and Dahl H D 1994 *Chem.-Ing.-Techn.* **66, No 2**, 223–229. (in German).

Muschelknautz E and Krambrock W 1970 *Chem.-Ing.-Techn.* **42, nr. 5**, 247–255. (in German).

Muschelknautz E and Trefz M 1990 *in* 'Proceedings of Second World Congress on Particle Technology' Kyoto, Japan pp. 52–71.

Muschelknautz E and Trefz M 1991 *VDI-Wärmeatlas.* **6 Auflage**, Lj1–Lj9. (in German).

Ng S Y, Priestman G H and Allen R W K 2006 *Chem. Eng. Res. & Des.* **84**, 884–894.

Nieuwstadt F T M and Dirkzwager M 1995 *Ind. Eng. Chem. Res.* **34**, 3344–3404.

Obermair S and Staudinger G 2001 *in* 'Proceedings PARTEC, 2001 International Congress for Particle Technology' Nürnberg, Germany.

Olszewski A and Strauss W 1978 *Atmos. Env.* **12**, 1559.

Overcamp T J and Mantha S V 1998 *Environmental Progress* **17 No 2**, 77–79.

Overcamp T J and Scarlett S E 1993 *Aerosol Sci. and Technol.* **19**, 362–370.

Patankar S V 1980 *Numerical heat transfer and fluid flow* Hemisphere Publishing Corp New York.

Peng W, Hoffmann A C, Boot P, Udding A, Dries H W A, Ekker A and Kater J J 2002 *Powder Technol.* **127**, 212–222.

Peng W, Hoffmann A C, Dries H W A, Regelink M A and Stein L E 2005 *Chem. Eng. Sci.* **60**, 6919–6928.

Peng W, Hoffmann A C, Dries H W A, Regelink M and Foo K K 2005 *Meas. Sci. Technol.* **16**, 2405–2414.

Perry R H 1997 *Perrys chemical engineers handbook* 7 edn McGraw-Hill New York.

Phyfe N M 1999 'Cfd modeling of cyclone separators'. Fluent Users Group Meeting.

Postma R, Hoffmann A C, Dries H W A and Williams C P 1998 *in* 'Proceedings of the World Conference on Particle Technology 3' Brighton, UK.

Prasad R O S and Bakker A 1999 'Cyclone modeling using les'. Fluent Users Group Meeting.

Rieger B and van Vliet L J 2002 *Image Processing, IEEE Transactions* **11**, 738–745.

Rietema K 1959 *De Ingenieur* **71 jaargang No. 39**, ch59–ch65. (in Dutch).

Rosin P, Rammler E and Intelmann W 1932 *Zeit. Ver. Deutscher Ing.* **76**, 433. (in German).

Sarpkaya T 1995 *Phys. Fluids* **7**, 2301–2303.

Schmidt P 1993 *Int. Chem. Eng.* **33 No 1**, 8–17.

Shepherd C B and Lapple C E 1939 *Ind. & Eng. Chem.* **31**, 972–984.

Shepherd C B and Lapple C E 1940 *Ind. & Eng. Chem.* **32**, 1246–1248.

Slack M D, Prasad R O, Bakker A and Boysan F 2000 *Trans IChemE* **78, Part A**, 1098–1104.

Slattery J C 1999 *Advanced transport phenomena* Cambridge University Press New York.

Smith,S Jr. J L 1962 *Journal of Basic Engineering, Trans. of the ASME* **Dec issue**, 609–618.

Stairmand C J 1949 *Engineering* **October issue**, 409–412.

Storch O and Pojar K 1970 *Staub-Reinhalt. Luft* **30 No 12**, 5–12.

Svarovsky L 1981 *in* J. C Williams and T Allen, eds, 'Handbook of powder technology' Elsevier Scientific Publishing Company New York.

Svarovsky L 1984 *Hydrocyclones* Holt, Rinehart and Winston East Sussex.

Swamee P K and Jain A K 1976 *Hydr. Engng. Div. ASCE* **102**, 657–664.

Ter Linden A J 1953 *Trans. of the ASME* **April Issue**, 433–440.

Trefz M 1992 *Forschritt-Berichte VDI* **295**. (in German).
UKAEA 1980 'Aere paper r9634'.
van Rossum J J 1959 *Chem. Eng. Sci.* **11**, 35–52.
Versteeg H K and Malalasekra W 1996 *An introduction to computational fluid dynamics: the finite volume method* Prentice Hall New Jersey.
Wang J, JH J H B and Dries H 2000 *Powder Technol.* **112**, 221–228.
Weisstein E W 1999 *The CRC concise encyclopedia of mathematics* Chapman and Hall London.
White C M 1940 *Proc. R. Soc. London, Ser. A* **174**, 322–338.
Wicks M 1971 *in* I Zandi, ed., 'Advances in solid-liquid flow in pipes and its application' Pergamon Press New York.
Wolf-Gladrow D A 2000 *Lattice-Gas Cellular Automata and Lattice Boltzmann Models: An Introduction* 1 edn Springer Verlag Berlin, Heidelberg, New York.
Yaodong W, Youhai J, Zhongli J and Mingxian S 1991 *in* 'Proceeding of INTERPEC CHINA '91'.
Zenz F A 2001 *Chemical Engineering* **108**, 60–64.
Zhao T S and Liao Q 2002 *International Journal of Heat and Mass Transfer* **45**, 2829–2842.
Zhongli J, Xiaolin W and mingxian S 1991 *in* 'Proceedings of Filtech Europa 91' Vol. 2 Karlsruhe, Germany pp. 583–589.

Index